AD-A278 075
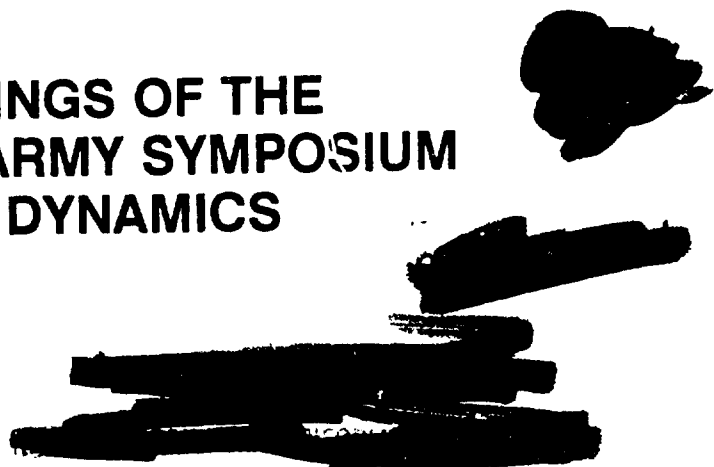
AD

ARCCB-SP-93034

PROCEEDINGS OF THE SEVENTH U.S. ARMY SYMPOSIUM ON GUN DYNAMICS

NEWPORT, RHODE ISLAND

11-13 MAY 1993

DTIC
ELECTE
APR 15 1994
S B D

THOMAS E. SIMKINS, EDITOR

US ARMY ARMAMENT RESEARCH, DEVELOPMENT AND ENGINEERING CENTER
CLOSE COMBAT ARMAMENTS CENTER
BENÉT LABORATORIES
WATERVLIET, N.Y. 12189-4050

BENÉT LABS

APPROVED FOR PUBLIC RELEASE; DISTRIBUTION UNLIMITED

94-11375

DTIC QUALITY INSPECTED 3

DISCLAIMER

The findings in this report are not to be construed as an official Department of the Army position unless so designated by other authorized documents.

The use of trade name(s) and/or manufacturer(s) does not constitute an official indorsement or approval.

DESTRUCTION NOTICE

For classified documents, follow the procedures in DoD 5200.22-M, Industrial Security Manual, Section II-19 or DoD 5200.1-R, Information Security Program Regulation, Chapter IX.

For unclassified, limited documents, destroy by any method that will prevent disclosure of contents or reconstruction of the document.

For unclassified, unlimited documents, destroy when the report is no longer needed. Do not return it to the originator.

REPORT DOCUMENTATION PAGE

Public reporting burden for this collection of information is estimated to average 1 hour per response, including the time for reviewing instructions, searching existing data sources, gathering and maintaining the data needed, and completing and reviewing the collection of information. Send comments regarding this burden estimate or any other aspect of this collection of information, including suggestions for reducing this burden, to Washington Headquarters Services, Directorate for Information Operations and Reports, 1215 Jefferson Davis Highway, Suite 1204, Arlington, VA 22202-4302, and to the Office of Management and Budget, Paperwork Reduction Project (0704-0188), Washington, DC 20503

1. AGENCY USE ONLY (Leave blank)	2. REPORT DATE	3. REPORT TYPE AND DATES COVERED
	September 1993	Final

4. TITLE AND SUBTITLE	5. FUNDING NUMBERS
PROCEEDINGS OF THE SEVENTH U.S. ARMY SYMPOSIUM ON GUN DYNAMICS	N/A

6. AUTHOR(S)

Thomas E. Simkins, Editor

7. PERFORMING ORGANIZATION NAME(S) AND ADDRESS(ES)	8. PERFORMING ORGANIZATION REPORT NUMBER
U.S. Army ARDEC Benét Laboratories, SMCAR-CCB-TL Watervliet, NY 12189-4050	ARCCB-SP-93034

9. SPONSORING/MONITORING AGENCY NAME(S) AND ADDRESS(ES)	10. SPONSORING/MONITORING AGENCY REPORT NUMBER
U.S. Army ARDEC Close Combat Armaments Center Picatinny Arsenal, NJ 07806-5000	

11. SUPPLEMENTARY NOTES

Presented at the Seventh U.S. Army Symposium on Gun Dynamics, Newport, Rhode Island, 11-13 May 1993.
This symposium was sponsored by the U.S. Army Research Office, the U.S. Army Armament Research, Development, and Engineering Center, and the U.S. Army Research Laboratory.

12a. DISTRIBUTION/AVAILABILITY STATEMENT	12b. DISTRIBUTION CODE
Approved for public release: distribution unlimited	

13. ABSTRACT (Maximum 200 words)

This publication represents a compilation of technical papers concerning analyses, design, measurement, and automation of gun dynamics. The authors represent a cross section of the scientific and technical community, including universities, industrial, and government research laboratories.

14. SUBJECT TERMS		15. NUMBER OF PAGES
Ballistics, Barrel Vibration, Dynamics, Precision, Controls, Target Acquisition, Accuracy		558
		16. PRICE CODE

17. SECURITY CLASSIFICATION OF REPORT	18. SECURITY CLASSIFICATION OF THIS PAGE	19. SECURITY CLASSIFICATION OF ABSTRACT	20. LIMITATION OF ABSTRACT
UNCLASSIFIED	UNCLASSIFIED	UNCLASSIFIED	UL

CONTENTS

i

-A CHRONOLOGY OF GUN DYNAMICS SYMPOSIUMS-

In-Bore Dynamics Symposium
> Naval Postgraduate School, Monterey, CA, 8-9 July 1976. Thomas N. Tschirn, Chairman.

First Conference of Dynamics of Precision Gun Weapons
> Rock Island, IL, 26-27 January 1977. Proceedings: R-TR-77-008, E.J. Haug, Editor.

Second U.S. Army Symposium on Gun Dynamics
> The Institute on Man & Science, Rensselaerville, NY, 19-22 September 1978. Thomas E. Simkins, General Chairman. Proceedings: ARLCB-SP-78013.

Third U.S. Army Symposium on Gun Dynamics
> The Institute on Man & Science, Rensselaerville, NY, 11-14 May 1982. Thomas E. Simkins, General Chairman. Proceedings: ARLCB-SP-82005.

Fourth U.S. Army Symposium on Gun Dynamics
> Riviera Beach, FL, 7-9 May 1985. Thomas E. Simkins, General Chairman. Proceedings: ARLCB-SP-85009.

Fifth U.S. Army Symposium on Gun Dynamics
> The Institute on Man & Science, Rensselaerville, NY, 23-25 September 1987. Thomas E. Simkins, General Chairman. Proceedings: ARCCB-SP-87023.

Sixth U.S. Army Symposium on Gun Dynamics
> Tamiment, PA, 15-17 May 1990. Thomas E. Simkins, General Chairman. Proceedings: ARCCB-SP-90015.

FOREWORD

-The Seventh Symposium-

Enclosed herein are the Proceedings of the Seventh U.S. Army Symposium on Gun Dynamics held at Newport, Rhode Island, 11-13 May 1993. These Proceedings contain thirty-three papers by authors from the military, academia, and industry. Papers from the U.S., England, and Canada are included covering the topics of fluid dynamics, gun accuracy, projectile motion, weapon simulation, tube deformation, controls theory and application, vibrations, and mathematical methods.

While past symposiums have been sponsored by a single laboratory or organization, this symposium was the collaborative effort of three U.S. Army organizations: the U.S. Army Research Office, the U.S. Army Armament Research, Development, and Engineering Center, and the U.S. Army Research Laboratory. The result was a wider scope of scientific and engineering topics providing for a greater cross-fertilization between academia and the military.

Once more, I am grateful to everyone who submitted a paper for inclusion in these Proceedings. As in previous years, I am delighted by the number of scientific and technical people who have gathered to share their knowledge and experience.

Thomas E. Simkins, Chairman
Seventh U.S. Army Symposium on Gun Dynamics

ATTENDEES

U.S. Army ARDEC
Benét Laboratories
ATTN: SMCAR-CCB-RT, Peter D. Aalto
Watervliet, NY 12189-4050

U.S. Army Research Office
ATTN: Gary L. Anderson
P.O. Box 12211
Research Triangle Park, NC 27709-2211

U.S. Army ARDEC
Benét Laboratories
ATTN: SMCAR-CCB-DS, Charles A. Andrade
Watervliet, NY 12189-4050

Purdue University
School of Mechanical Engineering
ATTN: Anil K. Bajaj
West Lafayette, IN 47907-1288

Sandia National Laboratories
ATTN: G.A. Benedetti, 8741
Livermore, CA 94550

U.S. Army ARDEC
Close Combat Armaments Center
ATTN: SMCAR-CCL-E, Philip Benzkofer
Bldg. #65
Picatinny Arsenal, NJ 07806-5000

U.S. Army Research Laboratory
ATTN: AMSRL-WT-PD, Morris Berman
2800 Powder Mill Road
Adelphi, MD 20783

U.S. Army Research Laboratory
ATTN: AMSRL-WT-PB, J. Bornstein
Aberdeen Proving Ground, MD 21005-5066

Royal Military College of Science
School of Mechanical, Materials, &
  Civil Engineering
ATTN: Prof. D.N. Bulman
Shrivenham, Swindon, Wiltshire
SN6 8LA
England, U.K.

U.S. Army Research Laboratory
ATTN: AMSRL-WT-PB, Mark L. Bundy
Aberdeen Proving Ground, MD 21005-5066

U.S. Army Research Laboratory
ATTN: AMSRL-WT-PD, Dr. Bruce Burns
Aberdeen Proving Ground, MD 21005-5066

U.S. Army Research Laboratory
ATTN: AMSRL-WT-PD, Larry Burton
Aberdeen Proving Ground, MD 21005-5066

U.S. Army ARDEC
Benét Laboratories
ATTN: SMCAR-CCB-RA, J.M. Coyle
Watervliet, NY 12189-4050

U.S. Army ARDEC
Close Combat Armaments Center
ATTN: SMCAR-CCL-LM, Francois Dahdouh
Bldg. #65N
Picatinny Arsenal, NJ 07806-5000

Defence Research Agency
Dynamics and Control Section
ATTN: Dilip K. Dholiwar
Chobham Lane
Chertsey, Surrey KT16 OEE
England, U.K.

U.S. Military Academy
Department of Civil & Mechanical Engineering
ATTN: LTC Robert E. Dillon, Jr.
Mahan Hall
West Point, NY 10996-1792

U.S. Army Research Laboratory
ATTN: AMSRL-WT-PD, Thomas F. Erline
Aberdeen Proving Ground, MD 21005-5066

U.S. Army ARDEC
Benét Laboratories
ATTN: SMCAR-CCB-SP, Richard Farrara
Watervliet, NY 12189-4050

U.S. Army ARDEC
Benét Laboratories
ATTN: SMCAR-CCB-DR, D. Finlayson
Watervliet, NY 12189-4050

U.S. Army ARDEC
Benét Laboratories
ATTN: SMCAR-CCB-DI, Russell Fiscella
Watervliet, NY 12189-4050

U.S. Army ARDEC
Benét Laboratories
ATTN: SMCAR-CCB-RA, T.E. Simkins
Watervliet, NY 12189-4050

U.S. Army ARDEC
Benét Laboratories
ATTN: SMCAR-CCB-DR, H.J. Sneck
Watervliet, NY 12189-4050

University of Illinois at Urbana-Champaign
Department of Mechanical
 & Industrial Engineering
ATTN: Alexander Vakakis
140 Mechanical Engineering Building
1206 West Green Street
Urbana, IL 61801

U.S. Army ARDEC
Benét Laboratories
ATTN: SMCAR-CCB-R, John Vasilakis
Watervliet, NY 12189-4050

University of Illinois at Urbana-Champaign
Coordinated Science Laboratory
ATTN: Petros Voulgaris
1308 West Main
Urbana, IL 61821

U.S. Army Research Laboratory
ATTN: AMSRL-WT-PD, Stephen Wilkerson
Aberdeen Proving Ground, MD 21005-5066

Massachusetts Institute of Technology
Intelligent Engineering Systems Laboratory
ATTN: J. Williams
77 Massachusetts Avenue
Cambridge, MA 02139

U.S. Army Research Office
Mathematical & Computer Sciences Division
ATTN: Julian J. Wu
P.O. Box 12211
Research Triangle Park, NC 27709-2211

SESSION I: FLUID DYNAMICS/GUN ACCURACY

SESSION II: PROJECTILE MOTION

SESSION III: WEAPON SIMULATION/TUBE DEFORMATION

SESSION IV: CONTROLS--THEORY AND APPLICATIONS

SESSION V: VIBRATIONS AND MATHEMATICAL METHODS

SESSION V: CONTINUED

SESSION I

FLUID DYNAMICS/GUN ACCURACY

SNECK

TITLE: Experimental Determination of Bore Evacuator Hole Flow
           Coefficients, Tube to Cannister
           H.J. Sneck
           U.S. Army Armament Research, Development, and
           Engineering Center
           Close Combat Armaments Center, Benét Laboratories
           Watervliet, NY 12189-4050
                also
           Professor of Mechanical Engineering
           Rensselaer Polytechnic Institute
           Troy, NY

ABSTRACT:

     The flow-rate of the propellant gases from the gun tube
through the bore evacuator holes controls the cannister charging
process and determines the maximum pressure available for tube
evacuation.   In an attempt to model this complex flow in simple
mathematical terms the holes are often treated as orifices.
Formulations of this type introduce dimensionless "orifice
coefficients" which are intended to embody the collective effect
of the details of the actual flow. The determination of these
coefficients is the central issue in the modeling. They are
expected to vary with changes in the hole configuration, fluid
properties and gross measures of the fluid motion. There have
been a few attempts to predict these coefficients analytically,
and even fewer to determine them experimentally. The results
presented here are a modest attempt to extend the empirical
database and verify previous mathematical predictions.

BIOGRAPHY:
PRESENT ASSIGNMENT: Mechanical Engineer - Benét Laboratories
(WAE), Watervliet, NY

PAST EXPERIENCE: Professor of Mechanical Engineering - 1953 to
present, consultant

DEGREES HELD: B.M.E., Rensselaer Polytechnic Institute, Troy, NY
1951; M. Eng., Yale University, New Haven, CT, 1952; PhD.,
Rensselaer Polytechnic Institute, Troy, NY 1961.

Experimental Determination of Bore Evacuator
Hole Flow Coefficients, Tube to Cannister

H.J. Sneck
U.S. Army Armament Research, Development, and Engineering Center
Close Combat Armaments Center, Benét Laboratories
Watervliet, NY 12189-4050

and

Professor of Mechanical Engineering
Rensselaer Polytechnic Institute
Troy, NY

INTRODUCTION:

A cannon bore evacuator system consists of a cannister surrounding a portion of the gun tube and a ring of small holes through the tube wall which connect the cannister cavity to the tube bore. The cannister is charged with high pressure propellant gases via these holes following the passage of the projectile and during a portion of the blow-down period. Since these holes are angled backward toward the breach, the tube gases must turn through an obtuse angle as they pass from the tube to the cannister. The charging process is further complicated by the generally high velocity down-tube gas flow passing the hole entrances.

While there is some experimental information available for flow through right angled holes [1], [2] and down-stream inclined holes, upstream inclined holes do not seem to have been investigated. The results of tests performed by the author on such holes using the USAF Academy Trisonic Wind Tunnel are reported here. The flow coefficients calculated from these tests are compared with the previous theoretical predictions [3]. An empirical correlation is presented which is suitable for coupling internal ballistics to the cannister pressurization process.

TEST FACILITIES

The Aeronautical Laboratory of the Department of Aeronautics at the USAF Academy has, among other facilities, a large blow-down wind tunnel capable of producing Mach numbers in the range of 0.24 to 4.5. Air at pressures ranging from 20 to 250 psia can be supplied to the stilling chamber from temperature stabilized storage tanks. This quiescent air then accelerates through nozzle blocks to a downstream straight 1.0' by 1.0' test section. The tunnel air is returned to the atmosphere via an adjustable diffuser following the test-section.

SNECK

To test bore evacuator holes one of the test section viewing
windows was removed and replaced with a metal plate. Three 1/8"
inch diameter 3/4" long holes were drilled through this plate at
30°, 45° and 60° to the tunnel centerline so that test section
air could flow through them, one at a time, into an external
plenum. Each hole was counter-bored on the downstream plenum
side to simulate actual evacuator holes. The plenum was
connected to the ambient air via a short length of pipe and a
flow control valve. Flow rates were measured by a rotameter
attached to the atmospheric pressure end of the pipe downstream
from the control valve. Plenum pressures were regulated by
opening and closing the throttling valve. Figure 1 shows a
schematic of the test system.
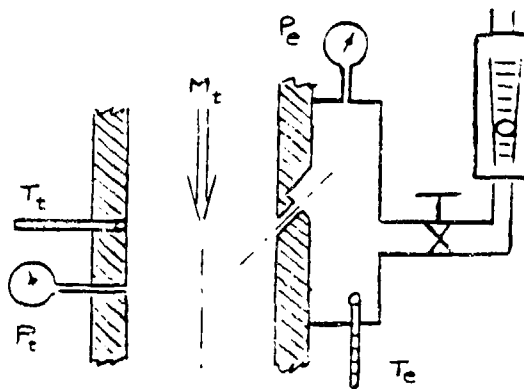
FIGURE 1 - Schematic of the Test System

TEST PROCEDURES

Three different test section Mach number ranges were run.
These were obtained by adjusting the wind tunnel nozzle/block and
diffuser configurations. Twenty to thirty second long tests were
performed for each hole angle and throttle valve setting.

The wind tunnel settling chamber pressure, settling chamber
temperature, test section pressure, and test section temperature
were measured during each run. The plenum pressure and
temperature were also measured, as well as the ambient pressure
and temperature. All of these were acquired via a
Kiethly data acquisition system and stored for further
processing. The rotameter reading was observed visually and via
a video camera - TV system and recorded on VCR tape for later
conversion to hole-flow rates.

A separate high pressure apparatus was used for the static
tests, $M_t = 0$. For these tests the wind tunnel was replaced by a
supply plenum connected to the wind tunnel air supply. The
supply plenum pressure and temperature were measured instead of
the wind tunnel test section pressure and temperature. The

3

results of these tests form a baseline for the wind tunnel tests
so that the effect of the tube Mach number could be assessed.

TEST OBJECTIVES

The test data was used to calculate the hole flow
coefficient K [3] defined by the equation

$$K = \frac{\dot{m}}{a\sqrt{gP_t\rho_t}} \qquad (1)$$

The coefficient itself is expected to depend upon the gas
specific heat ratio (γ), the tube Mach number (M_t), the hole
angle, and pressure ratio (P_e/P_t) across the hole. These tests
were performed to investigate the affect, if any, that these
variables (except γ) have on K.

Because of the large number of variable combinations (Mach
numbers, hole angles, pressure ratios) only a limited number of
tests could be performed on a given combination. Nevertheless,
some general trends did emerge from these tests. These are
presented in the following sections.

STATIC TESTS

Figure 2 shows the flow coefficient as a function of
pressure ratio for three hole angles. The predicted values from
[3] are shown by the hatched regions. Hatched region B is for a
"long" 45° hole, and hatched region C is for a short 90° hole.
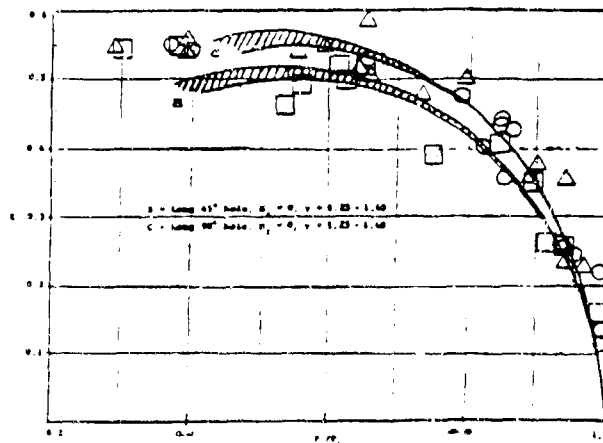
FIGURE 2. Flow Coefficient vs Pressure Ratio for $M_t = 0$.
Hole Angles: □-30°, △-45°, O-60°

4

SNECK

Since it is difficult to discern trends from Figure 2 the
data for each hole angle was least-square fit to the logarithmic
form of the equation

$$K = K_o \left(1 - \frac{P_e}{P_t}\right)^n \qquad (2)$$

The correlation coefficients obtained from regression analyses
were 0.93 to 0.94. The values of K computed from these equations
are shown in Table 1. As the hole angle is varied there appears
to be no significant variation in K at a given pressure ratio.
As a consequence, variations with the pressure ratio at a given
hole angle are also not significantly influenced by hole angle.

TABLE 1

K vs P_e/P_t Calculated from Least-Squares Correlation

$M_t = 0$			
$1 - P_e/P_t$	$30°$	$45°$	$60°$
0.2	0.38	0.43	0.40
0.4	0.48	0.53	0.51
0.6	0.55	0.60	0.59
$M_t \approx 0.4$			
0.2	0.30	0.27	0.22
0.4	0.39	0.38	0.36
0.6	0.45	0.47	0.47
$M_t \approx 0.8$			
0.2	0.24	0.23	0.25
0.4	0.33	0.34	0.36
0.6	0.40	0.43	0.45

SUBSONIC TESTS, $M_t \approx 0.4, 0.8$

Figure 3 shows the results for two ranges of tube Mach numbers, a low range of $0.35 < M_t < 0.45$ and in the high range of $0.72 < M_t < 0.85$. In each of the Mach number ranges the variation of K with hole angle was found not to be significant. However, there is a clear reduction in K with increasing Mach number. Correlation coefficients for the logarithmic regression analyses of this data range from 0.91 to 0.99.
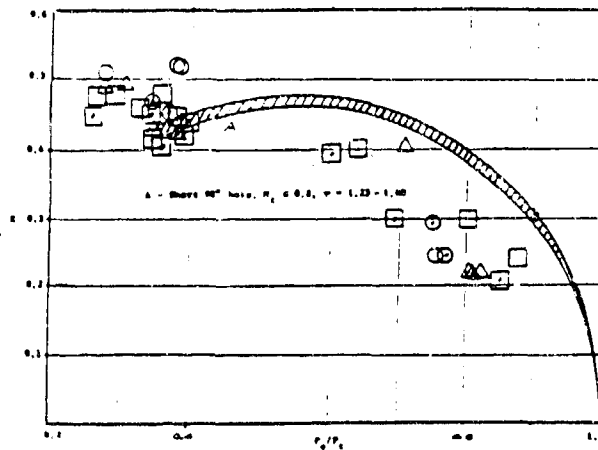
Figure 3. Flow coefficient vs Pressure Ratio.
$M_t \approx 0.4$: *Hole Angles*; □-30°,
   △-45°, ○-60°
$M_t \approx 0.8$: *Hole Angles*; ⊡-30°,
   ▲-45°, ⊙-60°

The test results are clearly not in agreement with curve A for a 90° hole [3] except at low pressure ratios near and at the onset of hole choking. Since the major portion of the evacuator filling is expected to occur under choked conditions, the low pressure ratio coefficients are important.

The least-squares calculated coefficients for each Mach number range are also given in Table 1. As with the $M_t = 0$ case no significant affect of hole angle is noted.

As usual, the onset of choking is difficult to pinpoint from the data with certainty. A comparison of Figures 2 and 3 suggest that the choking pressure ratio may shift toward lower values $(P_w/P_t < 0.5)$ with increasing tube Mach number.

SNECK

SUPERSONIC TEST, $M_t = 1.3$

As the wind tunnel test-section Mach numbers are increased the tunnel test-section pressure decreases. This reduces the range of pressure ratios that can be tested. Figure 4 shows the test results for pressure ratios in the range $0.64 \leq P_e/P_t \leq 0.74$.
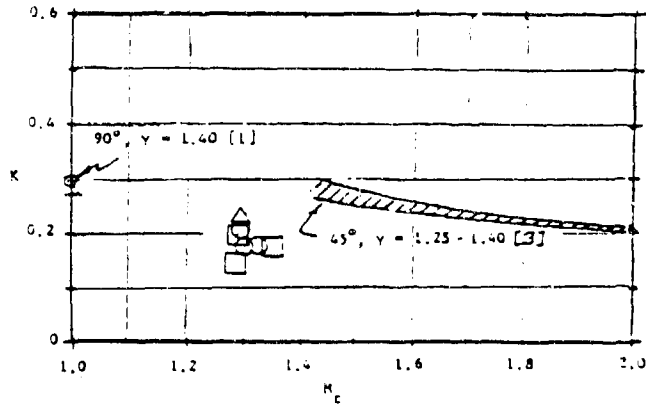
Figure 4. Flow Coefficient vs Tube Mach Number for $0.64 \leq P_e/P_t \leq 0.74$.

□-30°, △-45°, ○-60°,

Because of the scarcity of data the only thing that can be said for certain is that the coefficients are substantially less than the subsonic values for the same pressure ratios.

TEST CORRELATIONS

The variations of K and n in Equation (2) were least-squares curve fit obtain a relationship with the Mach number. These empirical equations are

$$K_o = 0.690(1-0.235M_t^{0.454}) \tag{3}$$

$$n = 0.331(1+0.643M_t^{0.546}) \tag{4}$$

A least-squares correlation of seventy six measured K_m vs calculated K_c using equations (2), (3) and (4) yields

$$K_m = 0.035+0.92K_c \tag{5}$$

7

SNECK

At high pressure ratios the correlation equations over-estimate the least-squares measured K_m. Very little data was obtained in this range. At the lower pressure ratio ($K_c > 0.2$) the correlation is within 10% of the least-squares K_m. Since most of the cannister filling is probably accomplished at lower pressure ratios, a high degree of correlation is desirable in this range. Extrapolation of the empirical equation into the supersonic regime yields values of K_c which are 30% to 50% higher than K_m. The few supersonic test results obtained make it difficult to assess the general accuracy of the correlating equation for $M_t > 0.8$.

Because sub and supersonic flows fields are so different there is no reason to believe that extrapolation from one to the other is possible. It is gratifying to find that the supersonic coefficients are not substantially different from the low values predicted (Figure 4) but that may just be fortuitous.

Supersonic tube flows, when they exist, last for only a short period of time compared to blow-down duration. However, very small pressure ratios accompany these Mach numbers so that there will probably be high flow rates despite the lower values of K.

SUMMARY

1   Correlation between theory and experiment appear to be in relatively good agreement for $M_t = 0$.

2. The same cannot be said for the correlation for $0 < M_t < 1.0$, where theory generally over-estimates K for a given pressure ratio.

3. Theory and experiment are in good agreement for small pressure ratios corresponding to choking when $M_t < 1.0$.

4. The subsonic flow coefficients do not seem to be significantly influenced by hole angles in the range 30° to 60°.

5. Increasing tube Mach numbers are accompanied by decreasing K.

6. Supersonic flow coefficients follow the subsonic trend of decreasing K with increasing M_t.

7. The few experimental supersonic coefficients obtained are in reasonable agreement with theory.

8. Limited supersonic tests do not permit correlation with the test variables.

SNECK

RECOMMENDATIONS

The following suggestions are made based on the existing state-of-knowledge.

Subsonic Tube Flow, $M_t < 1.0$

1. When $P_e/P_t > 0.3$ estimate the flow coefficient from equations 2, 3, and 4.

2. When $P_e/P_t < 0.3$ estimate the flow coefficient from equations 2, 3, and 4 with a constant $P_e/P_t = 0.3$.

Supersonic Tube Flow, $M_t > 1.0$

1. Conservatively estimate the flow coefficient as approximately 0.2 for $1.0 < M_t < 1.3$.

NOMENCLATURE

a   hole area

g   gravity acceleration

K   flow coefficient

K_o least-squares coefficient correlation with M_t

K_c least-squares calculated flow coefficient

K_m least-squares measured flow coefficient

$\dot{m}$ mass flow-rate

M_t tube Mach number

n   least-squares exponent correlation with M_t

P_e hole exit pressure (absolute)

P_t tube gas pressure (absolute)

ρ_t tube gas density

SNECK

REFERENCES

1. Smith, F. "Investigation of Fume Extractor Design by Model
    Techniques, RARDE Memo 13/67, Fort Halstead, 1967.

2. Rohde, J.E., Richards, H.T., Metzger, G.W. "Discharge
    Coefficients for Thick Plate Orifices with Approach Flow
    Perpendicular and Inclined to the Orifice Axis", NASA TN
    5467.

3. Sneck, H.J., Witting, P. "Bore Evacuator Hole Flows",
    Proceedings of the 6th Army Symposium on Gun Lynamics, I-61
    to I-75 (1990).

SNECK

TITLE: PRESSURE DISTRIBUTION AND PUMPING FORCE OF DISCHARGING
BORE EVACUATOR HOLES

MARIO RIVERA
BENÉT LABORATORIES
WATERVLIET ARSENAL, WATERVLIET, NY 12189-4050
also
PROFESSOR OF MECHANICAL ENGINEERING
UNION COLLEGE, SCHENECTADY, NY
-and-
H.J. SNECK
BENÉT LABORATORIES
WATERVLIET ARSENAL, WATERVLIET, NY 12189-4050
also
PROFESSOR OF MECHANICAL ENGINEERING
RENSSELAER POLYTECHNIC INSTITUTE, TROY, NEW YORK

ABSTRACT:

Bore evacuator holes are angled toward the muzzle end of a
gun tube so that the small jets created during the evacuator
discharge will entrain bore gases, forcing them to move toward
the muzzle. A control volume analysis of the gas in the tube
with an open breech shows that the only force acting in the
direction of the muzzle occurs at the nozzle entrance to the
tube. The pressure distribution at the nozzle entrance is
investigated theoretically and experimentally in this paper. An
empirical method of calculating the nozzle pumping force
component is presented for 30°, 45° and 60° nozzle angles.

BIOGRAPHY: M. Rivera
PRESENT ASSIGNMENT: Mechanical Engineer - Benét Laboratories
(WAE), Watervliet, NY
PAST EXPERIENCE: Associate Professor of Mechanical Engineering -
1985 to present, Assistant Professor of Mechanical Engineering
1978-85, Project Engineer 1973-78. consultant.
DEGREES HELD: B.S. (Aero) 1968, M.S. (Mechanics) 1970, Ph.D
(Mechanics) 1973; all at Rensselaer Polytechnic Institute, Troy,
New York

BIOGRAPHY: H. Sneck
PRESENT ASSIGNMENT: Mechanical Engineer - Benét Laboratories
(WAE), Watervliet, NY
PAST EXPERIENCE: Professor of Mechanical Engineering - 1953 to
present, consultant
DEGREES HELD: B.M.E., Rensselaer Polytechnic Institute, Troy, NY
1951; M. Eng., Yale University, New Haven, CT, 1952; PhD.,
Rensselaer Polytechnic Institute, Troy, NY 1961.

Pressure Distribution and Pumping Force
of Discharging Bore Evacuator Holes

Mario Rivera and H.J. Sneck
U.S. Army ARDEC
Close Combat Armaments Center
Benét Laboratories
Watervliet, NY

INTRODUCTION

During the discharge of a bore evacuator very small diameter jets issue into the bore from the evacuator nozzles. These jets are angled toward the muzzle end so that they can entrain the bore gases and pump them out of the muzzle and away from the breech. The process is similar to a jet-pump, i.e. jet momentum is imparted to the bore gas, albeit very inefficiently.

One would assume that decreasing the angle between the nozzle centerline and the tube centerline would increase the pumping effect. That is generally true. Such reasoning is based on the belief that the jet and nozzle centerlines are coincident, which is not true. Reference [1] shows that, depending on the angle of the nozzle and its pressure ratio, the two centerlines can be deflected by as much as 12° toward the breech. For a 45° nozzle that would mean that the effective jet angle is 57° at a nozzle pressure ratio of 4 [1].

The cross section of a deflected jet is also influenced by the nozzle angle. Photographs show that the jet is wider in the plane of the deflection angle than in the plane perpendicular. The resulting cross-section is oval, becoming more so in the flow direction. When the jet exits the nozzle supersonically complex shock patterns appear which only vaguely resemble the classical shock diamonds produced by 90° nozzles.

The detailed analysis of such jets and their pumping properties would clearly be a major computational undertaking, and one to be avoided if possible. One way to do that is to adopt a control volume approach closing the boundary so that the complex flows are within the control volume. If the problem can be solved using only the continuity and momentum equations then there is no need to study the details of the flow within the control volume. If an energy equation must also be considered, then the internal details of the flow need to be examined. Since the jets add very little thermal energy to the control volume, energy affects can be safely ignored.

In the case of a gun tube the breech end, muzzle end, and tube wall forces can be evaluated using well known fluid mechanics techniques. The only region where new information is required is at the nozzle entrance to the tube. The importance of the nozzle entrance is apparent if the control volume encloses

the muzzle and breech planes, the tube internal surface, and the hole entrance. Since the breech entrance pressure is below atmosphere while the muzzle exit pressure is at atmosphere, they combine to create a net force toward the breech. Drag forces on the tube surface also result in a force toward the breech. The only portion of the control volume boundary when a force toward the muzzle can be produced is at the nozzle entrance. The component of this force toward the muzzle must exceed the other two forces for pumping to occur. Thus, the success of a control volume analysis depends on determining the forces at the nozzle exit.

If it is assumed that the pressure inside the nozzle is uniform across its cross section near and at the exit cross section, then the force at the exit cross-section can be easily calculated. For most of the evacuator discharge phase the flow will be choked with an exit plane Mach number of unity. The remainder of the exit surface is the lip portion beyond the exit plane out to the tube surface. The pressure at the exit plane produces a force component toward the muzzle, while the lip surface yields a force component toward the breech. The net of these is the pumping force referred to earlier.

OBJECTIVE

The purpose of the research reported here is to obtain a simple method for determining the force exerted on the fluid by the lip. That force, combined with the exit plane force determines the total hole force, and its down-tube component is the pumping force.

The approach here is two-fold, i.e., analytical and experimental. A detailed three dimensional analysis of that portion of the jet adjacent to the lip is possible. The hope is it that may not be necessary if the lip forces can be reasonably well predicted by simpler means, in this case using the two-dimensional method of characteristics techniques.

The experimental portion of this effort was designed to measure lip pressures so that they could be compared with the results obtained from the two dimensional method-of-characteristics analysis, as well as to gain insight into the lip pressure distribution.

TEST PROCEDURES

Figure 1 is a Schematic of the Test Apparatus.
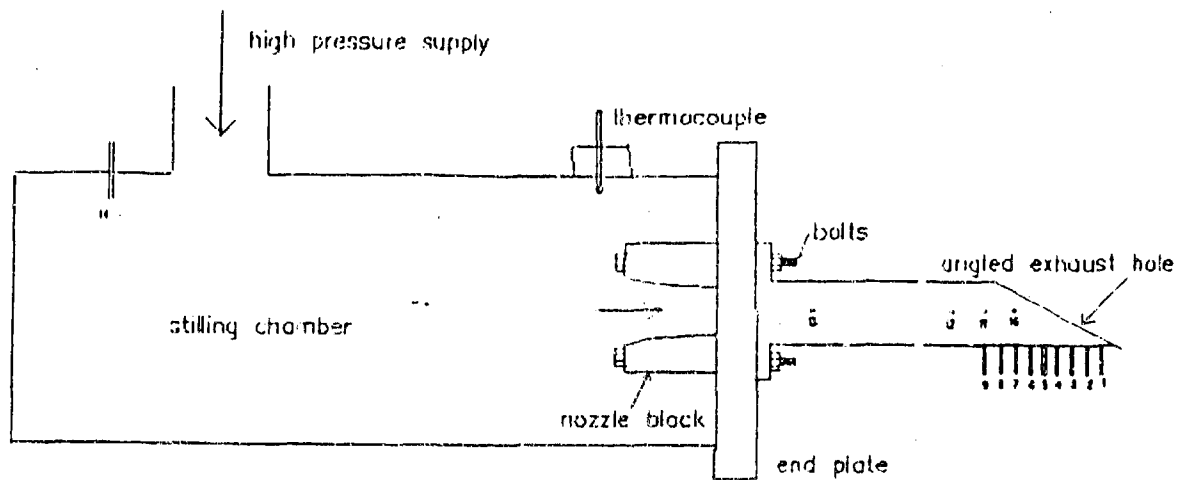
FIGURE 1 - SCHEMATIC OF TEST APPARATUS.

The nozzle angles were tested 30°, 45° and 60°. The nozzle diameter was approximately ten times the diameter of the actual nozzle exit so that small pressure taps could be used along the bottom and on the side of the lip.

The flow in the lip portion was examined usually using a shadow graph. Although it was not the purpose of these experiments to study the flow field, the oblique shock patterns observed were similar to those shown in reference [1]. The presence of shocks in the shadow graphs served to confirm that sonic conditions had been reached at the exit plane.

EXPERIMENTAL PRESSURE DISTRIBUTIONS

Figures 2-13 are typical of the pressure measurements. Pressures at the tip of the lip are at the left. Test points proceed upstream to the right along the lip and into the nozzle.
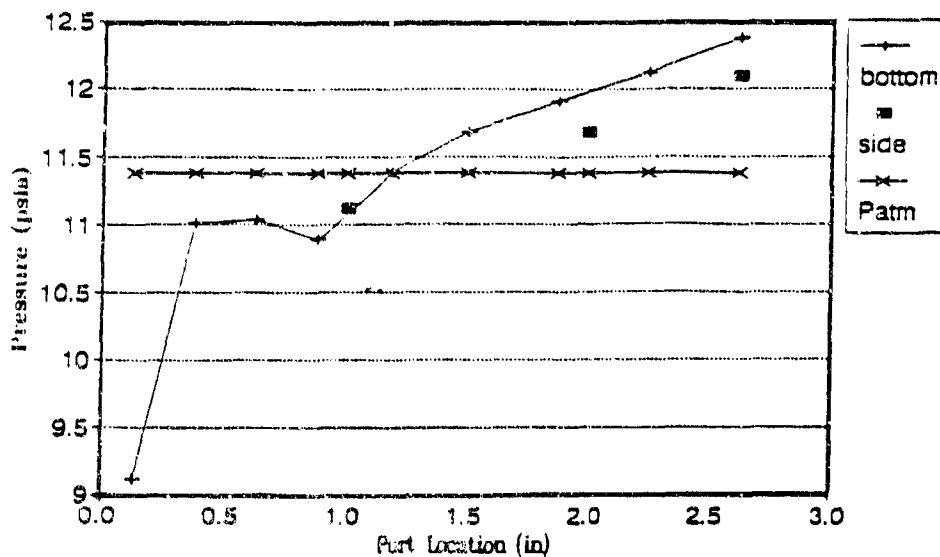
FIGURE 2 - 30° HOLE PRESSURE DISTRIBUTION, EPR = 1.86
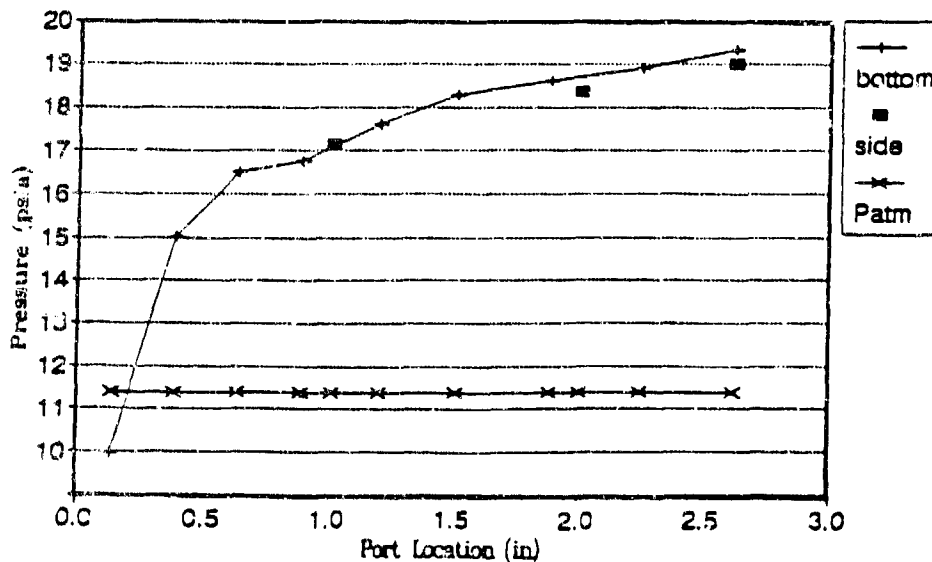
FIGURE 3 - 30° HOLE PRESSURE DISTRIBUTION, EPR = 2.91
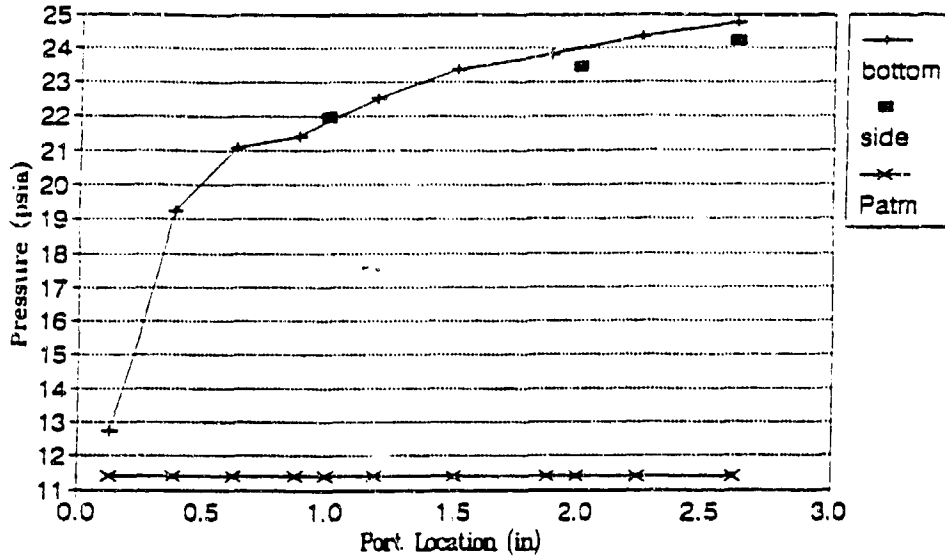
FIGURE 4 - 30° HOLE PRESSURE DISTRIBUTION, EPR = 3.73
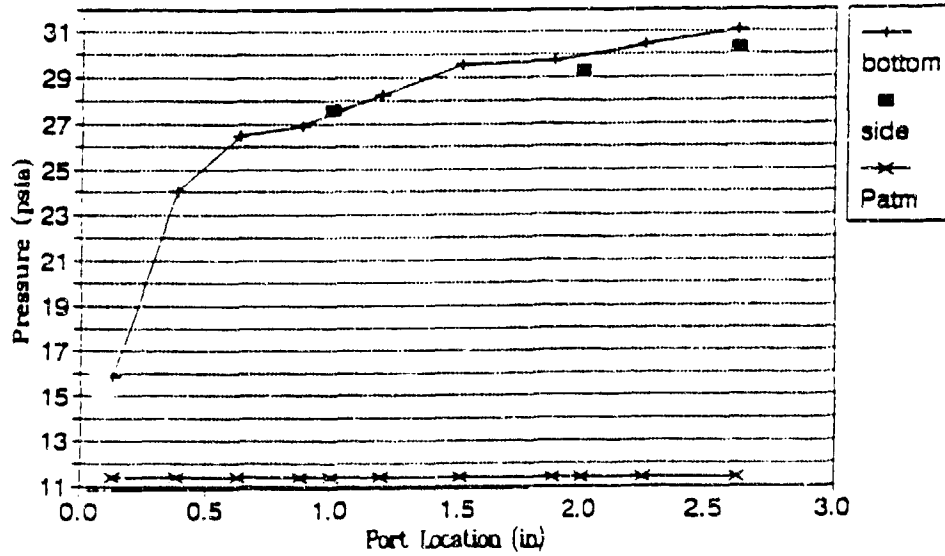
FIGURE 5 - 30°HOLE PRESSURE DISTRIBUTION, EPR = 4.64
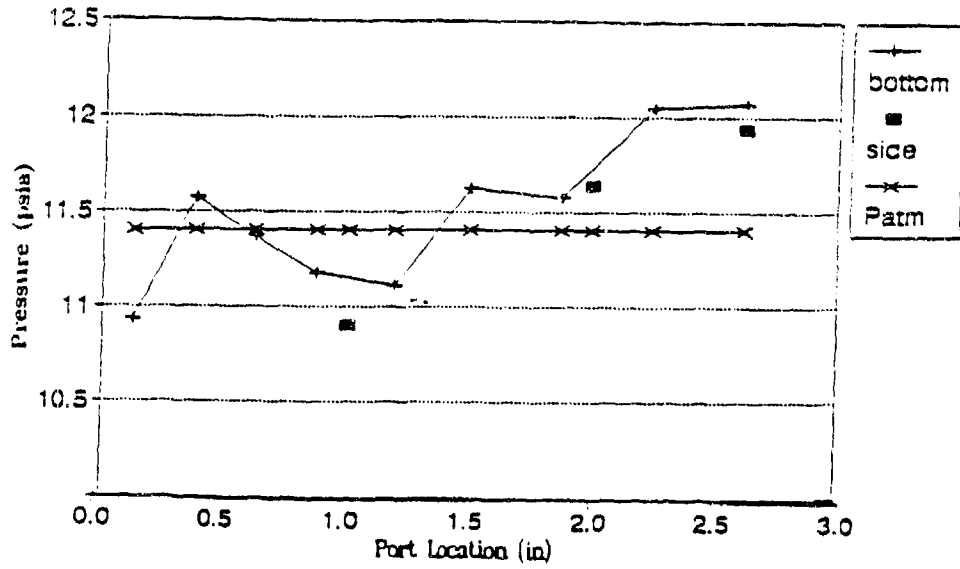
FIGURE 6 - 45° HOLE PRESSURE DISTRIBUTION, EPR = 1.85
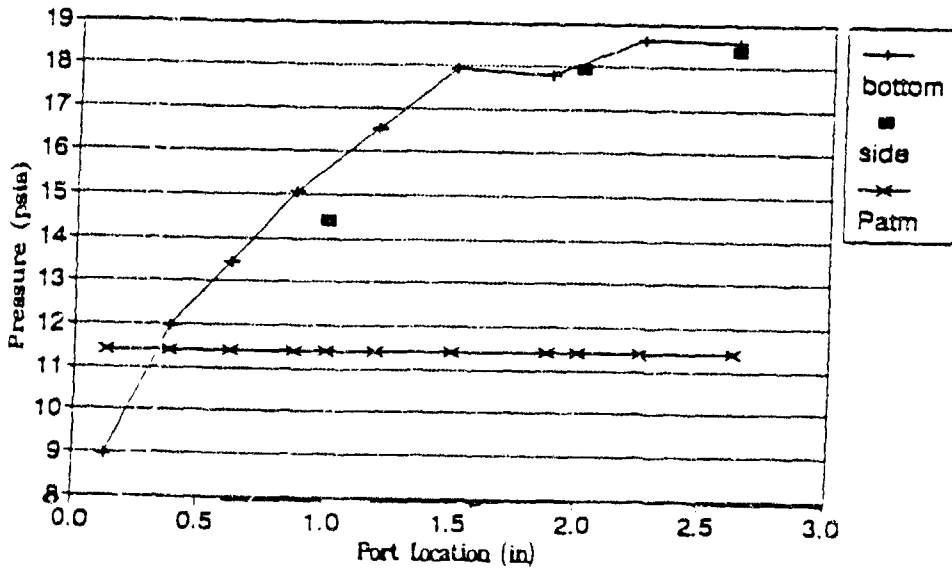
FIGURE 7 - 45° HOLE PRESSURE DISTRIBUTION, EPR = 2.89
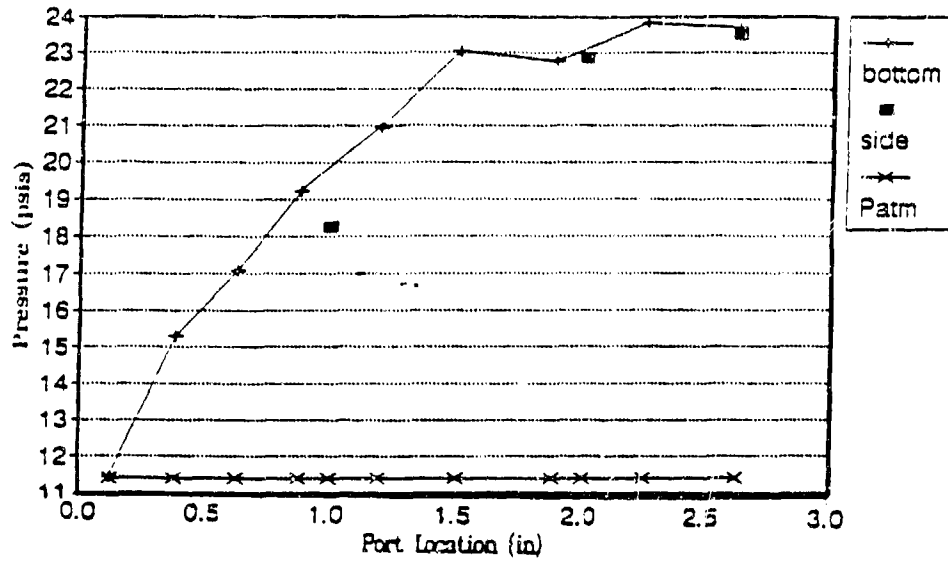
FIGURE 8 - 45° HOLE PRESSURES DISTRIBUTION, EPR = 3.69
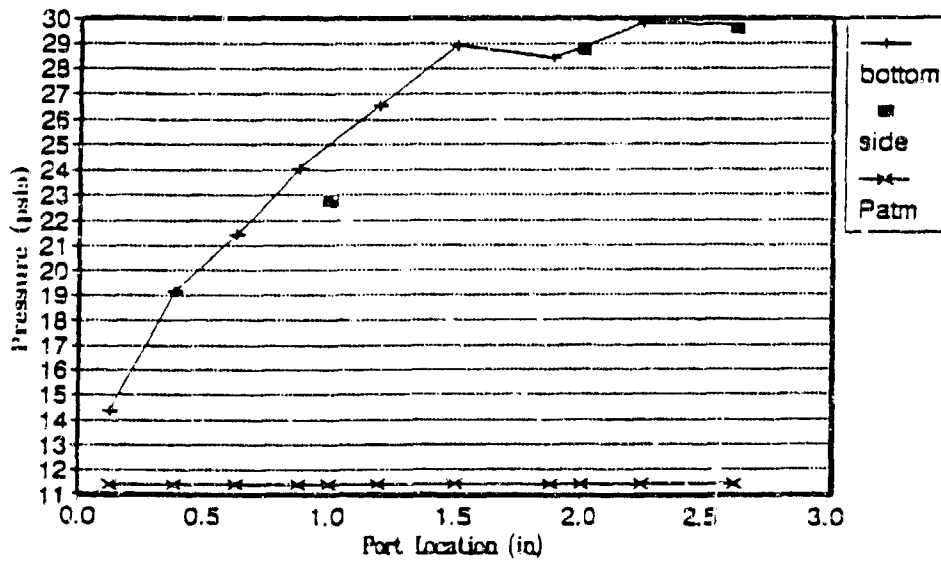
FIGURE 9 - 45° HOLE PRESSURE DISTRIBUTION, EPR = 4.56
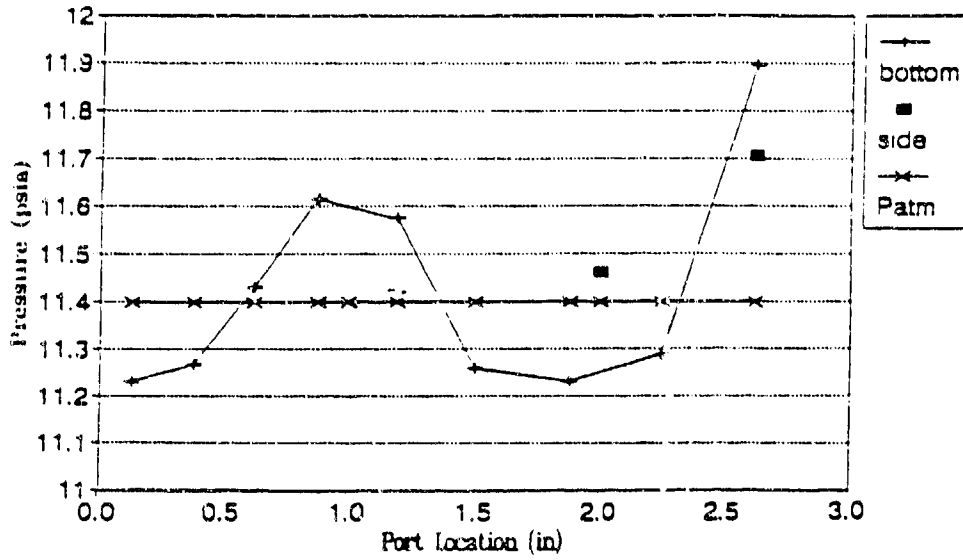
FIGURE 10 - 60° HOLE PRESSURE DISTRIBUTION, EPR = 1.87
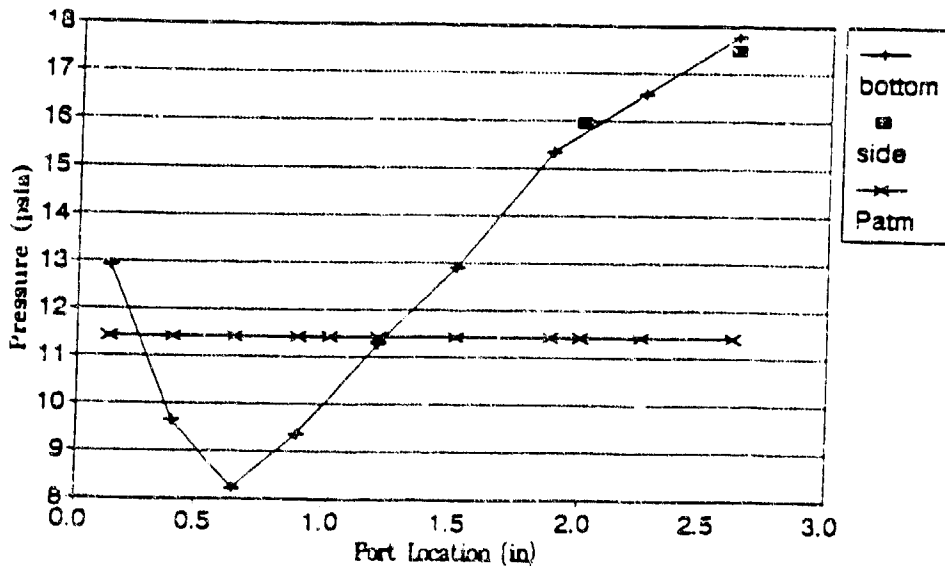
FIGURE 11 - 60° HOLE PRESSURE DISTRIBUTION, EPR = 2.86
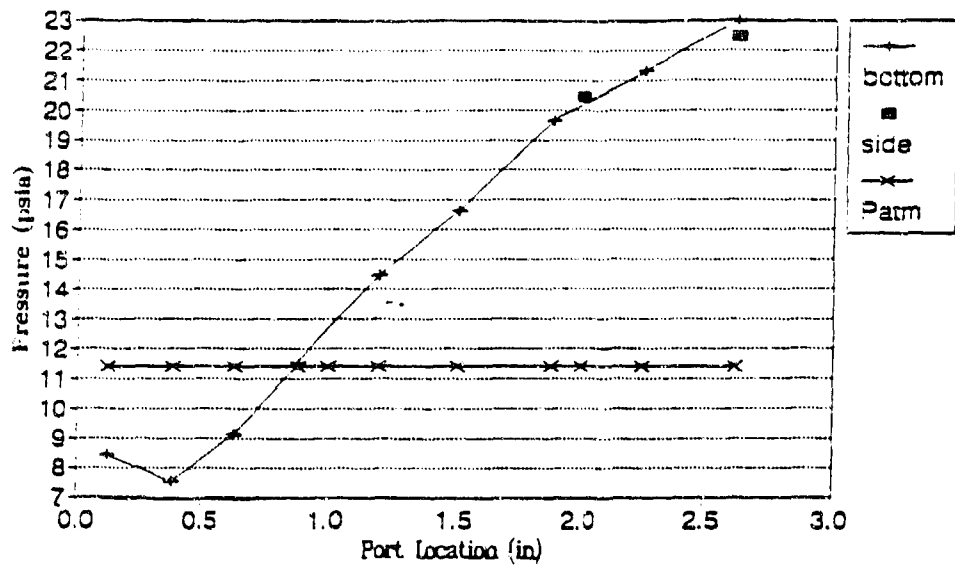
FIGURE 12 - 60° HOLE PRESSURE DISTRIBUTION, EPR = 3.68
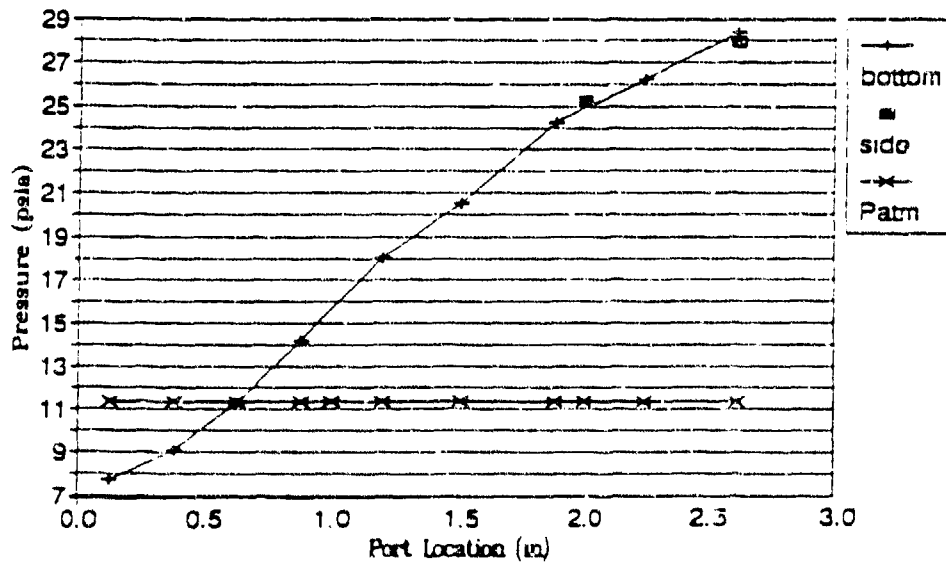
FIGURE 13 - 60° HOLE PRESSURE DISTRIBUTION, EPR = 4.54

Several interesting patterns emerge from these plots. In general the pressure declines from the nozzle exit toward the lip as expected. For the higher pressure ratios this decline is continuous, even to sub-ambient pressures at the tip of the lip. At lower pressure ratios the downward trend is interrupted by jumps in the pressure distribution. This effect is especially noticeable for the longer lipped nozzles, i.e. 45° and 60°. These jumps correlate with visually observed oblique shocks near these locations. Apparently the longer the lip, the more likely is the formation of a shock, especially at low pressure ratios.

Since most of the bore evacuator discharge will occur at high pressure ratios shock formation and sub-ambient pressures are probably of no concern.

Space constraints did not permit the inclusion of very many side-lip pressure taps. It is gratifying to see that the side pressures measured do not differ significantly from the bottom-lip pressures at the same axial position. This would indicate that at least on the lip surface the bottom-lip pressure is typical of the circumferential pressure distribution at each axial station. Symmetry at each station makes the summing of lip forces straight forward.

ANALYTICAL RESULTS

Prior to testing two-dimensional method of characteristics analyses were performed, first by hand and then using a computer. The computed lip-bottom pressures were normalized to the nozzle exit plan pressure where the Mach number was set to 1.01 to initiate the calculations. Distances along the lip-bottom, measured from the nozzle exit plane, were normalized to the exit diameter. The results for six different pressure ratios are shown in Figure 14 for all pressure ratios. Computations were performed to cover all lip angles, up to 60°.

The only distinguishing feature of the predicted pressure distribution is the distance at which the pressure stops declining and levels off. This point is a function of the exit pressure ratio.

Computations were continued beyond this point until they indicated that the formation of an oblique shock was imminent. (The computer code was not capable of crossing an oblique shock). The calculations indicated that the tendency to level-off and subsequently shock decreases with increasing EPR until the EPR was slightly above 3.36. For higher pressure ratios all three nozzle lips are predicted to be shock-free.
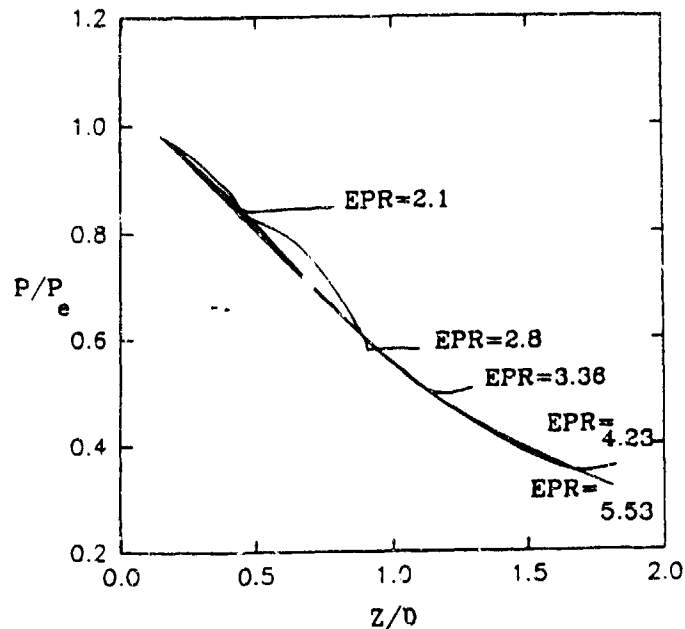
FIGURE 14 - LIP PRESSURE DISTRIBUTION γ = 1.4, 2-D METHOD OF
CHARACTERISTICS

Probably the most interesting feature of the theoretical curves is the universality of the pressure distribution for all pressure ratios up to the onset of the uniform pressure region.

COMPARISON OF EXPERIMENT AND ANALYSIS

Experimental and theoretical results are compared in Figures 15-18. Since it is difficult to control experimental conditions the EPR's are not exactly equivalent. Despite this it appears that agreement is reasonably good near the nozzle exit plane. This is expected since both theory and test pressures are initially normalize to unity. Farther along the lip the theory tends to underestimate the experimental pressures. The onset of the uniform pressure region occurs farther out on the lip than predicted.
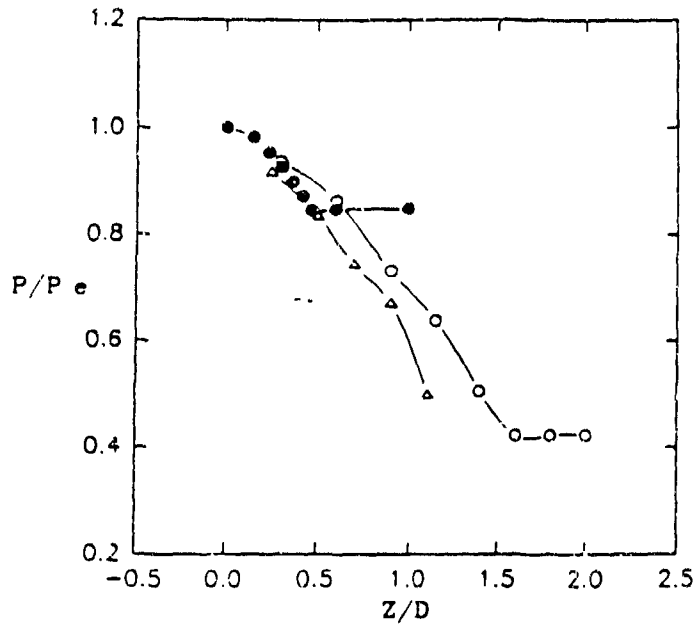
FIGURE 15 - ANALYTICAL LIP PRESSURE DISTRIBUTION;
● - *EPR* = 2.1 (*Experimental*), △ - *EPR* = 2.18, ○ -*EPR* = 2.13
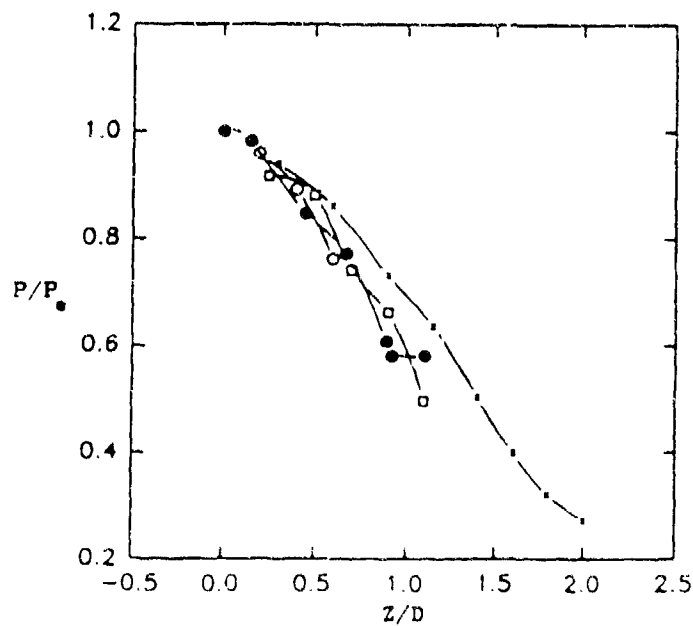
FIGURE 16 - ANALYTICAL LIP PRESSURE DISTRIBUTION;
● - *EPR* = 2.55 (*Experimental*), ○ - *EPR* = 2.49,
x - *EPR* = 2.65, □ -*EPR* = 2.54

23
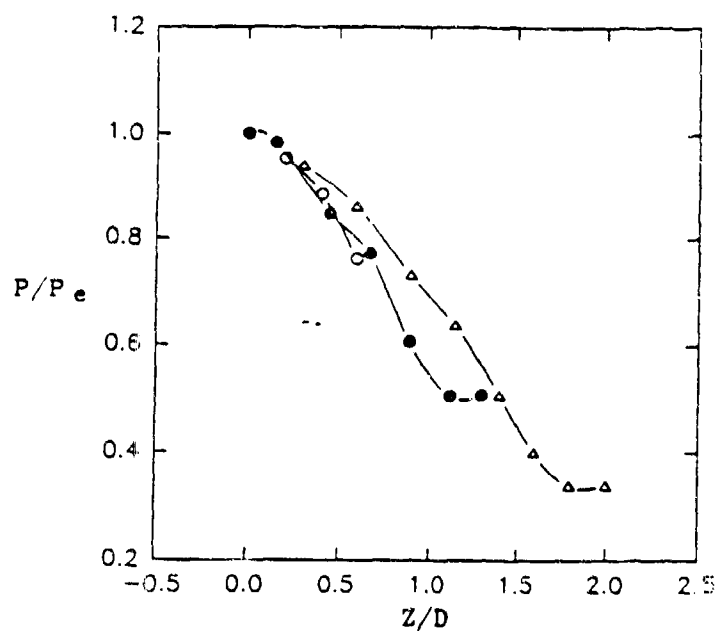
FIGURE 17 - ANALYTICAL LIP PRESSURE DISTRIBUTION;
● - EPR = 2.8 (Experimental), △ - EPR = 2.98, ○ - EPR = 2.65
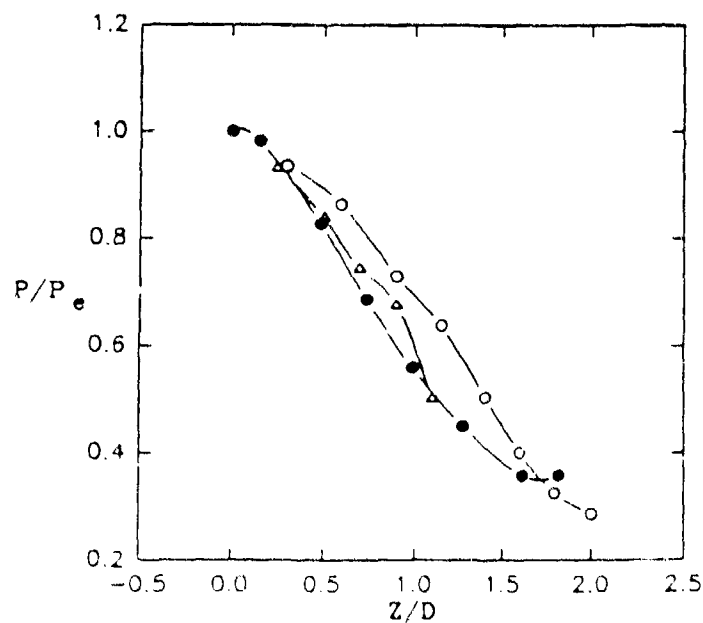
FIGURE 18 - ANALYTICAL LIP PRESSURE DISTRIBUTION;
● - EPR = 3.36 (Experimental), ○ - EPR = 3.11, △ - EPR = 3.15

AVERAGED LIP PRESSURES

Figure 19 shows the average pressure on the lip, P_w, relative to the nozzle exit pressure P_e. These averages were obtained by integrating the experimental lip pressure distributions over the lip area. The lip area in this case is the area seen when the nozzle exit is viewed normal to the nozzle center line. P_w times this area is the force the lip exerts on the gas perpendicular to the nozzle centerline. Smaller values of P_w/P_e result in larger pumping forces extended on the tube gases.
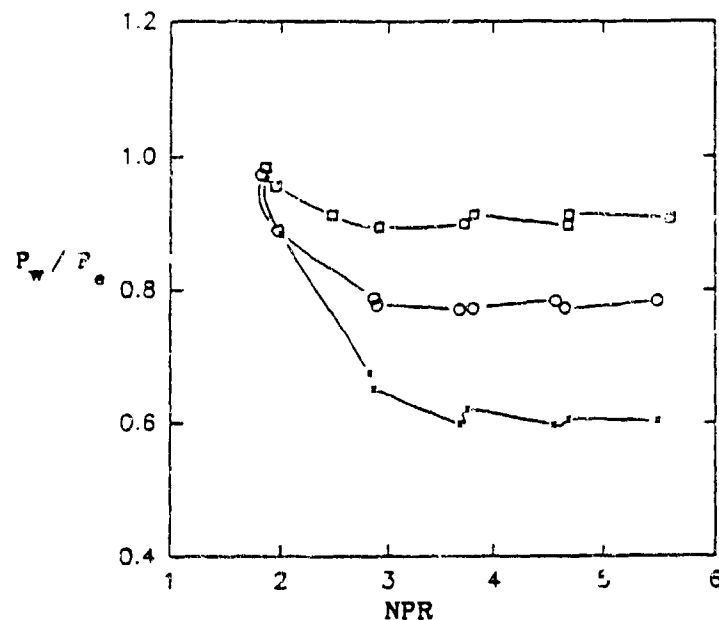
FIGURE 19 – NORMALIZED LIP PRESSURE VS NPR
$\beta = 30° - x, \quad \beta = 45° - \circ, \quad \beta = 60° - \square$

Below the critical NPR of approximately 1.9 the wall pressure (extrapolated and shown as a dashed line in Figure 19) is only slightly less than the nozzle exit pressure. Substantial decreases in P_w/P_e occur when the NPR is increased to about three or four, but beyond that increasing the NPR yields no further increase in P_w/P_e.

HOLE THRUST FORCES

The pumping force component provided by the nozzle pressures is given by:

$$F_p = P_e a_e \left(1 - \frac{P_w}{P_e}\right) \cos\beta$$

The factor $(1 - P_w/P_e) \cos\beta$ is the fraction of the maximum force $P_e a_e$ available as a pumping force. Figure 20 shows this term as a function of the NPR.
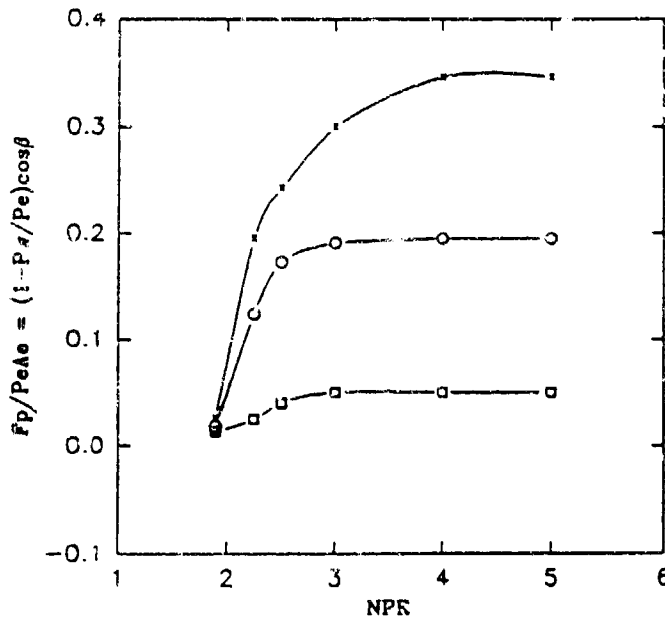
FIGURE 20 - NORMALIZED PUMPING FORCE VS NPR
$\beta = 30° -x$, $\beta = 45° - °$, $\beta = 60° - \square$

There is a dramatic increase in the pumping force as the NPR is increased to a level which eliminates shocks from the lip.

For NPR ≥ 1.9 the exit pressure P_e is theoretically related to the reservoir pressure P_R by $P_e = P_R/1.893$. Thus increasing P_R and NPR (to a limited extend) increases F_p. Once P_w/P_e reaches its asymptotic value F_p increases linearly with P_R.

RIVERA AND SNECK

OBSERVATIONS

1. The two-dimensional method of characteristics analysis underestimates the lip pressures. It also predicts a uniform pressure region, and the subsequent onset of an oblique shock, much closer to the nozzle exit plane than observed.

2. The universal character of the shockless wall pressure distribution predicted by theory appears to be at least approximately true for the actual flows.

3. The result of thirty tests indicates that the hole lip will be shockless if EPR > 1.5 for 30° nozzles, EPR > 2.5 for 60° nozzles.

4. The pressure along the bottom of the lip appears to be very nearly the same as the circumferential pressures at that axial location. This finding makes the calculation of the axial force component straight forward.

5. The ratio of the average wall pressure, P_w, to the nozzle exit pressure, P_e, decreases with increasing nozzle angle β, reaching asymptotic values as NPR is increased.

ACKNOWLEDGEMENTS

NOMENCLATURE

a_e	nozzle exit area
D	nozzle diameter
EPR	exit pressure ratio = P_e/P_t
NPR	nozzle pressure ratio = P_R/P_a
P	lip pressures
P_a	ambient pressure
P_e	nozzle exit plane pressure
P_w	area averaged lip wall pressure
Z	axial distance from the nozzle exit plane
β	nozzle angle
γ	specific heat ratio

REFERENCES

1. Wezien, R.W., Kibens, V.; "Influence of Nozzle Asymmetry on Supersonic Jets", AIAA Jour., Vol. 26, No. 1, Jan 1988.

TITLE: VALIDATION OF PROJECTILE TRANSIENT RESPONSE MODELS FOR THE STUDY OF PRESSURE OSCILLATIONS IN GUNS

David A Hopkins
Army Research Laboratory
Aberdeen Proving Ground, Maryland

Ting Li, Morris Berman
Army Research Laboratory
Adelphi, Maryland

ABSTRACT:

This paper presents results that provide a validated simulation approach to study the behavior of projectiles subjected to transient in-bore loadings. In this study, the PXR6353 instrumented round was modeled. The approach used features vibration studies of the components of this projectile. This includes a comparison of the vibration modes determined by finite element techniques with those modes determined using experimental modal analysis techniques. The ANSYS finite element code was used to generate the analytic model. Both impact and shaker excitation methods were used in the experimental modal analysis phase. The direct comparison between analytical and experimental data showed that the finite element model correctly captured the dominant modes of vibration of the projectile.

BIOGRAPHY:
PRESENT ASSIGNMENT: Mechanical Engineer, Mechanics and Structures Branch, Propulsion and Flight Division, Weapons Technology Directorate, Army Research Laboratory
DEGREES HELD: M.S. (Mechanical Engineering), University of Delaware, 1986; B.S. (Aerospace Engineering), University of Florida, 1983.

VALIDATION OF PROJECTILE TRANSIENT RESPONSE MODELS FOR THE STUDY OF PRESSURE OSCILLATIONS IN GUNS

DAVID A HOPKINS
ARMY RESEARCH LABORATORY
ABERDEEN PROVING GROUND, MARYLAND

TING LI
MORRIS BERMAN
ARMY RESEARCH LABORATORY
ADELPHI, MARYLAND

INTRODUCTION

The design of artillery projectiles has been based upon the presumed use of solid propellant as the propelling charge [1]. The pressure profile across the base is typically uniform for solid propellants. Also, the pressure-time history is smooth. However, with the nonconventional propelling charges now under consideration, neither of these conditions is necessarily true. Consequently, it is vital that the capability of existing munitions to survive these new launch environments be determined.

One means of addressing this issue is to conduct large scale firing tests using representative samples from all current munitions. This approach is time consuming. Also, limited information concerning the causes of failure is obtainable from this approach for munitions which do not survive the launch environment. Another approach is to use finite element (FE) methods to analytically determine the probable response of a projectile to the expected launch environment. This approach allows the determination of potential deleterious effects of the launch environment provided the FE model accurately represents the essential structural dynamic characteristics of the real projectile. For simple structures it is relatively straightforward to generate an appropriate FE model. However, complex structures such as artillery projectiles which have numerous internal components are a much more difficult task. Validation of these FE models is essential if confidence in the analytical results is expected.

Experimental Modal Analysis (EMA) has proven to be an extremely useful tool for validating complex FE models. In its simplest function, EMA determines the basic structural characteristics such as natural frequencies and modes of vibration of a structure. These measured characteristics can be compared with the predicted values obtained from an FE analysis to determine the accuracy of the model. Good agreement indicates that the FE model can be expected to realistically capture the basic dynamic behavior of the actual structure. For many FE models, this is all that is required for validation. Additional concerns such as the refinement of the FE model to account for stress concentrations are a separate issue and cannot be addressed by EMA. However, if the FE model cannot even reproduce the gross dynamic behavior of the structure correctly, then these additional concerns are moot.

Prior analyses [2,3,4,5] of projectiles typically used either the same FE model for the dynamic analysis as was used for the static analysis or relied upon the experience of the FE analyst to generate an acceptable FE model. For conventional solid propellant these approaches normally produced reasonable results. This success is due in part to the fact that the response of the projectile can be approximated as quasi-static when the loading is due to solid propellant. This is not true for analyses which attempt to simulate the liquid propellant (LP) launch environment. As is seen in Figure 1, the pressure-time curve exhibits high frequency oscillations. These oscillations can cause significant structural response if the frequency of the oscillations is near a fundamental frequency of some component of the projectile. Consequently, it is imperative for dynamic analysis that the FE model faithfully reproduces the correct dynamic response of the projectile. This paper examines the use of EMA in the development of an FE model of the PXR6353 instrumented projectile for use in dynamic analysis.

BACKGROUND

The basic goal of dynamic analysis is the determination of the dynamic response of a structure to a defined forcing function. For complex structures this often entails the development of an appropriate FE model. The discretized FE model yields a system of n equations describing the dynamic behavior of the structure. These equations can be written in the form
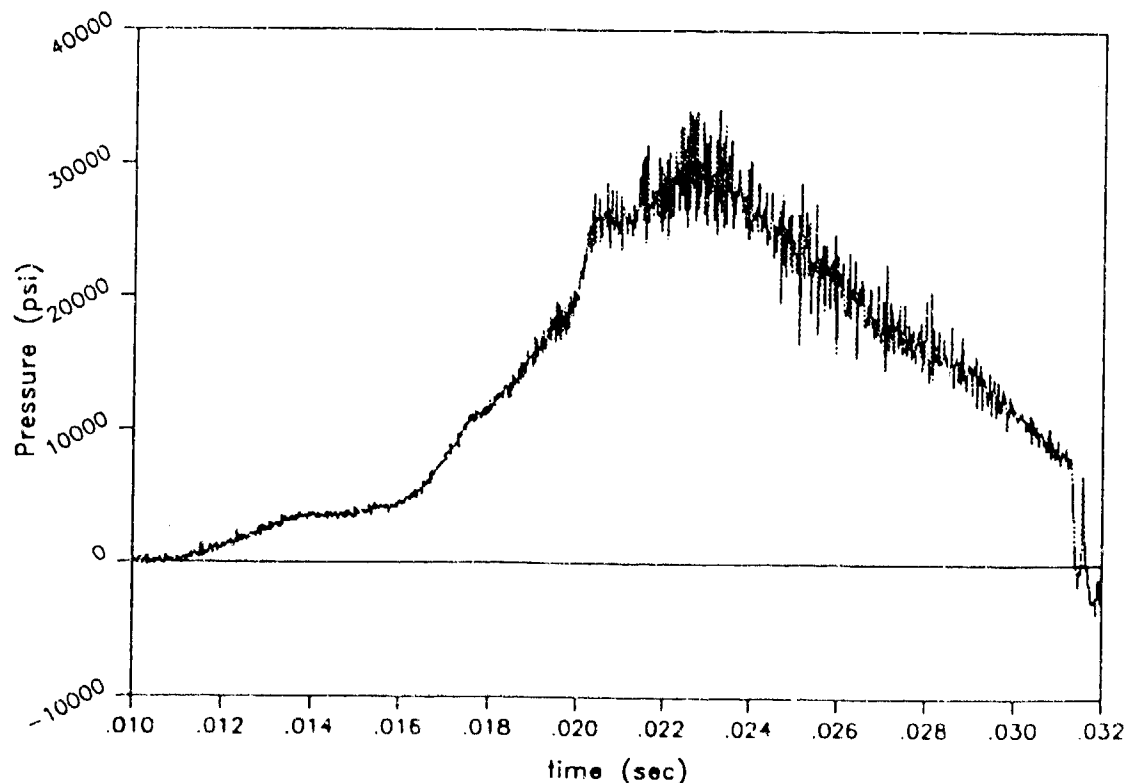
Figure 1. LP Pressure History

$$M \ddot{x}(t) + C \dot{x}(t) + K x(t) = f(t) \qquad (1)$$

where M, C, and K are the mass, damping and stiffness matrices, $f(t)$ is a defined forcing function, and $x(t)$ is the response. For linear structural analysis M, C, and K are symmetric and time invariant. Equation 1 can be rewritten in the Laplace domain as

$$s^2 M X(s) + s C X(s) + K X(s) = F(s) \qquad (2)$$

$X(s)$ and $F(s)$ are the transformed responses and forces, respectively. This equation represents an eigenvalue problem. For lightly damped structures, it is not unusual to neglect the damping and instead consider undamped free vibration response. The nontrivial solution of for this case is given by

$$\left| s^2 M + K \right| = 0 \qquad (3)$$

Solution of Equation 3 yields n natural frequencies, $s_n = j\omega_n$, and n modal vectors Ψ_n. These can then be used in a normal mode analysis to solve the forced vibration problem given by Equation 1. Also, the predicted natural frequencies and mode shapes can be compared with the corresponding experimentally determined quantities to determine the accuracy of the FE model.

The experimental determination of the natural frequencies and modal vectors constitutes EMA [6]. As with FEA, EMA starts with a system of equations written as in Equation 2. However, M, C, and K are now unknown. Instead, the response, $x(t)$, and the applied load, $f(t)$, vectors are the known quantities. Accordingly, neglecting damping, Equation 2 is rewritten as

$$B(s) X(s) = F(s) \qquad (4)$$

where $B(s) = Ms^2 + K$.

The transfer function $H(s)$ is then defined as

$$H(s) = [B(s)]^{-1} \qquad (5)$$

Therefore, Equation 4 can be expressed as

$$H(s) F(s) = X(s) \qquad (6)$$

The transfer function $H(s)$ relates the input to the system, $F(s)$, to the output, $X(s)$. In component form, Equation 6 relates the input at some point q to the output at a point p by the relation

$$H_{pq}(s) = \frac{X_p}{F_q} \qquad (7)$$

The individual components of $H(s)$, H_{pq}, are assumed to have the form

$$H_{pq} = \sum_{r=1}^{n} \left[\frac{Q_r \, \Psi_r \, \Psi_r^T}{s - s_n} + \frac{Q_r^{*} \, \Psi_r^{*} \, \Psi_r^{*T}}{s - s_n^{*}} \right] \qquad (8)$$

where Q_r is a scaling factor, Ψ_r is the rth modal vector, and $s_r = j\omega_r$ is the rth pole. This representation is based upon a simple one degree-of-freedom oscillator [7].

Assumptions in the derivation of Equation 1, and consequently Equation 6 imply that the entire transfer function matrix $H(s)$ can be reconstructed by measuring the transfer functions, Equation 7, of a single row or column of $H(s)$. To increase accuracy, it is common practice though to measure several rows or columns. These data are then used to determine the natural frequencies and modal vectors by curve fitting the data. Also, if multiple modes at a single frequency are to be resolved, then multiple rows or columns must be measured. As mentioned, agreement between the predicted and measured natural frequencies, ω_r, and the corresponding mode shapes Ψ_r is an indication of the accuracy of the FE model.

ANALYSIS

Experimental Modal Analysis

The PXR6353 instrumented projectile was analyzed both as a complete structure and as three separate components. In this paper discussion is limited to the results obtained for the separate components. The subdivision of the projectile into three components was made because these components represent logical substructures of the overall projectile. Section A consisted of the boattail and motor body, Figure 2. Section B was the body section, Figure 3. Section C consisted of all parts between the antenna section and nose inclusive, Figure 4. Section B was the simplest component consisting essentially of a cylinder with one end closed, while Section C was the most complex. All modal tests conducted simulated "free-free" boundary conditions by suspending the test sections by elastic cords with the axis of symmetry of the sections oriented horizontally. The "rigid body" frequencies for the test sections are substantially below 150 Hz which is well below the first flexural modes of all the sections. Data was collected in the frequency range of 0 to 10,000 Hz. Mode Indicator Functions (MIF) are shown in Figures 5-7 for Sections A, B, and C, respectively. Minimums in the value of the MIF indicate the location of a potential modes. The results of the modal test are summarized in Table 1.

Finite Element Analysis

The EMA results were used to validate both 2D and 3D FE models of the PXR6353 instrumented projectile. For the 2D model, four-node axisymmetric harmonic elements were used, while eight-node trilinear hexahedron elements were used in the 3D FE model [8]. The 2D and 3D FE meshes were generated such that in the r-z plane the mesh pattern was

Table 1. EMA and FEA Modal Results

	Mode	Frequency (Hz)			% Error		Damping (%)
		EMA	FEA				
			2D	3D	2D	3D	
Section A	1	1823	1941	1966	6.5	7.8	0.145
	2	4265	4748	4900	11.3	14.9	0.087
	3	5489	5717	5820	4.2	6.0	0.232
Section B	1	1897	1957	1984	3.2	4.6	0.207
	2	4679	4902	5075	4.8	8.5	0.142
	3	6111	6199	6332	1.4	3.6	0.122
Section C	1	1613	1696	1731	5.1	7.3	0.246
	2	3448	-	2508	-	-27.	4.00
	3	4034	4225	4345	4.73	7.7	0.583
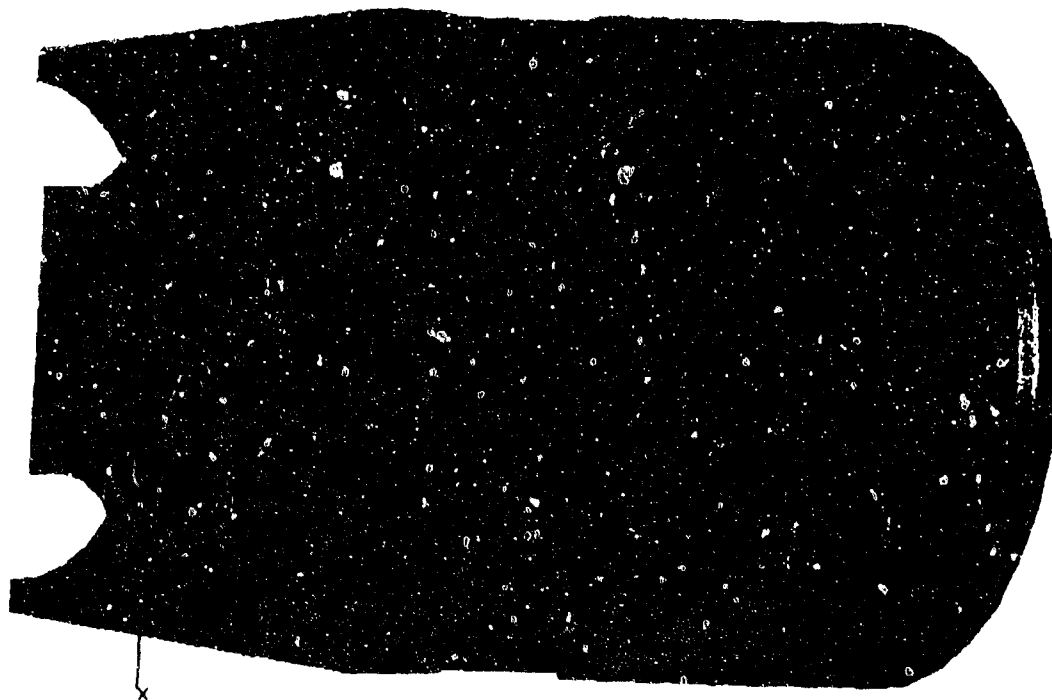
Figure 2. FEA Solid Model of Section A
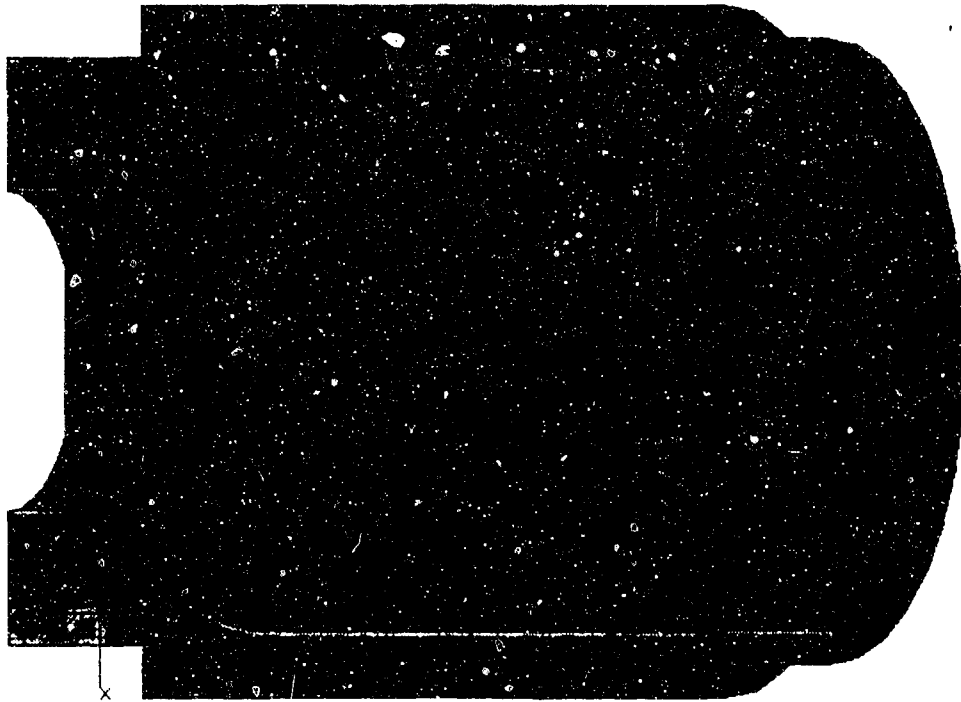
Figure 3. FEA Solid Model of Section B

Figure 4. FEA Solid Model of Section C
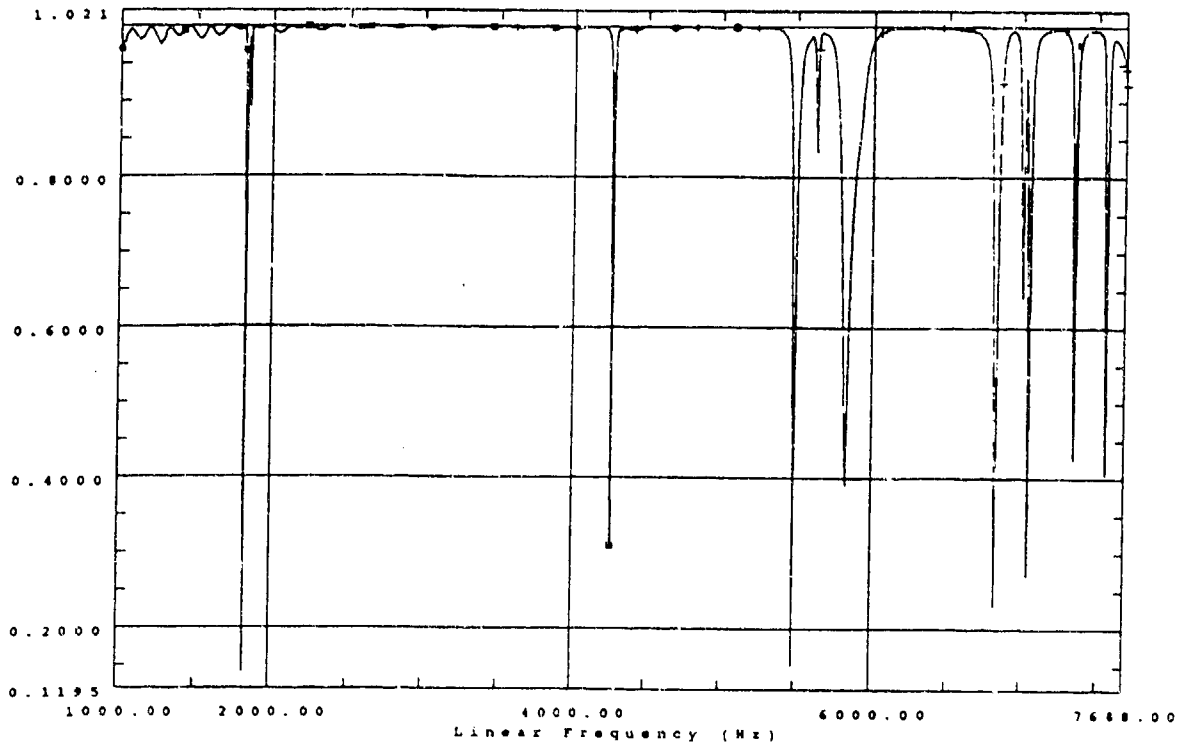
Figure 5. EMA MIF for Section A
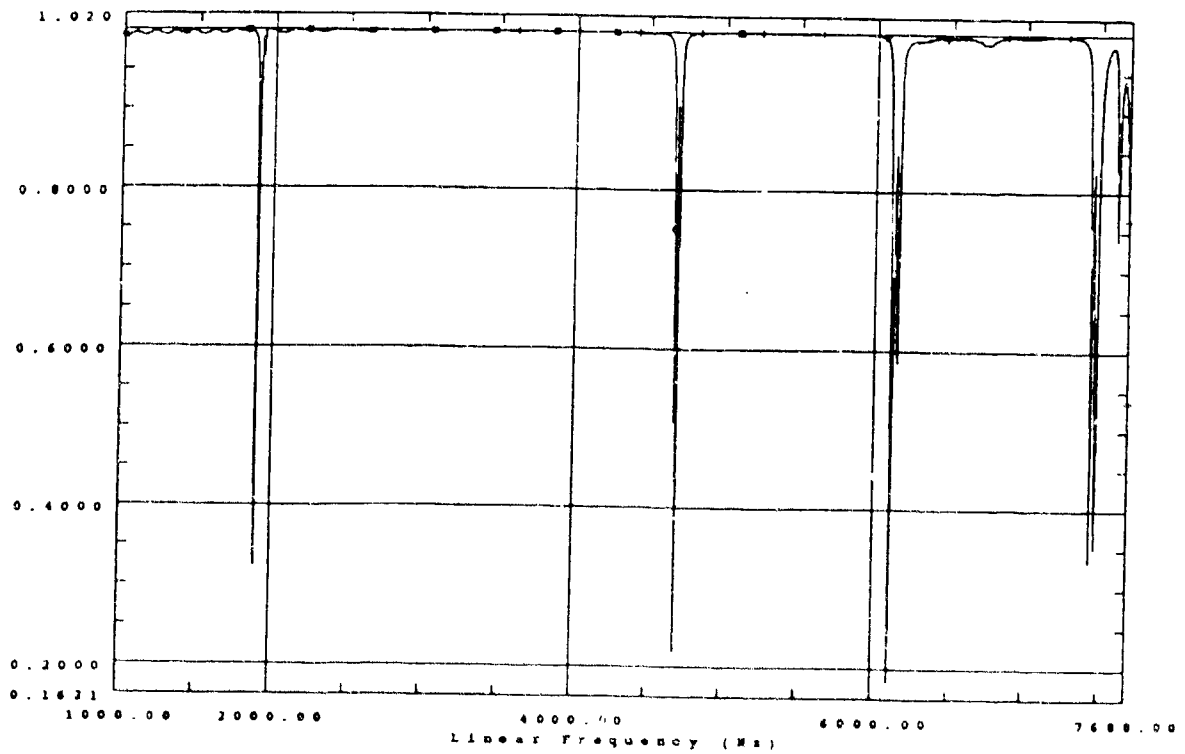
Figure 6. EMA MIF for Section B
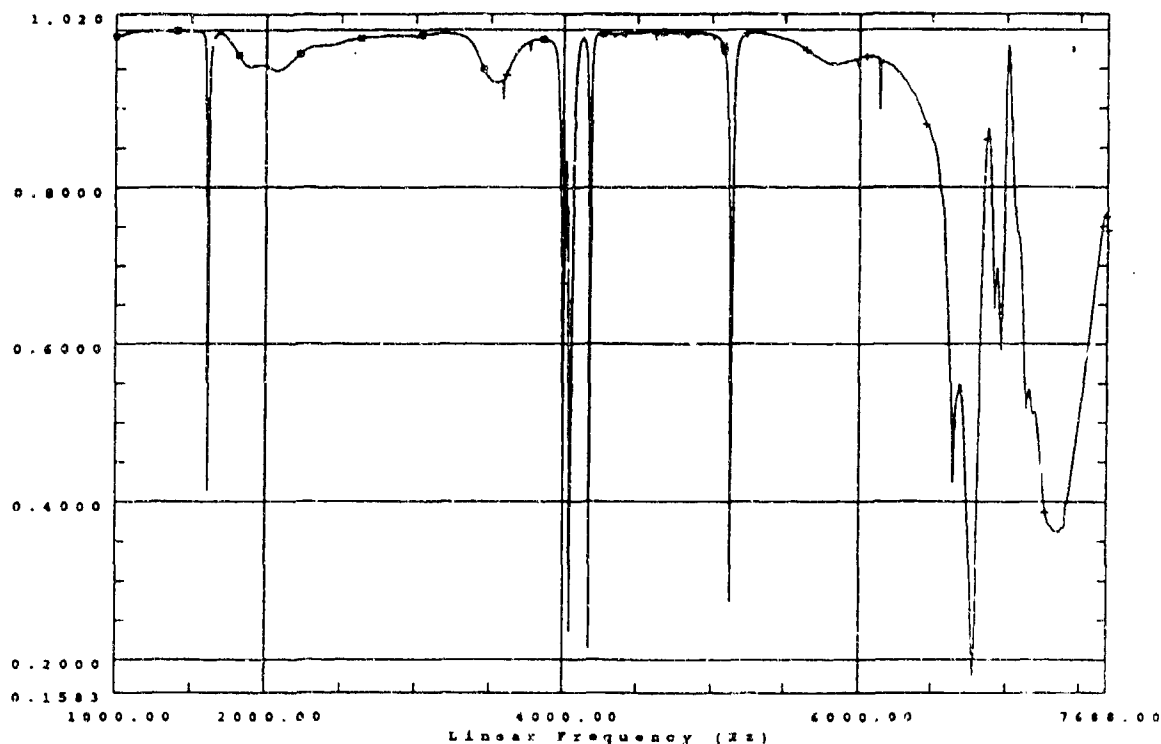
Figure 7. EMA MIF for Section C

the same. The mesh for Section B is shown in Figure 8 for illustration. The harmonic elements allow the specification of the mode shape in the circumferential direction by specifying the number of circumferential waves. The 3D FE model used 24 elements per 180 degrees in the circumferential direction. This number was arrived at by considering the effect of increasing the number of circumferential elements upon the frequency predictions for a simple hollow cylinder. The results of this cylinder problem are summarized in Table 2. It is seen that 24 circumferential elements give reasonable agreement with the same problem using quadratic elements. While increasing the number of circumferential elements would increase the accuracy, the results of this simple test problem indicate that the gains in accuracy would be minimal.

DISCUSSION

Frequency Comparisons

As mentioned, Section A consisted of the boattail and the motor body components of the projectile. The mass of the model for this section is 7,424.1 grams while the actual mass is 8,065 grams. The difference in mass is primarily due to the absence of the rotating band in the FE model. Inclusion of the rotating band mass in the FE model increases the model's mass to 7,935 grams. This indicates the model is approximately 1.6% lighter than the actual structure. In this study, this is considered an acceptable error. The FE frequency predictions
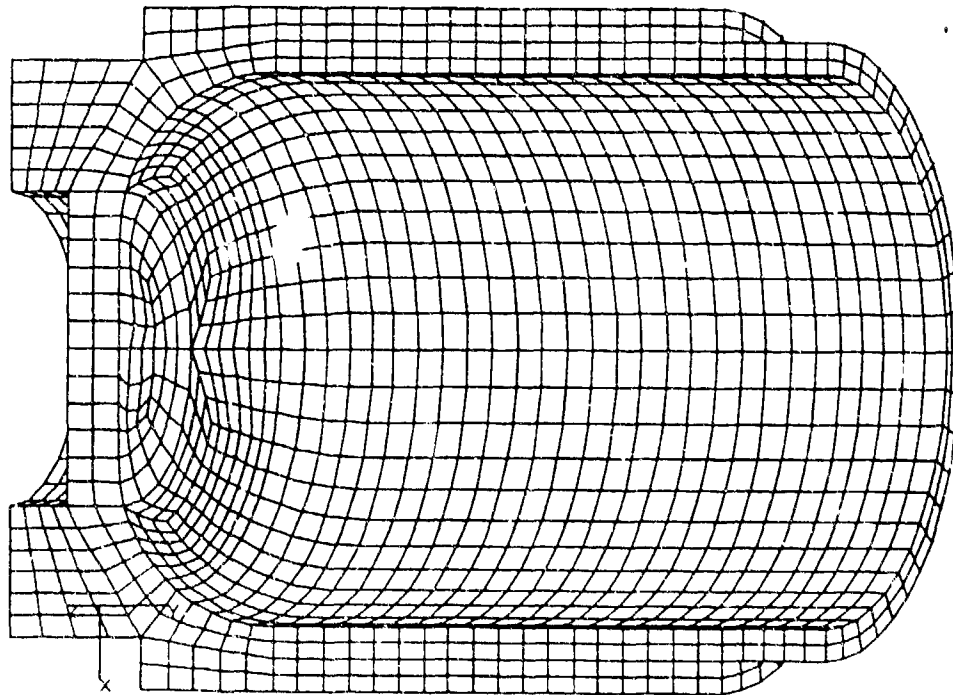
Figure 8. FE Mesh of Section B

Table 2. Convergence Examples

Element Type	# Circ. Elements	Frequency					
		Mode					
		1	2	3	4	5	6
Linear	6	1291	1335	1516	999	1959	2760
	12	853	873	1007	1012	1439	2236
	24	820	831	943	1015	1360	2145
Quadratic	6	1093	1098	1172	1001	1481	2085
	12	835	843	944	1003	1316	1983
	24	814	823	926	1004	1304	1976

are also included in Table 1. It is seen that the predicted frequencies are in good agreement with the experimental values.

The mass of the FE model of Section B is 11,024.2 grams while the actual mass of this section is 10,735 grams which constitutes an error of 2.7%. The difference in mass is due to the presence of transverse thru-holes in the base of Section B which are not included in the FE model. However, because the location of this extra mass in the FE model is in the base which is relatively rigid compared to the rest of the structure, the predicted natural frequencies are in good agreement with the experimentally measured frequencies.

Section C was the most complex section of the three sections. Each individual component of Section C though could be easily modelled. Consequently, the mass estimate is very good. The estimated mass is 10,033 grams while the measured mass is 10,007 grams which is an error of only 0.26%. This agreement is fortuitous since it is impossible to disassemble Section C to determine exactly which internal components are present. The close agreement between the FE model's mass and the actual structure's mass provides a measure of confidence that all internal components are included in the FE model. Despite the very good mass estimate, the predictions of the natural frequencies of Section C are not as accurate as might be expected. In particular, the second natural frequency is in error by -27.3%. It has since been determined that Section C was obtained from a round which had been used in a prior firing test and had sustained some internal damage. Therefore, it is highly unlikely that the FE model represents the actual internal boundary conditions between the internal components of this particular Section C correctly. Such errors in the internal boundary conditions can easily cause the large error in the predicted value of the second natural frequency since the second mode involves primarily components in the potentially damaged part of Section C.

Mode Shapes

One method of assessing the accuracy of the mode shapes determined using EMA is the modal assurance criterion (MAC) [9]. Ideally, for linearly dependent modal vectors, the MAC value should approach unity, while for linearly independent modal vectors the MAC value approaches zero. However, there are other considerations that can also lead to MAC values of zero or one [9]. Some of these reasons include non-stationarity of the structure, nonlinearity of the structure, noise, and an invalid modal parameter estimation. During the EMA, appropriate precautions were taken to minimize these possibilities so that the computed MAC values should indicate whether two modal vectors are linearly independent. The MAC values for the first three modes of Sections A, B, and C are shown in Tables 4-6. It is seen that the experimentally determined mode shapes used to validate the FE model are orthogonal. The fundamental mode shapes determined by EMA for these sections are shown Figures 9-11. The corresponding mode shapes predicted by the FEA are shown in Figures 12-14. The close agreement between the predicted and measured mode shapes is evident.

Table 3. MAC for Section A

Mode	1	2	3
1	1		
2	.001	1	
3	.331	.004	1

Table 4. MAC for Section B

Mode	1	2	3
1	1		
2	.001	1	
3	.331	.004	1

Table 5. MAC for Section C

Mode	1	2	3
1	1		
2	.001	1	
3	.061	.001	1
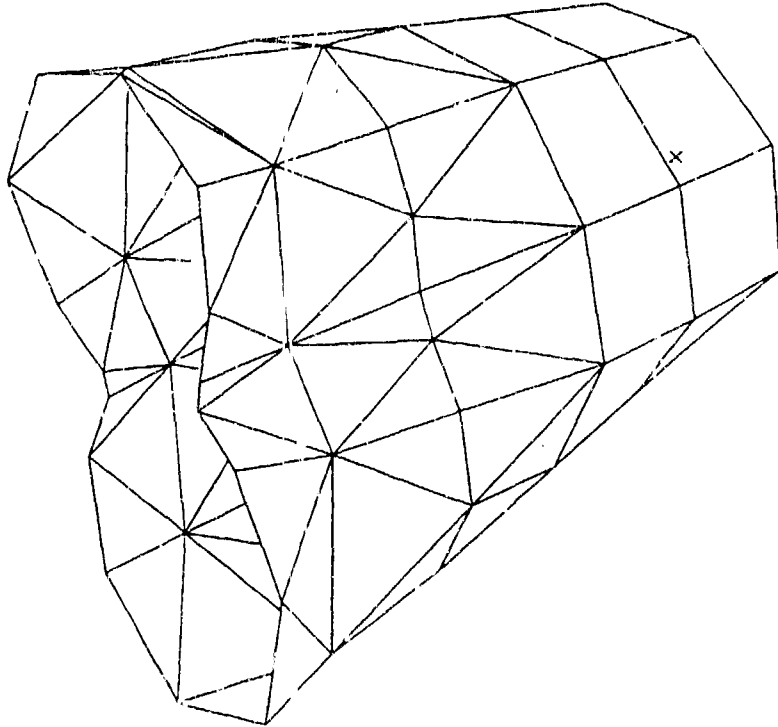
Figure 9. EMA Section A, Mode 1
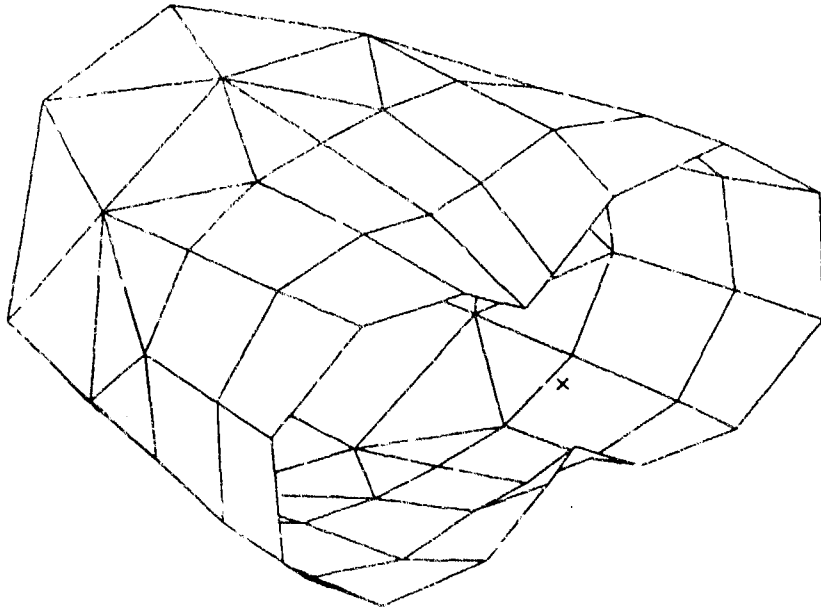
Figure 10. EMA Section B, Mode 1
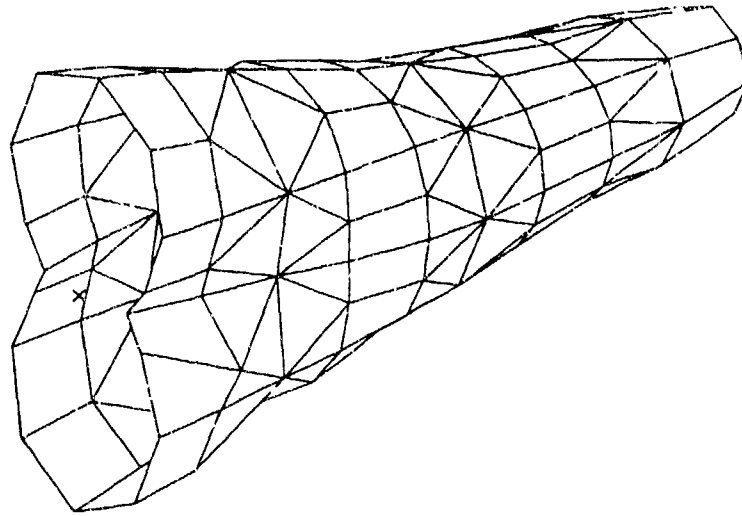
Figure 11. EMA Section C, Mode 1
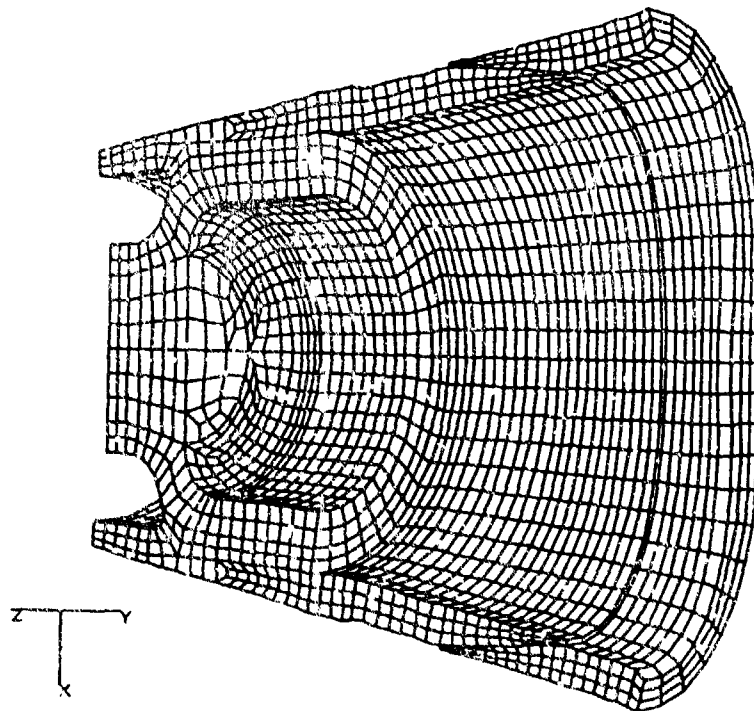
Figure 12. FEA Section A, Mode 1
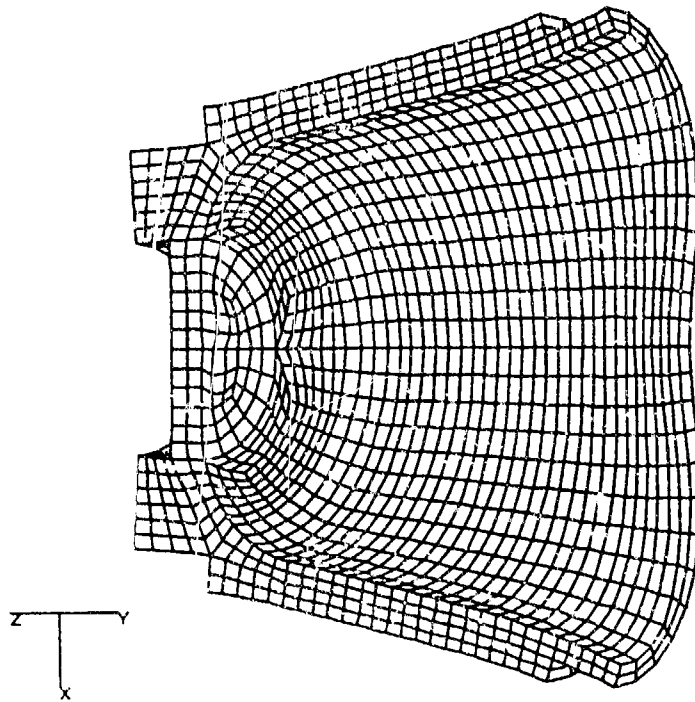
Figure 13. FEA Section B, Mode 1
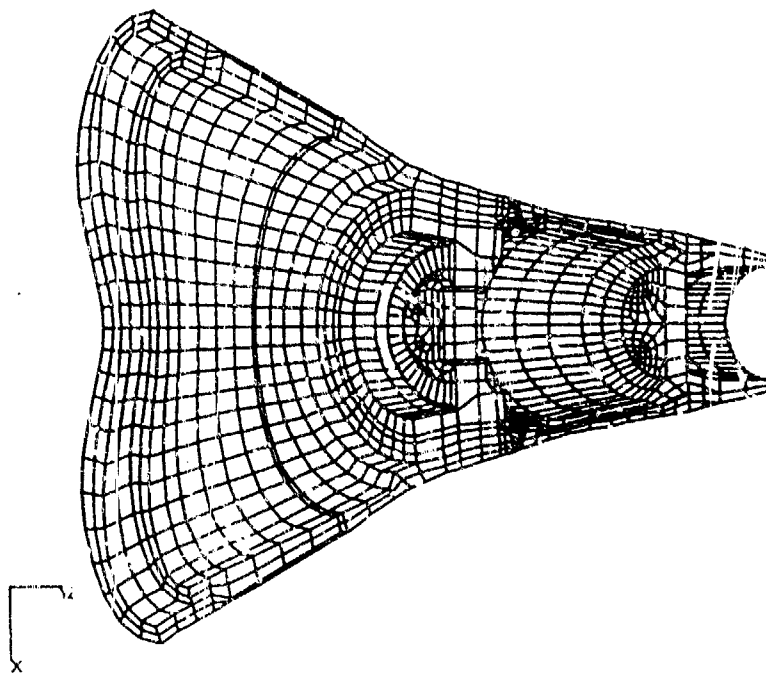
Figure 14. FEA Section C, Mode 1

CONCLUSIONS

The natural frequencies and mode shapes of the PXR6353 instrumented projectile and its components have been determined using EMA. Linear independence of the mode shapes obtained by EMA has been verified. These experimentally determined natural frequencies and mode shapes have been used to validate an FE model of this projectile. The agreement between the FEA and EMA results indicate that an acceptable FE model has been developed. The FE model can therefore be used with confidence to predict the structural response of the projectile when subjected to the LP interior ballistic environment.

REFERENCES

1) Bender, James M. and Burns, Bruce P., Dome Bases for Expellable-Munitioned and Saboted Projectiles, U.S. Army BRL-MR-3397, Aberdeen Proving Ground, Md, October, 1984.

2) Kaste, R.P. and Wilkerson, S.A., An Improved Sabot Design and DYNA3D Analysis for the XM900E1 Kinetic Energy Projectile, U.S. Army BRL-TR-3359, Aberdeen Proving Ground, Md, June 1992.

3) Rabern, D.A. and Bannister, K.A., Finite Element Models to Predict the Structural Response of 120-mm Sabot/Rods During Launch, Proceedings of the 6th U.S. Army Symposium of Gun Dynamics, Tamiment, Pa, May 1990.

4) Rabern, D.A., Numerical Simulation of Gun-Launched Kinetic Energy Projectiles Subjected to Asymmetric Projectile Base Pressure, 13th International Symposium on Ballistics, Stockholm, Sweden, June 1992.

5) Sorensen, Brett R., Finite Element Optimization of a Sabot for Use with Tungsten and Uranium Penetrators, 13th International Symposium on Ballistics, Stockholm, Sweden, June 1992.

6) Ewing, D.J., Modal Testing: Theory and Practice, John Wiley and Sons, Inc., New York, 1984.

7) Allemang, Randall J., Vibrations: Analytical and Experimental Modal Analysis, Structural Dynamics Research Laboratory Report, UC-SDRL-SN-20-263-662, University of Cincinatti, Cincinatti, Oh, 1992.

8) DeSalvo, Gabriel J. and Gorman, Robert W., ANSYS Engineering Analysis System User's Manual Vol I and II (Rev 4.3a), Swanson Analysis Systems, Houston, Pa., May 1989.

9) Allemang, R.J. and Brown, D.L., A Correlation Coefficient for Modal Vector Analysis, 1st International Modal Analysis Conference, Orlando, Fl., November 1982.

TITLE: Experimental Measurements of the Blast Pressure Profile for 20mm Perforated Muzzle Brake Designs

Douglas S. Savick
U.S. Army Research Laboratory
Propulsion and Flight Division
Aberdeen Proving Ground, Md 21005

ABSTRACT:

Pressure measurements were recorded at the Weapons Technology Directorate (WTD) of the Army Research Laboratory to verify predictions of a blast model used at Benet Weapons Laboratory (BWL). An array of eleven piezoelectric gages was placed in a vertical line perpendicular to the gun barrel and positioned at various locations behind the muzzle during the testing of two perforated muzzle brakes. The two muzzle brakes were designed and fabricated to fit on to a 20mm Mann barrel. The two brakes were compared to a third device with no perforations that served as a baseline. The first muzzle brake was a scaled down version of the EX35 and the second was a special design that had two rows of holes relocated between 7.5 and 9 calibers behind the muzzle ("split brake"). The pressure gage array was used to measure the portion of the blast profile that affected the area behind the gun.

This test was performed in conjunction with the first phase of the test where far field pressure measurements and blast wave shadowgraphs were obtained. This paper will present the characteristics of the blast pressure wave as it travels back along the gun axis correlating the pressure profile data with the shadowgraphs that were taken at the same locations. Results from the present blast profile test provided quantitative information for precise comparisons.

BIOGRAPHY: Douglas S. Savick
PRESENT ASSIGNMENT:
Aerospace Engineer for the Army Research Laboratory

PAST EXPERIENCE:
Began career with the Ballistic Research Laboratory as a co-op student and upon graduation returned there to a fulltime position

DEGREES HELD:
B.S., Aerospace Engineering, University of Cincinnati, 1987

Experimental Measurements of the Blast Pressure Profile for 20mm Perforated Muzzle
Brake Designs

Douglas S. Savick
U.S. Army Research Laboratory
Propulsion and Flight Division
Aberdeen Proving Ground, Md 21005

1. Introduction

Pressure measurements were recorded at the Weapons Technology Directorate (WTD) of the Army Research Laboratory to verify predictions of a blast model developed at Benet Weapons Laboratory (BWL) [1]. An array of eleven piezoelectric gages was placed in a vertical line perpendicular to a 20mm gun barrel and positioned at various locations behind the muzzle during the testing of two perforated muzzle brakes. The pressure gage array was used to measure the portion of the blast profile that affected the area behind the gun. The eleven gages were set at certain increments from the barrel's exterior wall.

This test was performed in conjunction with the first phase of the test where far field pressure measurements and blast wave shadowgraphs were taken [2]. This report will include the blast pressure data in comparison with the shadowgraphs that were taken at or about the same locations. The results from the blast profile test were useful in providing quantitative information for precise comparisons to the BWL's blast model [1].

2. Setup

The test was performed at WTD's indoor Aerodynamics Range. A schematic drawing of the test setup is shown in Figure 1. The firings and measurements took place in an anechoic chamber to eliminate reflecting blast waves that strike the range walls near the gun, as seen in the photograph of the test setup (Figure 2).

Two muzzle brakes (devices 5 and 7) were tested and compared to a baseline device (device 1) that had no perforations (Figure 3). Each device was designed and fabricated to fit on to a 20mm Mann barrel that was threaded at the muzzle. Each device had the same dimensions (approx. 28 cm in length) aside from their individual hole patterns. Device 5 is the scaled down version of the 105 mm EX35 perforated muzzle brake design that is being supplied as government furnished equipment for the Armored Gun System, currently in full development. Device 7 was tested for the 105mm gun and is of special interest because of its unique design as being a "split brake" (two rows of holes are spaced upstream from the other perforations). The ammunition used for this test was Cartridge, 20mm, TP, M55A2.

An array of piezoelectric gages was mounted in a steel block that was fabricated into a wedge shape (see Figure 4). The wedge was used to assure that the flow of the blast wave was not obstructed or interfered with before reaching the gages. The gages were fixed in the the wedge to measure static pressure with their measuring surfaces positioned flush to the

surface that the flow passed over. The array was adjustable to incremental distances behind the muzzle for the test requirements. The array consisted of eleven gages that were postioned in a line perpendicular to the gun barrel with the first six gages positioned at increments of 12.7 mm (.5 in) from the barrel exterior and the remaining five were at increments of 25 mm (1 in). Nicolet oscilloscopes recorded and stored the required data.

3. Procedure

Pressure data were recorded for the three muzzle devices at various distances behind the muzzle. The pressure gage array was initially positioned over the original muzzle (muzzle location when devices are absent, as seen in Figure 5) and repositioned at predetermined locations behind the original muzzle after each device had been tested at that location. Each device had 2-4 rounds fired through it for each location to establish a valid sample for averaging. The pressure was recorded at the following locations behind the muzzle: 0 cm, 5 cm, 10 cm, 15 cm, 20 cm, 25 cm, 30 cm, 40 cm, and 50 cm. The data were reduced and peak overpressure was analyzed and compared.

4. Analysis

4.1 Blast Pressure and Shadowgraphs Figures 6-16 represent the peak overpressures of the three muzzle devices at specified locations along the gun. Each figure displays the peak overpressure of each individual probe beginning with probe 1 (Figure 6). From these figures, the strength of the peak pressure could be studied as the blast wave traveled behind the muzzle and away from the barrel. From these figures, the following was observed. The pressures for device 1 have a consistent pattern in every figure. Most of the blast travels ahead of device 1, therefore the pressure sensed by each probe behind the muzzle was low at each location. Devices 5 and 7 produced higher pressures behind the gun than device 1 due to the gases emanating from the sides.

When the peak overpressures are measured behind the muzzle from 10-50 cm, device 7 produced weaker pressures than device 5. From Savick [2], it is found that the interaction between the two blast waves of device 7 weaken the strength of the blast wave as it travels rearward of the muzzle. This interaction can be observed in the shadowgragh of the blast waves of device 7 taken after the projectile exited the device (Figure 17). The blast wave of the front vents that travels rearward is intercepted by the blast wave of the rear vents that is traveling forward.

In the region before 10 cm, device 7 had a stronger peak overpressure than device 5 (for probes 1-7). This was due to the probes being almost over top of the the rear vents of device 7. In this position, the gages were measuring pressure that traveled outwardly as well as towards the back. As the probes were positioned further rearward (10 cm and beyond), the gages measured only the part of the blast wave that traveled towards the rear of the gun.

To demonstrate the difference in blast waves of devices 5 and 7, shadowgraphs of each blast wave taken separately at approximately the same location along the gun barrel. Figure

47

18 shows the blast wave for device 5 and Figure 19 shows the blast wave from device 7. The blast wave from device 5 is thicker and more defined in strength than the blast wave of device 7.

4.2   Blast Overpressure and Blast Code Analysis   The experimental results were compared to analytical data produced by BWL's blast code [1]. The code calculated the peak overpressure of each pressure probe for four different locations behind the the muzzle. The locations include 0 cm, 15 cm, 30 cm, and 50 cm behind the muzzle. Figures 20-22 show the comparison of the calculated data with the corresponding experimental data.

The predictions seem to be more accurate for the locations that are further away from the muzzle (i.e. 30 and 50 cm) for all three devices. The pressures that were measured at or near the muzzle are a result of a more complex flow field than could be predicted. Device 7 (Figure 22) is especially complicated due to the holes of the "split brake" being much closer to the probes than the other devices. The pressures at the 30 and 50 cm positions for device 7 were also difficult to predict. It appears that the interaction between the two blast waves from the "split brake" have a larger effect on each other than could be predicted. The 30 and 50 cm predictions do become consistent with the experimental data at the probes 6 and 7 region.

5.   Summary and Conclusions

1. Device 1 showed little variation in peak overpressure for any probe and/or any location.

2. Device 7 had lower blast overpressures than device 5 from 10-50 cm.

3. The two vent areas of device 7 provided interactions between blast waves that lessened the rearward overpressure.

4. The shadowgraph for device 5 showed a thicker and stronger looking blast wave than the shadowgraph of the blast wave from device 7.

5. The blast code provided close predictions for each device at locations 30 cm and beyond.

6. The predictions that were made closer to the muzzle were not able to account for all of the complexities of that flow field region.
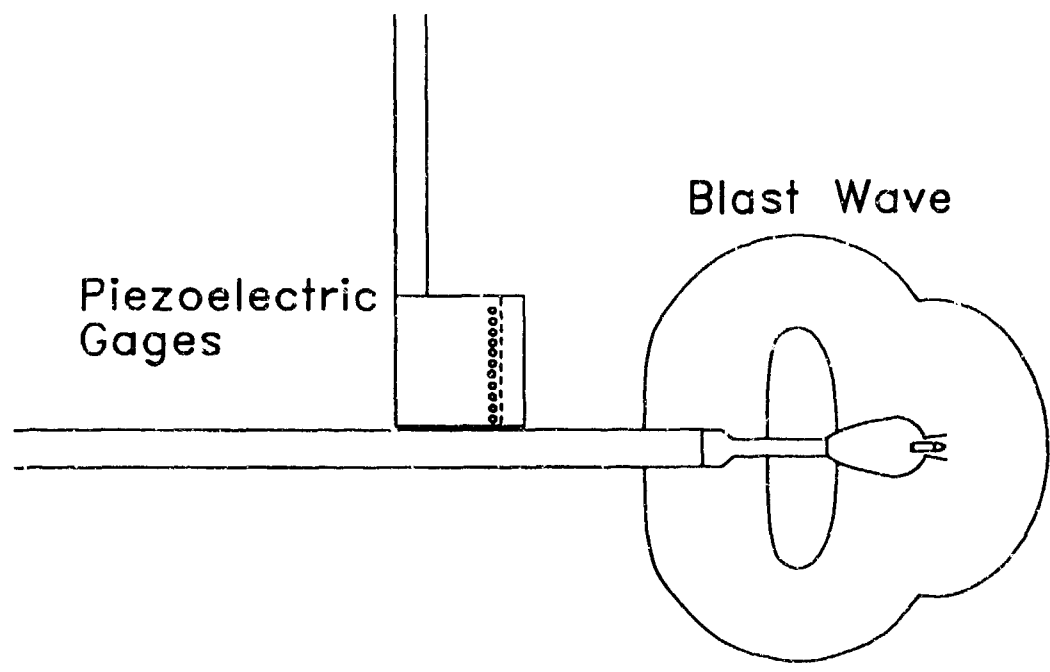
Figure 1. Schematic Drawing of Test Setup
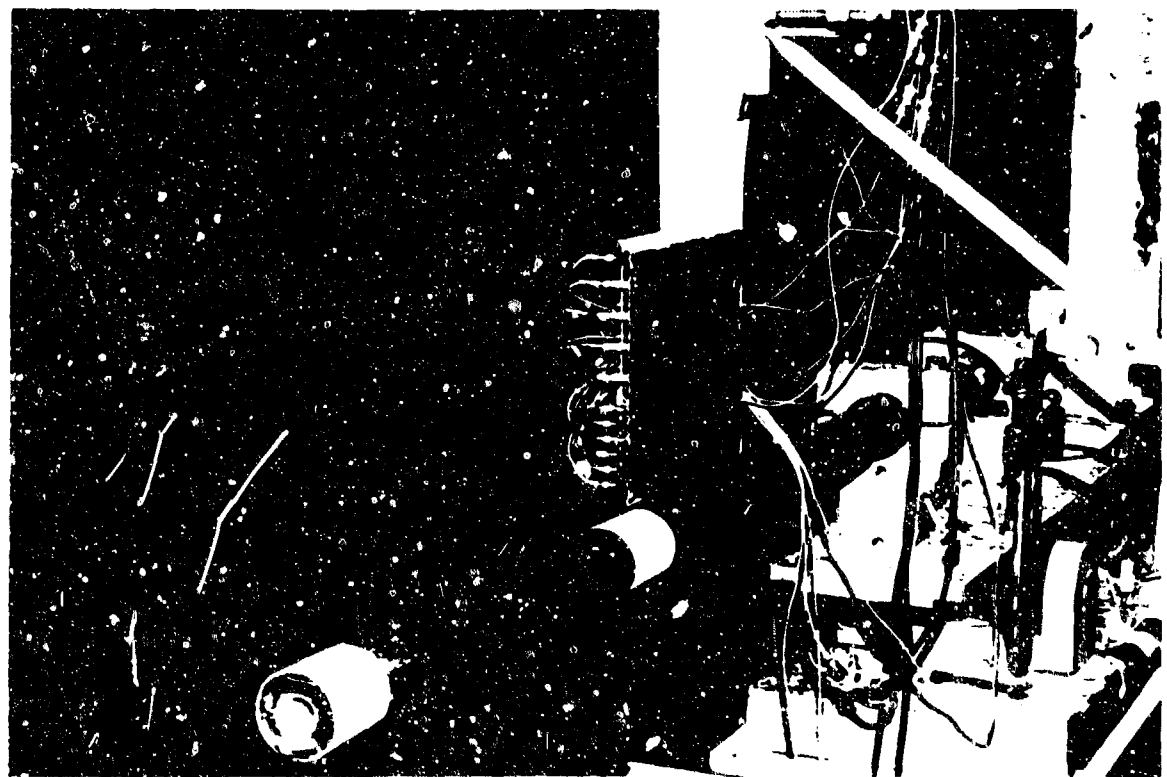
Figure 2. Photograph of Test Setup
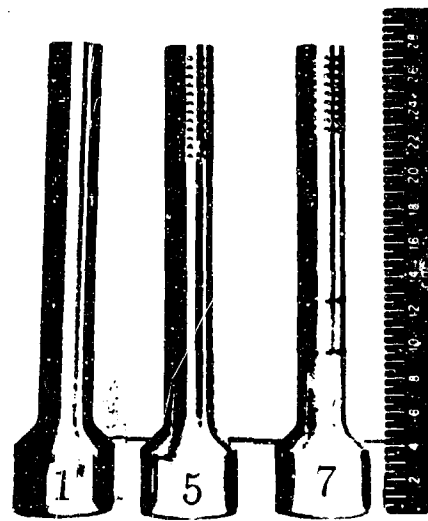
Figure 3. 20mm Perforated Muzzle Brake Devices
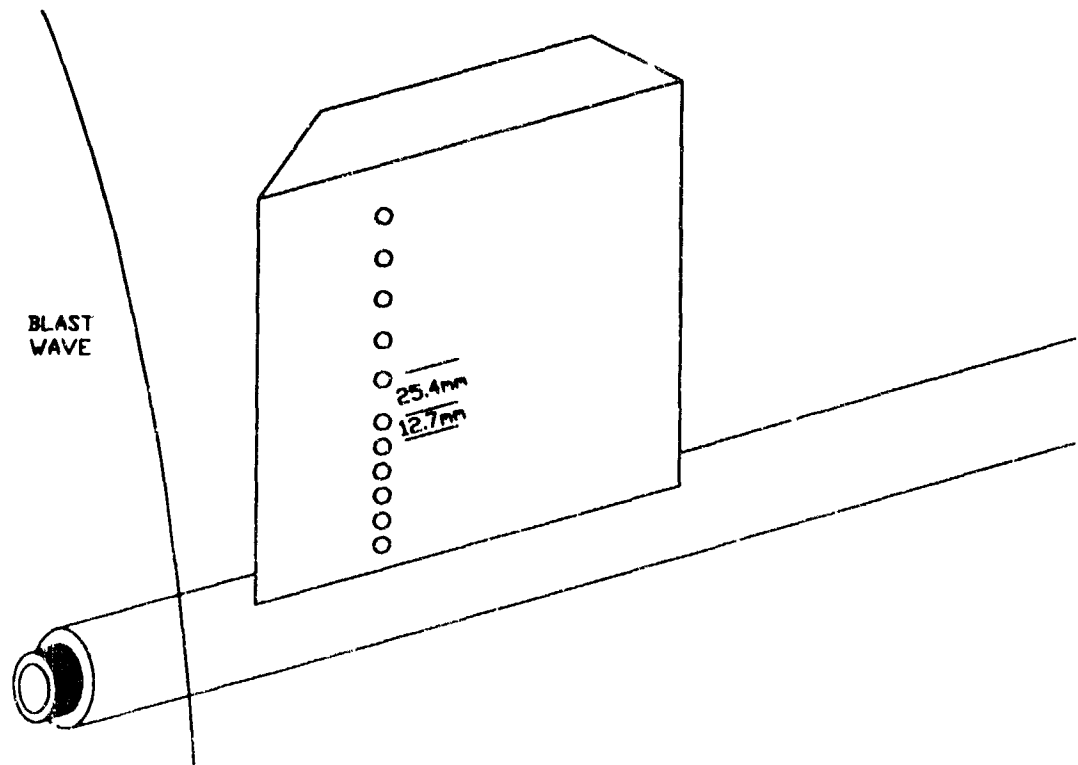
Figure 4. Piezoelectric Gages (Probes) Mounted in Steel Wedge.
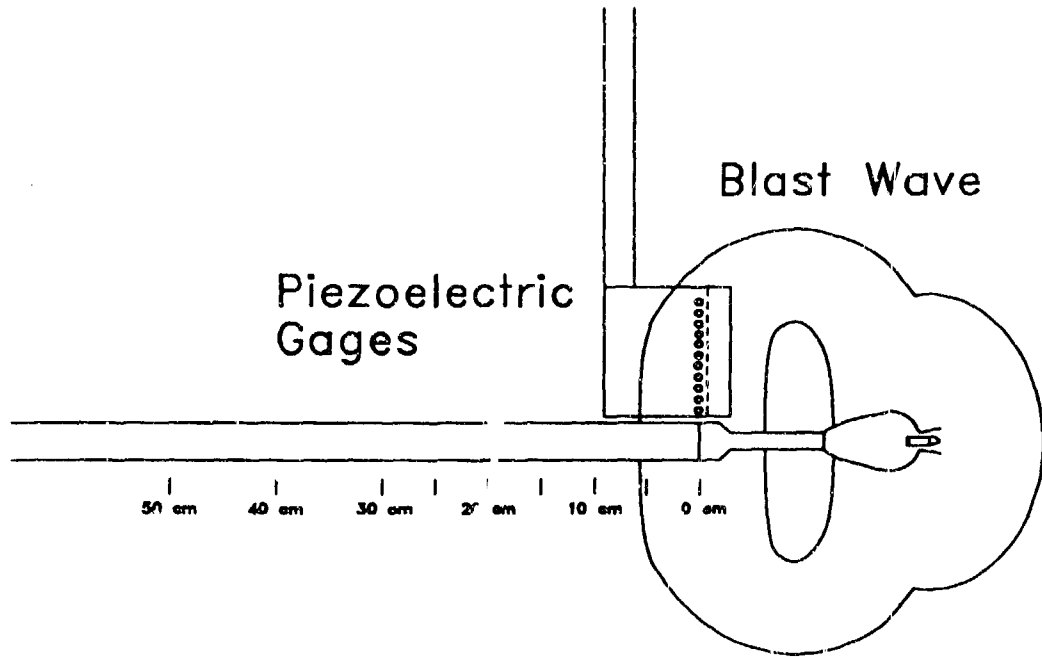
Figure 5. Schematic Drawing of Locations for Recording Overpressure.
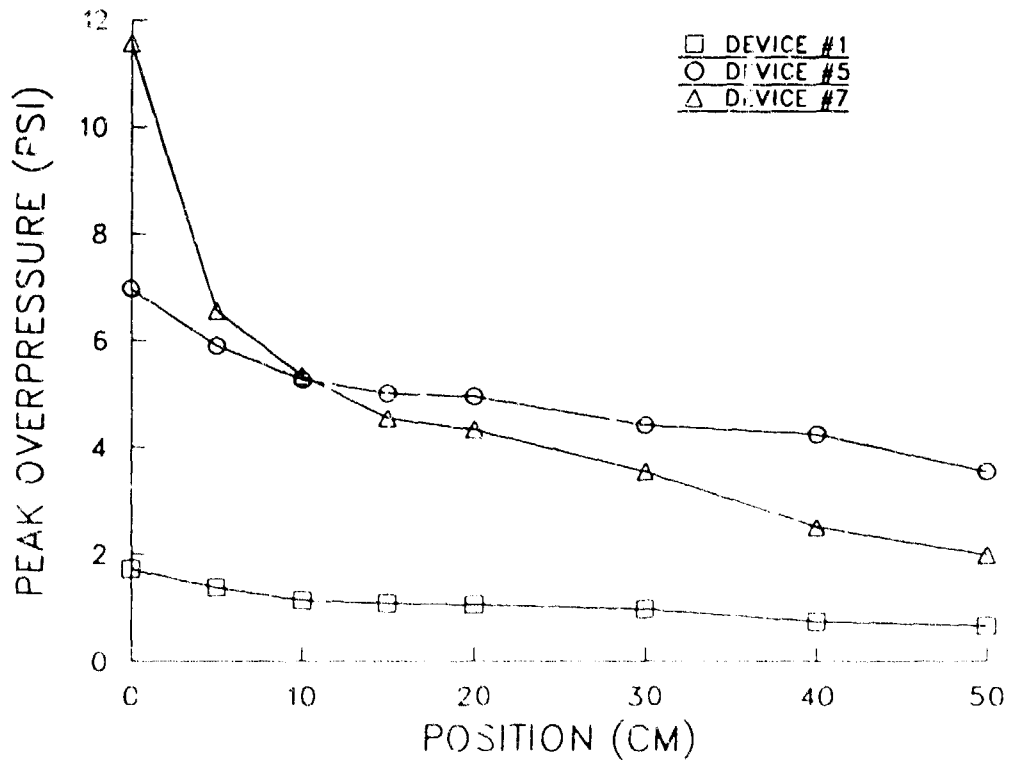
Figure 6. Peak Overpressure at Testing Locations for Probe 1.
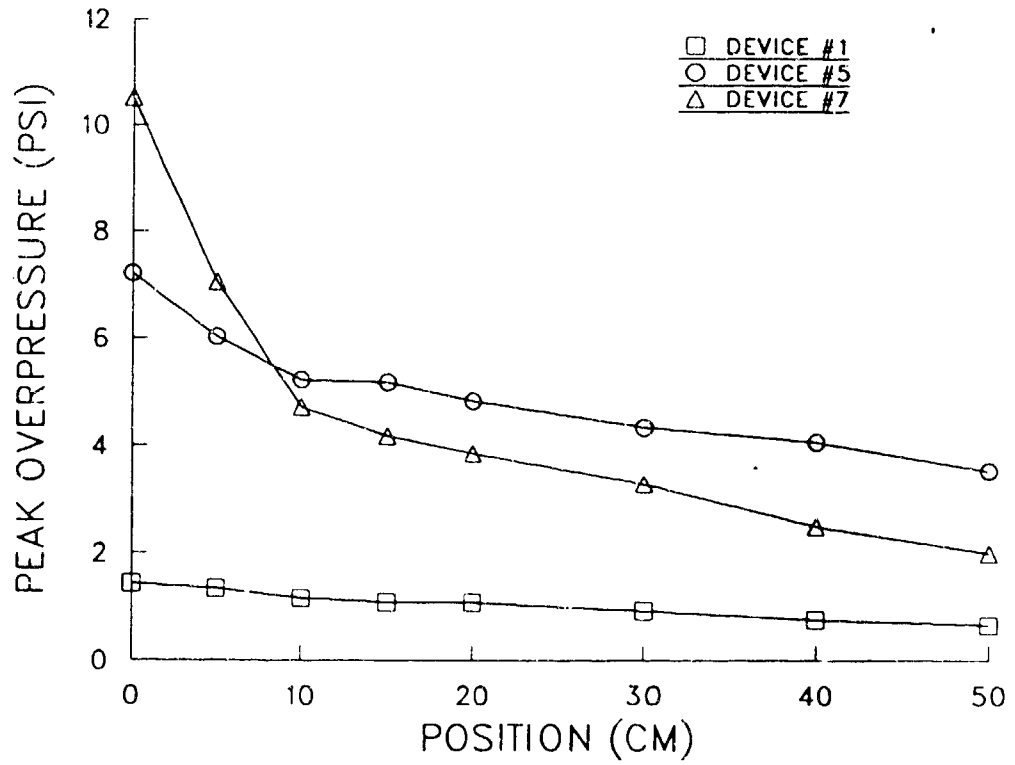
Figure 7. Peak Overpressure at Testing Locations for Probe 2.
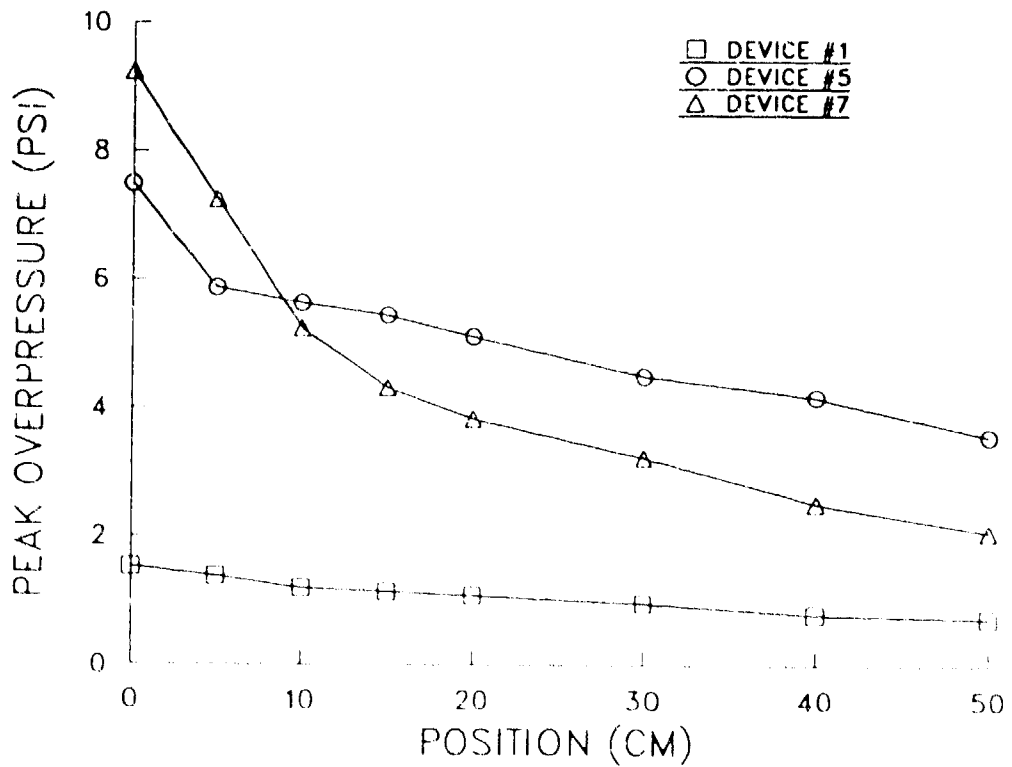
Figure 8. Peak Overpressure at Testing Locations for Probe 3.
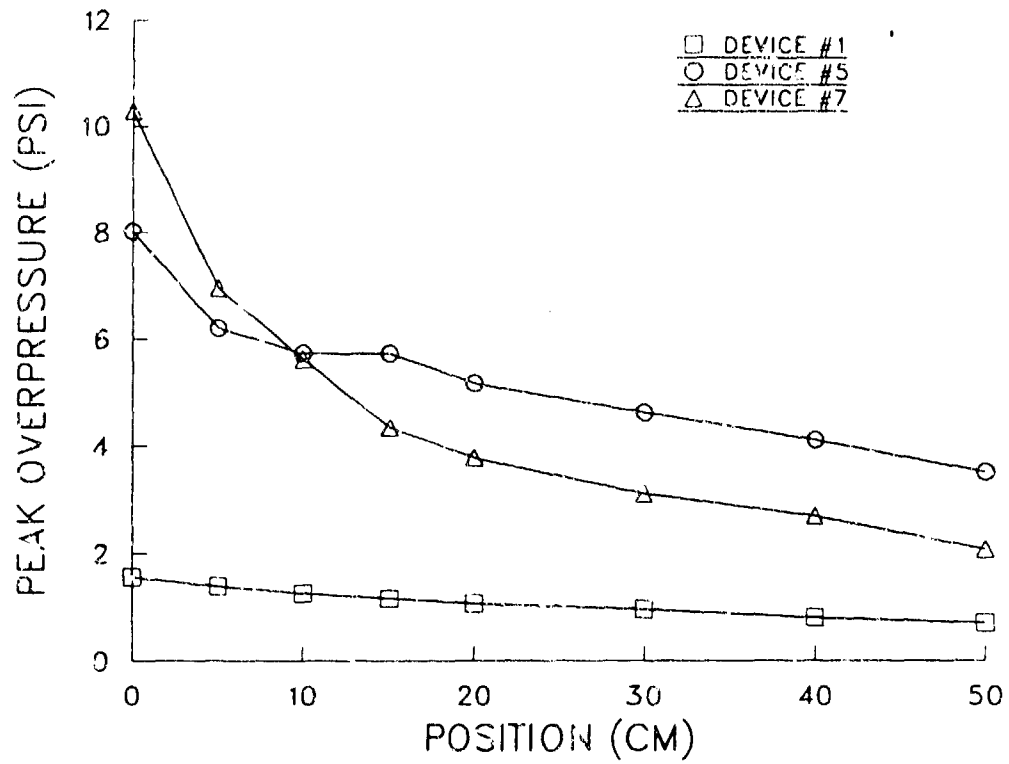
Figure 9. Peak Overpressure at Testing Locations for Probe 4.
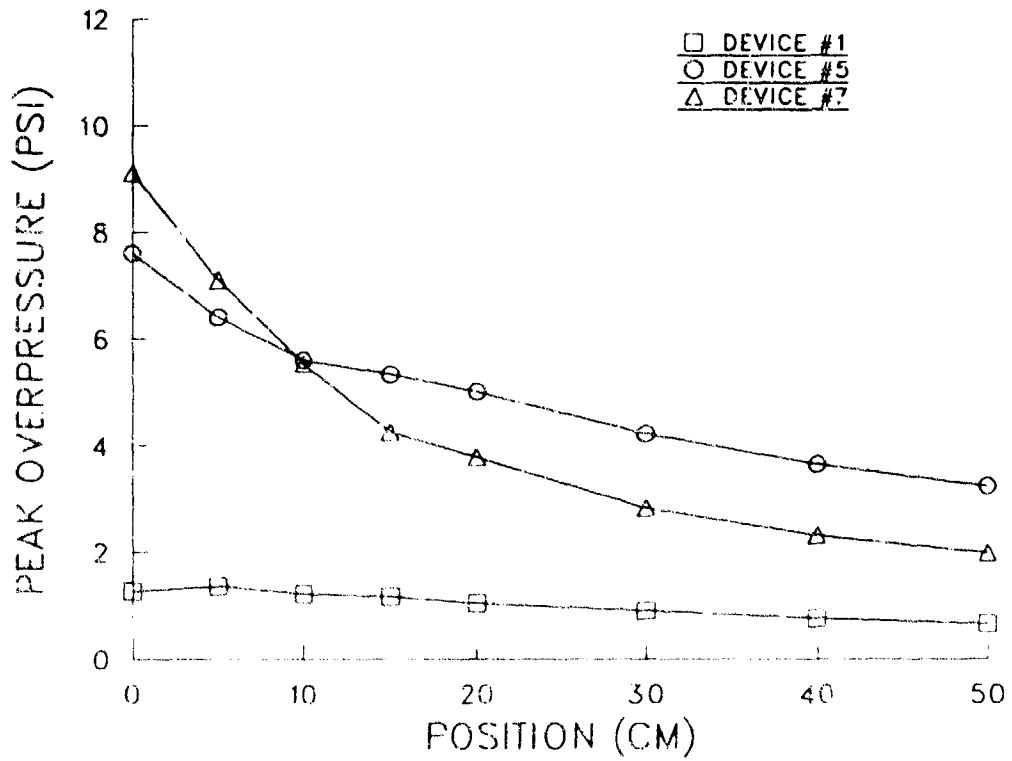
Figure 10. Peak Overpressure a. Testing Locations for Probe 5.
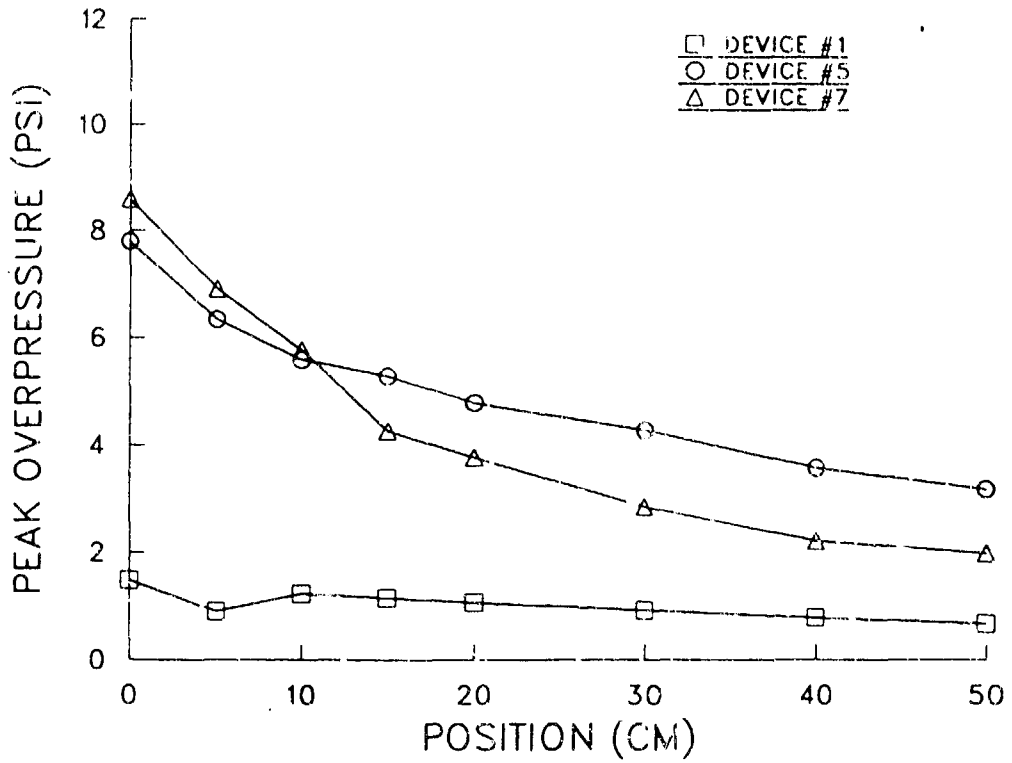
Figure 11. Peak Overpressure at Testing Locations for Probe 6.
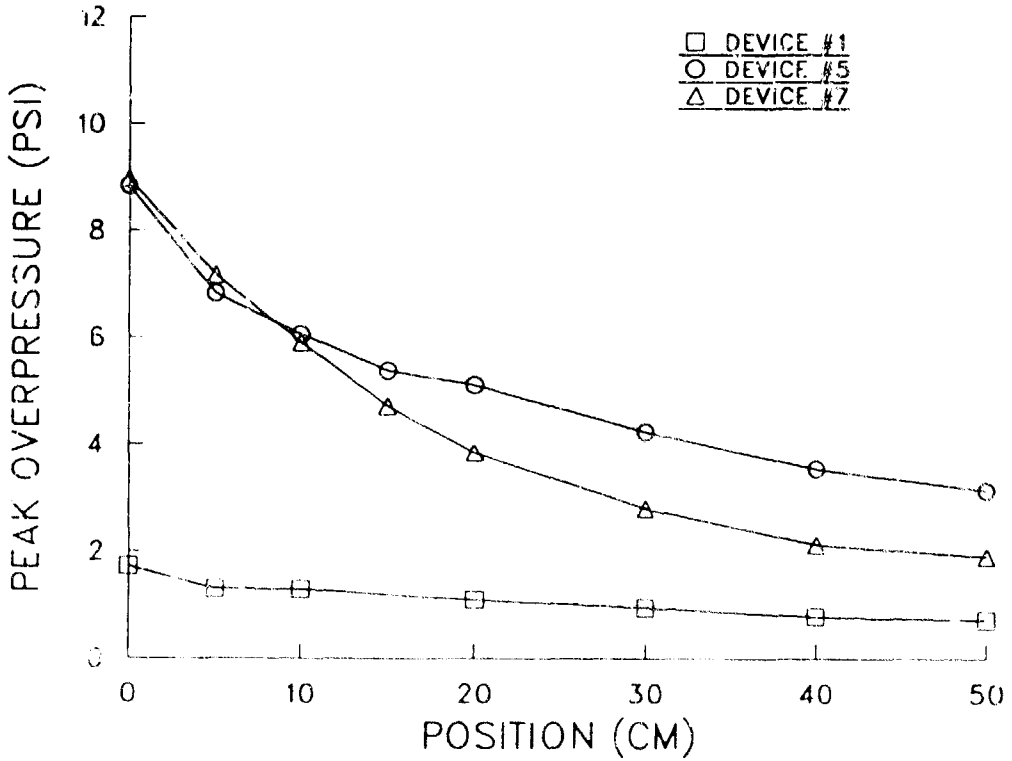
Figure 12. Peak Overpressure at Testing Locations for Probe 7.
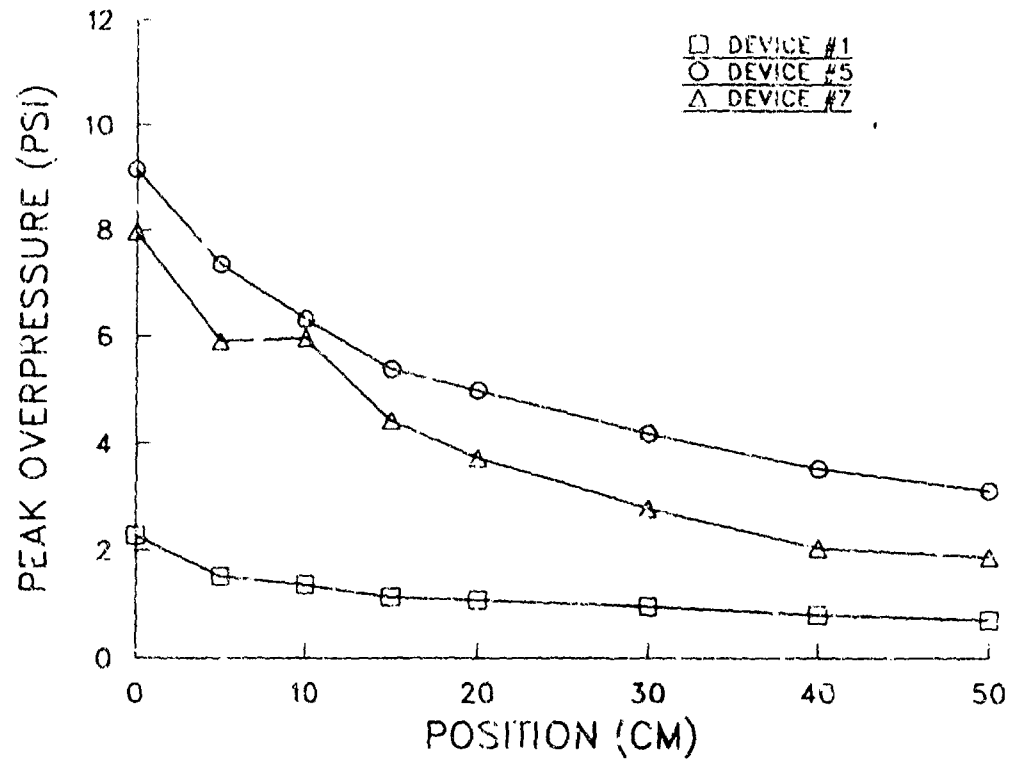
Figure 13. Peak Overpressure at Testing Locations for Probe 8.
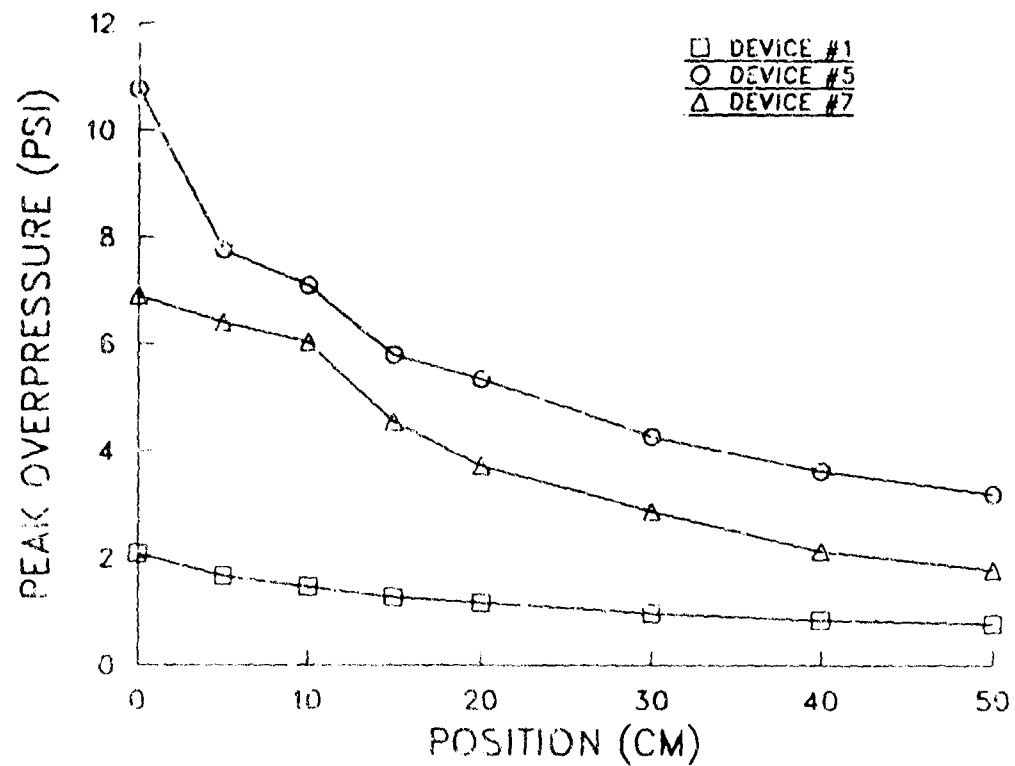
Figure 14. Peak Overpressure at Testing Locations for Probe 9.
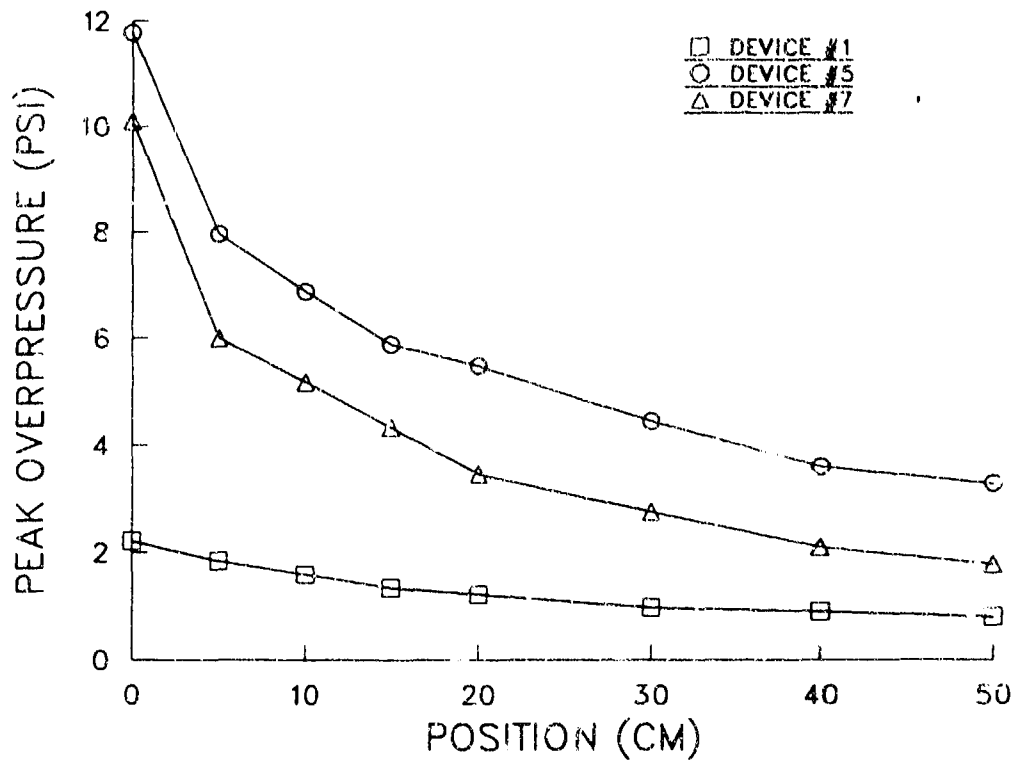
Figure 15. Peak Overpressure at Testing Locations for Probe 10.
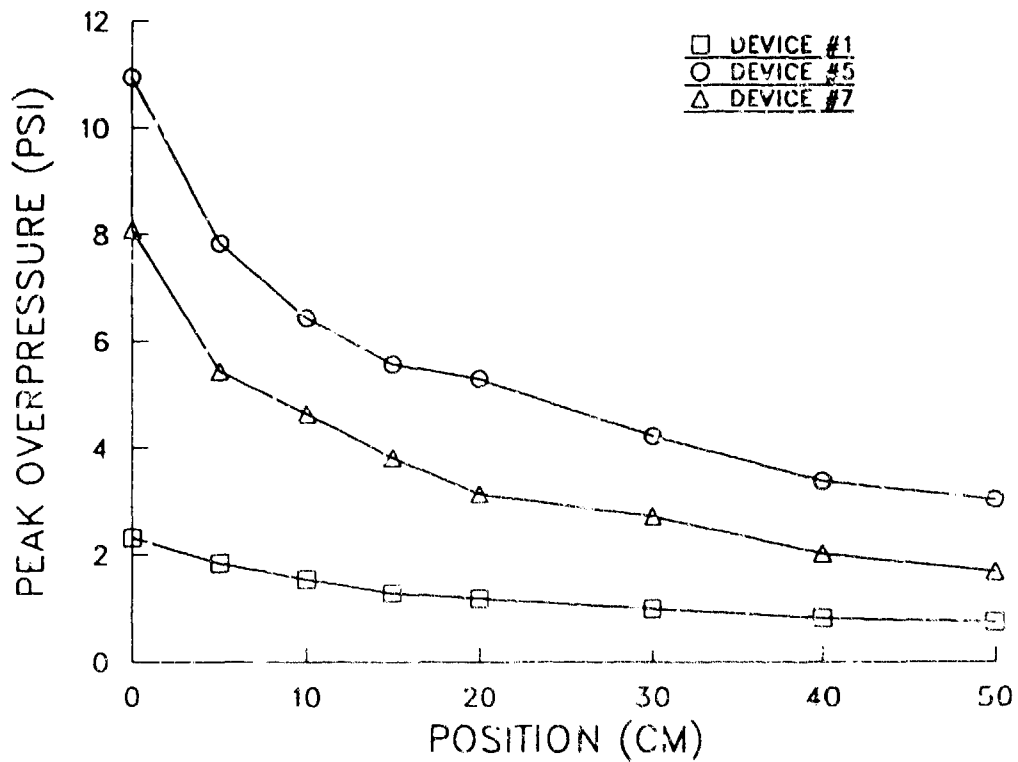
Figure 16. Peak Overpressure at Testing Locations for Probe 11.

Figure 17. Shadowgraph of the Blast Waves Exiting the Vents of Device 7.
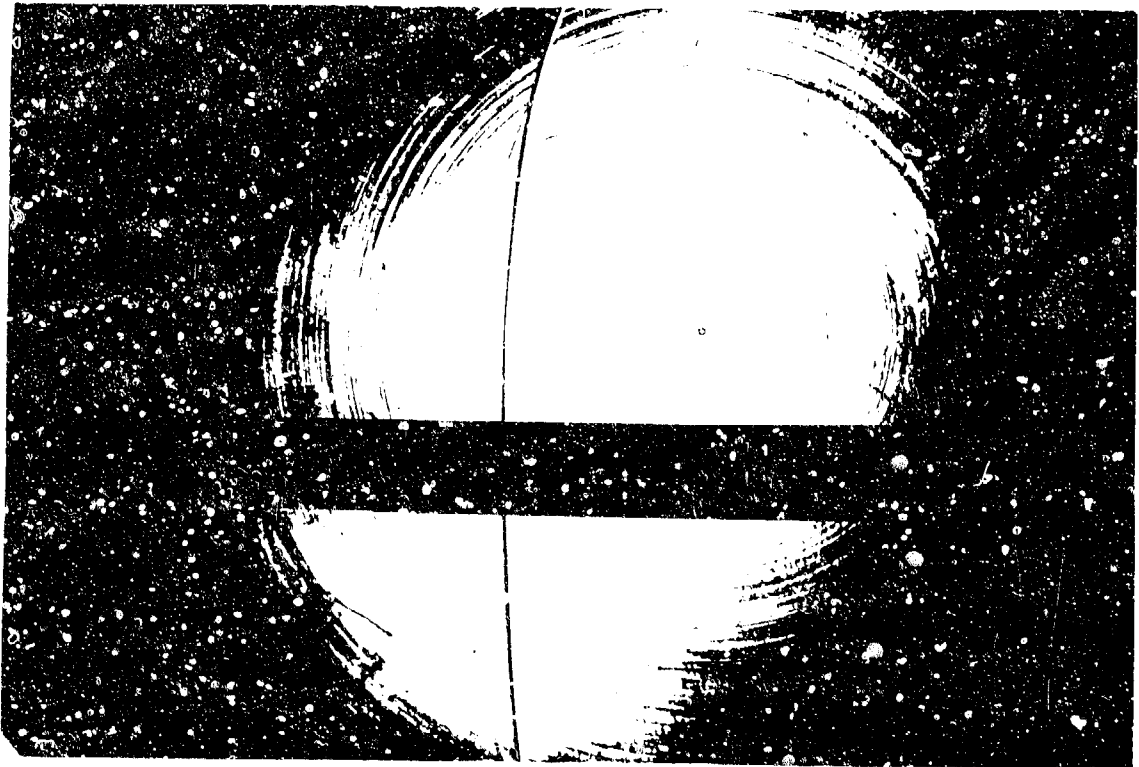
Figure 18. Shadowgraph of the Blast Wave of Device 5 at Approximately 50 cm.
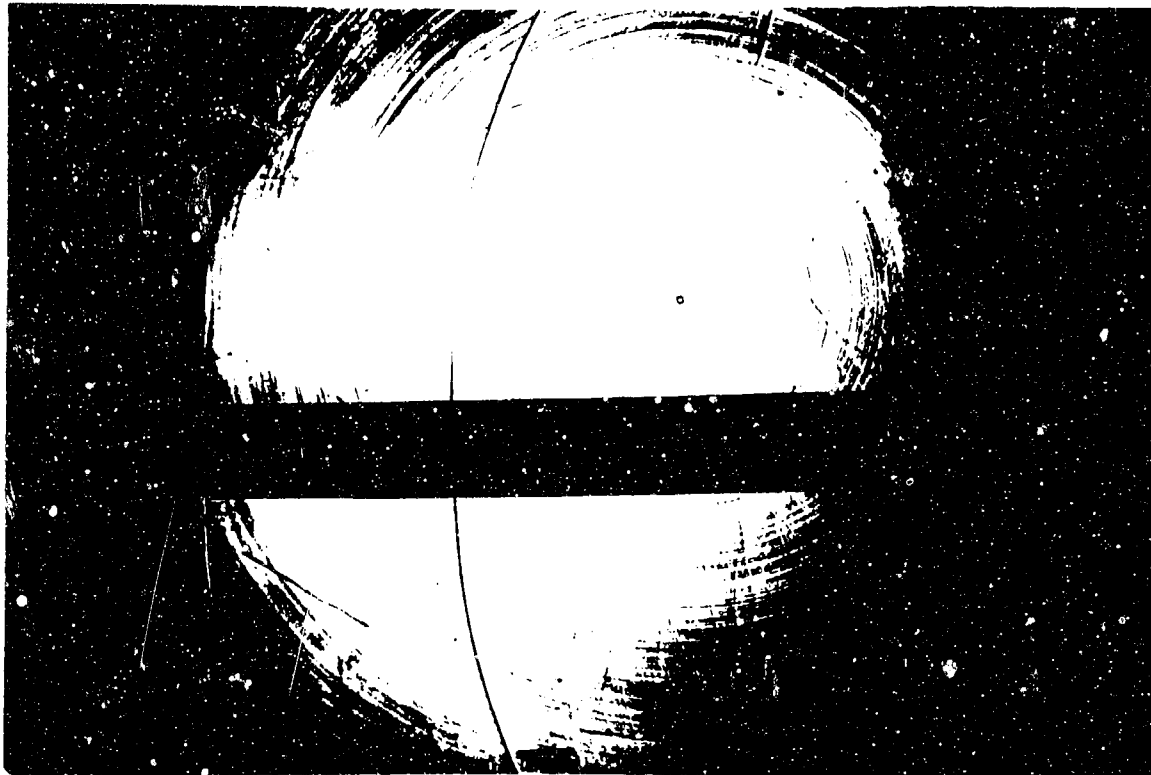
Figure 19. Shadowgraph of the Blast Wave of Device 7 at Approximately 50 cm.
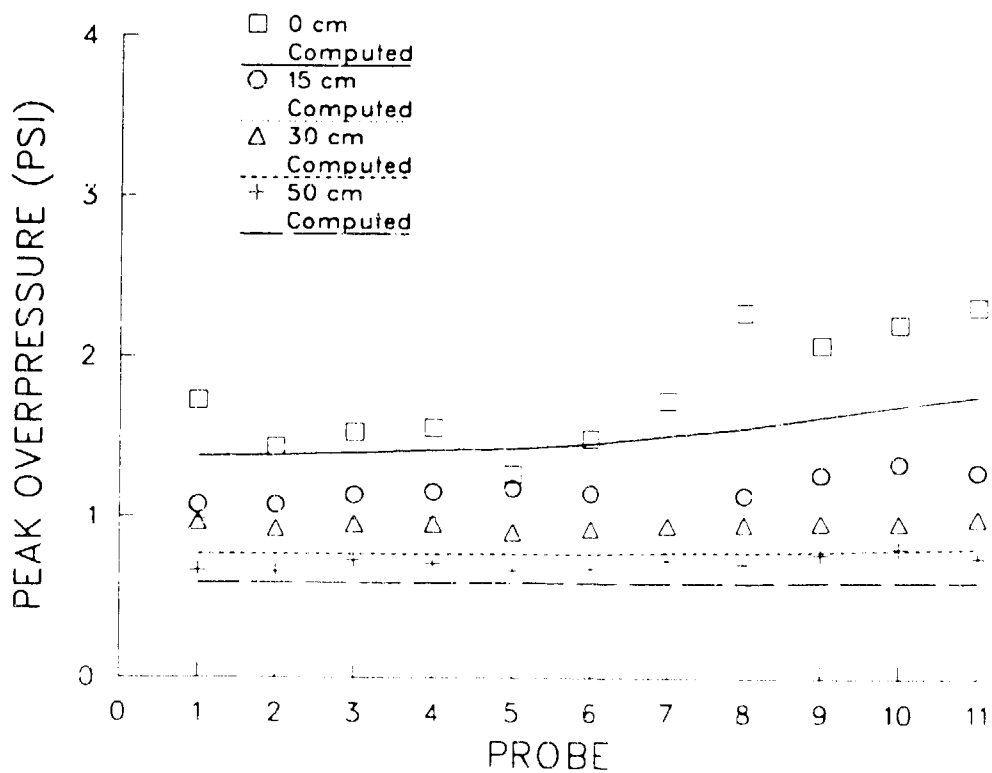
Figure 20. Computed and Empirical Peak Overpressure Comparisons for Device 1.
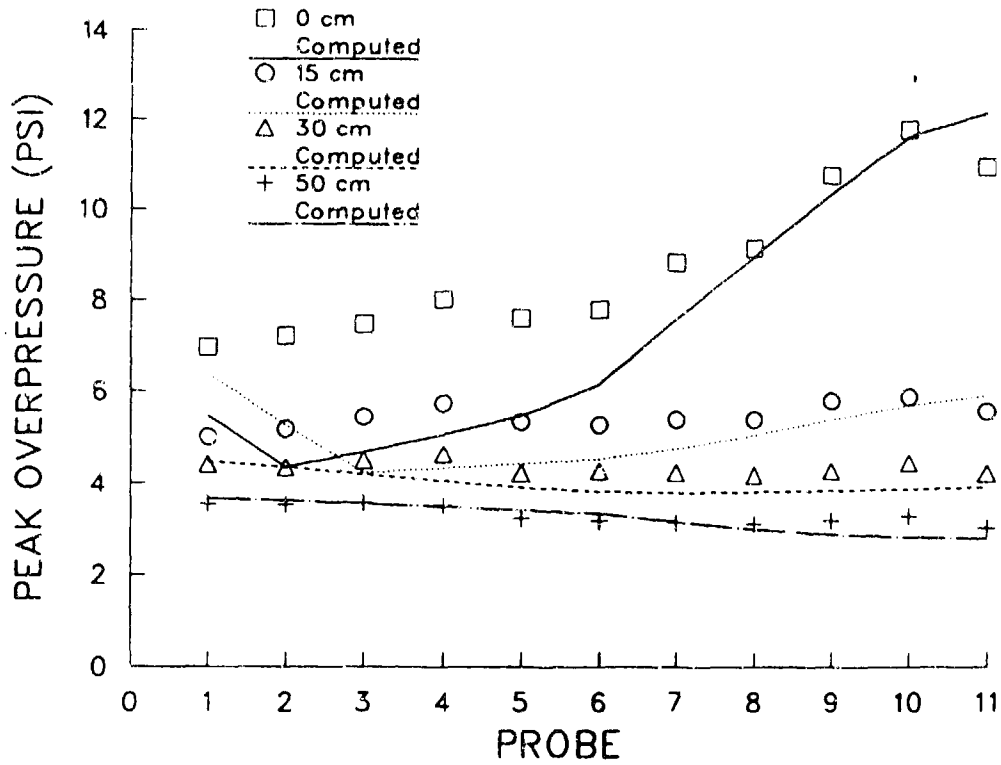
Figure 21. Computed and Empirical Peak Overpressure Comparisons for Device 5.
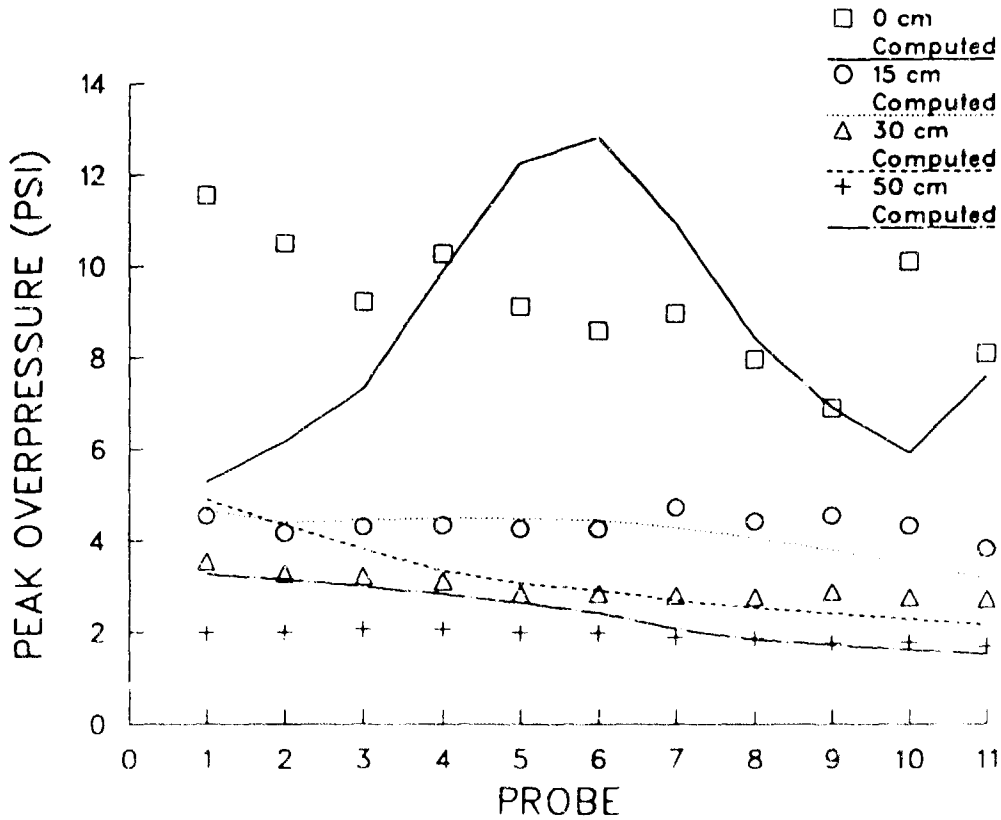
Figure 22. Computed and Empirical Peak Overpressure Comparisons for Device 7.

6. References

1. Carofano, G.C.,"Blast Field Contouring Using Upstream Venting", The Fourth International Symposium on Computational Fluid Dynamics, U. of California, Davis, Davis, California, September 9-12, 1991, p138-143, Benet Laboratories Technical Report in publication.

2. Savick, D.S., "Test Comparison for 20mm Perforated Muzzle Brakes", ARL-MR-31, U.S. Army Research Laboratory, Aberdeen Proving Ground, MD 21005-5066, February 1993.

TITLE: INVESTIGATION OF SHOCK IGNITION IN THE INJECTOR PORTS OF AN ANNULAR
         (BORE EVACUATOR) RESERVOIR[1]

         CHARLES A. ANDRADE AND CRAIG W. CLAUSS
         U.S. ARMY ARMAMENT RESEARCH, DEVELOPMENT, AND ENGINEERING CENTER
         CLOSE COMBAT ARMAMENTS CENTER
         BENÉT LABORATORIES
         WATERVLIET, NY 12189-4050

         HENRY T. NAGAMATSU, LEIK N. MYRABO AND DONALD G. MESSITT
         RENSSELAER POLYTECHNIC INSTITUTE
         GASDYNAMICS LABORATORY
         MECHANICAL ENGINEERING, AERONAUTICAL ENGINEERING AND MECHANICS
         TROY, NY 12180

ABSTRACT:

We observe that at first launch of the day, e.g., after the bore evacuator
reservoir is removed and resealed, peak reservoir pressures can double. As reported
in Ref 1, the measured peak reservoir pressure was about 1.4 MPa (200 psi) for the
M256 firing an M831 training projectile, whereas the next firing produced a reservoir
peak of about 0.7 MPa (100 psi). The explanation proposed is that *shock wave* ignition
occurs in the evacuator ports: fuel rich propellant gas in contact with heated air
at the shock contact interface reacts exothermally at the elevated states. Since
post-shock states must be established within μs of projectile arrival at the ports,
the proposed secondary combustion initiates during projectile travel. Air in the
reservoir is depleted for subsequent firings, replaced by burnt propellant gas, so
that secondary combustion is not likely then and evacuator pressures are predictable
by gas dynamical methods.

The initiation of 1st round secondary combustion in the bore evacuator is the
subject of this paper. We first cite further field test data for the 120 mm M256
evacuator. Then, using equilibrium thermochemistry, we perform shock tube analyses
that predict 1st round ignition in the evacuator ports of the 155 mm M284/185 at high
zone. To examine the hypothesis of 1st round secondary combustion in the M284/185
evacuator, and obtain measurements of the evacuator charge coefficient, a laboratory
investigation by Nagamatsu et. al., Ref 2, was established in which pressure and heat
transfer gauges confirm that shock processes occur in the injector ports at the port
opening event.

BIOGRAPHY:
PRESENT ASSIGNMENT: Charles A. Andrade is a Mechanical Engineer in the Systems
Engineering Branch at Benét Laboratories, assigned as Principal Investigator,
"Electro-Optical Sensors for Safe-to-Load Detection of Burning Case Residue."

PAST EXPERIENCE: gas dynamics and thermochemistry of bore evacuator flows; emission
spectroscopy of flames in a shock tube.

DEGREES HELD: Ph.D. Mechanical Engineering, Rensselaer Polytechnic Institute; M.S.
Physics, Rollins College; B.S. Engineering Physics, University of California.

INVESTIGATION OF SHOCK IGNITION IN THE INJECTOR PORTS OF AN ANNULAR RESERVOIR

CHARLES A. ANDRADE AND CRAIG W. CLAUSS
U.S. ARMY ARMAMENT RESEARCH, DEVELOPMENT, AND ENGINEERING CENTER
CLOSE COMBAT ARMAMENTS CENTER
BENÉT LABORATORIES
WATERVLIET, NY 12189-4050

HENRY T. NAGAMATSU, LEIK N. MYRABO AND DONALD G. MESSITT
RENSSELAER POLYTECHNIC INSTITUTE
GASDYNAMICS LABORATORY
MECHANICAL ENGINEERING, AERONAUTICAL ENGINEERING AND MECHANICS
TROY, NY 12180

INTRODUCTION

Bore Evacuator Design

1. __The Discharge Cycle__. To promote the reduction toxic gases and to better understand how a flareback event occurs, several aspects of the design of bore evacuators are being investigated. Simple. one-dimensional techniques for the evacuator pump flow were applied for the first time after WWII, based on Reynolds' Momentum Theorem -the control volume approach. Thus, References 3 and 4, and more recently, other investigations, References 5-7, have established use of control volume methods for the flow of room temperature air and/or propellant gases in the evacuator. More simplifications apply when __inviscid__ air is assumed for the discharge cycle because the energy and mass-flow equations uncouple and the resulting momentum, mass and state equations combine in an exact compressible flow algorithm, albeit nonlinear, that can be solved iteratively with a hand calculator to obtain the induced flow speeds at the breech and muzzle, given quasi-steady pressure in the reservoir for a given ejector geometry. This technique was extended to __an ideal propellant gas__ in which initial composition is established with a thermochemical code such as BLAKE, Reference 8. Then the higher energy state of the gas is given by the ratio of specific heats deduced from the composition. In this case, the energy and mass-flow equations must both be accounted for, together with the momentum and state equations, at each surface bounding the control volume, Reference 9. The addition of mixing-length losses, Reference 10, and experimentally obtained flow discharge coefficient, completes the steady-state discharge theory as applied to the 120 mm M256 and 155 mm M284 or M185 evacuators, Reference 11.

2. __The Charge Cycle Modeling Problem__. The bore evacuator charge cycle modeling presented an anomaly: It was found that the peak reservoir pressure could not be predicted for all firings. Since ballistics must drive all of the charge processes, the approach taken was to model the bore evacuator reservoir fill cycle by charging it with propellant gas from the dynamically variable high pressure reservoir bounded by the gun tube and projectile base prior to uncorking. Then, subsequent to the uncorking, charge it with gasdynamically expanding gas in the gun tube during gun blowdown. The process to peak reservoir pressure takes - generically for artillery and tank cannon -about 50 ms. This approach worked for all but, so called, 1st round firings since the computations fail to predict the peak charge pressure in that case. As reported in Reference 1 [Andrade and Haas] the measured peak reservoir pressure was about 1.4 MPa for the M256 firing a 1st round "warmer" M831 training projectile, whereas subsequent M831 firings produced a reservoir peak of about 0.7 MPa. Further evidence of elevated evacuator pressures in 1st round M256/M831 firings is given with recently obtained measurements summarized on Table I.

Table I. Peak Evacuator Pressure, Firing 120 mm M256/M831/DIGL "Warmers"
(Data obtained at Olin Ordnance Range, Socorro, NM, 12-16 April 1993)

Year		1993				1990	
Date		13 April		16 April			
Chamber Pressure		65		20		> 65	kpsi
Round No.		1st*	2nd	1st	2nd		
	Peak	1 2	1	1	1		
Gauge at 6 O'clock		382 188	160	186	115		psi
Gauge at 12 O'clock		275 119	125	141	67		psi
	Average	328 153	142	164	91		psi
Combustion Press (Difference of Avg):							
		98.5		73			psi
Ref 1						115	psi

*ENDEVCO gauges not torqued to specification for first 1st firing.

We note that "normal" evacuator peak pressures range from 91 to 160 psi and that the combustion pressures measured for the downloaded firing are about 2/3 that of the full charge rounds. Also, the asymmetric distribution of the ports, Figure 1a, favor a high pressure reflected shock wave region at the six o'clock gauge. The explanation proposed for these pressure observations is that the five reservoir injection ports accommodate *shock* wave ignition: by which the fuel rich propellant gas components react with shock heated air at the shock contact interface. Since post-shock states are established within µs of projectile arrival at the ports, a Mach 7.8 shock wave, computed in Ref 1, must traverse the 58 mm port length long before projectile exit.

Subsequent analysis and laboratory experiments aim at understanding the bore evacuator gas dynamic and reaction processes for possible applications to Advanced Field Artillery Systems. Fig 1b illustrates the process at the M284 charge valve.

THE SHOCK WAVE AS IGNITION SOURCE IN 155 MM M284/185 BORE EVACUATOR PORTS

Analysis.

1. **Interior Ballistics. (IBHVG2)**. To examine the hypothesis of secondary combustion at 1st round firing, as an explanation of evacuator reservoir pressures exceeding the gasdynamic prediction, a laboratory investigation was established, Ref 2, in which pressure and heat transfer gauges are to confirm that, at the port opening event, high Mach number ($M_s \approx 7$) shock processes can occur in the injector ports. These measurements and the existing reaction kinetics data, should then indicate that the port shocks are indeed the source of ignition of fuel rich propellant gas in the postshock state. Ballistic calculations for the 155 mm M284/M864, using M203A1 stick propellant give the gasdynamic state in the gun tube required for both the laboratory shock tube simulation at the charge/discharge ports and analyses of these process to be presented first. A summary of the ballistic database is shown on Figure 2 and Table II. These data are the basis of our work.

Table II. INTERIOR BALLISTICS DATA FOR THE 155 MM M284/M185/M203A1. (IBHVG2)

PROJECTILE   M864
PROPELLANT   M31 single perf slot stick, 12.7   kg

CHARGE WT. (Total)   13.7   kg*

COVOL   .0019837   m³/kg
TEMP   2587.   K
FORC   981908.4   m²/s²
GAMMA   1.2513
RHO   1641.418   kg/m³

Position:	Pmax	muzzle	charge port	discharge port	
Time	3.96	11.88	8.91	9.81	ms
Pres.	365.8	84.52	127.7	108.7	MPa
Temp.			1792.0	1742.0	K
Vel.			693.7	736.3	m/s

* For high zone, including combustible case components.

2. Initial Conditions for the 155 mm Bore Evacuator. At the time of passage of the projectile over the charge ports, e.g. Figs 1a and 1b, the physical properties of the propellant gases are given by IBHVG2, Table II, and the BLAKE/NASA Chemical Equilibrium & Transport Code (CET86) results. Appendix I, summarized as follows:

$$P_b = 127.7 \text{ MPa} \qquad \gamma_b = 1.2478$$

$$T_b = 1792 \text{ K} \qquad m_4 = 22.262$$

Where subscripts b or 4 will be used interchangeably for the propellant gas at the port opening; aka the shock tube state 4. Likewise, subscripts 1, 2, 3, 5 and 6 are for states ahead of the incident shock, behind the shock, in the expanded propellant gas, behind the reflected shock and in the Chapman-Jouguet (C-J) burned gas regions, respectively. Prior to a 1st firing, the evacuator reservoir is filled with air at normal temperature and pressure (NTP):

$$P_a = 14.7 \text{ psia} \qquad \gamma = 1.40$$

$$T_a = 300 \text{ K} \qquad m_a = 28.8$$

3. Ideal Gas Analysis of Shock Waves in the Ports and Evacuator Reservoir.

a. Incident Shock. By assuming the initial starting process in the charge ports at the time of projectile arrival at the opening of the ports to be similar to the diaphragm burst of a shock tube driver (Fig 3 is generic) the shock wave Mach number, M_s, created by the sudden burst at port opening is obtained, Refs 12 and 13, by solving

$$\frac{P_4}{P_1} = \left[\frac{2\gamma_1 M_s^2 - (\gamma_1 - 1)}{\gamma_1 + 1} \right] \left[\frac{1}{1 - \frac{\gamma_4 - 1}{\gamma_4 + 1} \frac{a_1}{a_4} \left(M_s - \frac{1}{M_s} \right)} \right]^{\frac{2\gamma_4}{\gamma_4 - 1}} \qquad (1)$$

where P_4, T_4, γ_4, a_4, and m_4 are the pressure, temperature, ratio of specific heats, velocity of sound, and molecular weight, respectively, of the driver gas. The corresponding physical parameters in the driven tube are P_1, T_1, γ_1, a_1, and m_1. The gas constant, R_b, for the propellant gas at 1792 K and molecular weight of 22.3 g/mole

is R_b = 2220 ft^2/sec^2/°R, and for air at NTP in the evacuator reservoir, the gas constant, R_e, is 1716 ft^2/sec^2/°R. Using these values in the equation for the acoustical speed, and continuing with mixed Engineering and SI units,

$$a = \sqrt{\gamma R T} \tag{2}$$

the sound speeds in the bore and the evacuator reservoir are, respectively,

$$a_b = 2230 \text{ ft/sec and } a_e = 1128 \text{ ft/sec}$$

The pressure ratio across the M284/M185 charge port entrance for $P_4 = P_b$ = 18,500 psi and $P_1 = P_e$ = 14.7 psi is

$$P_4/P_1 = P_b/P_e = 1260$$

Assuming, as a first approximation, that propellant gas in the gun bore corresponds to the shock driver gas and that air in the evacuator port is driven, the shock Mach number in the charge port passage is determined from Eq. (1) to be

$$M_s = 6.96$$

As shock waves propagate through the evacuator ports of any gun, Fig 1, or the ports of a laboratory simulation model, Fig 4, the pressure jump across the shock wave is given, Ref 14, by

$$\frac{P_2}{P_1} = \frac{2\gamma_1}{\gamma_1+1} M_s^2 - \frac{\gamma_1-1}{\gamma_1+1} \tag{3}$$

where P_1 = 14.7 psia is the initial pressure in the evacuator reservoir. For a shock Mach number of 6.96 in the charge ports, the pressure jump across the shock wave is

$$P_2/P_1 = 56.39$$

thus, the pressure behind the shock wave (state 2) is P_2 = 828 psi. The corresponding temperature jump is

$$\frac{T_2}{T_1} = \frac{\left[2\gamma_1 M_s^2 - (\gamma_1-1)\right]\left[(\gamma_1-1)M_s^2+2\right]}{(\gamma_1+1)^2 M_s^2} \tag{4}$$

where $T_1 = T_e$ = 300 K is the temperature in the evacuator reservoir. For a shock Mach number of 6.96 the temperature jump across the shock wave is

$$T_2/T_1 = 10.36$$

so that the charge port gas temperature in the shock heated state 2 is T_2 = 3100 K.

The velocity imparted to heated air by shock waves propagating through the evacuator ports, Figs 1 and 4, is

$$u_1 = u_2 = \frac{2a_1}{\gamma_1+1}\left(M_s - \frac{1}{M_s}\right) \tag{5}$$

where $a_1 = a_e$ for initial conditions at NTP. Thus, for a shock Mach number of 6.96 and a_1 = 1128 ft/sec, the imparted velocity is, u_2 = 6410 ft/sec in the charge port for a shock velocity,

$$u_s = M_s a_1 = 7854 \text{ ft/sec}$$

Assuming that propellant gases in the bore expand adiabatically like the driver gas in a shock tube, Fig 3, temperature of the expanded propellant gases can be determined upstream of the contact surface separating the cooling propellant gases from the shock heated air in the evacuator ports. Adiabatic expansion of a gas is given by

$$\frac{P}{\rho^\gamma} = \frac{P_4}{\rho_4^{\gamma_4}}$$ (6)

where ρ is the density of the gas in the driver. By using the equation of state of the gas

$$\frac{P}{\rho} = RT$$ (7)

the temperature of the driver gas expanding to the pressure behind the incident shock wave can be expressed as

$$\left(\frac{T}{T_4}\right) = \left(\frac{P}{P_4}\right)^{\frac{\gamma_4-1}{\gamma_4}}$$ (8)

Thus, hot propellant gas, initially at pressure $P_b = P_4 = 18.5$ kpsi, temperature $T_b = T_4 = 1792$ K, and specific heat ratio $\gamma_4 = 1.25$, expands to $P_3 = 828$ psi behind the shock wave in the port, with corresponding temperature at $T_3 = 967$ K.

b. Reflected Shock Wave at the Ball Valve for the Charge Ports. When the projectile traverses across the charge or discharge ports, Figs 1 and 4, a shock wave will propagate into the passage at a Mach number of 6.96, given the port opening pressure of 18,500 psi and a temperature of 1792 K, with the evacuator at NTP for a 1st round firing. Behind the incident shock wave the pressure is 828 psi with a temperature of 3100 K and an imparted velocity of 6410 ft/sec. By assuming the shock wave is reflected by the ball valve, Fig 1b, before the opening of the valve, the state of the air can be determined from the shock wave equations presented in Ref 12.

For an incident planar shock wave reflecting at a solid wall, the flow comes to zero velocity, $u_5 = 0$, behind the reflected shock wave which moves into the heated air region, heating it again. The twice heated region is called gas state 5. The contact surface boundary condition requires that the reflected shock Mach number, M_{sr}, and the incident shock Mach number, M_s, bear a similar relation to the imparted velocity, i.e., $u_2 = u_{is}$. Thus, by analogy to Eq 5, this is expressed as

$$u_{is} = \frac{2a_2}{\gamma_1+1}\left(M_{sr} - \frac{1}{M_{sr}}\right)$$ (9)

where $a_2 = 3630$ ft/sec is the sound speed in air that was heated and compressed by the incident shock wave and the reflected shock Mach number, M_{sr}, is given by

$$M_{sr} = \frac{u_2 + u_{sr}}{a_2}$$ (10)

where u_{sr} is the reflected shock wave velocity. By substituting the values for the velocity of sound, a_2, and imparted velocity u_2 into Eq. (9), the reflected shock wave Mach number can be solved from the equation

$$(M_{sr})^2 - \left(\frac{\gamma_1+1}{2}\right)M_2 M_{sr} - 1 = 0$$ (11)

where M_2 is the Mach number of the flow behind the incident shock wave, $M_2 = u_2/a_2 = 1.766$. The reflected shock Mach number for this value of M_2 is ,

$$M_{sr} = 2.517$$

and the corresponding reflected shock wave velocity is given by Eq. (10) as

$$u_{sr} = a_2 M_{sr} - u_2 = 2725 \text{ ft/sec}$$

The pressure behind the reflected shock wave is given by

$$\frac{P_5}{P_2} = \frac{2\gamma_2}{\gamma_2+1} M_{sr}^2 - \frac{\gamma_3-1}{\gamma_2+1} \tag{12}$$

and for $M_{sr} = 2.517$ the pressure behind the reflected shock wave becomes

$$P_5/P_2 = 7.225 \text{ and } P_5 = (7.225)(828) = 5982 \text{ psi}$$

By substituting the reflected shock Mach number into Eq. (4), the temperature becomes

$$T_5/T_2 = 2.154 \text{ and } T_5 = (2.154)(3100) = 6680 \text{ K}$$

4. <u>Summary of Ideal Shock Tube Flow Results</u>. The reflected pressure at the ball valves will be greater than the above values and the corresponding temperature will be less, as shown below for the thermochemical mixtures; however, as presently designed, the valves open at these pressures and combustion of the propellant gases, H_2 and CO, at 1st round fire, probably occurs in the expansion following the valve opening. The initial shock wave in the charge port passages, Fig 1, compresses and heats the ambient air to a pressure of 828 psi and a temperature of 3100 K, and therefore the combustion of H_2 and CO at the contact surface can occur. Behind the reflected shock wave, pressure and temperature are 5982 psi and 6680 K, respectively. As the check valves open this high pressure and temperature air will expand into the evacuator reservoir and be a source of high temperature gas to ignite the propellant gases, H_2 and CO, with O_2 in the reservoir.

5. <u>Thermochemical Shock Tube Flow Routine</u>. To simulate projectile base gas states including composition at the evacuator ports, the BLAKE program, Ref 8, was used. The program simulated combustion of the M31 stick propellant using the Lennard-Jones equation of state computing the equilibrium gas state at pressures and temperatures compatible with interior ballistics. The final composition from BLAKE was then transferred to the NASA code, Ref 15, giving additional thermochemical information, including the mixture mole fractions (partial pressures) for the port burst state, as summarized in Appendix I. To investigate shock ignition in the ports and secondary combustion in the reservoir, we observe that the port opening times for an M864 projectile, about 5 µs, is the same order of diaphragm burst time that establishes a shock wave in a shock tube, Ref 16. Fig 1b illustrates the projectile base at the charge port opening, with a cross section of the M284 check valves. By using the shock tube burst pressure equation, linked to the NASA code, we compute the real gas temperature, pressure and composition for shocked air in the evacuator charge ports, driven by M203A1 propellant gas . The equation for the burst pressure equation, i.e., the ratio of propellant gas pressure P_b, at the evacuator port to the initial air pressure there ($P_1 = 1$ atm) before arrival of the projectile base, is given by, Ref 1:

$$P_b/P_1 = P_{b1} = P_{21}/[1-(\gamma_4-1)*K*a_{1b}/2]^{2\gamma_4/(\gamma_4-1)}, \tag{13}$$

where the ratio $P_{21} = 1 + \gamma_1*M_1*K$ is the shock pressure rise, γ_4 is the propellant gas ratio of specific heats, $\gamma_1 = 1.4$ for air, M_1 is the incident shock Mach number in the port, which is driven by the propellant gas, $K = M_1(1-u_{21}) = v_3/a_1$, is the particle velocity imparted by the shock wave, normalized to the sonic speed in air, u_{21} is the cold to heated air density ratio, and a_{1b} is the air to propellant gas sonic speed

ratio. The subroutine was linked to the NASA code and iterations performed until shock jump conditions and mole fraction compositions are found such that Eq(13) is satisfied for a given pressure ratio and initial composition ahead of the shock. The results provide the heated air compositions, hence O_2 concentration at the postshock state.

From Table II, diaphragm burst occurs when the projectile opens the ports at the propellant gas to evacuator pressure ratio $P_{b1} = 1261$. The driver, M203A1 propellant gas, is characterized by its thermochemical properties, summarized in Appendix I, that must match the interior ballistic conditions at the port. The solution to Eq 13 is $M_s = M_1 = 6.72$ which is less than the ideal gas solution of 6.96 obtained above. By continuity, $u_{21} \equiv u_2/u_1$ is the inverse density ratio across the shock wave, viz.,

$$\rho_{21} = u_{21}^{-1}, \tag{14}$$

and is computed by subroutine SHOCK in the NASA code. We note that when the ideal gas expression for Eq 14 is substituted into Eq 13 one obtains the ideal burst pressure, Eq 1, and that for the high shock Mach numbers, the density ratio for the ideal (calorically perfect) gas cannot exceed 6 for diatomic gases, γ_1. However, at the same shock Mach number for a dissociated gas, chemical equilibrium yields density ratios in excess of six, decreasing the state temperature at nearly the same pressure (collision processes).

In the μs span of time to establish the shock wave, Ref 16, the propellant gas is assumed to expand isentropically into the ports, see Eq 8. Hence, the pressure drop from gun to port postshock state is given by the ratio:

$$P_{3b} = T_{3b}^{\gamma/(\gamma-1)} \times a_{3b}^{2\gamma/(\gamma-1)}, \tag{15}$$

where $T_{3b} = T_3/T_b$ is the expansion temperature ratio to be satisfied by the iterative process linking equations (13)-(15) to the NASA code. As in the ideal case, above, the expanded propellant gas temperature at the postshock state is $T_3 = T_{3b} \cdot T_b$, at pressure $P_3 = P_2$ (contact surface boundary value). Subroutine SHOCK also computes the reflected shock equilibrium properties, state 5, from the incident state 2 properties obtained from the shock tube iteration described and summarized in Appendix III.

It is convenient to use NASA's C-J detonation option, Ref 15. This requires the equilibrium propellant gas compositions in the postshock expansion (P_3, T_3), at the appropriate mix ratio for instantaneous combustion with the shock heated equilibrium air composition. Since the compositions are known from the equilibrium shock tube results, summarized in the Appendices and on Table III, one mole at each state is introduced into the C-J option, which yields the burned C-J state 6. The result is shown in Appendix IV and summarized on Table III. This calculation gives a detonation wave Mach number, $M_d = 2.8$ and raises the local pressure by a factor of 5. Actual combustion kinetics must account for diffusion and collision processes across the contact interface to produce the observed factor of 2 pressure rise in the reservoir.

Table III summarizes thermochemical results for the six states, beginning with the in-bore state 4 and proceeding to the burned gas, state 6, obtained from the assumed Chapman-Jouguet detonation initiated by the shock processes. A more detailed examination of all results, including initial and final compositions, are listed in Appendices I-IV. The most significant departure from the above ideal methods are the temperatures: $T_{5(ideal)} - T_{5(thermochem)} \geq 2000$ K. Appendix III shows that the mole fraction of O_2 is 11 % in the twice heated air at $T_5 = 4360$ K and $P_5 = 430$ Atm.

6. Ignition. An examination of postshock ignition delay measurements for stoichiometric hydrogen-air mixtures, published in the review by Schott and Getzinger, Ref 17, shows that ignition probably occurs in less than one μs as temperatures exceed 967 K and pressures exceed 35 psi in the postshock region, Fig 5. Consider a first round burst opening of the ports, with air in the reservoir at NTP (1 atm and 300 K).

The shock wave produced at $M_s = 6.72$ (Table III, Appendix II) corresponding to shock velocity $u_1 = 2310$ m/s, creates a post-shock environment in which ignition could initiate in about 0.10 of the time that it takes the shock wave to traverse the port. These postshock conditions are within the third explosion limit for stoichiometric H_2/O_2 mixtures, Refs 17 and 18, where branching chain kinetics mechanisms are known to support shock ignited detonation waves in the Chapman-Jouguet mode, Ref 18. Efforts to model the kinetic processes are scheduled under a Small Business Innovation Research Program now in Phase II. Benét is using NASA's CET code, Ref 15, to determine limiting values for this work.

INVESTIGATION OF THE M284 EVACUATOR IN THE RPI 4-INCH HIGH PRESSURE SHOCK TUBE

Bore Evacuator Model and Instrumentation.

1. RPI High Pressure Shock Tube. The Rensselaer Polytechnic Institute High Pressure Shock Tube, Fig 6, with a 4-in. diameter, 15-foot long driver and 55-foot long driven tube was used to simulate the flow conditions in the 155 MM cannon bore evacuator during live fire. **The laboratory investigation was required to simulate the port conditions, using a shock tube, and to measure the charge coefficient under evacuator charge flow conditions**. A photograph of the 65% scale bore evacuator model installed in the RPI High Pressure Shock Tube is shown in Fig 7, and a schematic of the bore evacuator model configuration for the charge phase tests is shown in Fig 4. A more detailed description of the RPI shock tube and tunnel is presented in Refs 2 and 19.

2. Gun Bore Evacuator Model. The bore evacuator model consists of a 38-in. long steel pipe with a 4-in. internal diameter, Figs 4 and 6, and the pipe has a wall thickness of 0.75 in. with 10 charge holes and 3 angled discharge holes to scale with the 155 MM gun bore evacuator. The evacuator casing is constructed of steel tubing with a 9-in. internal diameter and two 0.75-in. thick steel flanges. Six threaded tie rods were used to hold the model together and it was designed so that the length-to-diameter ratio (L/D) could be easily altered.

The operating x-t diagram for the shock tube and the pressure distribution along the shock tube at an early time is presented in Fig 3 for the evacuator charge tests. In Fig 8 the pressure ratios required with air or helium in the driver section to produce incident shock Mach numbers in the driven tube are presented with the experimental data and the theoretical predicted curves.

It is noted that during the first few μs after projectile arrival at the ports the initial shock transient is established, thus simulated by these laboratory conditions, and that the charge coefficient must be measured at several orders of magnitude later when flow into the evacuator is choked, establishing a quasi-steady state.

3. Shock Tube Instrumentation. The instrumentation installed in the shock tube and the bore evacuator model, Fig 4, consists primarily of piezoelectric pressure and thin-film platinum heat gauges, Refs 2 and 20. Kistler quartz pressure gauges are installed upstream of the bore evacuator to measure the shock wave conditions, and PCB quartz pressure transducers are used to measure pressures in the bore evacuator. One of the gauges, PG3, is installed in the outer wall in line with the discharge port, Fig 4.

Thin-film platinum heat transfer gauges with a response time of a few microseconds, Ref 21, are used to measure the shock wave speed in the shock tube and the transit time of the starting shock wave from the exit of the discharge port to the heat gauge HG3 placed at different distances from the port, Fig 4.

Several data acquisition systems are used in the RPI Shock Tube facility. A Tektronix 2520 mainframe with 18 channels is the primary data acquisition system. A Nicolet digital oscilloscope provides an additional four channels and Hewlett-Packard 54501A digitizing oscilloscopes are available.

Experimental Results for Gun Bore Evacuator Charge Cycle

For the tests to determine the charge coefficients for the charge and discharge ports, the initial pressure in the driven tube is 22.6 psia and air is used as the driver gas at 1100 psia. These conditions produce a shock wave Mach number of 1.89, Fig 8, and the Mach number of the flow after the shock wave is 0.89 with a bore pressure of 91.8 psia. The flow is steady for at least 4 ms for all tests, as shown in Fig 9 for the pressure gauge PG4 located in the shock tube wall, Fig 4.

To enable testing at high ratios of the bore pressure to the evacuator pressure, P_b/P_e, simulating the early charge cycle, diaphragms are placed over the charge and discharge orifices. Thin plastic diaphragm material is placed on a 1/8-in. thick steel tube, which is then inserted into the model from the muzzle end, Ref 2. The evacuator is evacuated to various low pressures to simulate the bore pressure ratio, P_b/P_e, of 2300 to 1 encountered during the firing of the gun.

Figure 10 shows the traces recorded from the two thin-film platinum heat gauges, HG3 and HG4 in Fig 4, to measure the starting shock wave through the discharge port for a bore evacuator pressure ratio, P_b/P_e, of 2372 with a bore pressure of 91.8 psia, and initial evacuator pressure of 2 Torr and temperature of 294 K. For these conditions the incident shock Mach number was 1.89, imparted flow Mach number of 0.89, and bore pressure of 91.8 psia, Fig 9, with a temperature of 467 K.

By assuming the flow through the discharge port to be similar to a shock tube with a bore pressure of 91.8 psi and evacuator pressure of 2 Torr, this condition corresponds to a pressure ratio, $P_b/P_e = 2373$. Using these flow conditions in the shock tube equation, Eq. (1), the shock Mach number in the discharge port is 4.25. For this shock Mach number the pressure and temperature behind the shock wave are 0.81 psi and 1321 K for an initial pressure of 2 T and temperature of 294 K in the evacuator. And the velocity in the port imparted by the shock wave is 3774 ft/sec.

The output traces of the heat gauges, Fig 4, located at the exit of the port, HG3, and downstream and in line with the port, HG4, are presented in Fig 10 for the bore evacuator pressure ratio P_b/P_e of 2373. The response time for these thin platinum heat gauges is a few microseconds so they can be used to detect the arrival of the shock wave and the output can be used to measure the heat flux as discussed in Ref 19. A sharp increase in the heat gauge output, as shown by heat gauge HG4 located downstream of the discharge port, is caused by the passage of the shock wave.

The corresponding pressure recorded by the pressure gauge, PG3, located at the evacuator housing and in line with the discharge port, Fig 4, is shown in Fig 11. A sharp increase in the pressure to approximately 2 psi from the initial pressure of 2 T in the evacuator occurs at 3.6 ms after the trigger of the Tektronix oscilloscope, while the time for the heat gauge output jump for heat gauge HG3 located close to the discharge port is approximately 3.4 ms. By assuming the shock wave reflection from the evacuator chamber surface produced the 2 psi, the incident shock Mach number in the evacuator for initial pressure of 2 T and temperature of 294 K is calculated to be 3.0, Ref's 12 and 13. The initial shock wave in the discharge port for a pressure ratio $P_b/P_e = 2373$ is 4.25, and thus the shock wave attenuates after exiting from the port to approximately Mach 3.0.

CONCLUSIONS

We applied the BLAKE and NASA/Lewis CET thermochemical codes to investigate shock wave processes as a possible source of ignition that may explain the high bore evacuator peak pressure observed at first firing. Second, we have applied laboratory experiments to verify the shock process in the evacuator ports.

The experiments show that for a bore evacuator pressure ratio of 2373, the shock Mach number in the discharge port is 4.25 with a temperature behind the shock wave of 1321 K, and both heat gauges and pressure transducer indicate the presence of a shock wave in the evacuator chamber. Thus, for the 155 MM cannon bore evacuator, higher shock Mach number with corresponding greater gas temperature will be produced due to higher propellent temperature of 1792 K and pressure of 18,500 psi at the time the projectile traverses the charge and discharge ports.

Thermochemical compositions obtained at postshock states and corresponding reaction kinetics data for the H_2/O_2 system described by Schott and Getzinger, Ref 17, indicate the likelihood of shock ignition in the ports. We believe these results give compelling evidence of shock ignition in the ports as the source of secondary combustion and corresponding elevated pressure in the evacuator at 1st fire.

The peak pressure observed at first round firing can be accounted for by a bulk calculation of hydrogen combustion in the evacuator reservoir initially filled with air. The calculation would proceed as in Ref 1 and would yield, nominaly, the pressure differences between the 1st and 2nd round firings given on Table I, above.

RECOMMENDATIONS FOR FUTURE WORK

Future investigation can establish visual flame imagery with shadowgraphs of the Mach bottle (shock wave structure) as it emerges from the ejector ports. We also note that the more time between firings, the more time for ambient air to diffuse through the port orifices into the reservoir, mixing to its equilibrium pressure with residual propellant gas. Given sufficient time, the diffusion process may result in conditions approximating those of a first round. At increased fire rates there is less time for this process, resulting in the reduced peak pressures observed for subsequent rounds.

The detailed kinetic processes of combustion might not be a critical issue if the bulk pressures due to exothermicity can be predicted. A possible use of these studies would be to support development of continuous air flow evacuators.

REFERENCES

1. Andrade, C. A. and Haas, J. E., "GENERIC BORE EVACUATORS II. NON-IDEAL AND REAL PROPELLANT GAS TRANSIENTS," Proc. 6th U.S. Army Symposium on Gun Dynamics, May, 1990

2. Nagamatsu, H.T., Myrabo, L.N., Messitt, D.G., Ekonomidis, C., Greenman, M., and Yagle, P., "An Experimental Investigation of the Gas Dynamic Performance of Gun Bore Evacuators Mounted on 155mm Self-Propelled Howitzers," Rensselaer Polytechnic Institute Final Report For Army Contract No. DAAA 2291-C-1149, Nov. 1992.

3. Fagen, W. and Henry, L. R., "Bore Scavenging Study for Case-Loaded Cannon Mounted in Closed Cab Vehicles", Am. Machine & Foundry Co., 1954

4. Smith, F., "Investigation of Fume Extractor Design by Model Techniques", RARDE Memo. 13/67, Fort Halstead, U. K., 1967

5. Sneck, H. J., "Gas Flows Through Small Holes In Gun Tube Walls", Proc of the 5th U. S. Army Symposium on Gun Dynamics, ARCCB-SP-87023, 1987 and "BORE EVACUATOR HOLE FLOWS", Proc. 6th U.S. Army Symposium on Gun Dynamics, ARCCB-SP-90015, May 1990

6. Andrade, C. A., et. al., "Theoretical Compressible Flow in Generic Bore Evacuators and Experimental Verification", AIAA 89-0652, January 1989

7. Nagamatsu, H. T., et. al., "GENERIC BORE EVACUATORS I. EXPERIMENTAL & AERODYNAMIC INVESTIGATIONS," 6th U.S. Army Symposium on Gun Dynamics, ARCCB-SP-90015, May 1990

8. Freedman, E., "BLAKE - A Thermodynamic Code Based on TIGER: Users' Guide and Manual", Tech. Rept. ARBRL-TR-02411, The Ballistic Research Laboratory, APG, MD, 1982

9. Nagamatsu, H. T., et. al., "Experimental and Numerical Study of Supersonic Jet Ejectors For Gun Bore Evacuators," AIAA-90-1620, June 1990

10. Schlichting, H. "Turbulent Flow Through Pipes," Chap XX in BOUNDARY LAYER THEORY, McGraw-Hill, 1955

11. Andrade, C. A., et. al, "Cannon Bore Evacuator Flow Theory, CFD, and Experimental Validation," AIAA-92-0832, January 1992

12. Glass, I.I. and Gordon Hall, J., *Handbook of Supersonic Aerodynamics, Section 18 Shock Tubes*, Navord Report 1488, Vol. 6, Dec. 1959.

13. Nagamatsu, H.T., Geiger, R.E., and Sheer, R.E., Jr., "Hypersonic Shock Tunnel", *ARS Journal*, May 1959, pp. 332-340.

14. Liepmann, H.W., and Roshko, A., *Elements of Gasdynamics*, Wiley, New York, 1957.

15. Gordon, S. and McBride, B. J., NASA SP-273, 1971.

16. White, D. R., "Influence of Diaphragm Opening Time on Shock Tube Flows", J. Fluid Mech. 4, 585, 1958

17. Schott, G. L. and Getzinger, R. W., "Shock Tube Studies of the Hydrogen-Oxygen Reaction System", Chapter 2. Physical Chemistry of Fast Reactions, Volume I: Gas Phase Reactions of Small Molecules (Ed. B. P. Levitt) Plenum Press, 1973

18. Lewis, B. and von Elbe, G., Combustion, Flames and Explosions of Gases, Chapters II and VIII, 2nd Edition, Academic Press, 1961

19. Minucci, M.A.S. and Nagamatsu, H.T., "An Investigation of Hypersonic Shock Tunnel Testing at an Equilibrium Interface Condition of 4,100 K: Theory and Experiment," AIAA Paper 91-1707, June 1991.

20. Dillon, R.E. and Nagamatsu, H.T., "Heat Transfer Rate for Laminar, Transition, and Turbulent Boundary Layers and Transition Phenomena on Shock Tube Wall," *AIAA Journal*, Vol. 22, 1984, pp. 1524-1528.

Table III. Thermochemical Gas States for the Charge Port Shock Tube

State 4: In-Bore Propellant

P_{41} = 1260
P_4 = 18517   psi
T_4 = 1791   K
γ_4 = 1.2513
w_4 = 22.26   g/mole
S_4 = 2.119   cal/g/K

State 1: Air at NTP

P_1 = 1 atm.

T_1 = 300   K
γ_1 = 1.4
w_1 = 28.8   g/mole
S_1 = 1.64   cal/g/K

M_s = 6.72

State 3: Expanded Propellant

P_{31} = 54.4
P_3 = 800   psi
T_3 = 967   K
γ_3 = 1.149
w_3 = 26.8   g/mole
S_3 = 1.91   cal/g/K

State 2: Shocked Air

P_{21} = 54.4
P_2 = 800   psi
T_2 = 2117   K
γ_2 = 1.254
w_2 = 28.84   g/mole
S_2 = 1.95   cal/g/K

State 6: Burned Gas, C-J

P_{61} = 280.6
P_6 = 4123   psi
T_6 = 3007   K
γ_6 = 1.189
w_6 = 27.5   g/mole
S_6 = 2.107   cal/g/K

M_d = 2.8
u_d = 1745   m/s

State 5: Reflected Air

P_{51} = 431
P_5 = 6334   psi
T_5 = 4359   K
γ_5 = 1.217
w_5 = 28.2   g/mole
S_5 = 2.02   cal/g/K

Bore Evacuator
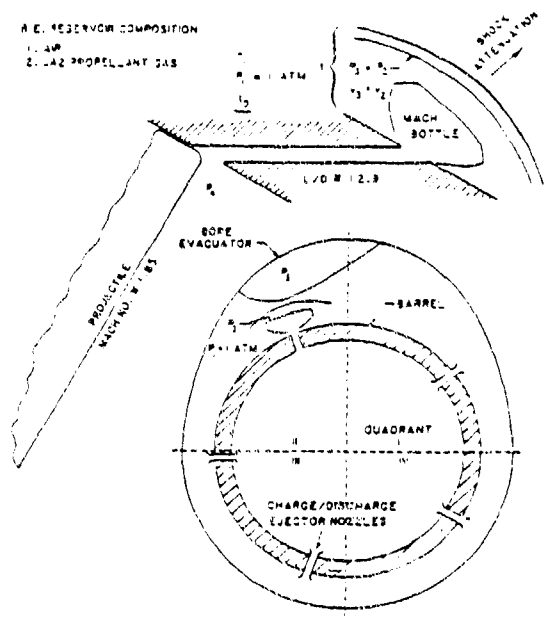
Figure 1a. Schematic of Initial Shock Transients M256
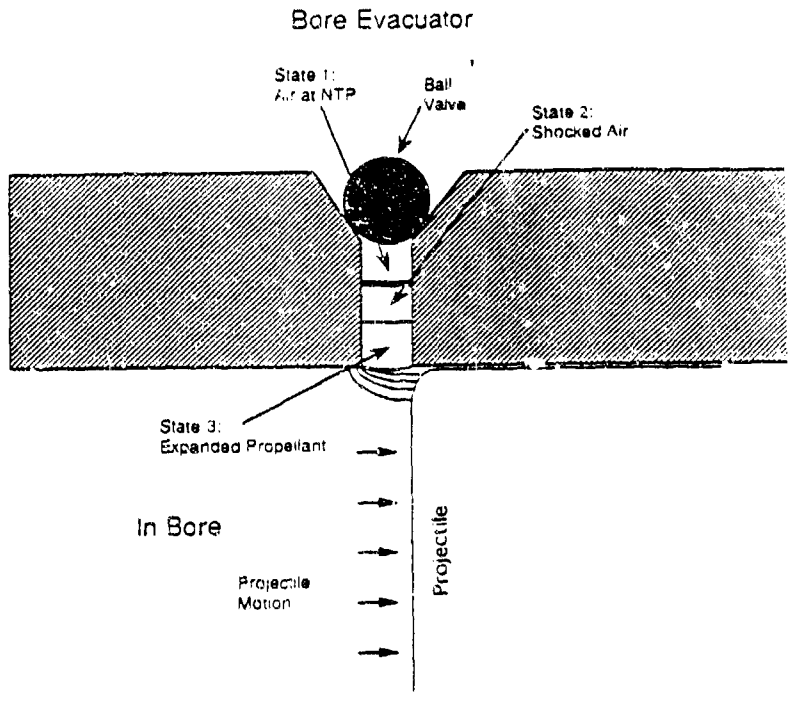
Fig. 1b. 155mm Charge Port Shock Configuration
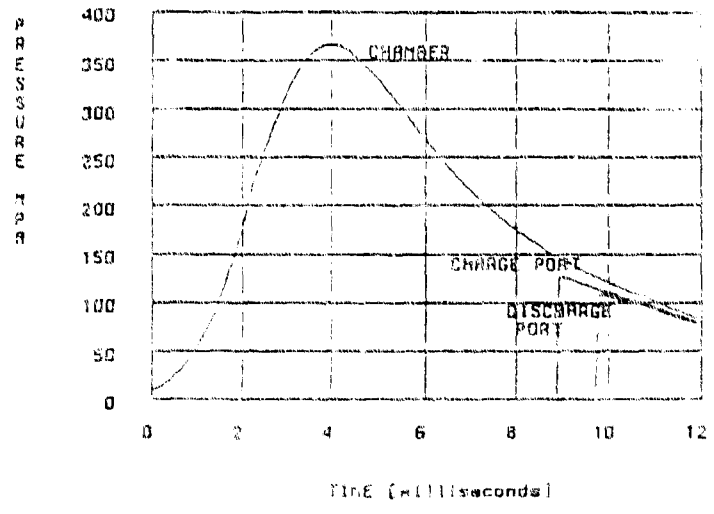
Figure 2. 155mm Cannon M284/M864 IBHVG2 Ballistics
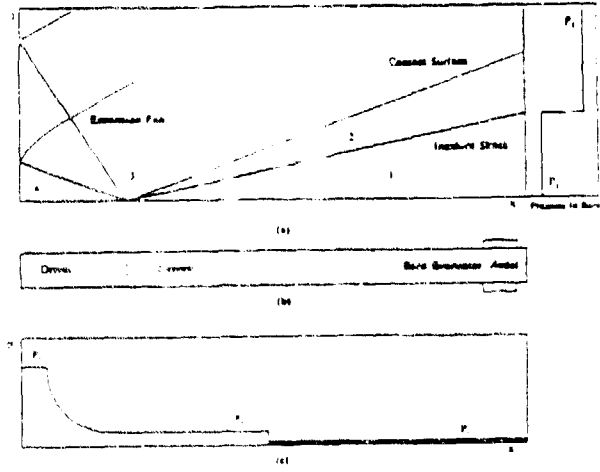
Fig. (a) Shock Tube X-t Diagram And Pressure History In The Model For The Charge Tests. (b) Shock Tube Configuration, and (c) Pressure Distribution Along Shock Tube At An Early Time

Fig. 4   Schematic Of The Bore
          Evacuator Model Configuration
          For The Charge Phase Tests

Fig. 2.10. Ignition delay as a function of postshock temperature and
pressure for a stoichiometric hydrogen air mixture (29.6% H₂, 5.8%
O₂, 55.6% N₂) near 1000 K. ■: 0.41-0.49 atm; ▲: 1.1-1.47 atm; ●:
1.95-2.37 atm. The solid curves were calculated with the low tempera-
ture mechanism discussed in the text and a selected set of rate coeffi-
cients (after Schott[20]).

Fig. 5   Shock Tube Studies of Hydrogen-Oxygen Reaction System (Ref. 3)

Fig. 6 RPI Low and High Pressure Shock
        Tubes

Fig   Photograph Of The 65% Scale
         Bore Evacuator Model Installed
         On The RPI High Pressure Shock
         Tube

Fig. 8 Driver-To-Driven Pressure Ratio Required For A Given Incident Shock Mach Number
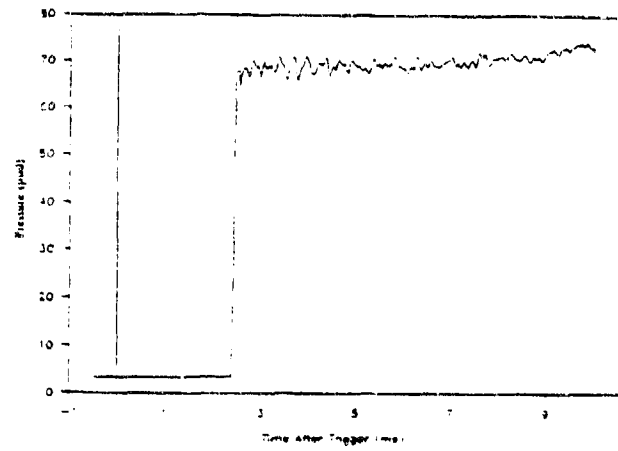
Fig. 9 Typical Pressure Trace From PG4 Showing The Time History Of The Bore Pressure
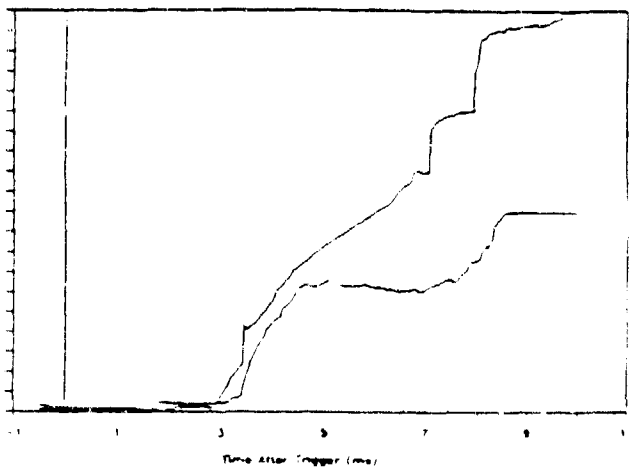
Fig 10 Output Of Heat Transfer Gauges In Bore Evacuator Model For P_b/P_e of 2300. Showing Presence Of Shock Waves
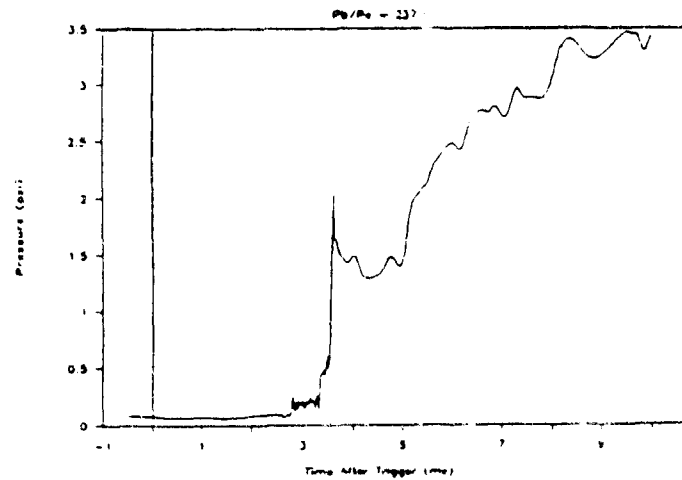
Fig. 11 Output Of Pressure Gauge PG3 Mounted In Evacuator Casing For P_b/P_e Of 2300

APPENDIX I

(a) NASA/CET86 INPUT COMPILED FROM BLAKE OUTPUT AT CHARGE PORT INTERIOR BALLISTIC STATE

THERMODYNAMIC EQUILIBRIUM PROPERTIES AT ASSIGNED TEMPERATURE AND PRESSURE

CHEMICAL FORMULA								MOLES	ENERGY CAL/MOL
H	2.00000	O	1.00000					8.348940	-42914.422
C	1.00000	O	1.00000					12.189	-14665.755
C	1.00000	O	2.00000					2.988750	-75212.375
H	1.00000							0.000161	59520.148
H	2.00000							8.448300	10970.967
N	1.00000	H	3.00000					0.009570	8998.009
C	1.00000	H	4.00000					0.206980	7385.011
H	1.00000	C	1.00000	N	1.00000			0.008940	49960.438
C	1.00000	H	2.00000	O	1.00000			0.002390	-6329.594
N	1.00000	O	1.00000					.0000003	33814.988
C	2.00000	H	2.00000					.0000295	78193.125
C	2.00000	H	4.00000					0.000154	44617.719
O	1.00000	H	1.00000					.0000091	20456.828
C	1.00000	H	3.00000					0.000105	55599.371
H	1.00000	C	1.00000	O	1.00000			.0000404	27147.545
N	2.00000							12.648	11625.187

(b) NASA/CET86 OUTPUT OF IN BORE THERMOCHEMICAL PROPERTIES AT CHARGE PORT INTERIOR BALLISTIC STATE

THERMODYNAMIC PROPERTIES

P, ATM	1260.20
T, DEG K	1792.0
RHO, G/CC	1.9079-1
H, CAL/G	-520.16
U, CAL/G	-680.12
G, CAL/G	-4316.83
S, CAL/(G)(K)	2.1187
M, MOL WT	22.262
(DLV/DLP)T	-1.01487
(DLV/DLT)P	1.1133
CP, CAL/(G)(K)	0.5184
GAMMA (S)	1.2478
SON VEL,M/SEC	913.8

MOLE FRACTIONS

FORMALDEHYDE	0.00005
FORMIC ACID	0.00003
CH4	0.00387
CO	0.27027
CO2	0.06889
HCN	0.00014
HNCO	0.00002
H2	0.19068
H2O	0.18307
NH3	0.00170
N2	0.28127

APPENDIX II

NASA/CET86 OUTPUT FOR AIR BEING SHOCKED IN CHARGE PORTS DURING FIRST FIRING CONDITIONS.

SHOCK WAVE PARAMETERS ASSUMING
EQUILIBRIUM COMPOSITION FOR INCIDENT SHOCKED CONDITIONS

INITIAL GAS (1)

MACH NUMBER	6.7158
U1, M/SEC	2337.00
P, ATM	0.99959
T, DEG K	300.0
RHO, G/CC	1.1708-3
H, CAL/G	4.7331
U, CAL/G	-15.943
G, CAL/G	-488.57
S, CAL/(G)(K)	1.6444
M, MOL WT	28.833
CP, CAL/(G)(K)	0.2413
GAMMA (S)	1.3998
SON VEL,M/SEC	348.0

SHOCKED STATE SATISFYING PG/P1 RELATION - EQN.(13)

SHOCKED GAS (2)--INCIDENT--EQUILIBRIUM

U2, M/SEC	360.37	MOLE FRACTIONS	
P, ATM	54.376		
T, DEG K	2517.3	AR	6.7466-3
RHO, G/CC	7.5926-3	CO	9.1508-6
H, CAL/G	641.89	CO2	7.1158-4
U, CAL/G	468.45	HE	7.2092-5
G, CAL/G	-4267.15	N	4.1072-8
S, CAL/(G)(K)	1.9501	NO	2.1830-2
		NO2	1.3088-4
M, MOL WT	28.843	N2	7.9287-1
(DLV/DLP)T	-1.00026	N20	9.0484-6
(DLV/DLT)P	1.0054	NE	1.4300-5
CP, CAL/(G)(K)	0.3431	O	8.9381-4
GAMMA (S)	1.2542	O2	1.7671-1
SON VEL,M/SEC	954.0	O3	1.7043-7
P2/P1	54.398		
T2/T1	8.391		
M2/M1	1.0003		
RHO2/RHO1	6.4850		
V2, M/SEC	1976.63		

APPENDIX III

NASA CET86 OUTPUT OF REFLECTED SHOCK STATE

SHOCKED GAS (5)--REFLECTED--EQUILIBRIUM

U5, M/SEC	567.98
P, ATM	431.27
T, DEG K	4358.5
RHO, G/CC	3.4016-2
H, CAL/G	1377.12
U, CAL/G	1070.08
G, CAL/G	-7439.39
S, CAL/(G)(K)	2.0228

M, MOL WT	28.209
(DLV/DLP)T	-1.01074
(DLV/DLT)P	1.1414
CP, CAL/(G)(K)	0.4859
GAMMA (S)	1.2168
SON VEL,M/SEC	1250.2

P5/P2	7.931
T5/T2	1.731
M5/M2	0.9780
RHO5/RHO2	4.4801
U5+V2,M/SEC	2544.61

MOLE FRACTIONS

AR	6.5982-3
CO	4.0925-4
CO2	2.9564-4
HE	7.0507-5
N	2.4165-4
NCO	6.1906-9
NO	1.0307-1
NO2	4.8567-4
NO3	4.8929-8
N2	7.3416-1
N2O	1.3141-4
N2O3	2.1284-8
N3	5.3703-8
NE	1.3985-5
O	4.4699-2
O2	1.0983-1
O3	4.4121-6

NASA/CET86 OUTPUT OF DETONATION CONDITIONS IN STATE 2/3 MIXING REGION

EQUIVALENCE RATIO= 1.1579
P, ATM   54.3980
T1, DEG K   959.54
H1, CAL/G   -239.95
M1, MOL WT   26.957
GAMMA1   1.2927
AE/AT   618.5

BURNED GAS

P, ATM   280.63
T, DEG K   3007.5
RHO, G/CC   3.1251-2
H, CAL/G   -5.2179
U, CAL/G   -222.68
G, CAL/G   -6341.94
S, CAL/(G)(K)   2.1070

M, MOL WT   27.483
(DLV/DLP)T   -1.00335
(DLV/DLT)P   1.0776
CP, CAL/(G)(K)   0.5172
(S)   1.1891
SON VEL,M/SEC   1040.1

DETONATION PARAMETERS

P/P1   5.159
T/T1   3.134
/M1   1.0195
RHO/RHO1   1.6780
MACH NUMBER   2.8218
DET VEL,M/SEC   1745.4

MOLE FRACTIONS

AR   0.00355
CO   0.07704
CO2   0.12748
H   0.00126
HO2   0.00001
H2   0.01726
H2O   0.20799
NO   0.00294
N2   0.55592
O   0.00023
OH   0.00520
O2   0.00110

TRACKING OF MANEUVERING TARGETS USING ℓ^1 ESTIMATORS

PETROS VOULGARIS

UNIVERSITY OF ILLINOIS AT URBANA CHAMPAIGN

COORDINATED SCIENCE LABORATORY

1308 WEST MAIN, URBANA, IL 61801

ABSTRACT:

In this paper we consider the problem of finding a filter that minimizes the worst case magnitude (ℓ^∞) of the estimation error in the case of linear time invariant systems subjected to unknown but magnitude bounded (ℓ^∞) inputs. These inputs consist of process and observation noise, as well as initial conditions; also, the optimization problem is considered over an infinite time horizon. Taking a model matching approach, suboptimal solutions are presented which stem from the resulting ℓ^∞-induced norm minimization problem. Examples are also presented that compare the performance of the so-obtained estimator with that of Kalman filters.

BIOGRAPHY:

Petros G. Voulgaris was born in Athens, Greece, on January 1963. He received his Diploma of Mechanical Engineering from the National Technical University of Athens in 1986, and the S.M. and Ph.D. degrees in aeronautics and astronautics from the Massachusetts Institute of Technology, Cambridge, MA, in 1988 and 1991, respectively. Since August 1991, he has been Assistant Professor at the Department of Aeronautical and Astronautical Engineering, University of Illinois, Urbana-Champaign where he also holds an appointment with the Coordinated Science Laboratory. His research interests lie in the areas of robust control, time-varying and nonlinear system theory with emphasis to aerospace applications, adaptive control, and robust estimation and identification.

OPTIMAL ℓ^1 ESTIMATION

PETROS VOULGARIS

University of Illinois at Urbana Champaign
Coordinated Science Laboratory
1308 West Main, Urbana, IL 61801

1 INTRODUCTION

Worst case estimation is an alternative approach to stochastic estimation when statistical information about the uncertainty is not available. The subject of worst case estimation for linear systems has been treated by several researchers and is often related to the advances in robust control. The reader is referred to [1,2,12,16] and references therein where, the subject of worst case estimation is treated in the presence of energy (ℓ^2 or $\mathcal{L}^2$) bounded input uncertainty with the objective to minimize the worst case energy of the estimation error. Also, the case where the noise is magnitude bounded and the objective is to minimize the worst case magnitude of the error, is treated in [3,10,15,11] and references therein. In particular, in [3] Euclidean norms for the magnitude are considered and the authors present a recursive algorithm (not necessarily optimal) with similar structure to Kalman filters. In [10,15] optimal algorithms are presented for pointwise estimation problems where the uncertainty is magnitude (ℓ^∞) bounded. More specifically, these algorithms are obtained by solving finite dimensional linear programs; also, time varying bounds on the magnitude of the noise can be handled. However, these algorithms are not recursive and cannot be easily implemented when the ammount of data is large, and in particular, for infinite horizon problems.

In this paper we consider the infinite horizon optimal filtering problem in discrete-time, linear-time-invariant systems (LTI), stable or unstable, when the sources of uncertainty are ℓ^∞-bounded process and observation noise together with uknown (but bounded) initial conditions. We set up the problem as a model matching problem [8] over ℓ^∞-bounded operators. In the case where the initial condition is known, the resulting problem is a model matching problem involving time invariant operators. Hence, a recursive suboptimal (arbitrarily close to optimal) estimator can be produced by solving a standard ℓ^1-optimization [4]. In the case where the initial condition is not known the resulting model matching problem is time varying. Yet, these time varying operators have a specific structure that is being exploited. A suboptimal solution consists of utilizing the suboptimal known-inital-condition (KIC) estimator after some *apriori* computable time index N which depends on the KIC solution, while up to time N the solution of $N + 1$ finite dimensional linear programs is required to construct the suboptimal estimates. This time index N, represents the time that takes the suboptimal KIC filter to make the error that is due only to initial conditions very small. Solving the $N + 1$ linear programs ammounts to finding the optimal pointwise estimator for the time interval $0 - N$ and is therefore equivalent with the approach in [10,15]. Also, conditions are given under which the suboptimal KIC filter is also suboptimal in the presence of unknown initial conditions; this, of course, would be the case whenever the initial condition is relatively small so that it does not affect the worst case estimation error.

The paper is organized as follows: in the next section the problem is defined in terms

of ℓ^∞ norms. In Section 3 the problem is put to a model matching form, and the solution follows for stable systems in subsection 3.1 where we separate the unknown initial condition case from the known (KIC); in subsection 3.2 the case of unstable systems is treated by appropriately transforming the problem to the stable case. In Section 4 we discuss other aspects of the problem such as performance of nonlinear filters and application of the previous results to control problems. Finally, we conclude in Section 5.

In the paper the following notation and terminology is utilized: $x(i)$, $A(i,j)$ represent the ith and the ijth element respectively of the real vector x and the real matrix A. Also, $A(i,.)$ represents the ith row of A, $|x|_\infty \stackrel{\text{def}}{=} \max_i |x(i)|$, $|A|_\infty \stackrel{\text{def}}{=} \max_i \sum_j |A(i,j)|$. If $y = \{y_0, y_1, \ldots\}$ represents a sequence of real matrices y_i, then its λ-transform is $y(\lambda) \stackrel{\text{def}}{=} \sum_{i=0}^\infty \lambda^i y_i$. Furthermore, $\ell^1 \stackrel{\text{def}}{=} \{y : \|y\|_{\ell^1} \stackrel{\text{def}}{=} \sup_i |(y_i \ldots y_0)|_\infty < \infty\}$; in the case where y_i's are vectors we define $\ell^\infty \stackrel{\text{def}}{=} \{y : \|y\|_{\ell^\infty} \stackrel{\text{def}}{=} \sup_i |y_i|_\infty < \infty\}$, $\ell_e^\infty \stackrel{\text{def}}{=} \{y : P_k y \in \ell^\infty \ \forall k = 0, 1, \ldots\}$ where P_k is the truncation operator defined as $P_k y = \{y_0, \ldots, y_k, 0, 0, \ldots\}$. An operator T on ℓ_e^∞ is called causal if $P_k T = T P_k$, $k = 0, 1, \ldots$; T is stable if it is a bounded operator on ℓ^∞. The space of all linear causal bounded operators T on ℓ^∞ is denoted by $\mathcal{L}_{TV}$. If $T \in \mathcal{L}_{TV}$ it can represented with the following lower triangular matrix $T = \begin{pmatrix} t_{00} & 0 & \cdots \\ t_{10} & t_{11} & \cdots \\ \vdots & \vdots & \ddots \end{pmatrix}$ and

$\|T\|_{\mathcal{L}_{TV}} = \sup_i |T(i,.)|_\infty$. $\mathcal{L}_{TI}$ is the subspace of $\mathcal{L}_{TV}$ which contains all causal time invariant ℓ^∞-bounded operators (i.e. Toeplitz matrices). Also, $\mathcal{L}_{TI}$ is isometrically isomorphic to ℓ^1 i.e., $\mathcal{L}_{TI} \simeq \ell^1$.

2 PROBLEM DEFINITION

Consider the following linear, time invariant, finite dimensional system

$$\begin{aligned} x_{k+1} &= A x_k + B w_k \\ z_k &= C_1 x_k \\ y_k &= C x_k + \zeta_k \end{aligned} \tag{1}$$

where w, ζ are process and measurement noise respectively with $\left\| \begin{pmatrix} w \\ \zeta \end{pmatrix} \right\|_{\ell^\infty} \leq 1$, z is an output to be estimated, and y is the measurment signal. Also, associated to the above system, there is an unknown initial condition x_0 which can be arbitrary as long as $|x_0|_\infty \leq 1$. The problem of interest is as follows (OBJ):

Based on the measurements y, construct a linear causal estimator Q of the output z i.e., $\hat{z} = Qy$ such that the following worst case error is minimized:

$$J \stackrel{\text{def}}{=} \sup_{w, \zeta, x_0} \|z - \hat{z}\|_{\ell^\infty}.$$

Note that there is no loss of generallity in assuming that the uncertainty bounds are all equal to 1. In the case where the norm bounds on w, ζ, x_0 are different than 1, we can always normalize the bounds by appropriate scaling. Next, we transform the problem to an

estimation problem where the initial condition is equal to zero. This is done by considering the time varying system

$$\begin{aligned}
\bar{x}_{k+1} &= A\bar{x}_k + Bw_k + L_k d_k \\
z_k &= C_1 \bar{x}_k + D_{1k} d_k \\
y_k &= C\bar{x}_k + \zeta_k + D_k d_k \\
\bar{x}_0 &= 0
\end{aligned} \tag{2}$$

where

$$L_k = \begin{cases} A, & k = 0 \\ 0, & k > 0 \end{cases}, \quad D_{1k} = \begin{cases} C_1, & k = 0 \\ 0, & k > 0 \end{cases}, \quad D_k = \begin{cases} C, & k = 0 \\ 0, & k > 0 \end{cases},$$

w, ζ are as before, d is a disturbance with $\|d\|_{\ell_\infty} \leq 1$, and the system has initial condition $\bar{x}_0 = 0$. Letting $\tilde{w} \stackrel{\text{def}}{=} \begin{pmatrix} w \\ d \\ \zeta \end{pmatrix}$ the following lemma can be easily verified:

Lemma 2.1 *The estimation problem (OBJ) is equivalent to finding a linear causal map Q for the system of Equation 2 such that the criterion*

$$\sup_{\tilde{w}} \|z - \hat{z}\|_{\ell_\infty}$$

is minimized with $\hat{z} = Qy$, $\|\tilde{w}\|_{\ell_\infty} \leq 1$ and $\bar{x}_0 = 0$.

3   PROBLEM SOLUTION

Pertaining to the system of Equation 2 let H, V represent the maps

$$H = (H_{zw} \; H_{zd} \; H_{z\zeta}) : \quad \tilde{w} \to z, \quad V = (V_{yw} \; V_{yd} \; V_{y\zeta}) : \quad \tilde{w} \to y$$

Note H_{zw}, $H_{z\zeta}$, V_{yw}, $V_{y\zeta}$ are time invariant with λ-transforms

$$H_{zw}(\lambda) = C_1((1/\lambda)I - A)^{-1}B, \quad H_{z\zeta}(\lambda) = 0, \quad V_{yw}(\lambda) = C((1/\lambda)I - A)^{-1}B, \quad V_{y\zeta}(\lambda) = I.$$

The map $\tilde{w} \to z - \hat{z}$ is given as

$$T \stackrel{\text{def}}{=} H - QV.$$

Lemma 2.1 states that we are seeking for Q to minimize the ℓ^∞ induced norm of the map T i.e., to minimize

$$\|T\|_{\mathcal{L}_{TV}} = \|H - QV\|_{\mathcal{L}_{TV}}.$$

Clearly, since the map $\zeta \to z - \hat{z}$ is equal to $-Q$ then Q should be a stable operator in $\mathcal{L}_{TV}$ so that the cost J is bounded. To make our point clearer we consider first the case where the system in Equation 1 is stable i.e., the eigenvalues of A have magnitude strictly less than 1.

3.1   Stable Systems

Note, that since we assumed that the system is stable then H, $V \in \mathcal{L}_{TV}$. In addition, H_{zw}, $H_{z\zeta}$, V_{yw}, $V_{y\zeta}$ are in $\mathcal{L}_{TI}$. First we consider the case of known initial conditions for the system of Equation 1.

3.1.1 Known initial condition

Without loss of generality, since the system is linear, we may assume that $x_0 = 0$ which ammounts to setting $d = 0$ in system of Equation 2. In this case the estimation problem transforms to a model maching problem involving time invariant systems

$$\mu_0 \stackrel{\text{def}}{=} \inf_{Q \in \mathcal{L}_{TV}} \|(H_{zw} \ 0) - Q(V_{yw} \ I)\|_{\mathcal{L}_{TV}} \tag{3}$$

In [14] it was shown that, for the above minimization, time varying Q offers no advantage over time invariant. As a matter of fact, for this type of problems even nonlinear Q does not perform better than LTI Q [5]. The problem of finding the optimal Q in $\mathcal{L}_{TI}$ is a ℓ^1-optimization problem. The reader is referred to [4,6,9,7] in order to see how solutions can be obtained using linear programming methods. More specifically, this problem has a "2-block" structure which implies that the optimization problem is, in general, an infinite dimensional linear programming problem. Approximate, finite dimensional, linear programming methods of solution are established in [4,6,9,7]. Using these methods one can obtain recursive Q's that achieve performance within any predefined distance from optimal.

Certain properties of the optimal solution to the above problem that provide intuition are presented in the propositions that follow.

Proposition 3.1 *Let* $\|V_{yw}\|_{\ell^1} \leq 1$. *Then,* $\mu_0 = \|H_{zw}\|_{\ell^1}$ *and hence,* $\overline{Q}_0 = 0$ *is an optimal filter.*

Proof First consider the scalar case i.e., when Q generates a scalar output $\hat{z}$. Then we have that

$$
\begin{aligned}
\|(H_{zw} - QV_{yw} \quad - Q)\|_{\ell^1} &= \|H_{zw} - QV_{yw}\|_{\ell^1} + \|Q\|_{\ell^1} \\
&\geq \|H_{zw}\|_{\ell^1} - \|QV_{yw}\|_{\ell^1} + \|Q\|_{\ell^1} \\
&\geq \|H_{zw}\|_{\ell^1} - \|Q\|_{\ell^1}\|V_{yw}\|_{\ell^1} + \|Q\|_{\ell^1} \geq \|H_{zw}\|_{\ell^1}
\end{aligned}
$$

Hence, the proof follows. For the vector case, i.e., when z and $\hat{z}$ are vectors, we can repeat the same arguments for each component involving only the corresponding rows of $H_{zw}(\lambda)$, $Q(\lambda)$ to conclude that the assertion is true. ∎

The above proposition has an interesting interpretation: recall that the map from the measurement noise ζ to the measurment signal y has norm $\|I\|_{\ell^1} = 1$; the interpretation therefore is that if the "signal to noise ratio" given by $\|V_{yw}\|_{\ell^1} / \|I\|$ is less than 1 then the best estimate is 0. Clearly, such cases are not interesting for estimation since any useful information is severely corrupted by measurment noise.

The next proposition gives a sufficient condition for the problem to have in fact a 1-block structure.

Proposition 3.2 *Let* $V_{yw}(\lambda) = \lambda V_o(\lambda)$ *where* V_o *has a left inverse* V_{ol} *in* $\mathcal{L}_{TI}$ *with* $\|V_{ol}\|_{\ell^1} \leq 1$. *Then, the optimal* Q *of Equation 3 is also optimal for the problem*

$$\mu_{01} = \inf_{Q \in \ell^1} \|H_{zw} - QV_{yw}\|_{\ell^1} .$$

Proof We will deal only with the scalar case i.e., z, $\hat{z}$ scalars. For the vector case, the same argument can be used for each scalar component and the corresponding rows of $Q(\lambda)$ and $H(\lambda)$. First note that $Q_1(\lambda) = \lambda^{-1}H_{zw}(\lambda)V_{ol}(\lambda)$ is in $\mathcal{L}_{TI}$ since $H_1(\lambda) = \lambda^{-1}H_{zw}(\lambda) \in \mathcal{L}_{TI}$; moreover, we have that $H_{zw} - Q_1 V_{yw} = 0 = \mu_{01}$ and hence Q_1 is the optimizer for μ_{01}. Given any $Q \in \mathcal{L}_{TI}$ let $\Phi = H_{zw} - QV_{yw}$; then, $\Phi_1(\lambda) = \lambda^{-1}\Phi(\lambda)$ is in $\mathcal{L}_{TI}$, $\|\Phi\|_{\ell^1} = \|\Phi_1\|_{\ell^1}$, and $Q = (\Phi_1 - H_1)V_{ol}$. Thus,

$$
\begin{aligned}
\|(H_{zw} - QV_{yw} \quad -Q)\|_{\ell^1} &= \|H_{zw} - QV_{yw}\|_{\ell^1} + \|Q\|_{\ell^1} \\
&= \|\Phi\|_{\ell^1} + \|(\Phi_1 - H_1)V_{ol}\|_{\ell^1} \\
&\geq \|\Phi\|_{\ell^1} + \|H_1 V_{ol}\|_{\ell^1} - \|\Phi_1 V_{ol}\|_{\ell^1} \\
&\geq \|\Phi\|_{\ell^1} + \|H_1 V_{ol}\|_{\ell^1} - \|\Phi_1\|_{\ell^1}\|V_{ol}\|_{\ell^1} \\
&\geq \|\Phi\|_{\ell^1} + \|H_1 V_{ol}\|_{\ell^1} - \|\Phi_1\|_{\ell^1} \\
&\geq \|H_1 V_{ol}\|_{\ell^1} = \|Q_1\|_{\ell^1} = \|(H_{zw} - Q_1 V_{yw} \quad -Q_1)\|_{\ell^1}
\end{aligned}
$$

which completes the proof. ∎

The above proposotion shows that under the stated conditions, the optimal KIC estimator is obtained by ignoring the measurement noise and minimizing the effect only of the process noise. In this case the solution is dominated by the 1-block structure. Note also that in this case $\|V_{yw}\|_{\ell^1} = \|V_o\|_{\ell^1} \geq \|V_{ol}\|_{\ell^1}^{-1} \geq 1$. However, the condition $\|V_{yw}\| \geq 1$ alone (i.e., "signal to noise" ratio ≥ 1) is not in general sufficient for a 1-block structure dominance. Next, we treat the more difficult case of unknown initial conditions.

3.1.2 Unknown initial condition

In the case where the initial condition is unknown but bounded as $|x_0|_\infty \leq 1$ the operators H and V are time varying and can be identified with the following lower triangular matrix representation

$$
H = \begin{pmatrix} h_{00} & 0 \\ h & H_0 \end{pmatrix}, \quad V = \begin{pmatrix} v_{00} & 0 \\ v & V_0 \end{pmatrix}
$$

where

$$
h_{00} = (0 \quad C_1 \quad 0), \quad v_{00} = (0 \quad C \quad I),
$$

$h = (h(i,.))_{i=0}^\infty$, $v = (v(i,.))_{i=0}^\infty$ are the $\infty \times 1$ block matrices given as

$$
h(i,.) = (C_1 A^i B \quad C_1 A^{i+1} \quad 0), \quad v(i,.) = (CA^i B \quad CA^{i+1} \quad 0),
$$

and H_0, V_0 are the time invariant operators with the Toeplitz representation

$$
H_0 = \begin{pmatrix} h_0 & 0 & \cdots \\ h_1 & h_0 & \cdots \\ \vdots & \vdots & \ddots \end{pmatrix}, \quad V_0 = \begin{pmatrix} v_0 & 0 & \cdots \\ v_1 & v_0 & \cdots \\ \vdots & \vdots & \ddots \end{pmatrix}
$$

with

$$
h_0 = (0 \quad 0 \quad 0), \quad h_i = (C_1 A^{i-1} B \quad 0 \quad 0), \quad i \geq 1
$$
$$
v_0 = (0 \quad 0 \quad I), \quad v_i = (CA^{i-1} B \quad 0 \quad 0), \quad i \geq 1
$$

Identifying the estimator $Q \in \mathcal{L}_{TV}$ as a $\infty \times \infty$ lower triangular matrix we can partition it as

$$
Q = \begin{pmatrix} q_{00} & 0 \\ q & Q_0 \end{pmatrix}
$$

where $q = (q(i,.))_{i=0}^{\infty}$ is a block $\infty \times 1$ matrix and Q_0 is a block $\infty \times \infty$ lower triangular matrix. We note that Q_0 is not necessarily a time invariant operator i.e., Toeplitz. The resulting map T is represented as

$$T = \begin{pmatrix} t_{00} & 0 \\ t & T_0 \end{pmatrix} = \begin{pmatrix} h_{00} - q_{00}v_{00} & 0 \\ h - qv_{00} - Q_0v & H_0 - Q_0V_0 \end{pmatrix}.$$

Note that H_0, V_0 are equal to $(H_{zw} \ 0 \ 0)$, $(H_{yw} \ 0 \ I)$ respectively which are in turn identical to $(H_{zw} \ 0)$, $(H_{yw} \ I)$ that we considered in the known initial condition case. Hence,

$$\mu_0 = \inf_{Q_0 \in \mathcal{L}_{TV}} \| H_0 - Q_0V_0 \|_{\mathcal{L}_{TV}}.$$

Let now

$$\mu \stackrel{\text{def}}{=} \inf_{Q \in \mathcal{L}_{TV}} \| H - QV \|_{\mathcal{L}_{TV}},$$

and define the "pointwise cost"

$$\nu_i \stackrel{\text{def}}{=} \inf_{Q(i,.)} |T(i,.)|_{\infty} = \inf_{Q(i,.)} |(H - QV)(i,.)|_{\infty}$$
$$= \inf_{Q(i,.)} |H(i,.) - Q(i,.)V|_{\infty}, \quad i = 0, 1, \dots .$$

This implies

$$\nu_0 = \inf_{q_{00}} |t_{00}|_{\infty} = \inf_{q_{00}} |h_{00} - q_{00}v_{00}|_{\infty}$$

and for $i \geq 0$

$$\nu_{i+1} = \inf_{q(i,.),Q_0(i,.)} |T(i+1,.)|_{\infty}$$
$$= \inf_{q(i,.),Q_0(i,.)} |(h(i,.) - q(i,.)v_{00} - Q_0(i,.)v \quad H_0(i,.) - Q_0(i,.)V_0)|_{\infty}.$$

Observe that because of the definition of the $| \bullet |_{\infty}$ matrix norm, the computation of ν_i as well as of the corresponding optimizer $\hat{Q}(i,.)$ is a finite dimensional linear programming problem. The variables to be specified are the elements of the (block) row $\hat{Q}(i,.)$ i.e., the elements in $\hat{Q}(i,j)$, $j = 0, \dots, i$ since $\hat{Q}(i,j) = 0$, $j > i$. Clearly, the optimal $\hat{Q}(i,.)$ should have bounded elements for, otherwise, the cost is infinite; hence ν_i can be achieved. The optimal cost ν_i is in fact the optimal (smallest) worst case error $|z_i - \hat{z}_i|_{\infty}$ that one can obtain based on the measurements $y_0, y_1, \dots, y_i$. In particular, the optimal pointwise estimate will be given by

$$\hat{z}_i = \sum_{j=0}^{i} \hat{Q}(i,j)y_j.$$

Our model matching approach for the pointwise optimal estimate is in essence equivalent with the approach of [10,15] where a general set membership uncertainty framework is utilized. Also note, that the above estimation algorithm will also be optimal for any finite horizon problem i.e., whenever the optimization criterion is taken to be

$$\sup_{\bar{w}} (\max_{k=0,1,\dots,T} |z_k - \hat{z}_k|_{\infty})$$

87

where T is a fixed time instant.

Next, we present a lemma that demonstrates a basic relation of the optimal infinite horizon cost μ with μ_0 and ν_i's :

Lemma 3.1 *Given any integer $N = 0, 1, \ldots$ the following holds*

$$\mu \geq \max(\nu_0, \nu_1, \ldots, \nu_N, \mu_0).$$

Proof   Given any $Q \in \mathcal{L}_{TV}$ it is clear that

$$\|T\|_{\mathcal{L}_{TV}} \geq \|H_0 - Q_0 V_0\|_{\mathcal{L}_{TV}} \geq \mu_0.$$

Also, for any such Q from the definition of ν_i's we get

$$\|T\|_{\mathcal{L}_{TV}} \geq |T(i, \cdot)|_\infty \geq \nu_i, \quad i = 0, \ldots, N.$$

∎

Therefore, if one can find a Q and a N such that

$$\|T\|_{\mathcal{L}_{TV}} \leq \max(\nu_0, \nu_1, \ldots, \nu_N, \mu_0) + \epsilon$$

for some given $\epsilon > 0$, then, Q is a ϵ-suboptimal solution. In the sequel we demonstrate how we can achieve this. To this end, let $\epsilon > 0$ and let $\overline{Q}_0$ be a time invariant operator in $\mathcal{L}_{TI}$ that satisfies

$$\left\| H_0 - \overline{Q}_0 V_0 \right\|_{\mathcal{L}_{TV}} \leq \mu_0 + \epsilon/2.$$

As we already mentioned in the known initial condition case, this is always possible. Let $\overline{Q}_0$ and $\overline{T}_0 \stackrel{\text{def}}{=} H_0 - \overline{Q}_0 V_0$ have the Toeplitz representations

$$\overline{Q}_0 = \begin{pmatrix} \overline{q}_0 & 0 & \cdots \\ \overline{q}_1 & \overline{q}_0 & \cdots \\ \vdots & \vdots & \ddots \end{pmatrix}, \quad \overline{T}_0 = \begin{pmatrix} \overline{l}_0 & 0 & \cdots \\ \overline{l}_1 & \overline{l}_0 & \cdots \\ \vdots & \vdots & \ddots \end{pmatrix}.$$

Also, define the following sequences in ℓ^1

$$\begin{aligned} h_{zd} &= \{C_1, C_1 A, C_1 A^2 \ldots\} \\ v_{yd} &= \{C, CA, CA^2, \ldots\} \\ \phi &= h_{zd} - \overline{Q}_0 v_{yd}. \end{aligned} \tag{4}$$

Note that $\phi = \{\phi_0, \phi_1, \ldots\}$ is associated with the map

$$d \to z - \hat{z} : \quad H_{zd} - \overline{Q}_0 V_{yd} = \begin{pmatrix} \phi_0 & 0 & \cdots \\ \phi_1 & 0 & \cdots \\ \vdots & \vdots & \ddots \end{pmatrix}.$$

In the transform domain we have $\phi(\lambda) = \lambda^{-1}(C_1 - \overline{Q}_0(\lambda)C)(\lambda^{-1} - A)^{-1}$. Since $\phi \in \ell^1$ there exists a computable integer N such that

$$|\phi_i|_\infty < \epsilon/2 \quad \forall i > N.$$

Let now $\hat{q}_{00}$, $\hat{q}(i,.)$, $\hat{Q}_0(i,.)$ be such that

$$\nu_0 = |h_{00} - \hat{q}_{00}v_{00}|_\infty,$$
$$\nu_{i+1} = |(h(i,.) - \hat{q}(i,.))v_{00} - \hat{Q}_0(i,.)v \quad H_0(i,.) - \hat{Q}_0(i,.)V_0)|_\infty, \quad i = 0,\dots,N-1. \quad (5)$$

As already mentioned, the computation of $\hat{q}_{00}$, $\hat{q}(i,.)$, $\hat{Q}_0(i,.)$ can be performed by solving the $N+1$ independent finite dimensional linear programs of Equation 5. The following theorem gives a ϵ-suboptimal estimator

Theorem 3.1 *The estimator*
$$\overline{Q} = \begin{pmatrix} q_{00} & 0 \\ q & Q_c \end{pmatrix}$$

with

$$q_{00} = \hat{q}_{00}, \quad q(i,.) = \begin{cases} \hat{q}(i,.), & 0 \le i < N \\ \overline{q}_{i+1}, & i \ge N \end{cases}, \quad Q_0(i,.) = \begin{cases} \hat{Q}(i,.), & 0 \le i < N \\ \overline{Q}_0(i,.), & i \ge N \end{cases},$$

achieves $\left\| H - \overline{Q}V \right\|_{\mathcal{L}_{TV}} \le \mu + \epsilon.$

Proof By construction of $\overline{Q}$ we have

$$|(H - \overline{Q}V)(i,.)|_\infty = \nu_i, \quad i = 0,1,\dots,N$$

and for $i \ge N+1$

$$\begin{aligned} |(H - \overline{Q}V)(i,.)|_\infty &= |(\overline{T}_0(i,.) \quad \phi_i)|_\infty \\ &\le |\overline{T}_0(i,.)|_\infty + |\phi_i|_\infty \\ &\le \mu_0 + \epsilon. \end{aligned}$$

Hence,

$$\left\| H - \overline{Q}V \right\|_{\mathcal{L}_{TV}} \le \max(\nu_0, \nu_1, \dots, \nu_N, \mu_0) + \epsilon$$

and the proof is complete. ∎

Note that for time $k \ge N+1$ the estimator of Theorem 3.1 coincides with the ϵ-suboptimal estimator $\overline{Q}_0$ that corresponds to the known initial condition problem i.e.,

$$(\overline{Q}y)(k) = (\overline{Q}_0 y)(k), \quad k \ge N+1.$$

Hence the meaning of the above theorem is that the known initial condition estimator will provide ϵ-suboptimal estimates after the precomputable time index N. This time N amounts to the time that takes the known initial condition estimator $\overline{Q}_0$ to drive the estimation error that is due only to initial conditions within a small bound $\epsilon/2$. For the time period 0 to N, the (sub)optimal estimates can be obtained by solving $N+1$ linear programs; these estimates correspond to obtaining the optimal pointwise esimates. Once time N is passed, optimal pointwise estimation does not improve on the infinite time cost J.

An interesting question is the following: under what condition does the estimator $\overline{Q}_0$ provide as good performance as $\overline{Q}$? Clearly, that will be the case whenever the initial condition uncertainty is small enough. In particular, for $\overline{Q}_0$ to be as good as $\overline{Q}$ it is sufficient that

$$|(H - \overline{Q}_0 V)(i,.)|_\infty \leq \mu_0 + \epsilon, \ i = 0, 1, \ldots, N$$

which means that $\mu_0 \leq \mu \leq \mu_0 + \epsilon$. Hence, we have the following

Corollary 3.1 *The known initial condition estimator $\overline{Q}_0$ is ϵ-suboptimal if*

$$|(T_0(i,.) \quad \phi_i)|_\infty \leq \mu_0 + \epsilon, \ i = 0, 1, \ldots, N.$$

In the case where the above condition is violated one can find by how much the initial condition uncertainty has to be reduced so that $\overline{Q}_0$ yields ϵ-suboptimal performance. To do this, let $a_m \in (0,1)$ be defined as

$$a_m = \max\{a \in (0,1): \ |(T_0(i,.) \quad a\phi_i)|_\infty \leq \mu_0 + \epsilon, \ i = 0, 1, \ldots, N\}. \tag{6}$$

Then, $\overline{Q}_0$ is ϵ-suboptimal whenever $|x_0|_\infty \leq a_m$, and $\left\|\begin{pmatrix} w \\ \zeta \end{pmatrix}\right\|_{\ell^\infty} \leq 1$. We conclude this subsection by considering the following example

Example 3.1 We consider the $\ell^\infty - \ell^\infty$ worst case filtering problem for the second order stable system

$$x_{k+1} = \begin{pmatrix} 0 & -.2 \\ 1 & 0 \end{pmatrix} x_k + \begin{pmatrix} 1 \\ 0 \end{pmatrix} w_k$$

$$z_k = \begin{pmatrix} 1 & 0 \\ 0 & 1 \end{pmatrix} x_k$$

$$y_k = (2 \quad 0)x_k + \zeta_k$$

where w, ζ are process and observation noise respectively with $|w_k| \leq 1$ and $|\zeta_k| \leq 1$ for $k = 0, 1, 2, \ldots$. The eigenvalues of the A-matrix are located at $\pm.4472j$. Furthermore, we assume that $x_0 = 0$ and hence we consider the KIC estimator. As mentioned previously, the problem becomes a ℓ^1-optimization which yields (using the Delay Augmentation method [7]) for the optimal map $\begin{pmatrix} w \\ \zeta \end{pmatrix} \rightarrow z - \hat{z}$

$$T_0(\lambda) = \begin{pmatrix} 0 & -.5 \\ 0 & -.5\lambda \end{pmatrix}.$$

The optimal cost is $\mu_0 = .5$ and the associated optimal KIC estimator is

$$\overline{Q}_0(\lambda) = \begin{pmatrix} .5 \\ .5\lambda \end{pmatrix}.$$

In fact, the resulting $\overline{Q}_0$ is also optimal for the 1-block problem

$$\mu_{01} = \inf_{Q \in \ell^1} \|H_{zw} - QV_{yw}\|_{\ell^1} = 0$$

since the conditions of Proposition 3.2 are satisfied: $V_{ol}(\lambda) = .5 + .1\lambda^2$, $\|V_{ol}\|_{\ell^1} \leq 1$.

Next, assume that an initial condition uncertainty of the form $|x_0|_\infty \leq 1$ is present in addition to the noise w, ζ. One can find a time index N above which the estimates of the optimal KIC estimator $\overline{Q}_0$ can be used. To do this, we form the sequence ϕ (Equation 4) which gives

$$\phi = \{\begin{pmatrix} 0 & 0 \\ 0 & 1 \end{pmatrix}, \begin{pmatrix} 0 & 0 \\ 0 & 0 \end{pmatrix}, \dots\}.$$

This implies that $N = 0$ and hence there is only one linear program that has to be solved in order to find the optimal $\overline{Q}$. This is simply a 2-dimensional linear program

$$\nu_0 = \min_{q_{00}} |h_{00} - q_{00}v_{00}|_\infty$$

which gives $\nu_0 = .5$ and $\hat{q}_{00} = \begin{pmatrix} .5 \\ .5 \end{pmatrix}$. Hence, the optimal estimator $\overline{Q}$ for the unknown initial condition will produce a cost of $\mu = \max(\nu_0, \mu_0) = .5$. The optimal filter $\overline{Q}$ is given as

$$\hat{z}_0 = \hat{q}_{00}y_0, \quad \hat{z}_k = (\overline{Q}_0 y)(k), \quad k = 1, 2, \dots .$$

Also note that the KIC filter is sensitive to initial condition uncertainty of size 1 since

$$|(\overline{T}_0(0,.) \quad \phi_0)|_\infty = 1 > \mu_0 = .5 .$$

From Equation 6 we obtain that $a_m = .5$ which implies that the optimal KIC filter will be also optimal for any initial condition with $|x_0|_\infty \leq .5$. Also, note that the first row of ϕ_i's is zero which implies that if only the first component z^1 of $z = \begin{pmatrix} z^1 \\ z^2 \end{pmatrix}$ were to be estimated, the KIC would have also been optimal for any initial condition uncertainty. This is also why $\overline{Q}$ and $\overline{Q}_0$ give the same estimates (as it can be easily checked) for the first component z^1. We conclude this example by presenting simulation results in the case where $x_0 = 0$: In Figures 3, 4 the estimation error is depicted for the inputs of Figures 1, 2 respectively. In particular, Figure 1 represents zero-mean Gaussian white noise input of unit intensity, whereas in Figure 2 a square wave type input of unit amplitude is shown (w is the solid whereas ζ is the dashed line). Figures 3, 4 show the estimation error in the first component z^1 of $z = \begin{pmatrix} z^1 \\ z^2 \end{pmatrix}$ for the optimal $\ell^\infty - \ell^\infty$ estimator $\overline{Q}_0$ (dashed line) together with the estimation error of the optimal Kalman Filter (solid line). As it can be observed the optimal $\ell^\infty - \ell^\infty$ estimator performs better than the Kalman Filter in the case of the input of Figure 2; the maximum error is .5 compared to .59 of the Kalman filter. Of course, this should be expected since the optimization criteria are different.

3.1.3   Discussion

In the previous sections we presented how suboptimal estimators can be constructed. Although the construction of a suboptimal recursive KIC estimator is easy, the construction in the case of unknown initial conditions is more involved. In particular, one has to solve the $N + 1$ linear programs of Equation 5 in order to obtain the optimal filter for the time $0 - N$,

and then "switch" to the KIC estimator. The time index N is computed from the knowledge of the KIC filter by requiring that the sequence ϕ in Equation 4 satisfies $|\phi_i|_\infty < \epsilon/2 \ \forall i > N$. In what follows we comment upon the size of N and relate it to the solution of the KIC case, when the latter results to a finite impulse response (FIR) map $\overline{T}_0$ from the input $\begin{pmatrix} w \\ \zeta \end{pmatrix}$ to the estimation error $z - \hat{z}$. First we have the following existence lemma

Lemma 3.2 *If (A, C) is an observable pair, then, given any $\epsilon > 0$, there exists a suboptimal map $\overline{T}_0 : \begin{pmatrix} w \\ \zeta \end{pmatrix} \to z - \hat{z}$ of the form*

$$\overline{T}_0(\lambda) = \overline{l}_0 + \overline{l}_1 \lambda + \ldots + \overline{l}_n \lambda^n$$

such that $\left\| \overline{T}_0 \right\|_{\ell^1} \leq \mu_0 + \epsilon$ for some n.

Proof see appendix ∎
Such a solution can be obtained with the methods in [4,6,9]. This of course implies that the suboptimal $\overline{Q}_0$ has also finite impulse response. The support n of the suboptimal solution will in general depend on the degree of desired accuracy: the larger n is allowed, the closer to the optimal value μ_0 the filter performance assumes. This is not to say however, that the optimal solution should necessarily have infinite support (see Example 3.1). Let now $\overline{Q}_0(\lambda) = \sum_{i=0}^{n} \overline{q}_i \lambda^i$ and let n_0 be the number of eigenvalues of A at the origin (if any). The following lemma characterizes a bound on the index N.

Lemma 3.3 *If (A, B) is a reachable pair, then $\phi_i = 0$ for $i > n_0 + n - 1$.*

Proof see appendix ∎
In view of the above, one can always take $N = n_0 + n - 1$. Note that this is in accordance with Example 3.1 for which $n_0 = 0$, $n = 1$, $N = 0$. Also, in the case where suboptimal solutions are FIR, the support of ϕ does not depend on the bound on the size $|x_0|_\infty$ of the initial condition uncertainty. More specificaly, if take $N = n_0 + n - 1$ suggested in Lemma 3.3 then $\phi_i = 0$, $i > N$ no matter what the bound on the initial condition uncertainty may be; i.e., the index N will be the same for any initial condition uncertainty. This is to say that the (sub)optimal filter $\overline{Q}$ produces the same estimates as the KIC filter $\overline{Q}_0$ for time larger than N no matter what the initial conditions are. Note however, that the estimates of $\overline{Q}$ for time $0 - N$ depend on the size of the initial condition uncertainty. Finally, we should also stress, that the index N does not represent the time that takes the initial condition response of the system to become arbitrarily small but rather, it represents the time that takes the KIC filter to bring the error due to initial condition to a small level. Hence, even in systems with very "slow" eigenvalues the resulting N need not necessarily be large as the following example indicates:

Example 3.2 Consider the system

$$x_{k+1} = \begin{pmatrix} 0 & -.9 \\ 1 & 0 \end{pmatrix} x_k + \begin{pmatrix} 1 \\ 0 \end{pmatrix} w_k$$
$$z_k = (1 \quad 0) x_k$$
$$y_k = (.5 \quad 1) x_k + \zeta_k$$

where w, ζ are process and observation noise respectively with $|w_k| \leq 1$ and $|\zeta_k| \leq 1$ for $k = 0, 1, 2, \ldots$. The eigenvalues of the A-matrix are located at $\pm .9487j$. For the known initial condition case we obtain (within 10^{-8} of the optimal) $\overline{Q}_0(\lambda) = .3673 - .7347\lambda$, $\overline{T}_0(\lambda) = (.8163\lambda \quad .3673 - .7347\lambda)$, and $\mu_0 = 1.9183$. For the index N we have that $\phi_i = 0$, $i > 0$ and hence, we can take $N = 0$; this means that if initial condition uncertainty is allowed, there is only 1 linear program to be solved in order to compute the suboptimal estimator.

3.2 Unstable systems

In the case of unstable systems i.e., when the eigenvalues of A are not in the open unit disk, the problem can be transformed using coprime factorization to a model matching problem involving only stable systems. Moreover, the resul~ng problem has the same structure as in the stable system case. This is done in the seque~ ~irst, we make the following assumption

Assumption 3.1 *The pair (A, C) is detectable.*

Due to the above assumption there is an estimator Q_1 such that the resulting error $z - \hat{z}$ is bounded. Such a Q_1 can be taken any observer of the form:

$$\hat{x}_{k+1} = A\hat{x}_k - K(y_k - C\hat{x}_k)$$
$$\hat{z}_k = C_1\hat{x}_k, \quad \hat{x}_0 = 0$$

where K is any matrix such that $A_K = A + KC$ is a stable matrix. Now, we can parametrize Q as $Q = Q_1 + Q_2$ where Q_2 is any system in $\mathcal{L}_{TV}$. If we define $\tilde{H} \overset{\text{def}}{=} H - Q_1 V$ then $\tilde{H} \in \mathcal{L}_{TV}$. A state space description of $\tilde{H}$ is

$$\tilde{H} = (A_K, (B \quad L_k + KD_k \quad K), C_1, (0 \quad D_{1k} \quad 0)), \quad k = 0, 1, \ldots \tag{7}$$

Then, the filtering problems becomes

$$\inf_{Q_2 \in \mathcal{L}_{TV}} \left\| \tilde{H} - Q_2 V \right\|_{\mathcal{L}_{TV}}$$

Note that $V = (V_{yw} \quad V_{yd} \quad V_{y\zeta}) = (V_{yw} \quad V_{yd} \quad I)$ is unstable; let G represent the map $\begin{pmatrix} w \\ d \end{pmatrix} \to y$ i.e., $G = (V_{yw} \quad V_{yd})$ and consider a coprime factorization $G = \tilde{M}^{-1}\tilde{N}$. A set of (left)coprime factors can be obtained from the following state space description [8,13]:

$$\tilde{M} = (A_K, K, C, I)$$
$$\tilde{N} = (A_K, (B_K)_k, C, (D_K)_k), \quad k = 0, 1, \ldots$$

where

$$(B_K)_k = (B \quad L_k + KD_k), \quad (D_K)_k = (0 \quad D_k), \quad k = 0, 1, \ldots.$$

Note that $\tilde{M} \in \mathcal{L}_{TI}$ whereas $\tilde{N} \in \mathcal{L}_{TV}$. The following lemma can now be derived

Lemma 3.4 *The estimation error $z - \hat{z}$ is bounded iff $Q_2 = \tilde{Q}\tilde{M}$, where $\tilde{Q}$ is any stable operator in $\mathcal{L}_{TV}$.*

Proof The "if" follows immediately since if $Q_2 = \tilde{Q}\tilde{M}$ then

$$T = \tilde{H} - \tilde{Q}(\tilde{G} \quad I) = \tilde{H} - \tilde{Q}(\tilde{N} \quad \tilde{M})$$

is stable. For the "only if" we have first that any causal Q_2 can be written as $Q_2 = \tilde{Q}\tilde{M}$ since $\tilde{M}$ is causaly invertible. In addition, $Q_2(G \quad \tilde{I}) = \tilde{Q}(\tilde{N} \quad \tilde{M}) \in \mathcal{L}_{TV}$ and $(\tilde{N} \quad \tilde{M})$ has a right inverse in $\mathcal{L}_{TV}$ since $\tilde{M}, \tilde{N}$ are left coprime; hence $Q_2 \in \mathcal{L}_{TV}$. ∎

In view of the above, if $\tilde{V} = (\tilde{N} \quad \tilde{M})$ then $\tilde{V}$ is in $\mathcal{L}_{TV}$ with state space representation

$$\tilde{V} = (A_K, (B \quad L_k + KD_k \quad K), C, (0 \quad D_k \quad I)), \quad k = 0, 1, \ldots \tag{8}$$

Moreover, the estimation problem transforms to

$$\mu = \inf_{\tilde{Q} \in \mathcal{L}_{TV}} \left\| \tilde{H} - \tilde{Q}\tilde{V} \right\|_{\mathcal{L}_{TV}} \tag{9}$$

where $\tilde{H}$, $\tilde{V}$ are stable maps in $\mathcal{L}_{TV}$. From the state space descriptions of $\tilde{H}$, $\tilde{V}$ it is clear that $\tilde{H}$, $\tilde{V}$ are of the same form as in the stable system case: the new A-matrix is A_K and the new B-matrix is $(B \quad L_k + KD_k \quad K)$ whereas the rest remain the same. In terms of input-output matrix representations they are of the form

$$\tilde{H} = \begin{pmatrix} \tilde{h}_{00} & 0 \\ \tilde{h} & \tilde{H}_0 \end{pmatrix}, \quad \tilde{V} = \begin{pmatrix} \tilde{v}_{00} & 0 \\ \tilde{v} & \tilde{V}_0 \end{pmatrix}$$

where $\tilde{h}$, $\tilde{v}$ are $\infty \times 1$ block matrices the rows of which decay exponentially fast (as the largest eigenvalue of $A + KC$) and $\tilde{H}_0$, $\tilde{V}_0$ are time invariant operators in $\mathcal{L}_{TI}$. In particular, $\tilde{H}_0$ and $\tilde{V}_0$ are given as

$$\tilde{H}_0 = (A_K, (B \quad 0 \quad K), C, (0 \quad 0 \quad 0)), \quad \tilde{V}_0 = (A_K, (B \quad 0 \quad K), C, (0 \quad 0 \quad I)) \tag{10}$$

Also, note that $\tilde{V}_0 = (\tilde{N}_0 \quad 0 \quad \tilde{M}_0)$ where $\tilde{M}_0$ and $\tilde{N}_0$ are the left coprime factors of V_{yw} given by

$$\tilde{M}_0 = \tilde{M}, \quad \tilde{N}_0 = (A_K, B, C, 0).$$

From the above discussion, it follows that the problem is exactly as in the case of stable systems and a ϵ-suboptimal $\tilde{Q}$ can be obtained similarly. The suboptimal estimator in this case is given as $\overline{Q} = Q_1 + \tilde{\overline{Q}}\tilde{M}$. Finally note that in the known initial condition case, one has to solve the following ℓ^1 optimization

$$\mu_0 = \inf_{\tilde{Q}_0 \in \mathcal{L}_{TI}} \left\| \tilde{H}_0 - \tilde{Q}_0 \tilde{V}_0 \right\|_{\mathcal{L}_{TI}} \tag{11}$$

Once a suboptimal $\tilde{\overline{Q}}_0$ is obtained the corresponding suboptimal filter is given as $\overline{Q}_0 = Q_1 + \tilde{\overline{Q}}_0 \tilde{M}_0$.

4 REMARKS

Herein, we discuss further various aspects of the problem and the implications of its solution given in the previous section.

4.1 Linear vs nonlinear filters

Throughout the paper we have assumed the filters Q were linear. In fact, one can prove that there is no additional advantage offered if a wider class that includes nonlinear filters is considered. In particular, let $\mathcal{N}$ denote the set of all bounded causal nonlinear (not necessarily linear) maps Q on ℓ^∞ which satisfy the linerizability condition [5]: there is a $Q_L \in \mathcal{L}_{TV}$ such that

$$\lim_{\alpha \to 0} \sup_{\|f\|_{\ell^\infty} \leq \alpha,\ f \neq 0} \frac{\|Qf - Q_L f\|_{\ell^\infty}}{\|f\|_{\ell^\infty}} = 0.$$

Clearly, $\mathcal{L}_{TV} \subset \mathcal{N}$. The following theorem can be derived along the lines of [5]

Theorem 4.1 *Let* $\mu_{NL} = \inf_{Q \in \mathcal{N}} \|H - QV\|_{\ell^\infty - \ell^\infty}$. *Then* $\mu = \mu_{NL}$.

Proof Let $Q \in \mathcal{N}$ and let $Q_L \in \mathcal{L}_{TV}$ be its linearization. We will show that $\|H - QV\| \geq \|H - Q_L V\|$ where $\|\bullet\|$ stands for the ℓ^∞ induced norm. From the linearization condition we have that given any $\epsilon > 0$,

$$\sup_{\|f\|_{\ell^\infty} \leq \alpha,\ f \neq 0} \frac{\|(Q - Q_L)Vf\|_{\ell^\infty}}{\|f\|_{\ell^\infty}} \leq \epsilon$$

for some $\alpha > 0$. Then,

$$
\begin{aligned}
\|H - QV\| &\geq \sup_{\|f\|_{\ell^\infty} \leq \alpha,\ f \neq 0} \frac{\|(H - Q_L V - (Q - Q_L)V)f\|_{\ell^\infty}}{\|f\|_{\ell^\infty}} \\
&\geq \sup_{\|f\|_{\ell^\infty} \leq \alpha,\ f \neq 0} \frac{\|(H - Q_L V)f\|_{\ell^\infty}}{\|f\|_{\ell^\infty}} - \sup_{\|f\|_{\ell^\infty} \leq \alpha,\ f \neq 0} \frac{\|(Q - Q_L)Vf\|_{\ell^\infty}}{\|f\|_{\ell^\infty}} \\
&\geq \|H - QV\| - \epsilon
\end{aligned}
$$

where we have used that $\sup_{\|f\|_{\ell^\infty} \leq \alpha,\ f \neq 0} \frac{\|(H - Q_L V)f\|_{\ell^\infty}}{\|f\|_{\ell^\infty}} = \|H - Q_L V\|$ since $H - Q_L V$ is linear. Since ϵ is arbitrary the proof follows. ∎

Hence, it is enough to search for linear filters.

4.2 Application to ℓ^1 optimal control with transients

The method presented of solving the estimation problem has also application to the problem of designing $\ell^\infty - \ell^\infty$ optimal controllers when there is, in addition to ℓ^∞-disturbances, a magnitude bounded uncertainty in the initial condition of the plant. In particular, for linear time invariant systems with unknown initial condition (but bounded, say by 1) the ℓ^∞ to ℓ^∞ optimization problem can be brought in the form

$$\inf_{Q \in \mathcal{L}_{TV}} \|T_1 - T_2 Q T_3\|_{\mathcal{L}_{TV}}$$

where T_1, T_2, T_3 are in $\mathcal{L}_{TV}$. For certain maps, (for instance from reference to control input in a unity feedback configuration) $T_2 = I$; moreover, T_1, T_3 are of the same form as in the estimation problem. Hence in these cases the same method of solution indicated herein applies.

5 CONCLUSIONS

In this paper we presented how suboptimal, infinite-horizon estimators can be constructed in the case of linear time invariant systems with ℓ^∞ bounded uncertainty. A model matching approach over ℓ^∞ bounded operators was taken. In the known initial condition (KIC) case the problem is simply a ℓ^1-optimization. In the unknown initial condition case, optimal pointwise estimation can be used until a precomputable time index after which, the KIC recursive estimator can be utilized. This time index corresponds to the time it takes the KIC filter to make small the estimation error that is due exclusively to initial conditions.

APPENDIX

Proof of Lemma 3.2

Following the same procedure as in the case of unstable systems (subsection 3.2) we can reformulate the problem as

$$\mu_0 = \inf_{\tilde{Q}_0 \in \mathcal{L}_{TI}} \left\| \tilde{H}_0 - \tilde{Q}_0 \tilde{V}_0 \right\|_{\mathcal{L}_{TI}}$$

where $\tilde{H}_0$, $\tilde{V}_0$ are as in Equation 10 and $A_K = A + KC$ where now K can be selected to make A_K have all of its eigenvalues at the origin. This is always possible due to the assumption that (A, C) observable. Thus, both $\tilde{H}_0$, $\tilde{V}_0$ are FIR. Moreover, $\tilde{V}_0 = (\tilde{N}_0 \ \tilde{M}_0)$ where $\tilde{M}_0$ and $\tilde{N}_0$ are the left coprime factors of V_{tw} given by $\tilde{M}_0 = \tilde{M}$, $\tilde{N}_0 = (A_K, B, C, 0)$. Hence [4,9], a FIR suboptimal solution can always be constructed. ∎

Proof of Lemma 3.3

Let $\overline{T}_0 = (\overline{T}_{01} \ \overline{T}_{02})$ and let $\overline{Q}_0 = \overline{T}_{02}$ have the realization $\overline{Q}_0 = (A_q, B_q, C_q, D_q)$. Then $\overline{T}_{01} = (A_0, B_0, C_0, D_0)$ where

$$A_0 = \begin{pmatrix} A & 0 \\ B_q C & A_q \end{pmatrix}, \ B_0 = \begin{pmatrix} B \\ 0 \end{pmatrix}, \ C_0 = (C_1 - D_q C \ C_q), \ D_0 = 0.$$

Moreover, if $\psi(\lambda) = \lambda\phi(\lambda)$ then ψ can be realized as $\psi = (A_0, B_1, C_0, D_0)$ where $B_1 = \begin{pmatrix} I \\ 0 \end{pmatrix}$. Clearly, the poles of A_0 consist of the poles of A and A_q with A_q having poles only at the origin. Now, the fact that $\overline{T}_{01}$ is FIR and that (A, B) is assumed to be reachable implies that all poles of A that are not at the origin are not observable through C_0: if not, i.e., if there exist a pole of A not at the origin that is observable through C_0 then necessarily (since T_{01} is FIR) this pole should not be reachable from B_0 which contradicts that (A, B) is reachable. Then, from the realization of ψ we have that the poles of A not at the origin are not observable and hence (since the rest of the poles are at the origin) $\psi(\lambda)$ is FIR with length bounded by $n_0 + n$ where n is the length of $\overline{T}_0$. Note also that the since $D_0 = 0$ the sequence $\lambda^{-1}\psi = \phi$ is well defined and is also FIR with support bounded by $n_0 + n - 1$. ∎

References

[1] T. Basar, "Optimum performance levels for minimax filters, predictors and smoothers," *Syst. Contr. Lett.*, vol. 16, 1991, pp. 309-318.

[2] D.S. Bernstein and W.M. Haddad, "Steady-state Kalman filtering with an $\mathcal{H}^{\infty}$ error bound," *Syst. Contr. Lett.*, vol. 12, 1989, pp. 9-16.

[3] D.P. Bertsekas and I.B. Rhodes, "Recursive state estimation for set membership description of uncertainty," *IEEE Trans. A-C*, Vol AC-16, 1971, pp. 117-124.

[4] M.A. Dahleh and J.B. Pearson. "Optimal rejection of persistent disturbances, robust stability and mixed sensitivity minimization," *IEEE Trans. Automat. Contr.*, Vol AC-33, pp. 722-731, August 1988.

[5] M.A. Dahleh and J.S. Shamma, "Rejection of persistent bounded disturbances: Nonlinear controllers", *Syst. Contr. Lett.*, vol. 18, 1992, pp. 245-253.

[6] M.A. Dahleh. "BIBO stability robustness in the presence of coprime factor perturbations," *IEEE Trans. A-C*, Vol AC-37, no 3, 1992.

[7] I. Diaz-Bobillo and M.A. Dahleh, "Minimization of the maximum Peak-to-Peak Gain: The general multiblock problem," to appear IEEE trans A-C.

[8] B.A. Francis. *A Course in H_{∞} Control Theory*, Springer-Verlag, 1987.

[9] J.S. McDonald and J.B. Pearson, "ℓ^1-Optimal control of multivariable systems with output norm onstraints," *Automatica*, Vol 27, 1991, pp. 317-329.

[10] M. Milanese and R. Tempo, "Optimal algorithms theory for robust estimation and prediction," *IEEE Trans. A-C*, Vol AC-30, 1985, pp. 730-738.

[11] M. Milanese and A. Vicino, "Optimal estimation for dynamic systems with set membership uncertainty: an overview," *Automatica*, Vol 27, 1991, pp. 997-1011.

[12] K.M. Nagpal and P.P. Khargonekar, "Filtering and smoothing in an H^{∞} setting," *IEEE Trans. A-C*, Vol AC-36, no 2, 1991, pp. 152-166.

[13] R. Ravi, P.P. Khargonekar, K.D. Minto and C.N. Nett. "Controller parametrization for time-varying multirate plants" *IEEE Trans on Automatic Control*, AC-35, no. 11, pp. 1259-1262, November 1990.

[14] J.S. Shamma and M.A. Dahleh, Time varying vs. time invariant compensation for rejection of persistent bounded disturbances and robust stability, *IEEE Trans. A-C*, Vol AC-36, July 1991, pp. 838-847.

[15] R. Tempo, "Robust estimation and filtering in the presence of bounded noise," *IEEE Trans. A-C*, Vol AC-33, no 9, 1988, pp. 864-867.

[16] I. Yaesh and U. Shaked, "Game theoty approach to optimal linear estimation in the minimum $\mathcal{H}^{\infty}$ norm sense," *Proc. 28th CDC*, pp.421-425, 1989.
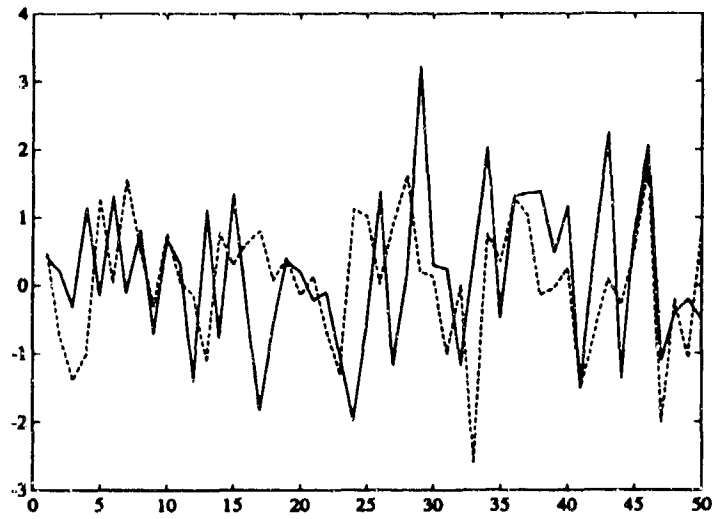
Figure 1: White noise input: w in solid, ζ in dashed line.
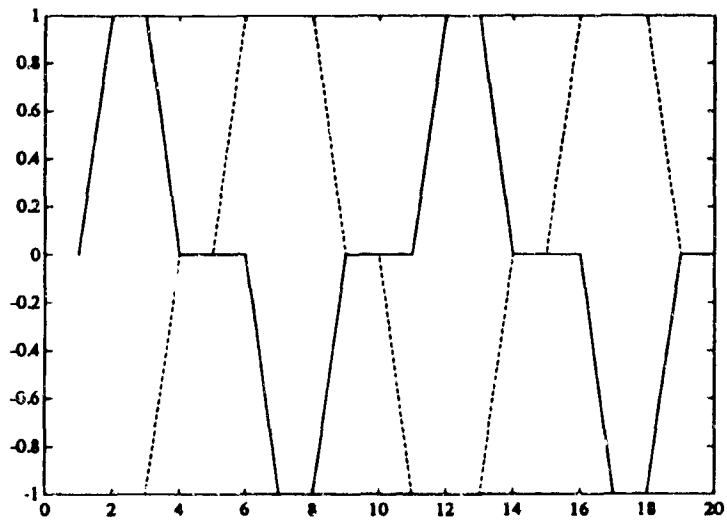
Figure 2: Square wave input: w in solid, ζ in dashed line.

99
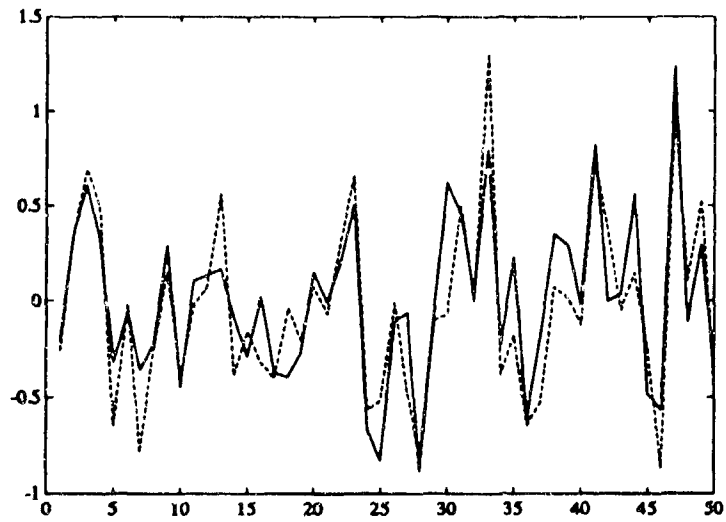
Figure 3: Estimation error of output z^1: Kalman filter in solid, Optimal $\ell^\infty - \ell^\infty$ filter in dashed line.
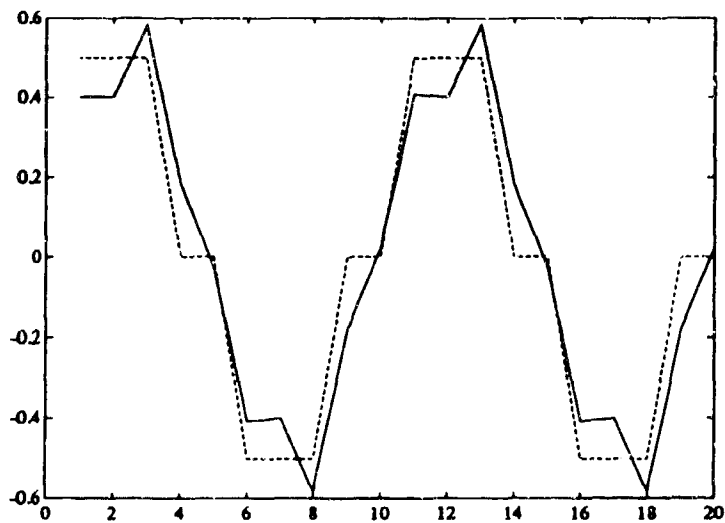
Figure 4: Estimation error of output z^1: Kalman filter in solid, Optimal $\ell^\infty - \ell^\infty$ filter in dashed line.

SESSION II

PROJECTILE MOTION

HELD, WEBB AND SCHMIDT

TITLE: IDENTIFICATION AND QUANTIFICATION OF SOURCES OF OCCASION-TO-OCCASION
         ELEVATION VARIABILITY IN TANK GUN ACCURACY
         BRUCE J. HELD, DAVID W. WEBB, EDWARD M. SCHMIDT
         AERODYNAMICS BRANCH, PROPULSION AND FLIGHT DIVISION
         U.S. ARMY RESEARCH LABORATORY
         ABERDEEN PROVING GROUND, MD 21005

ABSTRACTS:

        This paper describes the identification of some of the root causes of one of
the components of tank gun accuracy errors, namely occasion-to-occasion variability.
Occasion-to-occasion variability is the shift of the mean impact point for a given
tank/gun tube combination from one firing occasion to another. Unless the cannon
and fire control system of the tank can be calibrated for each firing event through
live fire zeroing, its occasion-to-occasion variability will have an adverse effect
on the accuracy of tank cannons. Unfortunately, live fire zeroing before each
firing event is impractical for several reasons. First and foremost is the cost.
Not only does each ammunition type require a separate zero, but each ammunition type
requires a minimum of three rounds to achieve calibration. Even given unlimited
ammunition, the logistical requirements of providing this much ammunition to each
tank unit is beyond the sustaining capability of those units. Additionally, the
tactical situation will rarely allow the time, space or security needed to zero each
of the unit's tanks. Finally, there is currently no way to determine the end and
start of new firing occasions. A calibration zero may be minutes or days long,
depending on many different variables.

        Many factors influence the magnitude of occasion-to-occasion variability.
Identification and analysis of these factors is critical to understanding and
solving the occasion-to-occasion variability problems in the M1 series tank. Over
the last several years, an effort by the Army Research Laboratory has identified and
quantified several components to this error source. These include: errors
associated with optical alignment of the cannon to the fire control system,
uncorrected gun jump which is dependent on the propellant temperature of the
ammunition, variation in the linear recoil motion which couples into the angular
motion of the gun and lot-to-lot variations of the ammunition used in the tank.

BIOGRAPHY: MAJ Bruce J. Held
PRESENT ASSIGNMENT: Currently an Armor Technology Manager for the Army Research
                     Laboratory, concentrating on issues related to the accuracy
                     of tank cannons.

PAST EXPERIENCE: Previous assignments include command and staff positions within
                  armor and armored cavalry units, to include command of a scout
                  platoon at Ft. Carson, Colorado and command of an armored
                  cavalry troop in Bamberg, Germany.

DEGREES HELD: BS, United States Military Academy (West Point), 1980
               MS, Stanford University, 1989

Identification and Quantification of Sources of Occasion-to-Occasion Elevation Variability in Tank Gun Accuracy

Bruce J. Held[*], David W. Webb and Edward M. Schmidt

Aerodynamics Branch, Propulsion and Flight Division
U.S. Army Research Laboratory
Aberdeen Proving Ground, MD 21005

1. INTRODUCTION

During the ground offensive of the 1991 Gulf War, one of the most spectacular examples of the high tech advantage enjoyed by the Coalition Forces was the accuracy of the M1 series tank. Historically, tank battles have been fought at ranges under 1000 meters. This has been due to a combination of intervisibility problems and the inability of tanks to accurately engage at longer ranges. This all changed during the Gulf War. Intervisibility problems were minimized by the flat desert terrain and the M1A1 tank was able to successfully engage targets out to three kilometers and beyond.

As a result of the example of the Gulf War, developers of tanks around the world can be expected to continue efforts aimed at improving the accuracy of their tanks. The implication for the U.S. Army is that we must also continue to improve the accuracy of our own tanks or lose the advantage that we currently enjoy. Given the current political and fiscal realities this means improving the M1 series tank for a number of years. Research efforts in this area can also extend to almost any other cannon system, direct and indirect fire, that may be employed on future U.S. weapons. This paper describes the identification and possible fixes for some of the root causes of one of the components of tank gun accuracy errors, namely occasion-to-occasion variability.

2. COMPONENTS OF TANK GUN ACCURACY

Generally, tank cannon accuracy is broken into several components for ease of analysis. The statistical means and standard deviations of groups of shot impacts on targets are used to describe these components of accuracy. The accuracy components generally used are round-to-round dispersion, occasion-to-occasion variability, central tendency and tank-to-tank variability. These various terms are described below and illustrated with Figure 1.

Figure 1 represents a target with the aim point located at the origin. In this example, rounds were fired over three occasions. On each occasion, three rounds were fired and the target impacts were recorded.

Each shot fired is represented on the target with open squares, circles or triangles to distinguish the impacts of the three firing occasions. The average of each of these groups is represented by a solid symbol of the same
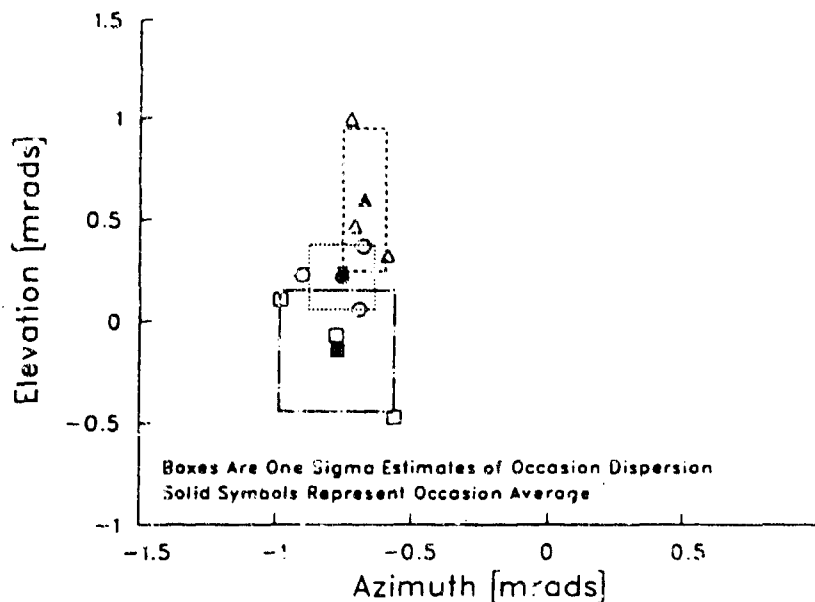
Figure 1.   Example Target and Shot Impacts

kind. This average value is known as the occasion zero and the standard deviations associated with these three-round groups are known as the round-to-round dispersion. On Figure 1, the estimate of the round-to-round dispersion for each occasion is indicated by the box surrounding each occasion's average impact point. In this example, the average value of the round-to-round dispersion is 0.14 milliradians (mrads) in azimuth and 0.27 in elevation. These are typical values, although this component of accuracy is very much round-type dependent.

The standard deviation of the means of the three-round shot groups represents occasion-to-occasion variability. Occasion-to-occasion variability in this example is 0.05 mrad in azimuth and 0.37 mrad in elevation. Generally, occasion-to-occasion variability is estimated to average 0.25 mrad in azimuth and elevation across the tank fleet and across ammunition types.

The mean value of all nine shots for this tank is an estimate of this tank's central tendency, represented by an X in Figure 1. In this example, the tank has an estimated central tendency of 1.26 mrad in azimuth and .23 mrad in elevation.

Finally, tank-to-tank variability for a particular ammunition type is a measure of the dispersion of the average central tendencies across the fleet of tanks. Tank-to-tank variability is estimated at 0.25 mrad in both azimuth and elevation. The mean central tendency across the fleet is normally referred to as the fleet zero value for an ammunition type.

3.   SOURCES OF OCCASION-TO-OCCASION ERROR

Determination of the sources of occasion-to-occasion error is primarily a process of looking for those events that cause a change between firing occasions, either in the armaments system of the tank itself or in the ammunition that will be fired. Some of these events, such as improper maintenance of the cannon system or damage to the ammunition, are obvious.

While the effect of such causes can be significant in the field, they will not be considered in this paper as they are correctable through training and proper procedure.

The other root causes of occasion-to-occasion variability are more subtle. They may happen slowly over time or by abrupt changes in the tank or environment. These are problems over which the soldier in the field can exercise little to no control. These problems must be corrected through hardware changes in the tank itself or by accounting for them in the fire control solution calculated for each round.

3.1 Definition of a Firing Occasion.

Different firing occasions are defined in terms of time, i.e. a long period (hours or days) between rounds; or in terms of significant events between rounds, such as maintenance on the weapon, large environmental changes or moving the tank to new firing positions. For the purposes of this paper, a firing occasion is defined to include all of those rounds fired from the same tank during a time period in which no significant events (with the exception of firing the weapon) have occurred that could affect the fire control system on the tank, the cannon system, or ammunition.

3.2 Muzzle Velocity Variation

Muzzle velocity variation affects accuracy by varying the projectile's time of flight to the target. The time of flight variation, in turn, varies the gravity drop of the projectile during its trajectory and hence there is an elevation error. Occasion-to-occasion variations in muzzle velocity are primarily caused by two distinct sources – the daily temperature cycle and a lot-to-lot variation in the average muzzle velocity for an ammunition type.

3.2.1 Muzzle Velocity Variations Due to Temperature Differentials

The ignition and burning rate of ammunition propellant varies with temperature. Warmer propellant ignites and burns at a faster rate than cooler propellant. This means that projectiles are accelerated more quickly when the propellant is warm and more slowly when the propellant is cool. This results in a relationship between muzzle velocity and propellant temperature. This relationship is well understood and is accurately modeled with a second degree polynomial. Therefore, if the propellant temperature of the ammunition is known, the muzzle velocity can be accurately calculated.

In modern tanks, ammunition temperature is estimated by measuring the air temperature in the ammunition storage compartment (hereinafter referred to as the bustle). There are two problems with this approach. First, there is a difference in the round temperature based on the round's location in the storage compartment. Because of this difference, one bustle air temperature measurement cannot be accurate for all the ammunition. Rounds stored near the top of the bustle tend to heat and cool more quickly due to thermal radiation transfer through the top of the turret, while ammunition in the bottom of the bustle is insulated to a greater degree by the air and ammunition above it. The second problem with measuring bustle air temperature to estimate ammunition temperature is that air and ammunition change temperature at different rates, producing a phase shift between the diurnal temperature cycles of the bustle air and the

ammunition in the compartment. Thus, during the day, the temperature cycle for ammunition near the top of the bustle precedes the bustle air temperature cycle by about 1.5 hours while the ammunition temperature cycle at the bottom lags the
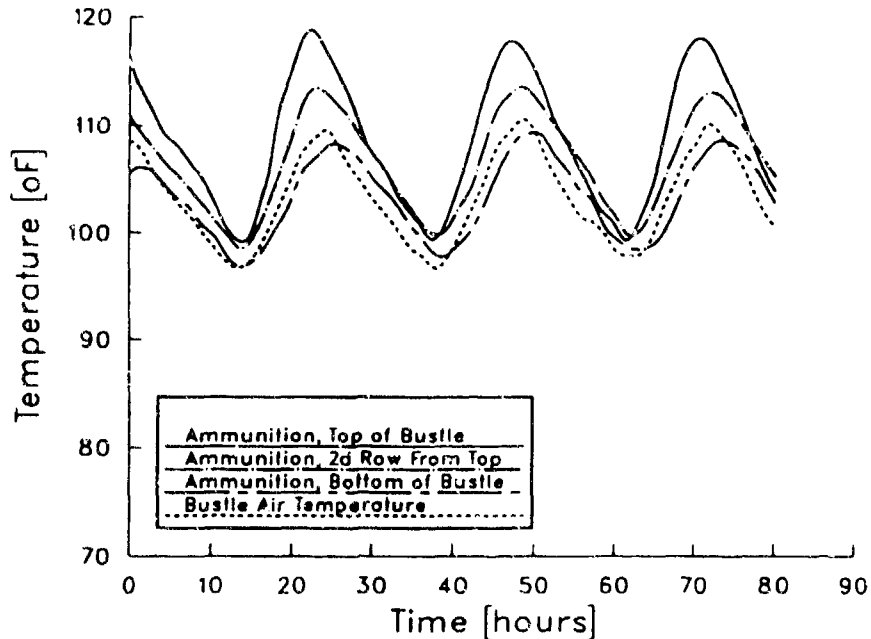
Figure 2. **Ammunition and Ammunition Compartment Temperature Cycles**

air temperature cycle by about an hour. The phase shift between the temperature cycles implies a differential between the average ammunition temperature and the measured air temperature.

Both the phase shift and the temperature difference associated with ammunition storage location are evident in Figure 2. This figure plots the temperature of ammunition stored at three locations in the ammunition storage compartment of an M1A1 tank and the storage compartment air temperature [1]. These plots were collected by instrumenting rounds of ammunition with thermo-couples and placing the rounds in the ammunition storage compartment. The tank was then placed in the open and the various temperatures were monitored for several days.

Difficulties in measurement of ammunition temperature prior to firing creates both round-to-round and occasion-to-occasion accuracy errors. The temperature difference between rounds of ammunition at a particular time creates a round-to-round error, since rounds with different muzzle velocities may be selected at that time. The temperature of the average round is different than the air temperature in the bustle and the magnitude of that difference varies through the diurnal cycle, thus, the diurnal temperature variation for all rounds creates an occasion-to-occasion accuracy problem.

The occasion-to-occasion error due to the use of the bustle air temperature to calculate muzzle velocity is estimated by comparing a muzzle velocity that is calculated using the average ammunition temperature with a muzzle velocity that is calculated using the bustle air temperature. Figures 3 and 4 plot these muzzle velocities for both M831 High Explosive, Anti-Tank,

Training Practice (HEAT-TP) and M865 Training Practice, Cone Stabilized, Discarding Sabot (TPCSDS) ammunition respectively. ΔMV is the difference between the average and calculated muzzle velocities.

A statistical analysis of the ΔMV provides an estimated mean ΔMV over the entire time of consideration (72 hours, or three complete cycles, for this analysis) and a standard deviation. When the mean ΔMV is not equal to zero, the muzzle velocity calculation based on the bustle air temperature is biased. A positive mean for ΔMV indicates that the muzzle velocity estimates tend to be underestimated, while a negative mean indicates an overestimation. Mean-squared error (MSE) is a measure of closeness that takes into consideration not only the variance of an estimator, but also the bias of that estimator. It is given by the formula, $MSE = (Bias)^2 + c^2$. MSE is used here as a measure of the muzzle velocity estimation error. Table 1 lists the mean ΔMV, the standard deviation and the velocity MSE resulting from temperature measurement errors.
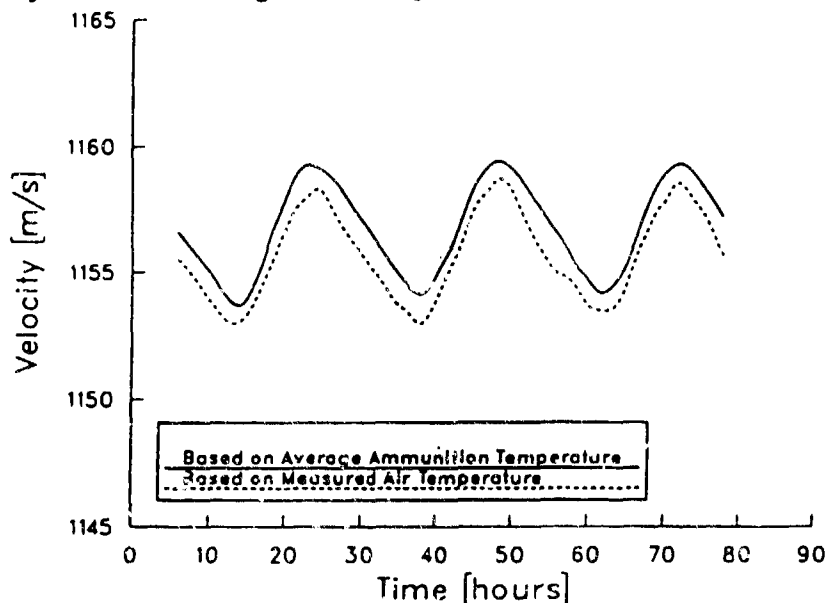
Figure 3. Average and Calculated Muzzle Velocity, M831
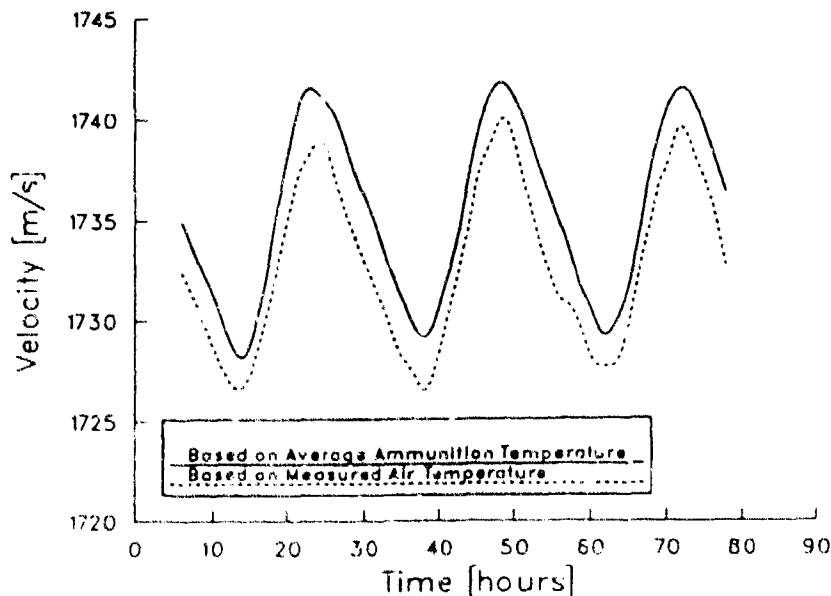
Figure 4. Average and Calculated Muzzle Velocity, M865

Table 1. Temperature Related Muzzle Velocity Statistics

	Mean ΔMV	$\sigma_{\Delta MV}$	$\sqrt{MSE}$
M831	-1.19	0.24	1.21
M865	-2.84	0.61	2.90

All Units Are Meters/Second

An estimate of the occasion-to-occasion elevation error caused by calculating muzzle velocity based on bustle air temperature is found by calculating two trajectories. One trajectory is calculated for a round launched at the muzzle velocity estimated with the bustle air temperature. The other trajectory is calculated with the same muzzle velocity plus or minus the error term from Table 1. The trajectories are differenced and an angular measure of the error is calculated as a function of range. The two trajectories were calculated using the Ballistic Research Laboratory General Trajectory Program [2]. Figure 5 plots the temperature related muzzle velocity error as a function of range for both the M831 and M865.
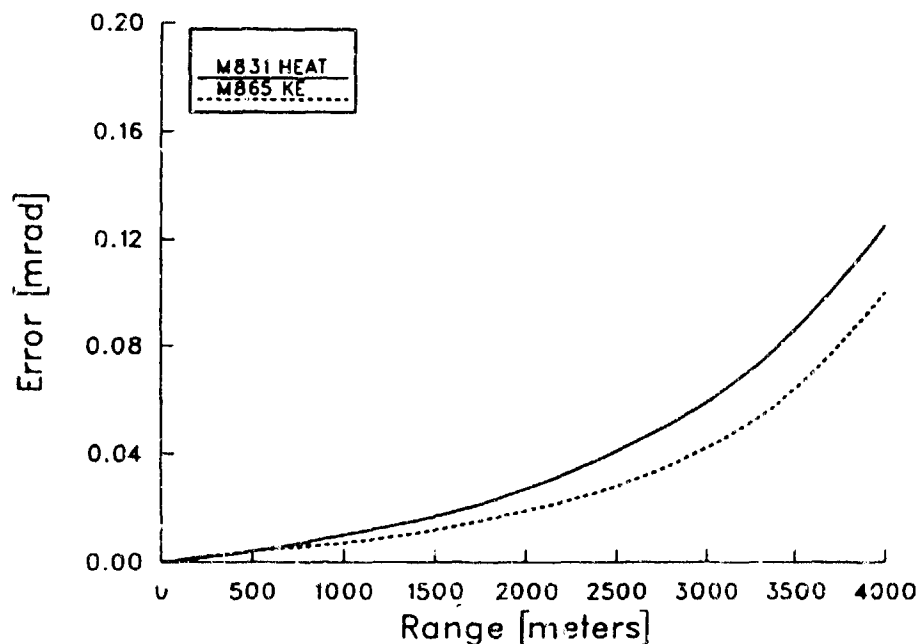
Figure 5. Error Due to Temperature Related Muzzle Velocity Variation

Notably, this error is range dependent and increases with range. The M831's error is 0.06 m ad a 3000 meters, while the error for the M865 is 0.04 mrad at the same range. The M831's greater sensitivity to muzzle velocity variation is due primarily to its lower initial velocity and its greater retardation (loss of velocity as a function of range). The high retardation is the result of the M831's high drag shape. It should be pointed out that the M865 is cone stabilized and is also a relatively high drag projectile. The occasion-to-occasion temperature related muzzle velocity error associated with a fin stabilized, service KE projectile is, therefore, significantly lower than that of the M865, due to the lower drag associated with fin stabilization.

3.2.2 Lot-to-Lot Muzzle Velocity Variations

Service ammunition is generally manufactured in lots of several thousand rounds. The quality of each lot is tightly controlled and is verified through lot acceptance testing. One way in which quality is controlled is through the use of single lots of component parts in the manufacture of completed rounds of ammunition. For example, only one lot of propellant will be used in the manufacture of a lot of completed rounds. While this reduces variability within a lot, variation between lots is to be expected.

For ease of accountability and accuracy, tank ammunition is normally issued to a unit from the same lot. This means that accuracy errors occuring as a result of lot-to-lot variations normally show up as occasion- to-occasion errors, rather than as round-to-round errors. One ammunition characteristic that varies from lot-to-lot is the average muzzle velocity for each lot of ammunition. Therefore, lot-to-lot muzzle velocity variations manifest themselves as occasion-to-occasion accuracy errors

The mean muzzle velocity for a lot of ammunition can be found in the lot acceptance test records for each lot of ammunition. Records for a total of 36 lots of M831 HEAT-TP ammunition and 29 lots of M865 TPCSDS ammunition were examined. The mean muzzle velocity and the standard deviation about the mean was calculated for each ammunition type to get an estimate of the lot-to-lot muzzle velocity variation. When the mean muzzle velocity is not equal to the required muzzle velocity, bias is introduced into the superelevation correction for the gun. As with the temperature related muzzle velocity variation, a mean-squared error term is used to estimate error in order to account for the bias and the variation. Table 2 is a listing of the required muzzle velocity, the mean muzzle velocity across the lots of tested ammunition, the standard deviation and the MSE resulting from the difference between the required and actual muzzle velocities.
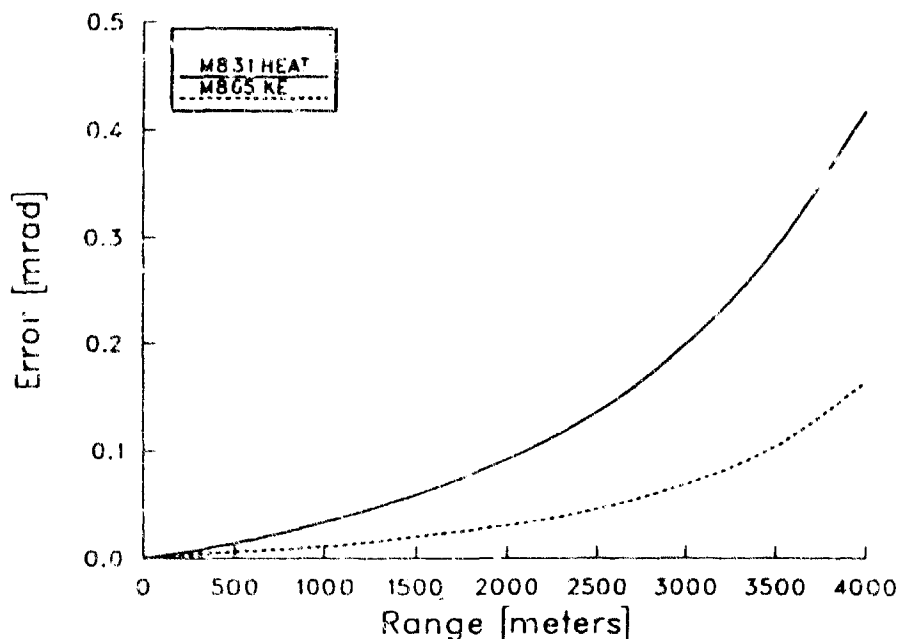
Figure 6. Error Due to Lot-to-Lot Muzzle Velocity Variation

Table 2. Lot-to-Lot Muzzle Velocity Statistics

	Standard MV	Mean MV	Mean ΔMV	$\sigma_{\Delta MV}$	$\sqrt{MSE}$
M831	1140.0	1139.03	-0.97	3.95	4.07
M865	1700.0	1700.90	0.90	4.65	4.74

All Units Are Meters/Second

An estimate of the occasion-to-occasion elevation error caused by lot-to-lot muzzle velocity variation may be found in a manner similar to that used to find the temperature related muzzle velocity variation error. Figure 6 plots the lot-to-lot error as a function of range for both the M831 and M865. This error is also range dependent and increases with range. The M831's lot-to-lot error is 0.19 mrad at 3000 meters, while the error for the M865 is 0.07 mrad at the same range. For the same reasons stated above, the M831's greater sensitivity to muzzle velocity variations is evident. Again, service KE ammunition can be expected to be even less sensitive to muzzle velocity variations than M865.

3.3 Gun Dynamics

A change in the pointing angle of the muzzle during the shot process will cause a projectile to exit the cannon at a different launch angle than was initially laid. When this effect is predictable, it may be accounted for in modern fire control computers with a computer correction factor (CCF). In fact, one component of the CCF in the M1 series tank is the average value of the muzzle pointing angle at shot exit. Variation in the average muzzle pointing angle at shot ejection between rounds and from firing occasion to firing occasion makes it impossible to provide a precise value for the CCF; therefore finding the cause of muzzle angle variation between firing occasions is needed to reduce occasion-to-occasion variability.

The dynamics of the cannon are known to affect occasion-to-occasion variability in at least two significant ways. First is a coupling of the linear recoil of the cannon into its angular motion, hence a coupling of linear recoil variation to muzzle angle variation [3]. Second, the temperature of the ammunition determines the amount of time it takes the projectile to travel the length of the cannon. If the cannon has any angular motion during this in-bore time, ammunition fired at different temperatures will exit the cannon with varying muzzle angle conditions [4].

In large tank cannons, there are several forces which create turning moments about the trunnions during firing. The dominant moment is due to a breech mass imbalance, which causes the center of gravity of the recoiling mass to be lower than the centerline of the gun. This offset acts as a lever arm when the pressure of the burning propellant accelerates the gun by pushing against the breech block along the centerline. The resultant couple, known as the powder pressure couple, induces a torque and subsequent rotation about the trunnion of the gun system [5]. In addition to the powder pressure couple, forces exerted by the radially expanding gun tube against the gun tube bearings and the resistance of the elevating mechanism to rotation create additional turning moments (Figure 7).

Simply modeling these forces results in the following equation of rigid body motion for the cannon:

$$\ddot{\theta} = \frac{\ddot{r}_1 r_2 m + \sum_{i=5}^{n} F_i r_i - [br_3 \dot{\theta} + kr_3 \theta]}{J_{cg} + m(r_1^2 + r_2^2)} = \frac{\ddot{r}_1 r_2 m + \sum_{i=5}^{n} F_i r_i - [br_3 \dot{\theta} + kr_3 \theta]}{I_T} \qquad (1)$$

where θ is the angular rotation of the cannon about the trunnion. The powder pressure couple is modeled by r_1, the magnitude of the linear recoil of the gun along its centerline; r_2, the offset between the center of gravity of the gun and the centerline of the cannon; and m, the mass of the cannon. The resistive forces at the elevating mechanism are modeled by b and k, the damping and spring constants of the elevating mechanism, and r_3, the distance between the elevating mechanism and the trunnion. The forces of gun tube expansion against the gun bearings are modeled by F_i, a distance of r_i from the center of gravity. I_{cg} equals the moment of inertia of the cannon about the center of gravity, and I_T equals the moment of inertia about the trunnion [3].
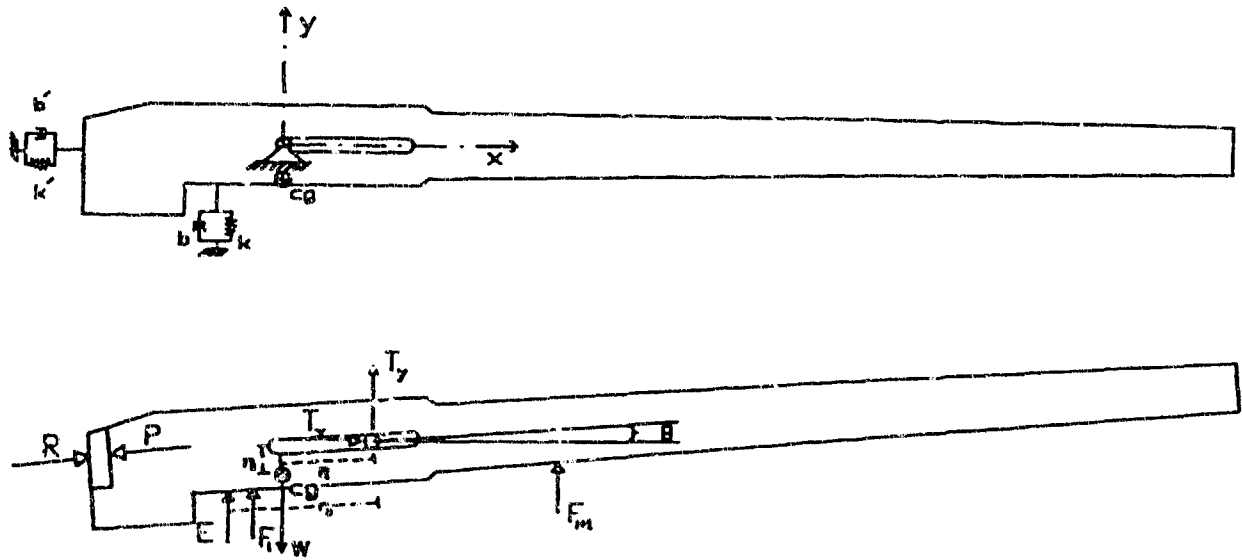
Figure 7. Simple Tank Cannon Model

3.3.1 Recoil Variation.

It is important to note that the equation of the angular motion has a term, $\ddot{r}_1 r_2 m$, that is dependent on the recoil acceleration. This implies that a change in recoil motion will be seen as a change in the angular motion of the cannon. Recoil motion can vary for a number of reasons. These include maintenance of the recoil system, changes in recoil hydraulic fluid temperature and viscosity, and varying hydraulic pressures between occasions. Also of note is the fact that this same term depends on the magnitude of the vertical offset, r_2, between the center of gravity and the centerline of the gun. By moving the cannon's center of gravity with balancing weights, the offset between the center of gravity and the centerline can be eliminated. With zero offset, all recoil loads act along the centerline of the cannon. Thus, the angular motion due to the powder pressure couple is eliminated. By comparing the motion of the cannon with and without the balancing masses, it is possible to gain some insight into the variability of the angular motion that results from changes in recoil motion.
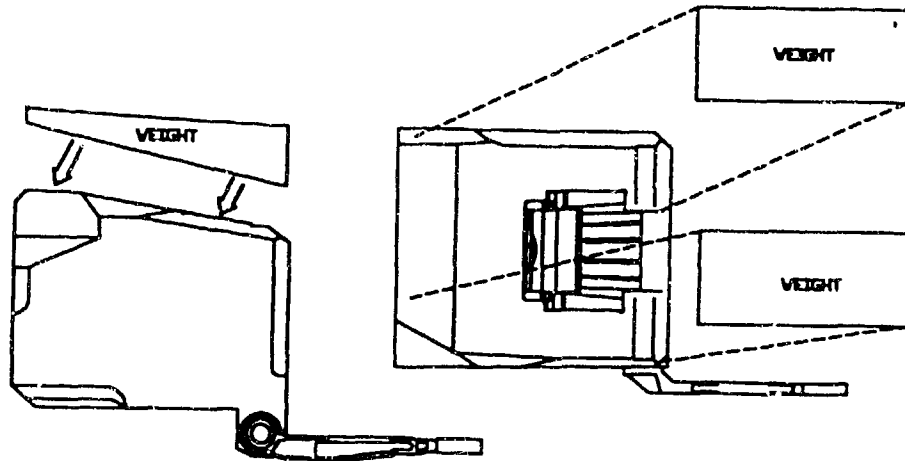
Figure 8.   Cannon Breech and Balancing Weights

A test was conducted in which the center of gravity of the recoiling mass of an M256 cannon was moved to the centerline of the gun [6]. This was accomplished by adding mass to the top of the breech of an M256 tank cannon (Fig. 8). This configuration will be referred to as the balanced breech. Reference to the standard breech will indicate that the weights were not attached to the breech. During this test, the muzzle angle of the cannon was measured with proximity probes [7]. Two different gun tubes were used for this test and both were configured with and without the balancing weights.

Figure 9 plots the muzzle pointing angle of one of the cannons during four firing occasions with M831 HEAT ammunition - two occasions with the balancing weights and two without. Shot exit time is at 0.0 milliseconds (msec). The occasions were separated by several days and movement of the tank. The muzzle pointing angle plots of the two occasions fired in the standard configuration fall into two populations, while those of the balanced firings cannot really be separated.
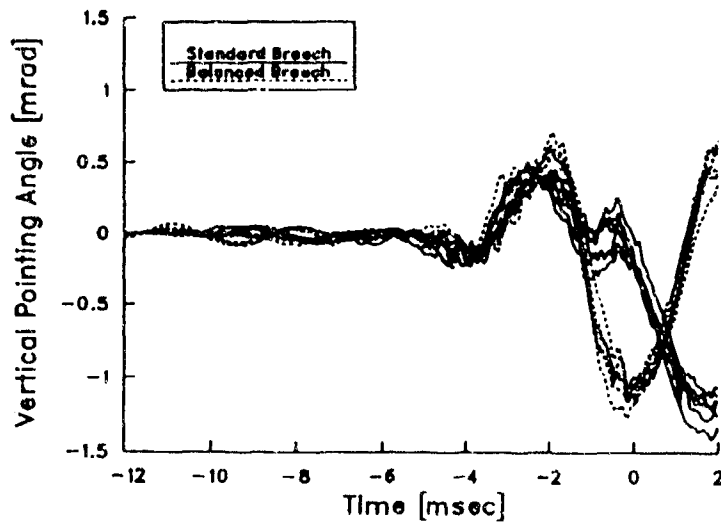
Figure 9.   Muzzle Pointing Angle, 2 x Firing Occasion, Balanced Breech and, 2 x Firing Occasion, Standard Breech

111
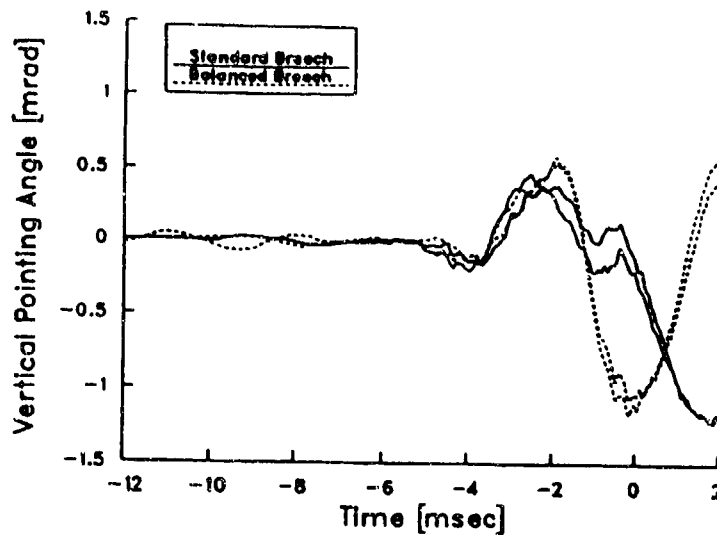
Figure 10. <u>Average Muzzle Pointing Angle, 2 x Firing Occasion, Balanced Breech and, 2 x Firing Occasion, Standard Breech</u>

This is seen more clearly in Figure 10, where the plots of individual shots in each firing occasion are averaged together. The averaged plots for the balanced configuration's two occasions nearly lie on top of one another, while those in the standard configuration are quite distinct.

These same trends are clear with the other gun tube and ammunition type [3]. Figures 11 and 12 are plots of the muzzle pointing angle variation for a cannon firing, respectively, M831 HEAT and a kinetic energy (KE) round whose in-bore characteristics are similar to M865.
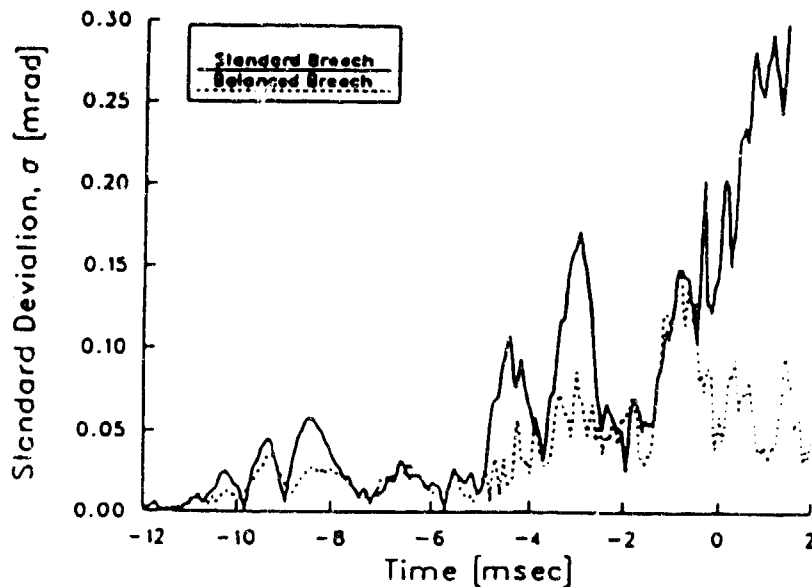
Figure 11. <u>Variation in Vertical Muzzle Pointing Angle, HEAT Ammunition, 4 Rounds/Occasions</u>
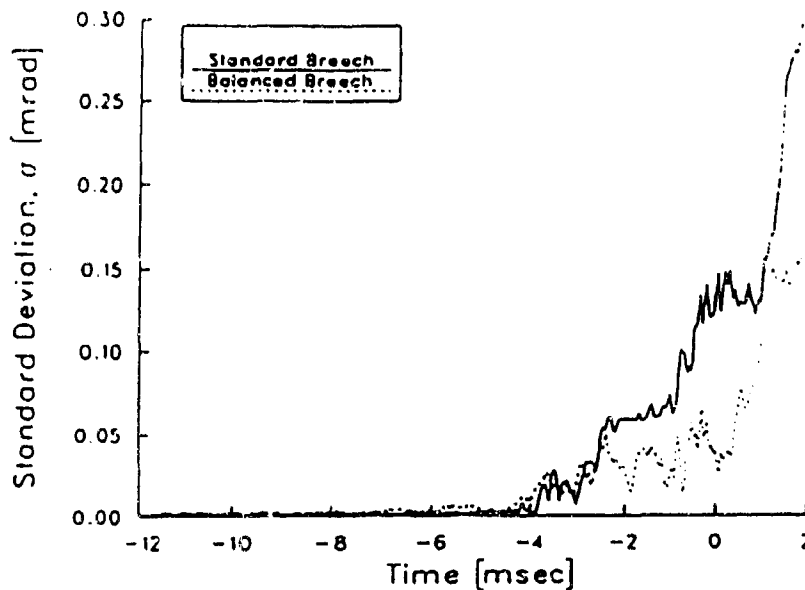
Figure 12. <u>Variation in Vertical Muzzle Pointing Angle,</u>
<u>KE Ammunition, 4 Rounds/Occasions</u>

Four rounds of each ammunition type were fired per gun to obtain estimates
of muzzle pointing angle variation. Combinations of time, movement of the tank,
and temperature change broke up the four round groups into firing occasions,
though each round did not necessarily represent a new occasion. The elevation
variation of muzzle pointing angle at shot exit for the standard configuration
is approximately .19 mrad with M831 HEAT-TP and .14 mrad with the KE ammunition.
The balanced configuration has variations at shot exit of .07 and .04 mrad
respectively for M831 and KE ammunition. The difference in variation between
the two configurations is due to the decoupling of the linear recoil motion and
the angular motion of the muzzle.

The residual muzzle angle variability seen in the balanced configuration
is a round-to-round effect. Assuming that the causes of the residual
varia'·ility are independent of the recoil effects, they may be removed in a
root-sum-square sense:

$$\sigma^2_{tmv} = \sigma^2_{rv} + \sigma^2_{rr} \tag{2}$$

For HEAT ammunition $\quad \sigma_{rv} = 0.177^2 = \sqrt{0.19^2 - 0.07^2}$ \tag{3}

For KE ammunition $\quad \sigma_{rv} = 0.134^2 = \sqrt{0.14^2 - 0.04^2}$ \tag{4}

where σ_{rv}-muzzle pointing angle variation that is due to recoil variation,
σ_{tmv}-total muzzle pointing angle variation and σ_{rr}-the residual round-to- round
muzzle velocity variation.

The muzzle angle variation that is the result of recoil variation has both
round-to-round effects and occasion-to-occasion recoil effects. While it is not
possible to separate the round-to-round and occasion-to-occasion effects, the
information gives some idea about the the magnitude of the two. Even assuming
that the occassion-to-occasion effects make up only half of the total, this
represents an error of .13 and .09 mrads for HEAT-TP and KE ammunition
respectively.

3.3.2 Propellant Temperature.

As mentioned earlier, propellant burn rates are a function of propellant temperature. As a result, muzzle velocity and in-bore time varies with temperature. In addition to the muzzle velocity errors, there is a significant impact bias for certain ammunition types that is dependent on ammunition temperature and is independent of the change in gravity drop associated with the muzzle velocity variation.

In order to determine the muzzle angle at shot exit, equation 1 is integrated twice. The muzzle angle at shot exit therefore depends on the limits of this integration, which are defined by the in-bore time of the projectile. Since the propellant temperature directly affects the in-bore time of the projectile, it will also affect the muzzle angle at shot exit [4].

Figure 13 is a plot of the muzzle pointing angle for firings of M831 HEAT ammunition which was conditioned to three different temperatures. Of note in these plots is that the general shapes of the curves are very similar. The major difference between the plots appears to be a time shift. Note that the pointing angle curve around shot exit time (0.0 msec) has a very steep slope. This causes a significantly different muzzle pointing angle at shot exit between the three conditions due to the time shift.

Currently, the muzzle pointing angles of only a limited number of ammunition types conditioned to different temperatures before firing have been measured. There are, however, computational methods for determining the pointing angles for different ammunition types across a range of temperatures [4]. There is also target data (i.e., measured holes in targets) for most current ammunition types that were fired after being conditioned to different temperatures. It is this target data that is used here to estimate the occasion-to-occasion effects of muzzle angle dependence on propellant temperature [8].
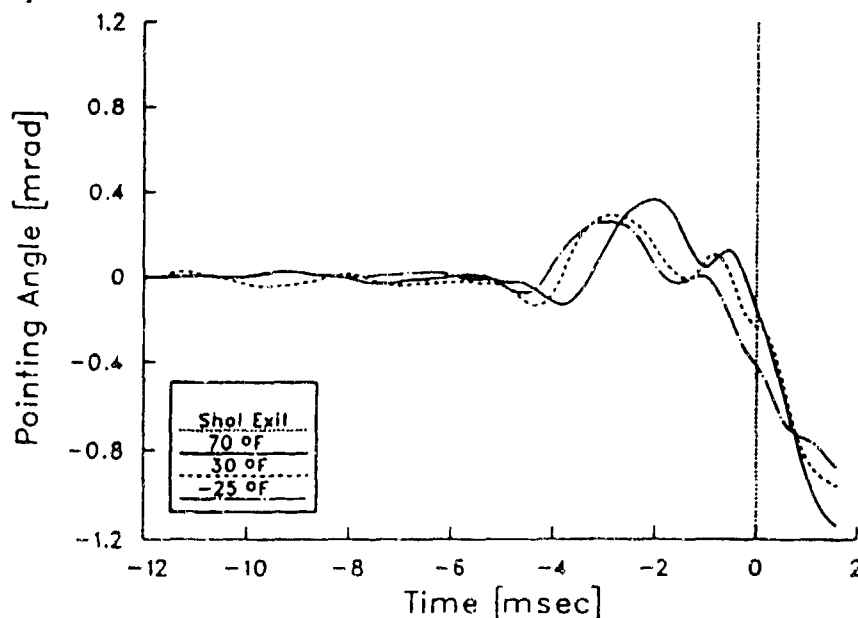
Figure 13. <u>Muzzle Pointing Angle, M831, 3 Propellant Temperatures</u>

Target impact data was collected over a period of several years. This data included ammunition type, temperature of the propellant and the impact point on the target. A regression analysis of propellant temperature versus mean impact point was used to determine the linear relationship between those two variables for each ammunition type. Because of the many differences in the tests themselves, only the simplest linear trends were sought in this analysis [8].

Figure 14 shows the plot of corrected target impact in elevation versus ammunition temperature for M831 HEAT ammunition. Visual inspection indicates a positive relationship between the two variables over the entire temperature range examined; a statistically significant slope confirmed the trend. The linear regression equation is given as;

$$\hat{y} = -.43 + .0046T \tag{5}$$

where $\hat{y}$ is the expected elevation impact point in mrad, .43 is the intercept in mils, .0046 is the slope in mrads/^{o}F, and T is the ammunition temperature in ^{o}F.
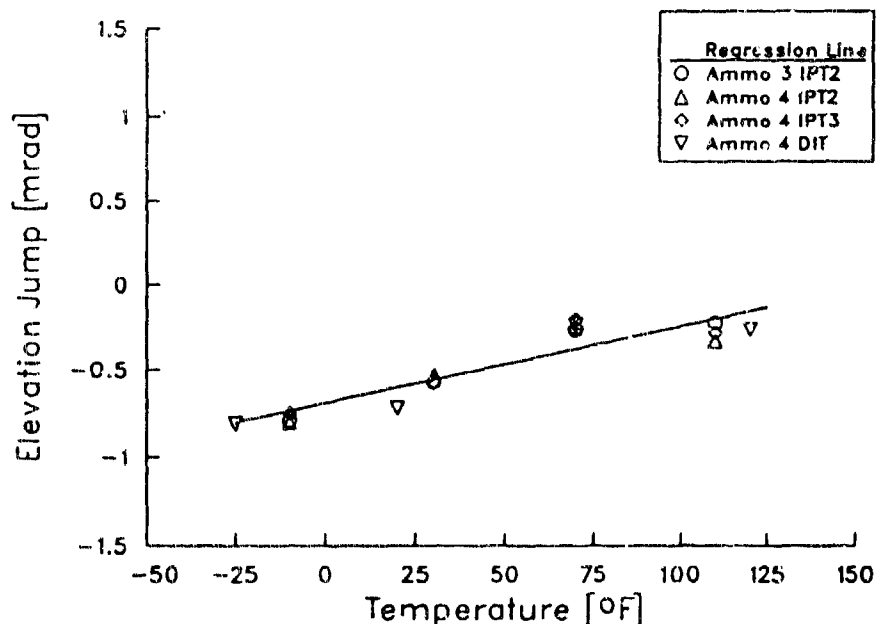
Figure 14. Target Impact Elevation vs. Temperature, M831

Figure 15 shows the plot of elevation impact versus ammunition temperature for M865. The interesting feature of this plot is the lack of a temperature dependency on elevation impact. This is due to the fact that around shot exit time for M865, the muzzle pointing angle is at a maximum point. This means that the time shift of the pointing angle plot does not result in large pointing angle differences for this ammunition type. Typically though, service KE ammunition has a temperature dependency whose slope is similar to M831 instead of M865.

Using the M831 regression equation as an estimate of the muzzle pointing angle dependence on propellant temperature, an approximate value of the occasion-to-occasion variability due to propellant temperature can be calculated. Temperature data in some likely area of operations is used to calculate muzzle pointing angles for a period of one year. From this population

of pointing angles the standard deviation is determined to provide an estimate
of the error. Since tanks are used all year and combat occurs 24 hours a day,
this approach seems reasonable.
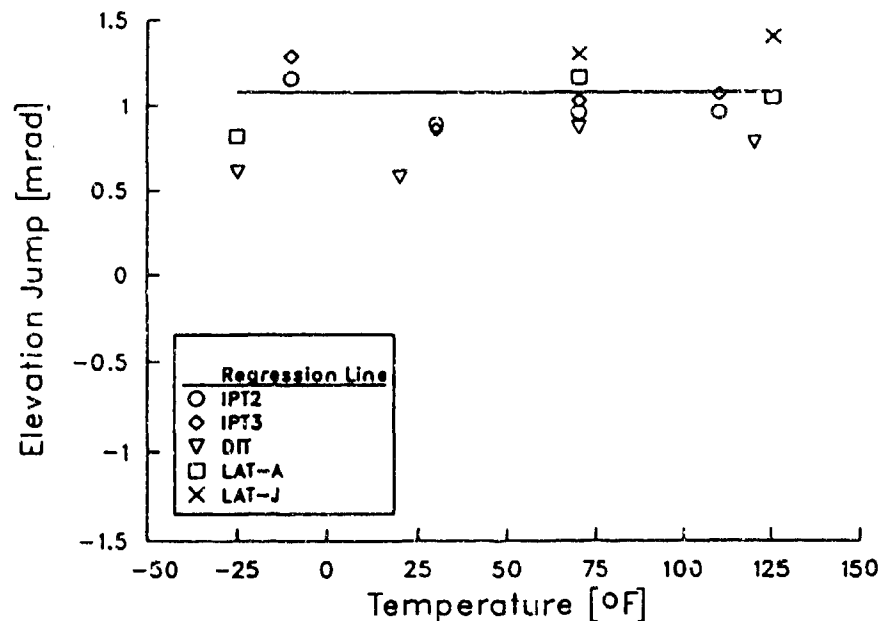
Figure 15. Target Impact Elevation vs. Temperature, M865

Temperature values were taken every three hours in a climate typical of
the middle latitudes in the northern hemisphere. Muzzle pointing angles were
calculated for each of these temperature values and the standard deviation of
the set of pointing angle data was calculated. The standard deviation thus
calculated provides an estimate of the occasion-to-occasion dispersion due to
propellant temperature of 0.093 mrad.

Calculating an estimate of the dispersion due to propellant temperature in
this way is necessarily dependent on the climate in the part of the world that
is used. Equatorial regions do not experience as much temperature variation
during the year and the dispersion should be correspondingly lower. High-desert
regions, on the other hand, experience greater temperature variation and the
dispersion may be greater. Since U.S. tanks have a world-wide contingency
mission, using a climate that is between these two extremes is reasonable.

One final note, the variation in ammunition temperature across the bustle
implies a round-to-round muzzle angle variability. From Figure 2, the maximum
temperature difference between rounds of ammunition is found at 21.45 hours.
The hottest round, at the top of the bustle is 118.3 °F and the coldest, at the
bottom of the bustle, is 104.9 °F. Applying equation 5 gives a maximum muzzle
angle spread of 0.06 mrad. The variability of ammunition temperature is much
smaller than the maximum spread. Over the three days of testing, the pooled
ammunition temperature variability was only 3.4 °F. Using this temperature
variability with equation 5 provides an estimate of the overall muzzle pointing
error produced by ammunition temperature variability within the bustle. This
error is only 0.02 mrad.

3.3.3 Lot-to-lot Muzzle Pointing Angle Variation

A muzzle angle error, similar to the temperature dependent error just described, occurs as a result of lot-to-lot muzzle velocity variations. Since the variable muzzle velocity implies a variable in-bore time for the projectile, the pointing angle at shot exit will vary with the lot-to-lot muzzle velocity variations.

It is possible to estimate the pointing angle error due to lot-to-lot muzzle velocity variations. This is accomplished by a similarity method. This method starts with the assumption that the general shape of the pointing angle-time plot will be similar for rounds shot at various muzzle velocities, but that the plot will shift in time. This assumption appears to be reasonably accurate for the muzzle velocity variations seen. Figure 13 above is an example of this phenomenon when the muzzle velocity variations are the result of propellant temperature variation, as opposed to lot-to-lot variation.

The idea behind the similarity solution assumes that the in-bore projectile velocity/time curve will be similar in shape across some small variation of muzzle velocities. With this assumption it is possible to write an algebraic equation that determines in-bore time. The dependent variable of the similarity function is a ratio of projectile velocity divided by muzzle velocity. At shot exit, this ratio is always equal to one. The independent variable is a ratio of the time (t) from propellant ignition, divided by some reference time (t_{ref}). t_{ref} is defined to be the gun length (L) divided by the muzzle velocity for that particular lot of ammunition (V_{mo}). Since the in-bore time vs. velocity curve is assumed similar for projectiles with variable muzzle velocities, the ratio of t/t_{ref} is a constant at shot exit for all lots. Using the values of a standard lot of M831 HEAT-TP [$t = 9.4$ msec, $t_{ref} = L/V_m = (4.83$ m)/(1140 m/sec) $= 4.237$ msec], the constant equals 2.219. This constant (C) is now used to find Δt, the time shift due to lot-to-lot muzzle velocity variation. t_1 is the in-bore time for a projectile that has a muzzle velocity (V_{m1}) equal to the standard muzzle velocity plus the lot-to-lot muzzle velocity variation from Table 2.

$$V_{m1} = V_m + \sigma_{V_{lot-to-lot}} \tag{6}$$

$$t_1 = C \cdot \frac{L}{V_{m1}} = 9.368 \text{ msec} \tag{7}$$

$$\Delta t = t - t_1 = 0.032 \text{ msec} \tag{8}$$

From Figure 13, the value of $d\theta/dt$ near shot exit time is found to be $-.94$ mrad/msec. The lot-to-lot muzzle pointing error is therefore calculated to be:

$$\left| \Delta\theta \right| = \left| \frac{d\theta}{dt} \cdot \Delta t \right| = \left| -.94 \text{ mrad/msec} \cdot 0.032 \text{ msec} \right| = 0.03 \text{ mrad} \tag{9}$$

3.4 Boresight Calibration.

In addition to the desire that the muzzle angle change from shot start to shot exit be the same from occasion to occasion, calibration between the muzzle of the cannon and the fire control optics used to point the cannon must be consistent from occasion to occasion. Currently, the U.S Army calibrates the cannon to the fire control optics with a muzzle boresight device. This is an optical device that is placed in the muzzle of the cannon. The muzzle boresight is used to aim the cannon at some target point. The fire control optics are then aimed at the same point to align them with the muzzle of the cannon. Any

inability to point the cannon at the same spot or to align the fire control optics at the same spot as the cannon will show up as occasion-to-occasion dispersion.

Recent tests have indicated that tank cannons may be aimed with an accuracy of 0.06 mrads (standard deviation) using the boresights currently in use with the U.S. Army. Included in this figure is the error associated with the boresight itself (i.e. parallax, reticule lines that obscure the target, etc.), the error associated with a slightly different placement of the boresight in the muzzle on each occasion and the error associated with moving the cannon [9].

The error inherent in the boresight itself (i.e. the inability to read the same spot with the boresight, independent of inserting the boresight in the muzzle and moving the cannon) was measured to be 0.02 mrads during the same test. This value can be used to make an estimate of the error associated with laying the fire control optics on the same spot as the muzzle of the cannon. Since the power of the optics in the fire control system and the boresight is the same (10 power), the ability to see the target spot should be about the same or less with the fire control optics (parallax problems inherent in the boresight are not applicable to the fire control optics). Combining the errors associated with aiming the cannon through use of the boresight (0.06 mrads) and those with placing the fire control optics on the target point (<0.02 mrad) leaves the total boresighting error at approximately 0.063 mrad.

IV. CONCLUSION

These six sources; temperature related muzzle velocity variation, lot-to-lot muzzle velocity variation, recoil variation, muzzle pointing angle dependence on propellant temperature, muzzle pointing angle dependence on lot-to-lot muzzle velocity variation and boresighting variation, represent major sources of occasion-to-occasion error that have been recently investigated and are now better understood. With this better understanding comes an increased ability to correct the problems. Reduction or elimination of these problems can significantly improve both the occasion-to-occasion error and the overall error for both current and future tanks.

V. REFERENCES

1. Twomey, D.J., J. Marchant, W. Hulcy, 'Final Report, Prototype Qualification Test-Government (PQT-G) Desert Phase of M1E1 Tank System, YPG Report No. 486, U.S. Army Yuma Proving Ground, Yuma Arizona, April 1984

2. FTB General Trajectory Program Users Guide, U.S. Army Ballistic Research Laboratory, Aberdeen Proving Ground, MD, 21005, May 1982

3. Held, B.J., Variability in Tank Gun Accuracy Due to Recoil Variation, BRL Technical Report, BRL-TR-3309, U.S. Army Ballistic Research Laboratory, Aberdeen Proving Grounds, MD, 21005-5066, January 1991.

4.   Bornstein, J. and E.M. Schmidt, *The Sensitivity of Tank Main Gun Ammunition Accuracy To Propellant Temperature*, BRL Memorandum Report, BRL-MR-3923,' U.S. Army Ballistic Research Laboratory, Aberdeen Proving Ground, MD, 21005-5066, June 1991.

5.   Gay, H.P. and A.S. Elder, *The Lateral Motion of a Tank Gun and Its Effect On the Accuracy of Fire*, BRL Report No. 1070, March 1959.

6.   Held, B.J. and T.F. Erline, *Dynamics of the Balanced Breech System for the 120mm Tank Main Gun*, BRL Technical Report, BRL-TR-3186, U.S. Army Ballistic Research Laboratory, Aberdeen Proving Grounds, MD, 21005-5066, January 1991.

7.   Bornstein, J., I. Celmins, P. Plostins and E.M. Schmidt, *Techniques for the Measurement of Tank Gun Cannon Jump*, BRL Memorandum Report, BRL-MR-3715, U.S. Army Ballistic Research Laboratory, Aberdeen, MD 21005-5066, December 1988

8. Held, B.J., D.W Webb and E.M. Schmidt, *Temperature Dependent Jump of the 120 mm M256 Tank Cannon*, BRL Memorandum Report, BRL-MR-3927, U.S. Army Ballistic Research Laboratory, Aberdeen, MD 21005-5066, December 1991

9.   Held, B.J. and D.W. Webb, *A Comparison of Muzzle Boresights For Tank Cannon*, BRL Memorandum Report, BRL-MR-3977, U.S. Army Ballistic Research Laboratory, Aberdeen, MD 21005-5066, June 1992

TITLE: FLIGHT DYNAMICS OF A SPINNING PROJECTILE DESCENDING ON A
        PARACHUTE

G. A. BENEDETTI
SANDIA NATIONAL LABORATORIES, LIVERMORE, CA 94550

ABSTRACT:

During the past twenty years Sandia National Laboratories and the U. S. Army have vertically gun launched numerous 155mm and eight-inch diameter flight test projectiles. These projectiles are subsequently recovered using an on-board parachute recovery system which is attached to the forward case structure of the projectile. There have been at least five attempts to describe, through analytical and numerical simulations, the translational and rotational motions of a spinning projectile descending on a parachute. However, none of these investigations have correctly described the large nutational motion of the projectile since all of them overlooked the fundamental mechanism which causes these large angular motions.

Numerical simulations as well as a closed form analytical solution show conclusively that the Magnus moment is responsible for the large nutational motion of the projectile. That is, when the center of pressure for the Magnus force is aft of the center of mass for the projectile, the Magnus moment causes an unstable (or large) nutational motion which always tends to turn the spinning projectile upside down while it is descending on the parachute. Conversely, when the center of mass for the projectile is aft of the center of pressure for the Magnus force, the Magnus moment stabilizes the nutational motion tending to always point the base of the spinning projectile down.

The fundamental quantity related to stability of the nutational motion is the direction of the Magnus moment. Since this is determined from such a basic result, it is profoundly simple. Consequently, it is surprising that the large nutational motion for a spinning projectile during parachute descent puzzled many investigators and went unexplained for nearly twenty years.

Projectile flight tests at Tonopah Test Range in Nevada conclusively demonstrated that the Magnus moment is responsible for the large nutational motion of a spinning projectile descending on a parachute.

The results of this work are utilized to render projectile parachute recovery systems more reliable and to explain what initially may appear to be a strange gyrodynamic behavior of a spinning projectile descending on a parachute.

BIOGRAPHY:
PRESENT ASSIGNMENT: Manager, Solid Mechanics Department, Sandia National
                         Laboratories/California

PAST EXPERIENCE: Member of Technical Staff, Sandia National Laboratories, Livermore,
                      California, 1962-present.

DEGREES HELD: Bachelor of Mechanical Engineering, Univ. of Santa Clara, California,
                   1960; Master of Science in Mechanical Engineering, Oregon State
                   University, Corvallis, Oregon, 1962; Ph.D., Arizona State University,
                   Tempe, Arizona, 1973.

FLIGHT DYNAMICS OF A SPINNING PROJECTILE DESCENDING ON A PARACHUTE

G. A. Benedetti
Sandia National Laboratories
Livermore, CA 94550

INTRODUCTION

During the past twenty years Sandia National Laboratories and the U.S. Army have vertically gun launched numerous 155mm and eight-inch diameter flight test projectiles. These projectiles are subsequently recovered using an on-board parachute recovery system which is attached to the forward case structure of the projectile. During this time there have been at least five or six attempts to describe, through analytical and numerical simulations, the translational and rotational motions of a spinning projectile descending on a parachute. However, none of these investigations have correctly described the large nutational motion of the projectile since all of them overlooked the fundamental mechanism which causes these large angular motions.

Numerical simulations as well as a closed form analytical solution show conclusively that the Magnus moment is responsible for the large nutational motion of the projectile. That is, when the center of pressure for the Magnus force is aft of the center of mass for the projectile, the Magnus moment causes an unstable (or large) nutational motion which always tends to turn the spinning projectile upside down while it is descending on the parachute in a normal manner. Conversely, when the center of mass for the projectile is aft of the center of pressure for the Magnus force, the Magnus moment stabilizes the nutational motion tending to always point the base of the spinning projectile down.

Projectile flight tests at Tonopah Test Range in Nevada conclusively demonstrated that the Magnus moment is responsible for the large nutational motion of a spinning projectile descending on a parachute.

A brief description of the projectile motion during a normal parachute descent may help the reader visualize the angular motions associated with a spinning projectile which tends to turn upside down.

At Tonopah Test Range, projectiles are usually fired 87° above the horizontal ground plane. When the projectile reaches apogee (60,000 feet to 75,000 feet; no spoiler plate), it begins to fall base first and the spin speed of the projectile is slightly less (~15%) than at barrel exit (~15,000 RPM for a 155mm diameter shell and ~10,000 RPM for an 8-inch diameter shell). After falling for about ten to twenty seconds, the forward mounted parachute is deployed and inflated.

As the spinning projectile descends on the parachute, it undergoes precession and nutation (refer to Figure 1). After the initial transients, which can last for several seconds, and prior to projectile-cable interaction, which takes several tens of seconds, the precession and nutation speeds are very low compared to the spin speed of the projectile. This has been shown by numerical simulation and observed experimentally.

In almost all flight test cases, the projectile slowly nutates until it is nearly upside down; that is, its nose is pointed towards the ground. When the nutation angle of the projectile is about 110° (this can take from 60 seconds to 150 seconds after parachute inflation), the spinning projectile begins to rub on the cable wear sleeve shown in Figure 1.

While the spinning projectile is in contact with the wear sleeve (~30 seconds to 60 seconds), severe lateral vibration of the cable and shroud lines occurs.

$\dot{\psi} \sim$ spin frequency or "speed"
$\dot{\phi} \sim$ precession frequency or "speed"
$\theta \sim$ nutation angle
$\phi \sim$ precession angle

PARACHUTE

BEARING

STEEL CABLE

$\dot{\psi}$

Θ

WEAR SLEEVE

NOSE SPIN BEARING

PROJECTILE CENTER
OF MASS

PROJECTILE

Z
FIXED
FRAME

$\dot{\phi}$

GROUND PLANE

Y

PROJECTION OF PROJECTILE CENTERLINE
ON TO GROUND PLANE

ϕ

X
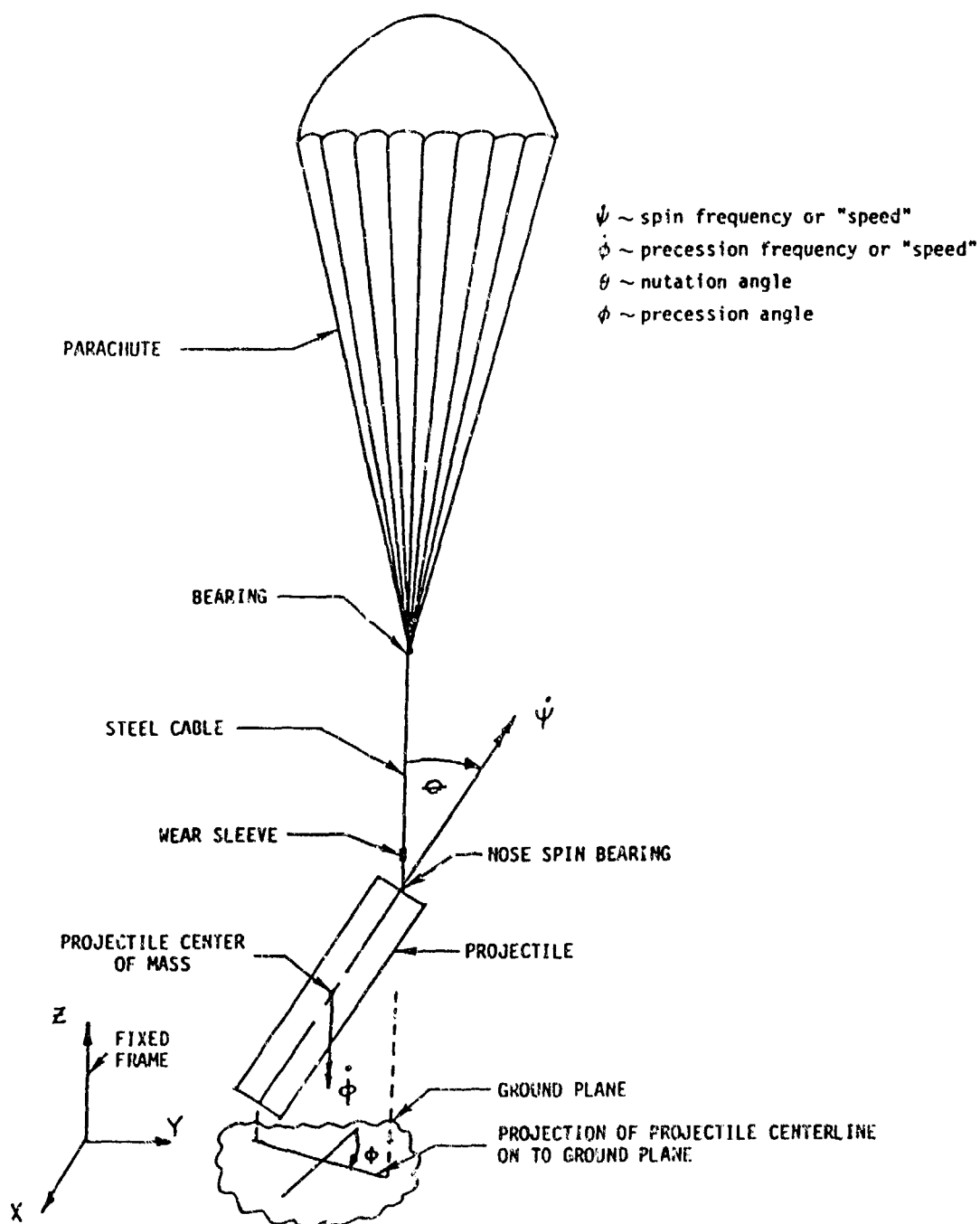
Figure 1. Spinning Projectile Descending on Parachute. Note that the upper bearing prevents the shroud lines from twisting due to precession especially when the nutation angle, θ, is near 90°.

During the time the projectile is in contact with the cable wear sleeve, its spin speed decreases significantly. Consequently, the projectile, with its greatly reduced spin speed, is now unstable in this upside down configuration and it rapidly nutates back to its original base down configuration impacting the

ground at 110 ft/sec and at a greatly reduced spin speed. The maximum flight time from gun launch to ground impact is about 400 seconds.

Numerical simulations in reference [1] describe this motion provided the center of mass for the projectile is forward of the center of pressure for the Magnus force in the post parachute deployment configuration.

The equations which describe the translational and rotational motions of the spinning projectile descending on its parachute are too lengthy to list here. However, the derivation of these equations is thoroughly documented in reference [1].

RESULTS

Projectile flight tests at Tonopah Test Range conclusively demonstrated that the Magnus moment is responsible for the large nutational motion of a spinning projectile descending on a parachute.

Flight Test Results

On June 26, 1985, two 155mm diameter flight test projectiles were successfully gun fired at Tonopah Test Range (TTR) to demonstrate whether or not the Magnus moment was responsible for the large nutational motions associated with a spinning projectile during a normal parachute recovery These projectiles were ballasted such that one would be stable and the other unstable according to the Magnus theory discussed previously. Both test units (FC891 ~ stable and FC892 ~ unstable) used Army parachute recovery systems.

It is important to note that the Sandia parachute recovery system incorporates a wear sleeve attached to a long steel cable between the projectile and the parachute shroud lines (refer to Figures 1 and 2) whereas the Army parachute recovery system utilizes a short loop (~6-inch loop) of steel cable between the projectile and the shroud lines (refer to Figure 2). Therefore, when a spinning projectile which uses an Army parachute recovery system nutates to about an upside down position, it will wear through the steel cable loop and, of course, separate itself from the parachute. This is precisely what occurred to the second flight test projectile (FC 892) which was ballasted such that it would turn upside down.

The first projectile (FC 891~ stable), which had its center of mass aft of the center of pressure for the Magnus force, impacted the ground base first with a vertical velocity of about 100 feet/second. The recovery was normal and the projectile and parachute were undamaged. The second projectile (FC 892 unstable), which had its center of mass forward of the center of pressure for the Magnus force, slowly nutated to approximately an upside down position and thus cut itself loose from the parachute about 70 seconds after parachute inflation. Consequently, the projectile impacted the ground nose first with a vertical velocity of about 1,100 feet/second. The parachute was subsequently recovered and the short loop of steel cable between the projectile and shroud lines was severed. The cut in the severed cable was clean with no frayed cable strands. This sequence of events had been predicted prior to the tests.

Therefore, it was concluded that the Magnus moment is responsible for the large nutational motion of a spinning projectile descending on a parachute. That is, when the center of pressure for the Magnus force is aft of the center of mass for the projectile, the Magnus moment causes an unstable (or large) nutational motion which always tends to turn the projectile upside down. Conversely, when the center of mass for the projectile is aft of the center of pressure for the Magnus force, the Magnus moment stabilizes the nutational motion tending to always point the base of the spinning projectile down.

Figure 3 shows a test projectile 7.5 x 10^{-3} seconds after barrel exit with an axial velocity of 2,700 feet/second.
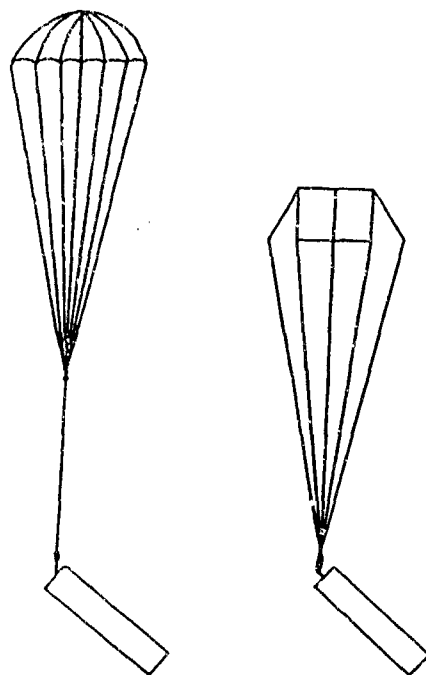
SANDIA   U.S ARMY

Figure 2. Parachute Recovery Systems.
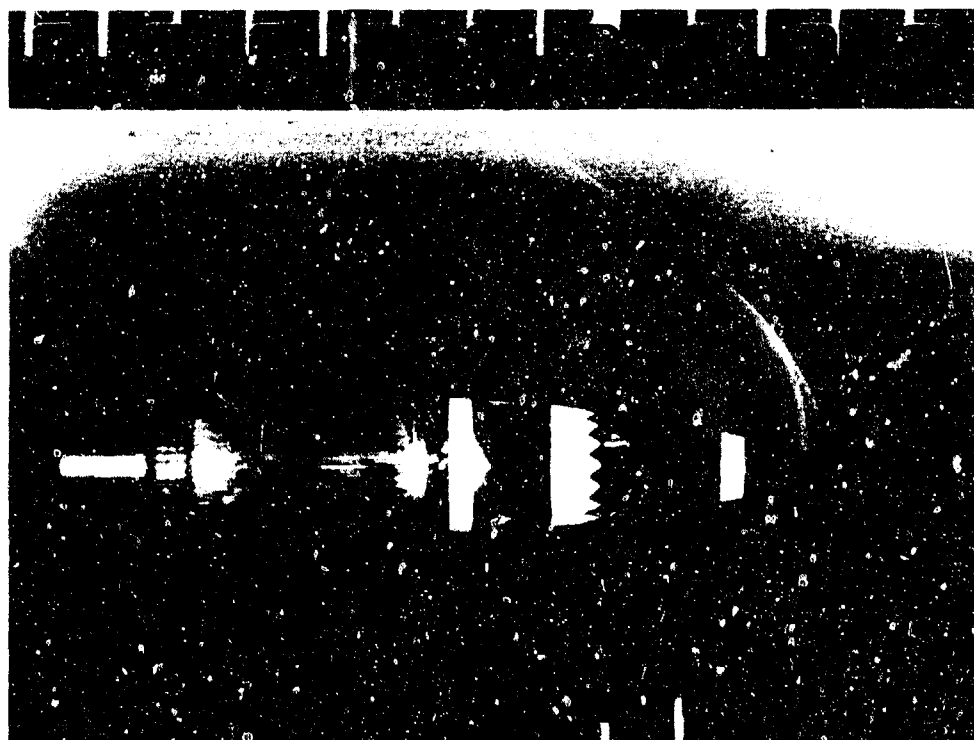
Figure 3. Test Projectile Fired from 155mm Diameter Tube at Tonopah Test Range. Note spoiler plate near nose of projectile.

124

Predicted Test Results

When the system equations of motion in reference 1 are numerically integrated to predict the translational and angular motions associated with a flight test projectile similar to FC892 (unstable), Figures 4 through 10 result. For these calculations, a Sandia parachute recovery system is utilized rather than an Army recovery system (refer to Figure 2). Consequently, when the spinning projectile nutates (θ) to θ_{rub} ($\theta_{rub} = 110°$), it begins to rub on the cable wear sleeve.

The normal interaction force (F_n) between the projectile and wear sleeve increases with the nutation angle (θ) provided $\theta > \theta_{rub}$. Therefore, during the time the projectile is in contact with the wear sleeve its spin speed $\dot{\psi}$ decreases and its precession speed ($\dot{\phi}$) increases significantly (refer to Figure 1). The decreased spin speed ($\dot{\psi}$) greatly reduces the Magnus force lift coefficient (C_ℓ) and, hence, the Magnus moment.

Subsequently the projectile impacts the ground in a near base down configuration and at a greatly reduced spin speed. A base down configuration is the optimum projectile configuration for ground impact since the projectile axial inertia loads are in the same direction as during gun launch. For some projectile designs a greatly reduced spin speed ($\dot{\psi}$) at ground impact is desirable since the projectile inertia torques during ground impact are opposite to those during gun launch.
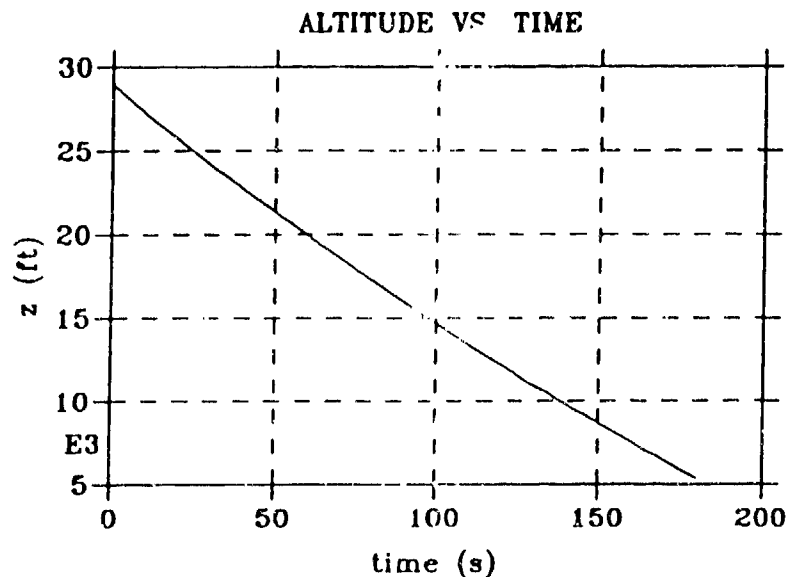
Figure 4. Altitude Above Mean Sea Level in Thousands of Feet Versus Time. Apogee occurs 34 seconds after gun launch and parachute inflation occurs 8 seconds after apogee. Zero time on the figure corresponds to parachute inflation.

VERTICAL VELOCITY VS. TIME
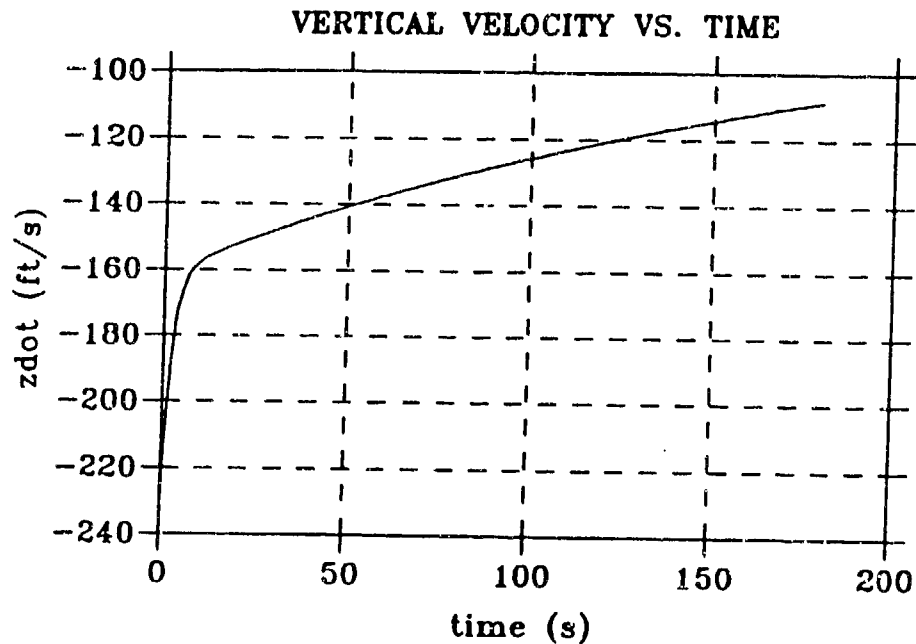
Figure 5. Vertical Velocity in Feet Per Second Versus Time. A negative vertical velocity indicates the direction of the velocity is towards the ground.

NUTATION ANGLE VS. TIME
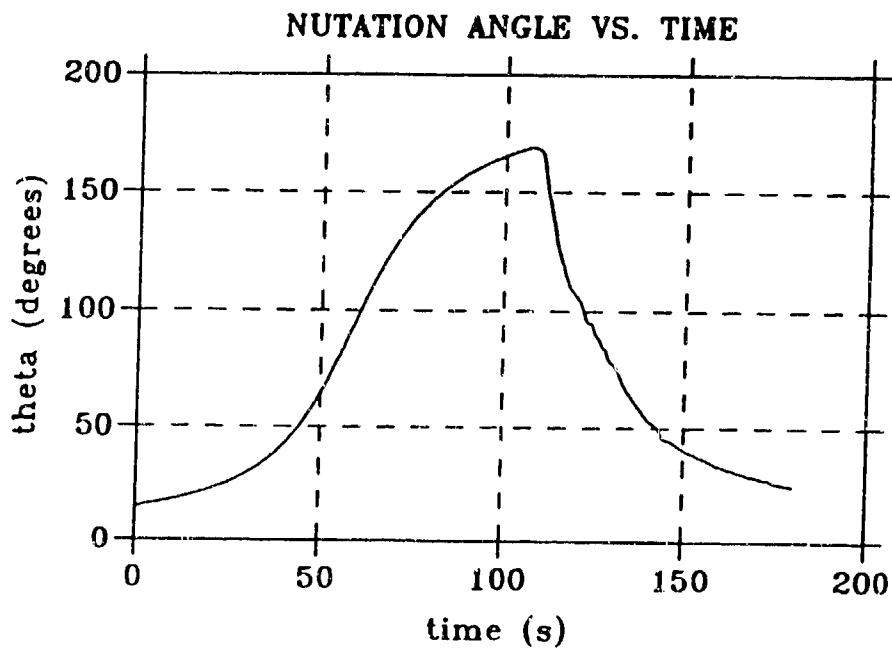
Figure 6. Nutation Angle, θ, versus Time for an Initial Nutation Angle of 15°. The maximum nutation angle is ~170° and occurs at ~107 seconds. Projectile-cable interaction begins at ~63 seconds ($\theta = 110°$) and ends at ~117 seconds.
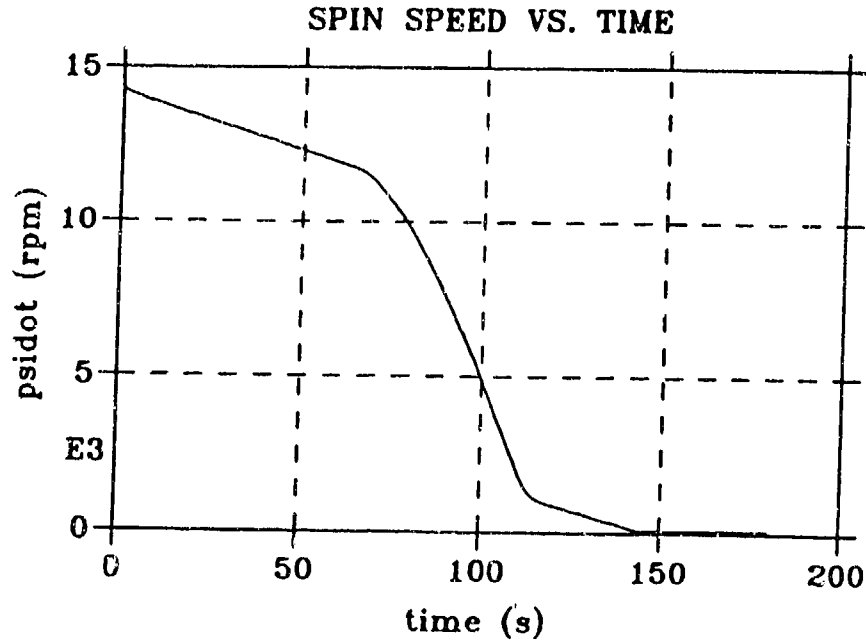
SPIN SPEED VS. TIME

Figure 7. Spin Speed, $\dot{\psi}$, in Thousands of Revolutions per Minute Versus Time. The spinning projectile begins to rub on the steel cable at ~63 seconds and projectile-cable interaction terminates at ~117 seconds.

PRECESSION SPEED VS. TIME
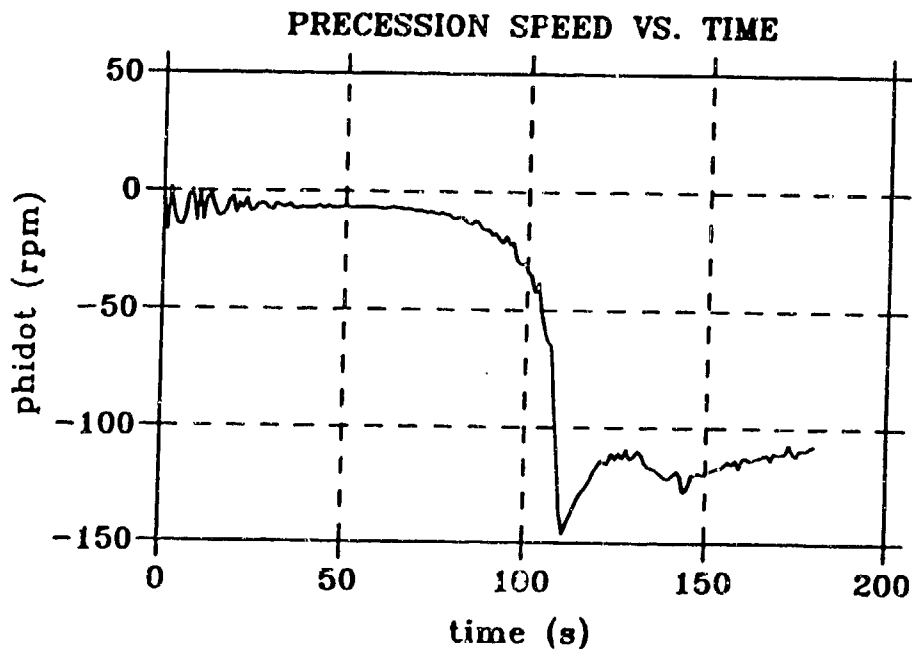
Figure 8. Precession Speed, $\dot{\phi}$, in Revolutions per Minute Versus Time. A negative precession speed, $\dot{\phi}$, indicates the direction of precession is clockwise when viewing the projectile from above along the negative Z axis. Refer to Figure 1. Projectile-cable interaction begins at ~63 seconds and ends at ~117 seconds.

MAGNUS FORCE VS. TIME
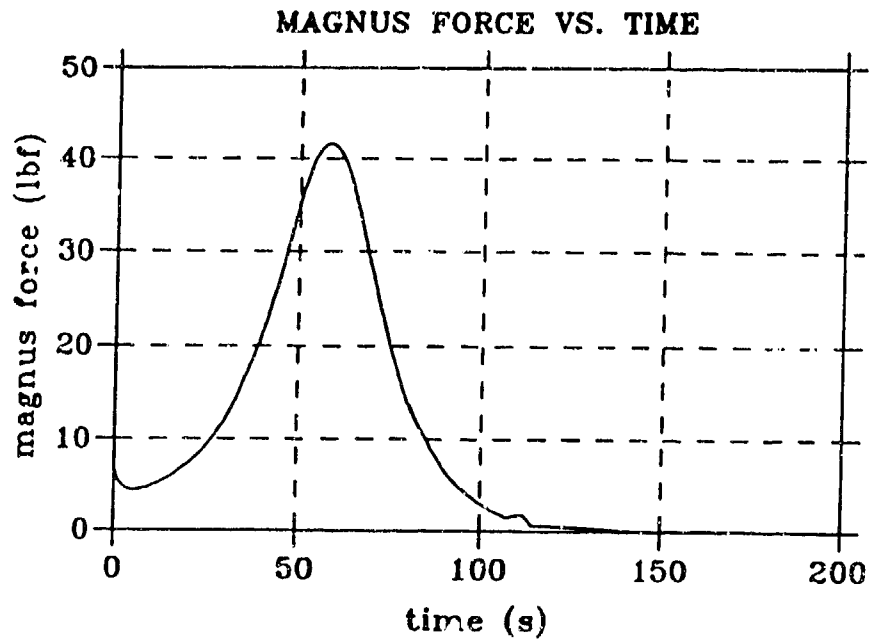
Figure 9. Magnus Force in Pounds Versus Time for an Initial Nutation Angle of 15°.

NUTATION ANGLE VS. TIME
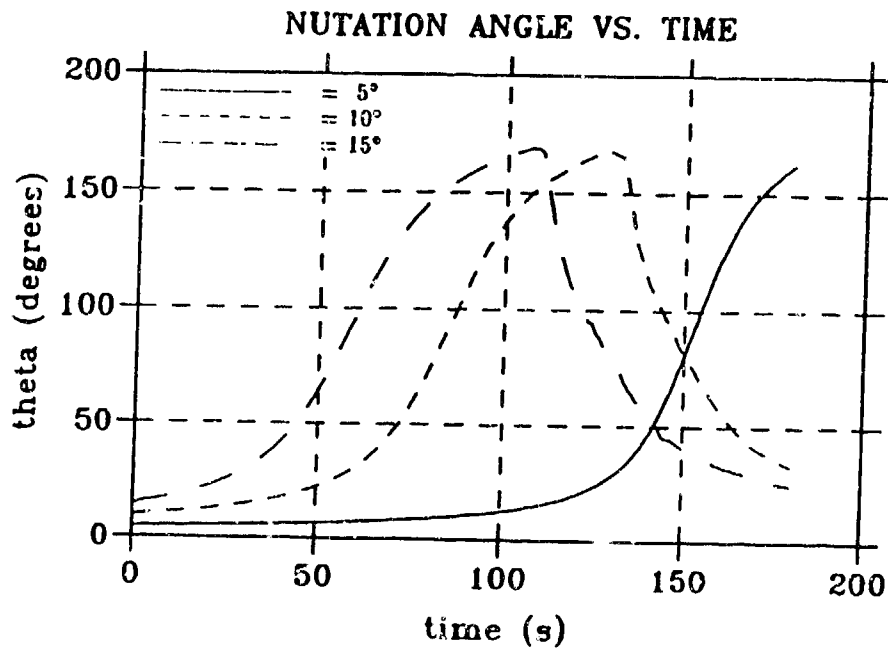
Figure 10. Nutation Angle, θ, Versus Time for Initial Nutation Angles of 5°, 10°, and 15°. Note that for an initial nutation angle of 5°, the projectile impacts the ground in a nearly nose down configuration.

CONCLUSIONS

The fundamental conclusion of this report is that the Magnus moment, which is caused by the Magnus force, is responsible for the large nutational motion of the spinning projectile during parachute descent. This conclusion was first determined analytically and then experimentally verified.

A. The following conclusions are for the case where the center of gravity (CG) for the projectile is *forward* of the center of pressure for the Magnus force (CP_{mag}) in the post parachute deployment configuration, and the spinning projectile is descending on the parachute in a normal manner. The spin is induced by firing the projectile from a right-hand twist tube.

    1A. The Magnus moment vector (magnitude and direction) is responsible for the large nutational motion (θ) of the spinning projectile. The projectile always tends to nutate (θ) toward the upside down or nose down position. This results because the Magnus moment causes the spinning projectile to rotate toward a position of stable dynamic equilibrium.

    2A. The maximum nutation angle (θ) attained by the projectile in a fixed amount of time from parachute inflation is highly dependent on the initial nutation angle (θ_0), the distance between the CG and CP_{mag}, the Magnus force and the axial angular momentum of the projectile.

    3A. The direction of projectile precession (refer to Figure 1) is always in the clockwise direction when viewing the projectile from above (along the negative Z axis).

    4A. Launching the projectile from a left-hand twist tube (if there are any) will still result in a large nutational motion (θ) of the projectile during parachute descent. However, in this case, the direction of precession will always be in the counterclockwise direction when viewing the projectile from above (along the negative Z axis).

    5A. If a base first impact with the ground and associated small axial and torsional inertial loadings are to be assured, the projectile must be de-spun or partially de-spun. This will spoil the Magnus effect and thus eliminate the de-stabilizing Magnus moment. When this is the case, the reliability of the recovery system can be increased (refer to conclusions 3B and 4B).

    6A. When the gun elevation angle is 87° above the horizontal, a substantial amount of descending flight time is required for the projectile to nutate upside down, rub on the cable wear sleeve to reduce its spin speed, and then return to the base down configuration prior to ground impact. To assure a base first impact with the ground, it is necessary to complete this sequence of events early during the descending flight. This can be accomplished by decreasing the gun elevation angle which, in effect, increases the initial nutation angle (θ_0) of the projectile prior to parachute inflation. Recall that small increases in the initial nutation angle (θ_0) will significantly decrease the total time required to return the projectile to its base down configuration prior to ground impact.

B. The following conclusions are for the case where the CG for the projectile is *aft* of the CP_{mag} for the Magnus force in the post parachute deployment configuration, and the spinning projectile is descending on the parachute in a normal manner. The spin is induced by firing the projectile from a right-hand twist tube.

    1B. The Magnus force remains unchanged but the Magnus moment vector reverses direction and the position for stable dynamic equilibrium for the projectile is now always in the base

down configuration. A base down configuration is the optimum projectile configuration for ground impact.

2B. Since the projectile is always in the base down configuration, the projectile does not rub on the cable wear sleeve. Consequently, severe cable and parachute vibration does not occur.

3B. When the base of the projectile always points toward the ground, the steel cable and associated hardware between the projectile and parachute can be eliminated. This reduces recovery system weight, decreases the complexity of the mechanical design and assembly procedure and also circumvents many functional and intractable engineering analysis problems associated with parachute deployment and projectile descent. Therefore, a more reliable parachute recovery system can be designed to "soft" recover artillery projectiles.

4B. Use of a spoiler plate attached to the forward portion of the recovery system during projectile ascent reduces the maximum altitude (~70,000 feet) and maximum flight time (~400 seconds) by a factor of approximately two. This increases reliability since there is less time for bearing failures, parachute failures, etc. to occur. Note that use of a spoiler plate is not recommended when the post deployment projectile configuration is such that the CG is forward of the CPmag. In this unstable configuration, a substantial amount of additional flight time is required so the projectile can nutate upside down, rub on the cable wear sleeve to reduce its spin speed, and then return to the base down configuration prior to ground impact. Recall that severe cable and parachute vibration occurs while the spinning projectile is rubbing on the cable wear sleeve.

5B. Since the projectile no longer rubs on the cable wear sleeve, its spin speed, $\dot{\psi}$, is high at ground impact. Consequently, higher inertia torques *may* result during ground impact. However, the inertia torque may be related to projectile penetration depth and a rapidly spinning projectile impacting the ground at only 110 ft/sec may not generate excessively large magnitudes of inertia torque relative to a slowly spinning projectile although the inertia torque may be longer in duration.

6B. The direction of projectile precession is always in the clockwise direction when viewing the projectile from above (along the negative Z axis).

C. General

1C. The system equations of motion are programmed and can predict the quantitative translational and rotational motions associated with a spinning projectile descending on a parachute. However, good applicable Magnus wind tunnel data is not available.

To accurately assess the instability of a spinning projectile (i.e., its tendency to turn upside down) during parachute descent, the Magnus force and the CP$_{mag}$ must be measured for the post deployment configuration and flight conditions. Once this wind tunnel data is obtained, quantitative evaluations of projectile behavior can be made.

The resources and facilities for obtaining these measurements are available (refer to reference 1).

2C. Some Army projectiles nutate to large angles during parachute descent and can subsequently wear through the short loop of steel cable between the projectile and parachute shroud lines (refer to Figure 2). When this happens, the projectile separates itself from the parachute and impacts the ground nose first.

Therefore, to prevent the spinning projectile from turning upside down during parachute descent, the projectile center of gravity (CG) must be located aft of the center of pressure (CP_{mag}) for the Magnus force. This, of course, applies to the post parachute deployment projectile configuration.

REFERENCE

1. Benedetti, G. A., *Flight Dynamics of a Spinning Projectile Descending on a Parachute*, Sandia National Laboratories Livermore, SAND89-8419, 1989.

TITLE: AN EXAMINATION OF IN-BORE PROJECTILE
MOTION FROM AN EM RAILGUN

LARRY BURTON
U.S. ARMY RESEARCH LABORATORY
WEAPONS TECHNOLOGY DIRECTORATE
ABERDEEN PROVING GROUND, MD 21005-5066

ABSTRACT:

An investigation was undertaken to examine electromagnetic
(EM) gun barrel/projectile interaction. The RASCAL code was
used in this study because of its ability to easily manipulate
relevant parameters such as gun tube centerline, projectile/bore
contact stiffness, and projectile design geometry. This work
centers around a comparison of projectile performance in the 9-MJ
EM railgun at the University of Texas Center for Electromechanics
(UTCEM) and a double-travel conventional gun. This comparison was
made by varying the parameters listed above for two different
projectile designs, one projectile being the M829 tank round, the
other, a preliminary EM design. It was hoped that adoption of this
format would identify specific areas of the EM gun/projectile
system that excite transverse loading, with the results of the
analysis presented here.

BIOGRAPHY:

PRESENT ASSIGNMENT: Mechanical Engineer, Mechanics &
Structures Branch, Propulsion & Flight Division, Weapons Technology
Directorate, U.S. Army Research Laboratory.

PAST EXPERIENCE: Nine years with the Mechanics & Structures
Branch.

DEGREES HELD: M.S.(Mechanical Engineering), The Johns Hopkins
University, Baltimore, MD, 1992; B.S.(Mechanical Engineering),
Virginia Polytechnic Institute and State University, Blacksburg,
VA, 1984.

An Examination of In-bore Projectile Motion from an EM Railgun

Larry Burton
U.S. Army Research Laboratory
Weapons Technology Directorate
Aberdeen Proving Ground, MD 21005-5066

INTRODUCTION

During the past decade, it has been recognized that a projectile's interaction with the gun tube during in-bore travel plays a major role in determining the terminal accuracy of the round. If the projectile is subjected to excessive transverse loading during this period, disturbances may be induced that lead to yawing motion and possibly even excitation of the projectile's natural frequencies. Obviously, it is important for the projectile designer to minimize the effects of these occurrences.

In recent years, much effort has been devoted to developing modeling techniques that may be used to estimate the disturbances that arise from projectile/gun tube interaction. These models range in scope from a one-dimensional beam element code, RASCAL [1], to three-dimensional, transient analysis with commercial finite element programs. The use of these techniques to investigate gun/projectile dynamics in conventional tank cannons is well documented [2,3,4,5,6].

Currently, however, there are ongoing programs to develop alternatives to conventional powder guns. One example is the electromagnetic (EM) gun system, which relies on passing current through an armature in an induced magnetic field to provide its propulsive force. The EM gun barrels are composite in nature, that is, having a non-homogeneous cross section (see Figure 1). This is a radical departure from the cylindrical steel tubes characteristic of current cannons. In addition, solid armature railguns typically rely on metal-to-metal contact to conduct current between the gun rails and the armature, which leads one to believe the EM system has characteristics that may lead to more excessive transverse disturbances being imparted to the projectile.

An analysis was undertaken to determine the severity of transverse loading in an EM barrel in comparison to a conventional steel gun tube. The details of the analytical investigation and the subsequent results are presented in the following sections.
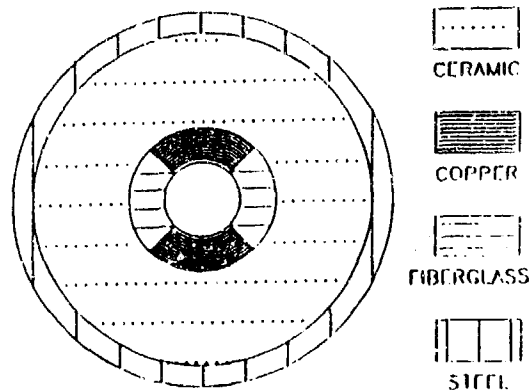
Figure 1. EM Railgun Barrel Cross Section

PURPOSE

The purpose of the analytical investigation was to determine the severity of transverse loading in an EM barrel in comparison to a conventional steel gun tube. It was hoped that by running numerous case studies while varying the parameters affecting in-bore projectile motion, a cause-and-effect relationship could be identified and the most deleterious conditions isolated.

PROCEDURE

Realizing the gross difference between conventional and EM gun systems, it was felt advantageous to exercise a simplistic in-bore dynamics code, which would allow for easy manipulation of the relevant parameters. This led to the RASCAL code [1] being chosen as the vehicle for conducting the investigation. RASCAL is a one-dimensional code, which employs beam elements and requires inputs of interior ballistic loading information, projectile geometry, barrel dimensions and centerline profile, and breech and gun system parameters. The specific values incorporated into the model are detailed in the following sections.

GUN BARREL MODELING

The study focused on a comparison of projectile motion in an EM railgun with that of a conventional gun. The 9-MJ railgun at the University of Texas Center for Electromechanics (UTCEM) was selected as the railgun gun to be modeled because centerline data for the barrel exists. The existence of centerline data is noteworthy for the EM community has only recently begun to recognize the important role the centerline profile plays in determining in-bore motion. It is also important to note the centerline profile changes drastically from shot to shot with current state-of-the-art railguns. Railguns are typically honed out after every shot to remove damage done by arcing and wear, thus placing the in-bore geometry in a continual state of fluctuation. Thus, the data employed in the model are a one-time barrel centerline meant to be representative of that found in the UTCEM gun.

The UTCEM gun is 9.5 m long and is mounted vertically. It has a constant diameter cylindrical cross section along its entire length. A double-travel conventional gun was chosen to serve as a comparator because its 10-m length is nearly equivalent to that of the UTCEM barrel and allows for velocities above those of standard ordnance. The gun barrel geometries are depicted below in Figure 2.

120-mm Tank Cannon

EM Gun Barrel
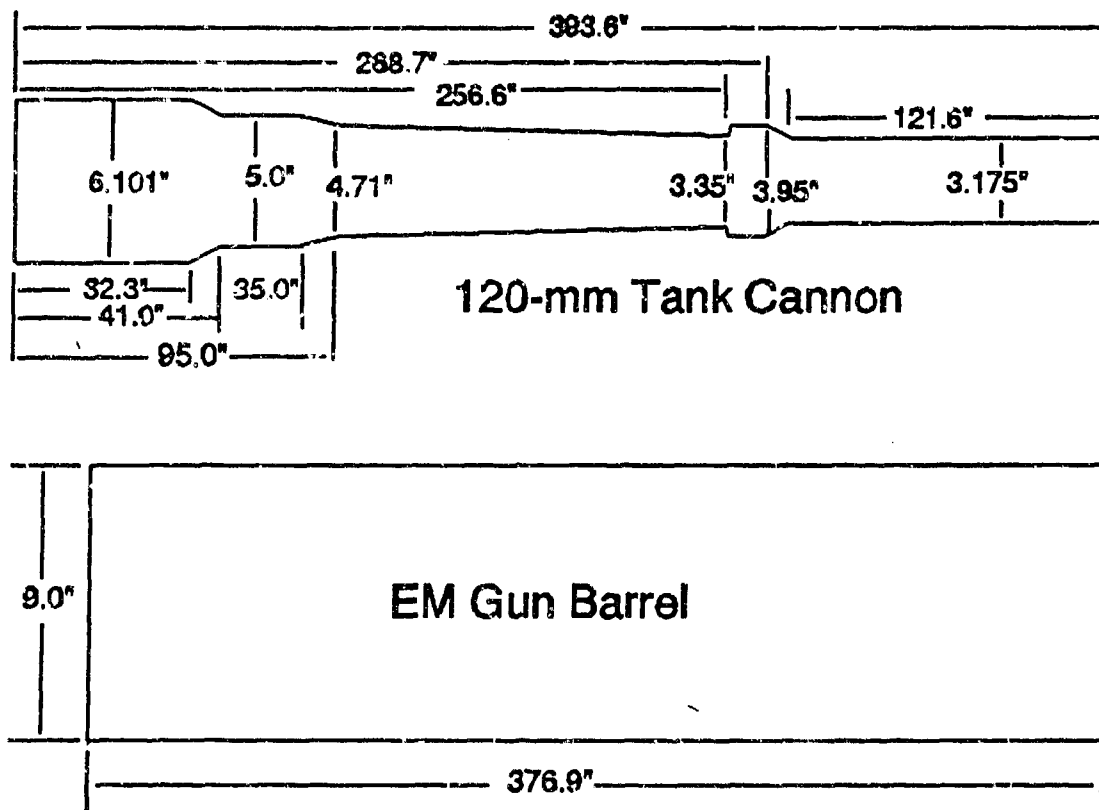
Figure 2. Barrel Geometries of EM and Double-Travel Guns

Note: the two barrels modeled have different bore diameters; the EM railgun has a 90-mm nominal diameter, while the double-travel cannon is 120 mm. One of the benefits of RASCAL is it does not require barrel geometry to be consistent with projectile geometry. In other words, it is possible to examine the motion of a 120-mm projectile in a 90-mm bore and vice versa. This capability results from RASCAL's use of beam elements to model the projectile with the projectile/barrel contact points represented with springs.

Figure 3 shows the centerline data incorporated into the gun barrel models. For the EM railgun, the vertical measurements are for the plane of the copper rails, while the horizontal are for the ceramic insulator. Tube 008 data refer to the double-travel cannon, and data line 2 simply is a verification of the original measurements of the UTCEM gun shown as data line 1.
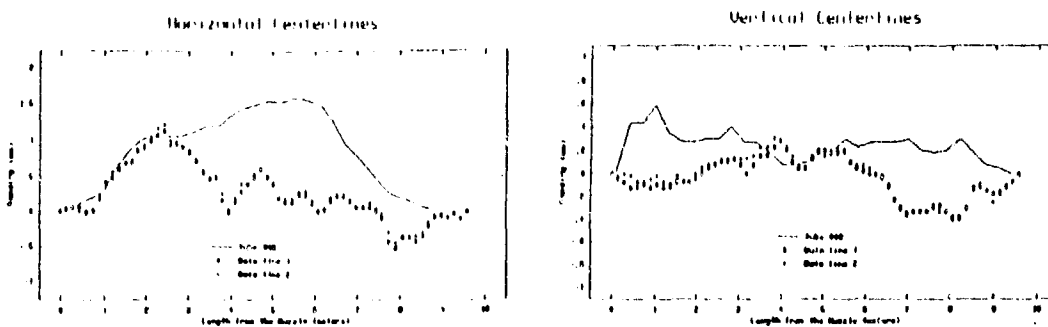
Figure 3. Gun Barrel Centerline Measurements

The final input requirement pertaining to the barrels was descriptions of the breech and gun system parameters. Since both guns are experimental, that is, not meant to be mounted in any vehicle, it was decided to use identical input files for the two guns except for bore and chamber radii particular to each gun, as well as the elastic modulus and material density of the barrels.

Obviously, for the case of the homogeneous steel conventional gun, the modulus ($30e06$ lb/in^2) and density (0.283 lb/in^3) are known. The EM barrel is not as straightforward for the laminate nature of its cross section calls for derivation of an effective modulus and density. An effective density was calculated using a simple rule of mixtures approach, whereby the density of each material layer was multiplied by its volume and these values were summed to give the total weight of the barrel. This weight was then divided by the total volume of the barrel to provide an effective density of the barrel (0.193 lb/in^3). A similar method was used to derive an effective modulus using a beam-deflection analysis. If each layer is considered a beam that maintains contact with its adjacent layer, the deflections are equivalent at coincidental points and have values of the form $y=(wl^4)/(8EI)$. This leads to

$$Y_1 = Y_2 = Y_3 = \frac{w_1 l^4}{8E_1 I_1} = \frac{w_2 l^4}{8E_2 I_2} = \frac{w_3 l^4}{8E_3 I_3} = Y_{eff} = \frac{w_{eff} l^4}{8E_{eff} I_{eff}}$$

where the subscripts denote the different layers. Since the barrel hangs vertically, there is no distributed gravity load, so $w_1=w_2=w_3=w_{eff}$ for any transverse distributed load. This results in

$$E_{eff} I_{eff} = E_1 I_1 + E_2 I_2 + E_3 I_3$$

The resultant effective density calculated equals $35.7e06$ lb/in^2.

INTERIOR BALLISTIC MODELING

One of the most significant differences between the EM railgun and the conventional gun system is the means of providing the propulsive force. However, the RASCAL code allows for interior ballistic data to be input as velocity versus time and is thus transparent to the mode of propulsion.

Two separate interior ballistic curves were used in the analysis and are shown in Figure 4. The first curve, and the more severe case, shows a peak velocity of 1965 m/s at muzzle exit. This curve was provided by UTCEM from a simulation code developed in-house. It is important to realize this simulation does not accurately reflect the current status of the UTCEM gun system for large caliber projectiles. At the present time, rise times of about 100 microseconds are typical, with efforts ongoing to control the staging of generators to reduce the rise time to that shown in the simulation. Therefore, this curve represents an optimal interior ballistic loading from the EM railgun.
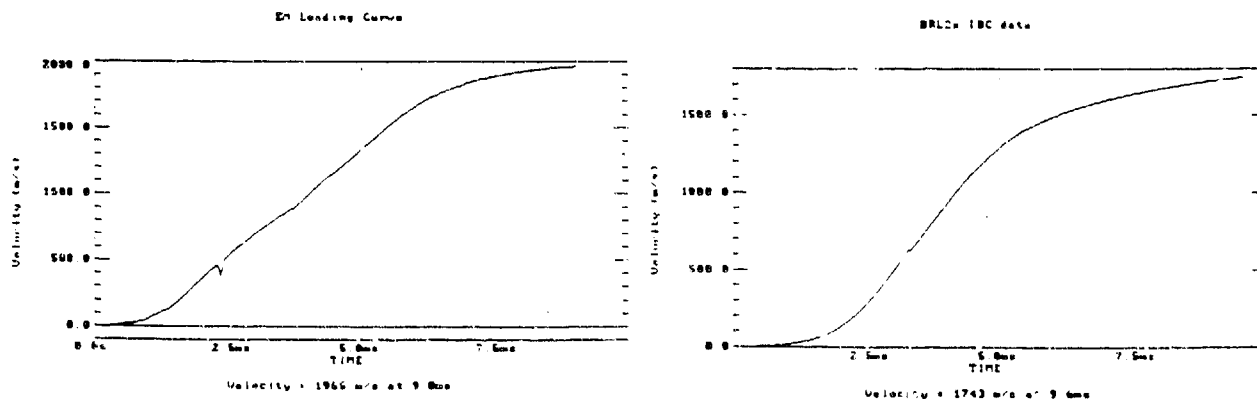
Figure 4. Interior Ballistic Curves used in RASCAL Analysis

The second load profile is for an M829 projectile fired from a double-travel cannon and does not include any charge optimization. This case achieves a maximum velocity of 1743 m/s at exit.

PROJECTILE GEOMETRY

RASCAL was written for specific application to projectiles operating in conventional tank cannons. Some of the assumptions required to apply the code to EM railgun cases have been detailed previously in the gun barrel modeling section. Similarly, a set of assumptions was required in modeling the EM projectile with RASCAL.

Two generic geometries are available within RASCAL for modeling projectiles. They are a double-ramp configuration as found in the M829 and the geometry of a Heat round. The EM projectile of interest is shown in Figure 5 and has the basic double-ramp configuration with two trailing armature contacts attached. Modeling these two trailing arms presents a difficulty since RASCAL's input is in the form of various tapers and a forward borerider as shown in Figure 6.
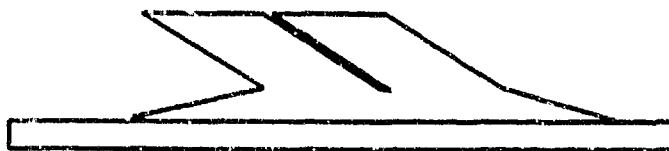
Figure 5. EM Projectile Configuraticn
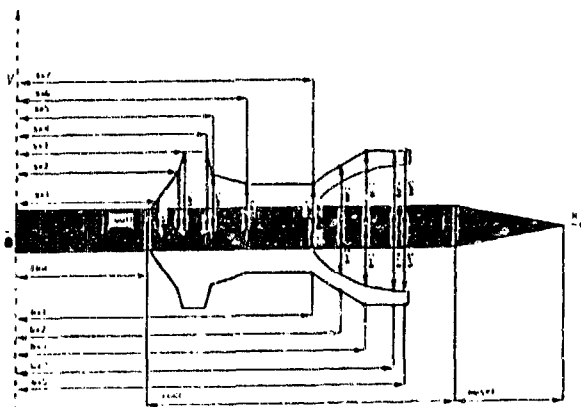
Figure 6. RASCAL Input Geometry for a Double-Ramp Sabot

The RASCAL model of the EM projectile is depicted in Figure 7.
The swept-back portion of the chevron armature design is not
included because of the limitations of the RASCAL geometry modeler.
However, it was felt that the overhanging structure provides only
minimal additional lateral stiffness, so that the model would
yield a response fairly representative of the projectile.

Some preliminary calculations were also made to investigate
the possibility of reversing the projectile direction to model one
of the armature leaves by taking advantage of the forward borerider
modeling capability (see Figure 8). However, from these
calculations, this technique was determined to be unfeasible for
this geometry because of the way RASCAL resolves the bore-riding
structure into beam elements. Therefore, the representation shown
in Figure 7 was chosen to best serve as the EM projectile model.

CONTACTS AT
7.74" & 9.2486"
L. - 15.4922 in
cg at .2Cm (7.87")
M - 1.97 kg
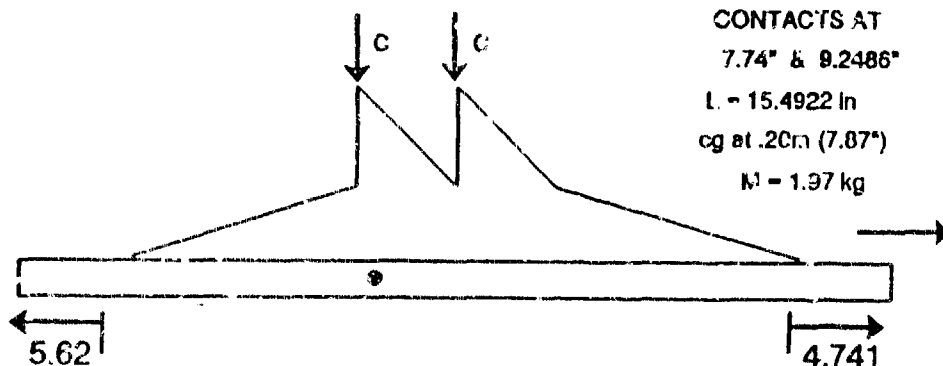
Figure 7. RASCAL Model of EM Projectile

CONTACTS AT
6.2436" & 7.7522"
L -14.6132 in
cg at .19m (7.48")
M - 2.06 kg

4.741   4.741
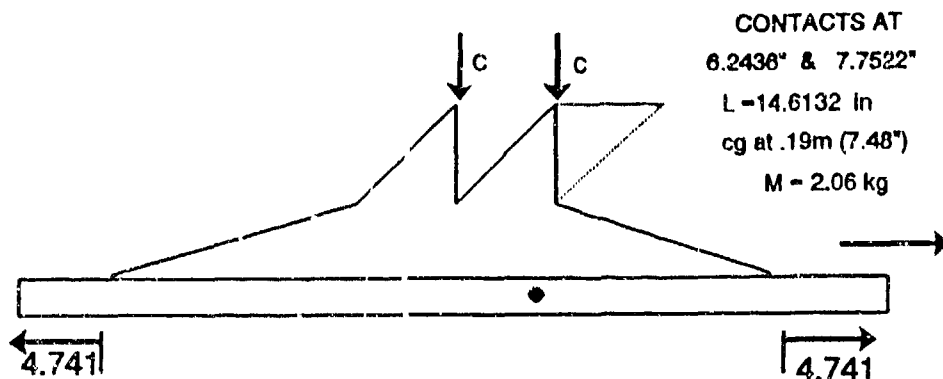
Figure 8. Alternate Model of the EM Projectile

The other projectile incorporated in the study was the M829, which is a standard ammunition for the 120-mm cannon. This was meant to serve as a baseline performer against which the EM design could be evaluated.

A key parameter in determining a projectile's in-bore performance is the stiffness associated with the projectile/bore interface. Attempts have been made to experimentally determine this contact stiffness value [7,8] with results ranging from approximately 1.0e05 to 1.0e06 lb/in in magnitude. Previous experience in matching the RASCAL output results with test firing data led to the use of 4.3e05 lb/in as a standard value [9]. For the purpose of this investigation, three different contact stiffness values were evaluated for each case studied to represent the lowest measured value (1.0e05 lb/in), the highest measured value (1.0e06), and a value used in previous evaluations with RASCAL (4.3e05 lb/in).

CASE STUDY MATRIX

The analysis involved the two projectile models with system parameters varied to look at 11 different scenarios as listed in Table 1. Each of the 11 cases were run with the three different stiffness values resulting in a total of 33 individual cases being investigated.

The study was set up so that Case 1 represented an estimate of the M829 projectile response from the double-travel gun having a conventional pressure profile loading. Case 2 was run to see how the more severe EM loading profile would affect the projectile. The third case isolated the effects attributable to the rail centerline, while Cases 4 and 5 provided data for the M829 in the EM gun system with rail and insulator centerlines, respectively. A final case, Number 11, was run during conditions similar to Case 1 except for use of the vertical centerline of the conventional double-travel gun instead of the horizontal centerline.

The other half of the investigation focused on the response of the EM projectile, with Case 6 serving as a baseline for the complete EM system. As with the M829 projectile cases, parameters were shuffled to see how singular changes affected in-bore

performance. Case 7 subjected the EM design to the conventional
loading in the EM system. Case 8 examined the projectile's actions
in an EM system having the double-travel gun's centerline. Case 9
analyzed the EM projectile in the conventional gun system, while
Case 10 looked at projectile response in the EM system with the
insulator centerline.

	Projectile	Loading	Centerline	Gun System	Barrel Geometry
Case 1	M829	Conventional	Double Travel 120mm	Double Travel Cannon	Double Travel Cannon
Case 2	M829	EM Profile	Double Travel 120mm	Double Travel Cannon	Double Travel Cannon
Case 3	M829	Conventional	UTCEM Rails	Double Travel Cannon	Double Travel Cannon
Case 4	M829	EM Profile	UTCEM Rails	UTCEM	UTCEM
Case 5	M829	EM Profile	UTCEM Insulator	UTCEM	UTCEM
Case 6	EM	EM Profile	UTCEM Rails	UTCEM	UTCEM
Case 7	EM	Conventional	UTCEM Rails	UTCEM	UTCEM
Case 8	EM	EM Profile	Double Travel 120mm	UTCEM	UTCEM
Case 9	EM	Conventional	Double Travel 120mm	Double Travel Cannon	Double Travel Cannon
Case 10	EM	EM Profile	UTCEM Insulator	UTCEM	UTCEM
Case 11	M829	Conventional	Double Travel 120mm (vertical)	Double Travel Cannon	Double Travel Cannon

Table 1. Listing of Parameters for Each Case Investigated

RESULTS

The output from RASCAL includes a wealth of information to determine both projectile and gun response. The focus of this effort was on the in-bore response of the round so the information extracted and examined from the RASCAL output included the transverse velocity at the projectile center of gravity and the projectile's angular velocity over the length of in-bore travel.

The transverse acceleration of each projectile's center of gravity was determined by taking a derivative of the RASCAL calculated velocity with a subsequent conversion made into g's. These values are tabulated in Table 2 for the 11 cases examined for all three contact stiffness values. Figure 9 is a graphical display of the same information. While the EM projectile cases generally exhibit higher transverse accelerations, they are the same order of magnitude as the M829 cases. The disturbing fact of these results is the dramatic rise in lateral acceleration for both projectiles traveling through the EM gun with the insulator centerline (Cases 5 and 10). The M829 cases exhibit increasing accelerations as the contact stiffness is increased. This is to be expected since the projectile's center of gravity is beneath the rear contact so that any increasing force transmitted through the stiffer contact acts directly on the center of gravity. Conversely, the EM projectile has its center of gravity between the two contact points. The data reveal the medium stiffness value (4.3e05 lb/in) results in more aggravated transverse accelerations than the stiffest contact (1.0e06 lb/in). This may be because one of the rod's natural bending frequencies is excited when the medium stiffness is used.

Maximum Transverse Acceleration, g's						
k, lb/in	1.0e05	4.3e05	1.0e06	k, lb/in	1.0e05	4.3e05	1.0e06
Case 1	534	649	1492	Case 6	1882	3152	2142
Case 2	552	857	1615	Case 7	1722	3215	1941
Case 3	247	845	2406	Case 8	1442	1563	2139
Case 4	296	1249	2585	Case 9	1185	1517	1122
Case 5	884	1868	8498	Case 10	2227	5973	4321
Case 11	211	594	673				

Table 2. Maximum Transverse Accelerations

It is also interesting to notice the trends in the magnitude of the transverse acceleration values. In proceeding from left to right on Figure 9, Cases 1 through 5 show increasing peak lateral accelerations. This corresponds to the M829 being subjected to more "EM-like conditions" with each subsequent case. That is, Case 1 employs a conventional gun system, Cases 2 and 3 have some aspects of the EM system integrated, and Cases 4 and 5 have the M829 in a full EM environment. Case 11 reinforces this notion that the conventional system produces a more benign response.

Similarly, Cases 6 through 9 show that as the EM projectile is introduced to more elements of the conventional gun system (again, moving left to right), it alleviates the severity of the transverse acceleration. Case 10 serves as a stark contrast to its predecessor, Case 9, pointing out the differences between the conventional system and the EM system with the insulator centerline.
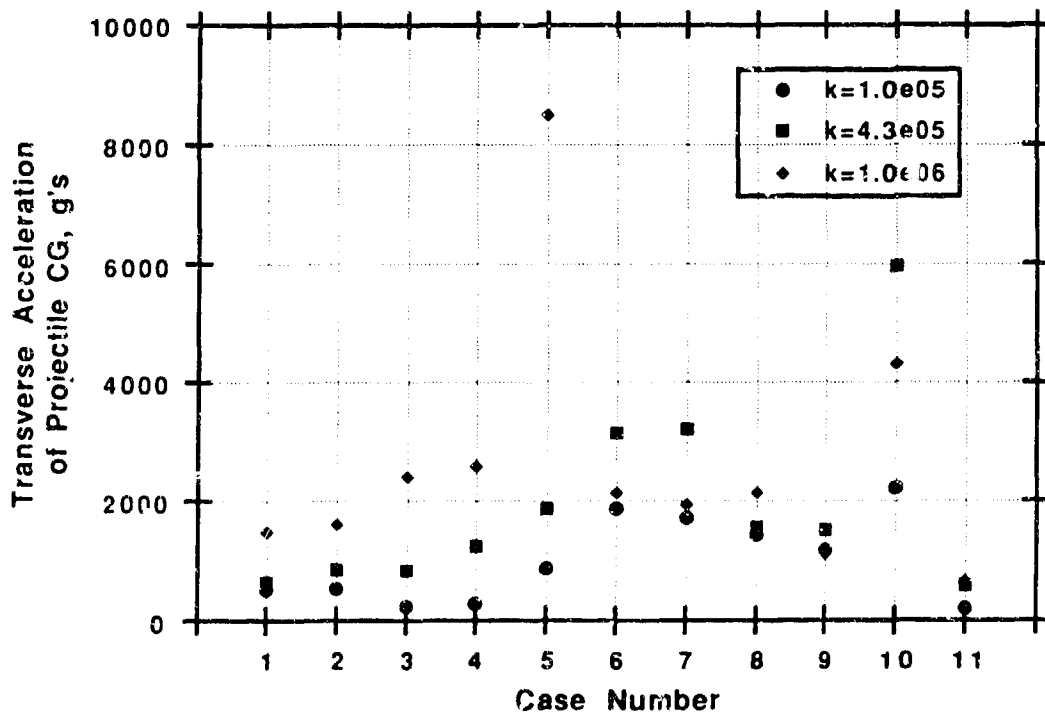
Figure 9. Comparison of Transverse Accelerations

The other output examined from the RASCAL analysis was the data for the angular rate of the projectile. These data are a measure of the instantaneous velocity of the projectile model slope, based on the displacement of the contact points. This provides a feel for the magnitude of a projectile's yawing motion while in bore. Plots of the angular velocity versus time are presented in Figures 10 through 42 for the 11 case studies with the various contact stiffness values.
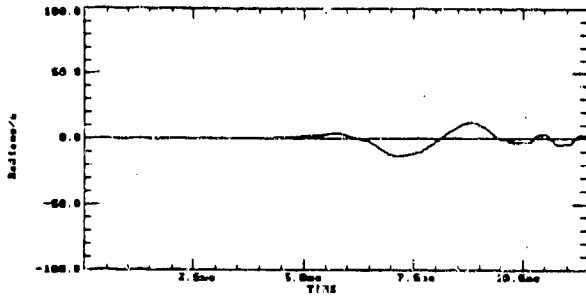
Figure 10. Angular Velocity of Case 1
b=1.0e05 lb/in
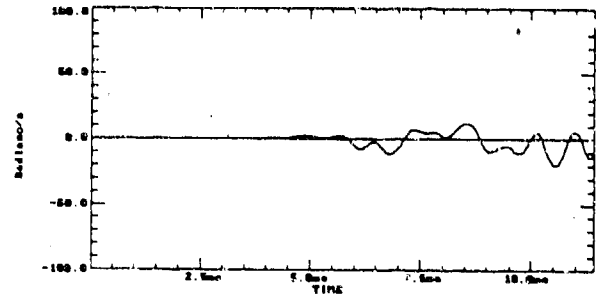
Figure 11. Angular Velocity of Case 1
b=4.2e05 lb/in
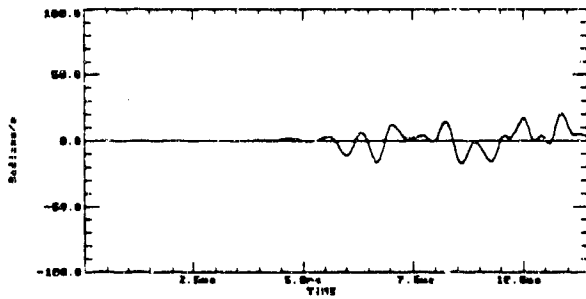
Figure 12. Angular Velocity of Case 1
b=1.0e06 lb/in
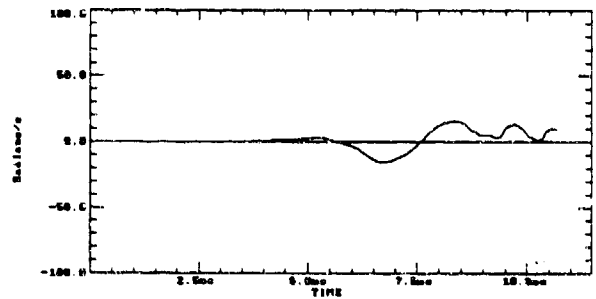
Figure 13. Angular Velocity of Case 2
b=1.0e05 lb/in
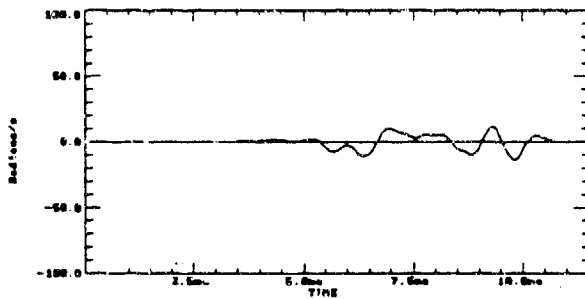
Figure 14. Angular Velocity of Case 2
b=4.2e05 lb/in
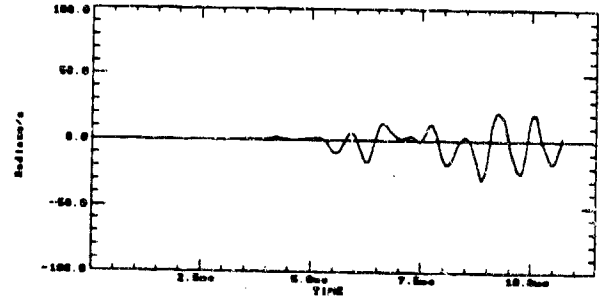
Figure 15. Angular Velocity of Case 2
b=1.0e06 lb/in
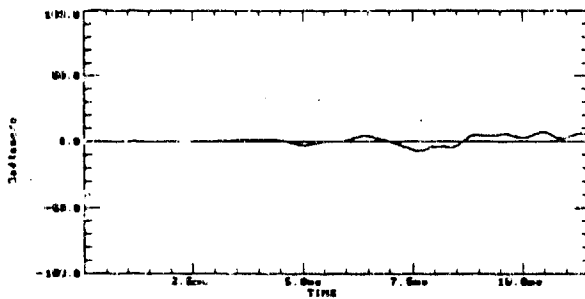
Figure 16. Angular Velocity of Case 3
b=1.0e05 lb/in
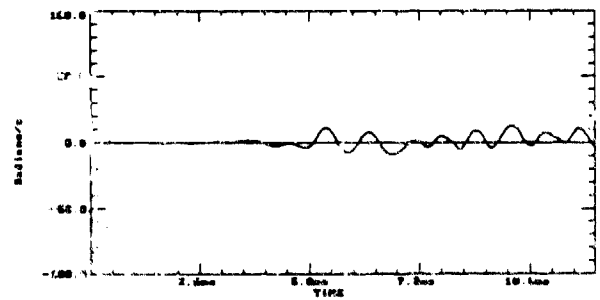
Figure 17. Angular Velocity of Case 3
b=4.2e05 lb/in

143
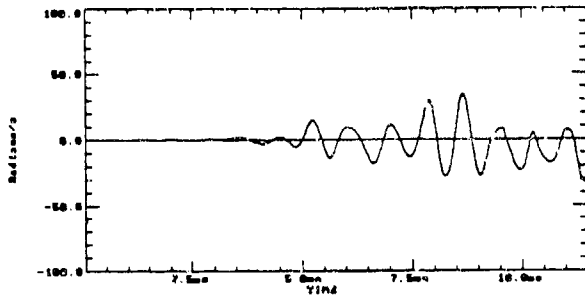
Figure 18. Angular Velocity of Case 3
h=1.0e05 lb/in
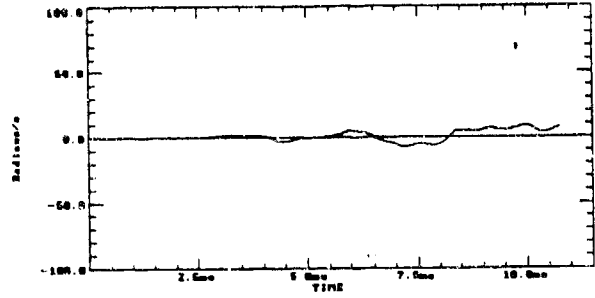
Figure 19. Angular Velocity of Case 4
h=1.0e05 lb/in
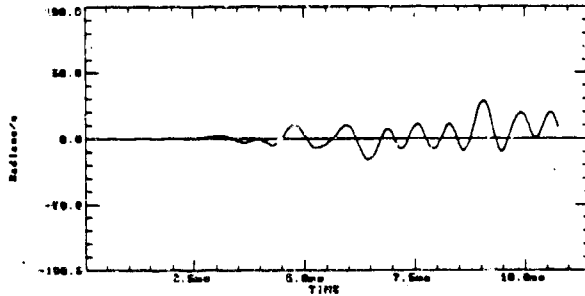
Figure 20. Angular Velocity of Case 4
h=4.3e05 lb/in
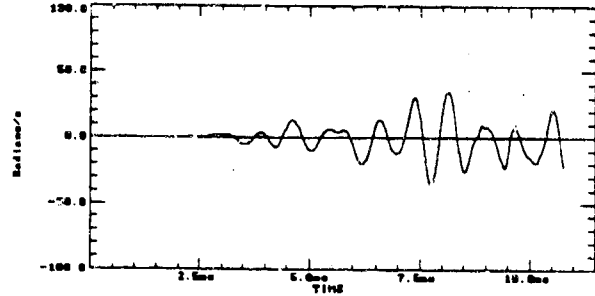
Figure 21. Angular Velocity of Case 4
h=1.0e06 lb/in
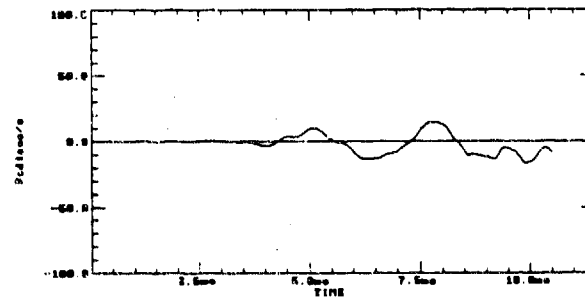
Figure 22. Angular Velocity of Case 5
h=1.0e05 lb/in
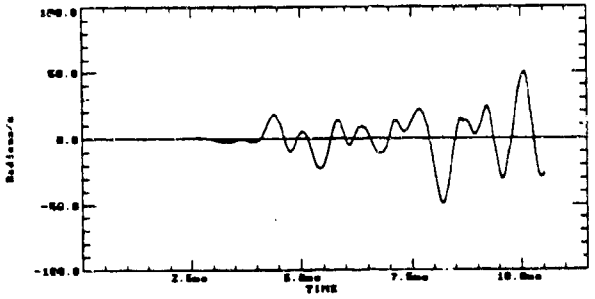
Figure 23. Angular Velocity of Case 5
h=4.3e05 lb/in
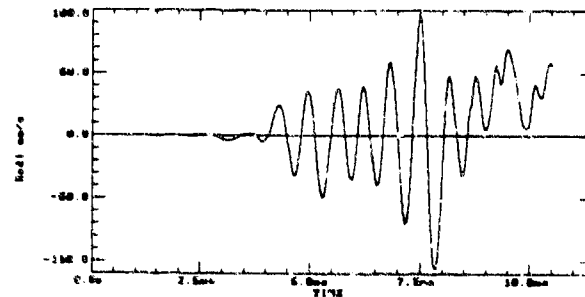
Figure 24. Angular Velocity of Case 5
h=1.0e06 lb/in
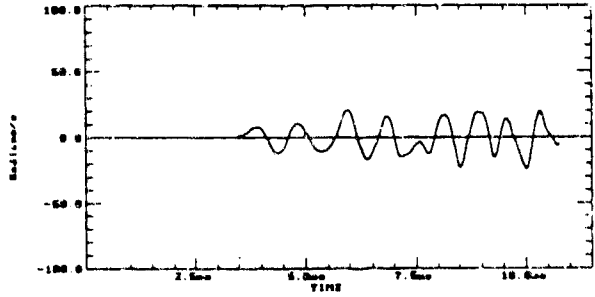
Figure 25. Angular Velocity of Case 6
h=1.0e05 lb/in
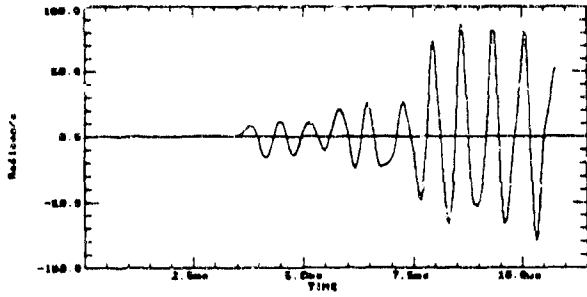
Figure 26. Angular Velocity of Case 6
b=4.3e06 lb/in
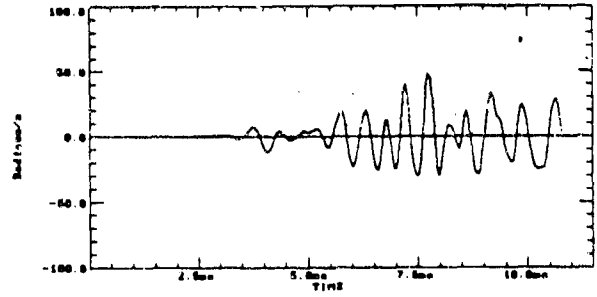
Figure 27. Angular Velocity of Case 6
b=1.3e06 lb/in
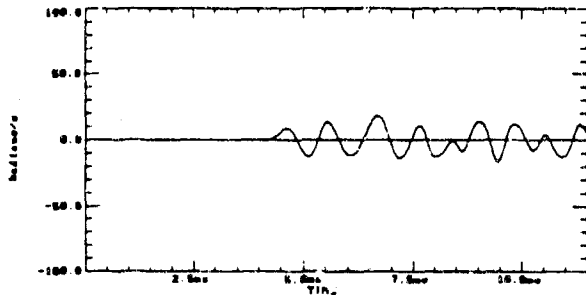
Figure 28. Angular Velocity of Case 7
b=1.0e06 lb/in
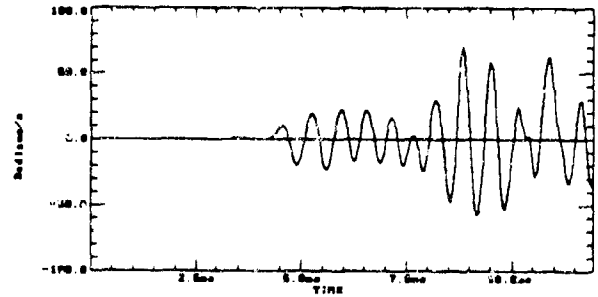
Figure 29. Angular Velocity of Case 7
b=4.3e06 lb/in
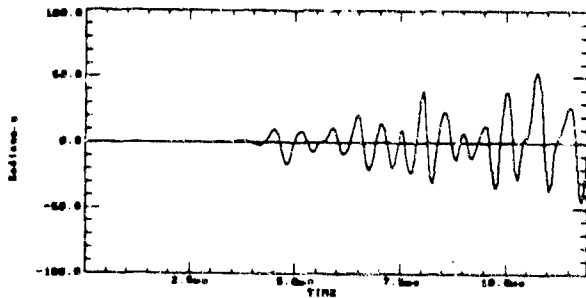
Figure 30. Angular Velocity of Case 7
b=1.0e06 lb/in
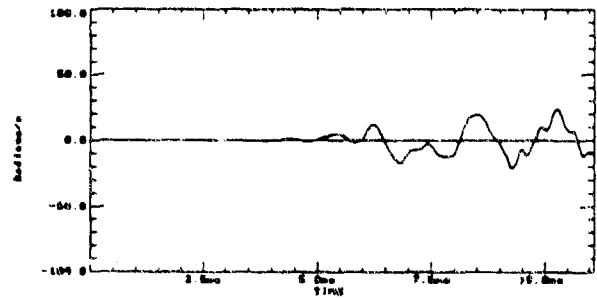
Figure 31. Angular Velocity of Case 8
b=1.0e06 lb/in
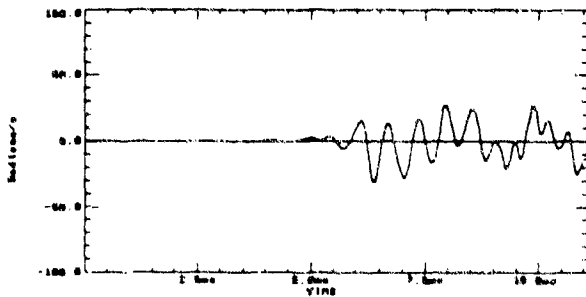
Figure 32. Angular Velocity of Case 8
b=4.3e06 lb/in

Figure 33. Angular Velocity of Case 8
b=1.0e06 lb/in

Figure 34. Angular Velocity of Case 9
h=1.0e05 lb/in

Figure 35. Angular Velocity of Case 9
h=4.3e05 lb/in

Figure 36. Angular Velocity of Case 9
h=1.0e06 lb/in

Figure 37. Angular Velocity of Case 10
h=1.0e05 lb/in

Figure 38. Angular Velocity of Case 10
h=4.3e05 lb/in

Figure 39. Angular Velocity of Case 10
h=1.0e06 lb/in

Figure 40. Angular Velocity of Case 11
h=1.0e05 lb/in
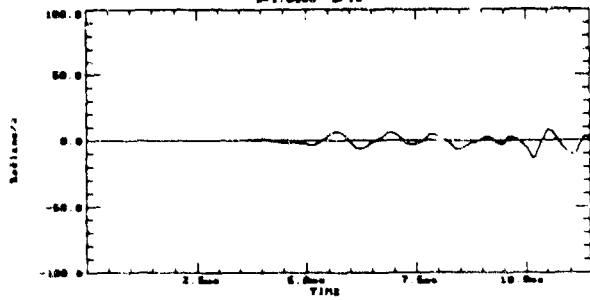
Figure 41. Angular Velocity of Case 11
h=4.3e05 lb/in
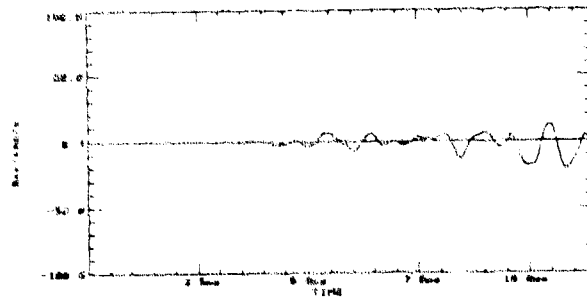
Figure 42. Angular Velocity of Case 11
h=1.0e06 lb/in

146

From the plots, it is seen that the M829 with the soft contacts (k=1.0e05 lb/in) yields a rather benign response for all cases (Cases 1 through 5, and 11). By comparing Cases 1 and 3 with Cases 2 and 4, respectively, one finds the projectile motion is mostly unaffected by a change in load profile. Substitution of the rail centerline profile for the conventional double-travel (Case 1 vs. Case 3 and Case 2 vs. Case 4) reveals a slight exacerbation of the in-bore motion. In general, the yawing motion worsens with an increase in contact stiffness. The case of the M829 through the EM insulator centerline, Case 5, is clearly the poorest performer from any of the analysis runs with this projectile.

The EM projectile cases exhibit trends comparable to those with the M829. Namely, the insulator centerline subjects the round to the most severe angular velocity, while the EM rail profile shows only slightly worse results than the conventional gun case does. Also, it is noted how a change in interior ballistic loading results in little difference between the EM and conventional cases. These EM projectile cases have an increasingly higher angular velocity when going from the soft to medium contacts, but the magnitude of the angular rate levels off and does not increase for the stiffest contacts. This is another indication that the medium contact stiffness excites a natural bending frequency of the rod.

In comparing the EM projectile to the M829, it is seen that the EM round has consistently higher angular rates for the soft contact cases. Also, given the conventional gun centerline, both projectiles show angular velocities of equivalent magnitude. Thus, nothing appears to be inherent in the different projectile designs that aggravates the in-bore yaw.

CONCLUSIONS

From this analysis, it is clear the EM gun system presents a more severe environment than does a conventional powder gun. The results point to the difference in centerlines as a primary cause. Changes in interior ballistic input are shown to have little effect on the transverse acceleration and angular velocity over the length of in-bore travel. However, further studies are required to ascertain if this holds true for velocities well above those of today's ordnance (2.5 km/s and up, for instance).

The differences between the M829 and EM projectile geometries do not greatly influence the in-bore yawing motion. In general, the EM projectile is consistently subjected to larger transverse accelerations, but the delta is minimal. Also, the apparent tendency to excite natural frequencies of the subprojectile for the medium spring stiffness case is certainly something that the EM projectile designer must concern himself with and try to avoid.

The choice of the gun barrel centerline profile acts as the principal driver in determining the projectile response for this

study. While the rail profile results in yawing motion only slightly worse than the powder gun, the insulator profile clearly brings about the worst response, with both the transverse accelerations and angular velocities being substantially higher.

The one-dimensionality of the RASCAL analysis fails to account for any coupling effects that result from traversing the rail and insulator centerlines simultaneously. Since it has been shown that the rail centerline imparts more motion to the projectile than a conventional gun does, and the insulator centerline produces even greater motion, it is feared that a more advanced code capable of modeling the full internal bore geometry will show even more deleterious results.

Finally, the results of this analysis point out a weakness of the current EM gun systems: an inability to maintain a relatively benign centerline through which the projectile traverses. At present, EM railguns have centerlines that fluctuate from shot to shot. Until a consistent, less severe centerline profile can be maintained, EM projectiles will have difficulty matching the in-bore, and subsequently, the flight and terminal performance of rounds fired from conventional guns.

REFERENCES

1. T.F. Erline, M.D. Kregel, and M. Pantano,"Gun and Projectile Flexural Dynamics Modeled by the Little RASCAL - a User's Manual", BRL-TR-3122, U.S. Army Ballistic Research Laboratory, Aberdeen Proving Ground, MD, July 1990.

2. T.F. Erline, M.D. Kregel,"Flexible Projectile Modeling Using the Little RASCAL Gun Dynamics Program", Proceedings of the Sixth U.S. Army Symposium on Gun Dynamics, Tamiment, PA, May 1990.

3. D.A. Hopkins,"Modeling Gun Dynamics with Three-Dimensional Beam Elements", Proceedings of the Sixth U.S. Army Symposium on Gun Dynamics, Tamiment, PA, May 1990.

4. N.D. Manners,"A Theoretical Study into the Effect of Sabot Stiffness on Projectile In-Bore Motion and Launch Accuracy", Proceedings of the Sixth U.S. Army Symposium on Gun Dynamics, Tamiment, PA, May 1990.

5. M.A. Polcyn, P.A. Cox,"The Adaptation of NASTRAN for Three-Dimensional Gun Dynamics Problems", Proceedings of the Sixth U.S. Army Symposium on Gun Dynamics, Tamiment, PA, May 1990.

6. D.A. Rabern, K.A. Bannister,"Finite Element Models to Predict the Structural Response of 120-mm Sabot/Rods During Launch", Proceedings of the Sixth U.S. Army Symposium on Gun Dynamics, Tamiment, PA, May 1990.

7. D.H. Lyon,"Radial Stiffness Measurements of 120-mm
    Projectiles", U.S. Army Research Laboratory, Aberdeen
    Proving Ground, MD, to be published.

8. C.D. McCall, D.L. Henry,"Flexural Characteristics of the M829
    Projectile Family", U.S. Army Research Laboratory, Aberdeen
    Proving Ground, MD, to be published.

9. T.F. Erline,"Projectile Spring Constants Significance to
    Modeling with the Little RASCAL Gun Dynamics Program",
    BRL-TR-3224, U.S. Army Ballistic Research Laboratory, Aberdeen
    Proving Ground, MD, April 1991.

TITLE: DYNAMIC ANAYSIS OF A PULLER SABOT CONCEPT

THOMAS F. ERLINE
US ARMY RESEARCH LABORATORY
WEAPONS TECHNOLOGY DIRECTORATE
AMSRL-WT-PD
ABERDEEN PROVING GROUND, MD 21005-5066

ABSTRACT:

Tank weapons have increased lethality in comparison to weapons of the past because of the development of high performance tank cannons and associated ammunition. This increase in lethality is due, in part, by the development of the armor-piercing, fin stabilized, discarding sabot (APFSDS) kinetic energy (KE) projectile.

The US ARMY presently uses the M829 as one of its main KE ammunition in the M1A1 tank. The M829 projectile sabot configuration is the double ramp design. The double ramp design with its central bulkhead and forward scoop bore rider provides dynamic stability during the launch cycle.

This paper examines the simulated lateral dynamics of two particular APFSDS KE rounds: the existing M829 a double ramp sabot design projectile and a conceptual "puller" sabot projectile. The lateral dynamics of these two KE rounds are simulations as fired from two particular 120-mm tank cannons. The simulations are performed by the Little RASCAL gun and projectile dynamics program. This program models dominant lateral loads of gun dynamics and the projectile interacting with the barrel. In-bore projectile lateral dynamics are predicted by the program which at muzzle exit provide initial launch conditions. Comparisons of the two KE projectile are made of mechanical flexure and shot exit conditions.

BIOGRAPHY:

PRESENT ASSIGNMENT: Mathematician, Mechanics and Structures Branch, Propulsion and Flight Division, Weapons Technology Directorate, US Army Research Laboratory.

PAST EXPERIENCE: Mathematician, Mechanics and Structures Branch, Interior Ballistics Division, Ballistic Research Laboratory, 1985-1992.
Research Scientist, Physics Division, Chemical Research and Development Center - PAD, 1982-1985.
Mathematician, Vulnerability Lethality Division, Ballistics Modeling Division and Concepts Analysis Laboratory, BRL, 1973-1982.

DEGREES HELD: BS - TOWSON STATE UNIVERSITY ,1973.

DYNAMIC ANALYSIS OF A PULLER SABOT CONCEPT

THOMAS F. ERLINE
US ARMY RESEARCH LABORATORY
ABERDEEN PROVING GROUND, MD 21005-5066

1. INTRODUCTION

Modern tanks have much more lethal weapon systems compared to the tanks of the past. This is possible because of the development of high performance tank cannons. These cannons are armed with highly lethal ammunition that can penetrate very thick armor. One major type of ammunition is the armor-piercing, fin stabilized, discarding sabot (APFSDS) kinetic energy (KE) projectile. This type of projectile, launched with a charge to projectile mass ratio of almost 1.0, has been developed to attain high muzzle velocity for increased range and penetration upon impact. Getting the penetrator to the target is the goal of the exterior ballistician. Launching the projectile is the goal of the interior ballistician, who studies the gun and projectile reacting to combustion and inertial loads as the bore riding projectile traverses the length of the barrel. At the moment the projectile leaves the muzzle, the interior ballistic end conditions become the initial conditions the exterior ballistician needs.

To provide the initial launch conditions of the projectile at exit, the interior ballistician needs to be able to predict the actions and reactions of the projectile during the launch cycle. When fired, the bore riding projectile undergoes a complex sequence of mechanical and gas dynamic interactions on its way down the barrel, until it reaches free flight.

This paper examines the simulated lateral dynamics of two particular APFSDS KE rounds: the existing M829 and a conceptual puller saboted KE projectile as fired from two particular 120-mm tank cannons. An analysis of the results of these simulations provides the lateral in-bore projectile dynamics which at muzzle exit then provide initial lateral launch conditions. The simulations are modeled by the Little RASCAL (LR) gun and projectile dynamics program [1]. The LR code is a fast running code that models the dominant lateral loads of gun dynamics and projectile/barrel interaction in a plane. The gun dynamics modeling has been shown to match experimental results quite well[2,3].

The M829 is the main 120-mm standard for the US Army APFSDS KE projectile for the M1A1 tank gun. This projectile with its double ramp design has excellent in-bore stability and dynamic characteristics. It is a design that has kept sabot weight down, and yet also appears to keep dynamic displacements at a minimum.

Even though the US Army has selected the double ramp sabot design (see figure 1) - a ramp from center to front and rear - as the most efficient type of discarding sabot design, this does not preclude investigations into other types of geometrical designs in an attempt to find more optimal configurations. One such design is known as the puller[4] sabot configuration (see figure 2). Somewhat recently (November 1991), a puller sabot (see figure 3). configuration was patented by R. Diel, A. Sippel, J. Meyer, and H-J. Kruse of the Federal Republic of Germany[5]. However, the puller configuration has been used by the US ARMY for projectiles in the past (for example, the 75mm ADMAG gun and other guns[6]).
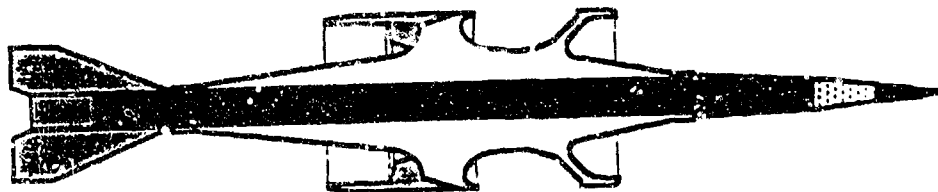
Figure 1. M829 - Double Ramp Sabot Design.
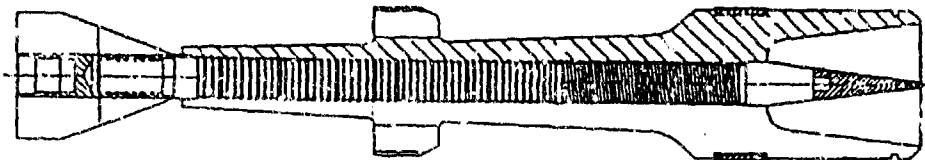
Figure 2. "Puller" - Alliant Concept Design.
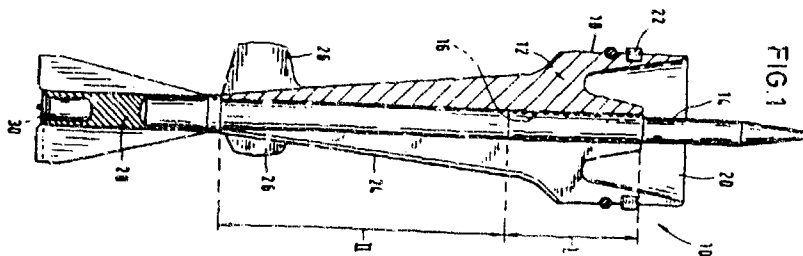
Figure 3. Patented Puller Design.

The puller concept represents an idea where the main bulkhead part of the sabot clamps the sub-projectile in a forward position. When firing this projectile the gas pressure of the combustion process is allowed to proceed to the forward bulkhead, which also acts as an obturator, propelling the projectile from this forward position. Thus, the trailing part of the projectile is literally "pulled" out of the tube. The gas pressure of the combustion process also compresses the long trailing ramp of the sabot against the sub-projectile. Interesting notes about the puller sabot projectile when firing it are: 1) the axial loading on a major percentage of the flight vehicle will be axial tension (the contrast is significant in comparison with the double ramp design where the front half of the projectile is in axial compression while the rear half is in axial tension); 2) shot exit conditions with combustion gases exiting along with a major portion of the puller projectile may have more turbulent disturbances than the double ramp design; and 3) lateral vibration characteristics will be completely different from those of the double ramp design.

The LR code used herein does not account for the first two of the above notes but does for the third. The Little RASCAL code can make predictions of shot exit conditions produced by the induced lateral vibrations as the projectile follows the centerline of a tank gun tube. Attempting to validate the projectile vibration part of the study, the M829 LR projectile model in-bore predicted displacement shapes are compared to the deformed rod shapes of M829 projectiles as taken by in-bore x-ray radiographic equipment[7]. Three different tests are documented on the lateral shapes of the M829 as captured on radiographic film within tube SN81. The three different experimental rod shapes are matched closely by the LR M829 projectile model simulated in tube SN81 in two out of three cases.

This study compares the M829 dynamics directly to the puller dynamics. To make the models as equal as possible for comparison purposes, the puller concept projectile model has its mass nearly equal to the M829 double ramp design model. This is accomplished by: 1) the puller is modeled using the exact same sub-projectile as the M829 model and 2) proper modeling ensuring the mass of the puller sabot is nearly the same as the M829 sabot. An analysis is made by observing the lateral responses of the puller concept projectile in comparison to the standard, M829 lateral responses. The different shot exit conditions produced by the two different designs as predicted by LR are a function of the dominant lateral mechanical loading of the projectile traversing the length of the barrel. These mechanical interactions are caused by the "powder pressure couple"[8] and the projectile interacting with the non-straight centerline of the barrel.

The particular puller configuration analyzed here and compared with the M829 double ramp design is based on the Alliant geometrical design, rather than the patented design. The Alliant design positions the rear fluted bulkhead significantly closer to the center of gravity of the projectile than the patented design,

which positions the fluted rear bulkhead support close to the
fins. On the otherhand, the M829 double ramp design positioned
the rear bulkhead over the projectile center of gravity.

2.   THEORY

The Little RASCAL gun and projectile dynamics program is a
lateral dynamic displacements code employing a direct structural
dynamics analysis approach to the simulation of firing a
projectile from a gun. Both the gun system and the projectile are
modeled using a series of equally spaced cylindrical elements.
Nodes are centered and assigned equivalent mass and stiffness
values based on standard engineering formulae. Inertial forces
and flexural forces are calculated using this simplified
description. Flexure at each node is approximated by a second
order finite difference method, which allows the bending forces to
be computed. Transverse nodal accelerations caused by these
forces are integrated with respect to time to obtain transverse
nodal velocities, and integrated again to obtain lateral node
displacements. Loads considered are pressure effects, mounting
conditions, breech center of gravity offset, and
projectile/barrel interactions. All forces are then integrated by
a predictor-corrector technique stabilized by a numerically stiff
ordinary differential equation solver[9,10].

The gun system (includes the breech, barrel and two gun
supports) and the projectile (includes the flight vehicle and the
sabot) are two separate models. They are accounted for
individually except for a variational algorithm which handles
their interaction. The interaction of the projectile with the
barrel occurs through contact points. The two contact points
defined on the projectile are usually positioned where they occur
geometrically at the bulkhead and scoop. The two projectile
contact points positions on the barrel are dynamic and change as
the projectile traverses the bore. The gun system model and the
projectile model are two separate flexible entities, with each
projectile contact point requiring a user defined spring constant.
The spring constants serve to define the interface loads between
the projectile model and the gun model. The importance of good
projectile spring constant values for accurate modeling results
has been shown [11]. The values used for spring constants in this
study are considered the most up-to-date. The values used are
within a range of values that were found in experimental work
performed at the Ballistic Research Laboratory[12].

3.   THE SIMULATIONS

The M256 120-mm gun system used in the M1A1 tank is a high
performance weapon system. It uses a smooth bore barrel and has a
concentric recoil design. The concentric design lends itself
readily to symmetric gun dynamics modeling. The M256 gun system
has been tested extensively for gun dynamics and mathematical

modeling has emulated its dynamic characteristics quite well [2,3]. In the vertical plane the dominant loadings of the "powder pressure couple" [8], gravity droop and the non-straight bore curvature contribute to the characteristic and repeatable barrel reactions including a muzzle whipping motion around the time of shot exit. Figure 4 shows a gun dynamics time and displacement surface trace of the vertical plane barrel centerline motion due to the "powder pressure couple" of tube SN104. The simulations use two centerlines: Tube SN81 considered a "bent" tube, and tube SN104 considered to be a fairly straight production tube. Figure 5 shows the tube vertical center line shapes where the muzzle is noted with an "x" and positioned at the origin.
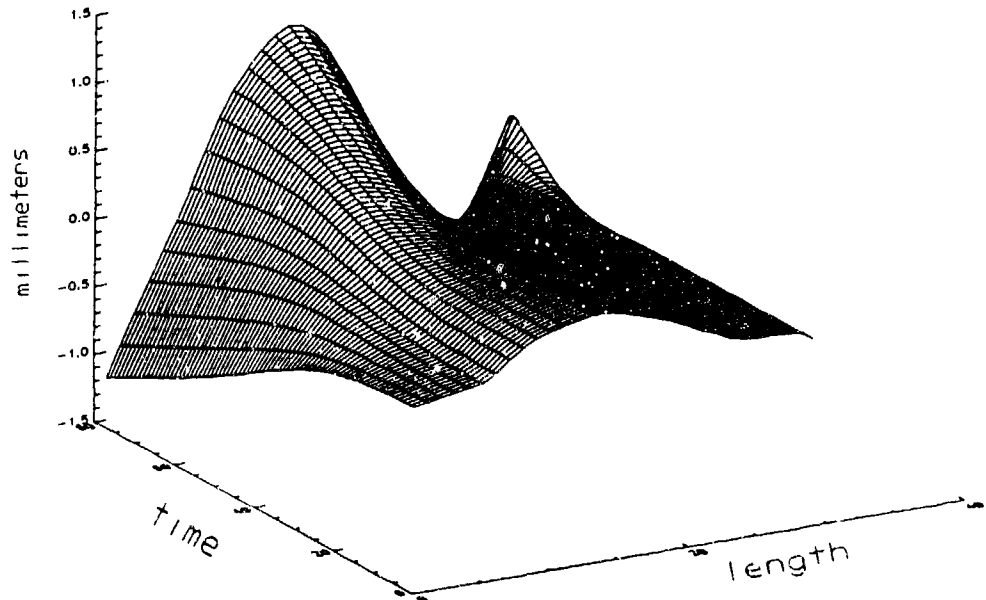
Figure 4. Centerline SN104 Gun Dynamics Motion from Ignition to Shot Exit.
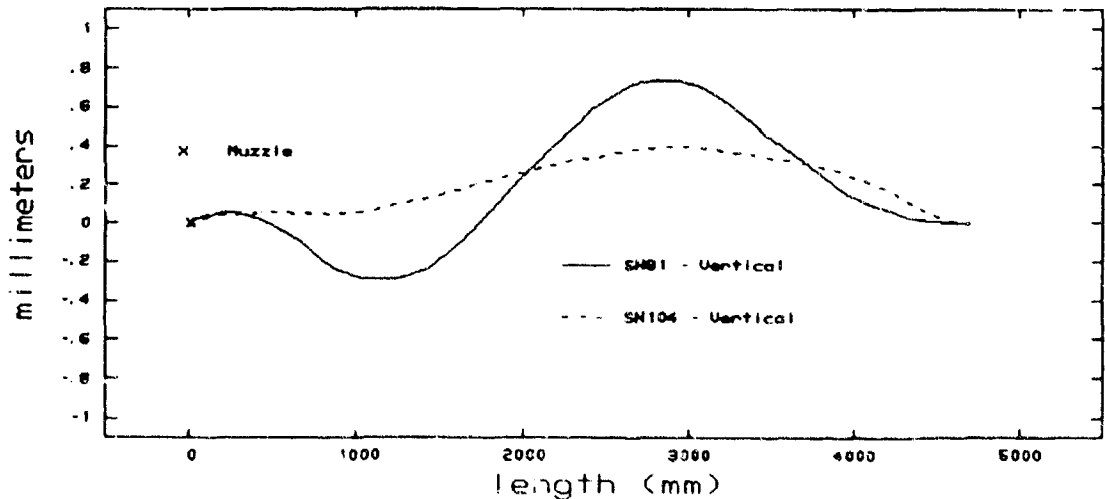
Figure 5. Vertical Centerlines – M256 Tubes SN81 and SN104.

Table 2. M829 Component Physical Properties

		Mass (kg)	Center of Gravity (mm)
Flight Vehicle (Rod, Fins and Tip)	Real	4.25	287.8
	Model	4.37	280.9
Bore Rider (Flight Vehicle, and Sabot)	Real	7.09	290.6
	Model	7.11	288.1

In-Bore Results Firing the M829 in the SN81

This projectile was experimentally fired from the non-straight 120-mm tube designated SN81. To capture the sub-projectile rod in-bore flexural shape while traversing the barrel a 2.3-MeV x-ray experiment was set-up. Dr. Rabern documents three separate test radiographs where the rod shapes are successfully extracted. The M829 rod shape was captured at 53, 66 and 52 inches from the muzzle and assigned as tests 1, 2 and 3, respectively. The captured experimental rod flexural shapes are shown with a "+" in figures 7, 8 and 9. Shown as a solid line in the figures 7, 8 and 9 are the Little RASCAL simulation results of the M829 model being fired in the SN81. The experimental shapes are slightly shorter than the model shape because only the rod shape is plotted, whereas the the fins and nose appear in the LR results. The LR displacement results and the experimental results are positioned with the projectile center of gravity at the 0.0, 0.0 coordinate. Neither shape represents actual projectile pitch. These plots are for the comparison of flexure only. The LR results are a snapshot of the projectile shape as close as possible to the actual barrel position indicated for that particular test.

Figure 8 shows the test 2 x-ray of the M829 projectile deformed shape at 66 inches from the muzzle appears to have a curvature that lies almost directly on top of the LR M829 model result. Figure 9 shows test 3 deformed projectile shape similar to the rear portion of the simulation curve with the front of the x-ray shape showing more bending than the model. Only figure 7 illustrates an x-ray vibration shape significantly different from LR modeling results.
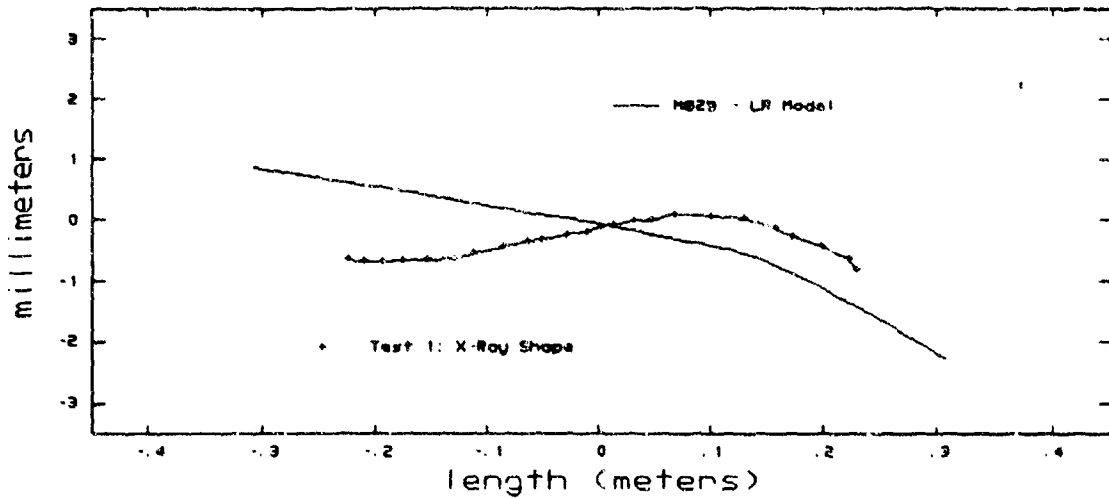
Figure 7. Test 1: M829 Deformed Shapes 58 Inches From the Muzzle.
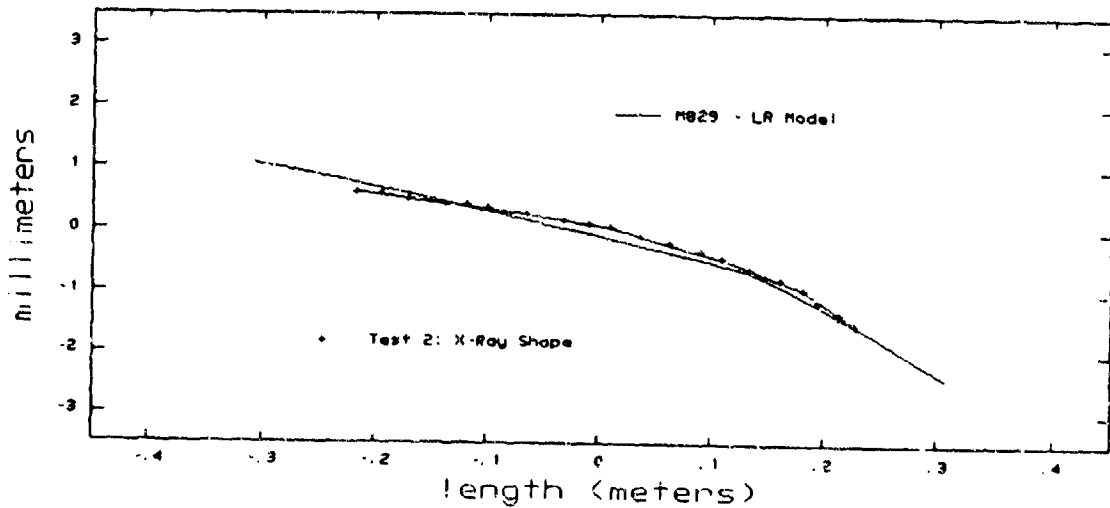
Figure 8. Test 2: M829 Deformed Shapes 66 Inches From the Muzzle.
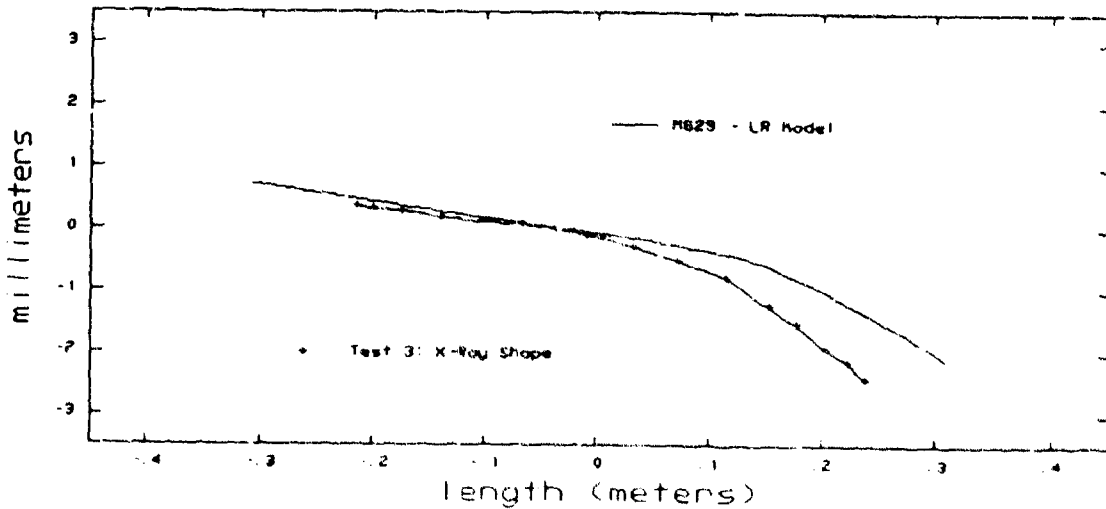
Figure 9. Test 3: M829 Deformed Shapes 52 Inches From the Muzzle.

4. MODELING PROJECTILES

The Interior Ballistics Parameters

The interior ballistics simulation used throughout these studies is based on the M829 fired from the M256 gun system. Both the M829 and the puller concept projectile models use this interior ballistics simulation because the two projectile models are mass equivalent. The firing simulation assumes an ambient temperature and a ratio of 1.17 to 1 propellant mass to projectile mass ratio[13]. The interior ballistics curves of projectile base pressure and projectile axial velocity are found in figure 6 with time zero representing shot exit. The interior ballistics propells the projectile model to shot exit in 7.2 milliseconds.
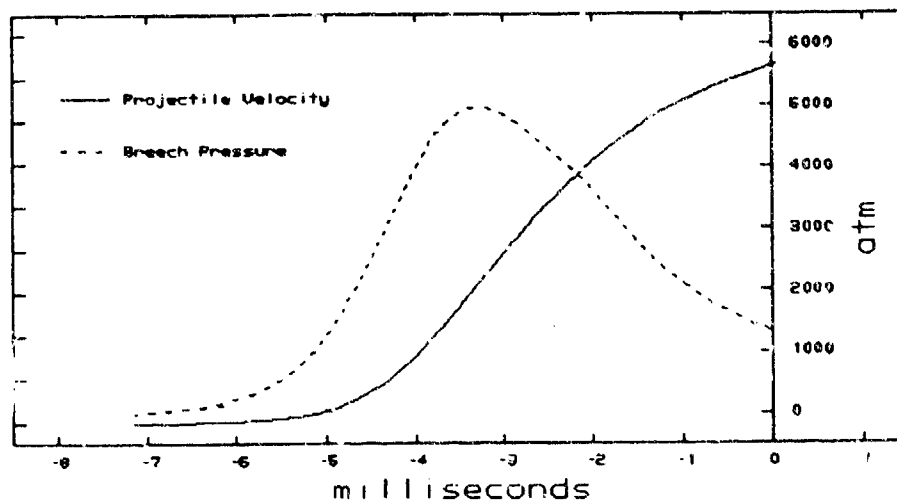
Figure 6. The M829 Interior Ballistics Curves.

The M829 Projectile

The M829 projectile modeled for the Little RASCAL program is based directly on the unmodified M829 projectile used in the experimental work of D. Rabern. The material parameters of the projectile are delineated in Table 1 and the component physical differences noted between the model and the real M829 are shown in Table 2.

Table 1. M829 Material Parameters

Material	Aluminum	Uranium	Steel
Density (kg/m^3)	2700.0	19000.0	7800.0
Young's Modulus (N/m^2)	6.89e10	1.7e11	2.0e11

The Puller Projectile

As indicated previously, the puller projectile model is based on the Alliant geometrical configuration as shown in figure 2. The puller flight vehicle is exactly the same flight vehicle used in the M829 model. To produce a puller model that is mass equivalent to the M829 some slight modifications to the original puller sabot were required, such as trimming material off the bulkheads and scoop. In Table 3 some of the physical properties of the two projectile models are given. Note the differences in the models: 1) the center of gravity of the puller projectile is forward of the M829 by almost 23 mm; 2) the distance between the contact points, also known as the "wheelbase", is 250 mm for the puller while it is just 94 mm for the M829; 3) the major bulkhead for each projectile (front for the puller and rear for the M829) is assigned a hefty spring constant, which is based on spring constant testing performed on double ramp projectiles by D. Lyon of ARL. The front scoop of the M829 is given a slightly softer spring constant, the value is sssumed appropriate because it is also within range of the measurements[11]. The rear bulkhead of the puller is then assumed to have the same softer spring value as the M829 scoop. In the absence of having any physical puller sabot specimens to test, this is assumed to be a reasonable value for this conceptual design because the puller rear bulkhead must be fluted open to allow the passage of the combustion gases.

Table 3. M829 and Puller Models Physical Properties

	Mass	Center of Gravity	(Located From the Base of the Fins)			
			Front		Rear	
			Scoop Contact	Spring Constant	Bulkhead Contact	Spring Constant
	(kg)	(mm)	(mm)	(N/m)	(mm)	(N/m)
M829	7.11	288.1	381.0	1.0e3	287.0	3.0e8
Puller	7.12	315.0	510.0	3.0e8	260.0	1.0e8

5. RESULTS AND DISCUSSION

With the models developed as noted, they were put on a CRAY supercomputer and run on a FORTRAN version of the Little RASCAL program. There are four simulations run for this study: the M829 fired from tubes SN81 and SN104, and the puller fired from the same two SN's. Figure 10 shows one in-bore comparison of the shape of the M829 model and the puller model at 58 inches before the muzzle of tube SN81. Different curvatures and orientations are predicted.
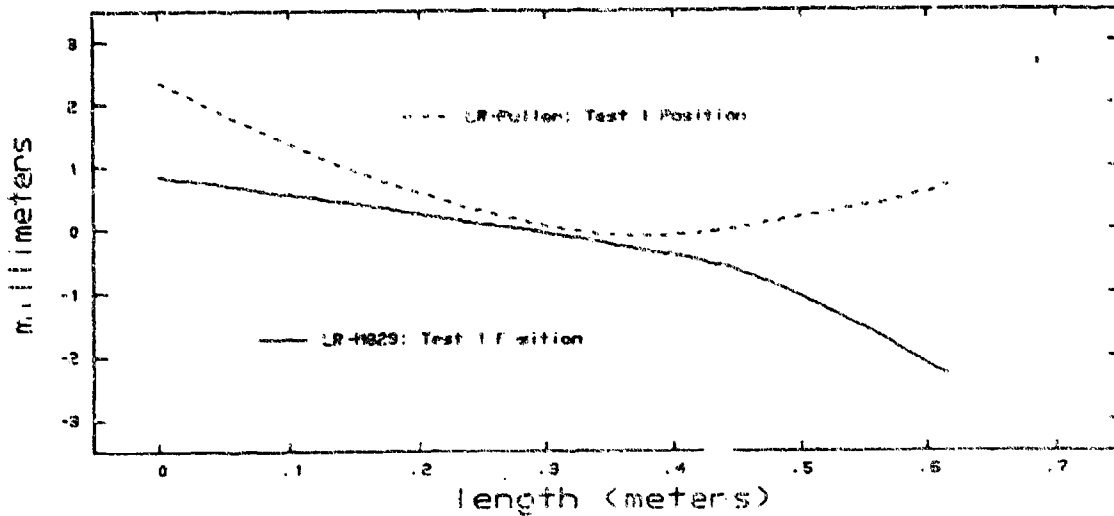
Figure 10. M829 LR Model Deformed Shape Compared to the
Puller LR Model In-bore 58 Inches From the Muzzle.

As the projectile exits the tube the mechanical interactions
cease. The shot exit conditions defined as the first step out
side of the barrel are recorded and they now become the initial
launch conditions for the exterior ballistician. The snot exit
conditions from the four simulations are noted in Table 4.

Table 4. Snot Exit Conditions

Projectile /Tube	Muzzle Slope	Muzzle Angular Rate	Pitch Angle	Pitch Rate	Projectile CG Velocity Vector
	Rads	Rads/sec	Rads	Rads/sec	m/sec
M829 SN81	1.58e-3	-3.00	6.97e-3	14.20	2.10
M829 SN104	1.15e-3	-2.15	2.83e-3	4.18	1.59
Puller SN81	1.35e-3	-1.86	2.67e-3	4.03	2.12
Puller SN104	9.95E-4	-1.65	1.98E-3	-1.89	1.59

Figure 11 illustrates the four different LR predictions of
pitch and shape of the M829 and puller models at shot exit from
the tubes SN81 and SN104. For comparative purposes some shot exit
results from the LR simulations are shown in Table 4, which
describes five shot exit parameters: 1)muzzle slope, 2)muzzle

slope angular velocity, 3)projectile pitch, 4)projectile pitch
rate, and projectile center of gravity(CG) velocity vector. In
figure 11 it appears that the bent tube of SN81 has a more violent
interaction with the projectiles than tube SN104. In the case of
the M829 from SN81 the lateral shape of the M829 predicted by the
LR model is very similar to the lateral shape as reported by Dr.
Rabern[7 (Figure 54. page 77)].   The puller reaction is quite
sensitive to the event in tube SN81 as indicated by its
exaggerated displacement "fish tailing" shape at shot exit.
The largest magnitudes for the exit angles of interest come from
the case of the M829 being fired from tube SN81.   Both muzzle and
projectile reactions are the most notable of all cases as can be
seen in table 4.   Even though the puller projectile reacts with
large displacements from tube SN81 as seen figure 11, the numbers
in table 4 show the puller pitch and pitch rates as significantly
lower.   Also, table 4 shows the puller with less gun and
projectile reaction to each other for tube SN104 than the M829.
As for the projectile center of gravity trace shown in figure 12
and given as the CG velocity vector in table 4, there appears to
be no significant difference.
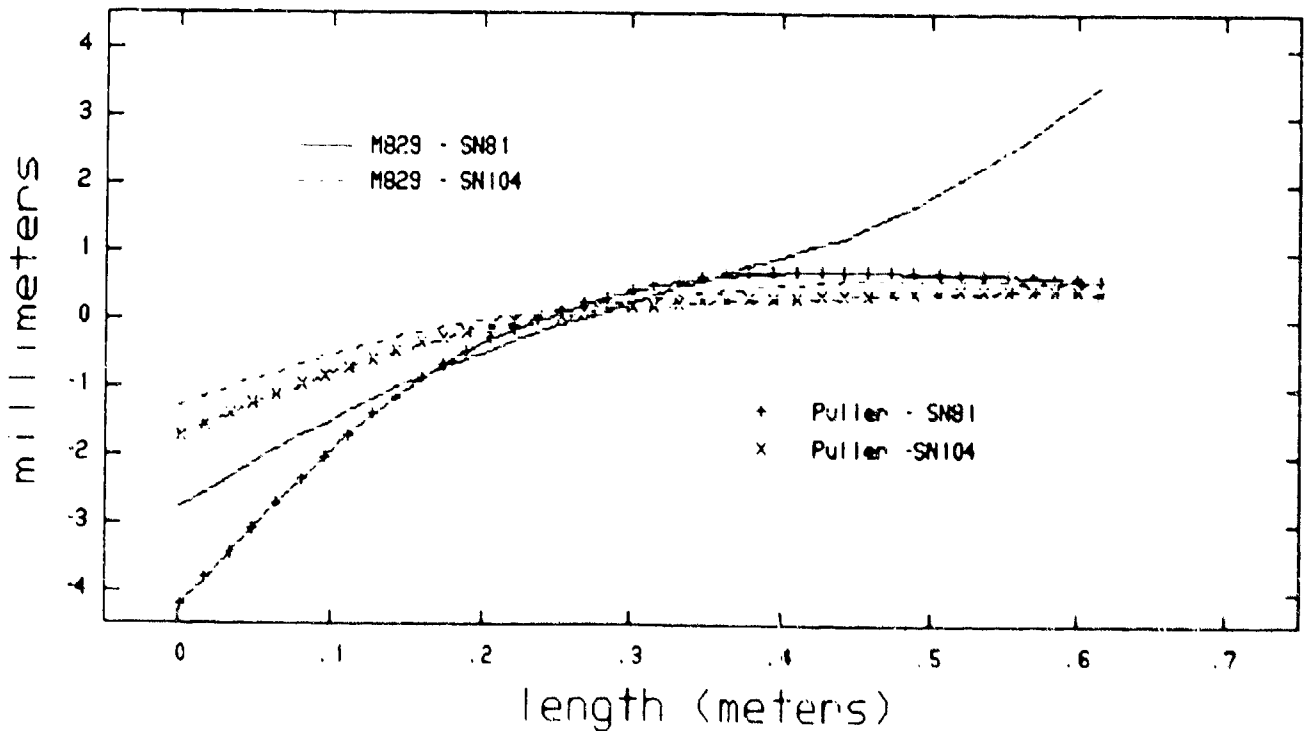
Figure 11. LR Projectile Models Pitch and Shape at Shot Exit.
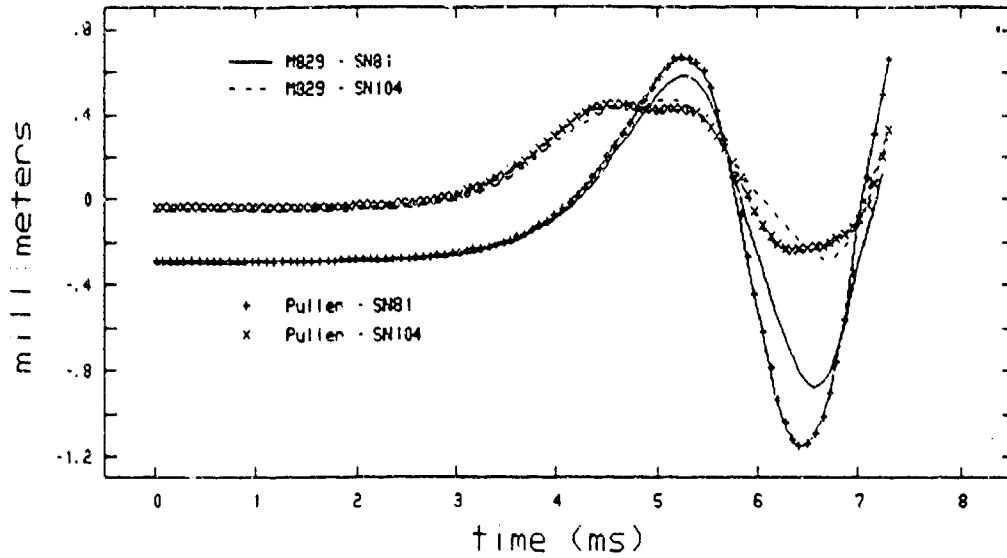
Figure 12. Projectile Center of Gravity Motion.

Figure 13 plots the tail displacement histories in the two tubes of the two projectile models from ignition to just past shot exit. Clearly the Puller projectile is being violently exercised. The other two models appear quiescent in comparison. Figure 14 illustrates the tip dynamics of the four simulations. Little tip motion was expected from a Puller projectile due the proximity of the forward main bulkhead. Despite this assumption it is noted that there is a fair amount of tip displacement, especially, in the case of the Puller in the SN81. From figures 13 and 14 it is noted that all the models tip and tail motion appear to maximize a negative displacement just after shot exit.
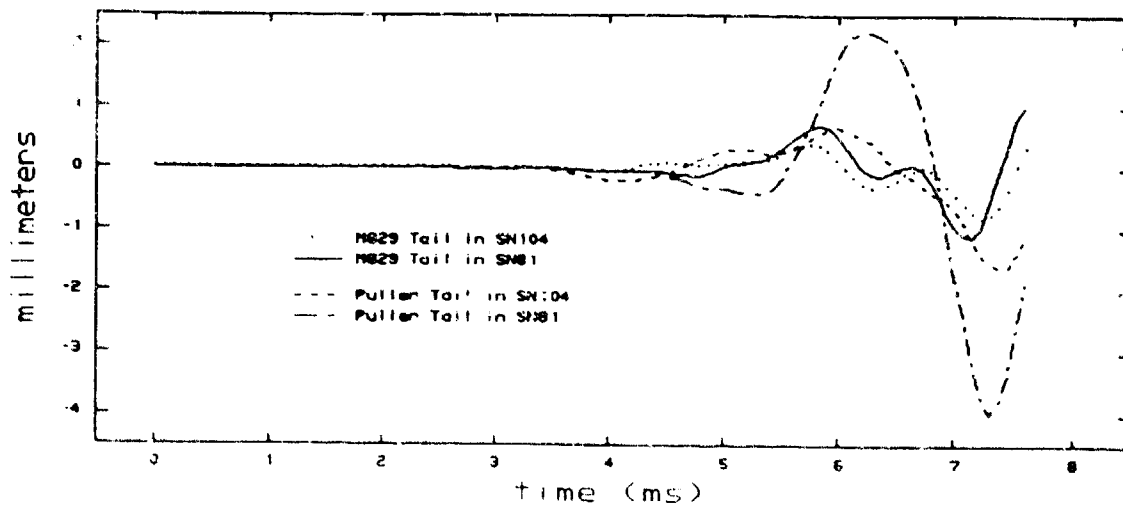
Figure 13. Tail Motion Histories of the LR Models M829 and Puller In the Tubes SN81 and SN104.
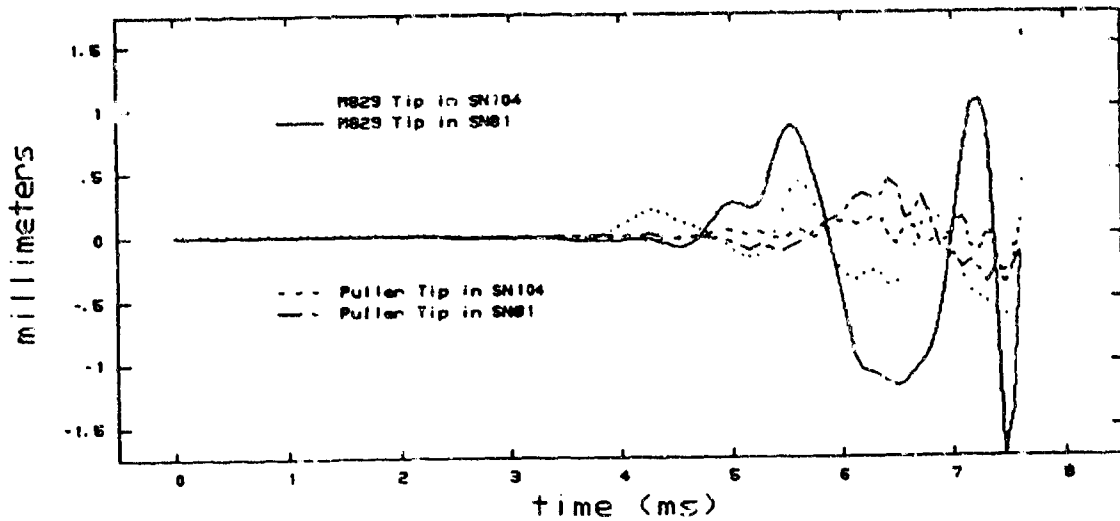
Figure 14. Projectile Tip Motion Reference the Contact Points.

As the projectile exits the tube the mechanical interactions cease. The shot exit conditions defined as the first step out side of the barrel are recorded and they now become the initial launch conditions for the exterior ballistician. The shot exit conditions from the four simulations are noted in Table 4.

Table 4. Shot Exit Conditions

Projectile /Tube	Muzzle Slope	Muzzle Angular Rate	Pitch Angle	Pitch Rate	Projectile CG Velocity Vector
	Rads	Rads/sec	Rads	Rads/sec	m/sec
M829 SN81	1.58e-3	-3.00	6.97e-3	14.20	2.10
M829 SN104	1.15e-3	-2.15	2.83e-3	4.18	1.59
Puller SN81	1.35e-3	-1.86	2.67e-3	4.03	2.12
Puller SN104	9.95E-4	-1.65	1.98E-3	-1.89	1.59

6. CONCLUSIONS

The puller concept saboted projectile as analyzed here allows an interesting comparison to the M829. As far as mechanical shot exit conditions are concerned the LR predictions indicate the puller design exits the barrel with smaller magnitudes for pitch, pitch rates, muzzle slope and velocity of muzzle slope. One way this can be explained is by the fact that the rear spring constant on the puller is softer than the rear bulkhead spring constant of the M829, thus the transverse loads induced at this location on the puller sabot should be less.

Completely different vibrational characteristics between the two different sabot designs are observed in this study. Though the shot exit conditions mentioned look promising for the puller concept, the puller sabot concept is significantly less stiff in the transverse direction which may allow excessive displacements. This flexing with larger displacements than the double ramp design in crooked tubes may therefore be a disadvantage. However, since modern tank gun tube straightness has been improving, this potential disadvantage may not be significant. Thus, if the puller sabot design can be shown to reduce in-bore weight, retain in-bore structural integrity and meet exterior ballistics criteria, then this design should to be studied seriously. Certainly, as far as modern materials (composites) are concerned the puller sabot design appears as a logical next step.

References

[1] T. Erline, M. Kregel, and M. Pantano, "Gun and Projectile Flexural Dynamics Modeled by the Little RASCAL - A User's Manual", Ballistic Research Laboratory, BRL-TR-3122, July 1990.

[2] J. Bornstein, T. Erline, B.T. Haug, and D. Hopkins, "Investigations On The Dynamics of Tank Guns", Proceedings of the 11Th International Symposium On Ballistics, Brussels, Belgium, May 1989.

[3] T. Erline and M. Kregel,"Modeling Gun Dynamics With Dominant Loads", BRL-MR-6383, JULY 1988.

[4] R. Becker, Alliant Techsystems, Inc. Private communication, September, 1992.

[5] R. Diel, A. Sippel, J. Meyer, H-J. Kruse, "Title: PROJECTILE ARRANGEMENT", U. S. Patent Number 5,063,855. All Inventors noted from the Federal Republic of Germany, Nov. 12,1991.

[6] W. Drysdale, BRL Private communication, January 1993.

[7]   D. Rabern, "Axially Accelerated Saboted Rods Subjected to Lateral Forces", Los Alamos National Laboratory Report LA-11494-MS, March 1989.

[8]   H.P. Gay and A.S. Elder, "The Lateral Motion of A Tank Gun and Its Effect On The Accuracy of Fire", Ballistics Research Laboratory Report No. 1070, March 1959.

[9]   M. Kregel and E. Lortie, "Description and Comparison of the "K" Method for Performing Numerical Integration of Stiff Ordinary Differential Equations", BRL Report No. 1733, July 1973.

[10]   M. Kregel and J. Heimerl, "Comments on the Solution Coupled Stiff Ordinary Differential Equations", BRL Report No. 2769, July 1977

[11]   T. Erline, "Projectile Spring Constants: Significance to Modeling with the Little RASCAL Gun Dynamics Program", BRL-TR-3224, April 1991.

[12]   D. Lyon, BRL Private communication, January 1992.

[13]   R. Dees, BRL Private communication, July 1986.

TITLE: RADIAL STIFFNESS MEASUREMENTS OF SEVERAL 120mm PROJECTILES

DAVID H. LYON
U.S. ARMY RESEARCH LABORATORY
WEAPONS TECHNOLOGY DIRECTORATE
ABERDEEN PROVING GROUND, MD 21005-5066

ABSTRACT:

An experimental technique for statically determining the radial stiffness of projectiles is presented. This technique utilizes a length of gun tube into which a modified projectile is fitted. In the case of APFSDS rounds, which contact the bore at two locations, a flat area is machined into the subprojectile at each of these locations. A corresponding clearance hole is drilled through the sabot and gun tube. When assembled, the holes align to allow a bar to apply loads directly onto the subprojectile. The resulting load versus deflection measurements, taken at the points of load application, allow the extraction of radial stiffness values. In addition, deflection measurements at various locations over the projectile length were recorded in order to observe the longitudinal bending response.

Accurate radial stiffness values are important parameters for in-bore gun dynamics models as the predictive capabilities of the codes are directly related to these numbers.

BIOGRAPHY

PRESENT ASSIGNMENT: Mr. Lyon is employed as a mechanical engineer for the Aerodynamics Branch, Propulsion and Flight Division of the Weapons Technology Directorate of ARL.

PAST EXPERIENCE: Mr. Lyon has previously served with the Launch and Flight Division of the the U.S. Army Ballistic Research Laboratory from 1983 to 1992. Mr. Lyon has been involved in the modeling and experimental verification of gun dynamics as they pertain to tank caliber systems for 8 years.

DEGREE: Mechanical Engineering, Drexel University.

RADIAL STIFFNESS MEASUREMENTS OF SEVERAL 120mm PROJECTILES

DAVID H. LYON
U.S. ARMY RESEARCH LABORATORY
WEAPONS TECHNOLOGY DIRECTORATE
ABERDEEN PROVING GROUND, MD 21005-5066

INTRODUCTION

Gun dynamics models attempt to simulate the in-bore behavior of projectile and gun/recoil components. The simpler models accomplish this by constructing the components from a series of beam elements. For modern APFSDS rounds, the simulated projectile is supported within the gun tube by means of two radial springs, one associated with the rear bulkhead contact point between the sabot and barrel, and the other with the front bourrelet contact point [1,2,3]. Stiffness values corresponding to these springs have been derived from finite element analysis [4] and limited static experiments [5]. However, values differing by as much as three orders of magnitude have been reported using these methods. In order to obtain accurate values, an important step towards improving the predictive capabilities of models, an experimental technique was devised and exercised on several 120mm projectiles; M829A1, M830E1 and M865.

NOTE: During the period between the initiation and publication of this work the M830E1 achieved type classification to become the M830A1.

Background

Several levels of modeling complexity can be employed in order to attempt a simulation of the in-bore behavior of projectiles. The most basic of which is the two-dimensional approach employed by RASCAL [6]. This allows modeling in only one plane at a time; therefore, no out-of-plane or coupling effects can be accounted for. If these effects prove to be significant, the accuracy of this approach will diminish. The next level of complexity incorporates axis-symmetric, three-dimensional beam elements, as incorporated into the SHOGUN [2] and BALANS [7] codes. This type of model includes coupling effects, allowing observation of both planes simultaneously.

Regardless of the type of beam element used, the projectile model is supported within the gun tube by linear springs, through which all forces between the projectile and tube are communicated. In the case of APFSDS rounds, two springs are utilized which simulate the rear bulkhead (or gas seal) and the front bourrelet, or bell. The design of the M830E1 is actually a hybrid between a saboted kinetic energy round and a full-bore HEAT round, with its discarding sabot and full-bore fins. This situation adds a third possible point of contact, that of the fins, and would require modification to the models in order to include this effect [8].

LYON

EXPERIMENTAL TECHNIQUE

In order to provide the data necessary to derive static radial spring constants at the proper locations, loads must be applied in the radial direction. Since the sabots of the rounds tested were divided into three segments, 120 degrees each, it was hypothesized that the orientation of the sabot may have an influence upon the stiffness values for the same projectile. Therefore, each projectile would be tested in two orientations, loaded parallel to a part line (0 degree), and rotated 60 degrees from that part line (60 degree).

Since the M830E1 utilizes grooves exclusively along the rod/sabot interface, this allowed the same subprojectile to be rotated to either the 0 or 60 degree configuration within one sabot. The sabot, in turn would have a hole at each orientation. Even though the M865 employs a V-thread along the entire length of engagement, the interface contains clearances which allow the subprojectile to rotate at least 60 degrees within the sabot, making both measurements again possible with a single projectile. However, since the M829A1 employs a fine friction thread over a portion of the rear sabot ramp, the rod is unable to freely rotate 60 degrees within the sabot. Therefore, two individual M829A1 projectiles were utilized, one for each orientation.

Experimental Methodology

In order to allow transverse loads to be applied to the penetrator while maintaining the projectile in constraints similar to those it would experience while traveling down the gun tube, various possibilities were considered. However, it was decided that using a rod to transfer the load directly to the subprojectile would be both physically feasible and mechanically correct. This would entail a clearance hole drilled through both the sabot and gun tube to provide a passage for the load bar as well as a flat area on the rod to accept the bottom of the rod and transfer the load without undesirable deflection at this interface. The location of these holes, with respect to the sabot, would also be important, since a direct comparison between sabots with different shapes would require some form of commonality.

The rationale concerning the selection of load points is described as follows. By loading the sabot/penetrator assemblage at indiscriminate locations, one could produce unwanted bending moments in addition to the desired transverse displacements, making separation of the two extremely difficult. Therefore, the load points must be positioned such that the load is transmitted through the structure while producing minimal bending moments.

The rear contact point on the M829A1 possesses a rather large bore footprint of 93mm, the majority of which, 81mm, is nylon obturator which can deform to allow contact between the sabot and the bore [9]. Therefore, the load bar at the rear contact point should be located such that it spans the forward edge of the full-bore portion of the sabot rearward into the obturator, as illustrated in Figure 1. At the front bell, the situation is somewhat different because the bell is angled and precludes loading in a similar manner. For this case a vertical line drawn tangent to the inner surface of the bell would serve as the forward edge of the load bar hole, also depicted in Figure 1. Although a load applied at this point will impart a moment, because it is not directly over the reaction point, it was felt this would not corrupt the results and could be accounted for if necessary. Further, applying a load directly over the front bell reaction point would induce longitudinal bending of the assemblage which would be included in the deflection measurement, an undesirable situation.

168
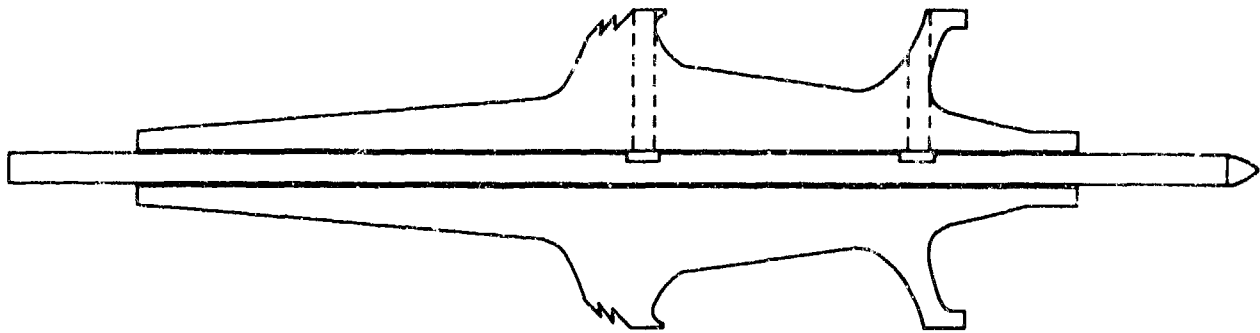
Figure 1. Section of Generic APFSDS Projectile, Showing Load Rod Locations.

Experimental Setup

First, each projectile was disassembled and appropriate load points established. The penetrators were then measured for machining of the flat areas and the fins were removed. Each set of sabots then had two load rod holes drilled at each of the two orientations. These again corresponded to the hole orientations relative to the sabot part lines. Next, the projectile was reassembled, obturator affixed, and rear sealed with JRTV in an attempt to simulate a production line condition. Finally, the obturator was lathe turned until it provided a light interference fit inside the tube.

The gun tube fixture consisted of a length of 120mm gun tube, the bottom of which was cross-drilled and threaded to accept two Linear Variable Displacement Transducers (LVDTs). Due to the length of the LVDTs, the gun tube was secured to a standoff plate for clearance. These devices were situated so that they would protrude up into the tube and rest in the saddle region of the sabots. Holes were also drilled through the top of the tube at corresponding load rod locations. Lastly, a third LVDT was threaded into the standoff plate in order to obtain deflection data approximately half way down the sabot rear ramp for M829A1. With the projectile properly aligned in the tube this entire assemblage was then situated on the base platen of a Baldwin hydraulic load frame. The load rod was inserted into the hole and alignment checked against the crosshead. Proper alignment was found to be critical in obtaining quality data. Next, dial indicators were arranged to measure the deflection at various points of interest along the subprojectile. These indicators were affixed to measure displacements with respect to the gun tube itself, rather than any part of the load frame, also found to be of critical importance. The details of this setup are shown in Figure 2.

Experimental Procedure

The maximum loads to be applied at each point were decided upon after considering RASCAL results for the DM13 APFSDS-T projectile. The peak loads transmitted through the front and rear contact points were 4,700 lb$_f$ and 6,500 lb$_f$ respectively. Although the current generation projectiles are somewhat more massive, loads in this range were felt to
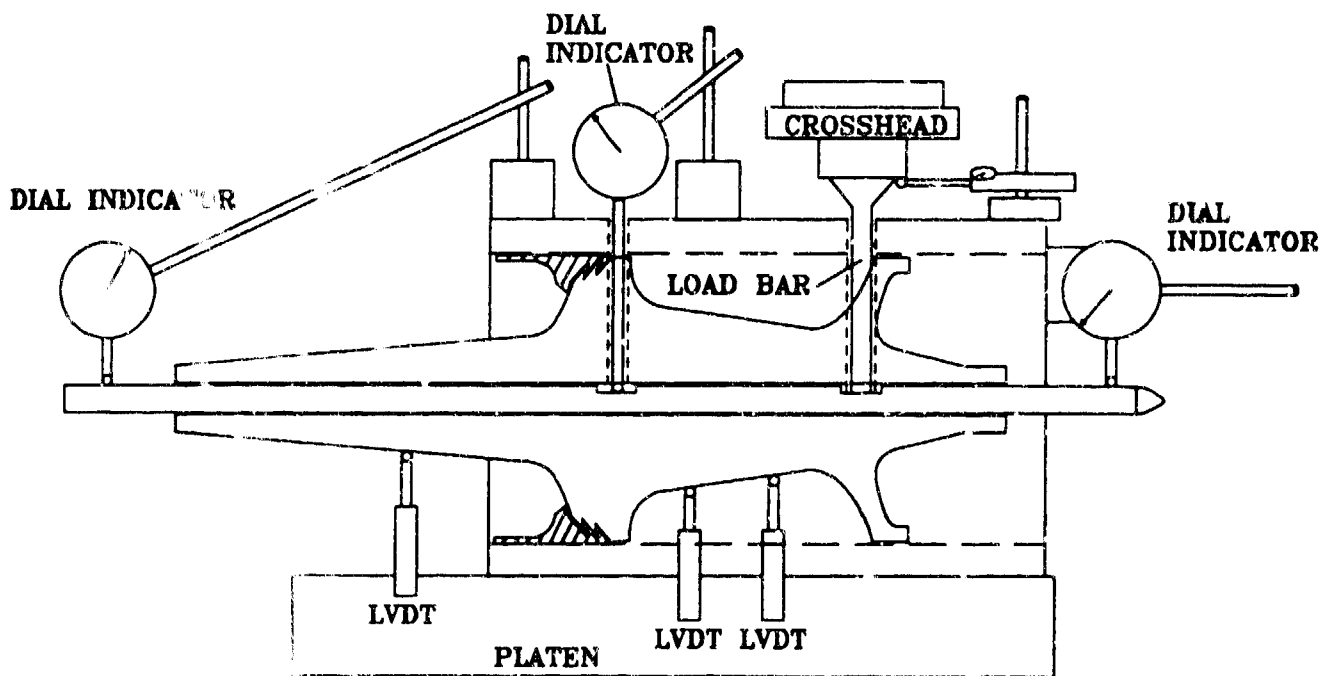
Figure **2.** Experimental Setup for Static Radial Stiffness Testing.

be l th   u. at and physically safe. Therefore, a maximum load of 5,500 lb/ for the front
bou. rele., .. 17,500 l for the rear bulkhead would be utilize 1.

Follow g inser on of the projectile into the tube and installation of all instrumentation,
the load roc was serted into the appropriate hole and its alignment checked against the
crosshead of he ad frame. Next, the setup was cycled to the maximum load and returned
to zero in an tte pt to further align all components and alleviate any clearances or initial
set. As this w repe ted several times it became clear that under very small loads, less than
50 lb/, the re p nses vere er atic and non repeatable. Therefore, it was decided that the load
profile would tart with a 50 lb/ pre-load and progress up to the maximum and then return
to 50 lb/ in 500 by in rement. in addition to the displacement data, clearances between
the tube and on bell as well a between the sabot petals themselves were measured in a.
attempt to sola any shifting or spreading that the petals may have undergone.

Lastly, since the deflection measureme t on the load rod would have to be taken near
the top, the c p ression of the rod itsel w uld be included in the measurement and would
have to be ren ed during data proce sing. Establishment of a spring constant for the load
bar itself was a mph hed utilizing linea Finite Element Analysis (FEA) software [10] and
comparing the ult w th the numerical calculation for an axially loaded rod [11]. The FEA
method produ d a value of 3.139 x 10⁶ lb/ n while the numerical calculation yielded 3.23.
x 10⁶ lb /in. Since the results provided by these two methods agreed within several percent,
and the EA took into count edge ffects at the measurement point, the FEA value was
selected In a dition, a l a frame exper ment was later conducted, providing even greater
confidence in these value. For this setup two identical load bars were stacked, end to end,
then axially compressed while the total deflection was measured. This technique served t

reduce the associated measurement error by increasing the deflections twofold. A spring constant of 3.191 x 10^6 lb$_f$/in was derived form this procedure.

EXPERIMENTAL RESULTS and DISCUSSION

APFSDS Projectiles

In order to validate the repeatability of the experimental technique, a minimum of four load cycles were recorded for each setup. The plots were then overlaid to disclose any variations. Figure 3, which contains the plots from four load cycles, serves as an illustratation. The only differences in response occurred during the first 1,000 lb$_f$ of load, and were most likely due to the take-up of clearances and shifting of components. These anomalies resulted in a bias of up to several thousandths of an inch. Otherwise, the composite plots revealed a very consistent response, even though the total deflections may have varied. This behavior provided adequate confidence in the repeatability of the experimental technique.
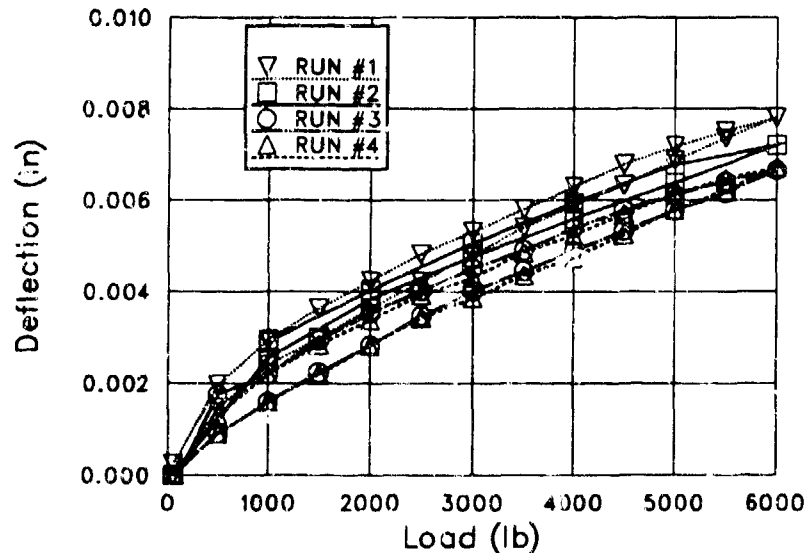
Figure 3. Results From Four Independent Load Cycles.

With the method established, it was then necessary to examine and compare the data more closely. Since the M829A1 and M865 are both APFSDS type rounds, with aluminum alloy (7075-T6511) sabots, they will be examined and compared first. Since the M830E1 is unique in design it therefore requires an alternate data analysis technique which will be discussed later.

While the M829A1 design has not changed noticeably since its type classification, the M865 projectile utilized for these measurements was manufactured according to the original sabot design, not the Product Improvement Program (PIP) design which decreased the distance between contact points, thickened the saddle region and changed the angle of the front bell. A photo of the subprojectile and sabot, with modifications completed, are shown in Figure 4. Also note that the obturator and forward band were fractured along one of the sabot part lines to facilitate disassembly. These components were then cemented after

reassembly in an attempt to introduce the original constraints.
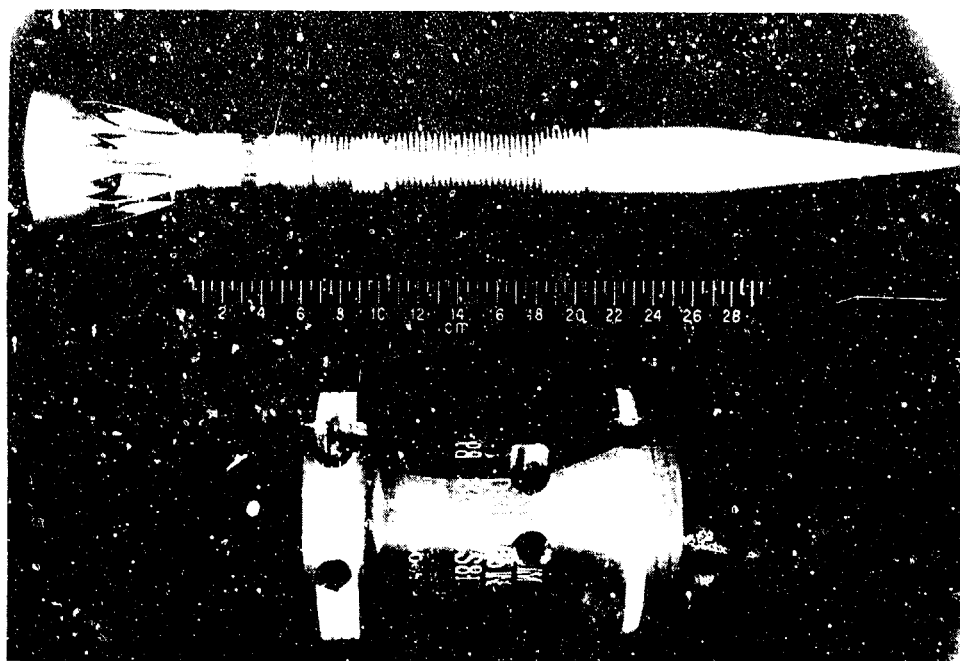
Figure 4. Modified M865 Subprojectile (top) and Sabot (bottom).

The responses due to front bell loading for the M829A1 and M865 are shown in Figure 5 with the 0 degree orientation in the top row and 60 degree below. This plot layout allows a direct comparison between projectile types, along the horizontal, as well as orientation, along the vertical. These particular plots were selected as being typical of that distinct configuration. In general, the plots are similar in shape and reveal a response that is non-linear over the lower load range, subsequently approaching a nearly linear behavior as the load increased beyond the 1,000 - 2,000 lb$_f$ region.

Furthermore, a very repeatable hysteresis differentiates the increasing load, or upload, response from the download response of the load profile. This effect was observed throughout all configurations of all projectiles as will be seen in later plots. Although slightly larger, in absolute terms, in some instances this hysteresis generally stayed within the .0003"-.0007" range. Several factors are believed to be possible contributors to this phenomena. First, the relatively soft obturator, compressing with time and load, may experience a recovery time lag and not return to its original shape within the elapsed time of the load cycle. Second, the friction between the petals and tube wall as well as between the petals themselves may introduce a hysteresis effect. Lastly, it was thought that the dial indicators may contain a certain amount of mechanical backlash, inherent to their internal gearing. However, after reviewing the LVDT data, a device which should exhibit zero backlash, a similar hysteresis was observed.

Comparing the plots along each row of Figure 5, the relative stiffness of each projectile can be observed by comparing the slopes of each linear region. This is possible because the stiffness is simply the inverse of the slope. Contrasting across both rows reveals that,

although the response shape is similar, both the magnitudes of total deflection and the slopes are quite different. Selecting the M829A1 as the baseline, the data indicate that the front bell of the M865 is considerably less stiff. This disparity is thought to be strongly geometry related, and was found to be consistent over both orientations.

Referring now to the columns of Figure 5, comparisons between the two orientations for the same projectile can be made. The M829A1 produced a larger total deflection in the 60 degree orientation, however, examination revealed that the majority of the difference occurred during the first 1,000 lb$_f$ of load and that the linear responses are quite similar. These differences are primarily attributed to initial spreading of the sabot petals and elimination of clearances. On the other hand, the M865 display almost identical behaviors over both orientations.

Turning now to Figure 6, which contains the same series of plots for the rear bulkhead data, a different set of results are depicted. First, these plots reveal greater differences due to orientation. The 0 degree configuration for M829A1 exhibits non-linear behavior out to the 2,000 - 3,000 lb$_f$ range, after which the response flattens out to follow a relatively shallow slope. The 60 degree orientation of the M829A1 displayed a more erratic response with increased hysteresis, especially in the medium load range. Smaller differences in slope tend to wash out any definitive transition from the non-linear to linear portions. Across the top row the M865 displayed less total deflection than the M829A1. However, a large portion of the M829A1 displacement occurred over the first 2,500 lb$_f$, indicative of clearances and sabot opening. Examining the bottom row shows almost the exact opposite, with the M865 experiencing greater deflection.

Results such as these warrant a closer examination of the details in order to offer possible explanations. First, the M865 employs a low-profile, plastic obturator which is injection molded in place. This is radically different from the thick, nylon obturator that is heated and pressed onto the M829A1. By nature, these systems possess different pre-stresses and exhibit unique constraining forces which oppose sabot petal spreading. Second, the M865 contains a thread along the sabot/subprojectile interface while the M829A1 uses a combination buttress groove and friction thread. Again, differences between the systems, such as tolerance stack-ups, can lead to differing behaviors. Lastly, the geometries of the two rear bulkheads are also different. The M865 uses a solid rear bulkhead with sabot material on both sides of the obturator, while the M829A1 relies upon a double saw-tooth taper, which reduces sabot contact to a small footprint just forward of the obturator. In conclusion, these distinctions most likely interact to produce a unique system response, which could explain the differences exposed in this series of rear bulkhead results.

M830E1 Projectile

The M830E1 projectile was designed to fulfill a multi-purpose function, to be used against ground targets as well as certain air threats. As stated previously, the configuration utilizes both a discarding sabot and full-bore fins. The sabot contacts the bore at two locations, the front bell and rear bulkhead, similar to an APFSDS round. However, since the thin-walled warhead body contains only explosive fill and a shaped charge liner, the entire assembly compresses appreciably when loaded in the radial direction. Therefore, a somewhat modified technique was employed to obtain the necessary data. The devised method entailed recording

data from two different setups and manipulating the results to produce the desired effect.

Because the explosive fill and shaped charge liner offer little to no radial stiffness, an empty warhead was utilized. This also alleviated many safety concerns. The projectile was prepared in a fashion similar to the previous rounds with two flat areas machined into the exterior of the warhead body and corresponding holes drilled through the sabot. The projectile was then assembled, fitted into the tube, and load cycled to obtain data. However, this arrangement compressed the entire warhead body as well as one half of the sabot. In order to isolate the compression of the warhead from that of the sabot, a second setup was used. The only modification to this setup was that a solid steel cylinder was inserted inside the warhead. The outer diameter of the disk formed a tight fit when situated within the warhead body, with clearances less than .0005". Then the load cycles were repeated to obtain data with essentially nc warhead compression. This lack of warhead compression was confirmed with differential dial indicator measurements. This setup therefore produced data for deflection of the sabot only. Utilizing linear spring theory, it is possible to deduce a spring constant for one half the projectile, the desired result. These calculations are included in the Appendix.

The plots in Figure 7 contain the front bell data for setups both with and without the steel disk. The hollow warhead results depict a graceful curve over the low loads, approaching a nearly linear response beginning in the 2,000 - 3,000 lb_f range. Focusing now on the solid warhead 0 degree configuration, the curve is actually of steeper slope initially, until the 2,000 lb_f load where it sharply turns to an almost horizontal line. This comparison blatantly depicts the effects of warhead compression. System clearances and sabot spreading account for initial deflections, however, after these are expended, the structure exhibits an extremely stiff response.

Studying the 60 degree results, a similar trend is revealed. Here the plots closely mimic one another until approximately the 2,000 lb_f load, beyond which divergence becomes prominent. However, the slope never diminished to that of the 0 degree plot. It is conjectured that some spreading of sabot petals continued throughout the load cycle for this orientation.

The rear bulkhead results are shown in Figure 8. Again the 0 degree plot exhibits a nearly linear behavior past the 2,000 lb_f load. Comparing this to the solid warhead plot beneath it, the difference in slopes, due to warhead compression, is once again obvious. Examining the last set of plots, those for 60 degrees, a similar reaction was observed. The 60 degree orientation displayed a greater total deflection then the 0 degree, both with and without the disk inside the warhead. The rationalization offered is that the spreading of sabots contributes a larger total deflection to the 60 degree than the 0 degree configurations. Notice, however, that a comparison of the plots for both solid warhead orientations indicates that the front bell exhibits greater stiffness than the rear bulkhead. Also, it is still unclear as to why the initial slope was greater for the solid warhead plot at 0 degrees, but this occurred for that one configuration only.

DATA ANALYSIS

Radial Spring Constants

Since the majority of gun dynamics codes allow only linear spring constants to com-

municate forces between the tube and projectile, it was necessary to describe the behavior illustrated by each configuration with a single slope, one for the front bell and one for the rear bulkhead. In order to arrive at this linear approximation, a Least Squares Fit (LSF) routine was applied over all the data points of each run. The resulting slopes for each configuration were then averaged and inverted to generate spring constants with the proper units, lb_f/in in this case. Utilizing this approach resulted in the values contained in Table 1. Although this reduction method provides first-order results, it includes data over the the entire load profile, combining all the effects that influence the response. While a LSF through the plots may produce an acceptable result for some configurations, others are clearly unable to accurately mimic the experimental behavior, as illustrated in Figure 9.

Table 1. Projectile Radial Spring Constants.

Projectile	Configuration			
	Front 0 Deg lb_f/in	Front 60 Deg lb_f/in	Rear 0 Deg lb_f/in	Rear 60 Deg lb_f/in
M829A1	.904 E+06	.610 E+06	1.45 E+06	1.56 E+06
M865	.373 E+06	.360 E+06	2.00 E+06	1.33 E+06
M830A1	.581 E+06	.438 E+06	1.39 E+06	1.21 E+06

Since several of the simulation codes are capable of utilizing spring constants which are constructed from a series of linear segments (BALANS) a somewhat more refined analysis is warranted. This improved method should attempt to allow the mechanical interactions, such as clearance elimination and sabot spreading, to be isolated from the compressive response of the structure itself. While it is somewhat impossible to experimentally isolate these effects, observation of the overall response can provide insight into contributing factors.

Another approach might be to eliminate the initial portion of data and fit the remaining section. However, this technique would yield a slope which was biased towards the higher load data, diluting the strongly non-linear effects associated with the lower load regions. And, since large forces are transmitted between the barrel and projectile for only a small portion of the in-bore travel (Erline 1991), this approach could significantly degrade code accuracy. However, by separating each response plot into two parts, the first of which contains the majority of non-linear behavior, and apply a LSF to each, it is possible to extract a spring constant composed of two linear segments, one from each region. Employing this method produced the results contained in Table 2. Since the dimensional clearances should have been eliminated in the lower load regions, the rightmost column of spring constants represent true sabot structural response and, therefore, should be used for comparisons between projectiles. Referring to the M829A1 as the baseline projectile, these numbers imply that the front bell of the M856 is considerably softer while the rear bulkheads are quite similar in stiffness in both directions. Regarding the derived results for the M830E1, these also show a front bell that is softer when compared to the M829A1, however, not as soft as the M865. Referring now to the rear bulkhead, the M830E1 is considerably lower in stiffness than either the M829A1 or M865.

Using this dual-slope approach to differentiate between the effects typical of the lower load region from those of the higher load data provided an analysis that was able to closely match the measured response over the entire load profile, again depicted in Figure 9.

Table 2. Dual Range Radial Spring Constants.

Projectile	Configuration	Load Range, lb$_f$	Dual Load Range Analysis		
			Spring Constant, lb$_f$/in	Load Range, lb$_f$	Spring Constant, lb$_f$/in
M829A1	Front 0 Deg	50 - 1103	.370 E+06	1103 - 6000	1.06 E+06
	Front 60 Deg	50 - 1118	.233 E+06	1118 - 5500	.860 E+06
	Rear 0 Deg	50 - 1597	.411 E+06	1597 - 7500	2.74 E+06
	Rear 60 Deg	50 - 2754	.887 E+06	2754 - 7500	2.30 E+06
M865	Front 0 Deg	50 - 1240	.204 E+06	1240 - 5500	.447 E+06
	Front 60 Deg	50 - 1888	.267 E+06	1888 - 5500	.425 E+06
	Rear 0 Deg	50 - 1966	.952 E+06	1966 - 7500	2.80 E+06
	Rear 60 Deg	50 - 2087	.513 E+06	2087 - 7500	2.32 E+06
M830E1	Front 0 Deg	50 - 1665	.267 E+06	1665 - 5500	.943 E+06
	Front 60 Deg	50 - 1777	.241 E+06	1777 - 5500	.684 E+06
	Rear 0 Deg	50 - 2215	.791 E+06	2215 - 7500	1.62 E+06
	Rear 60 Deg	50 - 1999	.583 E+06	1999 - 7500	1.80 E+06

Another quantity of importance, which is a contributing factor to the in-bore projectile response, is the ratio between front and rear spring constants, rather than their absolute values. Therefore, Table 3 was constructed which contains the spring constant ratios for each configuration. The spring constant values used to arrive at these ratios were extracted from the LSF of the higher load data previously discussed in Table 2.

Table 3. Projectile Radial Spring Constant Ratios.

Projectile	Orientation	Ratio (Rear/Front)
M829A1	(0 Degree)	2.58
M829A1	(60 Degree)	2.67
M865	(0 Degree)	6.26
M865	(60 Degree)	5.46
M830E1	(0 Degree)	1.72
M830E1	(60 Degree)	2.63

Sabot Separation Measurements

The clearance measurements between the front bell and tube wall indicated that after a load was applied, in either orientation, the front bell settled to the bottom of the tube where it remained, even after all load was removed. Furthermore, this clearance, which measured as much as .013" for several projectiles, remained nearly constant over the entire load profile.

The openings between sabot petals could only be measured in the forward bell area of the sabot, due to accessibility within the fixture. Opening measurements due to loading of the front bell varied with both the orientation and projectile type. Due to the tight fit of the forward retaining ring the M830E1 experienced no measureable opening between petals. The results are summarized in Table 4. Again, the table omits all rear loading configurations because gaps in the obturator region could not be measured.

Table 4. Clearances Between Sabot Petals due to Front Bell Loading.

Orientation	Load	Projectile Type		
		M829A1	M865	M830E1
0 Degree	Pre-Load	.001"	.0015"	NA
0 Degree	Max Load	.011"	.010"	NA
60 Degree	Pre-Load	.001"	.004"	NA
60 Degree	Max Load	.007"	.007"	NA

Projectile Axial Response

In addition to recording the deflections at the point of load application, the displacements at several other points along each projectile were measured. For both the M829 and M830E1 projectiles this included the nose, two sabot saddle points, the contact point were no load was being applied, a point along the rear sabot ramp and the tail end of the rod. For the M865 the rear ramp position was eliminated, due to the shorter sabot and subprojectile.

Displacements at the seven locations along the projectile were plotted at specific loads during the increasing portion of a load cycle. These results are portrayed to provide insight into the flexure over the entire projectile length and are illustrated in Figure 10. Examining the front bell of the M829A1 first, the response can be categorized as a rigid body rotation of the entire assemblage about the rear bulkhead in conjunction with a change in slope (bending) in the loaded region. Next, the M865 displays a pure rigid body rotation, pivoting about the obturator region. Note also the large magnitude of total deflections. Due to the relatively short and stiff subprojectile, this type of behavior was not surprising. In addition, the short wheelbase serves to magnify the total deflections. Finally, the sharp change in slope on the M830E1 is somewhat deceiving due to the fact that compression of the warhead is included, accounting for the majority of the deflection. Plots from the other orientations produced similar results and, for brevity, have not been included.

Referring now to Figure 11, the rear bulkhead plots reveal another set of projectile dependent shapes. The M829A1 responds almost as a simply supported beam subjected to a concentrated load near the mid-point, while the M865 portrays some bending through the saddle region. The M830E1 appears to display bending in the bulkhead area, however, warhead compression has again biased this observation.

SUMMARY and CONCLUSIONS

A unique measurement technique for extracting radial deflection versus load has been administered to three 120mm tank projectiles. The resulting data was then analysed using two methods. The first was a simple LSF of all data points for a particular load cycle. Results from this technique are applicable to the most rudimentary gun codes that allow only a single linear spring constant. The second method broke the response into two discreet segments, dependent upon the load, and performed a LSF on each segment. This dual-slope approach was able to fit the measured curves much more closely over the entire load cycle. Furthermore, an orientation sensitivity was shown to exist. This dependency was based upon the relation of the sabot part line to the load plane. Although only two orientations were measured for each projectile, presumably both the minimum and maximum, this relationship warrants

further investigated. Also, spreading of the sabot petals as well as longitudinal bending responses were recorded. The bending data revealed rigid body rotation in combination with various bending responses. The loads implied were not necessarily intended to simulate an inertial load of the type encountered in-bore, instead, they were simply utilized to elicit load versus deflection data at points of interest. In addition to absolute stiffness values, the ratios between contact points were presented as quantities of interest.

It is recommended that gun dynamics codes should allow input of at least a dual-slope spring constant in addition to a bore clearance dimension associated with the front bell in order to more accurately simulate the experimental data.

APPENDIX

In order to arrive at an equivalent spring rate for the M830E1, a two step experimental process was devised. This technique then utilized linear spring theory for multiple springs in a series arrangement.

The analysis began by rearranging the terms found in the definition for series springs [12] and isolating the spring constant associated with the entire warhead (K_{ew}). This value was then equated to the spring constant extracted form the experimental setup which compressed the hollow warhead.

$$K_{equiv} = \frac{(K_{ew})(K_{sabot})}{K_{ew} + K_{sabot}} \tag{1}$$

$$\frac{1}{K_{ew}} = \frac{(K_{equiv})(K_{sabot})}{K_{sabot} - K_{equiv}} \tag{2}$$

Next, the spring rate for one side of the sabot (K_{sabot}) was found during the second experimental setup which utilized the solid warhead. Substituting the appropriate variables allowed the calculation of the desired constant which is the effective stiffness for one half of the complete projectile (K_{eff}).

$$\frac{1}{K_{ew}} = \frac{1}{K_{\frac{1}{2}ew}} + \frac{1}{K_{\frac{1}{2}ew}} \tag{3}$$

$$\frac{1}{K_{eff}} = \frac{1}{K_{\frac{1}{2}ew}} + \frac{1}{K_{sabot}} \tag{4}$$
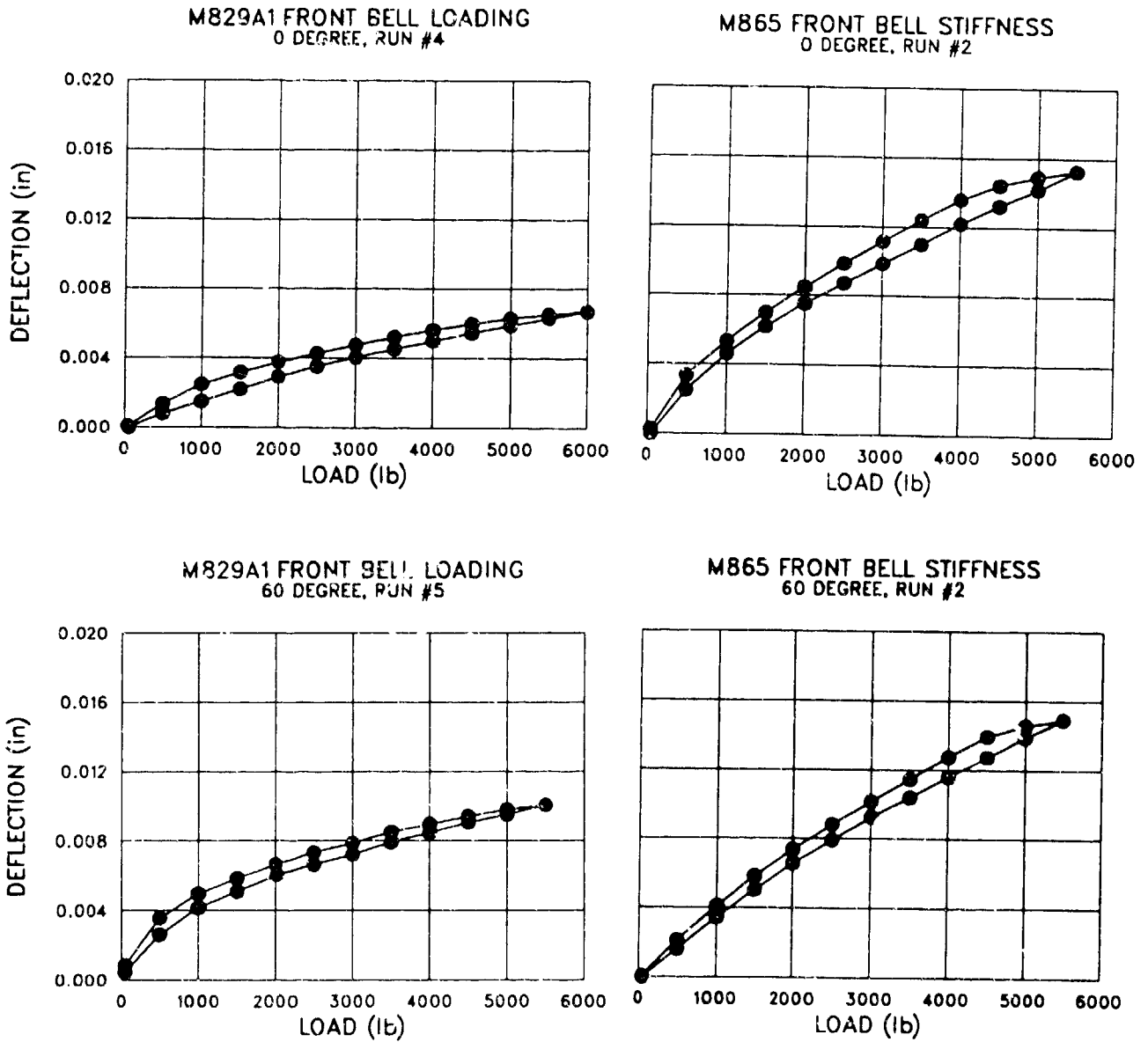
Figure 5. Deflection vs. Load Plots for M829A1 (left) and M865 (right) Due to Loading of the Front Bell.
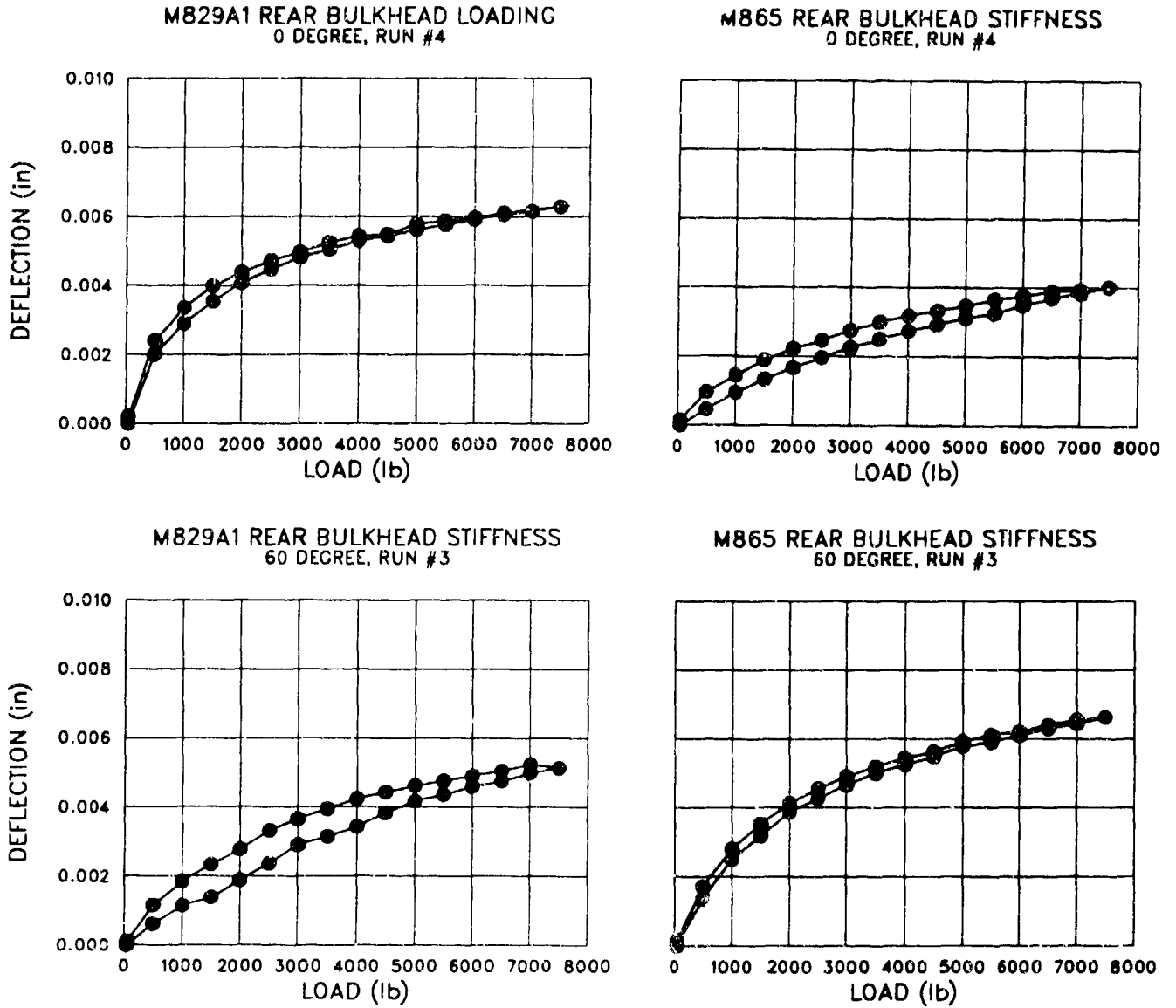
Figure 6. Deflection vs. Load Plots for M829A1 (left) and M865 (right) Due to Loading of the Rear Bulkhead.

M830A1 FRONT BELL STIFFNESS
0 DEGREE, DISK INSIDE WARHEAD, RUN #6

M830A1 FRONT BELL STIFFNESS
0 DEGREE, RUN #3

M830A1 FRONT BELL STIFFNESS
60 DEGREE, DISK INSIDE WARHEAD, RUN #6

M830A1 FRONT BELL STIFFNESS
60 DEGREE, RUN #3
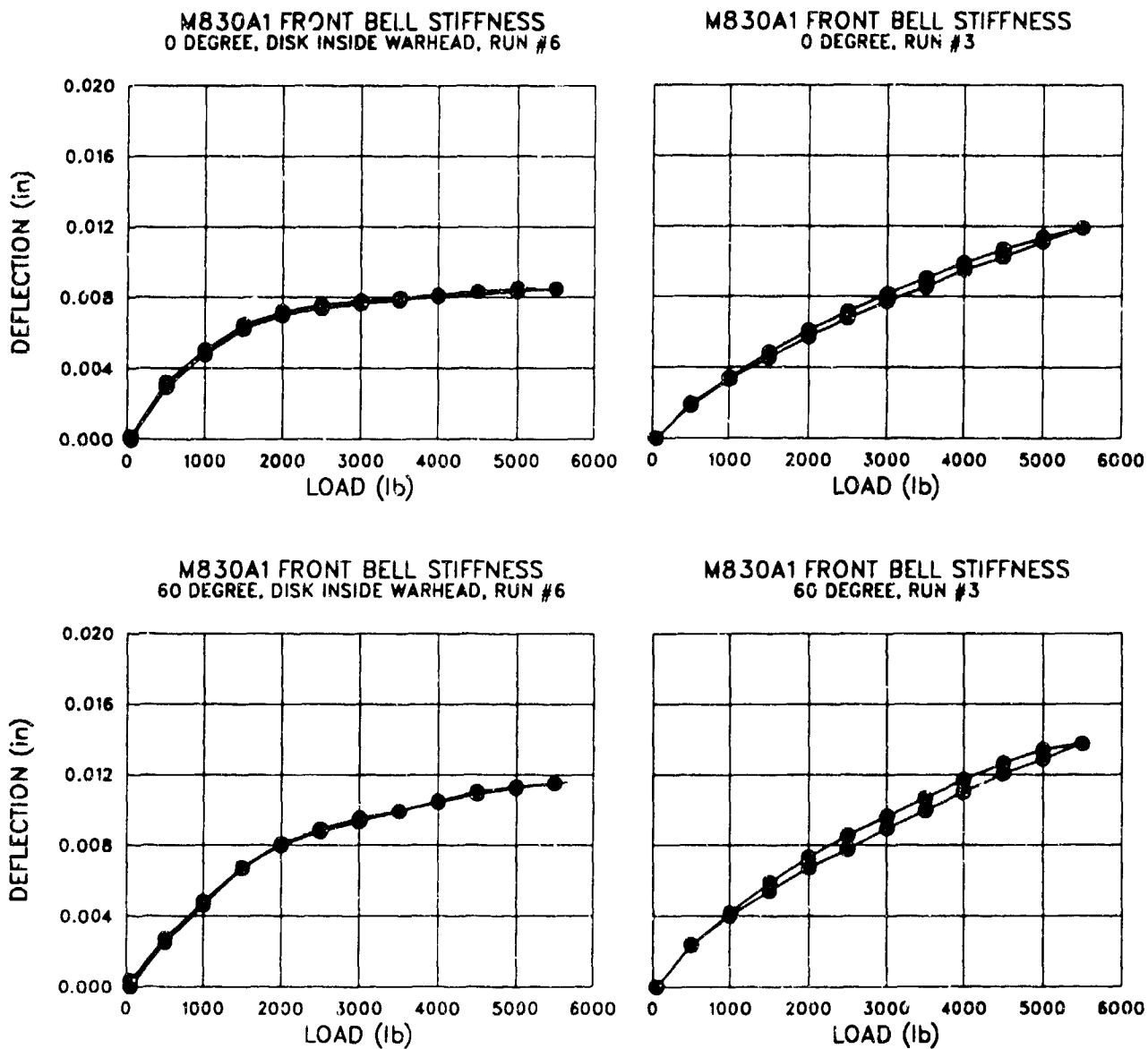
Figure 7. Deflection vs. Load Plots for M830E1 Due to Loading of the Front Bell.

M830A1 REAR BULKHEAD LOADING
0 DEGREE, RUN #4

M830A1 REAR BULKHEAD LOADING
60 DEGREE, RUN #4

M830A1 REAR BULKHEAD LOADING
0 DEGREE, DISK INSIDE WARHEAD, RUN #5

M830A1 REAR BULKHEAD LOADING
60 DEGREE, DISK INSIDE WARHEAD, RUN #6
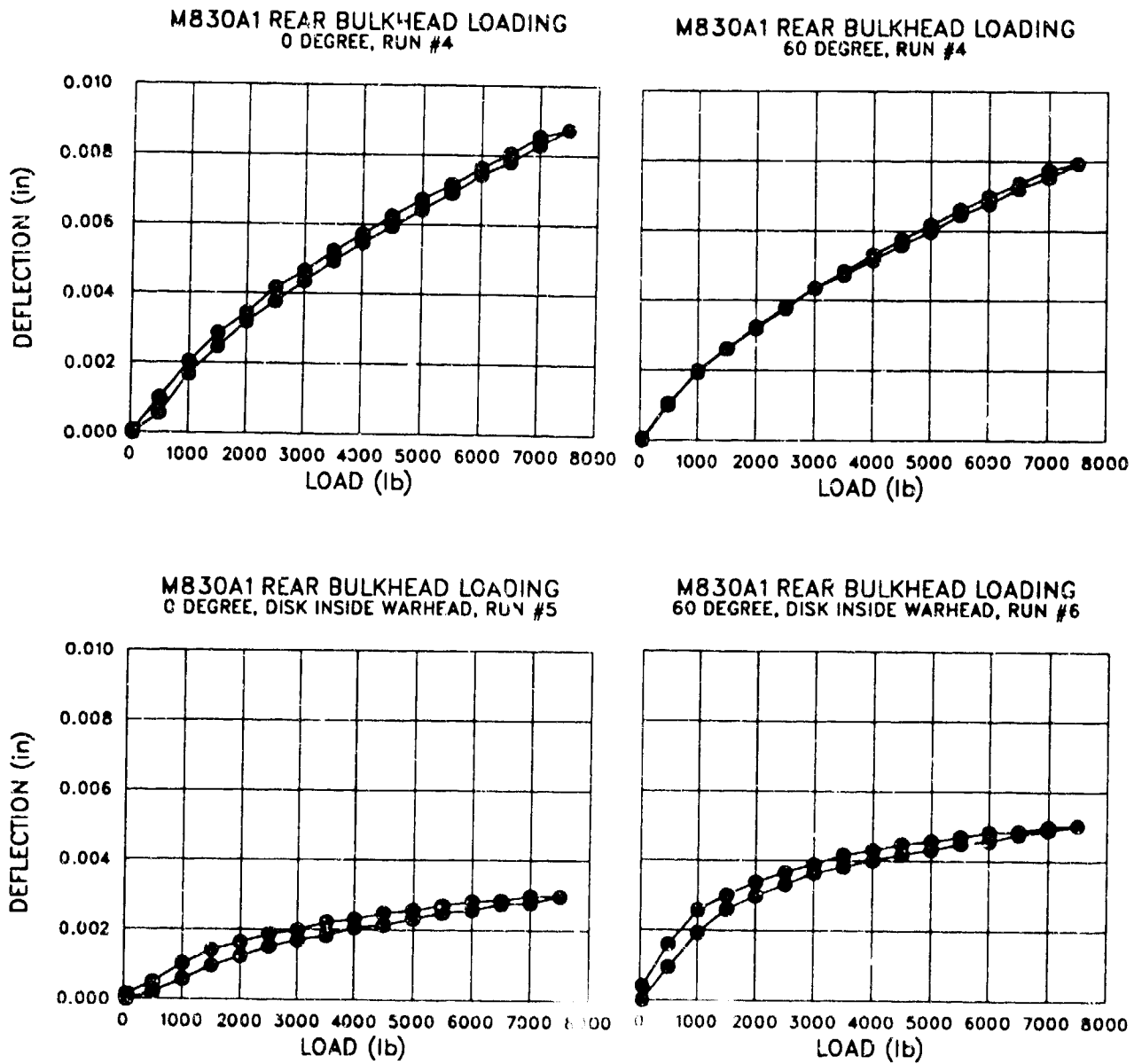
Figure 8. Deflection vs. Load Plots for M830E1 Due to Loading of the Rear Bulkhead.

M829A1 REAR BULKHEAD STIFFNESS
0 Degree, Run #4
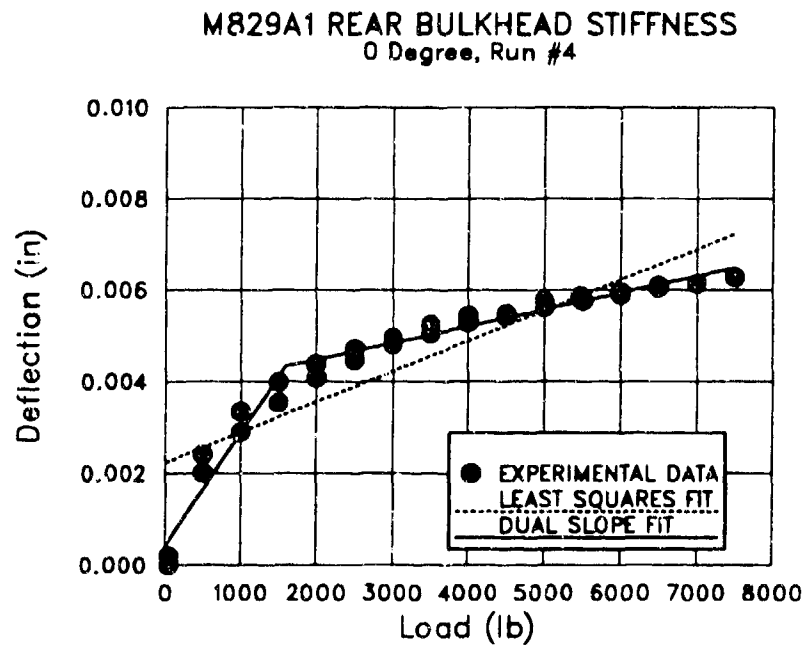
Figure 9. Deflection vs. Load Data with Fitting Techniques.

M829A1 FLEXURE, FRONT BELL LOADING
0 Degree, Run #3

M865 FLEXURE, FRONT BELL LOADING
0 Degree, Run #1

M830E1 FLEXURE, FRONT BELL LOADING
0 Degree, Hollow Warhead, Run #2
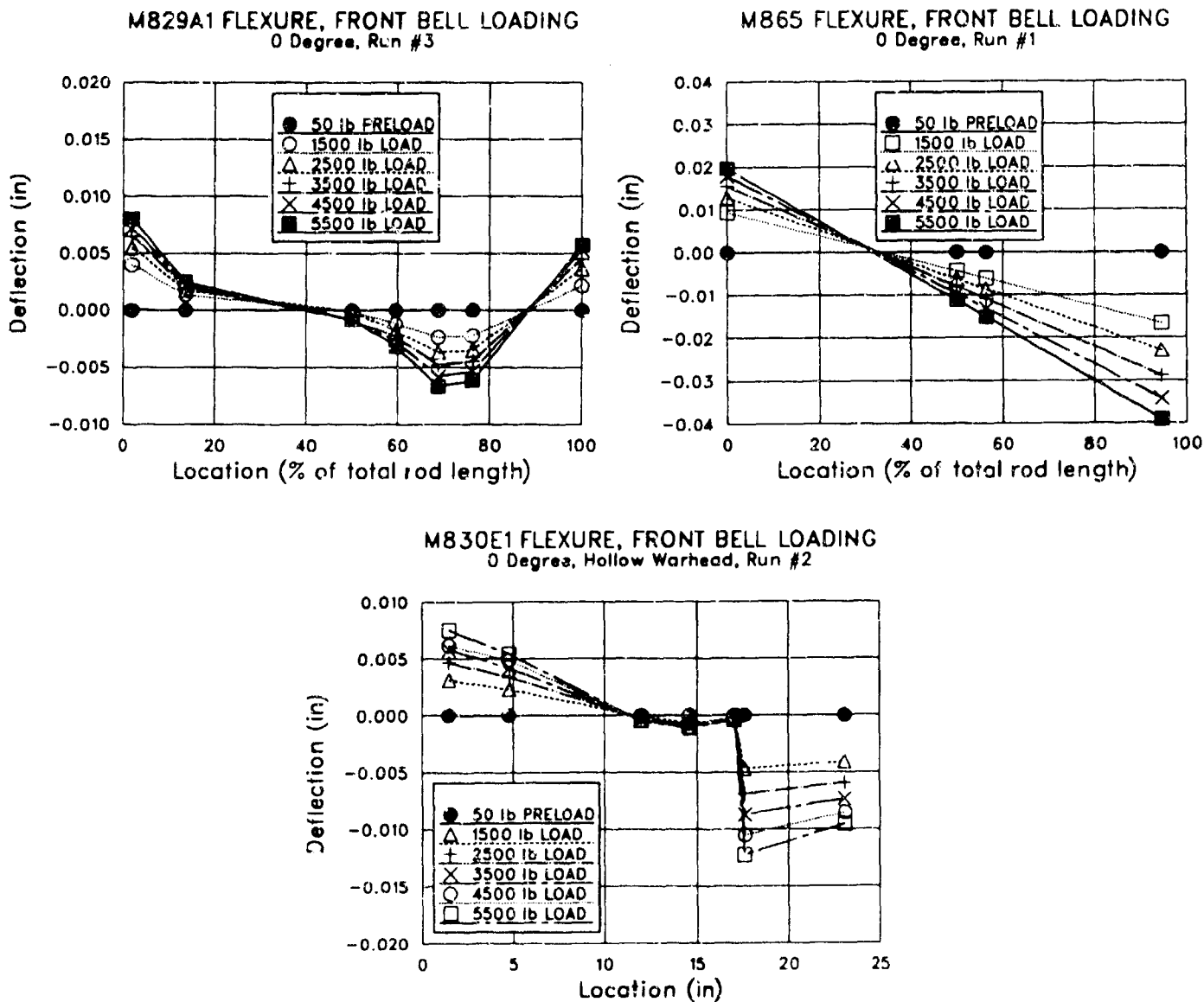
Figure 10. Projectile Flexure Due to Front Bell Loading for M829A1 (left), M865 (right) and M830E1 (bottom).
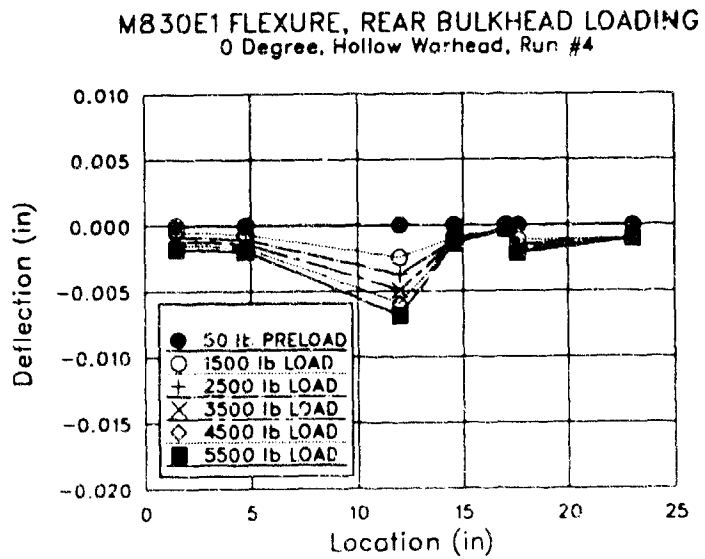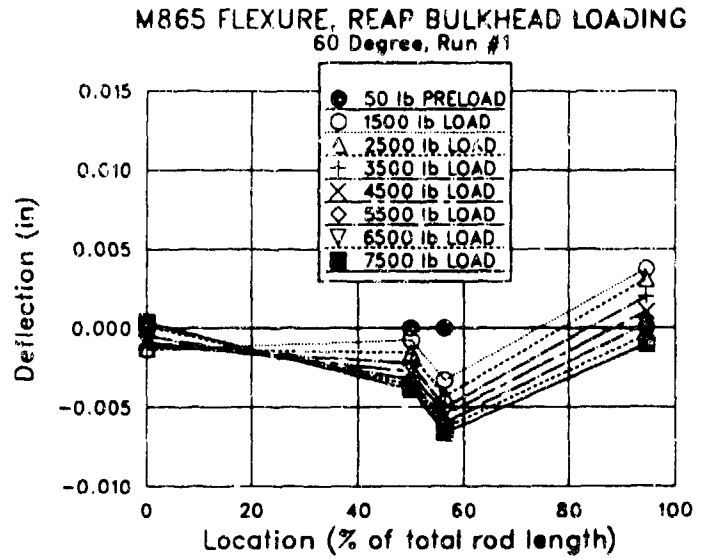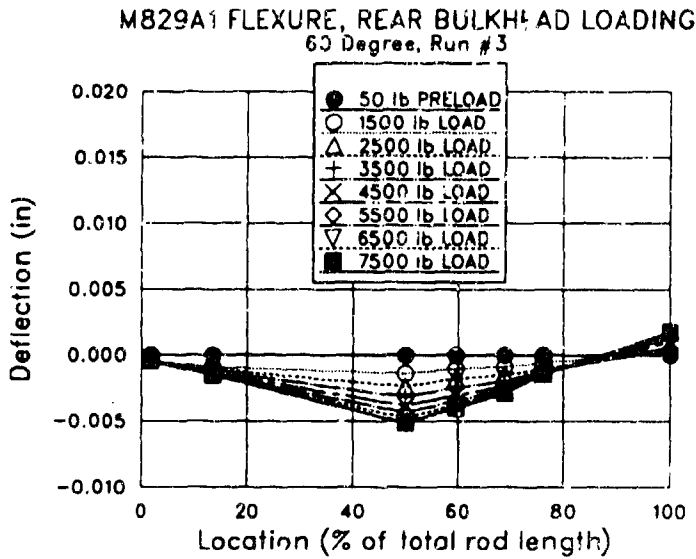
Figure 11. Projectile Flexure Due to Rear Bulkhead Loading for M829A1 (left), M865 (right) and M830E1 (bottom).

1. REFERENCES

[1] Erline, T. F., Kregel, M. D. and Pantano, M. "Gun and Projectile Flexural Dynamics Modeled by the Little Rascal -A User's Manual-." BRL Technical Report, BRL-TR-3122, U.S. Army Ballistic Research Laboratory, Aberdeen Proving Ground, MD, July 1990.

[2] Hopkins, D. A. "SHOGUN 3-D Gun Dynamics User's Manual." BRL Technical Report, BRL-TR-3128, U.S. Army Ballistic Research Laboratory, Aberdeen Proving Ground, MD, August 1990.

[3] Soifer, M. T. and Becker, R. S. "Projectile Motion in a Flexible Gun Tube." Contractor Report, BRL-CR-536, U.S. Army Ballistic Research Laboratory, Aberdeen Proving Ground, MD, October 1984.

[4] Stearns, B. K., Whyte, R. H. and Walton, W. "In Bore Structural Dynamic Behavior and Resultant Dispersion Characteristics of 105mm Projectile/Sabot Systems." Contract No. DAAK-78-M-3746, General Electric Company, Armament Systems Division, Burlington, VT, December 1978.

[5] Stearns, B. K. "105mm, M735 Projectile/Sabot Test Plan Outline." General Electric Company, Armament Systems Division, Burlington, VT, October 1979.

[6] Erline, T. F. and Kregel, M. D. "Modeling Gun Dynamics With Dominant Loads." BRL Memorandum Report, BRL-MR-3683, U.S. Army Ballistic Research Laboratory, Aberdeen Proving Grounds, MD, March 1988. AD B122387L

[7] Stearns, B. K., Maher, K. and Hathaway, W. "Projectile Balloting Dynamics: BALANS-90." Contract No. DAAD05-89-P-0401, Arrow Tech Associates, Burlington, VT, January 1990.

[8] Stearns, B. K. Telephone conversation with author. U.S. Army Ballistic Research Laboratory, Aberdeen Proving Ground, MD, May 1991.

[9] Drawing Number 12527402, "Projectile Sub Assembly, M829A1." U.S. Army Armament Research, Development and Engineering Center, Picatinny Arsenal, NJ, December 1986.

[10] Hollis, M. Conducted finite element analysis of load bar utilizing IDEAS software, Aberdeen Proving Ground, MD, September 1991.

[11] Popov, E. P. "Mechanics of Materials, Second Edition." Prentice-Hall Inc., Englewood Cliffs, NJ, 1976. pp. 37-41.

[12] Ogata, K. "System Dynamics." Prentice-Hall, Inc., Englewood Cliffs, NJ 1978. pp. 68-69.

BULMAN, HOYLE

TITLE

AN EXPERIMENTAL VALIDATION OF THE SIMBAD GUN DYNAMICS SIMULATION PACKAGE FOR FLEXIBLE SABOTED LONG ROD PROJECTILES

ABSTRACT

An experimental firing programme has been carried out using the RMCS 30mm Air Powered Gun to study the flexing of saboted long rod penetrators in-bore. A number of special two piece projectiles were developed, each with as nearly as possible the same mass, position of centre of gravity, pitch inertia, and band spacing, but with different rod diameters. A rigid one piece projectile was also developed, that had the same physical properties and band spacings.

A refined technique for measuring the in-bore motion of the shot was introduced into the experimental facility. This technique enabled the pitch and yaw motion of the front end of the rod to be measured, thus producing data that could be directly compared with theoretical simulations. The technique made use of an optical displacement transducer mounted perpendicular to and down range from the muzzle. A light beam from this transducer was directed on to a mirror on the front of the projectile via a circular mirror in the path of the shot. This latter mirror was formed by stretching a thin aluminised membrane over an annulus, through which the projectile passed without damage. The displacement of the returning light beam from the projectile was then measured by the transducer, from which shot pitch and yaw motions could be calculated.

Accurate measurement of the barrel profile was found to be necessary for the simulation work. This was achieved by pushing the rigid one piece shot slowly down the barrel, whilst measuring its pitch angle. The resulting data was then analysed to remove the gravity droop component, thus producing the barrel bend.

As the shots were required to be re-usable, a method of catching them in the indoor range without damage was required. A special catcher was therefore developed that consisted of a long horizontal tube filled with water, into which the projectile was fired, with no resulting damage.

The data obtained from the experimental work was used for the validation of the flexible saboted long rod projectile code as found in the gun dynamics simulation package SIMBAD. SIMBAD had been used in some earlier work to model the effects of cradle design on barrel motion, inclusion of this early work being necessary for the correct modelling of the system. The theoretical results obtained were then compared successfully with the experimental results.

This paper describes in more detail the work that has been carried out into the in-bore flexing of saboted long rod projectiles, as outlined above. It presents and compares results from both the experimental and theoretical work, discusses the findings, and gives conclusions.

AN EXPERIMENTAL VALIDATION OF THE SIMBAD GUN DYNAMICS SIMULATION PACKAGE FOR FLEXIBLE SABOTED LONG ROD PROJECTILES.

J.B. HOYLE & D.N. BULMAN
SCHOOL OF MECHANICAL, MATERIALS & CIVIL ENGINEERING
THE ROYAL MILITARY COLLEGE OF SCIENCE
SHRIVENHAM
SWINDON
WILTSHIRE

1.0 INTRODUCTION

Over the last few years, a considerable amount of work has been carried out world-wide in the area of tank gun dynamics. This work has generally included both theoretical simulation and experimental trials. The simulation work has been conducted in an attempt to gain a greater understanding of the dynamics involved, and to keep costs low. Mathematical simulation packages have been developed that can be used to model many of the parameters of these tank guns, and can include barrel dynamics, cradle dynamics, barrel to cradle interactions, shot in-bore dynamics and the interaction of the shot with the barrel [1,2,3,4,5]. The development of the very high L/D ratio long rod penetrators as used in modern APFSDS anti-armour rounds has required a further development of the shot models in order to correctly simulate the characteristics of these types of projectile.

Modern long rod penetrators generally consist of a rod with a high L/D ratio and are made of a high density material. They are usually supported in the barrel by a three piece sabot which separates from the penetrator on leaving the muzzle. The penetrator is supported axially by a screw thread along the part of its length in contact with the sabot, but the front of the penetrator can overhang the front of the sabot by a considerable fraction of its total length. When the penetrator is accelerated along the barrel, any bending of the penetrator due to transverse loads will be exacerbated by the tendency of the penetrator to buckle, and this will be most severe at the front overhang where it is transversely unrestrained by the sabot. The forces exerted on the penetrator by these bending and buckling loads can be very high, and have led in practise to penetrator and/or sabot failure.

The gun dynamics simulation package SIMBAD [6] has been developed in order to simulate the dynamics of modern tank guns. In particular, a recent version has included a facility for modelling the in-bore dynamics of saboted long rod penetrator APFSDS projectiles [7]. The model can utilize a flexible sabot with linear or non-linear stiffness rear bands and front cups, and a flexible penetrator. The screw thread type interface between the penetrator and sabot can be modelled, but other interface arrangements can also be included. The model places particular emphasis on the bending and buckling aspects of the penetrators' in-bore dynamics.

Validation of these simulation packages can often pose more problems than their initial development, as obtaining meaningful experimental data for comparison with their predictions is very difficult. These problems are even more severe where the in-bore dynamics of long rod projectiles are concerned. Deciding just what projectile parameter to measure is one concern, and any attempt to measure the projectiles' motion in a real gun using optical techniques poses difficulties due to obscuration by propellant gases. However, these problems can be largely overcome by using specially designed experimental guns as opposed to full sized guns. One such experimental gun is the RMCS 30mm Air Powered Gun [8], which has been used successfully to validate gun dynamic codes. This paper describes the use of the gun to assist in validating the flexible two piece shot model now incorporated in SIMBAD.

2.0   EXPERIMENTAL APPARATUS

A third generation development of the experimental RMCS Air Powered Gun has been used as the basis for studying the in-bore flexing dynamics of saboted long rod penetrators. The equipment used consists of a number of different sub-assemblies, which are described in more detail below.

2.1 THE AIR GUN.

The air gun used in the investigation consisted of a cylindrical pressure vessel with a quick release valve, which on firing, enabled rapid dumping of a compressed air charge to the 75 calibre smooth-bore barrel, thus propelling the projectile. The air gun was supported by a flexible cradle, and as it had been used in some earlier experimental work, the dynamic characteristics were known [9]. The transverse motions of the barrel and cradle were measured by inductive proximity transducers, and output data was captured and stored by computer.

FIGURE 1

189
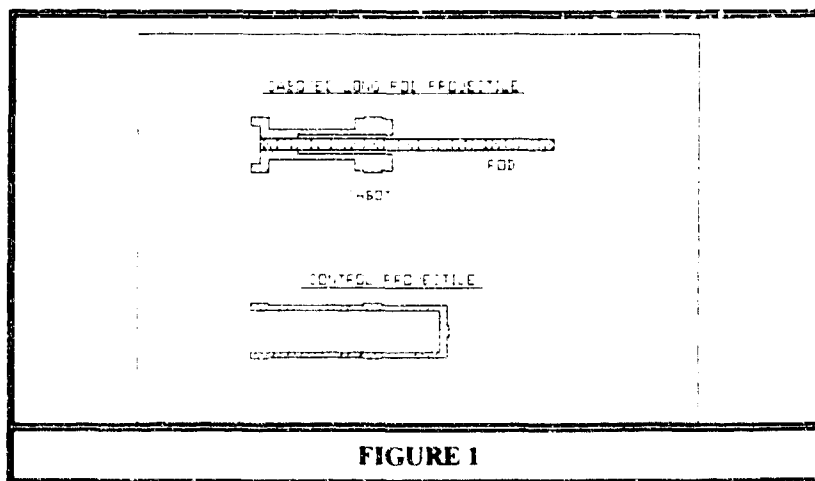
2.2 PROJECTILES.

As the investigation was carried out to study the in-bore dynamics of saboted long rod projectiles, the design of the experimental projectiles was particularly important. Each projectile had to incorporate a sufficiently long unsupported rod to enable a measurable amount of flexing to take place, while at the same time keeping overall projectile length to a minimum. A control projectile was also required for comparison with the saboted long rod projectiles. Both types of projectile were designed with the aid of SIMBAD, such that both had the same mass, position of centre of gravity, and pitch inertia. This meant that any differences in the measured pitch motion of the front of the projectile would be due to the different dynamics caused by bending of the rod. The different projectiles are discussed in more detail below.

2.2.1 Saboted long rod projectiles.

The saboted long rod projectile used in the investigation is shown as a cross section in Figure 1. The projectile consisted of a rigid sabot with two 10mm wide bands, front and rear, situated 60mm apart. Down the centre of the sabot was a 9mm diameter hole which extended to a point 20mm in front of the rear face of the sabot, the hole being continued at 8mm diameter. A 155mm long 8mm diameter rod was rigidly attached to the rear of the sabot, leaving 140mm unsupported. The front end of the long rod was polished to a mirror finish. A second saboted long rod projectile was also developed. This had a 6mm diameter rod of the same length as the 8mm rod, but as all the other dimensions of the projectile remained the same, it had a slightly reduced mass.

For practical reasons, both projectiles were designed with the aid of dynamic beam theory to enable the first natural frequency of the rod to be predicted. This would ensure that there would be a reasonable number of first mode beam vibrations (between 5 and 10) to be measured while the projectile was in the barrel. The first natural frequencies of the 8mm and 6mm rod projectiles were calculated to be 316 and 237 Hz respectively, giving about 9 and 6 oscillations while the projectile was in the barrel. These frequencies were subsequently measured to be 293 and 204 Hz respectively.

2.2.2 Control projectile.

The control projectile was designed for comparison with the saboted long rod projectiles. This projectile was made in one piece, and had a flexural stiffness many times greater than the flexible long rod, making it effectively a 'rigid' shot. The front end of this shot included a raised surface polished to a mirror finish. The control projectile was designed to have as nearly as possible the same mass, position of centre of gravity relative to the two bands, and pitch inertia as the saboted long rod projectiles. The control projectile is also shown in Figure 1.

2.3 MEASUREMENT OF IN-BORE PITCH MOTION AND BARREL PROFILE

For the measurement of projectile in-bore motion, a system based on an optical displacement transducer was developed [10]. This technique made use of a 'Zimmer' camera that produced and then measured the displacement of a collimated beam of light reflected off the mirror on the front of the projectile. Knowing the distance of the projectile from the camera, and the displacement of the reflected beam of light, the pitch angle of the front of the shot could be calculated. The distance travelled by the projectile down the barrel was derived from double integration of its acceleration curve, this being proportional to the measured pressure in the barrel.
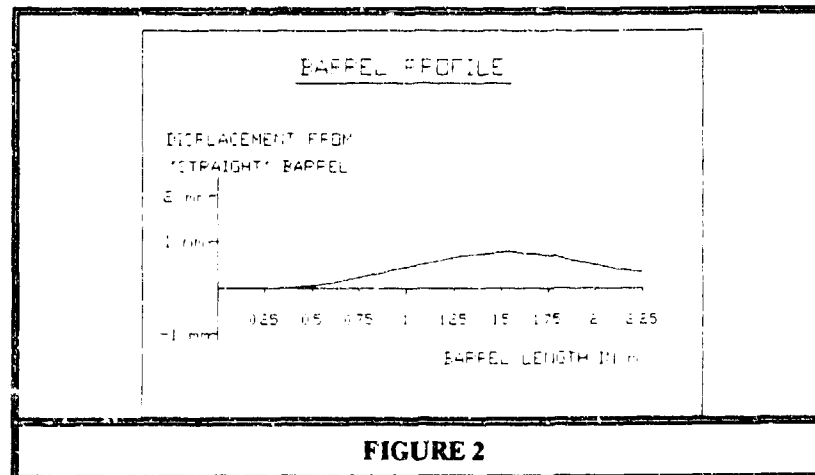
FIGURE 2

In order to avoid the projectile impacting the camera, the latter was situated down range of, and off-set perpendicular to, the muzzle. The collimated beam of light was then reflected down the barrel via a disposable mirror in the path of the projectile. This mirror was formed by stretching a thin film of aluminized plastic over an annulus, through which the projectile was fired, it being replaced after every firing.

The vertical barrel profile (shape) was measured in a similar fashion to the in-bore projectile motion using the Zimmer camera. Instead of firing the projectile, it was pushed down the barrel in increments of 3cm, the pitch displacement being recorded for each increment. Having obtained this data, it was analysed to give the barrel internal displacement at each increment relative to a "straight" (zero gravity droop and zero bend) barrel. Figure 2 shows the barrel profile.

2.4 PROJECTILE CATCHER

The projectiles needed to be captured after firing without damage in order that they might be reused. It was decided to develop a projectile catcher based on a cylindrical horizontal tube filled with water, into which the projectiles were fired. The catcher therefore consisted of a pipe, 3.5m long and 160mm bore. This was attached

to two drums, 0.6m diameter and 1.0m high, one at each end. This arrangement is shown in Figure 3 below. In operation, the water was retained in the pipe using a thin plastic membrane that was attached with a seal to the front end of the pipe. The rear drum and pipe were then filled with water to a level above the top of the pipe, making sure that all air was expelled from the pipe. The projectile was then fired through a hole in the front drum, through the membrane and into the pipe filled with water. The water in the pipe then flowed into the front drum and drained away. The projectile catcher as described was found to be very efficient at catching the projectiles without damage.
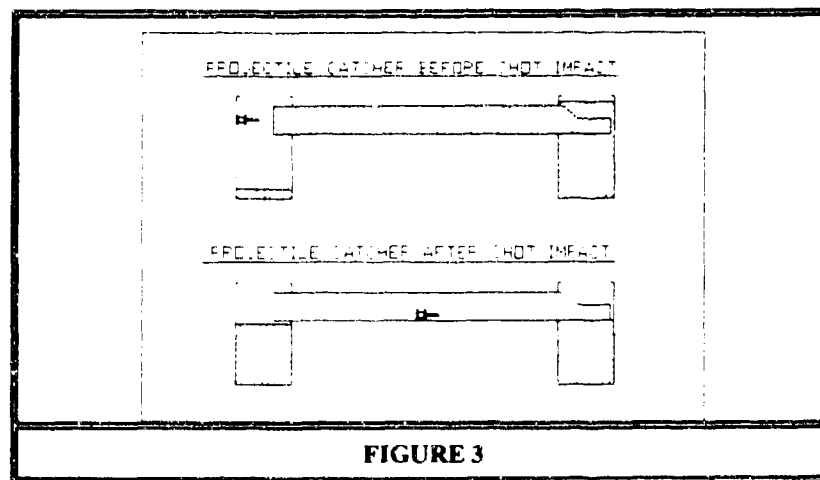
FIGURE 3

3.0   FIRING PROGRAMME AND EXPERIMENTAL RESULTS

A number of firings were made with each projectile in order to ensure consistency. Each of the projectiles weighed 230g, and were fired at a pressure of 2.67 MN/m.m (400 psi), giving a muzzle velocity of 150 m/s. Time to shot exit was 26 ms.

The experimental results are presented as graphs of shot pitch motion and muzzle motion. Figure 4 shows the pitch motion of the nose of the rod for the saboted 8mm diameter long rod projectile (dotted line), figure 5 shows the same motion for the nose of the saboted 6mm diameter long rod projectile (dotted line), and figure 6 shows the pitch motion for the rigid control projectile (dotted line).

Comparisson of the curves of muzzle motion for these three types of projectile show a high degree of similarity up to and including shot exit, hence one typical muzzle motion is shown in figure 7 (dotted line). This finding might be expected as only the projectile was varied between the different firings.

When the curves of projectile pitch motion are considered, there is a marked difference between the three firings. Figure 4 clearly shows the oscillatory type pitch motion of the front end of the 8mm diameter long rod

projectile (dotted line). This motion is due primarily to the flexing motion of the rod relative to the sabot, and has a frequency of about 285 Hz. This value compares very well with that predicted by the dynamic beam theory, of 316 Hz.

Note: The shot exit point shown for the experimental curves is slightly different to that of the same figure presented previously in Reference 7. It was realised that due to the length of the rod, shot exit was triggered while the sabot was still in-bore. The point of shot exit has therefore been altered by approximately one msec (time of flight over length of projectile) to take account of this fact.

Figure 5 shows the oscillatory type pitch motion of the front end of the 6mm diameter long rod projectile (dotted line). This motion is not as pronounced as that seen in figure 4, but close inspection reveals a frequency of about 220 Hz. This value is slightly lower than that predicted by the dynamic beam theory, of 237 Hz, but still compares favourably.

Figure 6 shows the pitch motion of the front end of the rigid shot (dotted line). As the shot is rigid, this motion can be assumed to represent the pitch motion of the whole projectile. The pitch motion is clearly quite smooth until after shot exit, the upward trend while the projectile is in the barrel being largely due to the projectile following the bend in the barrel.

4.0   THEORETICAL MODELLING AND RESULTS

4.1 THEORETICAL MODELLING

Two types of projectile were modelled in the simulation; a rigid projectile, and the two piece saboted long rod projectiles. These are discussed separately below.

4.1.1 RIGID (CONTROL) PROJECTILE

Rigid projectiles could be modelled as either 1; a lumped mass with linear or non-linear stiffness bands at front and rear, or 2; a very high stiffness flexible one piece projectile with similar front and rear bands. In this case the former was chosen, with linear stiffness bands front and rear.

4.1.2 FLEXIBLE SABOTED LONG ROD PROJECTILES

With this type of projectile, the sabot and penetrator were modelled separately. The sabot was modelled using Timoshenko elements, as shear was likely to be dominant mechanism by which deflection took place. The penetrator was modelled using Euler-Bernoulli beam elements, as bending was likely to be the dominant mechanism by which deflection took place.

As noted above, considerable emphasis was placed on the bending and buckling aspects of the saboted long rod projectiles. Simple finite element analysis would not normally consider the phenomenon of buckling in such a model, especially if the interaction between the axial forces (or accelerations) and the transverse deflections (bending) was small. However, with long rod penetrators that are partially unsupported transversely and which are subjected to very high levels of axial acceleration, this is not the case. In order to overcome this problem, the stiffness matrices of the penetrator and sabot were reformed a number of times during the simulation to take account of the change in position of the penetrator and sabot elements. Theoretically, the stiffness matrices need to be reformed after every time step in the simulation in accordance with each new position, but in practise, reforming the stiffness matrices 200 times during the simulation was sufficient to produce convergence of the solution.

The interaction between the sabot and the penetrator was made up of two components; axial and transverse. Both types of interaction could be linear or non-linear. In this case, the interface was modelled as a screw thread with an assumed square cross-section, with linear axial and radial stiffnesses [7].

4.2 THEORETICAL RESULTS

The theoretical results are presented as the pitch motion of the front end of the projectile against time. Figure 4 shows the oscillatory type motion for the 8mm diameter long rod projectile (solid line). Close inspection of this curve shows a frequency of about 260 Hz, which is lower than that seen experimentally.

Figure 5 shows the same type of motion for the 6mm diameter long rod projectile (solid line). Again, the frequency of vibration is lower than that seen experimentally, as it has a frequency of about 180 Hz.

Figure 6 shows the pitch motion of the rigid shot (solid line). It has a rather high pitch frequency of low amplitude that follows a general trend upwards.

Figure 7 shows the predicted motion of the muzzle (solid line).

5.0   DISCUSSION OF RESULTS

A comparison of the theoretical and experimental results both show essentially the same differences in in-bore pitch motion between the rigid projectiles and the saboted long rod projectiles. With the rigid projectiles, there is no significant pitch motion at low frequencies until shot exit, and the high frequency component for this projectile predicted by the simulation is of low amplitude. The pitch motion of the projectile is seen to follow a general trend upwards and is due primarily to the shot following the curve in the barrel. After shot exit, the experimental results show some pitch motion as the unstabilised projectile begins to tumble.

Both the theoretical and experimental results show a marked difference in the pitch motion of the saboted long rod projectiles as compared to the rigid projectiles. As noted above, this pitch motion is a measure of the flexing of the rod of the projectile, and clearly demonstrates that the rod does in fact flex while the projectile is in-bore.

The frequency of the flexing rod in-bore varies with its diameter, but not quite as one would expect. For the 8mm diameter rod projectile, the experimental flexing frequency in-bore is slightly lower than that predicted by the dynamic beam theory used in its design, 285 and 316 Hz respectively, but compares favourably. However, the flexing frequency predicted in the simulation is slightly lower at around 260 Hz. This is because the experimental projectile had the rod attached rigidly to the sabot, whereas the simulation projectile used a screw thread interface, thus effectively making the rod longer and less stiff.

For the 6mm diameter rod, a similar situation applied. The experimentally measured flexing frequency in-bore was about 220 Hz which is slightly lower than that predicted in the design of the shot, 237 Hz. Again, the frequency predicted by the simulation, 180 Hz, was lower than the measured frequency, for the same reasons as the 8mm diameter rod. The amplitude of vibration for the experimental curve is less than that of the theoretical curve due to incorrect damping values in the simulation.

The muzzle motion predicted by the simulation compares favourably with the experimental muzzle motion, both as to shape and amplitude.

Although not shown here, more simulations were carried out with slight changes to the barrel straightness data. This produced noticeable changes in the in-bore motion of both the rigid and saboted long rod projectiles, and could easily account for the discrepancies between the measured and predicted in-bore pitch motions.

6.0   CONCLUSIONS

1. Experimental long rod projectiles have been used successfully in the RMCS 30mm Air Powered Gun to study the in-bore flexing dynamics of saboted long rod projectiles.

2. The dominant frequencies in-bore were slightly lower than the first natural frequency of the rod as calculated using dynamic beam theory, and also measured by experiment.

3. The theoretical results agreed with the experimental results, but accurate data concerning the barrel profile needs to be used for the correct simulation of the in-bore dynamics.

7.0 REFERENCES

1. T.F. Erline, M.D. Kregel. Modelling Gun Dynamics with Dominant Loads. 5th US Army Symposium on Gun Dynamics, Rensselaerville, NY. 23-25 September 1987.

2. M.T. Soifer, R.S. Becker. DYNACODE-G/P and its application to the 120mm Tank Gun. 5th US Army Symposium on Gun Dynamics, Rensselaerville, NY. 23-25 September 1987.

3. D.N. Bulman. A comparison of theoretical jump for rifled and non-rifled barrels. 5th US Army Symposium on Gun Dynamics, Rensselaerville, NY. 23-25 September 1987.

4. S.E. Powell, P.G. Penny. The Theoretical Modelling of the Dynamics of Initially Non-straight Barrels using Finite Difference Techniques. 5th US Army Symposium on Gun Dynamics, Rensselaerville, NY. 23-25 September 1987.

5. D.A. Hopkins. Modelling Gun Dynamics with Three-Dimensional Beam Elements. 6th US Army Symposium on Gun Dynamics, Tamiment, Pennsylvania, 14-17 May 1990.

6. SIMBAD User Manual, Danby Engineering, Cirencester, UK.

7. D.N. Bulman. The In-bore Bending Dynamics of Long Rod Projectiles. 13th International Symposium on Ballistics, Stockholm, Sweden, 1-3 June, 1992

8. J.B. Hoyle. An Experimental Facility for the Study of Shot, Barrel and Cradle Dynamics. 6th US Army Symposium on Gun Dynamics, Tamiment, Pennsylvania, 14-17 May 1990.

9. D.N. Bulman, J.B. Hoyle. A Comparison of Theoretical and Experimental Results with Regard to the Effects of Gun Cradle Design on Barrel and Shot Motion. 6th US Army Symposium on Gun Dynamics, Tamiment, Pennsylvania, 14-17 May 1990.

10. G. Barker. An Experimental Investigation into In-bore Yaw in a Rifled Barrel using the RMCS Air Powered Gun. 5th US Army Symposium on Gun Dynamics, Rensselaerville, NY. 23-25 September 1987.

Maximum horizontal scale = 40msecs.
Maximum vertical scale = 0.5mrads.
Solid line shows theoretical result.
Dotted line shows experimental result.
Vertical line is shot exit.
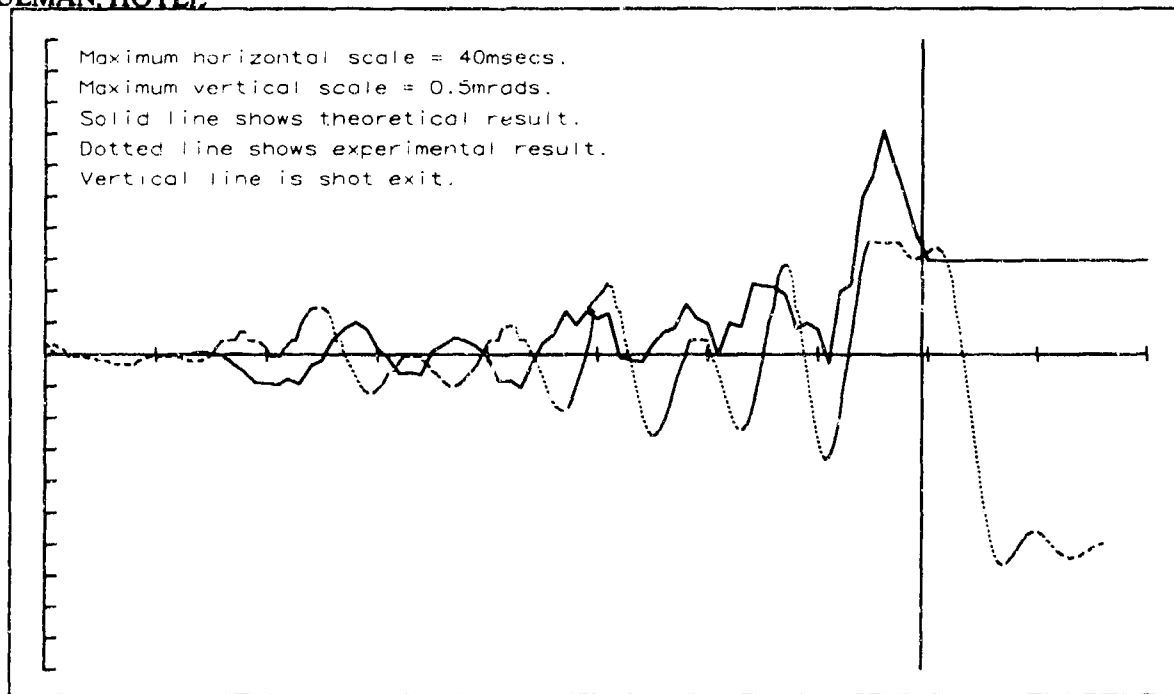
Fig 4.   Comparison of Theoretical and Experimental Results.
Pitch angle of the nose of the 8mm flexible rod.

Maximum horizontal scale = 40msecs.
Maximum vertical scale = 0.5mrads.
Solid line shows theoretical result.
Dotted line shows experimental result.
Vertical line is shot exit.
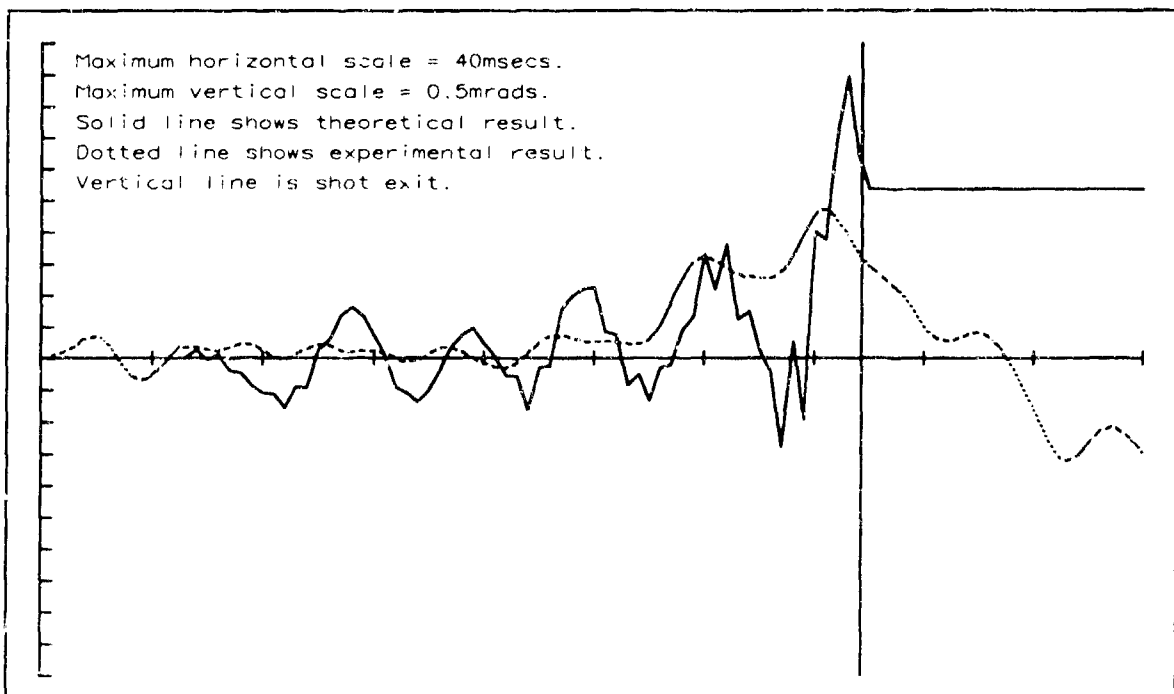
Fig 5.   Comparison of Theoretical and Experimental Results.
Pitch angle of the nose of the 6mm flexible rod.

```
Maximum horizontal scale = 40msecs.
Maximum vertical scale = 0.5mrads.
Solid line shows theoretical result.
Dotted line shows experimental result.
Vertical dashed line is shot exit.
```
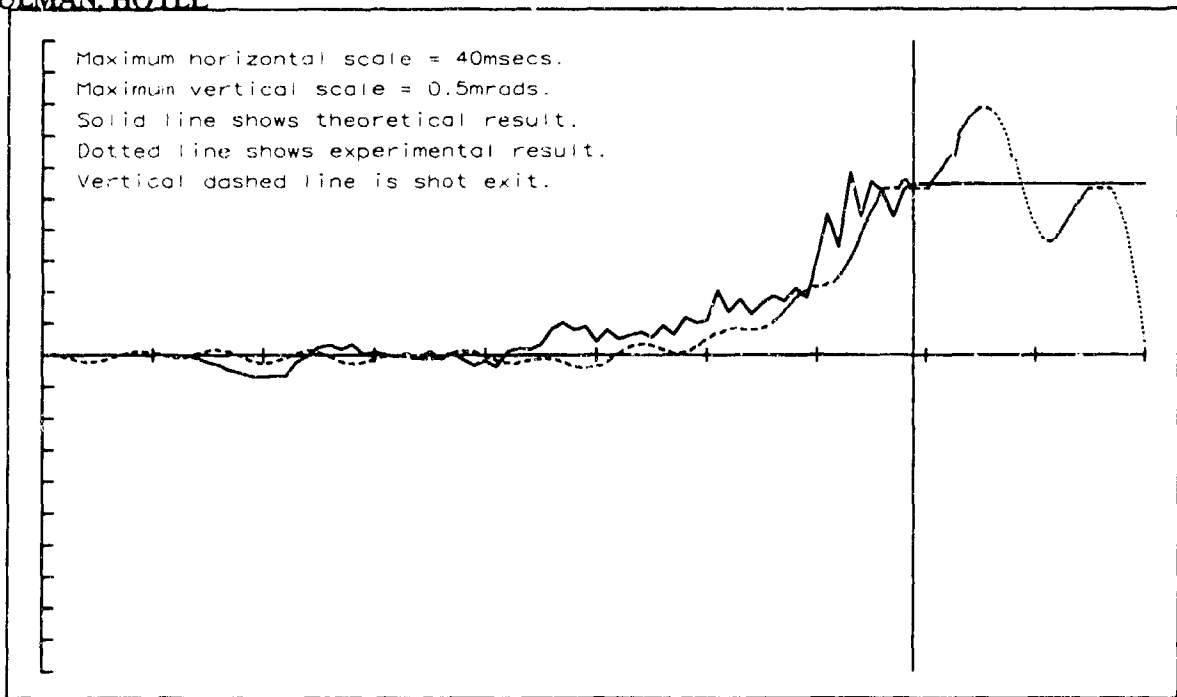
Fig 5.   Comparison of Theoretical and Experimental Results.
Pitch angle of the rigid shot.


```
Maximum horizontal scale = 40msecs.
Maximum vertical scale =  .5mm.
Solid line shows theoretical result.
Dotted line shows experimental result.
Vertical line is shot exit.
```
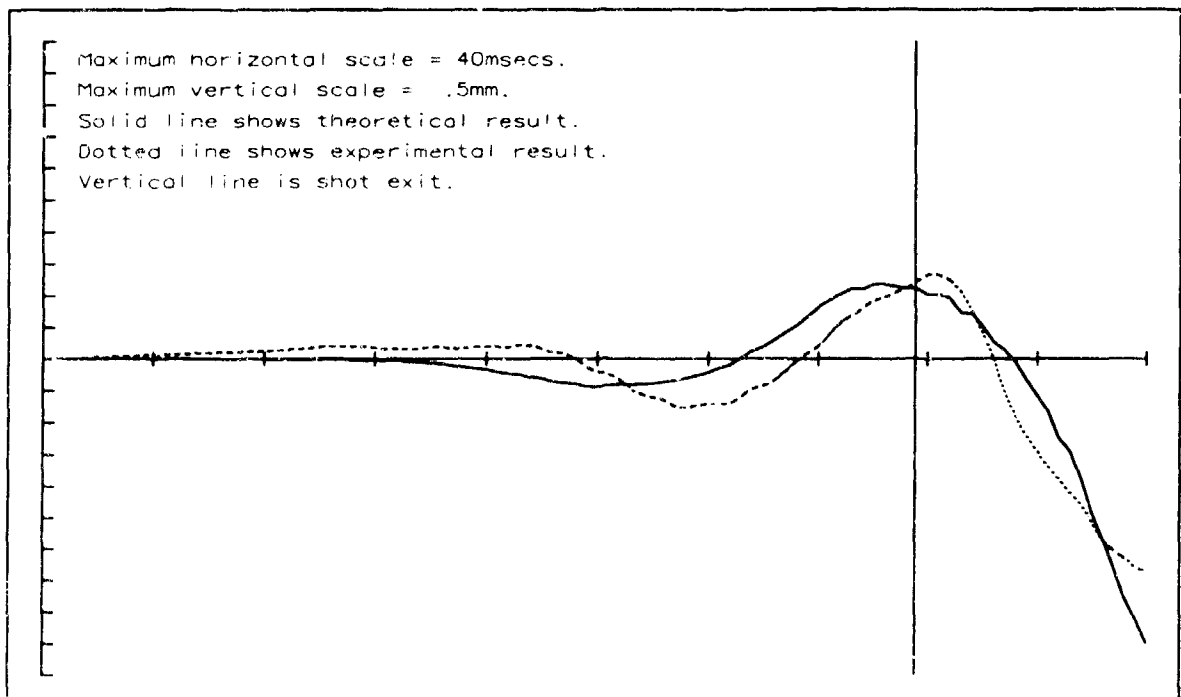
Fig 7.   Comparison of Theoretical and Experimental Results.
Vertical displacement of the muzzle

TRAJECTORY PATTERN METHOD APPLIED TO A TURRETED WEAPON SYSTEM

J. Rastegar, Department of Mechanical Engineering
State University of New York at Stony Brook, Stony Brook, New York 11794

Q. Tu, Department of Engineering, University of Redlands, Redlands, California 92373

F. Khorrami, School of Electrical Engineering and Computer Science
Polytechnic University, Brooklyn, New York 11201

M. Mattice and N. Coleman, U.S. Army Armament Research, Development,
and Engineering Center (ARDEC) Dover, New Jersey 07806-5000

ABSTRACT

The U.S. Army has built a test fixture called ATB1000 which emulates the types of nonlinearities and flexibilities found on most lightweight turreted weapon systems [2]. In this study, the Trajectory Pattern Method [1-5] is used to synthesize motion trajectories and generate inverse dynamics model based feedforward actuating signals for the test fixture. The main contribution of the present study is the derivation of the inverse dynamics model of the system in parametric form and synthesizing trajectories for point to point motions such that the resulting actuating torques do not contain the harmonic with frequency of the dominant first natural mode of vibration of the flexible beam representing the cannon. With this trajectory pattern, point to point motions with minimal residual vibration can be accomplished with zero end point jerk. A feedforward controller together with a PD feedback loop is constructed and implemented. Computer simulations of the open-loop response of the system are performed and the effectiveness of the approach is verified experimentally. The extension of this approach to vibration suppression problem is discussed.

Jahangir Rastegar received his BS from Southern Methodist University in 1970 and his MS and Ph.D. from Stanford University in 1972 and 1977, respectively. He is currently Associate Professor of Mechanical Engineering at State University of New York at Stony Brook. His research interests are in the areas of kinematics, dynamics and control of mechanical systems.

Qing Tu received her BS from East China Institute of Technology in 1982 and her MS and Ph.D. in Mechanical Engineering from State University of New York at Stony Brook in 1989 and 1992, respectively. She is currently Assistant Professor in the Engineering Department at University of Redlands. Her research interests are in the areas of kinematics, dynamics and control of high speed and high performance machinery.

Farshad Khorrami received his BS and Ph.D. in Electrical Engineering in 1984 and 1988, and BS and MS in Mathematics in 1982 and 1984, respectively, from Ohio State University. He is currently Assistant Professor of Electrical Engineering at Polytechnic University. His research interests are in the areas of robotics and automation, control of electro-mechanical systems, smart and flexible structures, and control theory and its implementation on nonlinear dynamics systems.

Michael S. Mattice received his BS from Michigan Technological University in 1985 and MS in Electrical Engineering from Polytechnic University in 1988. He is working on his Ph.D. in Mechanical Engineering at State University of New York at Stony Brook. He is currently an electronics engineer at the US Army Armament Research, Development and Engineering Center (ARDEC), Dover N.J. His interests include the application of advanced control theory to high performance motion control systems.

Norman P. Coleman is currently chief of the Automation and Robotics group of the Fire Support Laboratory, US Army Armament Research, Development and Engineering Center (ARDEC), Dover N.J. He received his BA degree in mathematics from the University of Virginia in 1965 (highest distinction) and the MA and Ph.D. in Mathematics from Vanderbilt University in 1967 and 1969, respectively. He is responsible for directing advanced research projects in the areas of digital weapon pointing and stabilization, adaptive control, sensor based robotics.

TRAJECTORY PATTERN METHOD APPLIED TO A TURRETED WEAPON SYSTEM

J. Rastegar, Department of Mechanical Engineering, State University of New York at Stony Brook
Stony Brook, New York 11794

Q. Tu, Department of Engineering, University of Redlands, Redlands, California 92373

F. Khorrami, School of Electrical Engineering and Computer Science
Polytechnic University, Brooklyn, New York 11201

M. Mattice and N. Coleman, U.S. Army Armament Research, Development, and Engineering Center
(ARDEC) at Picatinny Arsenal, Dover, New Jersey

ABSTRACT

The U.S. Army has built a test fixture called ATB1000 which emulates the types of nonlinearities and flexibilities found on most lightweight turreted weapon systems [2]. In this study, the Trajectory Pattern Method [1-5] is used to synthesize motion trajectories and generate inverse dynamics model based feedforward actuating signals for the test fixture. The main contribution of the present study is the derivation of the inverse dynamics model of the system in parametric form and synthesizing trajectories for point to point motions such that the resulting actuating torques do not contain the harmonic with frequency of the dominant first natural mode of vibration of the flexible beam representing the cannon. With this trajectory pattern, point to point motions with minimal residual vibration can be accomplished with zero end point jerk. A feedforward controller together with a PD feedback loop is constructed and implemented. Computer simulations of the open-loop response of the system are performed and the effectiveness of the approach is verified experimentally. The extension of this approach to vibration suppression problem is discussed.

1- INTRODUCTION

In the past, turreted weapon systems on helicopters were designed to be area weapon systems. Large dispersions about the main aim point were accepted and increased the probability of hit. If the targets were relatively vulnerable, this increased the probability of kill. Currently, these systems are being asked to serve as air-to-air weapons where much smaller dispersions are required not only to hit the target, but to hit it multiple times in order to increase the probability of a kill. Lightweight turret designs generally result in structures that are relatively more flexible. The structural flexibility causes vibration, control and accuracy problems. This means that the flexibility has to be included in the dynamics model and considered in the control algorithm.

The problems of modeling and control of flexible structures have been under intensive investigation in recent years [2, 6-18]. The dynamics models of flexible mechanical systems are more complex than their rigid counterparts since they are usually systems with distributed parameters. The equations of motion of such systems consist of a set of ordinary differential equations (O.D.E.) coupled with a set of partial differential equations (P.D.E.). The O.D.E. describe the rigid body motion and the P.D.E. describe the motion of the elements with distributed parameters. In general, the P.D.E. are transformed into O.D.E. using modal expansion techniques, lumped mass (lumped parametric beam) models, or finite element models. The equations of motion of the system are then derived using the Lagrangian equation, Euler-Newton equation, or Hamilton's principle. The control of the dynamic behavior of such systems is also more complicated due to the complexity of the inverse dynamics, nonlinearity of the system, stability, and controllability problems.

In this study, the Trajectory Pattern Method [1-5] is used to develop the inverse dynamics models of the system. The main contribution of this study is the derivation of the inverse dynamics model of the system in parametric form for point to point motions with trajectories that do not require actuating torque harmonic

with frequency of the dominant first natural mode of vibration of the flexible beam. A feedforward controller together with a PD feedback loop is constructed and implemented on the testbed. The effectiveness of the approach is experimentally verified. The extension of the approach to vibration suppression is discussed.

2- INVERSE DYNAMICS FORMULATION AND TRAJECTORY SYNTHESIS

The schematic of the testbed is shown in Fig. 1. The system consists of an inertia wheel with a moment of inertia I_w, to which a steel beam, representing the relatively flexible cannon and 0.915 m long and 0.476 cm in diameter is connected. The link mass is 0.1285 kg. The motor has an inertia I_m. The motor is connected to the inertia wheel by a torsional spring with spring constant k_s. The motor produces the torque τ. The angular position of the wheel and the motor relative to a fixed coordinate system are indicated by θ and θ_m, respectively. In the motions to be considered, the system starts at rest from some initial position and comes to rest at the completion of its motion. The flexible beam is initially undeformed and is desired to come to rest undeformed at the completion of motion. An assumed mode shape method is used to formulate the dynamics of the flexible beam. The approach is, however, general and can be used to formulate the inverse dynamics of systems modeled using finite elements, segmented beam elements, or lumped masses.
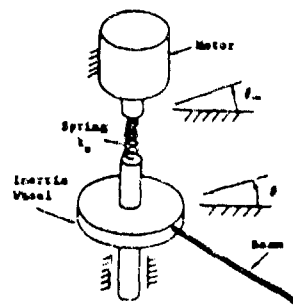
The flexible beam has a uniform cross section and a uniformly distributed mass along its length. The beam in the plane of its motion is shown in Fig. 2. In the coordinate system shown in Fig. 2, $w(\ell, t)$ is the deflection of a point along the link length with respect to its rigid position. Assuming that the beam is much stiffer in the longitudinal direction than in the transverse direction, the longitudinal deformation is considered to be negligible.

Using the assumed-mode method [19-20], the P.D.E. is reduced to O.D.E. as follows. Let
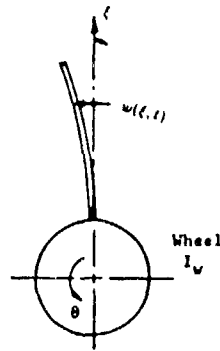
Fig. 2: The flexible beam.

$$w(\xi, t) = \sum_{j=1}^{n} \phi_j(\xi) q_j(t) \tag{1}$$

where n is the number of the assumed-modes, $\phi_j(\xi)$ is the comparison function, and q_j is the amplitude of the jth natural mode of vibration. In this study, the eigenfunction of a clamped-free beam is chosen to describe $\phi_j(\xi)$. Using the procedure described in [19-20], the equations of motion are obtained as [21]

$$r = (I_w + \frac{1}{3} m L^3) \ddot{\theta} + m \dot{\theta} \sum_{j=1}^{n} B_j q_j^2 + 2 m \dot{\theta} \sum_{j=1}^{n} B_j q_j \dot{q}_j + m \sum_{j=1}^{n} D_j \ddot{q}_j \tag{2a}$$

$$\ddot{q}_j + \omega_j^2 q_j = -\frac{D_j}{B_j} \ddot{\theta} + \dot{\theta}^2 q_j - \frac{\dot{\theta}^2 L^3}{B_j} \sum_{k=1}^{n} E_{jk} q_k \qquad j = 1, \cdots, n \tag{2b}$$

where m is the mass per unit beam length, L is the total beam length, and ω_j is the jth natural frequency. B_j, D_j, and E_{jk} are as given in [19-20].

In the present method, in order to avoid the introduction of the harmonic with the frequency of the first mode of oscillation of the beam in the actuating torque, r, the motion of the system is defined by the acceleration of the generalized coordinates q_1, i.e., the amplitude of the first natural mode of oscillation of the beam, using a number of basic sinusoidal time functions and a their harmonics. Here, in order to keep the derivations simple, the motions are considered to be point to point with zero end point acceleration and jerk, and synthesized using one basic (fundamental) sinusoidal time function and $(m-1)$ number of its harmonics as

$$\ddot{q}_1 = \sum_{i=1}^{m} [d_{q_1, 2i-1} \cos(i\omega t) + d_{q_1, 2i} \sin(i\omega t)] \tag{3a}$$

where ω is the frequency of the fundamental sinusoidal time function of the trajectory and the coefficients $d_{q_1, J}$, $(J = 1, 2, ..., 2m)$, are constant coefficients. The corresponding velocity and position expressions are found by integration as

$$\dot{q}_1 = \frac{1}{\omega} \sum_{i=1}^{m} \left[\frac{d_{q_1, 2i-1}}{i} \sin(i\omega t) - \frac{d_{q_1, 2i}}{i} \cos(i\omega t) \right] \tag{3b}$$

$$q_1 = \frac{1}{\omega^2} \sum_{i=1}^{m} \left[\frac{d_{q_1, 2i-1}}{i^2} \cos(i\omega t) + \frac{d_{q_1, 2i}}{i^2} \sin(i\omega t) \right] \tag{3c}$$

In equation (2b), the right hand side components of the centrifugal forces are usually very small and are, therefore, neglected. By substituting (3a) and (3c) in the first modal equation, i.e., equation (2b) for $j = 1$, the acceleration $\ddot{\theta}$ of the inertia wheel is determined in terms of the fundamental sinusoidal time function of the trajectory and its harmonics as

$$\ddot{\theta} = \sum_{i=1}^{m} [d_{\theta, 2i-1} \cos(i\omega t) + d_{\theta, 2i} \sin(i\omega t)] \tag{4a}$$

where

$$d_{\theta, 2i-1} = \frac{B_1}{D_1} \left(\frac{1}{i^2} - 1 \right) d_{q_1, 2i-1}$$

The inertia wheel velocity and position expressions are obtained by integrating (4a) as

$$\dot{\theta} = \frac{1}{\omega} \sum_{i=1}^{m} \left[\frac{d_{\theta, 2i-1}}{i} \sin(i\omega t) - \frac{d_{\theta, 2i}}{i} \cos(i\omega t) \right] \tag{4b}$$

$$\theta = -\frac{1}{\omega^2} \sum_{i=1}^{m} \left[\frac{d_{\theta, 2i-1}}{i^2} \cos(i\omega t) + \frac{d_{\theta, 2i}}{i^2} \sin(i\omega t) \right] + \theta_c \tag{4c}$$

where θ_c is the constant of integration. The constant of integration in the velocity equations (3b) and (4b) are set to zero in order to avoid the introduction of nonsinusoidal time terms in the position equation. Equation (2b) for $j = 2, 3, \cdots, n$, can then be written in the following form

$$\ddot{q}_j + \omega_j^2 q_j = f_j(\omega t) \qquad j = 2, 3, \cdots, n \tag{5}$$

where $f_j(\omega t)$ are in terms of the fundamental sinusoidal time function of the trajectory and its harmonics. The functions $f_j(\omega t)$ are readily shown to be

$$f_j(\omega t) = \sum_{i=1} f_{j, 2i-1} \cos(i\omega t) + f_{j, 2i} \sin(i\omega t) \tag{6}$$

where

$$f_{j, i} = -\frac{D_j}{B_j} d_{\theta, i}$$

Equations (5) are a set of second order decoupled ordinary differential equations with constant coefficients, and are readily solved for q_j, $j = 2, 3, \cdots, n$. For the desired zero initial modal displacements and velocities, i.e., for $q_j(0) = \dot{q}_j(0) = 0$, $j = 2, 3, \cdots, n$ the solution can be shown to be

$$q_j = \frac{D_j B_1}{B_j D_1} \sum_{i=1}^{m} (\frac{1}{i^2} - 1) \frac{1}{\omega_j^2 - (i\omega)^2} \{ d_{q_1, 2i-1} [\cos(\omega_j t) - \cos(i\omega t)] +$$

$$d_{q_1, 2i-1} \left[\frac{i\omega}{\omega_j} \sin(\omega_j t) - \sin(i\omega t) \right] \} \tag{7}$$

The corresponding modal velocities, accelerations, and jerks are obtained by differentiating equations (7) with respect to time. The right hand terms in the equation of motion (2a) are now known. The required (feedforward) actuating torque r is, therefore, obtained in terms of the fundamental sinusoidal time function of the trajectory and its m harmonics.

Now consider point to point motions that begin at time $t = 0$ and end at time $t = t_f$. At the start and the end of motion, the flexible beam is considered to be undeformed and stationary. In order to ensure smooth motions, the end point acceleration and jerk are desired to be zero. The starting position of the inertia wheel is arbitrary and is considered to be zero. The following end conditions must, therefore, be satisfied

$$\theta(0) = \dot{\theta}(0) = 0 \tag{8a}$$

$$q_1(0) = \dot{q}_1(0) = \ddot{q}_1(0) = \dddot{q}_1(0) = 0 \tag{8b}$$

$$q_j(0) = \dot{q}_j(0) = 0 \qquad j = 2, 3, \cdots, n \tag{8c}$$

$$\theta(t_f) = \theta_f, \qquad \dot{\theta}(t_f) = 0 \tag{8d}$$

$$q_1(t_f) = \dot{q}_1(t_f) = \ddot{q}_1(t_f) = \dddot{q}_1(t_f) = 0 \tag{8e}$$

$$q_j(t_f) = \dot{q}_j(t_f) = 0 \qquad j = 2, 3, \cdots, n \tag{8f}$$

where θ_f is the final position of the inertia wheel.

A total number of $(4n + 8)$ initial and final conditions must therefore, be satisfied in order for the aforementioned motions to be realized. By setting $t = 0$ and $t = t_f$ in equations (1), (4), (7) and their time derivatives, and using the conditions (8)

(4n + 8) relationships between the trajectory coefficients $d_{q_i,j}$, $(j = 1, 2, ..., 2m)$, and the constants of integration θ_c, equation (4c), are obtained. Note that since each harmonic provides two coefficients, the minimum number of harmonics with which such trajectories may be synthesized is $2(n+2)$. By including more harmonics in the trajectory, trajectories that are optimal according to some criterion are synthesized.

Once the required feedforward torque τ, equation (2a), is determined, the corresponding motor torque, τ_m, is obtained as follows. From Fig. 1, the required motor trajectory is found as

$$\theta_m = \frac{\tau}{k_s} + \theta \qquad (9)$$

θ_m is therefore in terms of the fundamental sinusoidal function of the trajectory and its harmonics. $\ddot{\theta}_m$ is obtained by differentiating θ_m twice with respect to time. From Fig. 1, it is readily seen that

$$\tau_m = I_m \ddot{\theta}_m + k_s(\theta_m - \theta) \qquad (10)$$

Having found θ, θ_m and $\ddot{\theta}_m$, the feedforward actuator torque τ_m is obtained from equation (10) in terms of the fundamental sinusoidal function of the trajectory and its harmonics. Note that the computed actuating torque does not contain the harmonic with the first natural frequency of the beam. One can obviously choose to eliminate any one of the natural frequencies from the actuating torque.

Note that in order to eliminate the actuating torque component corresponding to more than one natural frequency of the beam, the inertia wheel must have more than one independent (actuated) motion, e.g., translational motions in the X and Y directions in the XY plane, Fig. 2. In which case and not considering special situations, actuating torque (force) components corresponding to three natural frequencies may be eliminated.

3- EXAMPLE

The system parameters are identified to be $I_w = .15\ kg - m^2$, $I_m = .0023\ kg - m^2$ and $k_s = 24.5\ N - m/rad$. The PD gains are set at $k_p = 80$ and $k_v = 1$, and the resulting signal is added to the control signal after the planned motion time has elapsed. The maximum motor torque is $10\ N - m$. The motor friction torque is measured to be approximately $.5\ N - m$ and is compensated for. A 100 Hertz dither signal of $.6\ N - m$ is used to reduce the effects of sticking at low velocities. During the experiments, the position of the motor shaft and the inertia wheel are measured by optical encoders. The position signals are differentiated numerically to obtain the corresponding velocities. The deformation of the beam is determined using tip accelerometer and strain gage outputs measuring lateral bending strains at two equally spaced locations along the beam. The first three natural frequencies of the beam are calculated to be $\omega_i = 24.6$, 138.7 and 345.5 rad/sec, for $i = 1, 2, 3$. The first natural frequency is verified experimentally. The frequencies of the fundamental sinusoidal time functions of the synthesized trajectories are selected such that the above natural frequencies of the beam are not excited. For more information about the testbed and the control hardware and software, the reader is referred to [2].

In the following experiment, the trajectory is synthesized for the generalized coordinate q_1, equation (3), corresponding to the first natural mode of vibration of the beam. The higher modes of vibration are determined to have negligible contribution, and are therefore neglected. The trajectory of the generalized coordinate q_1 is synthesized using a fundamental sinusoidal time function with frequency $\omega = \pi\ rad/sec$, and five of its harmonics. The time taken to complete the motion is $t_f = 1\ sec$.

The expression indicating q_1, equation (3c), contains 12 coefficients, $d_{q_1,i}$, $(i = 1, 2, ..., 12)$, and there is an integration constant θ_c in the θ expression, equation (4c). There are, therefore, a total number of 13 trajectory parameters that can be used to satisfy the 12 end conditions given by equations (8a), (8b), (8d) and (8e).

With the selected trajectory, fundamental frequency and t_f, the remaining end conditions are automatically satisfied.

Following the aforementioned procedure, for a total rotation of $\theta(t_f) = 0.5\ rad$ and by arbitrarily setting an extra trajectory coefficient, in this case $d_{q_1,12} = 0$, the remaining 12 trajectory harmonic coefficients in (3c), i.e., $-[(1/\omega^2)/i^2]d_{q_1,i}$, $(i = 1, 2, ..., 11)$ and θ_c are determined as

$$d_{q_1,i} = -3.033E-4,\ 0.000,\ 15.528,\ 0.000,\ 4.549,\ 0.000,\ -24.845,$$
$$0.000,\ -1.516,\ 0.000,\ 9.317,\ 0.000$$
$$\theta_c = 0.000$$

The structure of the resulting inverse dynamics based controller is shown in the block diagram of Fig. 3. The feedforward (actuator) signal is generated using the sinusoidal time functions and the constant trajectory coefficients. The desired motor position and velocity signals are generated using the sinusoidal time functions and the constant trajectory parameters in the block indicated as the "trajectory synthesizer". An outer loop PD control action is used to correct for model inaccuracies and noise.
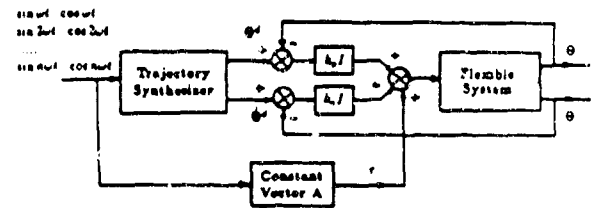
Fig. 3: The structure of the inverse dynamics model based controller.

For the aforementioned motion, the synthesized and the measured motor trajectories are shown in Fig. 4. The corresponding velocities are shown in Fig. 5. Note that the high frequency velocity signal is due to the input 100 Hertz dither signal. In Fig. 6, the computed feedforward torque, the measured PD and tip accelerometer signals are illustrated, respectively. In this illustration, due to the way that the hardware connections are made, a negative tip acceleration corresponds to a positive actuating torque. The total deformation of the torsional spring, i.e., the position of the wheel relative to the motor, is shown in Fig. 7. The
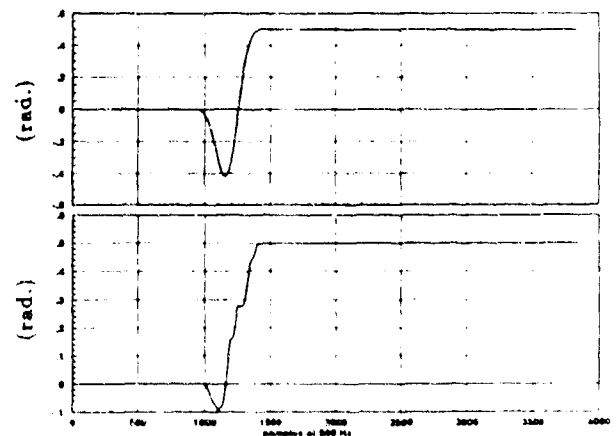
Fig. 4: The synthesized (top) and the measured (bottom) motor trajectories

experiments are done at a sampling rate of 500 Hertz. Trajectory synthesis and the feedforward torque computation are performed on-line using separate processors [2]. As can be seen from the above illustrations, the tip motion closely follows the intended pattern, and the tip comes to rest at the completion of motion. In the measured acceleration signal, the slowly decaying signal is due to the charge amplifier. The authors are currently involved in the process of implementing a tip position vibration suppression algorithm based on the present methodology. The algorithm involves the use of the measured wheel position and velocity and the tip acceleration to generate the required initial conditions to replace their zero values in (8), and on-line synthesis of trajectories to bring the system to rest or to the desired end conditions for the case of tracking motions.
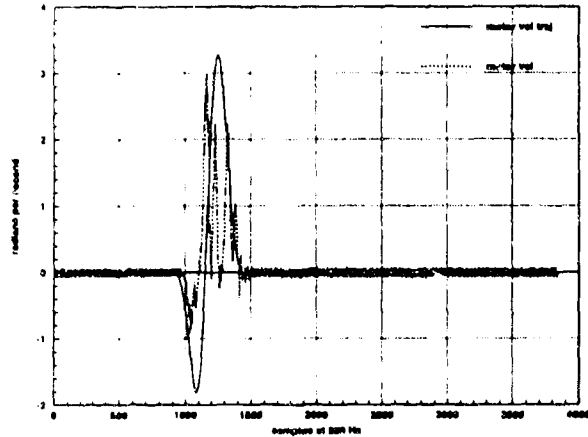
Fig. 5: The synthesized (top) and the measured (bottom) motor velocities.
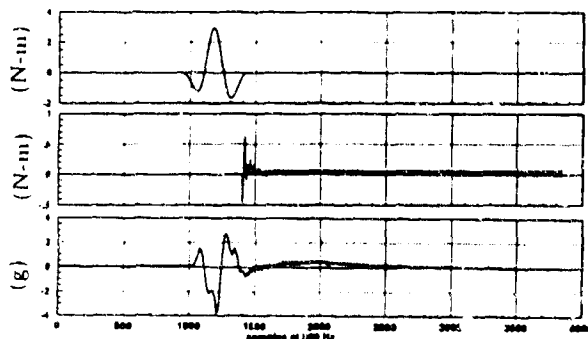
Fig. 6: The computed feedforward torque (top), measured PD signal (middle) and tip accelerometer (bottom).

4- DISCUSSION AND CONCLUSIONS

One of the advantages of the trajectory pattern method is the fixed structure of the resulting inverse dynamics model, and the fact that all derivations related to the trajectory synthesis and feedforward signal generation are made in parametric form. For systems that are not too complex and for classes of trajectory patterns, explicit analytical formulations can be performed. This makes the trajectory pattern method ideal for use in model based controllers requiring minimal on-line computations that can be performed mostly in parallel.
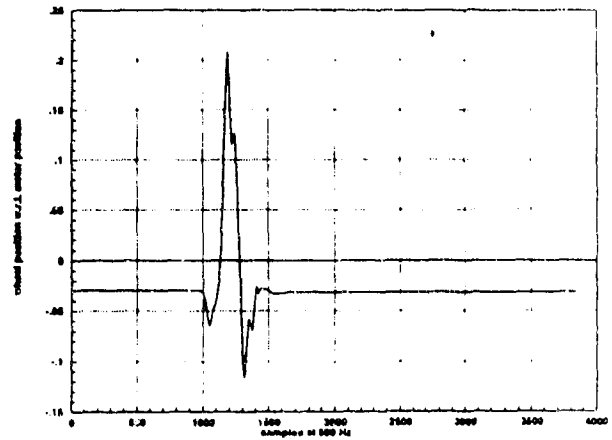
Fig. 7: The position of the wheel relative to the motor.

The present approach is shown to permits trajectory synthesis such that the component corresponding to the dominant (one) natural modes of vibration of the flexible beam is not present in the required actuating signal. In general, for each actuator affecting the rigid body motion, the component corresponding to one mode of vibration can be eliminated from the actuating signal. The synthesized (tracking and regulatory) motions produce minimal residual vibration which are accomplished with zero end point jerk.

REFERENCES

[1] Fardanesh, B., and Rastegar, J., 1992, "A New Model Based Tracking Controller for Robot Manipulators The Trajectory Pattern Inverse Dynamics," *IEEE Trans. Robotics and Automation* 8 *(2)*, pp. 279 284.

[2] Rastegar, J., Tu, Q., Fardanesh, B., Coleman, N., and Mattice, M., 1992, "Experimental Implementation of Trajectory Pattern Inverse Dynamics Model Based Controller for a Flexible Structure," *American Control Conference*, Chicago.

[3] Tu, Q., and Rastegar, J., 1991, "On the Inherent Characteristics of the Dynamics of Robot Manipulators," *13th Biennial ASME Conf. on Mechanical Vibration & Noise*, Miami, pp. 299-305.

[4] Rastegar, J. and Fardanesh, B., 1990, "Trajectory Pattern Specific Inverse Dynamics Formulation of Robot Manipulators, and its Applications" *ASME 1990 Mechanisms Conf.*, Chicago. Illinois.

[5] Rastegar, J., and Fardanesh, B., 1991, "Inverse Dynamics Models of Robot Manipulators Using "Trajectory Patterns - With Application to Learning Controllers," *Eighth World Congress on the Theory of Machines and Mechanisms*.

[6] Book, W. J., and Majette, M., 1983, "Controller Design for Flexible, Distributed Parameter Mechanical Arms Via Combined State Space and Frequency Domain Techniques," *ASME J. of Dynamic Systems, Measurement, and Control*, 105, *(2)*, pp 245-254.

[7] Asada, H., Ma, Z. D., and Park, J. H., 1990, "Inverse Dynamics of Flexible Robot Arms: Modeling and Computation for Trajectory Control", *ASME J. of Dynamic Systems, Measurement, and Control*, 110, *(2)*, pp. 177-185.

[8] Tomei, P., and Tormambe, A., 1989, "Approximate Modeling of Robots Having Elastic Links," *IEEE Trans. Syst. Man Cybern.*, SMC-18, *(5)*, pp 831-840.

[9] Cannon, R. H., and Schmitz, E., 1984, "Initial Experiments on the End-Point Control of a Flexible One-Link Robot," *Int. J. of Robotics Res.*, 3, *(3)*, pp. 62-86.

[10] Bayo, E., 1987, "A Finite Element Approach to Control the End-Point Motion of a Single-Link Flexible Robot," *J. of Robot. Sys.*, 4, *(1)*, pp. 63-75.

[11] Naganathan, G., and Soni, A. H., 1988, "Nonlinear Modeling of Kinematic and Flexibility Effects in Manipulator Design," *ASME J. of Mechanisms, Transmissions, and Automation in Design*, 110, *(3)*, pp. 243-254.

[12] Tilley, S. W., Cannon, R. H., and Kraft, R., 1986, "End Point Force Control of a Very Flexible Manipulator With a Fast End Effector," *ASME Proc. WAM*.

[13] Harashima, F., and Ueshiba, T., 1986, "Adaptive Control of Flexible Arm Using the End-Point Position Sensing," *Japan-U.S.A. Symp. on Flexible Automation* 1, pp. 225-229.

[14] Farrenkopf, R. L., 1979, "Optimal Open-Loop Maneuver Profiles for Flexible Spacecraft," *AIAA J. of Guidance and Control*, 2, *(6)*, pp. 491-498.

[15] Aspinwall, D. M., 1980, "Acceleration Profiles for Minimizing Residual Response," *J. of Dynamic Systems, Measurement, and Control*, 102, *(1)*, pp. 3-6.

[16] Swigert, C. J., 1980, "Shaped Torque Techniques," *AIAA J of Guidance and Control*, 3, *(5)*, pp. 460-467.

[17] Meckl, P. H., and Seering, W. P., 1985, "Minimizing Residual Vibration for Point-to-Point Motion," *ASME Journal of Vibration, Acoustics, Stress, and Reliability in Design* 107 *(4)*, pp 378-382.

[18] Bayo, E., and Paden, B., 1987, "On Trajectory Generation of Flexible Robots," *J. of Robot Sys.*, 4, *(2)*, pp. 229-235.

[19] Meirovitch, L., 1967, *Analytical Methods in Vibrations*, Mac-Millan Co.

[20] Meirovitch, L., 1986, *Elements of Vibration Analysis*, McGraw-Hill.

[24] Tu, Q., 1992, *Ph. D. Dissertation*, Mechanical Engineering Department, The State University of New York at Stony Brook.

SESSION III

WEAPON SIMULATION/TUBE DEFORMATION

BENZKOFER

TITLE: DYNAMIC ANALYSIS OF SHOULDER-FIRED WEAPONS
         PHILIP D. BENZKOFER
         U.S. Army Armament Research, Development & Engineering Center
         Light Armament Division
         Simulation & Evaluation Branch
         Picatinny Arsenal, NJ 07806-5000

ABSTRACT:

        A recoil analysis to assess several recoil mitigating
technologies applied to shoulder-fired weapons such as a grenade
launcher or shotgun has been conducted.   Parameters such as weapon
weight, recoil impulse, recoil velocity and recoil energy were
identified as critical. A range of values were selected for
evaluation. In order to monitor and assess the dynamics occurring
during its cyclic motion, a mathematical model for a 12 Gauge weapon
has been developed. The model defines each major component and the
relative connectivity between them is defined in terms of kinematic
joints. A Lagrangian methodology is utilized to formulate the rigid
body dynamic equations of motion. Three commercial recoil reducing
devices were evaluated in the model to determine their specific effect
on recoil motion, both on the weapon and on the soldier firing the
weapon. A full test program was conducted at the Armaments Research
Laboratory (ARL) on a modified 12 Gauge shotgun to measure recoil
control for each of the recoil devices. An additional model was
formulated for this fixture. Comparisons between model and
experimental test results were made. Further tests and evaluation
include combinations of recoil devices. Documentation of sample model
output is included.

BIOGRAPHY:
PRESENT ASSIGNMENT: Armament/Weapon/Mechanisms Analysis, US Army
Armament Research and Development Center, 1977 to present.
PAST EXPERIENCE: Math Analysis, GEN T.J. Rodman Laboratory, Rock
Island Arsenal, IL, 1966 to 1977.
DEGREES HELD: B.S., Mathematics, Iowa State University, 1965, M.S.,
Mechanical Engineering, University of Iowa, 1980.

DYNAMIC ANALYSIS OF SHOULDER-FIRED WEAPONS

PHILIP D. BENZKOFER

U.S. Army Armament Research, Development and Engineering Center
Close Combat Armaments Center
Picatinny Arsenal, NJ 07806-5000

INTRODUCTION

The primary objective of the Parametric Recoil Analysis program was to create computer models that are capable of quantifying the effectiveness of recoil mitigating devices in shoulder fired grenade launchers/weapons with known weapon weights and cartridge characteristics. Early models were concentrated on the M203 system as a baseline. Followon analyses were concentrated on modeling a 12 Gauge weapon installed in a firing fixture designed and fabricated by the Armaments Research Laboratory's Weapons Branch at Aberdeen Proving Grounds. This decision was based upon the fact that physical data obtained from firing from the test fixture would provide the basis for model comparison. The ARL fixture was designed to simulate the motion of a shooter's shoulder, represented by a sliding mass, when firing a weapon. The capability to incorporate shock absorbers and recoil pads was designed into the fixture. By comparing the model results to the actual test fixture results, a good correlation could be obtained. By obtaining this correlation, the necessity to test future shock absorber designs is substantially reduced or eliminated.

The ultimate goal was to produce a model for use in determining the characteristics of an "ideal damper" based upon known ammunition parameters and weapon configuration. In this way, damping parameters can be input to the model until the best recoil mitigating results are obtained. The damper can then be designed around those damping characteristics. This provides the background for the subject paper. A detailed description of the system and the analysis performed along with the results follows below.

WEAPON SYSTEM MODELING

In order to address the analysis of the weapon, a brief description of the weapon is relevant. Initial analyses were based upon the 40mm M203 grenade launcher system. However, based upon a test program conducted at ARL using a 12 Ga Remington, this system was selected for a modeling effort. A test fixture for the test firing program was designed and built (see figures 1 and 2) at the ARL facility, where the test firings were conducted. A later fixture was developed which substantially reduced the weight of the sliding mass,
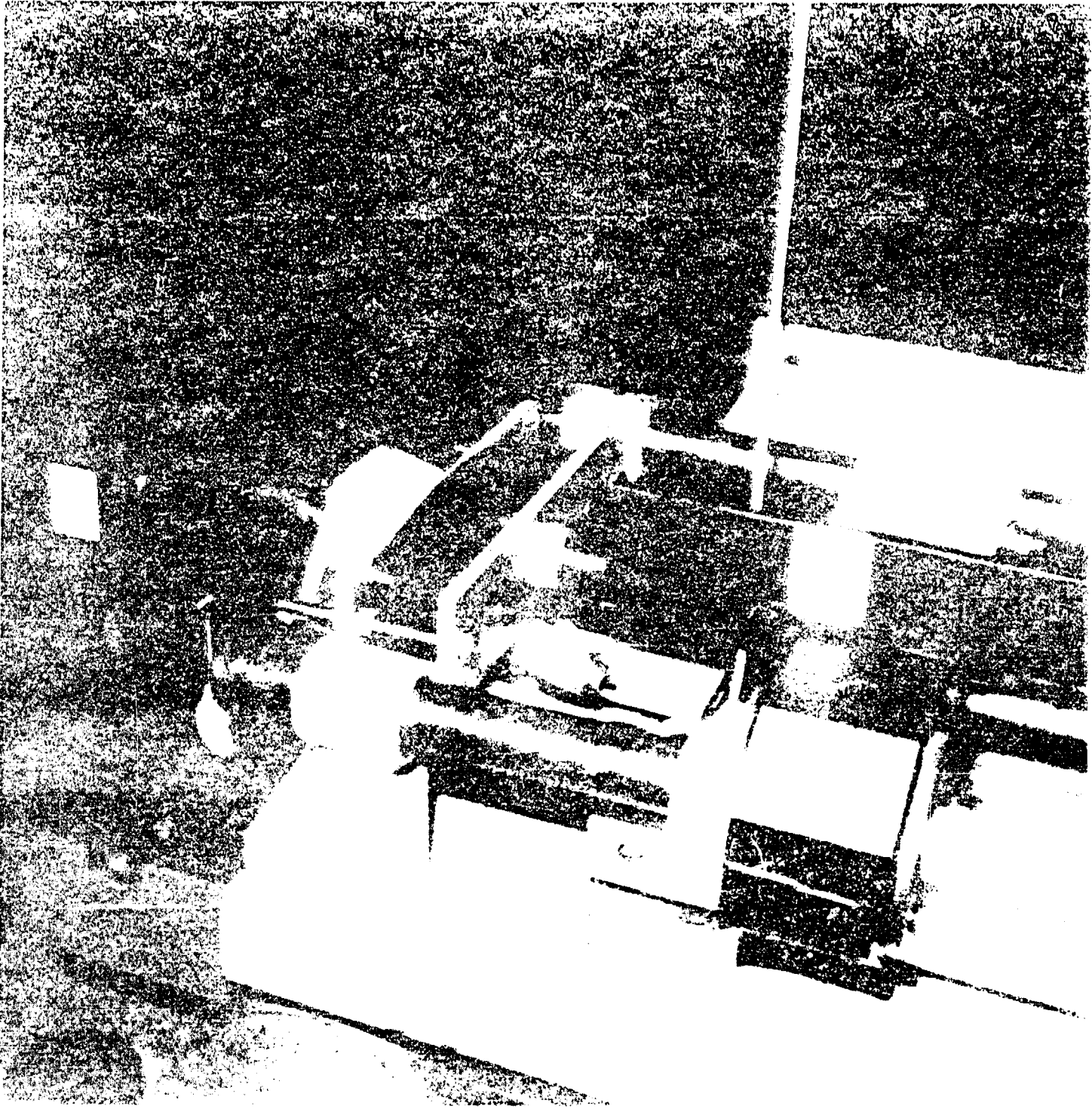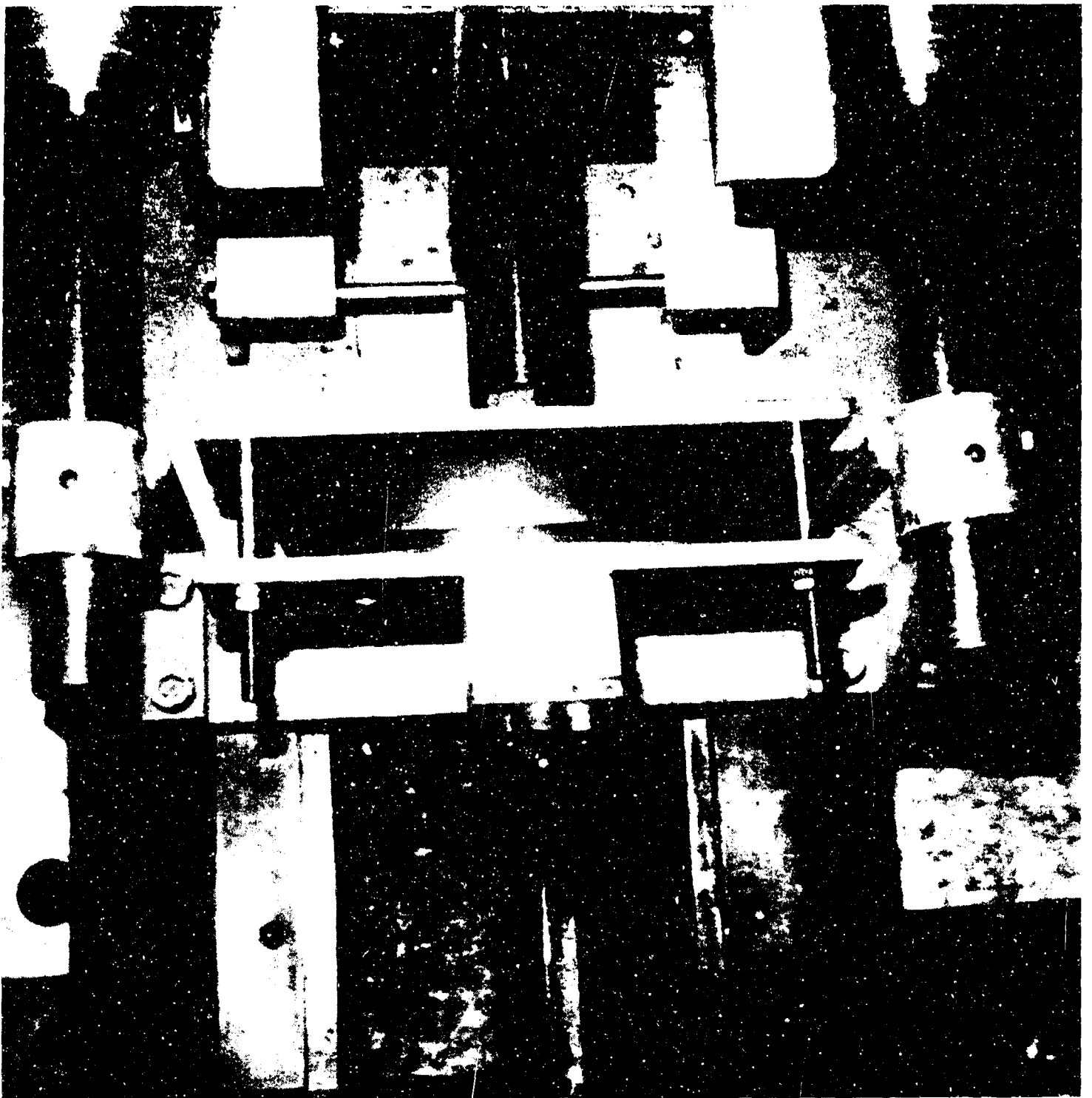
Figure 2. ARL test fixture and weapon

which represents the shoulder mass. This reduction in mass was based upon initial testing results, indicating the first translating mass shown in figures 1 and 2 did not replicate actual motion. The fixture did, however, allow for the development of a generic computer model. The 12 Ga weapon was modified by cutting the stock and constructing a translating fixture which would allow for insertion of the recoil devices and pads. Three specific rounds of ammunition - a target load, a rifled slug load and a heavy magnum load, were utilized in testing, consequently their pressure-time curves were used in the model as system drivers. A typical curve is shown for the magnum round in figure 3. A schematic drawing representing the ARL fixture/weapon system is shown in figure 4. This schematic actually represents the later test fixture described above which was developed to change the mass of the translating mass. Mass one with coordinates x_1, y_1 represents the Inertial Reference Frame from which all global measurements are made. Mass two with coordinates x_2, y_2 represents the mass center of the shoulder, mass three with coordinates x_3, y_3 represents the mass center of the rifle and finally mass four with coordinates x_4, y_4 represents the mass center of the projectile. The associated coordinates are shown on the figure. Connectivity is indicated by spring and damper pairs k_1, c_1 and k_2,c_2 between masses one and two and k_3,c_3 and k_4,c_4 between masses two and three. The spring and damper pairs between masses one and two represent two springs with $k_1 = k_2 = 149$ lbs/inch and $c_1 = c_2 = 0$. The operating height of these two springs is 4.4 inches, which is also the free length. The spring and damper pair represented by k_3, c_3 is a recoil dissipating device such as a shock absorber where k_3 is a constant value and c_3 is variable with velocity. The spring and damper pair represented by k_4, c_4 is a secondary dissipative device such as a pad where measured values are utilized for k_4 and c_4. The variable pressure time curve for the ammunition is applied to the projectile in the forward direction and conversely applied to the rifle in the rearward direction. The dynamic equations of motion are code generated [1] and are in the Lagrangian form given by

$$\frac{d}{dt} \left(\frac{\partial T}{\partial \dot{q}_i} \right) - \frac{\partial T}{\partial q_i} - Q_i + \frac{\partial \phi}{\partial q_i}^T \lambda = 0 \ , \qquad i = 1,\ldots,N \tag{1}$$

where

    T is the kinetic energy
    q_i are the generalized coordinates
    Q_i are the generalized external forces acting on the system
    λ is the set of Lagrange Multipliers associated with the
constraints imposed on the system
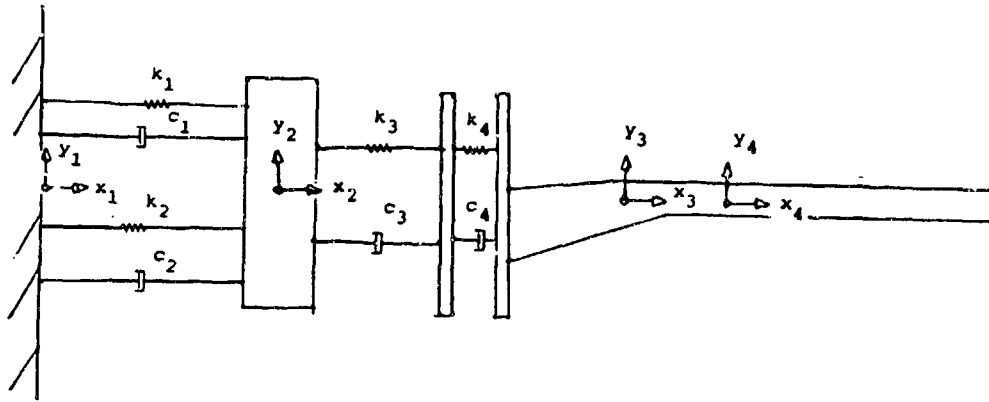
Figure 3.   Schematic model of weapon
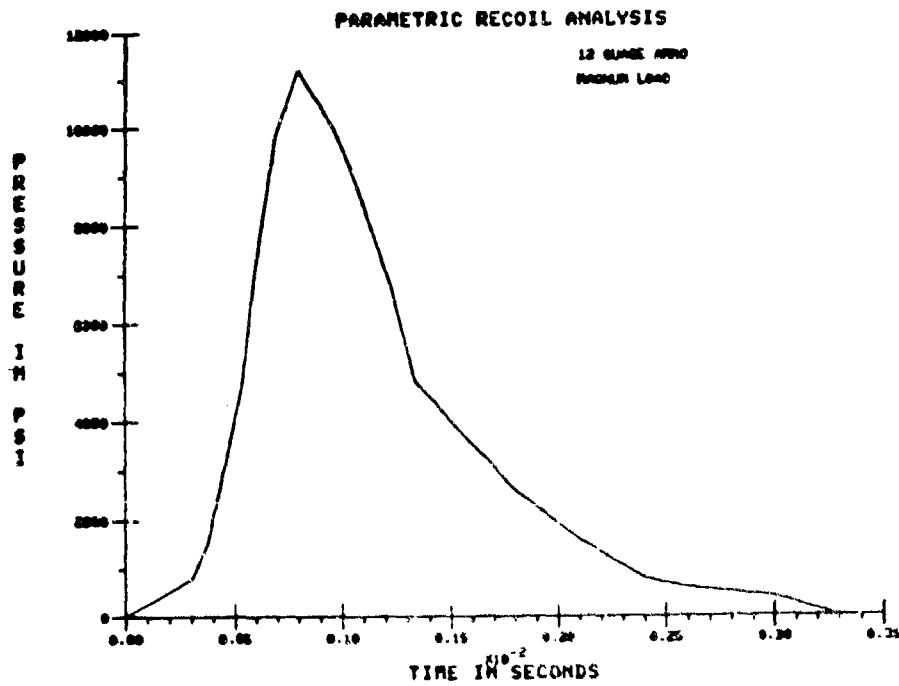
Figure 4.   Pressure-Time curve for 12 Ga ammo

210

BENZKOFER

The equations of constraint are of the form

$$\phi(q,t) = 0 \tag{2}$$

These equations represent the mathematical description of constraining motion. The model, then, can be exercised to obtain the dynamic motion for given parameter changes such as spring damper rates. This analysis provides the basis for any future design and/or redesign efforts. The author has has significant experience in application of dynamics code to weapon and armament system analysis in [3] through [11].

ANALYSIS

Mass two, the shoulder, on the ARL fixture, (see figure 4) weighed 32 pounds. This weight was utilized based upon a previous man-weapon analysis [2]. There were no springs between masses one and two, so effectively $k_1 = c_1 = k_2 = c_2 = 0$. as shown in figure 4. Two of the most promising shock absorbers based upon initial testing and analysis were selected for inclusion in this paper. Curves depicting velocity versus damping coefficients for these two shocks are shown in figures 5 and 6, and provide the force effects of the shock absorbers. These data were furnished by the manufacturers.

The first series of output given in figures 7, 8 and 9 depict displacement, velocity and acceleration versus time, respectively, for the translating mass, or shoulder (for the early BRL test fixture model shown in figures 1 and 2). In each of the figures the motion for the cases of no shock, an Ace and a Taylor shock absorber is shown. The ammunition round is the magnum round with its P-T curve shown in figure 4. The significant difference in absorber effect is best shown in figure 9 for accelerations, where the magnitude is substantially greater for the case with no shock absorber. Similarly the displacement, velocity and acceleration versus time for the rifle is shown in figures 10, 11 and 12, respectively. The velocities in figure 11 are significantly higher for cases with the shock absorbers as compared with the translating mass in the previous figures, as is also the case in figure 12 for accelerations of the rifle. For the case of the ARL test fixture with the lighter translating mass, specifically 11-12 pounds, it is shown schematically in figure 4. The early ARL test fixture weighed 32 pounds and did not have the two large springs represented by k_1, k_2, c_1 and c_2 in figure 4. The displacement, velocity and acceleration versus time for the translating mass, or shoulder, are shown in figures 13, 14 and 15, respectively. The significant difference in shock absorber effect is best shown in figure 15 for acceleration, with the magnitude being substantially greater for the case of no shock absorber. The displacement, velocity and acceleration versus time for the rifle are shown in figures 16, 17 and 18, respectively. Some increase in velocities over that for the translating mass, or shoulder, is noted for the cases with shock
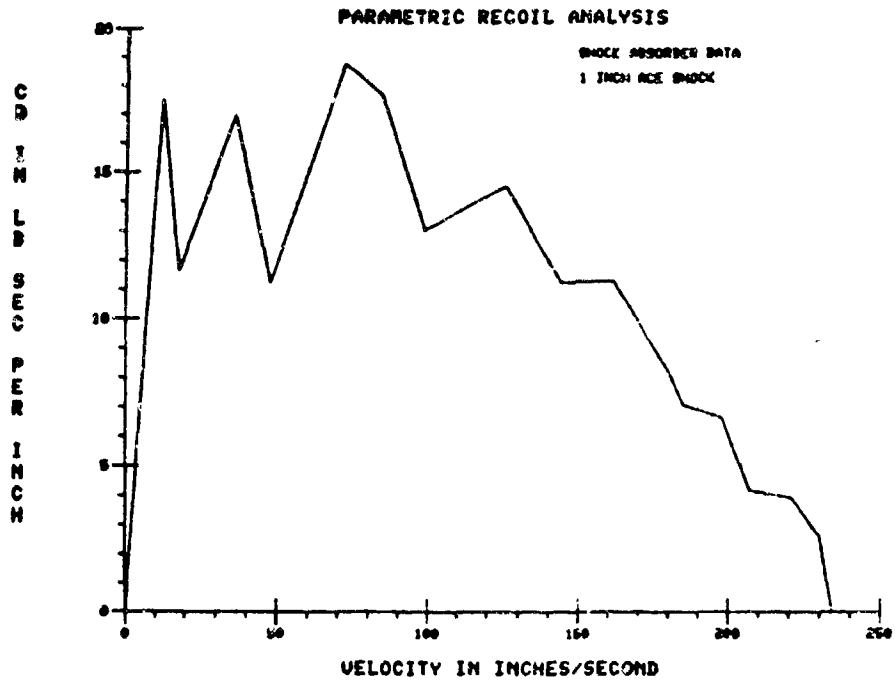
Figure 5.   Damping coefficient versus velocity for Ace shock
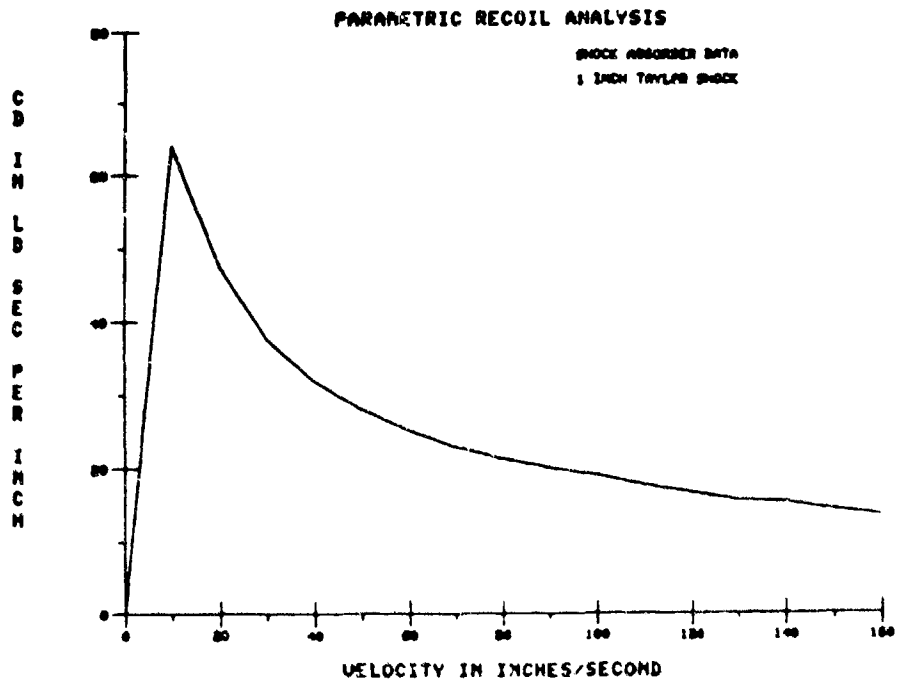
Figure 6.   Damping coefficient versus velocity for Taylor shock

212

PARAMETRIC RECOIL ANALYSIS
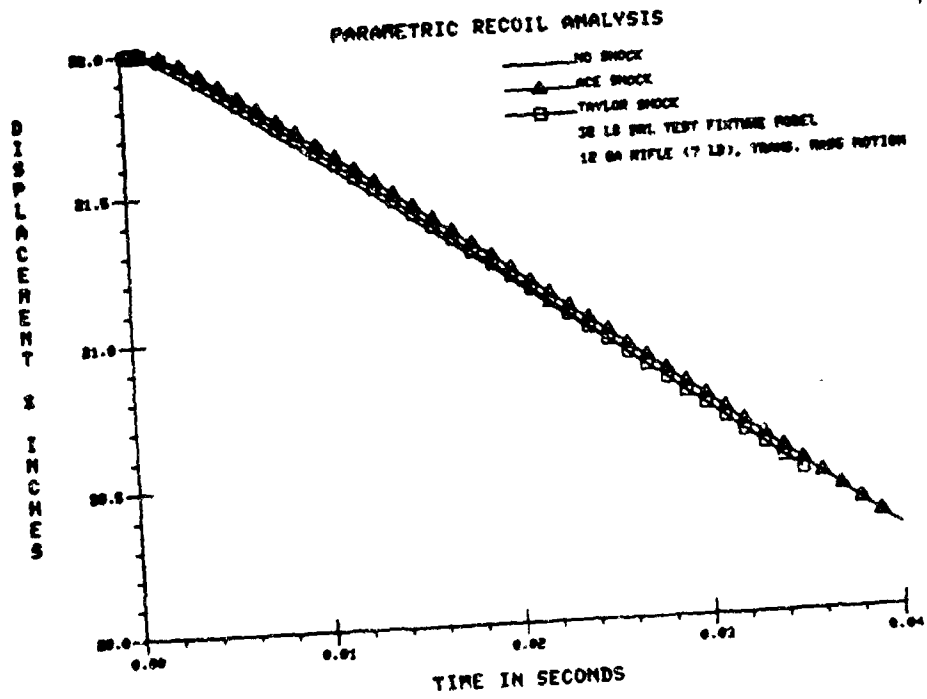
Figure 7. Displacement versus time for shoulder mass

PARAMETRIC RECOIL ANALYSIS
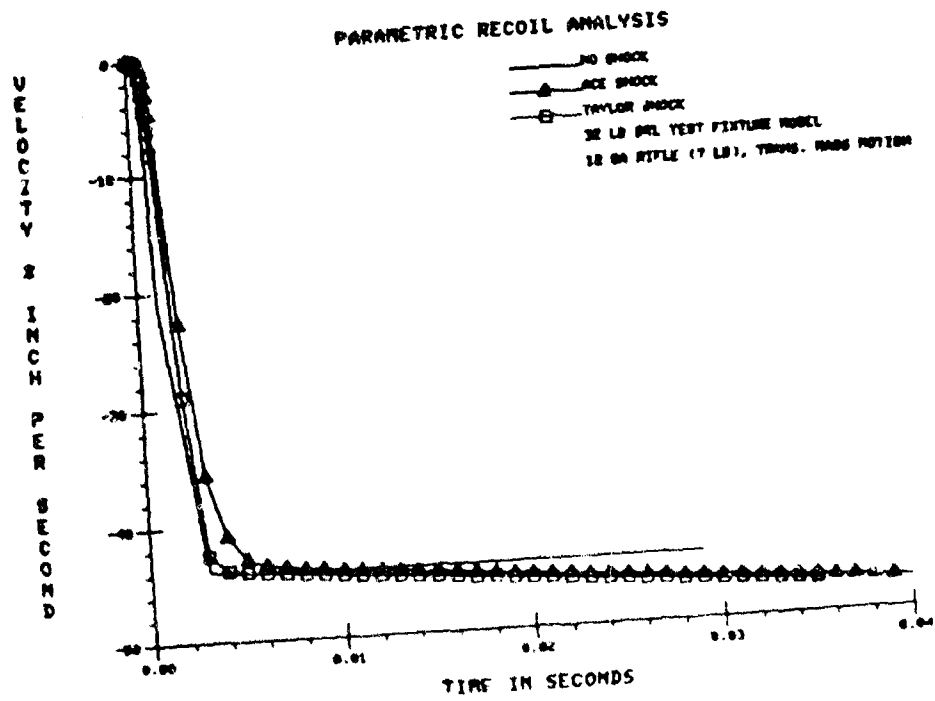
Figure 8. Velocity versus time for shoulder mass
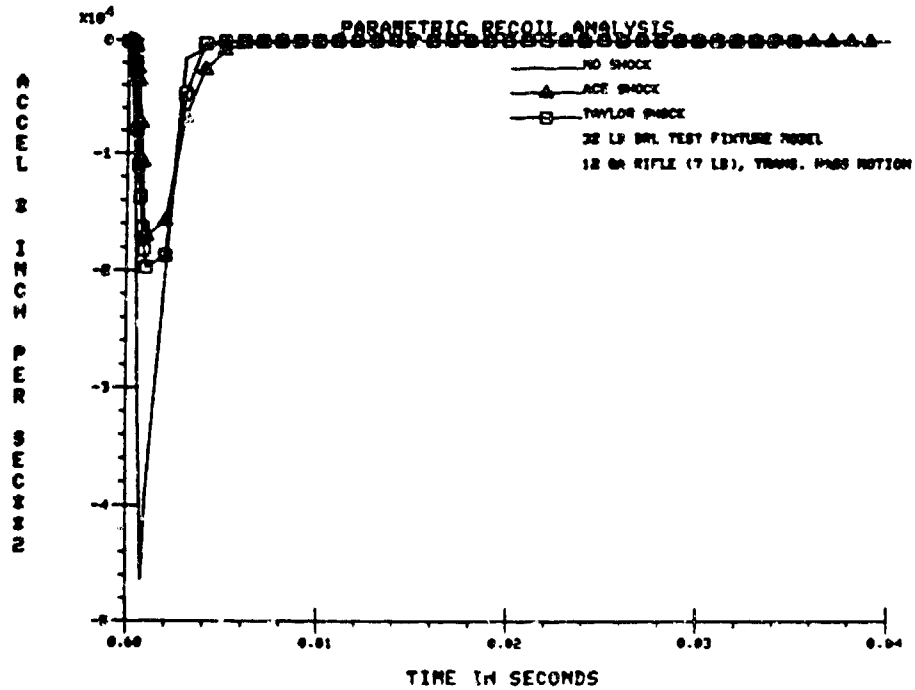
Figure 9.   Acceleration versus time for shoulder mass
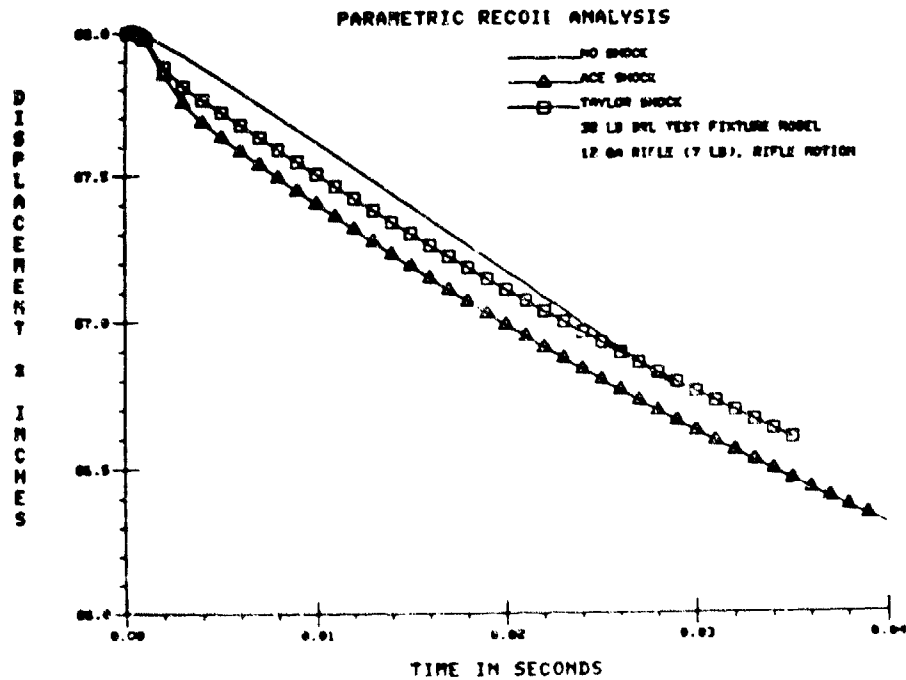
Figure 10.   Displacement versus time for rifle
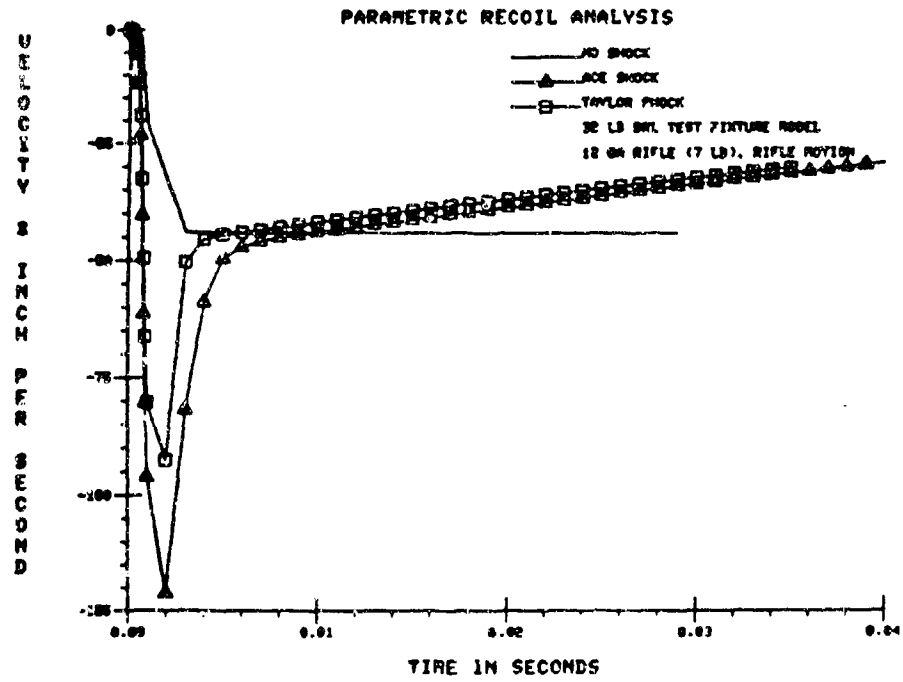
Figure 11.   Velocity versus time for rifle
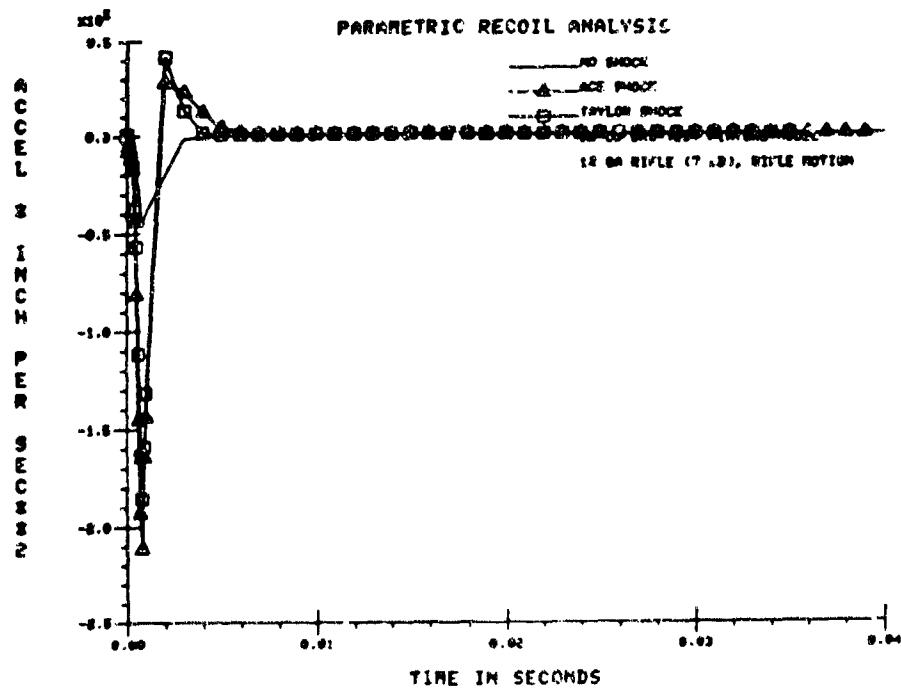
Figure 12.   Acceleration versus time for rifle

PARAMETRIC RECOIL ANALYSIS
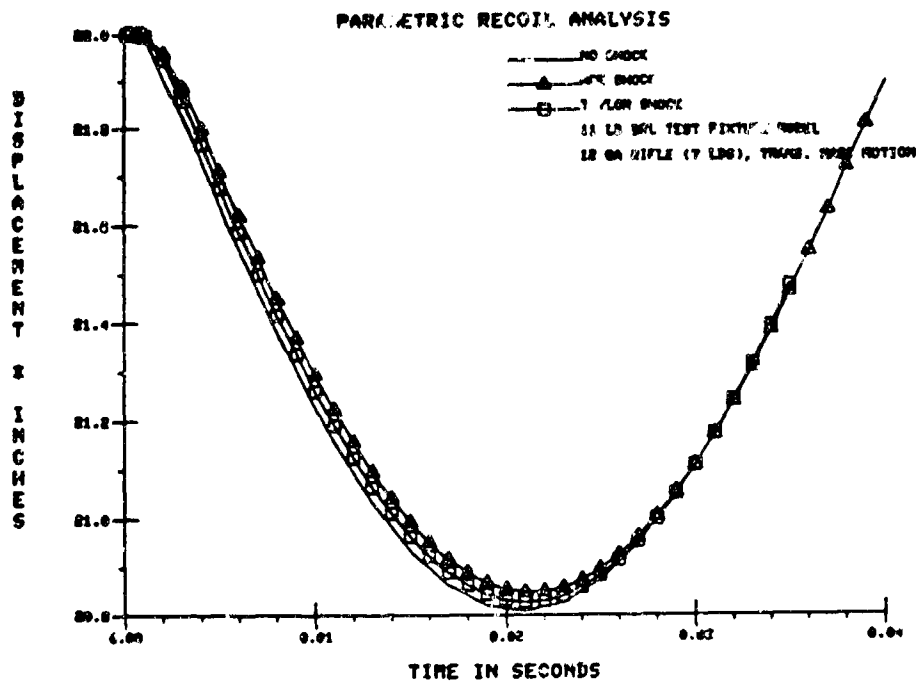
Figure 13. Displacement versus time for shoulder mass

PARAMETRIC RECOIL ANALYSIS
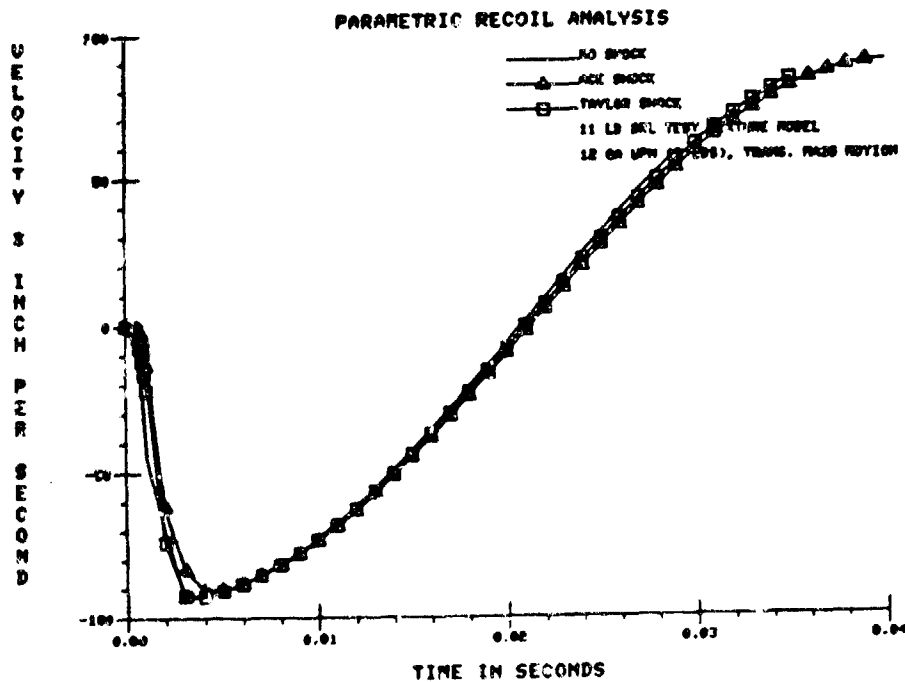
Figure 14. Velocity versus time for shoulder mass

216
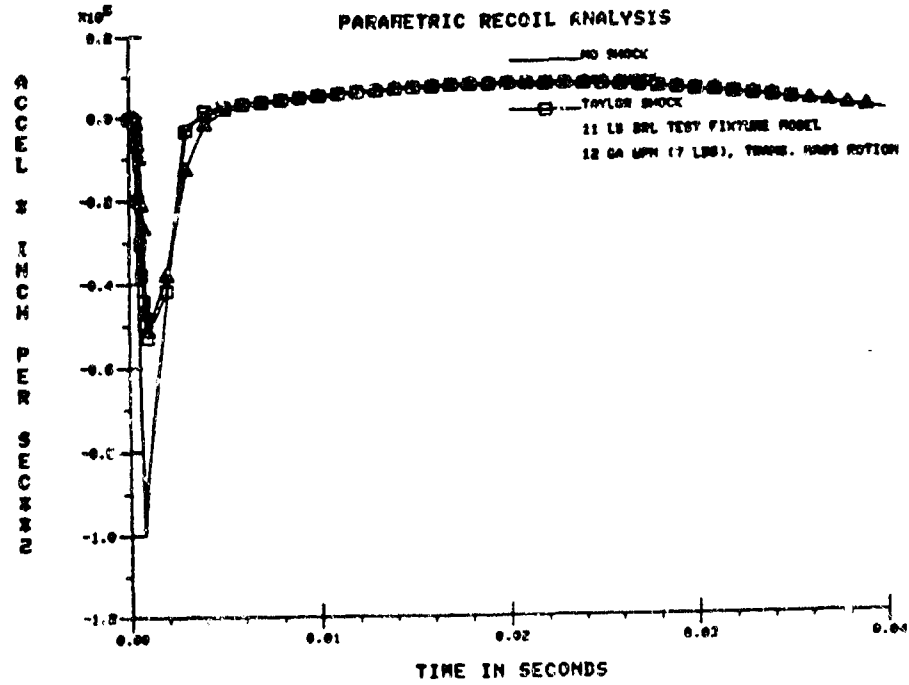
Figure 15. Acceleration versus time for shoulder mass
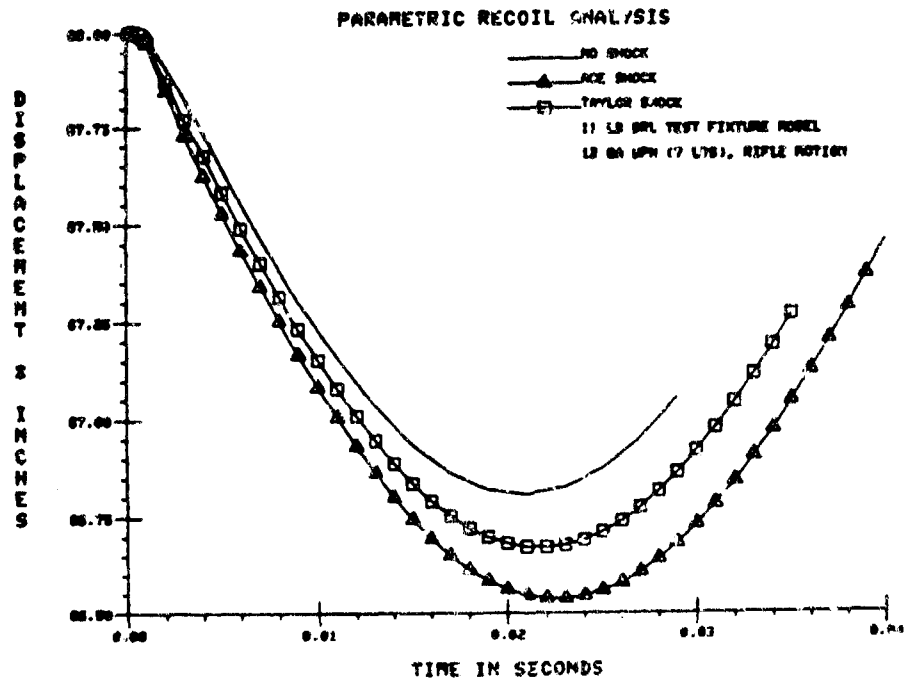
Figure 16. Displacement versus time for rifle

PARAMETRIC RECOIL ANALYSIS
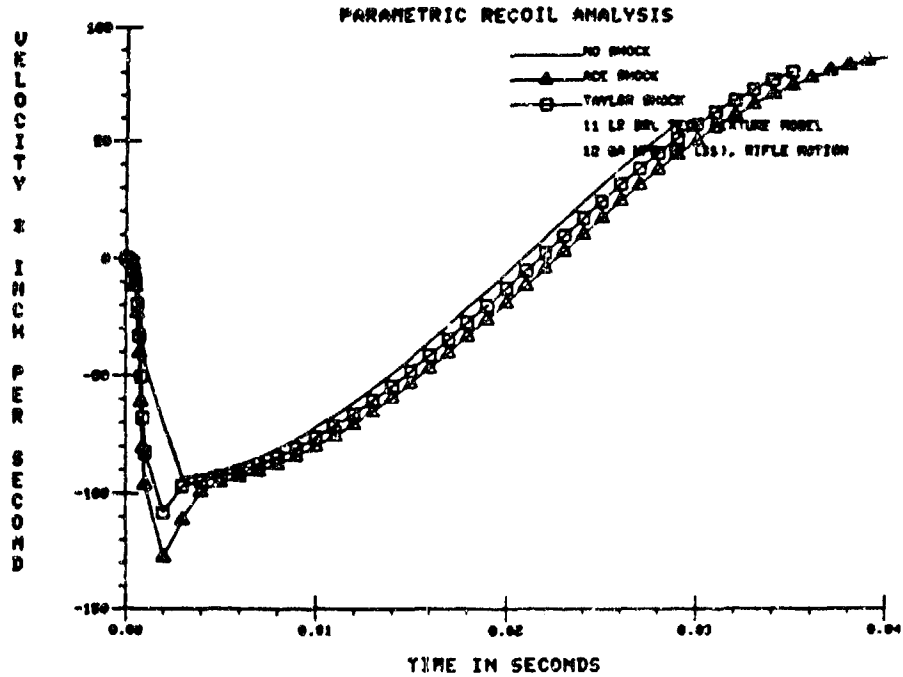
Figure 17. Velocity versus time for rifle

PARAMETRIC RECOIL ANALYSIS
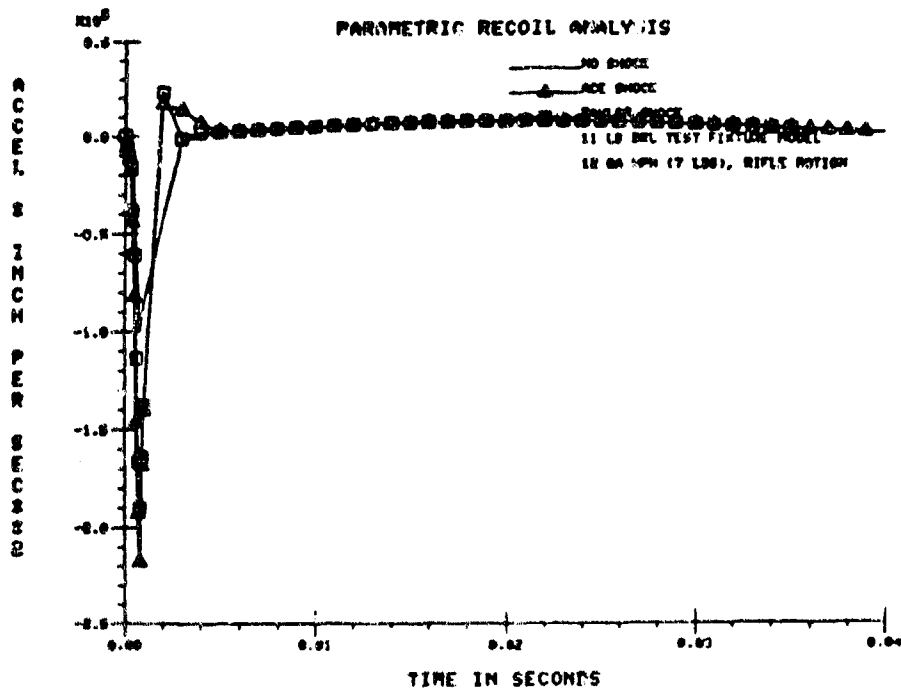
Figure 18. Acceleration versus time for rifle

absorbers. Substantial increases in accelerations for the shock absorber cases over that for the shoulder are also depicted in figure 18.

In order to assess the effect of varying the damping rates associated with the shock absorbers, a series of analyses were made. The Ace shock was arbitrarily selected to evaluate differences in performance. The case for a damping rate equal to that used in the analyses to date was used as a reference, and two additional rates were selected. These are specifically fifty percent and thirty percent of the damping rate used to date. The displacement, velocity and acceleration versus time for the translating mass, or shoulder, for the three cases are shown in figures 19, 20 and 21, respectively. Interestingly, a decrease in damping rate decreases peak velocities and accelerations. Conversely, looking at the displacement, velocity and accelerations versus time for the rifle, respectively, shown in figures 22, 23 and 24, a decrease in damping rate increases peak velocities and accelerations. A change in damping rate, then, has significant impact on the motion.

Several comparisons between simulation results and experimental data from ARL testing are shown in figures 25, 26, 27 and 28. Figure 25 shows displacements versus time for the magnum round with no shock absorber for ARL test data versus simulation results. Similarly, displacements for the case when a shock absorber is used is shown in figure 26. Figure 27 shows velocities for a magnum round and finally figure 28 shows accelerations for the case of no shock absorber. In general, good comparison is made in terms of displacements and velocities. Acceleration tracks relatively good up to peak and even after peak except a shift does occur.

CONCLUSIONS AND RECOMMENDATIONS

Some inaccuracies are apparent when observing motion results as simulation values do not fully coincide with test data. Several significant factors may well have affected the results as provided in the figures above. One, the pressure-time curve used for the 11 pound shoulder mass model is based on Remington's Magnum round, and the round used at ARL for the 11 pound system was the Duplex round. Even though the impulse measured was similar, there very well could be a shift in the actual curve's shape. The second important factor is that the damping curves used in the simulation are based on manufacturer-furnished data, and some error may exist in this data. The last factor is is the accuracy of the model itself. Although a good check has been made of the math model and the input to the code, and the fact that the code itself is felt to be a verified one, further investigation is warranted. Good match with displacement and velocity is shown, and in general peak accelerations are matched. However, some shift in curve shape and magnitude values are evidenced. Further Remington data has been requested and further interface with the shock absorber manufacturers will be pursued. A good model of the ARL fixture has been developed and will provide the basis for further analysis and investigation.

PARAMETRIC RECOIL ANALYSIS
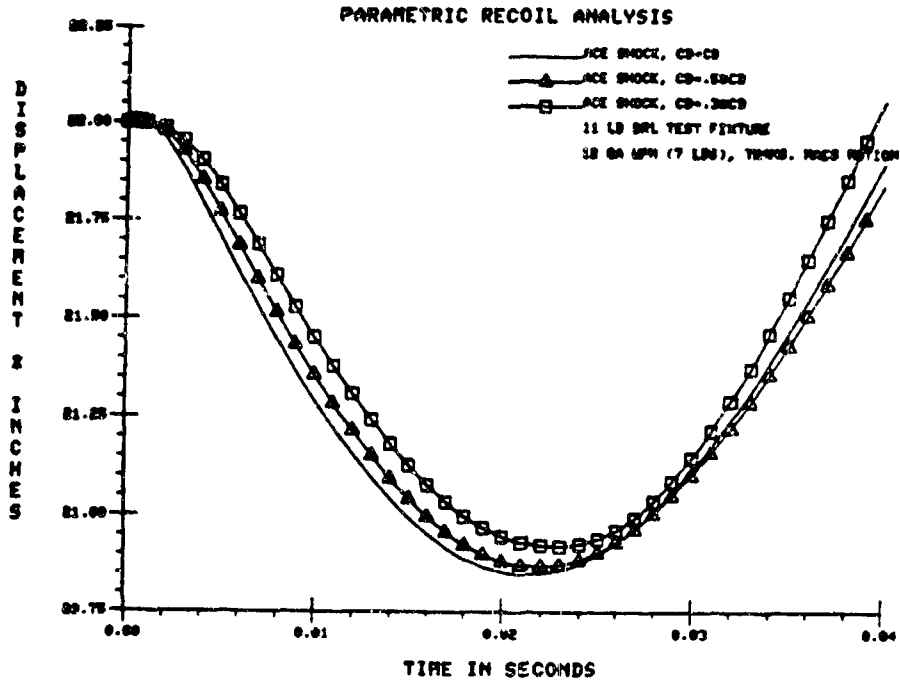
Figure 19.   Displacement versus time for shoulder mass

PARAMETRIC RECOIL ANALYSIS
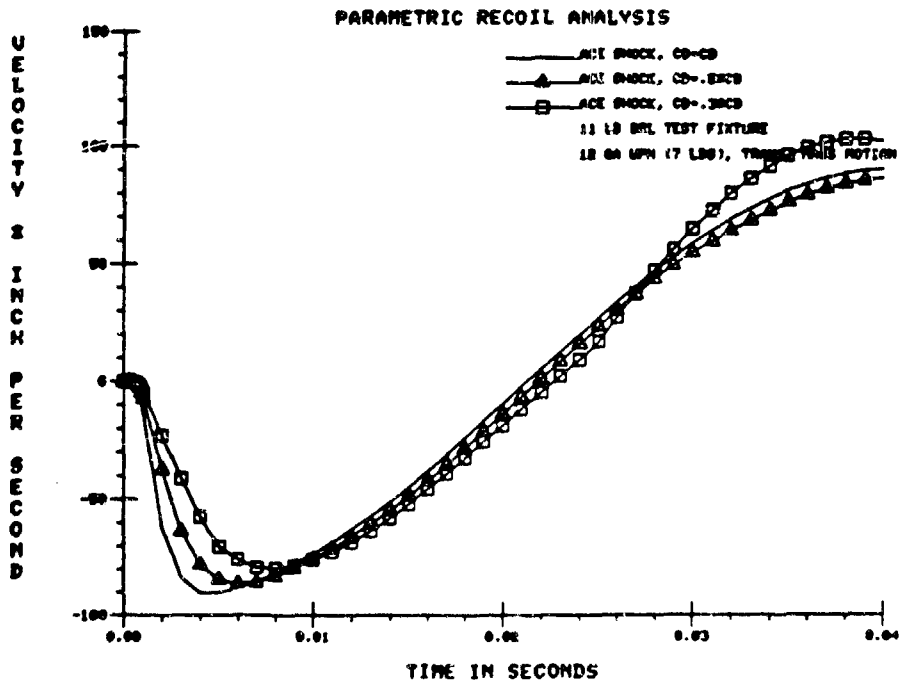
Figure 20.   Velocity versus time for shoulder mass
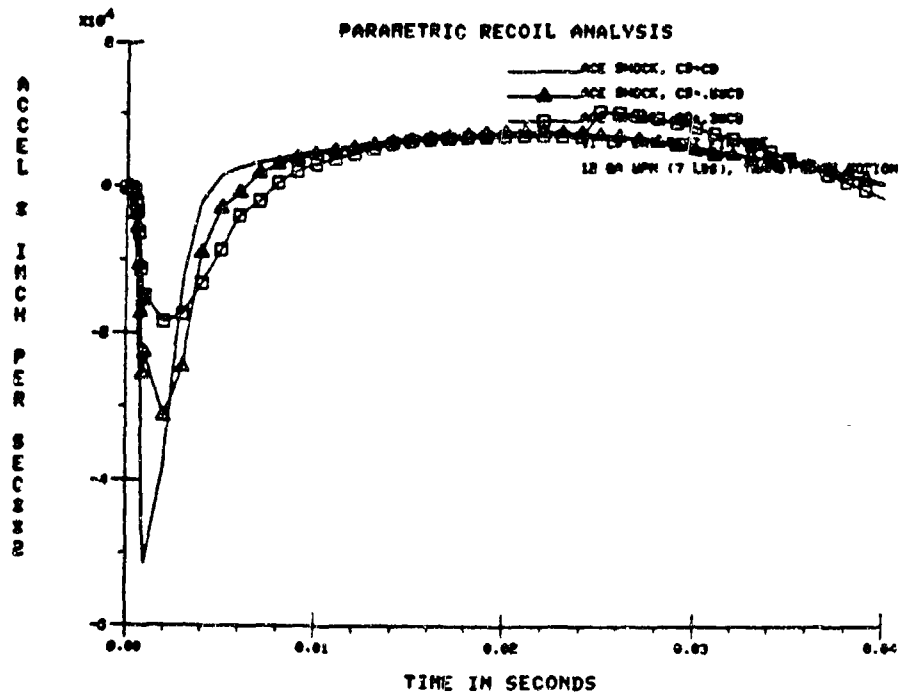
Figure 21.   Acceleration versus time for shoulder mass
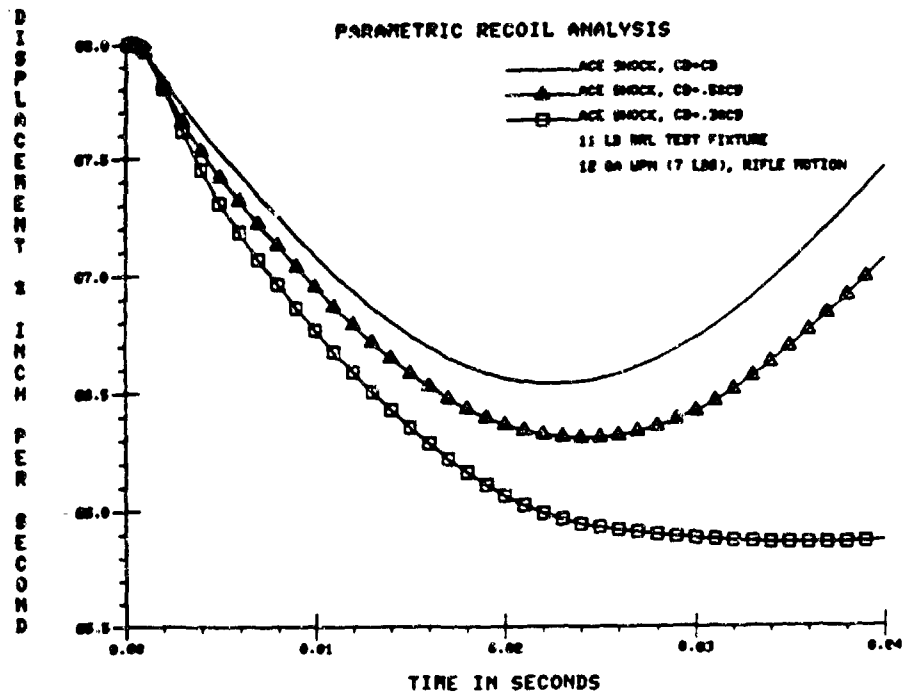
Figure 22.   Displacement versus time for rifle

PARAMETRIC RECOIL ANALYSIS
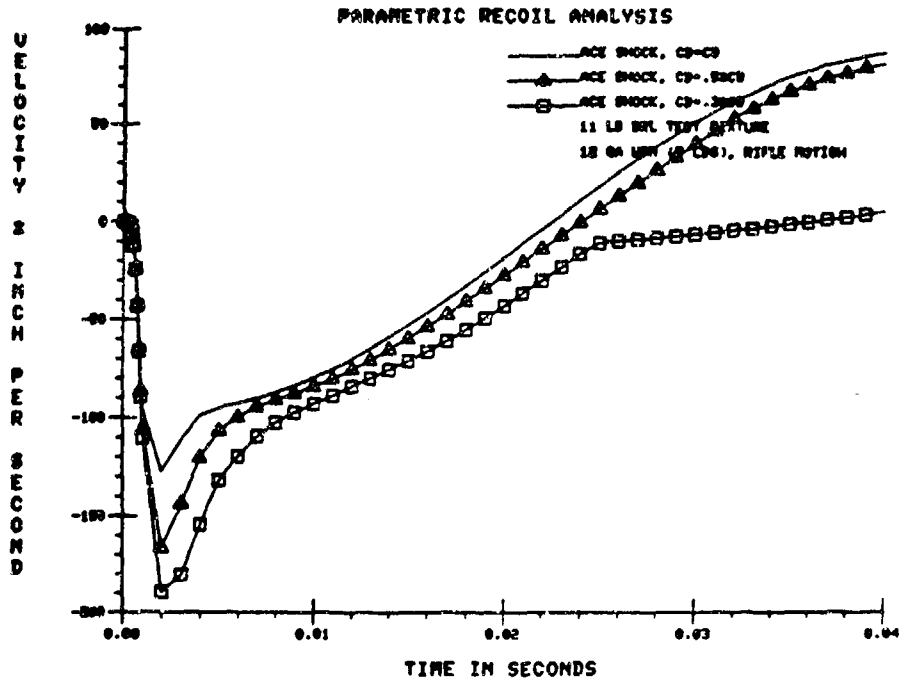
Figure 23. Velocity versus time for rifle
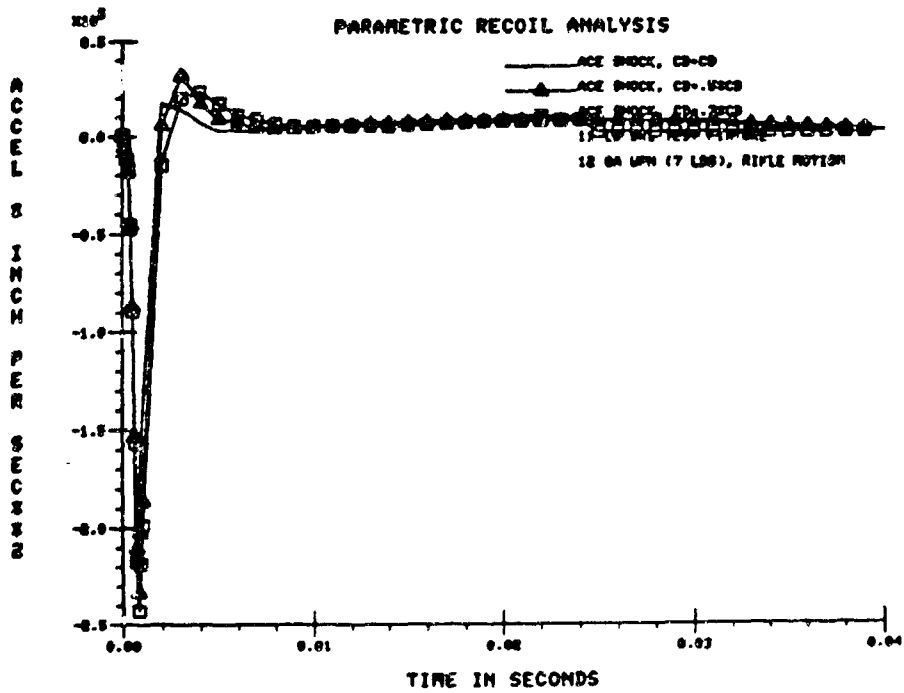
Figure 24. Acceleration versus time for rifle

PARAMETRIC RECOIL ANALYSIS
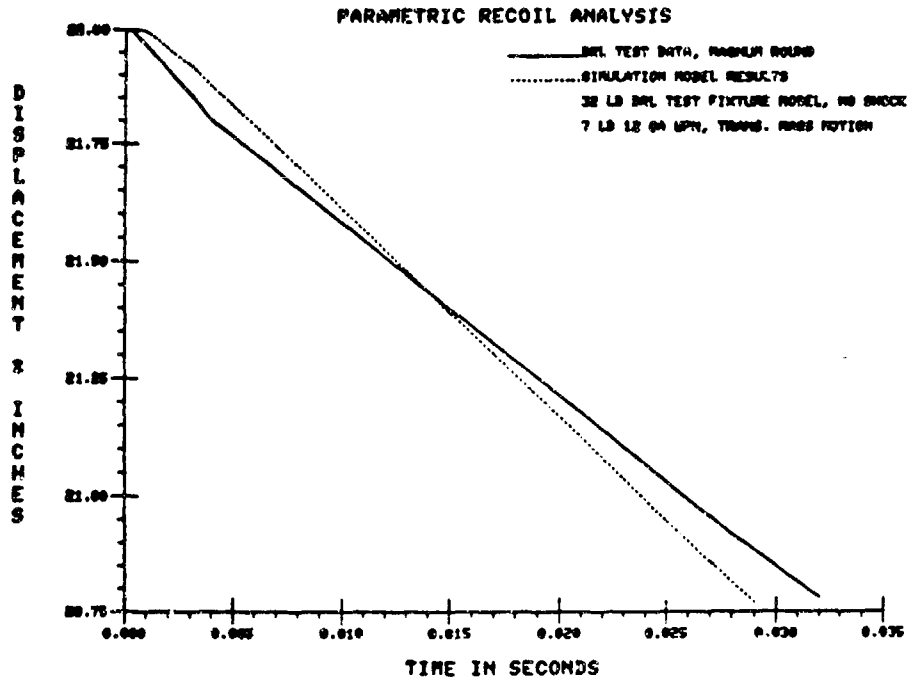
Figure 25. Displacement versus time for shoulder mass

PARAMETRIC RECOIL ANALYSIS
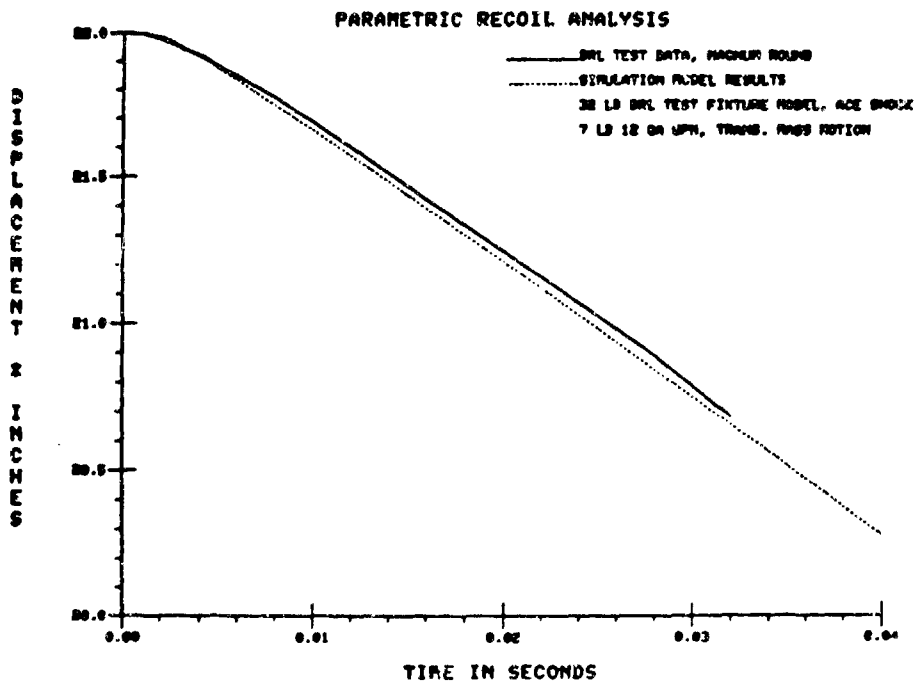
Figure 26. Displacement versus time for shoulder mass

PARAMETRIC RECOIL ANALYSIS
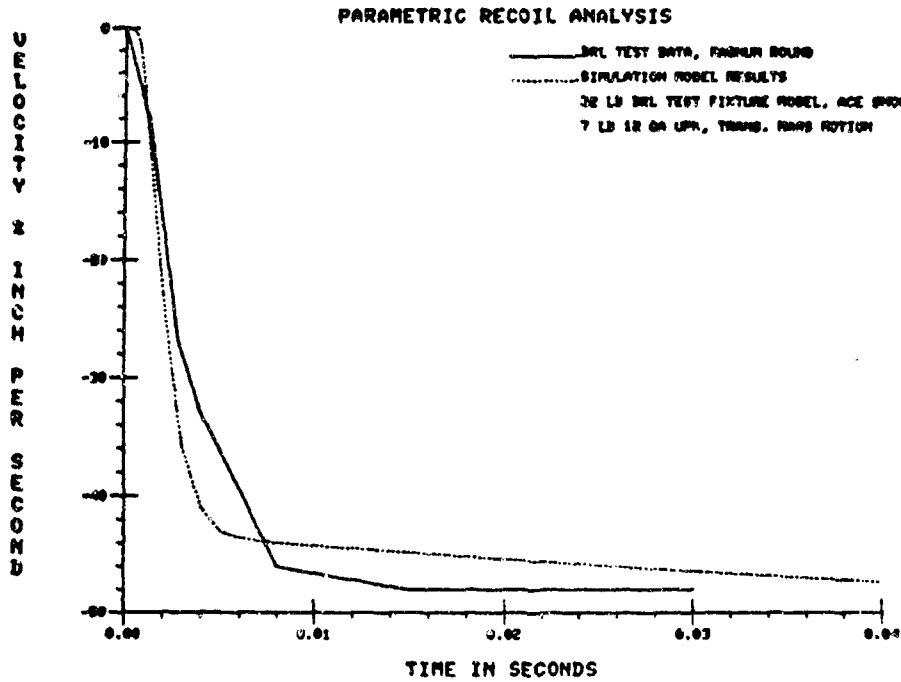
Figure 27. Velocity versus time for shoulder mass

PARAMETRIC RECOIL ANALYSIS
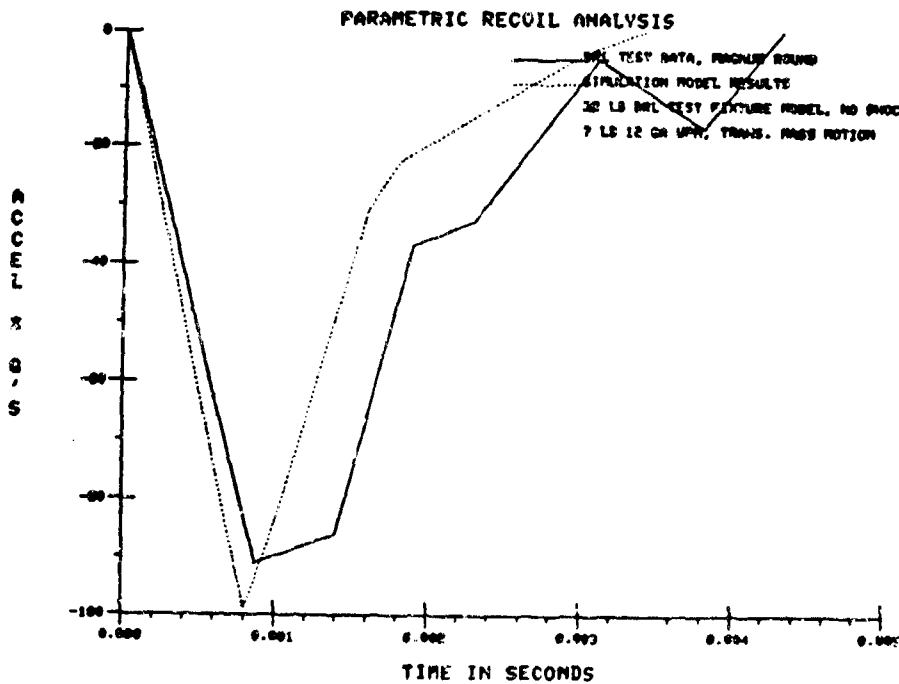
Figure 28. Acceleration versus time for shoulder mass

224

BENZKOFER

REFERENCES

1.   DADS 2D/3D Theoretical and User Manuals, University of Iowa, Iowa City, IA, 1982.

2.   Thomas D. Hutchings and Albert E. Rahe, "Study of Man-Weapon Reaction Forces Applicable to the Fabrication of a Standard Rifle Firing Fixture", Technical Report, Gen. Thomas Rodman Laboratory, Rock Island Arsenal, IL Oct 1975.

3.   Philip D. Benzkofer, "Dynamic Analysis of a Hand-Held Weapon", proceedings of the Sixth U.S. Army Gun Dynamics Symposium, May 1990.

4.   Philip D. Benzkofer, "Dynamic Analysis of the Caliber .45 M1911A1 Pistol", Technical Report, U.S. Army Armament Research, Development and Engineering Center, ARDEC, Picatinny Arsenal, NJ, Dec 1989.

5.   Philip D. Benzkofer, "Precision Aircraft Armament Control Experiment Armament System Dynamics", U.S. Army Armament Research, Development and Engineering Center, ARDEC, Picatinny Arsenal, NJ Jan 1988.

6.   Philip D. Benzkofer, "An Evaluation of the Dynamics Inherent in an Advanced Primer Ignition Weapon System", Technical Report, U.S. Army Armament Research, Development and Engineering Center, ARDEC, Picatinny Arsenal, NJ, Jan 1988.

7.   Philip D. Benzkofer, "Dynamics of High Cyclic Rate Weapon Systems", proceedings of the Fifth U.S. Army Gun Dynamics Symposium, Sep 1987.

8.   Philip D. Benzkofer, "Automated Dynamic Analysis in Support of a Future Air Defense Test Bed", Technical Report, U.S. Army Armament Research, Development Center, ARDC, May 1986.

9   Philip D. Benzkofer, "Automated Dynamic Analysis of Weapon Systems", proceedings of the Fourth U.S. Army Gun Dynamics Symposium, May 1985.

10.   Philip D. Benzkofer, "Dynamic Analysis of the 20mm General Purpose Heavy Machine Gun", proceedings of the Third U.S. Army Gun Dynamics Symposium, May 1982.

11.   Philip D. Benzkofer, Master of Science Dissertation, "An Equation-Generating Computer Code for the Dynamic Analysis of a Class of Mechanisms", University of Iowa, College of Engineering, Graduate College, Dec 1980.

SIMULATION OF TANK CANNON LAUNCH DYNAMICS

*J. Bornstein, D.S. Savick, D.H. Lyon, E.M.Schmidt
J. Kietzman & D. Deaver
U.S. Army Research Laboratory
Weapons Technology Directorate
Aberdeen Proving Ground, MD 21005-5066

ABSTRACT

Improvements have been made in a suite of computer simulations designed to model the launching of saboted, fin-stabilized projectiles from smooth bore guns. These modifications include modeling of the projectile release from the gun tube, subsequent sabot petal shape alteration because of the release of the gun tube constraints on the launch package and inclusion of more realistic initial conditions for the sabot discard model. Inclusion of these modifications has altered the resulting initial linear and angular motion of the projectile as it enters free flight from the motion reported in earlier papers. It has also modified the degree of agreement with experimental results. Additionally, mechanisms now exist within the model to provide some variability in the initial free flight projectile motion, resulting in target impact dispersions, heretofore not present in this simulation suite.

*BIOGRAPHY
PRESENT ASSIGNMENT: Aerospace Engineer, Advanced Weapons Concepts Branch, Weapons Concept Division
PAST EXPERIENCE: Aerospace Engineer, Fluid Physics Branch, BRL concerned with investigation of launch dynamics for large and medium caliber ammunition.
DEGREES HELD: PhD, Aeronautics & Astronautics, Polytechnic Institute of Brooklyn

INTRODUCTION

A principal goal of modelling the launch process for direct fire ammunition is to correctly predict the impact of rounds on target. Once this is achieved, the sensitivity of impact to variations in launch conditions can be studied for the purpose of analyzing bias and dispersion. A previous paper[1] discussed the application of a suite of computer simulations to describe the launch process for saboted 120mm tank main gun ammunition, including gun dynamics, in-bore projectile motion, and sabot discard. The primary elements of this simulation suite, also used in the current implementation, are "The Little Rascal"[2] gun and in-bore projectile Dynamics model and the AVCO sabot discard model[3] as modified by Sepri[4]. Predicted impacts for 120mm training ammunition were compared with experimental results. Discrepancies between prediction and test results were noted and suggestions for further improvements of the model, which might lead to the resolution of these disparities, were mentioned.

The current paper discusses three extensions of the earlier model. The first, developed by Kietzman[5], examines the initial stage of the sabot discard process immediately after the launch package exits the muzzle and is released from the constraint of the gun tube. At this point in the projectile trajectory, the relatively elastic sabot petals have been deformed from their initial shape through interaction with the gun tube resulting from in-bore balloting motion. Once released from the gun tube, the petals are free to return to their original, undeformed state. This latter process is referred to as sabot decompression. The resulting redistribution of energy and momentum among the individual components comprising the launch package (three or more sabot petals and the projectile) can modify both the linear and angular motion of the projectile.

In his original work, Kietzman simplified the problem by assuming that both the front and rear bore-riding surfaces are released simultaneously from the constraints of the gun tube. Given the relatively high projectile velocity at the muzzle and fairly close spacing of the two boreriding surfaces, it was presumed that the time span required for passage of the two surfaces by the muzzle would be small compared to the time required for the decompression process to finish. Subsequent computations showed that this assumption was incorrect. In the second extension, Deaver[6] modified the analysis to consider the sequential release of the front and rear bore-riding surfaces, together with the interaction between the launch package and gun tube during this transitional phase.

The final extension of the model suite is the use of a more complete set of initial conditions for the sabot discard model. In the earlier paper, it was assumed that the sabot is firmly attached to the penetrator and shares a common pitching motion during sabot discard initiation. In the current implementation, individual pitch and yaw rates are specified for each petal and a separate pitch rate is specified for the penetrator. Inclusion of projectile release from the gun, sabot decompression and more complete initial conditions for sabot discard have resulted in changes of the predicted target impact point and have modified the degree of agreement with experimental data. The sensitivity of these enhancements of the initial roll orientation of the projectile within the gun has also injected mechanisms that produce target impact dispersion.

SABOT DECOMPRESSION MODEL

During in-bore travel, projectiles are subjected to lateral loads brought about by both curvature of the bore and motion of the gun tube. At the same time, the projectile remains radially constrained, leading to elastic deformation of both the penetrator and sabot petals. The majority of this deformation normally occurs to the sabot petals. Since the forces exerted by the gun

tube upon the sabot elements are directed inward toward the centerline, the induced stress will be compressive. Once the projectile exits the muzzle, the radial constraint is removed, permitting the petals to return to their original shape and giving each sabot element a linear and angular velocity relative to the penetrator.

The model developed by Kietzman describes the situation for a projectile consisting of a rigid penetrator surrounded by three rigid sabot petals. Extension of the model for systems consisting of four or more sabot petals can, however, be easily accomplished. Following the lead of lumped parameter in-bore dynamics models, e.g., "Little Rascal", the forces resulting from interaction among the four components are modeled using six linear springs, with two springs connecting each sabot petal to the penetrator (see Figure 1). The contact points for each spring are located on the longitudinal axes of the appropriate bodies, at axial positions roughly corresponding to the locations of the front bore rider and rear obturator.

The model begins with the state of the projectile immediately before it exits the gun tube. At this stage, the sabot is represented as a solid annular body surrounding the penetrator and connected to it by the linear springs. The initial compression of each spring is determined by the location of the projectile axis with respect to the tube center. The "Little Rascal" simulation is used to provide the initial position and orientation of the projectile.

The Kietzman model assumes that the launch package is ejected from the gun tube instantaneously, i.e., the radial constraints on both bore-riding surfaces are removed simultaneously. Once this occurs, the petals are no longer connected to one another, and each petal is affected only by interaction with the penetrator. Thus, the effect of any side forces acting between sabot petals is neglected.

Another limitation of this model is the treatment of the sabot compressibility. While the overall volumes of the actual petals compress, the model assumes that all the compression effects can be described by a spring placed between a rigid body petal and a rigid body penetrator. This implies that all of the energy of sabot compression is transformed into kinetic energy of the petal and penetrator, rather than into other effects, such as deformation or vibration of the petal itself.

The mechanics of the simulation are centered about the temporal integration of equations defining Newton's second law

$$\sum F_{x_i} = m\ddot{x}_i \tag{1}$$

$$\sum F_{y_i} = m\ddot{y}_i \tag{2}$$

$$\sum F_{z_i} = m\ddot{z}_i \tag{3}$$

Euler's equations of motion ,

$$\sum M_{x_i} = I_{xx_i}\dot{\omega}_{x_i} + (I_{zz_i} - I_{yy_i})\omega_{y_i}\omega_{z_i} \tag{4}$$

$$\sum M_{y_i} = I_{yy_i}\dot{\omega}_{y_i} + (I_{xx_i} - I_{zz_i})\omega_{z_i}\omega_{x_i} \tag{5}$$

$$\sum M_{z_i} = I_{zz_i}\dot{\omega}_{z_i} + (I_{yy_i} - I_{xx_i})\omega_{x_i}\omega_{y_i} \tag{6}$$

and the orientation of each body in space

$$\dot{\psi}_i = (\omega_{y_i} \sin \phi_i + \omega_{z_i} \cos \phi_i) \sec \theta_i \tag{7}$$

$$\dot{\theta}_i = \omega_{y_i} \cos \phi_i - \omega_{z_i} \sin \phi_i \tag{8}$$

$$\dot{\phi}_i = \omega_{x_i} + (\omega_{y_i} \sin \phi_i + \omega_{z_i} \cos \phi_i) \tan \theta_i \tag{9}$$

for each of the four bodies considered in the simulation. The parameters ψ, θ, and ϕ represent Euler angles describing the rotation of a point from the inertial coordinate system into the non-inertial body fixed systems employed within the simulation and are chosen as a "3-2-1" system.

To simplify the integration process, multiple coordinate systems are used. The majority of the computations and the reporting of results is done in an inertial system. For convenience, the current version of the model employs the same coordinate system as the Little Rascal model. Four separate body-fixed coordinate systems have also been defined to simplify the computation of angular velocities. Each of these coordinate systems is centered at the body center of gravity (c.g.).

For the integration process, the system of equations is reformulated into a system of 48 first order differential equations, 12 equations describing the motion of each of the 4 bodies. The model uses the IMSL subroutine DIVPRK[7], which employs fifth and sixth order Runge-Kutta-Verner methods to solve the initial value problem. In its current configuration, a complete run for the model requires a few minutes time on a VAX8600 operating in a multi-user environment. Since there are no external forces acting upon the system, checks for the conservation of linear momentum, angular momentum, and total energy are performed at each time step to ensure the correctness of the integration process.

APPLICATION OF THE SABOT DECOMPRESSION MODEL

A series of computations was performed for an XM866 fin stabilized, discarding sabot training practice (TPFSDS-T) round fired from the 120mm M256 main gun of an M1A1 tank. Three cases were examined, each representing one of the three gun tubes discussed in the original paper by Lyon et al. Results from the "Little Rascal" in-bore projectile dynamics model were used to provide initial conditions. For the simulation, the flight body mass was 2.73 kg, the total launch package mass was 5.43 kg and the c.g. was 0.216 meter from the projectile base. These values differ somewhat with those used in the earlier paper but more closely represent measured values.

In both the in-bore dynamics and sabot decompression models, the interaction between each sabot and the penetrator is assumed to take place at a single contact point rather than spread over a circular arc. Thus, the compression of the individual springs will vary as the initial roll angle is modified, changing the magnitude and direction of the net forces initially acting upon the penetrator and affecting projectile trajectories once the sabots are decompressed. This apparently artificial variation of force is, to some degree, mirrored in reality. Lyon[8] has shown that the force-displacement relationship at the forward and rear bore riders of real sabots depends on the roll orientation of the sabot, i.e., location of the interfaces between petals.

Based upon the simulation results, the complete decompression process, from the point that the front bore rider exits the gun until the sabot attains its initial undeformed state, requires approximately 0.5 ms for a 120mm saboted training round. Some variation in this figure does

occur because of differing initial sabot deformation brought about by differing in-bore trajectories, gun-tube bore straightness profiles and initial roll orientation, does occur. The sabots should be fully decompressed when the projectile is approximately 0.8 meter downrange.

Sabot decompression has a negligible effect upon the axial penetrator velocity component (u). It does, however, have a measurable impact upon both transverse components. For example, the vertical velocity component for an XM866 round launched from gun #104 varies between 0.71 m/s and 0.95 m/s. This differs substantially from the initial muzzle value of 0.58 m/s, that was used in earlier simulations. In the horizontal direction, the velocity varies between -0.65 m/s and -1.0 m/s compared with a value of -0.76 m/s at the muzzle.

Figure 2 displays the trajectories of rounds launched from the three gun tubes used in the earlier paper of Lyon et al. For purposes of comparison, the experimentally measured values at a point 1.8 meters downrange have also been included. It should be noted, however, that at the 1.8 meter downrange position, sabot discard disturbances may already be having some effect upon projectile motion. Also, in the experimental measurements, a muzzle bore telescope was used to orient the gun in the range coordinate system. The telescope has mounting feet approximately 70 mm and 301 mm uprange from the muzzle when the unit is fully seated in the gun tube. The local slope of each gun tube at those points was used to rotate the simulation results into a coordinate system consistent with the measurements. This convention will be used in the further comparisons of simulation and experimental results.

From the figure, it is apparent that the decompression process adds not only a bias but also a variability to the projectile trajectory. The introduction of a large variability is especially true in the cases of guns 84 and 85 which, as noted by Lyon et al., contain significant bore curvatures. The large curvature results in major in-bore accelerations of the launch package, with subsequent deformation of the sabot petals. By lumping all the compressibilty of each sabot petal along a single axis (represented by the spring), there is a tendency for the simulation to enhance the influence of initial roll orientation. Although differences exist between trajectories determined by simulation and those reported from experiments, the simulations do tend to follow the trends seen in the test results, suggesting that it captures many of the essential elements of the actual physical processes.

Projectile angular rates are also affected by the decompression process. Figure 3 depicts the rates predicted by the simulation, together with the rates determined from measurement. Here, the agreement between simulation and reality is far less encouraging, suggesting that a more detailed model is required.

PROJECTILE RELEASE MODELING

One of the principal assumptions in the original sabot decompression model was that one could allow both the front and rear bore-riding surfaces of the launch package to be simultaneously released from the constraints of the gun tube. This was based upon the presumption that the decompression process would be relatively long compared with the elapsed time between passage of the two bore-riding surfaces by the muzzle. Unfortunately, this is not truely the case. For the cases currently being examined, decompression requires approximately 500 microseconds while the rear bore rider passes the muzzle roughly 90 microseconds after the front bore rider. Thus for a appreciable portion of the decompression process, the front of each sabot petal is free to move in space, while the rear portion is still constrained and driven by the motion of the gun.

Deaver modified the original model by dividing the sabot decompression into a two-stage process. The initial phase begins as the front bore-riding surface reaches the muzzle and lasts until the rear obturator reaches the muzzle. During this stage, the front spring between each sabot element and the penetrator is permitted to decompress and the front portion of each sabot is permitted to interact only with the penetrator. At the same time the rear portion of the launch package is treated as a single solid body, constrained to follow the motion of the gun tube. Given the relative masses of gun tube and launch package, it is assumed that the gun motion will be determined primarily by its vibrational characteristics and that the solutions obtained by the lumped parameter gun dynamics models, which do not treat the release process, remain valid. During the second phase of the model, both front and rear bore-riding surfaces are free of the gun, and the model proceeds according to the original formulation of Kietzman.

Figures 4 and 5 depict the projectile trajectory and angular motion after sabot decompression, as obtained using the modified version of the model. Comparison with Figures 2 and 3 indicates that while introduction of sequential release of the front and rear bore-riding surfaces has increased the variability of linear and angular motion with roll orientation, it has not drastically altered projectile behavior. Thus, some other aspect of the model must be responsible for its inability to reproduce the angular rate of the projectile.

SABOT DISCARD MODEL

The AVCO sabot discard code describes the flight dynamics of the sabots and projectile and calculates the forces and moments acting on the projectile. The flight dynamics are affected by sabot interactions with the projectile. If the forces and moments are distributed asymmetrically around the projectile, the penetrator flight path will be disturbed. Three types of interactions are considered in the code. First is the contact or mechanical interaction that occurs as the sabot pivots off the projectile. Second is the aerodynamic interaction caused by pressure variations because of the sabot shock waves impinging on the projectile. Third is aerodynamic interaction caused by the sabots as they lift off and temporarily shield the fins from the oncoming flow causing an uneven pressure distribution across the control surfaces.

The code requires a number of parameters to make the necessary calculations. These include the geometry of the sabot, the initial position of the sabot segments with respect to the penetrator, the aerodynamic coefficients for the bodies and their inertial properties.

The version of the code used in the earlier paper by Lyon et al assumed that penetrator and sabot initially behaved as a single rigid body which could possess only a pitching motion. This should approximate the expected behavior of an inelastic, saboted round, subject to in-bore balloting motion, as it exits the muzzle. For those simulations, the projectile pitch rate was provided by the gun dynamics codes Rascal and SHOGUN[9].

The current version of the discard model permits each of the individual sabot petals to have both a linear and angular velocity with respect to the penetrator. Thus, the sabot and penetrator can act as elastic bodies within the gun, storing energy through compression of the sabot petals and ultimately causing motion of the petals with respect to the penetrator as the energy is released when the round leaves the tube.

While the sabot petals can have independent linear velocities and rates at the outset of the integration process, it is assumed that the position and orientation of each petal with respect to the

penetrator are identical to those found before the round was launched. Strictly speaking, there is an improper matching of conditions between the sabot decompression code and the discard model. However, given the small magnitudes of the angles and offsets between the penetrator and sabot elements given by the decompression code, the error introduced was presumed to be small.

Both versions of the program yield two output parameters that are used to compute the total projectile jump: $\dot{\alpha}$, the angular rate of the projectile, and α, the c.g. trajectory of the projectile. The parameters are computed by integrating the forces and moments applied to the projectile. Results obtained through the application of the code are discussed in the following section.

COMPARISON WITH EXPERIMENTAL RESULTS

To evaluate the ability of the model to accurately predict target impact and the magnitude of the intermediate disturbances acting upon the projectile, comparisons were made with earlier experimental data for XM866 projectiles fired from an M1A1 tank. In its current configuration, the sabot discard code is limited to the treatment of cases for which the initial angular motion of the penetrator is a pure pitching motion. Thus, only two computations were performed for each of the three gun tubes considered in the investigation: one case in which the projectile was pitching up and another in which it was pitching down. For each gun tube these two situations occur for roll orientations that are approximately, though not exactly, 180° apart.

Figure 6 presents a comparison of the target impacts predicted by the current version of the simulation suite with the results of the earlier paper and the centers of impacts obtained from test firings XM866 projectiles from those gun tubes[1]. Two features become immediately apparent. First is an increased spacing between impact locations as a function of gun tube. For example, the impacts for rounds launched from gun #85 have moved over 0.5 mil toward the left, somewhat closer to the center of impacts from firing exercises. Second is the large variation of impact point for projectiles launched from the same gun tube but with differing initial roll orientation. This is particularly noticeable for the projectiles fired from gun tube #84.

To determine which of the simulation program modifications has provided the more significant contribution to the observed change in projectile impact location, the simulation was run with the sabot decompression program (simultaneous release), but with the older version of the sabot discard code, which only permits a uniform initial pitching motion for both the penetrator and sabot petals. The results of this computation for projectiles fired from gun #84 is shown in Figure 7. At least for this case, it can be clearly seen that the addition of the sabot decompression code minimally altered the trajectory of the projectile. This suggests that the introduction of asymmetrical initial conditions for the discard code had the greatest impact. The initial conditions are, however, the result of the decompression code, albeit indirectly. Additionally, the sabot decompression process contributes substantially to the angular projectile motion (though discrepancies between computed and measured values exist). Thus, it is difficult to say which model extension has made the greater contribution to the changes in the predicted impact location.

Finally, while the impact locations predicted by the simulation have moved toward the impacts measured during test firings, significant differences between the two values still exist, implying that the current model still does not fully capture the physics of the launch process.

CONCLUDING REMARKS

This paper has discussed an extension of the suite of models being used at the U.S. Army Research Laboratory to quantitatively describe the launch dynamics of large caliber ammunition for direct fire weapons. The extension has considered the process by which sabot petals, deformed by in-bore balloting motion, decompress once the constraints of the gun tube are released, causing the relative motion between each of the petals and the flight body. It has also used an improved version of the AVCO sabot discard code which permits the initial state of the projectile to include the relative motion of the penetrator and sabot petals. While the results obtained by using this improved version of the model show somewhat better agreement with experiment than the previously reported model, room for further improvement exists.

REFERENCES

[1] Schmidt, E.M., Savick, D.S., Lyon, D.H. & Plostins, P., 1990, "Comparison of Computed and Measured Jump of 120mm Cannon," Sixth U.S. Army Gun Dynamics Symposium.

[2] Erline, T.F., Kregel, M & Pantano, M., 1990, "Gun and Projectile Flexural Dynamics Modeled by 'The Little Rascal' - A User's Manual," Technical Report 3122, U.S. Army Ballistic Research Laboratory, Aberdeen Proving Ground, MD (July).

[3] Siegelman & Crimi, P., 1979, "Projectile/Sabot Discard Aerodynamics," 1979, Contractor Report CR-00410, U.S. Army Ballistic Research Lab, Aberdeen Proving Ground, MD (Dec).

[4] Sepri, P., 1986, "Aerodynamic Interaction Between Projectile Fins and Sabot Petals," U.S. Army Ballistic Research Lab, Aberdeen Proving Ground, MD 21005 (Sept).

[5] Kietzman, J.W., "Sabot Decompression and its Effect upon the Angular Rates of APFSDS Sabots and Penetrators," U.S. Army Research Laboratory, Technical Report in preparation

[6] Deaver, D., "Private Communication"

[7] IMSL, Inc, 1987, Math/Library User's Manual, pp. 633-639.

[8] Lyon, D.H. "Radial Stiffness of Several 120mm Projectiles," Technical Report to be published, U.S. Army Ballistic Research Laboratory, Aberdeen Proving Ground, MD.

[9] Hopkins, D.A., "Modeling Gun dynamics with Three- Dimensional Beam Elements," Sixth U.S. Army Symposium on Gun Dynamics, 1990

LIST OF SYMBOLS

F force
M moment
m mass
u,v,w x,y & z velocity components
X,Y,Z coordinates in the inertial coordinate system
x,y,z coordinates in the body-fixed coordinate system
α projectile pitch angle
ψ, θ, ϕ Euler angles
ω angular velocity
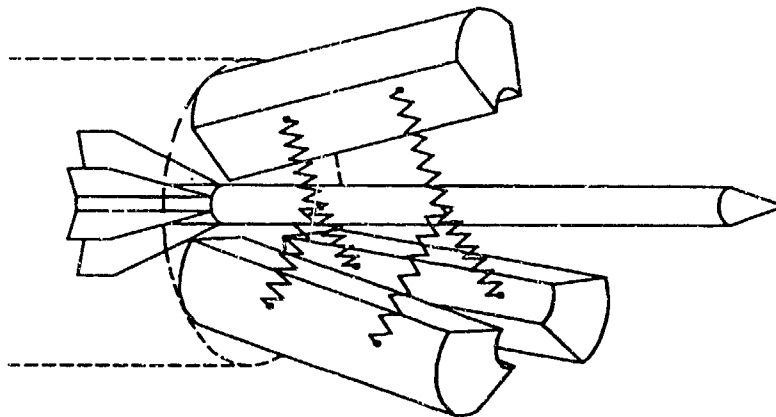
Figure 1. Geometry of projectile used for sabot decompression model
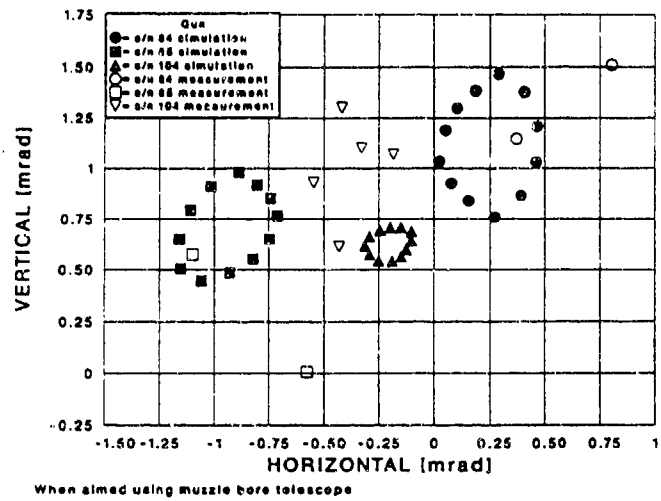
Figure 2. Projectile trajectories after sabot decompression – Kietzman model.
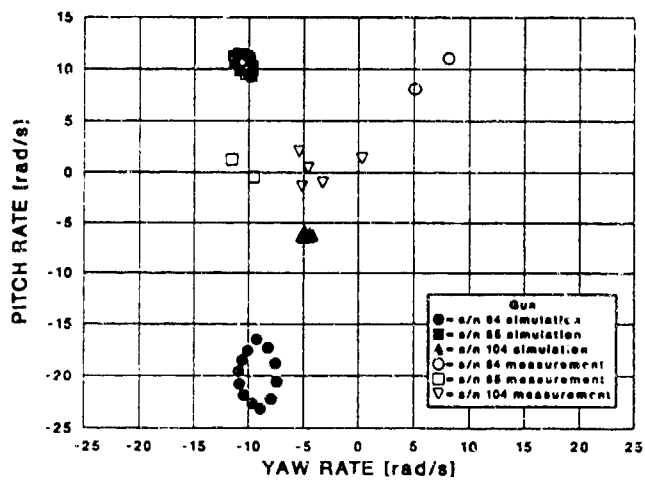
Figure 3. Projectile angular velocity after sabot decompression – Kietzman model
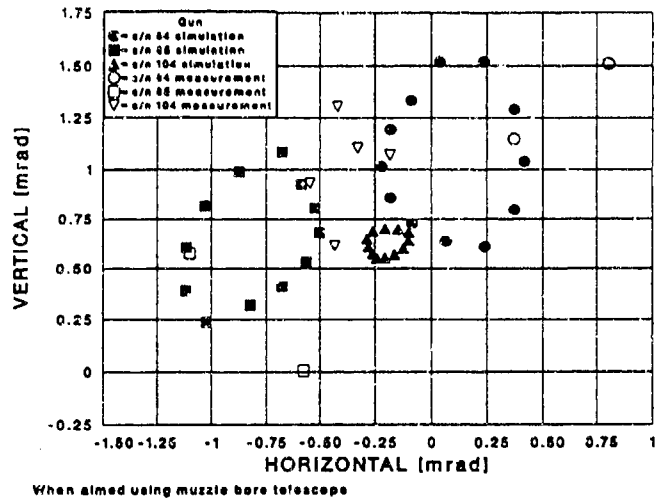
Figure 4. Projectile trajectories after sabot decompression – with sequential release of front and rear bore-riding surfaces.
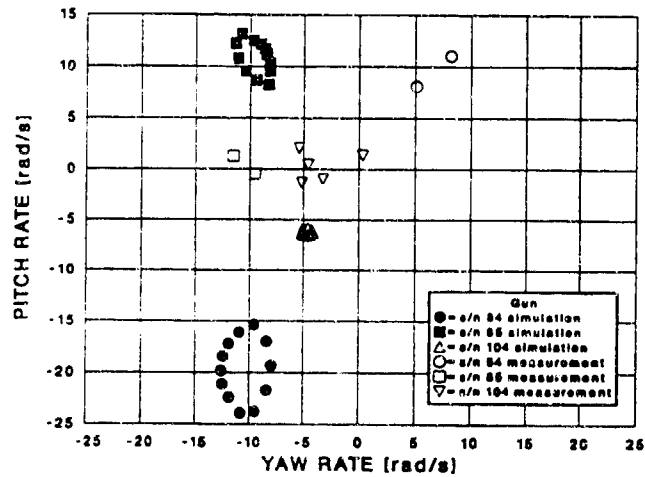
Figure 5. Projectile angular velocity after sabot decompression – with sequential release of front and rear bore-riding surfaces.

236
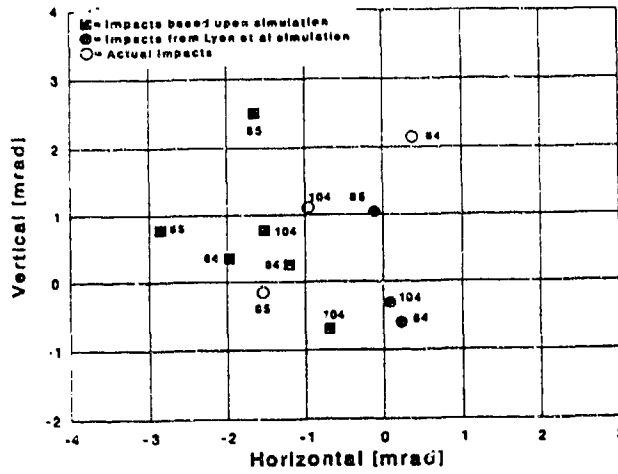
Figure 6. Comparison of impacts obtained from simulation and test firings.
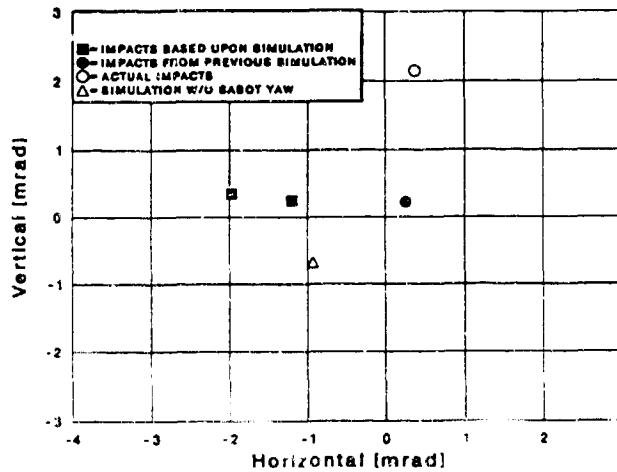
Figure 7. Comparison of impacts obtained for rounds launched from gun #84, using different simulation suites.

*TITLE: A CONSISTENT METHOD FOR DETERMINING GUN-TUBE STRAIGHTNESS ON THE M256 120MM GUN

AUTHOR: Dr. Stephen Wilkerson
U.S. Army Research Laboratory
ATTN: AMSRL-WT-PD
Aberdeen Proving Ground, MD 21005-5066

*ABSTRACTS:

Currently, each 120mm gun-tube, as part of the manufacturing and inspection process, undergoes a series of measurements to determine whether the tube's centerline profile meets critical tolerances. The measuring apparatus consists of a chain-driven plunger that is inserted down the gun-tube from the muzzle end toward the breech. At the same time, a laser device, which is positioned at the breech end of the gun-tube just in front of the forcing cone, transmits a laser signal to the plunger that records the location of the beam using a photo sensor. The "true centerline" is estimated as the straight line between the laser device and the plunger at the muzzle. Then as the plunger is inserted further down the gun-tube toward the laser, variations in the laser light are correlated with actual vertical and horizontal displacements to produce an estimate of the gun-tube's profile with regards to its "true centerline."

When a bullet is fired out of a gun-tube, the bullet is forced to follow the tube's profile. Due to the huge forces applied on the bullet by the propellant gases, considerable interaction between the bullet and gun-tube are possible during the interior ballistic cycle. These interactions manifest themselves in the form of out-of-plane vibrations. (Out-of-plane refers to any direction other than the intended axial or down bore motion.) Shot to shot variations in those vibrations can lead to scatter and a loss of gun accuracy. Therefore, duplicating the current response of the system's dynamic behavior numerically requires an accurate representation of the gun-tube's centerline profile. This paper describes two methods for acquiring an acceptable gun-tube profile for use with numerical models of the M256 weapon system. Problems associated with the measurement techniques and the numerical modeling of this system are discussed. Recommendations in both areas are additionally made.

*BIOGRAPHY:

*PRESENT ASSIGNMENT: 10/89 to Present: Research Engineer, The Army Research Laboratory, Aberdeen Proving Ground, MD 21005-5066.

*PAST EXPERIENCE:

7/83 to 10/89: Mechanical Engineer, The Naval Surface Weapons Center, 10901 New Hampshire Ave., Silver Spring, MD 20903-5000.

1982 to 1983: Aerospace Engineer, Naval Air Systems Command, Washington, D.C.

*DEGREES HELD:

The Johns Hopkins University, Baltimore, MD. Ph.D., Department of Mechanics, April 6, 1990. Dissertation title "A Boundary Integral Approach to Three-Dimensional Underwater Explosion Bubble Dynamics."

George Washington University, Washington D.C. Masters of Science, Structural Engineering, May 1985. Thesis Title: "Ship and Submarine Response to an Underwater Explosion." GPA - 3.50.

The Johns Hopkins University, Baltimore, MD. Bachelor of Science, Mechanical Engineering, May 1982, GPA - 3.00.

A CONSISTENT METHOD FOR DETERMINING GUN-TUBE STRAIGHTNESS ON THE M256 120MM GUN

Dr. Stephen Wilkerson
U.S. Army Research Laboratory
ATTN: AMSRL-WT-PD
Aberdeen Proving Ground, MD 21005-5066

INTRODUCTION

When a gun system is fired, typically the aiming point and muzzle pointing direction do not coincide. The aim point is located as to compensate for gravity, aerodynamic drag, and some estimate for the effects of cross winds[1]. Under ideal conditions, each time the weapon is fired the projectile would impact in the exact same location. However, every aspect affecting the flight path of the projectile is not fully understood and therefore not compensated for. The term "jump" is used to classify things that are not properly balanced for by the weapons control systems. Such motions as introduced into the projectile, due to gravity-droop, projectile initial seating, sabot liftoff, thermal heating of the gun-tube, and motions which are possibly introduced by a non-straight gun-tube, are at present not considered. Since bullets are forced to follow a gun-tube's center line, which can also be affected by thermal heating conditions, gravity-droop, mount vibrations (the tank may be moving) etc., it is felt that representing this important attribute of the system accurately will be critical to any numerical simulation of the gun and projectile's dynamic response to the firing cycle. For years analysts have estimated the gun's centerline profile from measurements taken during manufacturing at Watervliet Arsenal and subsequent measurements taken occasionally at Aberdeen Proving Ground Combat Systems Test Activity (CSTA). These measurements are routinely included in numerical simulations of the gun and projectile's dynamic behavior[2,3,4]. This paper examines how these measurements are taken and how best to incorporate the data into a numerical simulation of the weapon systems performance. The paper also makes specific recommendations regarding these measurements and how they might be changed or better quantified for use with numerical formulations of gun dynamics.

BACKGROUND

Watervliet Arsenal in New York has designed and maintains equipment to measure the variations of the gun-tube's centerline profile accurately[5]. Basically, the measuring device consists of a laser which is positioned just forward of the forcing cone and a photo sensor which is attached to a plunger and pushed down the gun-tube, from the muzzle end, by a mechanical device. Initially, the plunger is inserted just into the muzzle and a straight line of sight is established between the laser device and the plunger. Then as the plunger is pushed down the gun-tube toward the laser, variations from the established straight line of sight are measured to produce a profile in the vertical and horizontal planes. A typical profile in the vertical direction is shown for gun-tube 5065 in Figure 1. A number of important issues regarding the calibration of the instrument have been and continue to be addressed by Watervliet[5]. This will be discusses in more detail later on.

On the other hand, the method currently employed at USACSTA is based on an alignment telescope which had subsequently been used at Watervliet Arsenal. The older method employed at CSTA typically requires more operator skill and is not as accurate as the method being employed at Watervliet[6] Nonetheless, efforts/proposals are underway to improve both techniques[5]. In a compatibility test between the CSTA method and Watervliet's more robust equipment, a mean discrepancy of approximately 0.07mm was observed. However, the maximum discrepancy observed was 0.25mm. It is pointed out by Weddle[6], these discrepancies are too large, particularly when two successive measurements were conducted on the same tube using the same CSTA equipment and produced a mean discrepancy of 0.02mm and a maximum of 0.06mm. In as much as the maximum discrepancy between the two methods is nearly of the same magnitude as the actual displacements being measured, this is of some concern when trying to incorporate this as a parameter in a finite element simulation of the system. It is understood that these measurements are adequate in assuring that reasonable tolerances have been achieved during manufacturing. Nonetheless, they may need additional safeguards when looking closely at tube-to-tube variations with regard to jump.
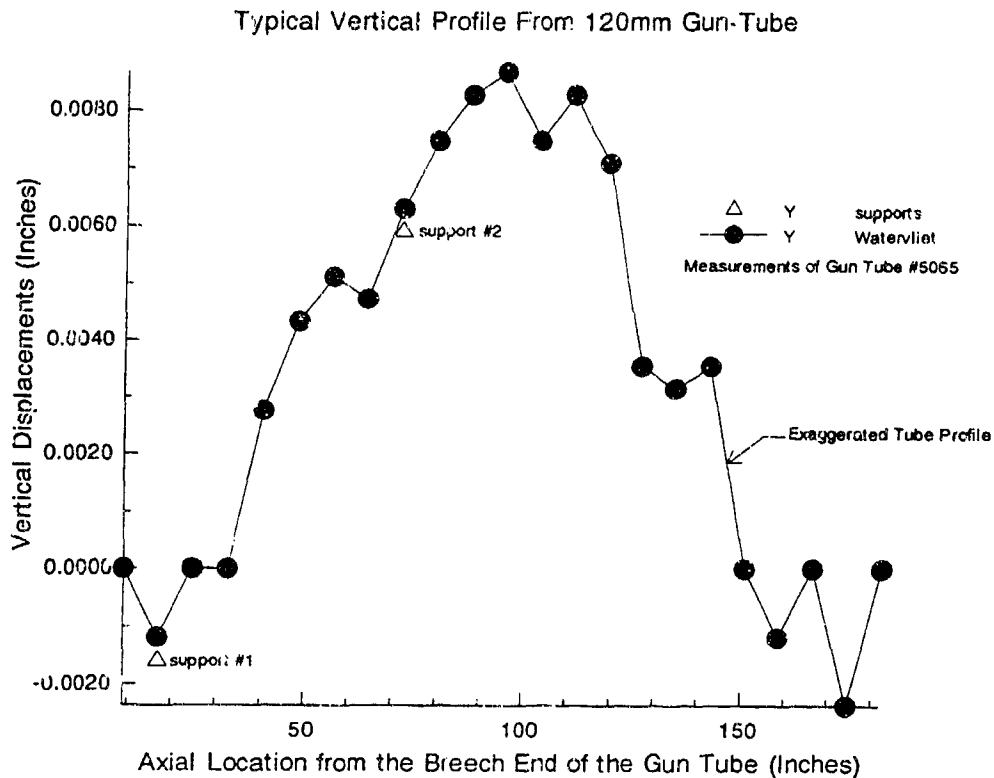
Figure 1. Watervliet measurement of gun-tube 5065.

When developing a finite element model of the gun-tube and projectile, it is desirable to include the influence of the gun-tube's profile and gravity-droop in the model. Since the gun-tube's gravity droop and actual profile are dependent on how the tube is supported as well as any additional weights that are attached to it, and since the measurement conditions are not identical to the firing conditions, this is not always a simple procedure. In the past, two basic techniques have been employed to incorporate this information in dynamic models of the system. For example, Rabern and Lewis[7], and Rabern[2] used a linear combination of a calculated gun-droop and the measured profiles and included them directly in their model. On the other hand, Hopkins[4] used the measured profile to calculate interferences between the projectile and gun-tube from the measured profile alone. Similarly, Erline et al.[5] used the profiles alone to estimate a curve representing the forcing function; typically, that curve estimate is of second order. All three methods have their merit and use the measured profile in a straightforward way. In this report, a somewhat in-depth investigation was undertaken into how the measurements were being gathered, possible sources of error, and how best to incorporate the measurements into a finite element model. In particular, this study considered the two gun-tubes that were used in the balanced breech test[8]. They were gun-tubes 5064 and 5065.

METHODOLOGY

Initially, only the measurements taken at CSTA, on tubes 5064 and 5065, were available. USACSTA measurements on those two tubes consisted of a single-pass test. Subsequently, the measured profiles taken at Watervliet Arsenal were obtained. The measurements at Watervliet typically measure the vertical profile on the initial pass and then rotated the gun-tube 180 degrees and repeated the measurement. Therefore, for that case, the Watervliet data consisted of two measurements in the vertical plane. This is important in that using the Watervliet data allowed a direct comparison with the CSTA measurements for each tube, thereby giving an estimation of error between the two measuring techniques. Furthermore, Watervliet's method, being redundant, gave more information, which was used for better estimates of the gun-tube's actual profile. In this paper, two methods are developed: the first can be used when only one pass data is available while the other incorporates the information from both tests and calculates an actual estimated profile. In both cases described here, the data from Watervliet is used. After checking Howd's[5] examination of Watervliet's methods and then reviewing Weddle's[6] methodology, it became clear that Watervliet's data was more consistent and complete for the purposes described herein.

For the first technique, method 1, Watervliet's data gave a second measurement from which to check the estimated profile. Consequently, method 1, which uses only the data from a single pass, designated y(0), is checked with the second pass, designated y(180). Conversely, method 2, which linearly combines the data from both passes for an estimated profile, verifies the estimate via the original data. This will become more evident as the methods are presented. The math involved in reducing the measured profiles is elementary, but nonetheless important in producing an accurate finite element representation of the gun-tube model. For example, the profile used in the finite element model should have the same profile as the experiment under identical test conditions. This is a simple thing to show. An illustrative example is given here. If a gun tube's finite element model is supported at the same locations and then gravity-droop is added into the finite element model, the tube will have a particular profile with respect to the supports (see Figure 2). Then if a straight line is established between the muzzle and forcing cone, (the approximate locations of the laser and plunger used in the test), then the profile as seen from that straight line should have the same shape as the measured profile in the test. What is important to note here is that the tests conducted at Watervliet are done on the gun-tube alone based on the German Method[9]. This method supports the tube at 405mm and 1853mm from the chamber end of the tube. These support locations were picked to simulate where the tube is supported in the actual recoil mechanism. Therefore, the finite element model and experiment should both have used these boundary conditions. Nonetheless, it is understood that the profile measured at Watervliet on the gun-tube alone may not have the same shape as when that particular tube is mounted in a tank.
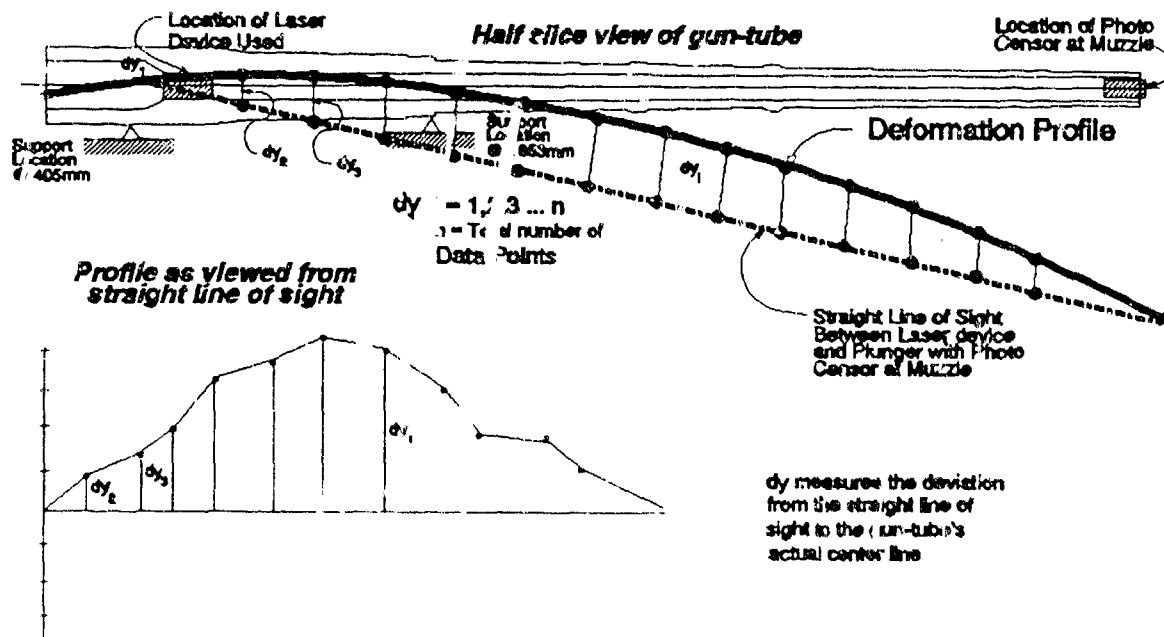
Figure 2. Technique for calculating gun-tube profile in experiment and from finite element model.

The presentations of the two methods focus on the vertical component only. This was done because the horizontal data can be applied directly and is not affected by gravity. Therefore, the need to separate the actual profile and gun-droop, caused by gravity, does not exist in that plane. The reason for wanting these two components to be separated in the vertical plane is to allow for geometry and boundary condition changes, of an actual firing test configuration, in the model. For example, when an M256 is fired in a tank, there is a breech, piston, cradle assembly, a front armored shroud attached to the cradle, a bore sight, and thermal shrouds all attached to (in one manner or another) or influencing the vertical profile of the gun-tube. By using the combination of the measured profile and an associated finite element model, it is possible to find a close estimate of the actual path that the projectile must follow down the gun-tube. This will become clear as the specifics of the methods used here are examined in detail.

METHOD # 1

Single Data Set

The initial step in method 1 is to assemble a finite element model of the 120mm M256 gun-tube alone and simulate the experimental measurements taken at Watervliet with the identical boundary and geometric properties. Since a gun-tube is similar to a long piece of pipe, a beam element model of the gun-tube's geometry is sufficient to accurately calculate displacements in the tube under specified loads[10]. For this particular model, 106 elements with varying geometric properties to account for the tapered section and changes in inner and outer diameters of the gun-tube are used. Figure 3 shows a half-plane view of the gun-tube outline used in the model. Figure 4 shows an exaggerated displacement profile, from the finite element calculation, of the gun-tube's deflection under its own weight. The figure also indicates the location of the supports at 405mm and 1853mm. Slight variations of an inch or two in the support location made almost no difference in the calculated displacements of the gun-tube's droop due to gravity. This means that if the test configuration had slight variations in the support positions, it should not have a noticeable effect. In order to relate the test configuration to the finite element calculations, two common points are required. The logical choice would be the supports, which for this case would also establish a common horizontal plane. However, the measurements taken at Watervliet are of the gun tube section that the bullet must follow and do not include the propellant chamber section near the first support. As can be seen in Figure 4, the experimental measurements do not go as far aft as the first mount. To account for this small discrepancy, this technique uses a correction factor which is equal in magnitude to the displacements caused by gravity-droop, in that same range, as calculated in the finite element model for gravity-droop alone. As can be seen in the figure, the correction is small in comparison with the particular deformed profile being examined. As it turned out, though, the addition of a correction factor was not necessary. Therefore, assuming that the support was at the same location as the laser device was sufficient to assure accuracy in both methods being presented. Just the same, method 1 includes a correction factor while method 2 does not. Figure 4 indicates the approximation line of sight that is used in the experiment to measure the tube's profile. If, for example, the tube's manufacturing was "perfect," (i.e., no bending of the gun-tube was done and there were no manufacturing irregularities; therefore only gravity-droop would exist.) then the profile measured would look as if it were being viewed from this straight line. However, this is not the case. In fact, due to extensive cold working of manufactured tubes, the actual gun-tube which has residual stresses in its material at different locations has a better profile than what would be observed in an un-worked "perfect" gun-tube. Gun-tube 5064's profile, as measured at Watervliet, is shown in Figure 5. Now it is understood that the actual profile measured is a linear combination of the gun-tube's actual profile in a gravity-free environment plus the displacements as imposed by gravity:

$$y_{M_i} = y_{A_i} + y_{g_i} \tag{1}$$

where y_M is the measured displacements, y_A is the actual curvature of the tube independent of gravity, y_g is the curvature as introduced by gravity, and the index i represents i=1,2,3,...,n where n=number of data points. Watervliet measures y_M twice and uses the data to calculates y_A. The first measurement is taken, giving y(0); and then by rotating the gun-tube 180 degrees and re-measuring the profile, giving y(180), Watervliet can assure that these tolerances are adhered to during the manufacturing process while getting a reasonable estimate of y_f. For this study, y_A is the only parameter of importance for the finite element model because y_g can be obtained with a high degree of accuracy with the finite element model. Once a good estimate of y_A is obtained from the experiments, then using the displacements for gravity found in the finite element calculation with the same supports, the results from the experiment can be duplicated. Therefore, the same finite element model, as assembled with the y_A profile as part of its shape, can then be re-supported in a M256 cradle with the breech, recoil-mechanism, bore sight, bore-evacuator, thermal shrouds, etc; and gravity can be added back into the model to find the actual shape of the gun-tube inside the tank. In summary, the finite element model will incorporate any additional droop as introduced into the system by weights attached on the tube and have a realistic or accurate estimate of the gun-tube's actual profile.

In order to directly compare the finite element and measured profile, two common reference points which establish a horizontal plane must be established. An obvious choice is the two support points. These points are already used in the finite element calculation. However, as mentioned before, the experimental measurements are not taken at the first support point at 405mm, rather, the experimental measurements start from approximately 602mm or 198mm in front of the first support. Since the gun curvature due to gravity in that first 198mm is of an order of magnitude less than the measured change from one data point to the next, it would not be unreasonable to neglect this short span. Neglecting a correction factor for the
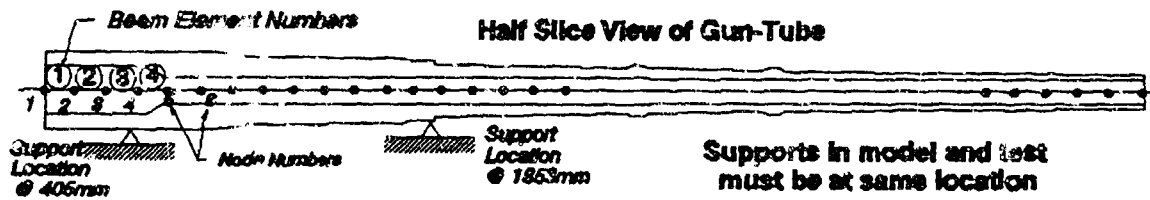
Figure 3. Half-slice view of gun-tube geometry with beam element methodology.
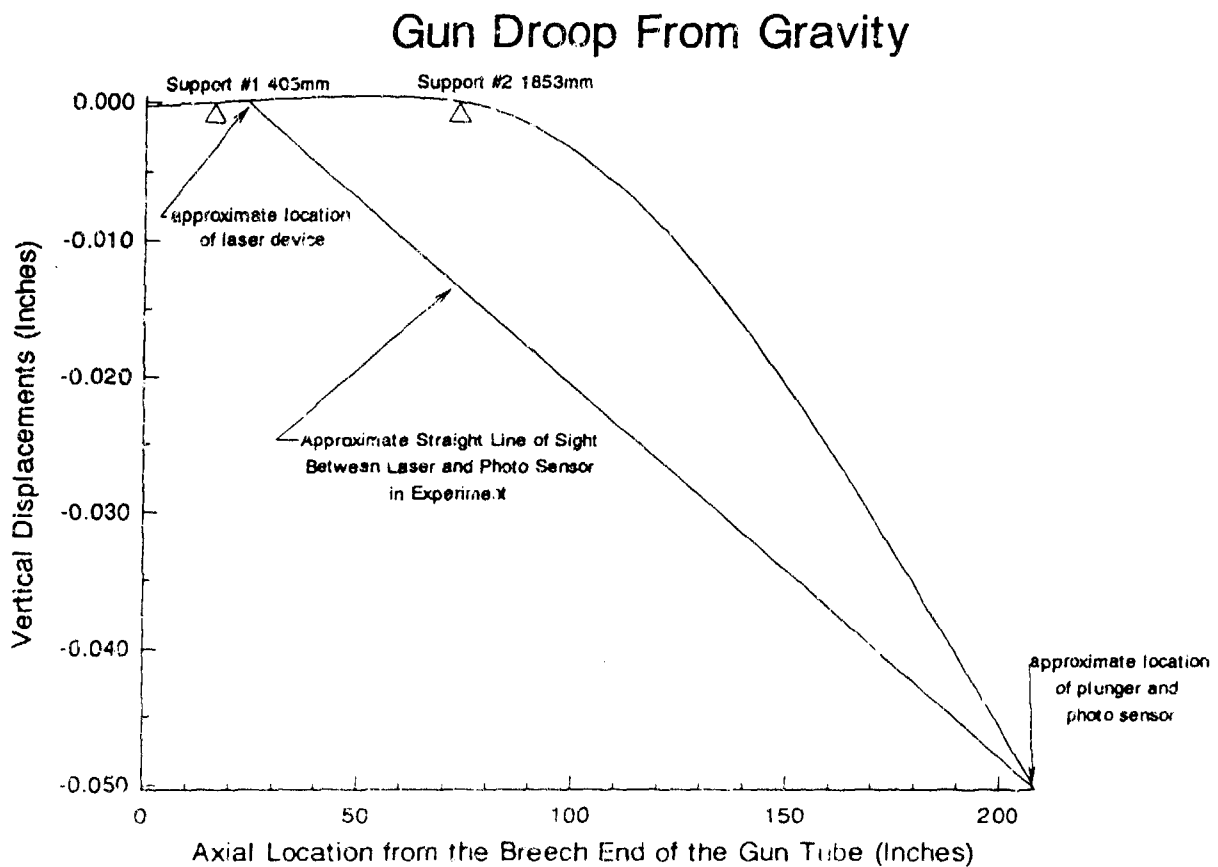
Figure 4. Gun-tube profile due to gravity alone (calculation made with ANSYS finite element program and beam element model of 120-mm gun-tube).

243

Measured Profile
Vertical Displacements for Gun-Tube 5064
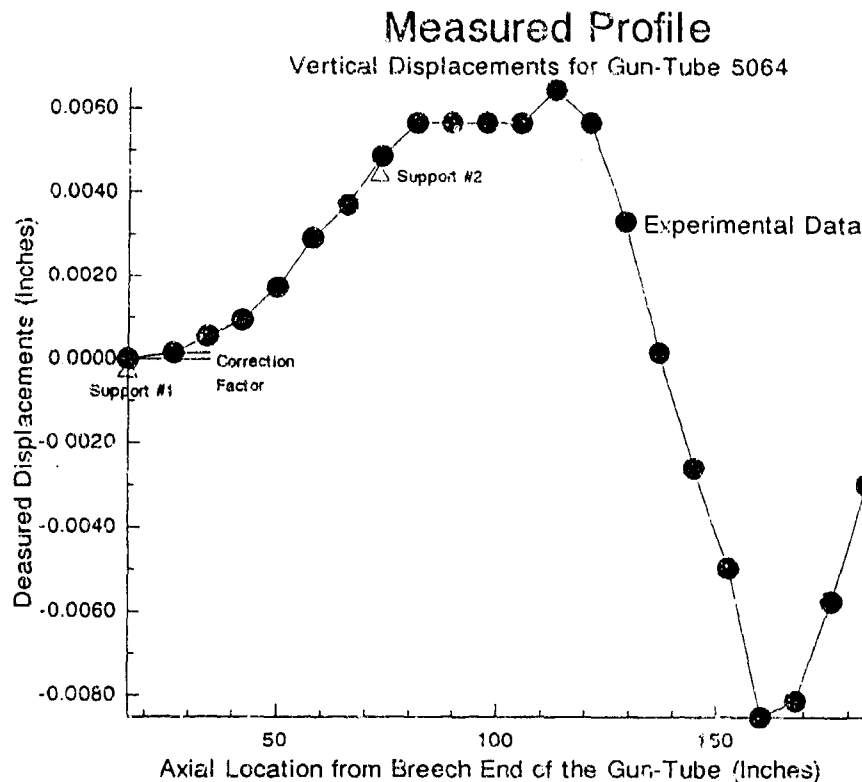
Figure 5. Measured tube profile from Watervliet with correction factor far offset in support location.

difference in support locations made no noticeable difference in the results. Nonetheless, a correction factor was added in accordance with the displacement changes observed in the finite element model and is shown in Figure 5. Then Figure 6 shows a straight line segment which can be drawn through the two support points. Now by rotating the straight line back to the horizontal along with the associated measurements taken at Watervliet (see Figure 7), both measurements and calculation have two common reference points. Recalling equation 1, where y_m is represented by the rotated curve given in Figure 7, and y_g is given in Figure 4, y_A can be obtained by subtracting y_g from the y_M which has been rotated, at each data point. Since the finite element model and experimental data did not have a one-to-one data point correspondence, linear interpolation routines were used to establish a correlation between associated points. The actual profile y_A is given in Figure 8. If only one pass data is available, then it is felt that this method would give a reasonable representation of the gun-tube profile in a finite element model. Now the displacements in Figure 8 can be applied directly to the finite element model's construction. Then if the finite element model is supported as in the test and gravity is applied in the model, the gun tube's profile will be identical to the original measurements taken. However, if the model is assembled into the cradle, with all the attachments in the actual gun system (i.e., breech etc.), and gravity is re-applied to the model, the gun-tube's profile should closely resemble the actual profile for that system. If a second set of data is available, y(0) & y(180), Method 2 should always be used. For this case, a second set of data was available from Watervliet, and that information can now be used to check or get an estimate of the scatter and error in this method.

If y_A, as given in Figure 8, is the actual gun profile independent of gravity and if that curve is rotated 180 degrees and gravity is reintroduced, the calculated curvature for that case should be identical to the second measurement made at Watervliet for y(180). Figure 9 shows a comparison of $(-y_A + y_g)$ to the second measurements taken at y(180). As can be seen, there is reasonably good agreement in magnitudes and shape of the two profiles except along the range from 50 to 90 inches from the breech end of the gun-tube. In this area, measurements varied by more than 10%, which was considered unacceptable. Therefore, method 2 was adapted. Some speculations on the source of this error will be discussed at length after method 2 is presented.
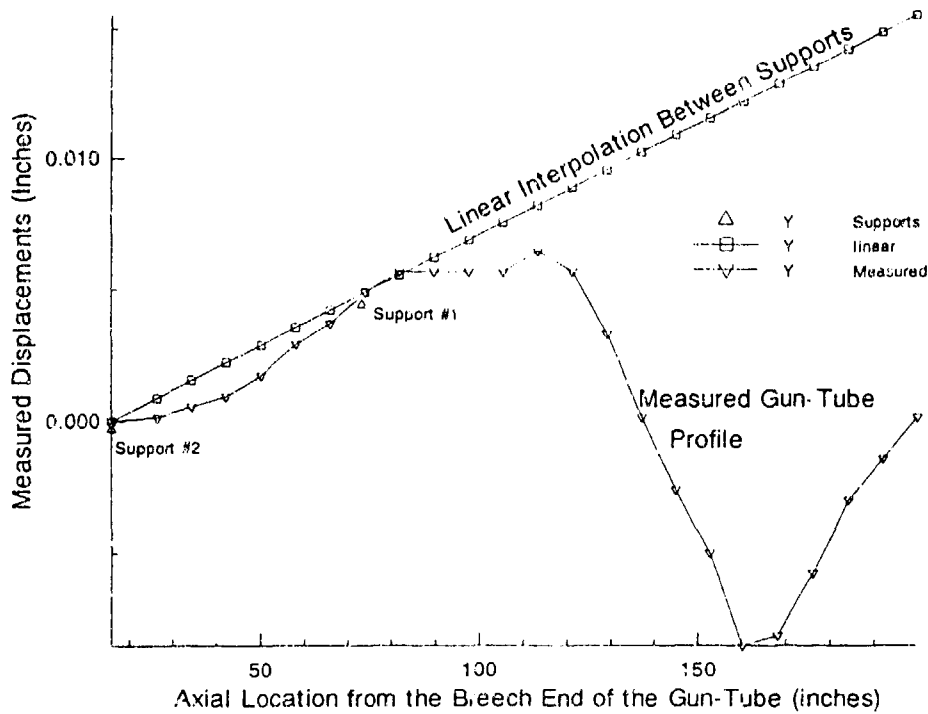
Figure 6. Measured profile with linear interpolation between supports (The straight line segment between the supports establishes a horizontal correlation between measurement and calculation.)
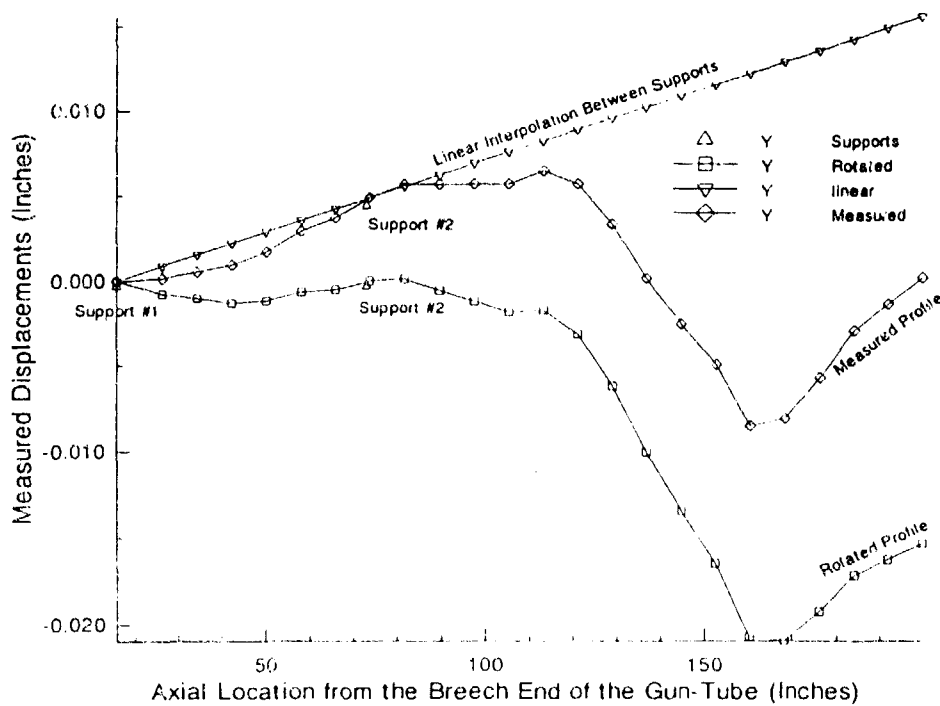
Figure 7. Shows Watervliet measurement, linear interpolation between supports, and the resulting curve when the Watervliet measurements are rotated with the linear curve to a common horizontal plane.

245

Gun-Tube Profile Independent of Gravity

This Curve represents the
The Difference Between
The Rotated Curve Given
in Figure 7 and the Gravity
Curve Given in Figure 4
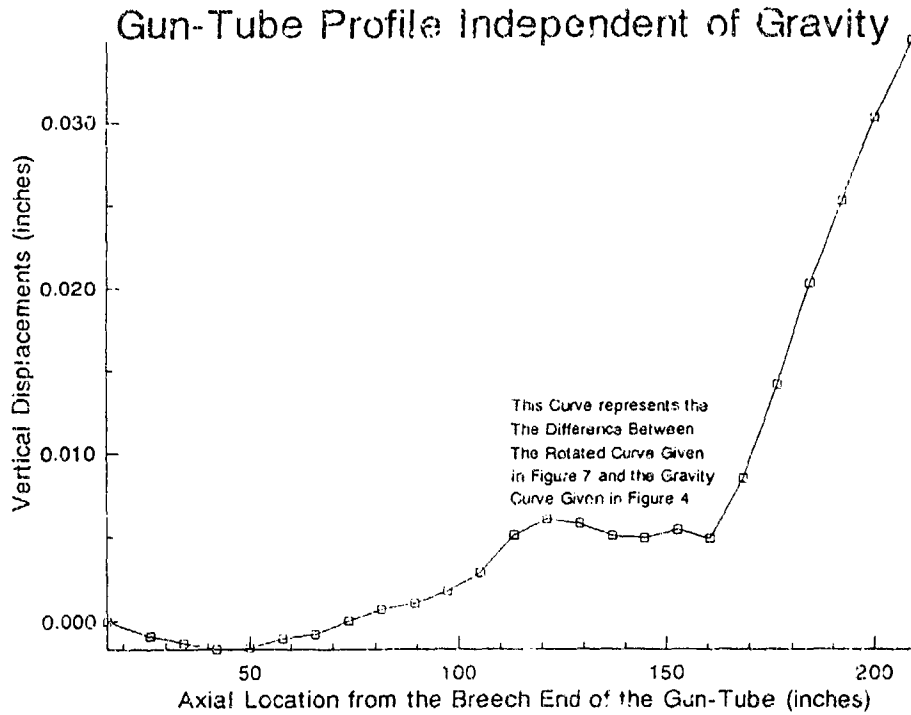
Figure 8. Estimated gun-tube profile Y_a using measured displacements and calculated gravity-droop.

Calculated versus Measured Curve
for Gun-Tube 5064

Measurements Taken y(180)

Calculated Curve as Given by
figure 8 rotated 180 degrees
and added to gravity droop
as given by figure 4

Y — Original
Y — Calculated
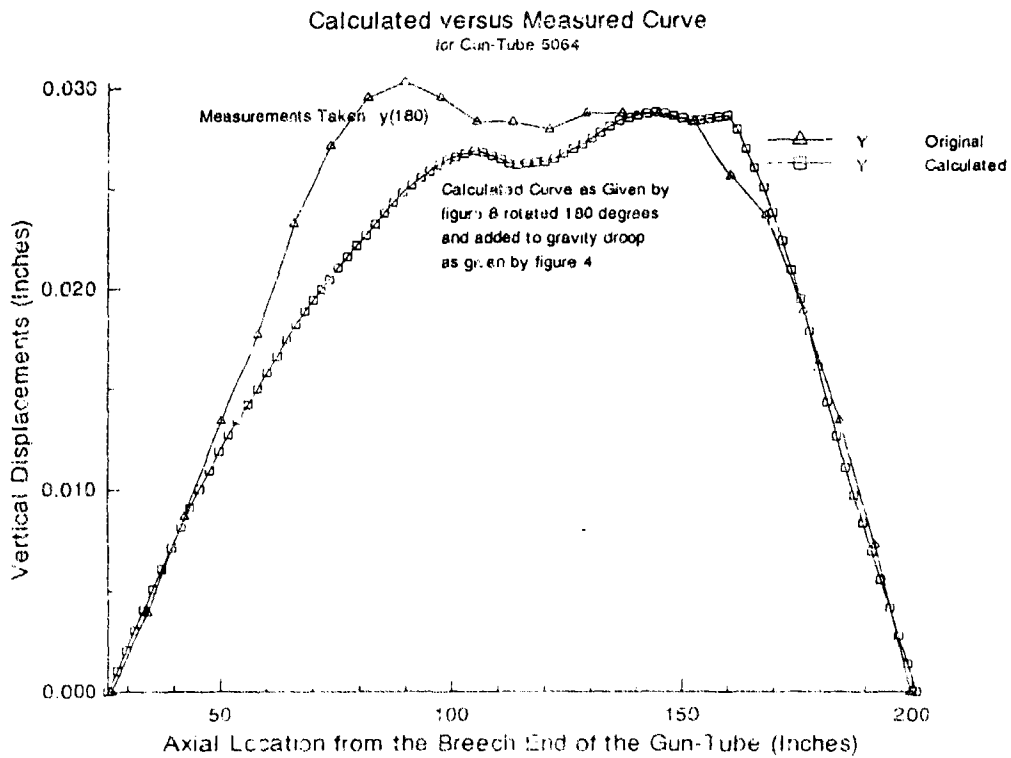
Figure 9. Comparison of measured profile at $Y_{(180)}$ and calculated profile based on $(-Y_a + Y_g)$.

WILKERSON

METHOD #2

Redundant Data Set

Method 1 concentrates on a consistent procedure when only one measurement is available. However, this is rarely the case inasmuch as Watervliet routinely measures a gun-tube's profile in the vertical plane and then rotates the tube 180 degrees and repeats the measurements. Furthermore, Watervliet keeps a data base on the gun-tubes that have been manufactured there so that this data can be obtained for a 120mm gun-tube. For this case, equation 1 can be written as:

$$y_{M_i}(0) = y_{A_i} + y_{g_i} \tag{2}$$

or

$$y_{M_i}(180) = -y_{A_i} + y_{g_i} \tag{3}$$

where $y_{M_i}(0)$ denotes the first measurements taken and $y_{M_i}(180)$ represents the measurements taken after the tube is rotated 180 degrees. Subtracting one from the other yields:

$$y_{A_i} = \frac{y_{M_i}(0) - y_{M_i}(180)}{2} \tag{4}$$

where y_A is routinely included in the Watervliet data set.

Figure 10 shows a plot of y_A, gun-tube 5064 from equation 4. Once again, to establish a horizontal plane, the two supports in the test are connected via a straight line, and the line and associated curve are rotated to the horizontal. This procedure is depicted graphically in Figure 11. The similarity between the new curve and the curve that was estimated using method 1 is noticeable. Now if the profile shown in Figure 11 is assumed to be the gun-tube's actual profile independent of gravity, then gravity can be added to the curve and compared with the measured profile. Similarly, the profile could be rotated 180 degrees, gravity could be added in, and the resulting profile could be compared to the measurements taken for that condition. Once again, profiles in the calculation are estimated using the same procedure as in the experiment. That is, a straight line is drawn between where the laser and plunger would be in the gun tube, and deviations from that line are used to find the gun-tube's estimated profile. By including both data sets in determining the gun-tube's actual profile, the resulting curve with gravity should more closely duplicate the measurements. (This technique can be thought of as an averaging or smoothing of the experimental results.) Figure 12 shows a comparison between the estimated profiles used in the finite element approximation as compared with the actual measurements. As can be seen, there still exists some error, between 60 to 90 inches from the breech end of the tube, as was observed using method 1. However, these errors have been substantially reduced.

DISCUSSION

Notwithstanding, errors exist and are a source of concern in the context of being able to qualify them. If, for instance, the errors are in the methods described here, then perhaps a higher order technique could be developed. On the other hand, if the measurement technique has a $\pm 10\%$ deviation, this would be sufficient to account for a majority of the discrepancies observed in method 2; then perhaps more robust testing could be done. One possibility for improving the experimental data would be to make additional measurements. Additional profiles could be linearly combined, as was done in method 2, to produce a better profile. This could be accomplished by rotating the gun-tube only 90 degrees after the initial vertical measurement. Then y_A would be obtained directly in the horizontal plane and could be compared to the linear combination of terms given by equation 4. Additionally, if one additional pass was taken, let's say at -90 degrees, a reasonable estimation of error or the boundaries of the error could be estimated using both of the 90 degree off-vertical measurements.
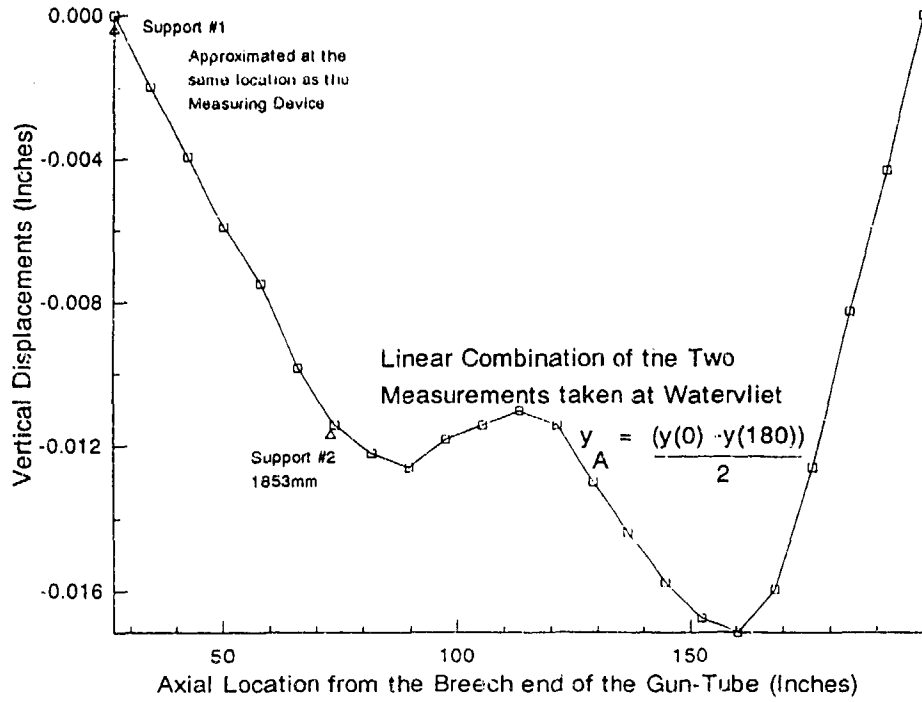
Figure 10. Linear combination of the two measurements taken at Watervliet in the vertical plane.
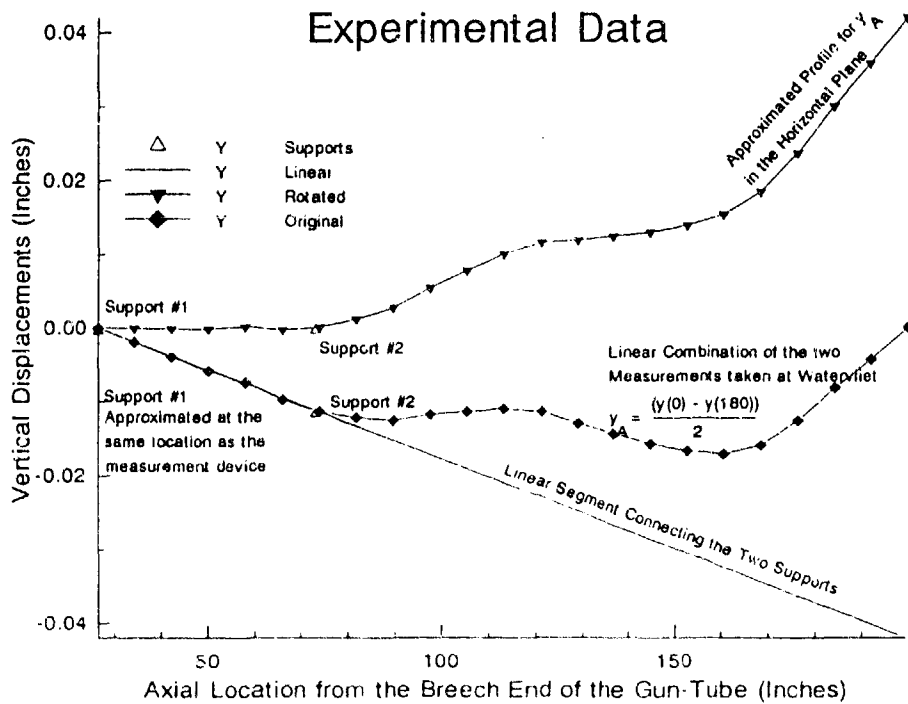
Figure 11. Linear combination of Watervliet's two vertical measurements, the linear line passing through the two supports, and the approximation for Y_a in the horizontal plane.

Comparison
Between Exp. and Calc. at y(0) & y(180)
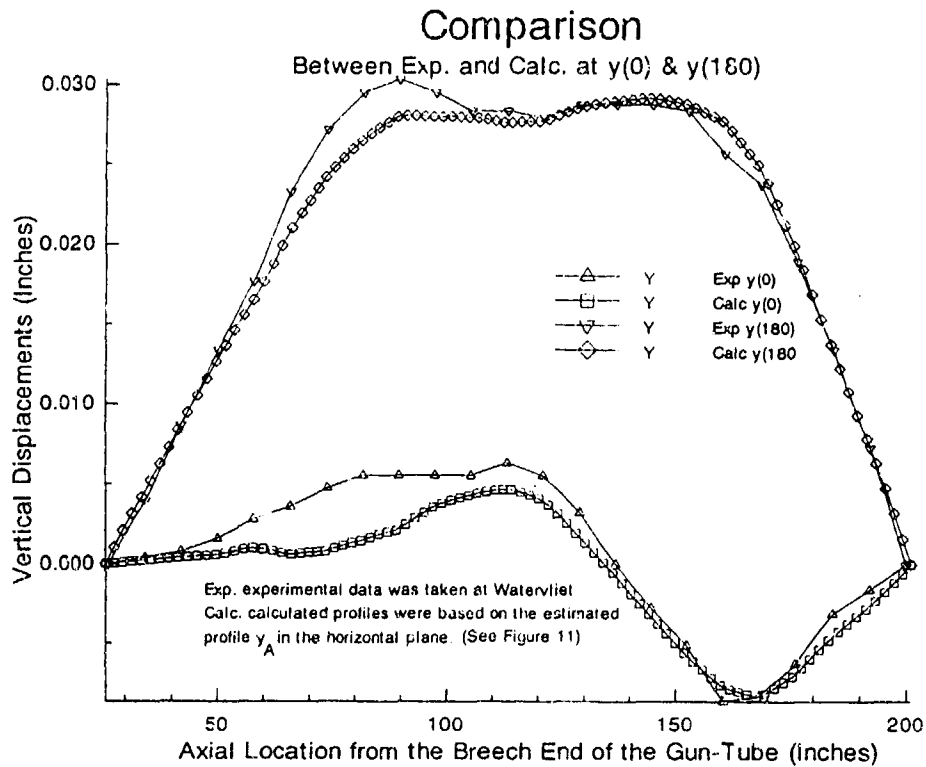
Figure 12. Comparison between experimental and calculated profiles at y (0) and y (180).

Another source of concern is how the measuring device might be affecting the measurements. The plunger head, which weighs 18 pounds, has to be supported by the gun-tube. A quick finite element calculation reveals that an 18-pound load at the muzzle will deflect the muzzle approximately four thousandths of an inch. Additionally, the chain that drives the device weighs a fair amount, and it was pointed out to us by Watervliet personnel that the forces on the chain and plunger as it is pushed down the tube were sufficient to deflect the muzzle in both the vertical and horizontal planes.

It would be beneficial, in terms of quantifying the mechanical error associated with gun-tube profile measurements, to conduct an additional series of measurements during the routine profile examinations at least once. First, one could record x-y measurements at 90-degree intervals instead of 180 as already mentioned. This would give four redundant pieces of data by which to quantify possible scatter in the measurement techniques. Secondly, a small apparatus could be built which would record and control typical mechanical displacements caused by the measuring apparatus[11].

CONCLUSIONS

An accurate estimate of the gun-tube's profile can be made for use in finite element dynamic simulations, using measured profiles and simple numerical techniques. The methods employed rely on obtaining an accurate estimate of the gun-tube's profile in a gravity-free environment. It was shown that using experimental measurements and numerical calculations of gravity-droop provided accurate gun-tube profiles which compared favorably with actual observed measurements. The error associated with the methods presented were in the order of 10 percent when compared with the maximum observed displacements. However, they were not as good when compared with the actual magnitude of the measurement being taken at a particular location along the gun-tube (see Figure 12).

The source of the errors observed was examined in terms of the measurement techniques used to find them. Specific recommendations were made with regards to improving or quantifying sources of error which may be occurring from the measurement techniques. It is equally important to note that the measurements that are being taken are sufficient for the purposes of quantifying and assuring the manufacturing quality of each 120mm gun-tube.

However, the purpose of this paper was to determine how best to use the experimental data for an accurate estimate of a particular gun-tube profile for analysis purposes which, in this case, warranted closer examination of the measuring techniques. In summary, the methods presented make use of the experimental data to estimate a gun-tube's profile which can then be incorporated into a dynamic simulation of that same gun-tube mounted in a tank. It is further stipulated that the estimated profile, coupled with a finite element calculation, accounts for varying boundary conditions, and will yield consistent estimations of the actual gun-tube's profile during firing tests. Similarly, it is understood that thermal effects for a given test need to be accounted for as well[12]. It is further recommended that the Watervliet measurements, which have proven to be more reliable, be used whenever possible in determining a particular gun-tube's profile. Finally, it was shown that by using a linear combination of the two measurements made at Watervliet (a form of smoothing the data) more consistent estimates of the tube's profile could be obtained than when using only a single measurement.

REFERENCES

1. Schmidt, E.M. et al. "Jump From M1A1 Tank." BRL-IMR-868 June 1986.

2. Rabern, D.A. "Axially Accelerated Saboted Rods Subjected to Lateral Forces." Los Alamos National Laboratory LA-11494-MS UC-706 March 1989.

3. Erline, T.F. et al. "Gun and Projectile Flexural Dynamics Modeled by the Little Rascal - A USER'S MANUAL." BRL-TR-3122 1990.

4. Hopkins, D.A. "Shogun 3-D Gun Dynamics User's Manual." BRL-TR-3128 August 1990.

5. Howd, C.A. "In-Process Straightness Measurement of Gun-tubes." Watervliet Arsenal WVA-QA-9101 August 1991.

6. Weddle, A.L. "Methodology Investigation of Gun-tube Straightness Measurements." Aberdeen Proving Ground USACSTA-6439 October 1986.

7. Rabern, D.A., Lewis, M.W. "Projectile and Gun-tube Simulations with a Moving Pressure Front in Two - and Three Dimensions." Los Alamos National Laboratory MEE4-90-451 October 1990.

8. Cpt. Heid, B.J., Erline, T.F. "Dynamics of the Balanced Breech System for the 120mm Tank Main Gun." BRL-TR-3186 Ballistic Research Laboratory January 1991.

9. Rowekamp, B.J. "Breech Mechanism Interchangeability Documentation for Hybrid Cannon." Benét Laboratory Watervliet, NY August 1987.

10. Wilkerson, S.A. et al. "Static Load Test on the M256 System." Report in Print March 1993.

11. Letter Wilkerson, S.A. to Howd, C. March 1993.

12. Bundy, M. L. "Gun Barrel Cooling and Thermal Droop Modeling." ARL TR in Print March 93.

TITLE: EXPERIMENTAL INVESTIGATION AND MODELLING OF THE EFFECT OF BORE
CURVATURE ON MUZZLE MOTIONS OF 60-MM GUNS

RONALD G. GAST
U.S. ARMY ARMAMENT RESEARCH, DEVELOPMENT & ENGINEERING CENTER
BENET LABORATORIES
WATERVLIET, NY 12189-405

ABSTRACT:

In recent years, great strides have been made regarding isolation of the dominant loads that cause beam-type vibrations in tank cannons during ballistic operation. A more subtle load type is due to the characteristic bore profile of the gun tube itself. While curvature and inertia-induced loads due to gravity droop are known to have little effect on gun motions, a similar in regard to center line profile produced by other conditions (manufacturing, thermal failure, e cannot be made. Very little controlled testing has been conducted to establish the severity of this condition. This lack of data was the driving force behind the development and conduction of the tests and the simulation modelling reported herein.

Tests were conducted using two 60-mm in tubes 63 calibers long. One of the tubes possessed a great deal of in-plane curvature, while the second was relatively straight. In the test, the tubes were isolated from all known dominant loads by using braided cords for supports and a centered breech. For both tubes, the primary plane of curvature was incrementally varied with respect to gravity, and a number of rounds were fired from each orientation.

Benet Laboratories' Uniform Segments in Vibration model was used to conduct the simulations. The mathematical relationships regarding load functions for beam vibrations and the statistical aspects of curvature estimates were addressed and incorporated in the modelling. Both test data and modelling results confirmed that the profile of the bore and its orientation with respect to gravity has an impact upon the magnitude and characteristic of muzzle motion throughout the shot.

BIOGRAPHY
PRESENT ASSIGNMENT Mechanical Engineer, Tank Turret Branch, Development Engineering
Division, Benet Laboratories (to present).

PAST EXPERIENCE Mechanical Engineer, Special Projects Section, Benet Laboratories (1971-1985) and
Mechanical Engineer, Automatic Weapons Section, Benet Laboratories, (1968-1971).

DEGREES HELD B.S.M.E. Rensselaer Polytechnic Institute, 1968; M.S.M.E., Rensselaer Polytechnic
Institute, 197; Ph.D., Rensselaer Polytechnic Institute, 1988.

EXPERIMENTAL INVESTIGATION AND MODELLING OF THE EFFECT OF BORE CURVATURE ON MUZZLE MOTIONS OF 60-MM GUNS

Ronald G. Gast
U.S. Army Armament Research, Development, and Engineering Center
Benet Laboratories
Watervliet, NY 12189-4050

BACKGROUND

In recent years, great strides have been made regarding isolation of the dominant loads that cause beam-type vibrations in tank cannons during ballistic operation [1-4]. A mo e subtle load type is due to the characteristic bore profile of the gun tube itself. While curvature- and inertia-induced loads due to gravity droop are known to have little effect on gun motions [4], a similar claim in regard to center line profile produced by other conditions (manufacturing, thermal flexure, etc.) cannot be made. Very little controlled testing [5] has been conducted to establish the severity of this condition. This lack of data was the driving force behind the development and conduction of the tests and the simulation modelling reported herein.

Tests were conducted using two 60-mm gun tubes 63 calibers long. One of the tubes possessed a great deal of in-plane curvature, while the second tube was relatively straight. In the test, the tubes were isolated from all known dominant loads by using braided cables for support and a centered breech. For both tubes, the primary plane of curvature was incrementally varied with respect to gravity and a number of rounds were fired from each orientation.

Benet Laboratories' Uniform Segments Gun Vibration model [6,7] was used to conduct the simulations. The mathematical relationships regarding load functions for beam vibrations and the statistical aspects of curvature estimates were addressed and incorporated in the modelling. Both test data and modelling results confirmed that the profile of the bore and its orientation with respect to gravity has an impact upon the magnitude and characteristic of muzzle motion throughout the shot.

TEST SETUP AND FIRING SCHEDULE

The test consisted of firing 2.25 kilogram (kg) slug projectiles 100 millimeters (mm) long through the two 60-mm gun tubes, while the motion of the tubes' outer diameter (OD) in two orthogonal directions at two axial stations near the muzzle was recorded. Both propellant gas pressure and projectile in-bore travel were also recorded. The guns, which have a length of 63 calibers, were suspended by braided cables (stiffness of 260 newton/mm) and allowed to recoil freely during projectile acceleration. External buffers mounted to the stand decelerated recoil after the projectile had cleared the bore. The OD of the initial 12.5 calibers of tube length is 140 mm. A tapered section 6.25 calibers long reduces this OD to 75 mm for the last 44.25 calibers. An overall view of the test setup is shown in Figure 1.
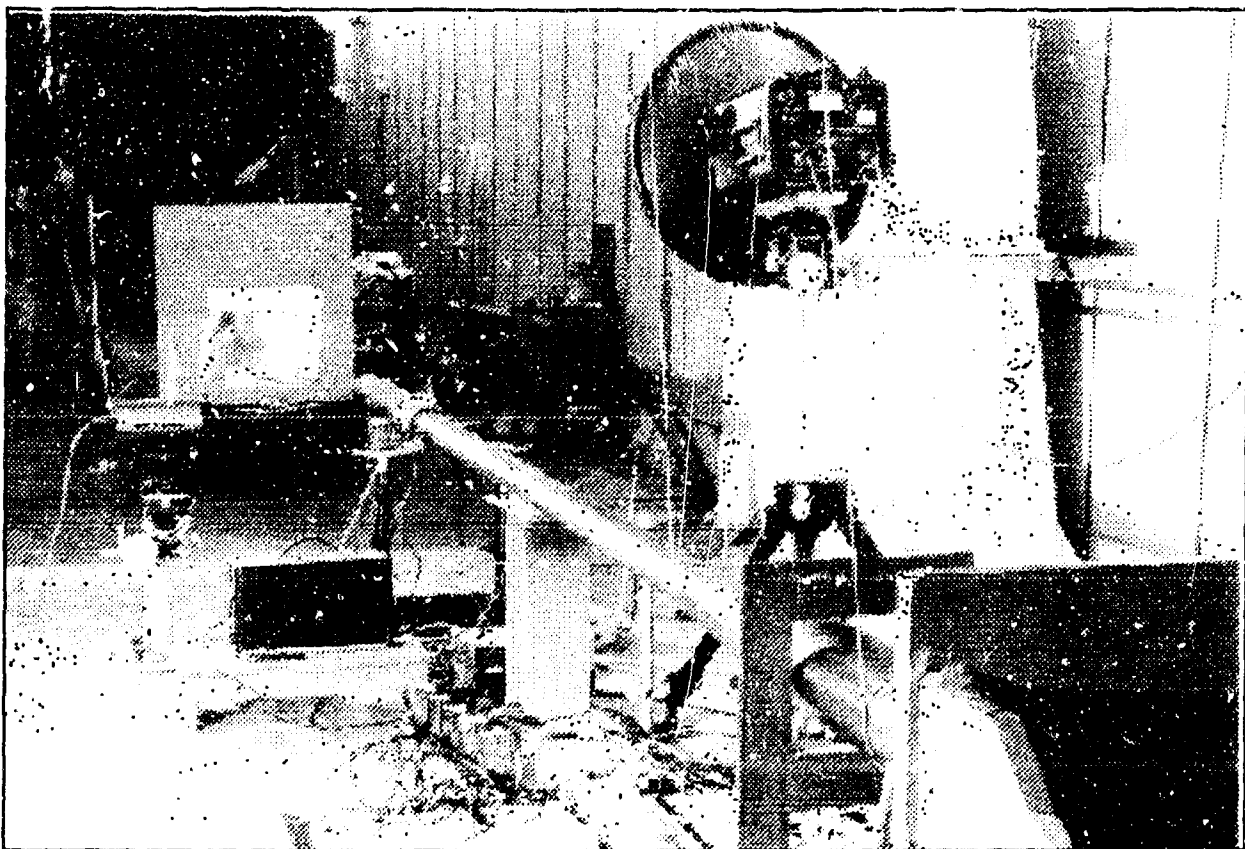
Figure 1. Test Setup.

Two tubes were manufactured for this test. The bore profile of the first tube (Serial #2) had a significant in-plane bow about 0.635-mm total indicator reading (TIR). The second tube (Serial #3) was much straighter. Profile variations in both directions did not exceed 0.072-mm TIR. The top vertical center line (TVCL) for each gun was established as the plane of maximum curvature. This position is referred to as the 12 o'clock position with all reported o'clock rotations as viewed from the breech. The static condition of the bore profiles is shown in Figure 2.

To determine transverse motions and expansion of the OD at the muzzle, six eddy probes were mounted in a cylindrical carrier that slips over the muzzle of the gun. Two axial locations at 2.5 and 5.0 calibers from the muzzle were selected for motion monitoring. Three gages were used at each location: two of them monitor horizontal movement, whereas the third monitors vertical movement of the tube's outer surface. Therefore, both expansion of the tube and motion of the bore's center line are included in the data. Appropriate calculations must be made to extract tube movement. With E1 through E6 as the eddy probe responses, the equations for center line motion and OD expansion are:

$$EXP_{2.5} = (E4 + E5)/2 \quad \text{OD expansion at 2.5 calibers}$$
$$EXP_{5.0} = (E2 + E3)/2 \quad \text{OD expansion at 5.0 calibers}$$
$$HRZ_{2.5} = (E5 - E4)/2 \quad \text{Horizontal motion at 2.5 calibers}$$
$$HRZ_{5.0} = (E3 - E2)/2 \quad \text{Horizontal motion at 5.0 calibers}$$
$$VRT_{2.5} = (E1 - EXP_6) \quad \text{Vertical motion at 6 inches}$$
$$VRT_{5.0} = (E6 - EXP_{12}) \quad \text{Vertical motion at 12 inches}$$

253

60mm GUN TUBES: BORE PROFILES

TEST TUBE #2

CENTERLINE DEVIATION (MILLI-INCHES)

AXIAL LOCATION RFT (INCHES)

TEST TUBE #3

CENTERLINE DEVIATION (MILLI-INCHES)

AXIAL LOCATION RFT (INCHES)
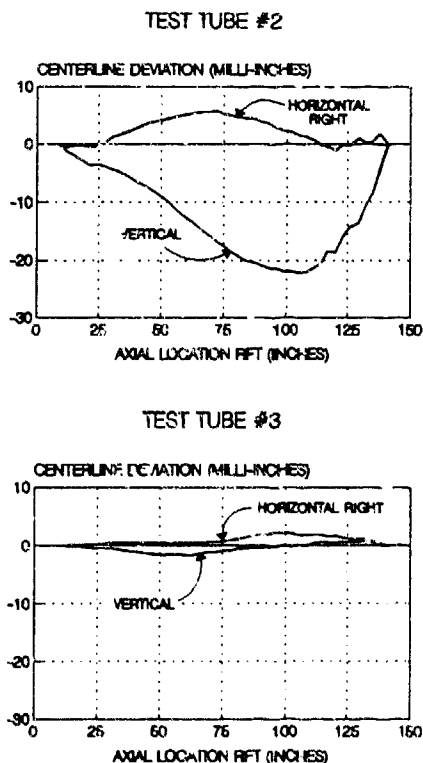
Figure 2. 60-mm Test Guns: Comparison of Bore Profiles.

Figure 3 contains the raw data for one particular eddy probe signal and its assumed response after filtering with a 1000-Hertz low-pass filter.

To locate the projectile with respect to the muzzle, a radar emitting and receiving unit located along the side of the gun directs its beam at a foil-lined foam sacrificial target that is 8.5 calibers in front of the muzzle. The emitted wave is reflected from this target towards the face of the projectile travelling through the bore. As the projectile accelerates, the frequencies of the returning waves are recorded. These frequencies vary in direct proportion to the projectile's velocity. By performing Fast Fourier Transforms (FFT) at discrete time intervals and plotting the results as a function of time, a response proportional to the projectile velocity can be reproduced. The results for a particular round are indicated as a waterfall plot in Figure 4. The dominant frequencies at each time interval when multiplied by the appropriate scale factor (1 cm/sec per Hertz) yield the projectile' speed. This information is then integrated to locate the projectile with respect to the muzzle.

The basic parameter of the test was the effect of curvature on muzzle motion. Since gravity produces additional curvature, orientation of the static profile with respect to gravity was a test parameter leading to the schedule of rounds shown in Table 1.

60mm TEST DATA ROUND #23   EDDY PROBE #4 DATA

RAW & FILTERED OUTPUT VOLTAGE vs TIME
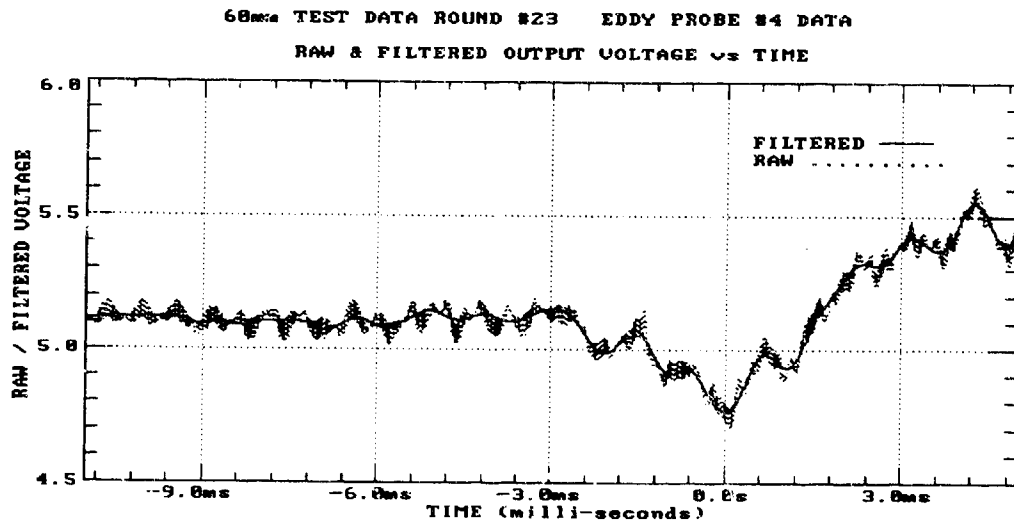
Figure 3. Round #23: Raw Voltage Eddy #4 Probe.

**60mm FIRING TEST: ESTIMATE of
PROJECTILE VELOCITY
(WATERFALL PLOT)**
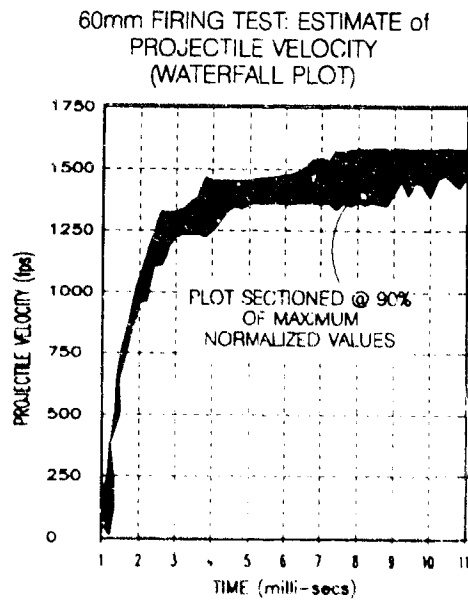
Figure 4. Round #23: Waterfall Plot Projectile Velocity.

GAST

As shown in the table, this portion of the test was conducted over many months. This was due to the amount of time needed for a precision setup before each shot and the subsequent data reduction. A number of additional rounds were fired to establish consistency of the ballistic response and integrity of the recorded data. Approximately 128,000 data points were generated for each shot.

Table 1. Firing Schedule for 60-mm Tubes #2 and #3

Round Number	Date	Tube Number	Profile Orientation
22 23	10-04-90 10-10-90	2	12:00
24 25	10-12-90 10-16-90	2	09:00
26 27	10-18-90 10-23-90	2	06:00
28 29	10-25-90 10-26-90	2	03:00
30 31	01-08-90 01-14-90	3	12:00
32 33	02-12-91 02-20-90	3	09:00
34 35	02-26-91 02-28-91	3	06:00
36 37	03-05-91 03-12-91	3	03:00

DETAILS OF SIMULATION MODEL

The simulation package chosen for this analysis was Benet Laboratories' Gun Vibration Model (Uniform Segments Method). Basically, it is a modal analysis technique in which the gun-beam is segmented into a number of uniform cross sections. The Euler-Bernoulli beam equation for a free-free boundary condition is applied to each segment. Across segment boundaries continuity of displacement, slope, moment, and shear are invoked. This results in a set of simultaneous equations relating the geometry and material properties to the displacement coefficients and mode shape frequencies. The total number of equations is four times the number of uniform segments chosen. This system of equations is set up in matrix form and used for continuing analyses. Setting the determinant to zero and solving the resulting algebraic equations yields the mode shape frequencies. By solving the linear system at each frequency calculated, the mode shape coefficients are found. Standard numerical techniques are used for these calculations and for the time-stepping integrations that follow.

There are three areas of concern in developing a gun model for use by the Uniform Segments Method (USM). The first requires that the modal parameters of the model accurately represent the modal parameters of the component. Secondly, since bore curvature is the main driving function in this exercise, an accurate functional representation of it is imperative. The third regards numerical convergence when using modal analysis techniques for vibration modelling. A minimum number of mode shapes must be selected to establish model convergence before any reliable calculations can be made. In this section, the above three concerns are addressed.

GAST

Establishment of Modal Parameters

To model a gun-beam undergoing forced vibration using the USM, an accurate representation of the natural frequencies and mode shapes of the bare tube are required. Control of these modal parameters is accomplished by segment definition. This entails the selection of the boundary locations, normalized weight, and bending resistance of each segment such that the free vibration frequencies and mode shapes of the entire model accurately mimic the component. The geometry of the tube and its USM representation are shown in Figure 5.

60mm TEST GUN TUBE
COMPARISON of FREQUENCY ESTIMATES

FEM MODEL: 72 ELEMENTS

5.40" DIAM   4.25" DIAM   3.00" DIAM

USM MODEL: 3 SEGMENTS
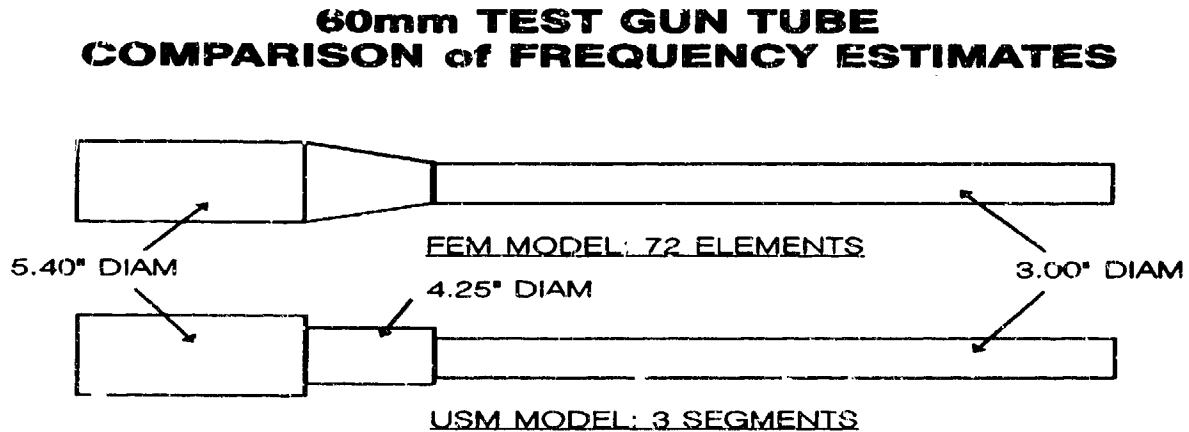
COMPARISON OF FIRST 6 BENDING MODES (HERTZ)

FEM	26.3	80.1	176.0	311.5	469.8	623.6
USM	26.4	83.1	187.4	329.5	478.2	656.4

Figure 5. 60-mm Guns: Geometric Comparisons.

In the absence of experimental results, a finite element method (ABAQUS) was used to provide a comparative set of modal parameters. The ABAQUS model employed a total of 72 prismatic beam elements containing two nodes (total degrees of freedom (dof) was 144), whereas the USM model has three segments that were chosen such that total beam weight was preserved. The first six natural bending frequencies are shown in Figure 6. Frequencies match very well with at most a 5.3 percent difference in the third mode.

Sensitivity of Functional Fit of Bore Profile

The primary loads applied during the 60-mm test, which are to be modelled in this investigation, are proportional to bore curvature, which is a function of the second spatial derivative of the profile. Since bore curvature is to be derived from the measured profile by a numerical differencing technique, a precise functional representation is required for accurate modelling of the related loads. A module is available in the USM software whereby gravity droop, which is determined by standard equations of mechanics, may be added to any additional initial straightness deviation. The user has the option of selecting the type of functional fit to represent the profile. The choices are a set of cubic spline polynomials between each pair of data points or an Nth order polynomial (up to N=10) based upon a least squares fit of the data.

Figure 6. 60-mm Guns: Mode Shape Comparisons.

To indicate the sensitivity of curvature, a modelling experiment was performed in which four different polynomial functions (orders 2,4,6,8) were used to define the static profile of tube #2 oriented in the 6 o'clock position. The result of this exercise is shown in Figure 7, where the transverse vibration of the muzzle in the vertical direction is shown as a function of projectile position in-bore. The four plots represent the response to the four different profile functions. As indicated, the displacement is locally sensitive to the polynomial order, however, the overall shape is not. Since a high level of accuracy is needed to estimate muzzle motions during projectile approach, it is imperative that the bore profile from which curvature is derived be represented as accurately as possible.

Since the static profile is based upon measurements containing systematic errors, a statistical method [8] to evaluate the goodness of fit is used to test competing polynomials used to represent bore profiles. Basically, a statistic called chi-squared is calculated at each measurement point. Its value is the square of the deviation between the measured and estimated value divided by the square of the measurement error in the dependent variable. All calculations are summed and compared to the dof, which is the number of test points minus the order of estimating polynomial. If both the summation and the dof are approximately equal, then the fit is good. If the dof is much greater than the summation, then the fit is too restrictive, and vice versa when the dof is much less than the summation.

60mm TEST GUN TUBE #2
COMPARISON of DISPLACEMENT vs PROFILE
VARIOUS FUNCTIONAL LEAST SQUARE FITS

DISPLACEMENT AT MUZZLE (INCHES) X 10^3

2nd ORDER POLY

4th ORDER POLY

6th ORDER POLY

8th ORDER POLY

PROJECTILE LOCATION FROM MUZZLE (INS)
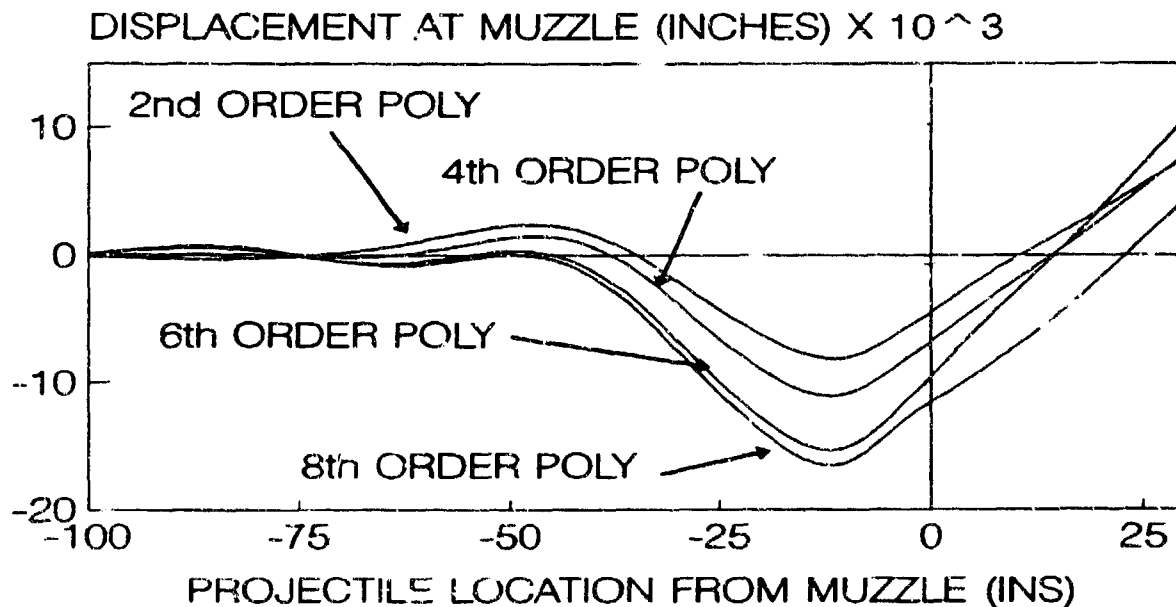
Figure 7. Dynamic Response to Profile Order.

For the given accuracy of the inspection data and the statistical approach used to estimate the validity of a fit, a fourth order polynomial proved to be the best for each tube in both vertical and horizontal directions. Quadratic curvature will result when these functions are twice differentiated, thus yielding a spatially varying driving function for projectile/tube interactive loads.

COMPARISON OF TESTING AND MODELLING RESULTS

A series of computer runs were made to simulate the test conditions. Due to the consistency of ballistic pressure and projectile travel realized during the test, a common ballistic driving load was used for all runs. This removed the burden of establishing the ballistic driving loads from the individual test records.

Four of the nine resident load functions were used. They were the curvature-dependent loads (i.e., projectile path and pressure curvature), the support reaction load, and the breech inertia load. The recoil inertia load was not included due to the nature of the support system. Unlike a conventionally mounted cannon that recoils over a fixed slide surface, the reaction provided by the pendulum-type cable support does not drive the gun in the same manner. With this support, the entire gun recoils as a rigid body without exciting any of the transverse modes.

259

Tra   Motions at the Muzzle

During the initial phase of the simulations, it was determined that the response level due to the projectile path load dominated all others. The results heuristically establish the effect upon muzzle motion of a fired mass projectile travelling along a curved path in a ballistically typical fashion. To this end the dynamic results (both model and test) are presented along with the main scaling factor--the spatially varying bore curvature. This function scales directly in magnitude and inversely in direction the product of the projectile weight and the square of the speed. This is a point load that travels with the projectile. In the remainder of this section, comparisons between the modelling and test results are discussed. Each of the figures that follow contain the curvature and displacement results for diametrically opposing bore profile orientations for a given gun tube. The graphs on the left present the curvature function along the axial coordinate of the tube, whereas the graphs on the right present the muzzle displacement results for both the test data and model.

Tube: #2; Direction: Vertical; Profile Orientation: 12 & 6 O'Clock

Results for these conditions are found in Figure 8. In the vertical plane there are two contributions to bore curvature. The first is a result of gravity droop, which for this particular gun tube contributes approximately -21 micro-inches[1]. Added to this is the static curvature, which for gun tube #2 in this plane varies monotonically from 0 at the breech end to 50 micro-inches[1] at the muzzle. The combined effect at the 12 o'clock orientation is shown on the upper left graph, and the effect for the 6 o'clock orientation is shown on the lower left graph in Figure 10. The displacement responses are shown on the right.

At the 12 o'clock position, the predominant motion is downward for the in-bore duration of projectile travel. When the projectile reaches the muzzle, however, this response rate increases rapidly, and upon exit, vertical motion nearly stops. In the 6 o'clock position, the plane of curvature is reversed, as is the response, as the data indicates. By comparing the records at 12 o'clock with 6 o'clock, significant differences in vertical response are noted. Much greater vertical motion is shown at the 6 o'clock orientation than at 12 o'clock. At 6 o'clock the static profile is additive with gravity droop, thus presenting a path of greater curvature.

For both orientations, the model tracks the test results quite well. At 12 o'clock the muzzle moves in a consistently negative direction achieving a value of -0.005 inch at exit. At 6 o'clock a sharp negative change in displacement occurs at a projectile location of -40 inches. This trend continues achieving a value of -0.013 inch at a projectile location of -15 inches. From this point, displacement quickly reverses and moves in a positive direction as the projectile passes. A timing shift of approximately 10 inches is indicated between the test data in the 6.00 orientation. This is likely due to the experimental uncertainty in locating the projectile with respect to the muzzle. At best a tolerance band of ± 10 inches for projectile location has been estimated.
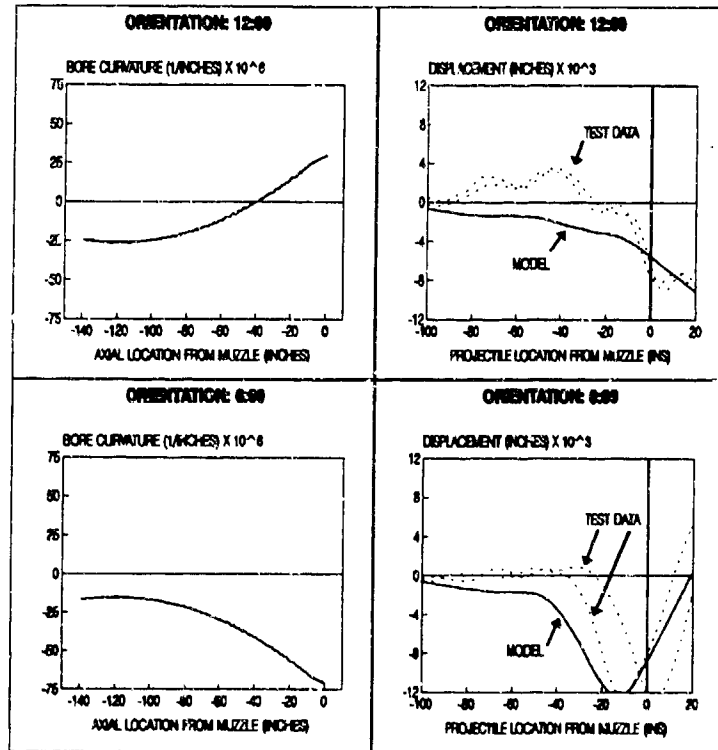
Figure 8. Gun #2: Muzzle Displacement Vertical Direction 12 and 6 O'Clock.

Tube: #2; Direction: Vertical; Profile Orientation: 3 & 9 O'Clock

Results for these conditions are found in Figure 9. When the TVCL is orientated in this manner, the total vertical curvature follows a parabolic path mirrored about the droop value of -21 micro-inches[1]. At 3 o'clock, the curvature function is concave downward and vice versa at the 9 o'clock orientation. Data indicates a steady downward motion as the projectile approaches and maintains this displacement after exit. In comparison, the responses for the model are more similar at these orientations mainly due to the lower overall curvature along the bore, but as before, they track the test data quite well. A response shift of about 20 inches is noticeable in the data at the 3 o'clock orientation. The shift is much less at 9 o'clock.

GAST
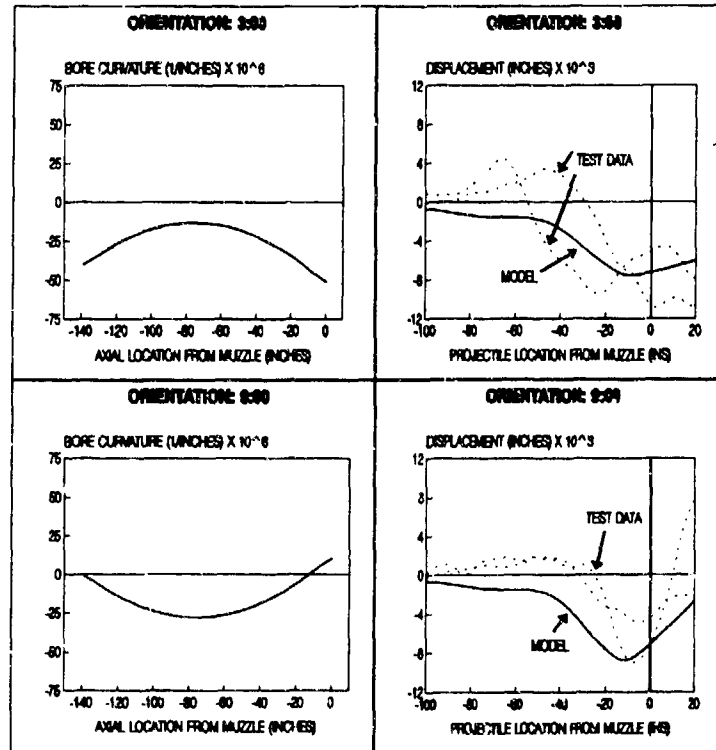
Figure 9. Gun #2: Muzzle Displacement Vertical Direction 3 and 9 O'Clock.

Tube: #2; Direction: Horizontal; Profile Orientation: 12 & 6 O'Clock

Results for these conditions are found in Figure 10. In this plane the curvature function lacks the droop component. The shape is still parabolic. However, it is shifted much closer to the axis. The overall effect of this shift is to present a scaling factor of lower magnitude that reverses in direction during projectile excursion. The responses of the model and the data are much lower relative to any of the previous conditions. At the 12 o'clock orientation, the muzzle moves slightly to the right during projectile approach, then reverses direction and moves left at exit and beyond. The data response shows a similar tendency, although it is somewhat masked by noise. At the 6 o'clock orientation, both data and model responses appear to be mirror images of those at the 12 o'clock orientation. The data, however, shows a 20-inch timing shift between each shot which, if both were shifted, would produce responses that are more consistent.

262
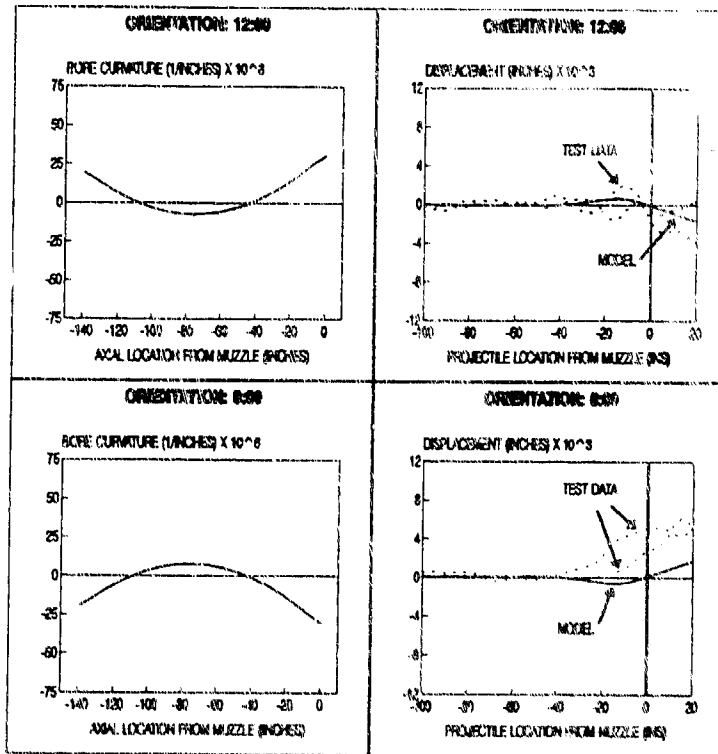
Figure 10. Gun #2: Muzzle Displacement Horizontal Direction 12 and 6 O'Clock.

Tube: #2; Direction: Horizontal; Profile Orientation: 3 & 9 O'Clock

Results for these conditions are found in Figure 11. The curvature function presented at these orientations begins at a zero value at the breech, monotonically increases to +50 micro-inches[1] at the 3 o'clock orientation, and decreases to -50 micro-inches[1] at 9 o'clock. Due to the characteristic of this function, the model is driven in a consistent direction with an increasing scale factor as the speed of the projectile increases and approaches the muzzle. A significant disturbance is indicated at projectile approach and passage. Model responses at the two orientations are again mirror images of each other. Data responses show similar tendencies with a timing shift quite evident at the 3 o'clock orientation. Greater disturbance values in the data are indicated at the 9 o'clock orientation.

Figure 11. Gun #2: Muzzle Displacement Horizontal Direction 3 and 9 O'Clock.

Tube: #3; Direction: Vertical; Profile Orientation: 12 & 6 O'Clock

Results for these conditions are found in Figure 12. The static curvature function for tube #3 is quite different from tube #2. As previously shown, very little profile deviation exists for tube #3 in either direction, therefore, its static curvature function is orders of magnitude less than tube #2. Less than 1 micro-inch[1] deviation exists over the entire length of tube #3 in either direction. In the vertical direction, therefore, gravity droop dominates overall curvature. With a value of -21 micro-inches[1], the difference from 12 to 6 o'clock is very slight. Shot-to-shot repeatability in the data at a given orientation is demonstrated. Moreover, the response does not change dramatically as the orientation is changed. Basically, the muzzle rises slightly at initiation of projectile travel, then falls as the projectile approaches. At passage the motion reverses itself and moves upward. The differences in model responses are also slight. Very little change in response snape can be observed when the two orientations are compared.

GAST

60mm COMPARISON of TEST and ANALYSIS
TUBE #3 CURVATURE and MUZZLE DISPLACEMENT
DIRECTION: VERTICAL; ORIENTATION: 12:00 & 6:00
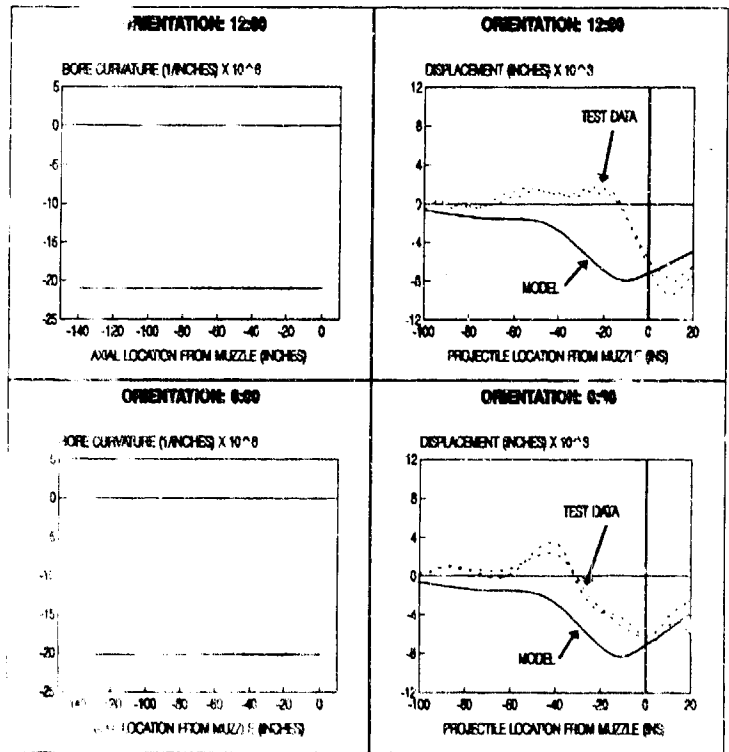
Figure 12. Gun #3: Muzzle Displacement Vertical Direction 12 and 6 O'Clock.

Tube: #3; Direction: Vertical; Profile Orientation: 3 & 9 O'Clock

Results for these conditions are found in Figure 13. For these orientations, the results are the same as those for the 12 and 6 o'clock orientations. Gravity droop dominates total curvature, and the model and data responses show the same tendencies.

Figure 13. Gun #3: Muzzle Displacement Vertical Direction 3 and 9 O'Clock.

Tube: #3; Direction: Horizontal; Profile Orientation: 12 & 6 O'Clock

Results for these conditio s re found in Figure 14 In the horizontal direction at these orientations, a curvature value of 0 micro-inch⁻¹ at 12 o'clock and -0.7 micro-inch⁻¹ at 6 o'clock is indicated. These values are nearly two orders of magnitude less than the droop value in the vertical direction. The model and data responses are very slight but comparable.

GAST

Figure 14. Gun #3: Muzzle Displacement Horizontal Direction 12 and 6 O'Clock.

Tube: #3; Direction: Horizontal; Profile Orientation: 3 & 9 O'Clock

Results for these conditions are found in Figure 15. In the horizontal direction at these orientations, a curvature value of -0.3 micro-inch^{-1} at 3 o'clock and +0.3 micro inch^{-1} at 9 o'clock is indicated. These values are even less than those at 12 and 6 o'clock. The model and data responses are again very slight.

GAST

Figure 15. Gun #3: Muzzle Displacement Horizontal Direction 3 and 9 O'Clock.

Point Values at Exit

A succinct method of data reporting, which highlights the overall dependency of profile curvature and orientation on muzzle motions and exit conditions, is shown in Figures 16 and 17. In these figures, point values at projectile exit for experimental data and modelling results for muzzle displacements and exit vectors are contained within elliptical envelopes in which the boundaries enclose the values reported at the four TVCL orientations.

Displacement results are reported in Figure 16. The area enclosed by the ellipses indicates the amount of sensitivity the gun has upon orientation of its bore curvature. As seen, the data envelope for tube #2 is rather large compared to its counterpart for tube #3. The enclosure for tube #2 is roughly 0.007 inch horizontal by 0.006 inch vertical, whereas for tube #3 the boundaries are 0.003 inch by 0.004 inch, respectively. This indicates that tube #2 is more sensitive to orientation of its bore profile than tube #3. Modelling results show the same trend because the enclosed area for tube #2 is about 0.003 inch in both directions and for tube #3 it is about 0.001 inch. However, when the test and model are compared, this sensitivity is not as pronounced. The model's area for tube #2 is about one-third as large and completely enclosed within the data for tube #2. For tube #3, the ratio is less.

GAST

EXIT CONDITIONS for 60mm TEST and MODEL
MUZZLE DISPLACEMENT ENVELOPES

GUN TUBE #2

GUN TUBE #3
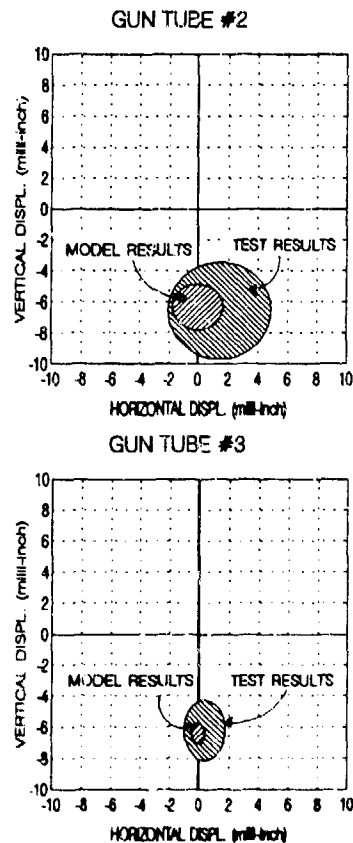
Figure 16. Point values @ Exit: Muzzle Displacements.

The exit vector is a calculated number. Its value is the sum of the muzzle's slope and transverse velocity divided by the projectile velocity at exit. It is essentially a measure of the initial direction that the tube imparts upon an exiting projectile. For the data, it is essentially a second order calculation in that neither the velocity nor the slope are measured directly. Velocity is derived by differentiating displacement, and slope is estimated as the secant angle between the two reporting stations near the muzzle. In the model this value is calculated directly from the muzzle motions.

The data and modelling results for this parameter are shown in Figure 17. The data indicates that the response for tube #2 is biased in the vertical direction. The vertical length is 0.75 milliradians (mr) and the horizontal is 0.5 mr. For tube #3, the enclosure is nearly circular with a diameter of 0.6 mr. The sensitivity between a curved and straight profile is not well established for the test results. The enclosed area for tube #2 is slightly greater than for tube #3 and roughly centered at the same location. For the model, the results show that tube #2 should have much greater sensitivity than tube #3, as indicated by the respective enclosed areas. The center of each enclosure is at the same location, however, the radii for tube #2 is much greater than for tube #3.

EXIT CONDITIONS for 60mm TEST and MODEL MUZZLE EXIT VECTOR ENVELOPES

GUN TUBE #2

GUN TUBE #5
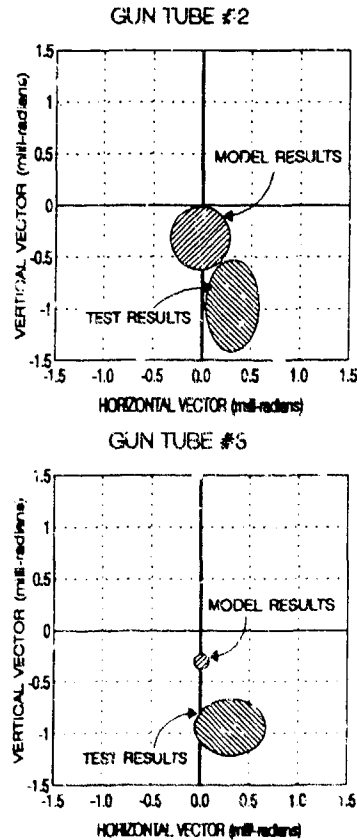
Figure 17. Point values @ Exit: Exit Vector.

RECOMMENDATIONS AND CONCLUSIONS

There were two reasons for conducting the test and simulation modelling reported herein. The first was to determine if the magnitude and orientation of the static curvature of a gun influences motions at the muzzle during projectile acceleration. The second was to verify a computer simulation model developed at Benet Laboratories.

In regard to the former, the data clearly demonstrates the existence of a relationship between bore profile and the kinematic state of the muzzle during projectile acceleration in the absence of all other known loads. Moreover, the magnitude and orientation of the spatially-curved bore center line alters the pointing angle of the muzzle at projectile exit, directly influencing the accuracy of the shot. The muzzle of a relatively straight tube is much 'quieter' than that which is not straight.

The model tracked the test results, but it is quite sensitive to the analytical representation of the profile. In order to achieve this level of similarity, great care must be taken in both profile measurement and its representation in the simulations. To this end, a statistical approach based upon the number of data points and the precision of their measurement was used to determine the 'best' functional fit. Since it is the second derivative that affects the response and not the actual profile, one may appreciate the care exercised in this area.

GAST

As a result of conducting this test, a great deal of experimental information now exists regarding not only gun dynamics but ballistics in general. Specific to gun dynamics, information regarding the kinematic response of the muzzle end is such that detailed predictions inherent to most computer models can be compared with actual data. This link has been sorely lacking in previous tests conducted on production weapons in a field environment where 'background noise' often infiltrated test parameters and corrupted results. The data generated from this test should be well suited for comparison with the predictive gun dynamics computer model developed at Benet. Both ballistic and dynamic consistency existed among similarly conditioned shots. This leads one to place a great deal of faith upon the test data and its use for model verification.

The rewards are immense in regard to analytically predicting shot accuracy. The first regards sustaining crew survival. For example, in a tank application, the probability of firing a second shot after a first round miss is very small. Most likely the return fire will defeat the attacking tank. In artillery applications, a first round kill is not as important, however, efficiency of operation and preservation of ammunition would certainly benefit if the initial shots of a firing mission were more accurate. The second benefit involves the concept of 'fleet zero' currently being studied for tank weapons. The knowledge of a tube's dynamic characteristics and its impact upon accuracy without the use of live firing would most definitely preserve ammunition. The results reported herein establish the worth of Benet Laboratories' Gun Vibration Model and its predictive capabilities in regard to modelling gun motion as a function of the magnitude and orientation of the bore's profile.

REFERENCES

1.   T.F. Erline and M.D. Kregel, "Modeling Gun Dynamics with Dominant Loads," *Proceedings of the Fifth U.S. Army Symposium on Gun Dynamics*, ARCCB-SP-87023, Benet Laboratories, Watervliet, NY, 23-25 September 1987, p. 150.

2.   R.G. Gast, "Analytical Comparison of the Accuracy of Tank Weapons," ARDEC Technical Report ARCCB-TR-89023, Benet Laboratories, Watervliet, NY, September 1989.

3.   T.E. Simkins, "Transverse Response of Gun Tubes to Curvature-Induced Load Functions," *Proceedings of the Second U.S. Army Symposium on Gun Dynamics*, ARLCB-SP-78013, Benet Weapons Laboratory, Watervliet, NY, 19-22 September 1978, pp. I-66 - I-77.

4.   D. Warken, K. Wolf, R. Heiser, J. Ballman, and W. Pavel, "The Effect of Barrel Curvature and Projectile Unbalance on Excitation of Gun Vibrations," *Proceedings of the Third U.S. Army Symposium on Gun Dynamics*, ARLCB-SP-82005, Vol. II, Benet Weapons Laboratory, Watervliet NY, 11-14 May 1982, pp. III-42 - III-63.

5.   E. Schmidt, "Jump From the M1A1 Tank," BRL IMR 868, Ballistic Research Laboratory, Aberdeen Proving Ground, MD, 1987.

6.   R.G. Gast, "Modal Analysis of the Dynamic Flexure in Tank Weapons by the Uniform Segments Method," Ph.D. Thesis, Rensselaer Polytechnic Institute, Troy, NY, April, 1988.

7.   R.G. Gast, "Normal Modes Analysis of Gun Vibration by the Uniform Segment Method," ARDEC Technical Report ARCCB-TR-87033, Benet Laboratories, Watervliet, NY, November 1987.

8.   G.J. Borse, *FORTRAN 77 and Numerical Methods for Engineers*, PWS-Kent Publishing Co., Boston, 1985, pp. 469-71.

AUTHORS: BUNDY, GERBER AND BRADLEY

TITLE: THERMAL DISTORTION DUE TO WALL THICKNESS VARIATION
AND UNEVEN COOLING IN AN M256 120-MM GUN BARREL

ABSTRACT:

During firing, the gun barrel centerline profile and muzzle pointing angle
change due to thermal distortion. There are several causes of thermal
distortion; we will discuss two: uneven cooling, and non-uniform wall
thickness. We will briefly explain the mechanisms by which these two effects
produce gun barrel bending and describe how these effects are modeled. We
will demonstrate our model by predicting the muzzle pointing angle change for
a particular gun tube firing five rounds, one every two minutes. The
predictions are compared with experimental results; some agreement is noted.

BIOGRAPHY: Dr. Mark L. Bundy

PRESENT ASSIGNMENT: Currently a Research Physicist with the U.S. Army
Research Laboratory, working in the area of tank
and artillery accuracy.

PAST EXPERIENCE: Temporary Assistant to the Director at the former
Ballistic Research Laboratory; Taught college math and
physics.

DEGREES HELD: B.A. Physics, Math from Augsburg College, Mpls. MN, 1972
M.S. Physics from Drake University, Des Moines, IA, 1975
Ph.D. Physics from the University of Maine, Orono, ME, 1980

THERMAL DISTORTION DUE TO WALL THICKNESS VARIATION AND UNEVEN COOLING IN AN M256 120-MM GUN BARREL

Mark L. Bundy*, Nathan Gerber and James W. Bradley

Aerodynamics Branch, Propulsion and Flight Division
U.S. Army Research Laboratory
Aberdeen Proving Ground, MD 21005

1. INTRODUCTION

High temperature propellant gas transfers heat to the barrel on every shot. If one side of the barrel has a slightly thicker wall than the other side, then the firing heat input will cause a greater change in temperature on the thin-walled side. This will produce a cross-barrel temperature difference, CBTD, which will create a non-uniform thermal expansion, and thereby bend the barrel away from the high temperature side.

Gerber and Bundy [1] computed the effect of wall thickness variation on CBTD in the 120 mm M256 gun. Their numerical model uses as input: the propellant temperature for a given 120-mm round type (e.g., DM13, M829, etc.), obtained from the NOVA code [2]; and the convection coefficient, obtained from the Veritay code [3,4], which utilizes the method of Stratford and Beavers [5]. The CBTD model will compute a non-zero temperature difference across the barrel at any point where the wall thickness is not uniform (a symmetric chrome layer is assumed).

When the firing heat input reaches the outer wall of the barrel, it will begin to transfer heat to the surrounding air. Since heated air rises in the earth's gravitational field, the hot air rising past the top of the barrel will remove less heat than the ambient temperature air moving past the bottom. And thus, a positive top-minus-bottom CBTD is established. Bundy [6] has recorded (plotted) CBTDs versus above-ambient barrel temperature at several locations along the bore. In addition, he has formulated a thermoelastic model that predicts barrel bend for any specified distribution of CBDTs along the barrel.

We will use the above two models, and reference data, to predict barrel bend due to CBDTs caused by wall thickness variation and uneven cooling for five rounds (DM13 kinetic energy penetrators) fired through a particular barrel (serial number 4251). We will compute the total muzzle angle change due to the combined CBTD effects after each shot and compare the predictions with measurements.

2. INPUT DATA:

A representative plot of the propellant gas temperature, T_g, and , convection coefficient, h_g, for the DM13 round at two locations, z=2.85 m and z=4.45 m from the breech, is shown in Figures 1 and 2, respectively.
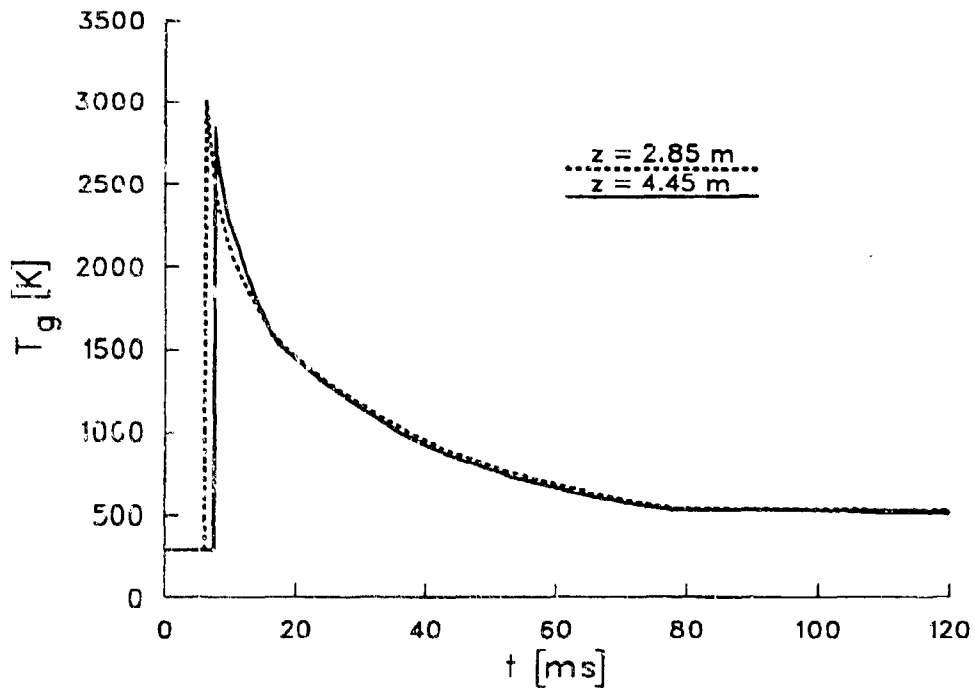
Figure 1. Propellant Gas Temperature versus Time, at z=2.85 m and z=4.45 m from the Breech, Computed from the NOVA code
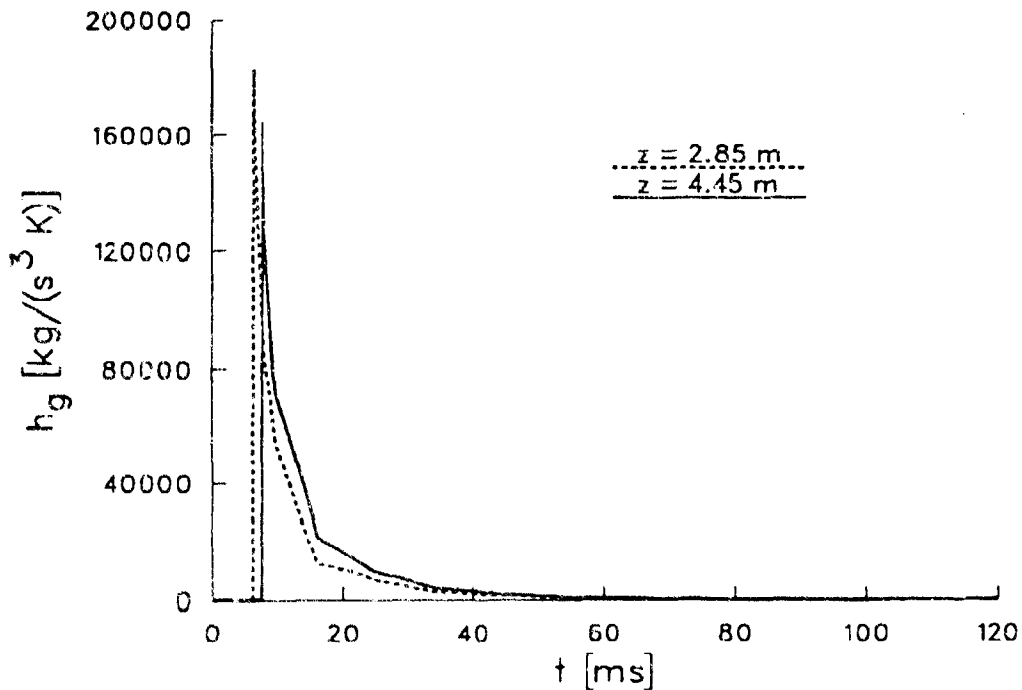
Figure 2. Heat Transfer Convection Coefficient, at z=2.85 m and z=4.45 m from the Breech, Computed from the Veritay Code

274

It is standard procedure at the time of manufacture to measure the inner and outer barrel radii at four positions around the bore (every 90 degrees), at numerous axial locations. Thus, wall thickness variation can be determined from these measurements. We will model wall thickness variation at a point along the bore axis by assuming that a plane, normal to the bore axis, will intersect the inner and outer walls of the barrel in two circles. The inner circle will have a radius R_I and the outer circle will have a radius R_o. Where there is wall thickness variation, the two circles will not be concentric. Viewed from the breech, we can describe the outer circle as displaced a distance ε at an angle φ relative to the origin and gunner's right of the inner circle, see Figure 3.

A listing of R_I, R_o, ε, and φ for the M256 gun barrel, serial number 4251 (manufactured in 1987), is given in Table 1. Since the barrel is relatively thick and the ε's are relatively small over that portion of the tube which lies within the recoil cradle (roughly the first two meters from the breech), we have assumed, a priori, that the majority of the thermal distortion due to wall thickness variation will originate from the region outside the cradle. Therefore, we have only specified values in Table 1 for R_I, R_o, ε, and φ over that portion of the barrel which extends beyond the recoil cradle.

The maximum value of ε for serial number 4251 is 0.13 mm, which corresponds to a maximum wall thickness variation of $2\varepsilon = 0.26$ mm. The maximum acceptable wall thickness variation for any M256 barrels is 1.5 mm (outside the chamber), which is almost six times larger than that of serial number 4251. Nevertheless, it is typical of barrels produced in recent years to have their maximum wall thickness variation several times smaller than the maximum allowed.

Table 1. Geometry for M256 Gun Barrel, Serial Number 4251

Distance, z, from Breech (m)	R_I (mm)	R_o (mm)	ε (mm)	φ (deg)
5.24	60	77.1	0.080	-128
5.09	60	77.2	0.075	-79
5.02	60	80.9	0.065	-90
4.45	60	82.7	0.100	-108
3.95	60	85.4	0.056	-63
3.45	60	109.1	0.027	-158
2.85	60	109.1	0.125	+81
2.35	60	103.0	0.130	+61

3. CBTD COMPUTATIONS

3.1 Wall Thickness Variation

Given the wall thickness variation described in Table 1, the model of Gerber and Bundy is used to calculate top-minus-bottom and left-minus-right CBDTs that result from propellant gas heating of the asymmetric barrel. For example, Figure 4 plots the CBTD history at the z=5.02 m location. From Table 1 and Figure 3, we can deduce that the bottom of the barrel is thicker than the top at z=5.02 m from the breech (ϕ = -90°); thus, we would expect the top-minus-bottom temperature difference to be positive, as predicted in Figure 4. Also, since the origins of the inner and outer wall radii are both aligned in the vertical plane at z=5.02 m, there should be no wall thickness variation, and hence no CBTD, in the horizontal plane, which is also shown to be the case in Figure 4.

For later comparison with experiment, we will tabulate the CBTD roughly one minute after firing each of the five rounds. These values are listed in Table 2, with the left-minus-right temperature difference denoted $CBTD_x$, and top-minus-bottom temperature difference denoted $CBTD_y$.

Table 2. Predicted CBTDs in the Horizontal and Vertical Planes Due to Wall Thickness Variation

Distance, z, from Breech (m)	$CBTD_x$ One Minute After Firing Round Number (°C)					$CBTD_y$ One Minute After Firing Round Number (°C)				
	1	2	3	4	5	1	2	3	4	5
5.24	-.07	-.13	-.16	-.18	-.19	+.10	+.16	+.21	+.23	+.25
5.09	+.03	+.04	+.05	+.06	+.06	+.11	+.19	+.24	+.27	+.29
5.02	0.00	0.00	0.00	0.00	0.00	+.07	+.11	+.15	+.17	+.19
4.45	-.02	-.04	-.05	-.06	-.07	+.08	+.13	+.17	+.19	+.21
3.95	+.01	+.03	+.03	+.04	+.04	+.03	+.05	+.07	+.08	+.08
3.45	-.01	-.01	-.01	-.01	-.02	0.00	0.00	+.01	+.01	+.01
2.85	0.00	+.01	+.01	+.01	+.01	-.03	-.05	-.07	-.08	-.09
2.35	+.02	+.03	+.04	+.05	+.06	-.04	-.06	-.07	-.09	-.10

3.2 Uneven Cooling

To estimate the top-minus-bottom CBTD due to uneven cooling one minute after firing at each of the locations in Table 1, we must first find the average above-ambient barrel temperature at each of these locations and times. This data can be obtained, and is displayed in Table 3, from the same Gerber and Bundy model used to predict the CBTDs due to wall-thickness variation.

As aforementioned, Bundy [6] has measured and plotted the CBTDs in the vertical plane due to uneven cooling as a function of the average above-ambient M256 barrel temperature. Using this reference data, we can estimate the CBTDs associated with the temperatures in Table 3. Since the data in Bundy is not given at the same locations as Table 3, we must use interpolation and extrapolation to determine the CBTD values listed here.
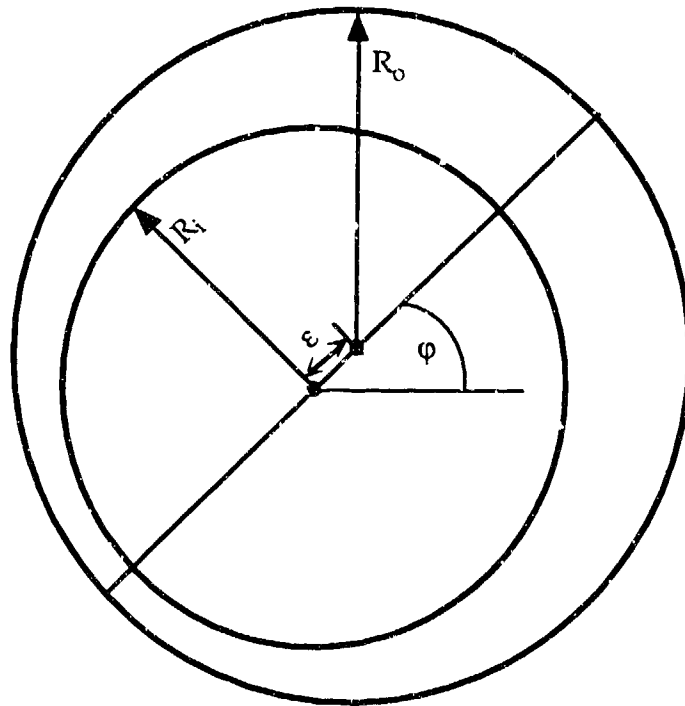
Figure 3. Transverse Cross Section of a Gun Barrel of Non-uniform Thickness, Viewed from the Breech
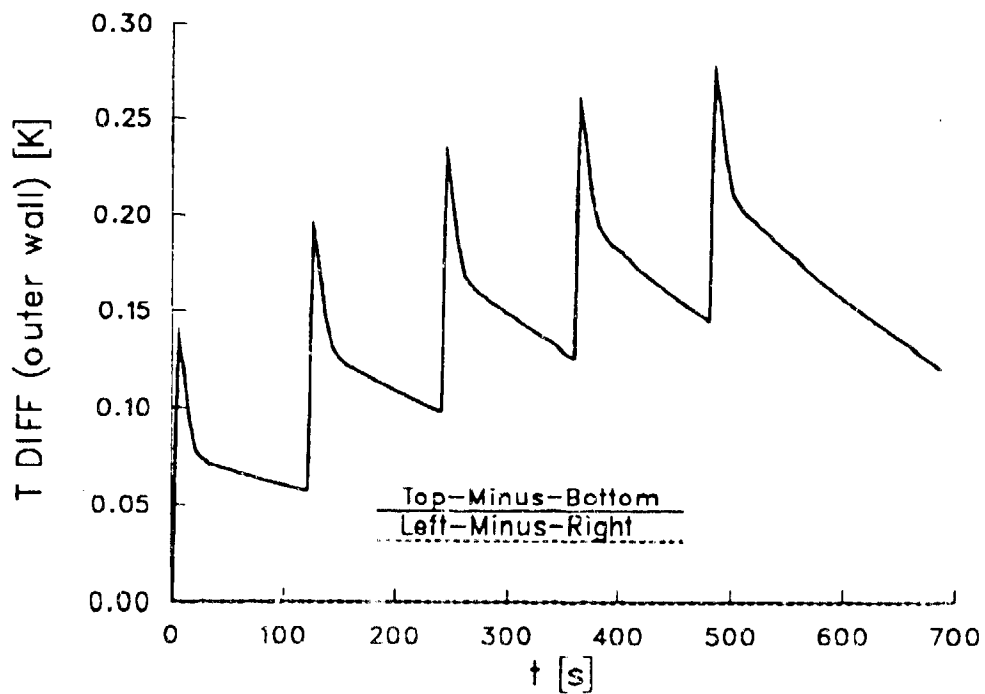
Figure 4. Predicted CBTDs in the Horizontal (Azimuthal) and Vertical (Elevation) Plane Due to Wall Thickness Variation at z=5.02 m from the Breech, from Gerber and Bundy code

277

Table 3. Predicted CBTDs in the Vertical Plane Due to Uneven Cooling

Distance, z, from Breech (m)	Average Above-Ambient Barrel Temperature One Minute After Firing Round Number (°C)					CBTD$_y$ One Minute After Firing Round Number (°C)				
	1	2	3	4	5	1	2	3	4	5
5.24	14	28	40	52	64	+1.8	+3.4	+4.6	+6.0	+7.2
5.09	14	28	40	52	64	+1.5	+2.8	+3.8	+4.1	+6.0
5.02	12	22	33	43	52	+1.4	+2.6	+3.5	+3.7	+5.4
4.45	10	18	26	34	42	+.30	+.40	+.55	+.75	+.90
3.95	8	15	22	29	35	+.25	+.35	+.50	+.65	+.75
3.45	3	7	10	13	16	+.16	+.25	+.35	+.45	+.53
2.85	4	7	11	14	18	+.04	+.08	+.10	+.13	+.16
2.35	5	9	13	17	21	0.00	0.00	+.01	+.01	+.02

4. BARREL BEND

The predicted barrel bend will be determined using the model described in Bundy [6]. This model computes the barrel bend of an M256 cannon due to uneven thermal expansion associated with a given set of CBTD input values. It is based on thermoelastic theory [7], which is applicable for small bends, such as the case here. The model assumes the barrel is supported at 0.36 m and 1.52 m from the breech, which is approximately the region where the barrel is upheld in the M256 recoil cradle. The change in elastic modulus with temperature at each CBTD location can be included in the barrel bend calculations, however, Bundy has shown that for tank gun firings this has an insignificant effect.

We will first compute thermal distortion due to wall thickness variation alone. In particular, Figure 5 shows the predicted change in horizontal and vertical muzzle angle due to the CBTD pairs (CBTD$_x$ and CBTD$_y$) given in Table 2. In general the muzzle angle is predicted to move down and to the gunner's right. However, the angular changes are extremely small. For comparison, we next plot, Figure 6, the predicted change in muzzle angle due to uneven cooling, from the CBTD$_y$ values in Table 3. It can be seen that the effect of uneven cooling dwarfs that of uneven wall thickness (for this particular barrel, under these firing conditions).
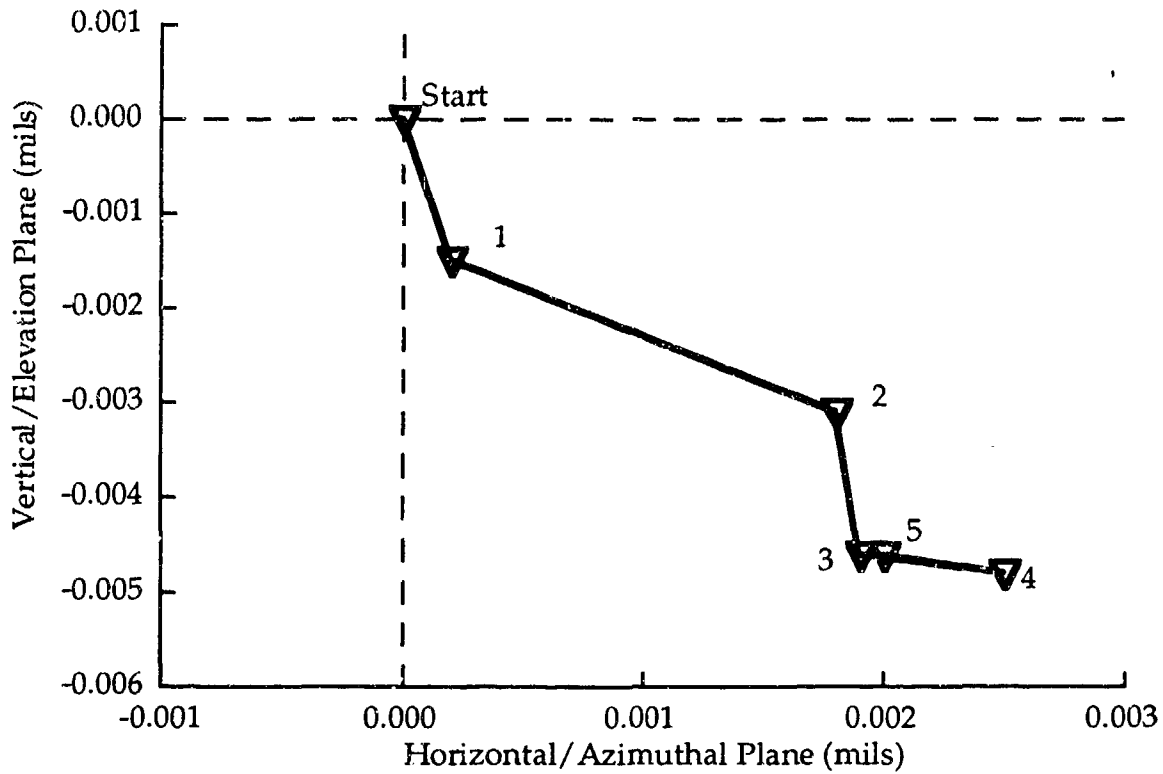
Figure 5. Predicted Muzzle Angle Change Due to Wall Thickness Variation, Associated with the CBTD Values of Table 2
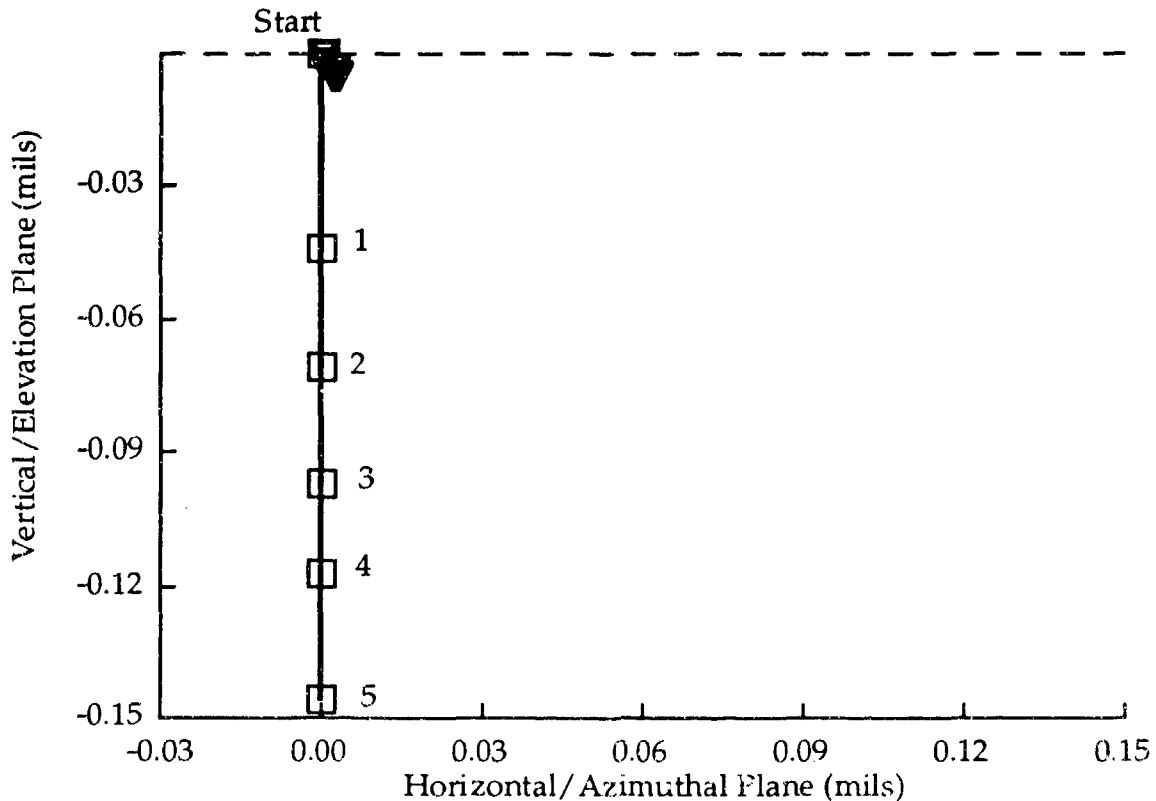
Figure 6. Predicted Muzzle Angle Change Due to Wall Thickness Variation and Uneven Cooling, Associated with the CBTD Values of Tables 2 and 3

279

The experimentally observed change in muzzle pointing angle at the times corresponding to Figure 6 are shown in Figure 7.* (Note, to correct for movement in the recoil cradle after firing each round, we have subtracted the angular change in the recoil cradle from the actual muzzle angle change for each measurement shown in Figure 7.) There is general agreement in the downward trend, most predictions in the vertical plane are within the experimental error of the measurements. However, in the horizontal plane the predicted movement to the gunner's right is much smaller than the measured movement to the right, nevertheless, the predictions are still within the measurement error of the instruments.
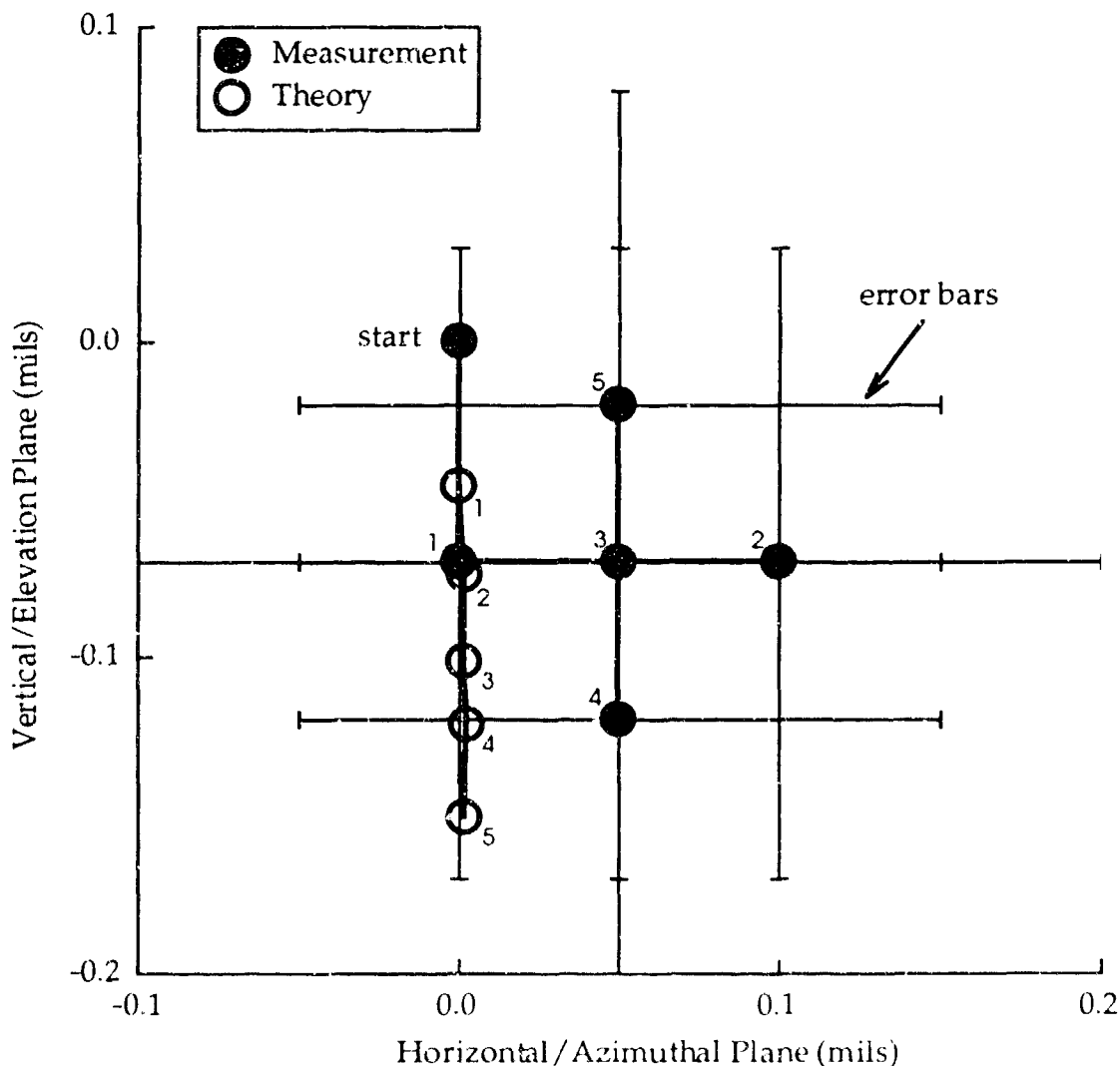
Figure 7. Predicted and Measured Muzzle Angle Change, One Minute after Firing each of Five DM13 Rounds (One Every Two Minutes) Through an M256 Barrel, Serial Number 4251

---

* Data was taken from a firing test done in November, 1991, APG, MD. Five DM13 rounds were fired through M256 barrel, serial number 4251 at a rate of roughly one round every two minutes.

5. SUMMARY

In theory, we have shown that thermal distortion of the gun barrel due to wall thickness variation in a typical M256 gun barrel is almost an order of magnitude smaller than the measured thermal distortion.

Thermal distortion due to uneven cooling accounts for most of the measured muzzle angle droop in our test case. However, for this particular barrel we observed changes in the horizontal muzzle angle which could not be accounted for in our analysis.

In view of our findings that wall thickness variation has a small effect on distortion, it seems unlikely that our a priori decision to neglect the wall thickness effect from that portion of the barrel which lies within the recoil mount would explain the noted differences.

There is, however, a third mechanism related to gun barrel manufacture, viz., variation in the chrome thickness, that could account for some of the differences between theory and experiment. Future work will add the contribution of chrome thickness variation to the predicted thermal distortion of Figure 7, in hopes of improving the agreement.

6. REFERENCES

1. Gerber, N., and M.L. Bundy, *Cross-Barrel Temperature Difference Due to Wall Thickness Variation*, ARL-TR-100, U.S. Army Research Laboratory, Aberdeen Proving Ground, MD, March 1993.

2. Gough, P.S., *The NOVA Code: A User's Manual - Volume 1. Description and Use*, IHCR-80-8, Naval Ordnance Station, Indian Head, MD, December 1980.

3. Chandra, S., and E.B. Fisher, *Simulation of Barrel Heat Transfer*, DAAA15-88-D-0014, U.S. Army Ballistic Research Laboratory, Aberdeen Proving Ground, MD, June 1989.

4. Chandra, S., and E.B. Fisher, *Analysis of 16-inch/50 Gun Chamber Heating*, Veritay Report No. C68-1, Naval Ordnance Station, Indian Head, MD, October 1989.

5. Stratford, B.S., and G.S. Beavers, *The Calculation of the Compressible Turbulent Boundary Layer in Arbitrary Pressure Gradient - A Correlation of Certain Previous Methods*, No. 3207, Aeronautical Research Council R&M, 1961.

6. Bundy, M.L., *Gun Barrel Cooling and Thermal Droop Modeling*, To be Published, U.S. Army Research Laboratory, Aberdeen Proving Ground, MD.

7. Boley, B.A., and J.H. Weiner, <u>Theory of Thermal Stresses</u>, New York: Wiley, 1960.

FINLAYSON

TITLE

Quantifying Gun Barrel Curvature: From Derivation of the Basic
Formulas to Evaluating Derivatives, Estimating Errors, and
Selecting Measurement Intervals.

David F. Finlayson

U.S. Army ARDEC
Close Combat Armaments Center
Benét Laboratories
Watervliet, NY 12189-4050

ABSTRACT

Following a discussion on the need to measure the curvature
of gun barrels are given the derivations of the unit tangent and
normal vectors; and the definitions of the binormal vector, and
the curvature and torsion of a space curve. Formulas for
curvature and torsion and the tangent, normal, and binormal
vectors are given in terms of cartesian coordinate derivatives.
The derivatives in these formulas must be evaluated numerically
using measurements of the deviation from straightness of the
barrel centerlines. Various methods for obtaining derivative
formulas (e.g. Taylor's series, and differentiating interpolating
polynomials derived by finite difference and least squares
methods) and the requirements of a derivative formula are given.
Origins and definitions of types of error are given as an
introduction to error estimation and measurement interval
selection. Finally a new method for selecting derivative
formulas and measurement intervals based on the treatment of
error as a random variable is introduced.

BIOGRAPHY:

PRESENT ASSIGNMENT:

Mechanical Engineer, Engineering Analysis Branch, Benét
Laboratories, Watervliet, NY, 1967-Present

PAST EXPERIENCE:

Mechanical Engineer (Ordnance), U.S. Naval Weapons Laboratory,
Dahlgren, VA, 1963-1966.
Packaging Engineer, Springfield Armory, Springfield, MA, 1961-
1963.

DEGREES HELD:
B.S. (Mechanical Engineering), Worcester Polytechnic Institute,
Worcester, MA, 1961.
M.S. (Mechanical Engineering), Rensselaer Polytechnic Institute,
Troy, NY, 1968.

FINLAYSON

Quantifying Gun Barrel Curvature: From Derivation of the Basic
Formulas to Evaluating Derivatives, Estimating Errors, and
Selecting Measurement Intervals.

David F. Finlayson
U.S. Army ARDEC
Close Combat Armaments Center
Benét Laboratories
Watervliet, NY 12189-4050

INTRODUCTION

It is well known that in the manufacture of gun barrels -
from initial forging to final machining-residual stresses are
created in the workpiece such that upon subsequent material
removal the developing barrel becomes crooked. Indeed, some of
the residual stresses are deliberately introduced in
straightening operations that occur between machining operations.
The object is, of course, to produce a gun barrel that is as
straight as possible or at most has a small amount of beneficial
curvature as would, for example, counteract gravity effects
(droop). And the reason for wanting a straight gun barrel is
accuracy; for even if the point of aim of a crooked barrel were
known, the disturbance of the barrel caused by the forces of a
projectile traveling in a crooked bore would make the point of
aim of the barrel at projectile exit essentially probabilistic.

Nevertheless, as much as we desire to make barrels that are
straight, practical limitations in the manufacturing process
preclude full attainment of that goal. This raises two
questions: (1) how do we specify what is an acceptable gun
barrel from the standpoint of straightness, and (2) given that
the barrels we make are not perfectly straight, how may we use
measurements of the deviation from straightness of individual gun
barrel bores to predict the most probable point of aim of that
gun barrel at projectile exit.

Obviously, the answers to the above questions would have to
be based on a rigorous analysis of the firing dynamics of gun
barrels which in turn would require a rigorous description of the
geometrical state of the gun barrel as defined by the bore
centerline. Such a description will, for every point on the
curve of the centerline, consist of values for the curvature
(κ), and torsion (τ) of the curve; and the components of the
vectors comprising the tangent, principal normal, and binormal
vector triad ($\vec{T}$, $\vec{N}$ and $\vec{B}$, respectively). In the following
section an introduction to the theory of space curves is given.
The section following that contains the formulas for the above
desired quantities in terms of derivatives of the centerline
curve with the detailed mathematical derivations omitted. For
the interested reader the details are available from the author.
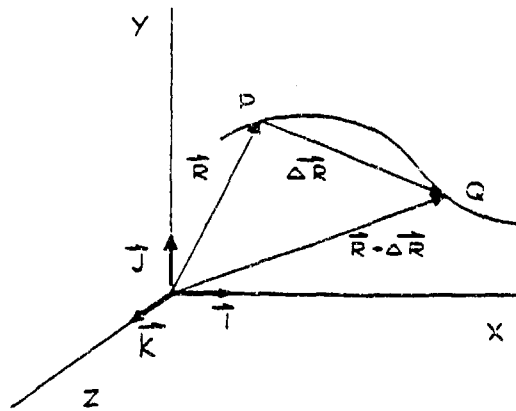
FIGURE 1.   Position Vectors for Points on a Curve in Space

A point in space, say P, can be described with the respect
the origin of a coordinate system by a position vector, $\vec{R}$, as
shown in figure 1.   In the figure $\vec{I}$, $\vec{j}$, and $\vec{k}$ are unit vectors
in the direction of the x, y, and z axes respectively.   Also
shown is the position vector $\vec{R} + \Delta\vec{R}$ to the point Q.   If the
vector difference between points P and Q is divided by the length
of the curve from P to Q, Δs, we have

$$\frac{\Delta\vec{R}}{\Delta s} = \frac{\Delta x}{\Delta s}\vec{I} + \frac{\Delta y}{\Delta s}\vec{j} + \frac{\Delta z}{\Delta s}\vec{k} \tag{1}$$

which in the limit as $\Delta s \to 0$ becomes

$$\frac{d\vec{R}}{ds} = \frac{dx}{ds}\vec{I} + \frac{dy}{ds}\vec{j} + \frac{dz}{ds}\vec{k} \tag{2}$$

Since it is apparent that $\frac{\Delta\vec{R}}{\Delta s} \to \frac{\Delta\vec{R}}{|\Delta\vec{R}|} \to \frac{d\vec{R}}{|d\vec{R}|}$ and $\Delta\vec{R}$

approaches tangency to the curve as $\Delta s \to 0$ we conclude that $\frac{d\vec{R}}{ds}$

is a unit vector, say $\vec{T}$, tangent to the curve at point P.
Taking the scalar product of $\vec{T}$ with itself gives therefore

$$\left(\frac{dx}{ds}\right)^2 + \left(\frac{dy}{ds}\right)^2 + \left(\frac{dz}{ds}\right)^2 = 1, \ or \ ds = \sqrt{(dx)^2 + (dy)^2 + (dz)^2} \tag{3}$$

FINLAYSON

Taking the derivative of the tangent vector with respect to curve length gives formally

$$\frac{d\vec{T}}{ds} = \frac{d}{ds}\left(\frac{d\vec{R}}{ds}\right) = \frac{d^2x}{ds^2}\vec{\imath} + \frac{d^2y}{ds^2}\vec{\jmath} + \frac{d^2z}{ds^2}\vec{k} \ . \tag{4}$$

Now since $\vec{T}$ is a vector of constant (unit) length its derivative can have no component parallel to $\vec{T}$ so that it must be normal to $\vec{T}$ and point in the direction of change of $\vec{T}$. This is expressed as $\frac{d\vec{T}}{ds} = \kappa \vec{N}$ where $\vec{N}$ is a unit vector called the principal normal which points in the direction of change of $\vec{T}$ and κ is a scalar multiplier called the curvature and is the rate of change in direction of $\vec{T}$ with respect to distance along the curve. Taking the scalar product of $\frac{d\vec{T}}{ds}$ with itself gives therefore

$$\left(\frac{d^2x}{ds^2}\right)^2 + \left(\frac{d^2y}{ds^2}\right)^2 + \left(\frac{d^2z}{ds^2}\right)^2 = \kappa^2, \ or \ \kappa = \sqrt{\left(\frac{d^2x}{ds^2}\right)^2 + \left(\frac{d^2y}{ds^2}\right)^2 + \left(\frac{d^2z}{ds^2}\right)^2} \tag{5}$$

If we were to construct a circle of radius ρ through the points P and Q of figure 1 and designate the central angle between radial lines to P and Q as $\Delta\theta$, then the length of the included arc would be given as $\Delta s = \rho\Delta\theta$, or $\frac{1}{\rho} = \frac{\Delta\theta}{\Delta s}$. And, as $\frac{\Delta\theta}{\Delta s} \to \frac{d\theta}{ds}$ as $\Delta s \to 0$ then $\frac{1}{\rho} = \frac{d\theta}{ds}$. But $\frac{d\theta}{ds} = \kappa$ so we have $\frac{1}{\rho} = \kappa$ and ρ is called the radius of curvature.

A third unit vector, called the binormal vector, which is perpendicular to both the tangent and principal normal vectors is defined by $\vec{B} = \vec{T} \times \vec{N}$. The unit vector triad thus defined is shown in figure 2.
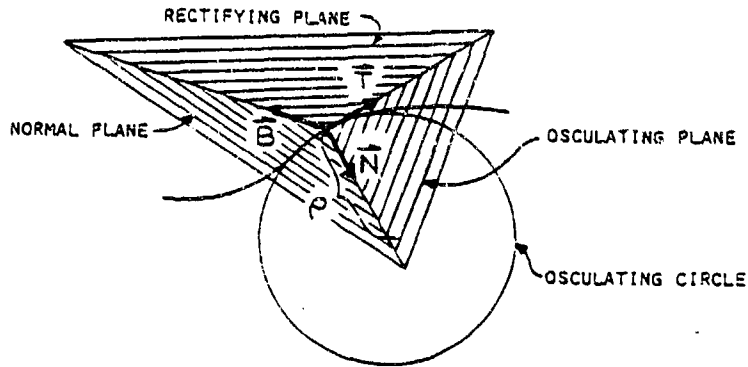
Figure 2. The unit vector triad on a curve.

In the figure the circle of radius ρ labeled the osculating circle is so named because it is just tangent to (kisses) the curve. The plane defined by the tangent and principal normal vectors is called the osculating plane because it contains the osculating circle. Also shown is the rectifying plane defined by the binormal and tangent vectors which is so named because, when viewed in the perspective of the plane, the curve is rectified or seen in its full length. Finally there is the normal plane defined by the principal normal and binormal vectors and so named because it is normal, or perpendicular, to the curve.

Taking the derivative of the binormal vector with respect to curve length provides a useful relationship as follows:

$$\frac{d\vec{B}}{ds} = \frac{d}{ds} (\vec{T} \times \vec{N}) = \vec{T} \times \frac{d\vec{N}}{ds} + \frac{d\vec{T}}{ds} \times \vec{N} = \vec{T} \times \frac{d\vec{N}}{ds}.$$

(Since the vectors $\frac{d\vec{T}}{ds}$ and $\vec{N}$ are parallel, their vector product is zero.) The definition of the vector product gives $\frac{d\vec{B}}{ds}$ perpendicular to $\vec{T}$ and, since $\vec{B}$ is a vector of constant (unit) magnitude, $\frac{d\vec{B}}{ds}$ must also be perpendicular to $\vec{B}$. Therefore we must conclude that $\frac{d\vec{B}}{ds}$ is parallel to $\vec{N}$ so we can say

$$\frac{d\vec{B}}{ds} = -\tau \vec{N}. \tag{6}$$

The scalar multiplier τ is called the torsion of the curve and is a measure of the rate of "twist" of the curve. A negative sign is attached to the multiplier so that positive torsion is indicated with positive rotation of $\vec{B}$ in the right handed sense.

Lastly, the derivative of the principal normal with respect to distance along the curve is

$$\frac{d\vec{N}}{ds} = \frac{d}{ds}(\vec{B} \times \vec{T}) = \vec{B} \times \frac{d\vec{T}}{ds} + \frac{d\vec{B}}{ds} \times \vec{T} \tag{7}$$

$$= \kappa(\vec{B} \times \vec{N}) - \tau(\vec{N} \times \vec{T}) = \tau\vec{B} - \kappa\vec{T}$$

Equations (6) and (7) are known as the Frenet-Serret formulas after the French mathematicians who independently discovered them about one hundred and fifty years ago.

The relationship between κ and τ can be found by taking the scalar product of $\vec{N}$ and $\frac{d\vec{B}}{ds}$:

$$\vec{N} \cdot \frac{d\vec{B}}{ds} = -\tau(\vec{N} \cdot \vec{N}), \quad or$$

$$\tau = -\frac{1}{\kappa}\frac{d^2\vec{R}}{ds^2} \cdot \frac{d}{ds}\left(\frac{d\vec{R}}{ds} \times \frac{1}{\kappa}\frac{d^2\vec{R}}{ds^2}\right)$$

$$= -\frac{1}{\kappa^2}\frac{d^2\vec{R}}{ds^2} \cdot \left(\frac{d^2\vec{R}}{ds^2} \times \frac{d^2\vec{R}}{ds^2} + \frac{d\vec{R}}{ds} \times \frac{d^3\vec{R}}{ds^3}\right) \tag{8}$$

$$= -\frac{1}{\kappa^2}\frac{d^2\vec{R}}{ds^2} \cdot \left(\frac{d\vec{R}}{ds} \times \frac{d^3\vec{R}}{ds^3}\right)$$

$$= \frac{1}{\kappa^2}\frac{d\vec{R}}{ds} \cdot \left(\frac{d^2\vec{R}}{ds^2} \times \frac{d^3\vec{R}}{ds^3}\right).$$

Substitution of (2) into the scalar triple product (8) and performing the indicated vector multiplication gives a formula which can be expressed in determinant form as

$$\tau = \cfrac{\begin{vmatrix} \dfrac{dx}{ds} & \dfrac{dy}{ds} & \dfrac{dz}{ds} \\[2ex] \dfrac{d^2x}{ds^2} & \dfrac{d^2y}{ds^2} & \dfrac{d^2z}{ds^2} \\[2ex] \dfrac{d^3x}{ds^3} & \dfrac{d^3y}{ds^3} & \dfrac{d^3z}{ds^3} \end{vmatrix}}{\kappa^2} \tag{9}$$

Curvature, Torsion; and the Components of the Tangent, Principal Normal, and Binormal Vectors in Parametric Form.

For purposes of expressing these quantities in terms of measurable variables it will be more convenient to express x, y, and z in terms of a parameter that is directly determinable. This parameter could be one that is totally independent, say t (not necessarily time), or what is best for our purposes, x. That is we shall say that y=f(x) and z=g(x). Without showing the somewhat lengthy mathematical operations required to obtain them, the formulas for curvature and torsion are

$$\kappa = \left\{ \cfrac{\left(\dfrac{dy}{dx}\dfrac{d^2z}{dx^2} - \dfrac{dz}{dx}\dfrac{d^2y}{dx^2} \right)^2 + \left(\dfrac{d^2z}{dx^2} \right)^2 + \left(\dfrac{d^2y}{dx^2} \right)^2}{\left[1 + \left(\dfrac{dy}{dx} \right)^2 + \left(\dfrac{dz}{dx} \right)^2 \right]^3} \right\}^{\frac{1}{2}} \tag{10}$$

and

$$\tau = \cfrac{\left(\dfrac{d^2y}{dx^2}\dfrac{d^3z}{dx^3} - \dfrac{d^2z}{dx^2}\dfrac{d^3y}{dx^3} \right)}{\left(\dfrac{dy}{dx}\dfrac{d^2z}{dx^2} - \dfrac{dz}{dx}\dfrac{d^2y}{dx^2} \right)^2 + \left(\dfrac{d^2z}{dx^2} \right)^2 + \left(\dfrac{d^2y}{dx^2} \right)^2} \tag{11}$$

FINLAYSON

For a curve that lies in a plane, say z = constant,
$\frac{dz}{dx} = \frac{d^2z}{dx^2} = \frac{d^3z}{dx^3} = 0$ so that $\tau = 0$ and we get the familiar formula

$$\kappa = \frac{\dfrac{d^2y}{dx^2}}{\left[1 + \left(\dfrac{dy}{dx}\right)^2\right]^{3/2}} . \tag{12}$$

And the formulas for the tangent, principal normal, and binormal vectors are respectively

$$\vec{T} = \frac{\vec{i} + \dfrac{dy}{dx}\,\vec{j} + \dfrac{dz}{dx}\,\vec{k}}{\left[1 + \left(\dfrac{dy}{dx}\right)^2 + \left(\dfrac{dz}{dx}\right)^2\right]^{\frac{1}{2}}} , \tag{13}$$

$$\vec{N} = \frac{\begin{array}{l} -\left[\left(\dfrac{dy}{dx}\right)\left(\dfrac{d^2y}{dx^2}\right) + \left(\dfrac{dz}{dx}\right)\left(\dfrac{d^2z}{dx^2}\right)\right]\vec{i} \\[2mm] + \left\{\left[1 + \left(\dfrac{dz}{dx}\right)^2\right]\left(\dfrac{d^2y}{dx^2}\right) - \left(\dfrac{dz}{dx}\right)\left(\dfrac{d^2z}{dx^2}\right)\left(\dfrac{dy}{dx}\right)\right\}\vec{j} \\[2mm] + \left\{\left[1 + \left(\dfrac{dy}{dx}\right)^2\right]\left(\dfrac{d^2z}{dx^2}\right) - \left(\dfrac{dy}{dx}\right)\left(\dfrac{d^2y}{dx^2}\right)\left(\dfrac{dz}{dx}\right)\right\}\vec{k} \end{array}}{\left[\left(\dfrac{dy}{dx}\dfrac{d^2z}{dx^2} - \dfrac{dz}{dx}\dfrac{d^2y}{dx^2}\right)^2 + \left(\dfrac{d^2z}{dx^2}\right)^2 + \left(\dfrac{d^2y}{dx^2}\right)^2\right]^{\frac{1}{2}}\left[1 + \left(\dfrac{dy}{dx}\right)^2 + \left(\dfrac{dz}{dx}\right)^2\right]^{\frac{1}{4}}} , \tag{14}$$

and

$$\vec{B} = \frac{\left(\dfrac{dy}{dx}\dfrac{d^2z}{dx^2} - \dfrac{dz}{dx}\dfrac{d^2z}{dx^2}\right)\vec{i} - \dfrac{d^2z}{dx^2}\,\vec{j} + \dfrac{d^2y}{dx^2}\,\vec{k}}{\left[\left(\dfrac{dy}{dx}\dfrac{d^2z}{dx^2} - \dfrac{dz}{dx}\dfrac{d^2y}{dx^2}\right)^2 + \left(\dfrac{d^2z}{dx^2}\right)^2 + \left(\dfrac{d^2y}{dx^2}\right)^2\right]^{\frac{1}{2}}} . \tag{15}$$

EVALUATING THE FORMULAS

As equations (10), (11) and (13) - (15) show, the problem comes down to evaluating first and second order derivatives (and third order for equation (11)) of y and z with respect to x. This must be accomplished numerically by substituting measurements of barrel deviation from straightness into derivative formulas. One such measurement could be that of the offset of the barrel centerline from an established straight reference line at specified intervals along its length, much as is done now in final acceptance inspection. Substitution of measurements taken in orthogonal directions representing the x and y coordinates then allows evaluation of the equation.

Another measurement could be that of the slope (first derivative) of the barrel centerline relative to the horizontal or some other reference slope. Evaluation of the formulas would then be accomplished by substitution directly for the first derivatives and into first and second order derivatives, respectively. Again, the measurements would be taken at intervals along the barrel and in orthogonal planes. This method of evaluating the formulas not only has the obvious advantage of reducing numerical error through calculating fewer derivatives, but the measurements themselves would probably be more precise.

In any case it will be desired to obtain derivatives having some limit on their error if not the most precise possible. These derivatives require some care in computing as numerical differentiation can be considered an unstable process that may lead to large errors. The reasons for this should become apparent in the sections to follow where the methods for obtaining the derivative formulas are outlined and a result of a theory for determining the required precision and spacing of the measurements is presented.

OBTAINING DERIVATIVE FORMULAS

One method of obtaining derivative formulas for the function of x, f(x), is to write the Taylor series expansion for f(x) about the point of interest, x_o, as

$$f(x_o+h) = f(x_o) + hf'(x_o) + \frac{h^2}{2!} f''(x_o) + \frac{h^3}{3!} f'''(x_o) + \ldots \qquad (16a)$$

or

$$f(x_o-h) = f(x_o) - hf'(x_o) + \frac{h^2}{2!}f''(x_c) - \frac{h^3}{3!}f'''(x_o) + \ldots \qquad (16b)$$

Rearrangement of these equations gives

$$f'(x_o) = \frac{f(x_o+h) - f(x_o)}{h} - \frac{h}{2!}f''(x_o) - \frac{h^2}{3!}f'''(x_o) - \ldots \qquad (17a)$$

and

$$f'(x_o) = \frac{f(x_o) - f(x_o-h)}{h} + \frac{h}{2!}f''(x_o) - \frac{h^2}{3!}f'''(x_o) + \ldots \qquad . \quad (17b)$$

By truncating these equations after the first term the first approximations to the first derivative at $x = x_o$ are obtained as

$$f'(x_o) \approx \frac{f(x_o+h) - f(x_o)}{h} \equiv \frac{f_1 - f_o}{h}, \qquad (18a)$$

and

$$f'(x_o) \approx \frac{f(x_o) - f(x_o-h)}{h} \equiv \frac{f_o - f_{-1}}{h}. \qquad (18b)$$

where the f_i represent the function values at $x = x_o + ih$. Now, since the derivative formulas (18a, b) are the result of truncating equations (17a, b) there has been introduced what is called truncation error. It can be shown that this truncation error is

$$E_T = \pm \frac{h}{2} f''(\xi) \qquad (19)$$

where $\xi = \xi(x)$ is an unknown function of x evaluated on the interval. The error in this case is said to be of order h, O(h). Formulas (18a, b) are the simplest examples of what are called forward and backward difference formulas, respectively. If the average of these two formulas is taken the result is

$$f'(x_o) = \frac{f_1 - f_{-1}}{2h} \tag{20}$$

which is the simplest example of what are called central difference formulas. Adding equation (17b) to equation (17a) and solving for $f'(x_o)$ gives formula (20) as well with the truncation error

$$E_T = -\frac{h^2}{6} f'''(\xi) \tag{21}$$

being determined from the first truncation term as before. It is obvious that, since the truncation error for formula (20) is $O(h^2)$ as compared to $O(h)$ for formulas (18a, b), for small enough values of h, formula (20) will be the more precise. In general central difference formulas give better results than forward or backward difference formulas and will be the only type considered hereinafter. One more example of this method of formula derivation is provided by subtracting equation (17b) from equation (17a) to give

$$f''(x_o) = \frac{f_{-1} - 2f_o + f_1}{h^2} \tag{22}$$

which has error $O(h)$.

Although the method of the preceding paragraph could be used to obtain derivatives of higher order than two, as above, and formulas with more points than three, as above also, it is more efficient to use interpolating formulas and take their derivatives. It should be noted that interpolating polynomials are meant to interpolate between the value of tabular points and in that way represent the underlying but unknown function. Even though they may do that well, that does not mean that their derivatives will accurately approximate the derivatives of the function. More will be said about the control of error in the section to follow.

In any case it is convenient to normalize the variables according to

FINLAYSON

$$s = \frac{x - x_o}{h} \tag{23}$$

where h is the tabular or measurement interval and s is the interpolating function variable. Differentiating (23) gives

$$\frac{ds}{dx} = \frac{d}{dx}\left(\frac{x - x_o}{h}\right) = \frac{1}{h} . \tag{24}$$

Applying the chain rule for derivatives gives first

$$\frac{df}{dx} = \frac{df}{ds}\frac{ds}{dx} = \frac{1}{h}\frac{df}{ds} \tag{25}$$

and then

$$\frac{d^2 f}{dx^2} = \frac{1}{h}\frac{d^2 f}{ds^2}\frac{ds}{dx} = \frac{1}{h^2}\frac{d^2 f}{ds^2} \tag{26}$$

and so on. The observation to be made here is that continuing in the above manner would produce the general result

$$f^d(x) = f^d(x_o + sh) = \frac{1}{h^d}f^d(s) \tag{27}$$

where d is the order of the derivative.

Without presenting the laborious details, some formulas obtained by differentiating Stirling's central difference interpolation formula (the average of Newton's forward and backward difference interpolation formulas) and setting s = o are:

$$f'(x_o) = \frac{f_{-2} - 8F_{-1} + 8f_1 - f_2}{12h} , \tag{28}$$

$$f''(x_o) = \frac{-f_{-2}+16f_{-1}-30f_o+16f_1-f_2}{12h^2} , \qquad (29)$$

$$f'(x_o) = \frac{-f_{-3}+14f_{-2}-85f_{-1}+85f_1-14f_2+f_3}{120h} , \qquad (30)$$

and

$$f'''(x_o) = \frac{3f_{-3}-32f_{-2}+55-f_{-1}-55f_1+32f_2-3f_3}{40h^3} . \qquad (31)$$

The formulas above are just a few of a very large number of formulas that are obtainable not only from Stirling's but other differencing schemes as well as the method of least squares using orthogonal polynomials, and even by substituting formulas back into themselves or other formulas. What is significant is that it is possible to estimate the value of a derivative of a function with a weighted average of the values of the function at equally space intervals away from the point of interest divided by the interval spacing raised to the order of the derivative. (The observant reader will note the apparent rules of symmetry and summation for the coefficients of the function values in the formulas). In the next section the important question of what the interval spacing should be will be addressed.

ERRORS AND INTERVALS

As in any calculation one should be concerned with errors when calculating derivatives numerically-indeed, especially concerned when calculating derivatives numerically. The reason for this is as follows. Recalling that what was called truncation error was, in absolute magnitude, on the order of the measurement or tabulation interval, h, raised to some power, it would seem that by simply making h smaller the error could be made as small as one wished. But as h is made smaller the values of the f_n in the formulas get closer. If carried far enough, making h smaller would make the differences between the f_n as small as the error in measurement and cause them to be "lost in the noise." Clearly there is more than one kind of error that must be considered and a balance struck in regard to the size of h in order to minimize total error.

FINLAYSON

To get a start at this the following kinds of errors will be recognized:

Truncation Errors arise from limiting the number of terms in a series or polynomial used to approximate the function of interest and increase in size as the number of terms is diminished.

Discretization Errors derive from the size of the measurement or tabulation interval used and increase in size as the size of the interval is increased.

Round-off Errors accumulate from the use of irrational numbers of necessarily finite length and increase in size with the number of athematical operations performed with the numbers.

Input Errors are the result of limitations on the precision of the input data such as would occur in physical measurements and increase in size with the number of mathematical operations performed with the data.

The above listed kinds of errors are not entirely unrelated. For instance, truncation and discretization errors are related by the fact that the measurement or tabluation interval is equal to the overall interval over which the measurements or tabulations are made divided by the degree of the approximating polynomial which collocates at the measurement or tabulation points. The choice between the terms truncation and discretization is mainly one of viewpoint based on how the derivative formulas are derived and thus how the error arises. Since the term truncation error has already been introduced, it will be used in what follows. Round-off and input errors, on the other hand, are both examples of what could be called resolution error; however, since the effect of measurement errors is the issue here, the term input error will be used here.

Whatever terms are used for these kinds of error it is the total error that is of interest in the end. By definition it can be said that

$$Total\ error = Calculated\ value - Exact\ value$$

$$= (Calculated\ value - Formula\ value) \qquad (32)$$

$$+ (Formula\ value - Exact\ value)$$

And, recognizing the meaning of the terms in parentheses,

$$Total\ error = Input\ error + Truncation\ error. \tag{33}$$

Alternatively, dividing through by Exact value gives

$$\frac{Total\ error}{Exact\ value} = \frac{Input\ error}{Exact\ value} + \frac{Formula\ value}{Exact\ value} - 1. \tag{34}$$

From the foregoing discussion one would be led to believe that there is some optimum value of h which would result in minimum total error; indeed, at least in theory, setting the derivative of equation (33) equal to zero would result in an expression for optimum h. In practi e, however, it is not possible to obtain expressions for input error and truncation error that are definite enough to permit that. In an effort to get around this difficulty the author has recently utilized equation (34) taking into account the probabilistic nature of the input error.

Only a brief outline of the theory and results will be given here as follows: Since Input error/Exact value is a random variable, Total error/Exact value is also a random variable. The expected value of (Total error/Exact value) squared can easily be shown to be

$$E[X^2] = E[Y^2] + C^2 \tag{35}$$

where $E[Y^2]$ is the expected value of (Input error/Exact value) squared and C^2 is (Formula value/Exact Value - 1) squared. Evaluating the latter term can be accomplished by considering the data over the interval of interest to represent the values of a cyclic function which meets the Dirichlet conditions and has a period equal in length to that of the interval, thus allowing the assumed underlying function to be expressed as a Fourier series. Based on this it would seem reasonable to take a sine (or cosine) function as representative, in a sense, of the function whose derivative is required.

FINLAYSON

The result of analyzing error in this way can be shown graphically as in Figure 3 where for different values of $(E[X^2])^{1/2}$ (percent expected error) are plotted values of the ratio measurement precision to wave amplitude ($|e_M/a|$) versus the ratio measurement interval to wavelength (h/L). A plot such as this can be used to compare different derivative formulas as well as support the best measurement interval to use based on some knowledge of the underlying function such as would be obtained from Fourier analysis.
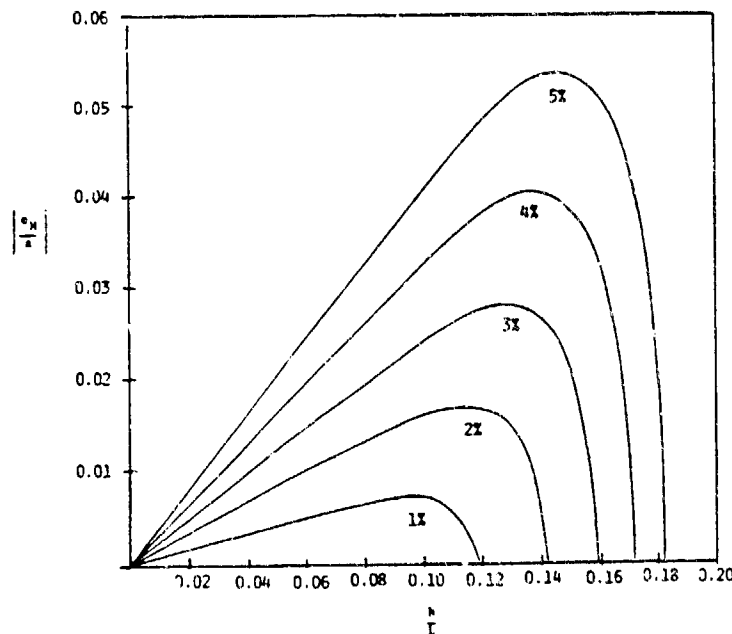
Figure 3. Measurement Precision vs. Measurement Interval for Various Expected Errors

SESSION IV

CONTROLS--THEORY AND APPLICATIONS

STABILITY ANALYSIS AND CONTROL OF A ROTARY FLEXIBLE BEAM

M.F. Golnaraghi and G.R. Heppler
ConStruct Group, Department of Mechanical Engineering
University of Waterloo
Waterloo, Ontario N2L 3G1

ABSTRACT

This paper addresses the stability analysis and control of a two degree of freedom flexible rotary beam with a flexible joint. The beam has been modelled as a lumped mass system with flexibility in two planes represented by torsional springs. The nonlinear equations of the system are coupled and contain gyroscopic terms. It is shown that the system can exhibit both divergence and flutter instabilities as the rotational speed and/or the beam and joint stiffnesses vary. It is demonstrated that the stabilization of the system is possible by adjusting the joint flexibility, via position feedback. Furthermore, addition of damping to the joint through velocity feedback, could remove the oscillations in one direction and significantly reduce the vibrations in the other, once the joint stiffness is properly tuned (at internal resonance).

BIOGRAPHY: M.F. Golnaraghi

PRESENT ASSIGNMENT: Assistant Professor, Department of Mechanical Engineering, University of Waterloo

DEGREES HELD: PhD, Theoretical and Applied Mechanics, Cornell University

STABILITY ANALYSIS AND CONTROL OF A ROTARY FLEXIBLE BEAM

M.F. Golnaraghi and G.R. Heppler
ConStruct Group, Department of Mechanical Engineering
University of Waterloo
Waterloo, Ontario N2L 3G1

INTRODUCTION

Gyroscopic systems have been the subject of numerous studies [1-4]. One of the most important properties of the gyroscopic systems is that they can display static instabilities (divergence) and dynamic instabilities (flutter) [1]. Application of gyroscopic systems can be encountered in helicopter rotors and robotic systems where the above mentioned instabilities can be detrimental. In this paper, a simple model which retains the fundamental features and behaviour of these type of systems is studied. As a first step, a rotational lumped mass rigid body model with flexibility in two directions is considered. The effects of flexibility and the rotor angular speed on the stability of the system are presented. Furthermore, a simple control strategy, based on feedback control theory and internal resonance [5,6], is proposed to stabilize the system and to regulate the oscillations in both directions. The control torque in this method is applied in only one plane. The goal of this research is to extend these preliminary results to the above mentioned physical systems.

MATHEMATICAL MODEL

The lumped mass system of concern is a simple model of a flexible joint/ flexible beam rotary system, as shown in Figure 1. The X,Y,Z coordinate frame is stationary and the x,y,z frame rotates with the rigid link, l_4, with a constant angular velocity Ω about the Z axis. Masses M_1 and M_2 represent the masses of links l_1 and l_2, respectively (and any additional payload and counterweight elements). The generalized variables θ_1 and θ_2 are measured relative to the x,y,z reference frame. The stiffness coefficients K_1 and K_2 represent flexibility in x and z directions. The control torque T is applied, at the joint, in the direction along the y axis. This torque is used to attain any static equilibrium configuration defined by $\theta_1 = \theta_{1ref}$ and $\theta_2 = 0$. Furthermore, it can be used to adjust the torsional flexibility in the y direction (i.e. K_1).

EQUATIONS OF MOTION

The equations of motion of the system in nondimensional form are:

$$
\begin{bmatrix} a_{11} & a_{12} \\ a_{21} & a_{22} \end{bmatrix} \begin{Bmatrix} \ddot{\theta}_1 \\ \ddot{\theta}_2 \end{Bmatrix} + \begin{bmatrix} 0 & b_{12}\theta_2 \\ b_{21}\theta_1 & 0 \end{bmatrix} \begin{Bmatrix} \dot{\theta}_1 \\ \dot{\theta}_2 \end{Bmatrix} + \begin{bmatrix} 0 & c_{12}\theta_1 \\ c_{21}\theta_2 & 0 \end{bmatrix} \begin{Bmatrix} \dot{\theta}_1 \\ \dot{\theta}_2 \end{Bmatrix}
$$

$$
+ \begin{bmatrix} 0 & d_{12} \\ d_{21} & 0 \end{bmatrix} \begin{Bmatrix} \dot{\theta}_1 \\ \dot{\theta}_2 \end{Bmatrix} + \begin{bmatrix} e_{11} & 0 \\ 0 & e_{22} \end{bmatrix} \begin{Bmatrix} \theta_1 \\ \theta_2 \end{Bmatrix} + \begin{bmatrix} f_{11} \\ f_{21} \end{bmatrix} = \begin{bmatrix} T \\ 0 \end{bmatrix}
\tag{1}
$$

$$a_{11} = \left(M^* \ell_2^{*2} + 1\right)\left(\cos^2\theta_1 \cos^2\theta_2 + \sin^2\theta_1\right) ,$$

$$a_{12} = \left(M^* \ell_2^{*2} + 1\right)\left(\cos\theta_1 \sin\theta_1 \sin\theta_2\right) , \quad a_{21} = a_{12} ,$$

$$a_{22} = \left(M^* \ell_2^{*2} + 1\right)\cos^2\theta_1 ,$$

$$b_{12} = \left(M^* \ell_2^{*2} + 1\right)\cos\theta_1 \sin\theta_1 \left(1 + \cos\theta_2\right) ,$$

$$b_{21} = \sin\theta_2 \left(M^* \ell_2^{*2} + 1\right)\left(\cos^2\theta_1 \cos\theta_2 - \sin^2\theta_1 + \cos^2\theta_1\right) ,$$

$$c_{12} = -2\left(M^* \ell_2^{*2} + 1\right)\left(\cos^2\theta_1 \cos^2\theta_2 \sin\theta_2\right) ,$$

$$c_{21} = -2\left(M^* \ell^{*2} + 1\right)\cos\theta_1 \sin\theta_1 ,$$

$$d_{12} = -\Omega^*\left(M^* \ell_2^{*2} + 1\right)\left(\cos\theta_1 \sin\theta_2\right)\left(2 + \cos\theta_2\right)$$
$$+ \ell_4^* \Omega^*\left(M^* \ell_2^* - 1\right)\cos\theta_1 \sin\theta_2 ,$$

$$d_{21} = \Omega^*\left(M^* \ell_2^{*2} + 1\right)\left(2 + \cos\theta_1\right)\sin\theta_1 \cos\theta_1$$
$$- \ell_4^* \Omega^*\left(M^* \ell_2^* - 1\right)\cos\theta_1 \sin\theta_2 ,$$

$$e_{1i} = 1 ,$$

$$e_{22} = K^* ,$$

$$f_{11} = \Omega^{*2}\left(M^* \ell_2^{*2} + 1\right)\cos\theta_1 \sin\theta_1 - \ell_2^*\Omega^{*2}\left(1 - \ell_2^* M^*\right)\sin\theta_1 \cos\theta_2$$
$$- g^*\left(1 - \ell_2^* M^*\right)\cos\theta_1 ,$$

$$f_{21} = \ell_4^* \Omega^{*2}\left(1 - \ell_2^* M^*\right)\cos\theta_1 \sin\theta_2 ,$$

where,

$$M^* = \frac{M_2}{M_1} \ , \ \ell_2^* = \frac{\ell_2}{\ell_1} \ , \ \ell_4^* = \frac{\ell_4}{\ell_1} \ , \ \Omega^* = \frac{\Omega}{\left\{\dfrac{K_1}{M_1 \ell_1^2}\right\}^{\frac{1}{2}}} \ ,$$

$$g^* = g\frac{M_1}{\ell_1} \ , \ K^* = \frac{K_2}{K_1} \ .$$

The control torque T which forces the system to any desired angle $\theta_1 = \theta_{1ref}$ and $\theta_2 = 0$ is defined as:

$$T = \theta_{1ref} + \Omega^{*2}\left(M\ell_2^{*2} + 1\right)\cos\theta_{1ref} \sin\theta_{1ref} - \ell_4^* \ \Omega^{*2}\left(1 - \ell_2^* M^*\right)\sin\theta_{1ref}$$
$$- g^*\left(1 - \ell_2^* M^*\right)\cos\theta_{1ref} \tag{2}$$

Note that to simplify the analysis from this point on $\ell_1^*, \ell_2^*, \ell_4^*$ and $g^* = 1$.

STABILITY ANALYSIS

Upon setting $\dot\theta_1$, $\ddot\theta_1$, $\dot\theta_2$, $\ddot\theta_2$ equal to zero in (1), we obtain the following equations for the system equilibria:

$$e_{11}\theta_1 + f_{11} = T \ ,$$
$$e_{22}\theta_2 + f_{21} = 0 \ . \tag{3}$$

The solution to (3) must be obtained numerically because of the complexity involved in the equations. It is clear that the equilibrium points obtained from (3) are functions of M^*, K^*, Ω^* and T. These parameters can directly influence the number and the value of the system equilibria. As an example consider the system when $\theta_{1ref} = 3\pi/20$ is selected as the operating position. The number of equilibria can vary as Ω^* is increased. Figure 2 shows that the system can possess between three to five fixed points as Ω^* varies from 0.1 to 1.2 for $\theta_2 = 0$, $M^* = 5$ and $K^* = 1.5$. Note that $(\theta_1 = \theta_{1ref}, \theta_2 = 0)$ is always an equilibrium point. Furthermore, depending on system parameters, other equilibria could exist when $\theta_2 \neq 0$, but they are not shown here.

To determine the local stability of the equations of motion (1) about the equilibrium values, the equations are linearized. The eigenvalues of the resulting system determine the stability. The linearized system for $\theta_1 = \theta_{1ref} = \theta^0_1$, $\theta_2 = 0$ when $0 < \theta_{1ref} < \pi/2$ may be written in the form:

$$\begin{bmatrix} a_{11} & 0 \\ 0 & a_{22} \end{bmatrix} \begin{bmatrix} \ddot{\theta}_1 \\ \ddot{\theta}_2 \end{bmatrix} + \begin{bmatrix} 0 & b_{12} \\ -b_{12} & 0 \end{bmatrix} \begin{bmatrix} \dot{\theta}_1 \\ \dot{\theta}_2 \end{bmatrix}$$

$$+ \begin{bmatrix} c_{11} & 0 \\ 0 & c_{22} \end{bmatrix} \begin{bmatrix} \theta_1 \\ \theta_2 \end{bmatrix} = \begin{bmatrix} 0 \\ 0 \end{bmatrix} \tag{4}$$

or,

$$A\ddot{\theta} + B\dot{\theta} + C\theta = 0 \tag{5}$$

The elements of the matrices are as follows:

$$a_{11} = \left(1 + M^* \ell_2^{*2}\right)$$

$$a_{22} = \left(1 + M^* \ell_2^{*2}\right) \cos^2\theta_1^0$$

$$b_{21} = \Omega^* \left(3 \cos\theta_1^0 + \ell_4^* + M^* \left(3\ell_2^{*2} \cos\theta_1^0 - \ell_2^* \ell_4^*\right)\right) \sin\theta_1^0$$

$$c_{11} = g^* \sin\theta_1^0 + \Omega^{*2}\ell_4^* \cos\theta_1^0 - \Omega^{*2}\left(\sin^2\theta_1^0 - \cos^2\theta_1^0\right)$$

$$- M^* \left(\Omega^{*2}\ell_2^{*2}\left(\sin\theta_1^2 - \cos^2\theta_1^0\right) + \Omega^{*2}\ell_2^* \ell_4^* \cos\theta_1^0 + g^* \ell 1_2^* \sin\theta_1^0\right) + 1$$

$$c_{22} = \Omega^{*2}\ell_4^* \cos\theta_1^0 - M^* \Omega^{*2}\ell_4^* \ell_2^* \cos\theta_1^0 + K^*$$

We note that the A and C are the mass and stiffness matrices and are diagonal; B is the gyroscopic matrix and is skew symmetric.

To discuss stability properties, we assume a solution to this linear system of the form

$$\begin{bmatrix} \theta_1 \\ \theta_2 \end{bmatrix} = \begin{bmatrix} v_1 \\ v_2 \end{bmatrix} e^{i\lambda t} . \tag{6}$$

Substituting these equations into (4), we obtain

$$\begin{bmatrix} c_{11} - \lambda^2 a_{11} & b_{12} i\lambda \\ -b_{12} i\lambda & c_{22} - \lambda^2 a_{22} \end{bmatrix} \begin{bmatrix} v_1 \\ v_2 \end{bmatrix} e^{i\lambda t} = \begin{bmatrix} 0 \\ 0 \end{bmatrix} \tag{7}$$

For nontrivial solutions we set the determinant of the matrix of coefficients in (7) equal to zero and obtain the characteristic equation

$$\Delta(\lambda^2) = a_{11}a_{22}\lambda^4 - \left(a_{11}c_{22} + a_{22}c_{11} - b_{12}^2\right)\lambda^2 + c_{11}c_{22} = 0 \qquad (8)$$

where $\lambda^2 = \omega$. The possible solutions and the corresponding stability types where $\gamma, \beta > 0$ are shown below.

	Roots	Solution	Stability Type
1.	$\lambda_{1,2} = \pm\gamma$ $\lambda_{3,4} = \pm\beta$	$\underline{v}\,e^{\pm i\gamma t}$ $\underline{v}\,e^{\pm i\beta t}$	Stable
2.	$\lambda_{1,2} = \gamma \pm i\beta$ $\lambda_{3,4} = -\gamma \pm i\beta$	$\underline{v}\,e^{(i\gamma\pm\beta)t}$ $\underline{v}\,e^{(-i\gamma\pm\beta)t}$	Flutter instability
3.	$\lambda_{1,2} = \pm\gamma$ $\lambda_{3,4} = \pm i\beta$	$\underline{v}\,e^{\pm i\gamma t}$ $\underline{v}\,e^{\pm\beta t}$	Divergence instability
4.	$\lambda_{1,2} = \pm i\gamma$ $\lambda_{3,4} = \pm i\beta$	$\underline{v}\,e^{\pm\gamma t}$ $\underline{v}\,e^{\pm\beta t}$	Divergence instability

The root locus of the system, representing the values of λ in (8) when $M^*=5$, $K^*=1.5$ and Ω^{*2} is varied from 0.1 to 1.5, is shown in Figure 3. As Ω^{*2} increases, the roots of (8) go from divergence instability to stable, flutter, and back to stable regions. The system is stable when all the roots are real. The system undergoes divergence instability when one or both roots are imaginary. The boundaries of the divergence regions satisfy $a_{11}a_{22}=0$. The flutter instability boundaries are obtained from $\partial\Delta(\omega)/\partial\omega=0$, inside which the roots are complex conjugate. The regions of stability for the system for $M^*=4$ and $M^*=5$, are shown in Figure 4. As shown, the system with larger mass has a larger flutter region in the first quadrant of the K^*-Ω^{*2} parameter space (realistic motion can only occur in the first quadrant).

To verify the linear stability analysis, the nonlinear equations (1) were simulated numerically when $M^*=5$, $K^*=1.5$ and Ω^{*2} is increased from 0.04 to 1.44 (Figures 5-7). The phase portraits of θ_1 and θ_2 motions correspond to a divergence solution in Figure 5, where $\Omega^{*2}=0.04$. Figure 6 depicts a stable solution at $\Omega^{*2}=0.25$, while Figure 7 shows a flutter instability at $\Omega^{*2}=1.44$. In all the above cases, the behaviour of the nonlinear system confirms the linear stability results.

CONTROL EXAMPLES

The most important observation from the previous section, particularly upon considering Figure 4, is that adjusting the stiffness ratio, K^*, may stabilize or destabilize the system depending on the value of Ω^{*2}. This task is achieved (physically) by changing the joint flexibility in (1), or by using position feedback control (i.e. $K_p(\theta_{1\,ref}-\theta_1)$ added to the torque equation).

Once the system is stabilized, the oscillations could be reduced using a velocity feedback controller. Thus, the torque equation (2) is modified to illustrate the addition of the feedback controller as follows:

$$T = \theta_{1ref} + \Omega^{*2}\left(M\ell_2^{*2} + 1\right)\cos\theta_{1ref}\sin\theta_{1ref} - \ell_4^*\,\Omega^{*2}\left(1 - \ell_2^*M^*\right)\sin\theta_{1ref}$$
$$- g^*\left(1 - \ell_2^*M^*\right)\cos\theta_{1ref} - K_v\left(\dot\theta_1\right) \qquad (9)$$

where K_v is the velocity feedback gain.

An example of the controlled system for $\Omega^*=1$, $M^*=0.1$, $K^*=1.5$, and $K_v=2.5$ is shown in Figure 8. Note that the controller is activated after 50 nondimensional time units. The initial condition was set at $\theta_1=0.4$ and $\theta_2=0$. Although the reference position $\theta_1{}_{ref}=0.4712$ is reached, the θ_2 has oscillatory behaviour, and ringing in the θ_1 respo $\backsim$ is the result of these oscillations. The exponential reduction of the amplitude of θ_2 suggests that damping can be transferred from one mode to another. Adjusting the stiffness ratio to $K^*=2.0$ (Figure 9), the system is forced into the state of internal resonance, where energy transfer between θ_1 and θ_2 is significantly enhanced [5,6]. At this value of K^*, the oscillations in θ_2 motion are reduced significantly through the damping in θ_1. Upon increasing the mass ratio M^*, the number of equilibria increase which make control an extremely hard task. At $M^*=4$, for $\Omega^*=0.7$, the system is at internal resonance when $K^*=1.0$. The controller can be used to completely eliminate both θ_1 and θ_2 oscillations when $K_v=2.5$, as shown in Figure 10. However, the response settles at a point different than the desired operating value, which reflects the controller limitation.

CONCLUSIONS

For the system shown in Figure 1, the divergence and flutter boundaries were obtained from the linearized equations (4). The equations of motion were linearized about a desired operating point . It has been demonstrated that the nature of the static and dynamic instabilities (divergence and flutter) depend on the nondimensional system parameters, particularly the mass ratio, stiffness ratio, and the angular velocity. Stabilization of the system was possible by adjusting the stiffness ratio. The oscillations were completely eliminated in one mode and significantly reduced in the other, once the stiffness ratio was tuned so that the system was at the state of internal resonance, and damping was added through a control torque applied in one direction. The control approach was proven successful for small mass ratios.

ACKNOWLEDGEMENTS

REFERENCES

1.	Huseyin, K. (1978) *Vibrations and Stability of Multiple Parameter Systems*, Noordhoff International Publishing, Alphen van den Rijn, Netherlands.
2.	Yamanka, K., Heppler, G.R., and Huseyin, K. (1992) "On the Stability of Gyroscopic Systems," *ConStruct Group Technical Report* No. 1992-1, *Journal of Mathematical Modelling and Scientific Computing*, 2, 1993, pp. 438-443.
3.	Damaren, C.J., D'Eleuterio, G.M.T. (1989) "Optimal Control of Large Space Structures Using Distributed Gyricity," *J. Guid. Control and Dynamics*, 12, pp. 723-731.
4.	Golnaraghi, M., Keith, W. , and Moon, F.C. (1985) " Stability Analysis of a Robotic Mechanism Using Computer Algebra," *Applications of Computer Algebra*, editor: Richard Pavelle, Kluwer Academic Publishers, Boston. pp.281-292.
5.	Golnaraghi, M.F. (1991) "Vibration Suppression of Flexible Structures Using Internal Resonance," *Mechanics Research Communications Journal* 18-2/3, pp. 135-143.
6.	Tuer, K.L., Golnaraghi, M.F., and Wang, D. (1992) "Development of a Generalised Active Vibration Suppression Strategy for a Cantilever Beam Using Internal Resonance," To appear in *The Journal of Nonlinear Dynamics*.
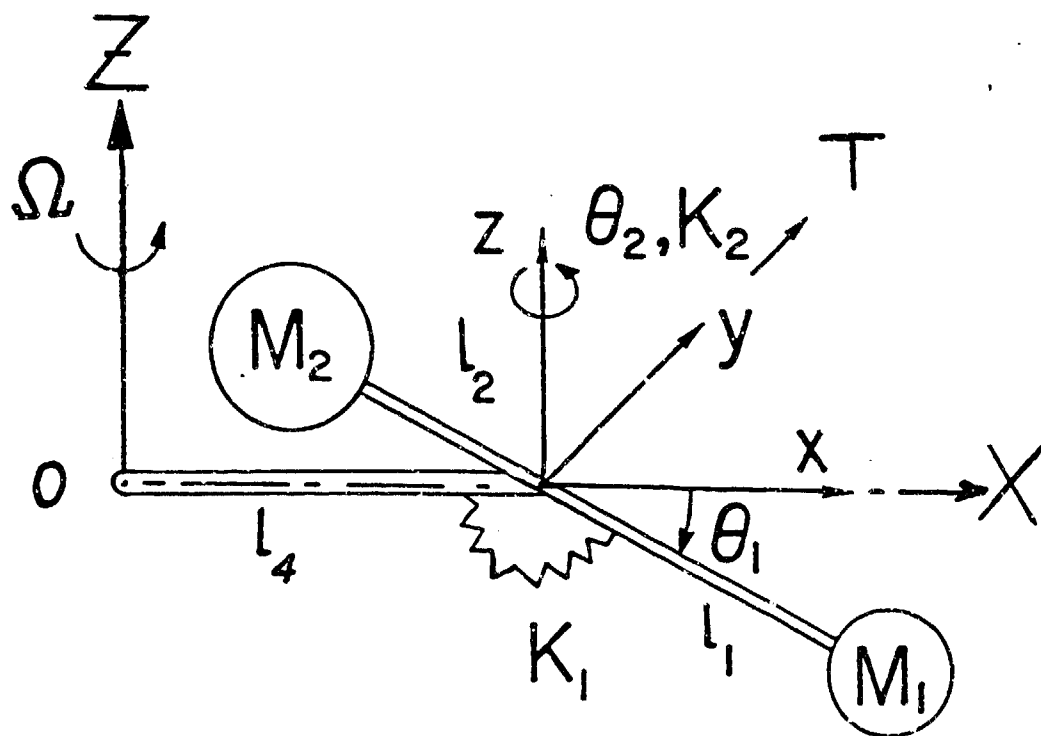
Figure 1. A lumped mass beam with flexibility in two directions.
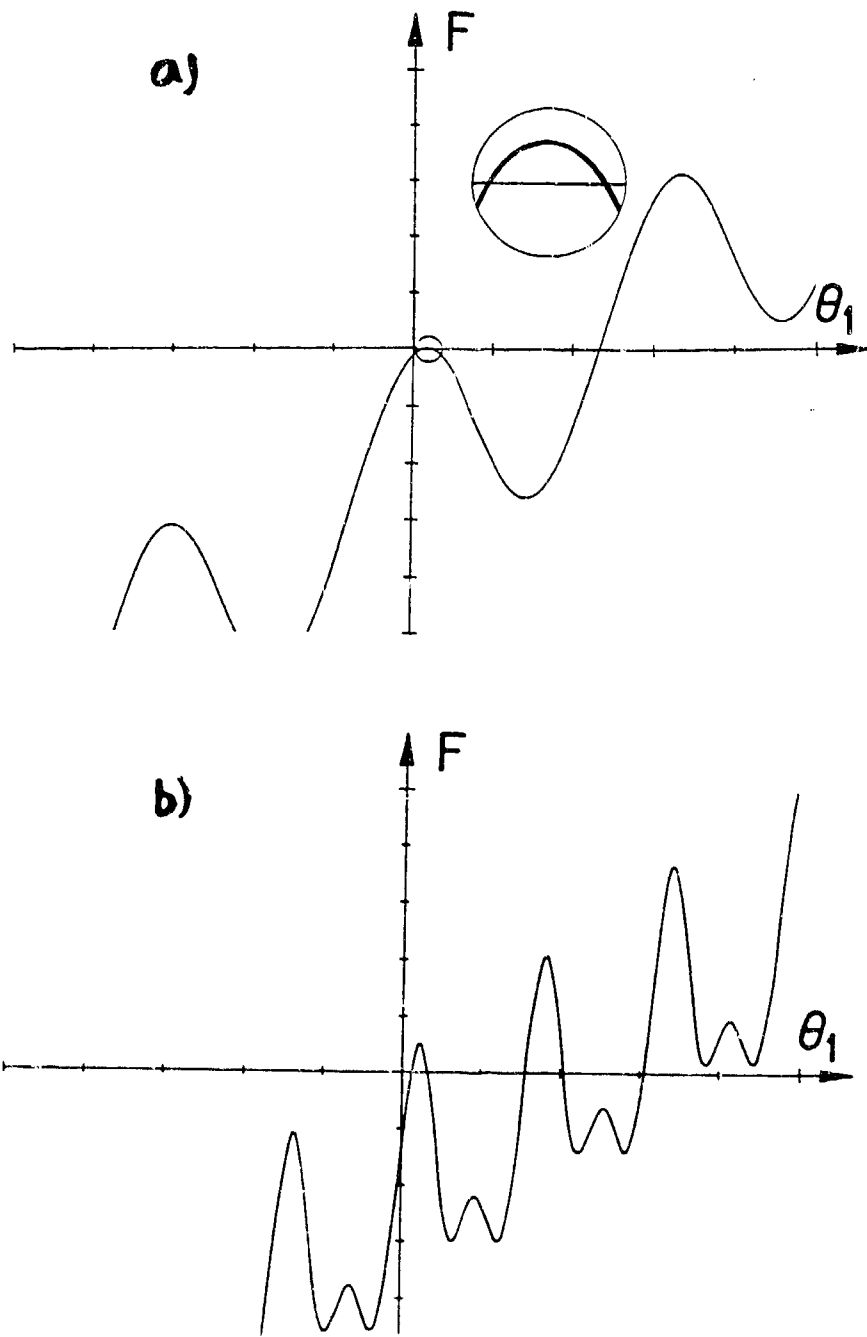
Figure 2. The system equilibria when $\theta_2=0$, $M^*=5$ and $K^*=1.5$; a) $\Omega^*=0.1$, b) $\Omega^*=1.2$.
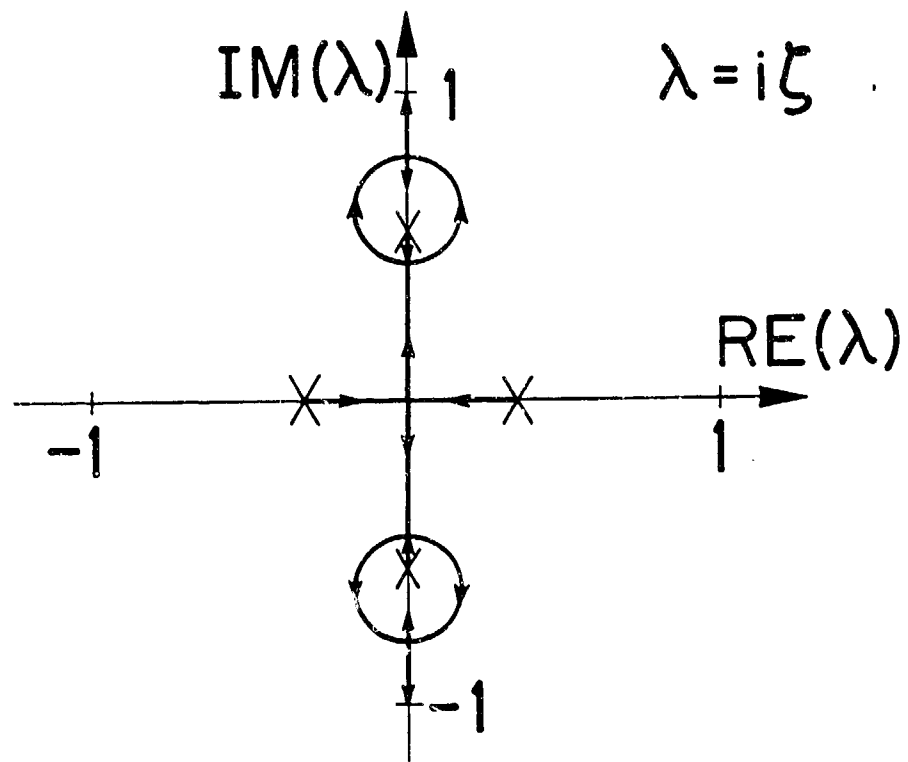
Figure 3. The root locus for $M^*=5$, $K^*=1.5$ and Ω^{*2} varying from 0.1 to 1.5.

a)

b)
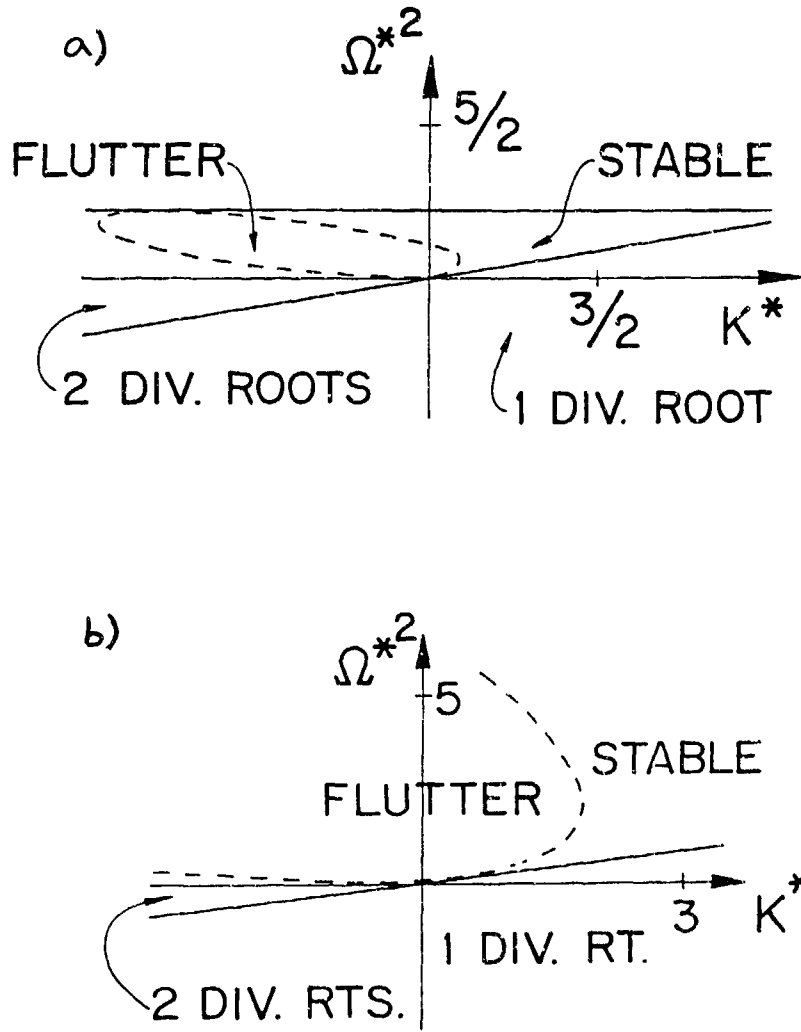
Figure 4. The regions of stability; in K^*-Ω^{*2} parameter space; a) M^*=4, b) M^*=5.
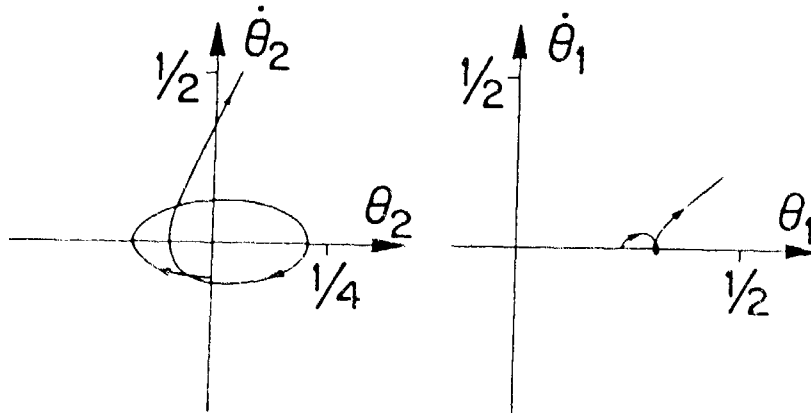
Figure 5. Phase portraits of the response of (1) when M^*=5, K^*=1.5 and Ω^{*2}=0.04.
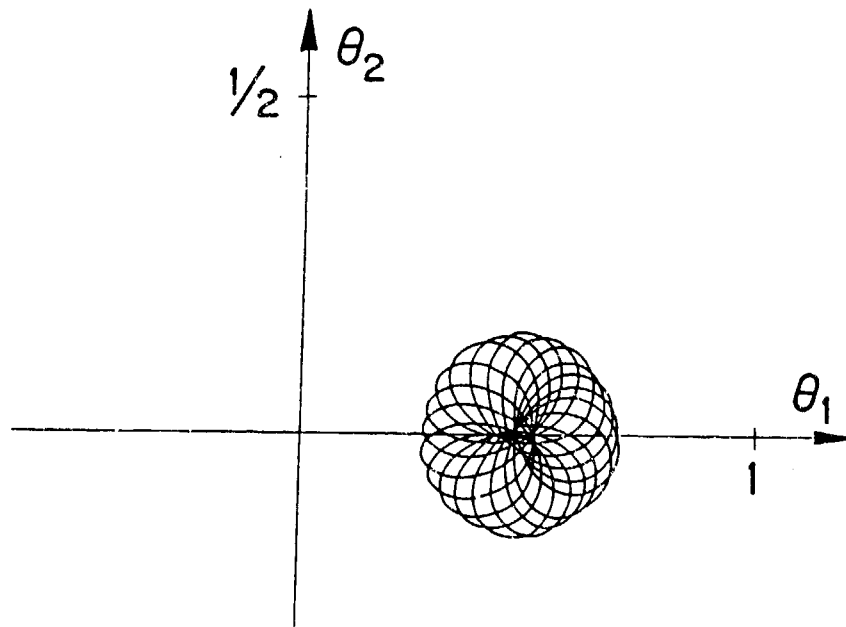
Figure 6. Response of (1) at $M^*=5$, $K^*=1.5$ and $\Omega^{*2}=0.25$.
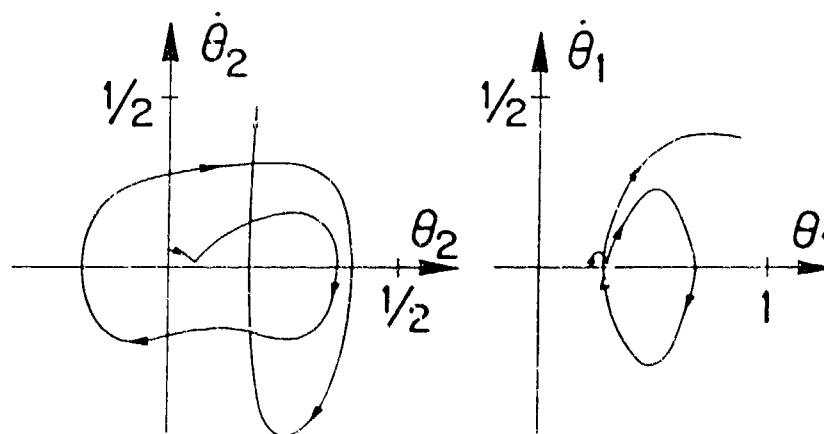
Figure 7. Phase portraits of the response of (1) when $M^*=5$, $K^*=1.5$ and $\Omega^{*2}=1.44$.
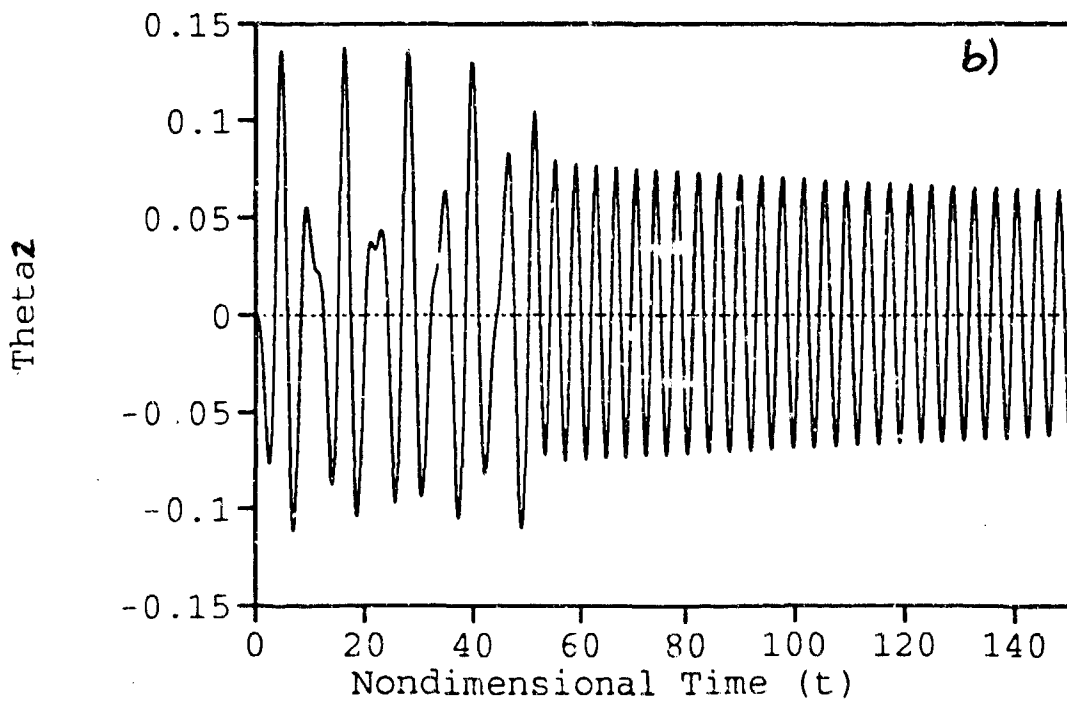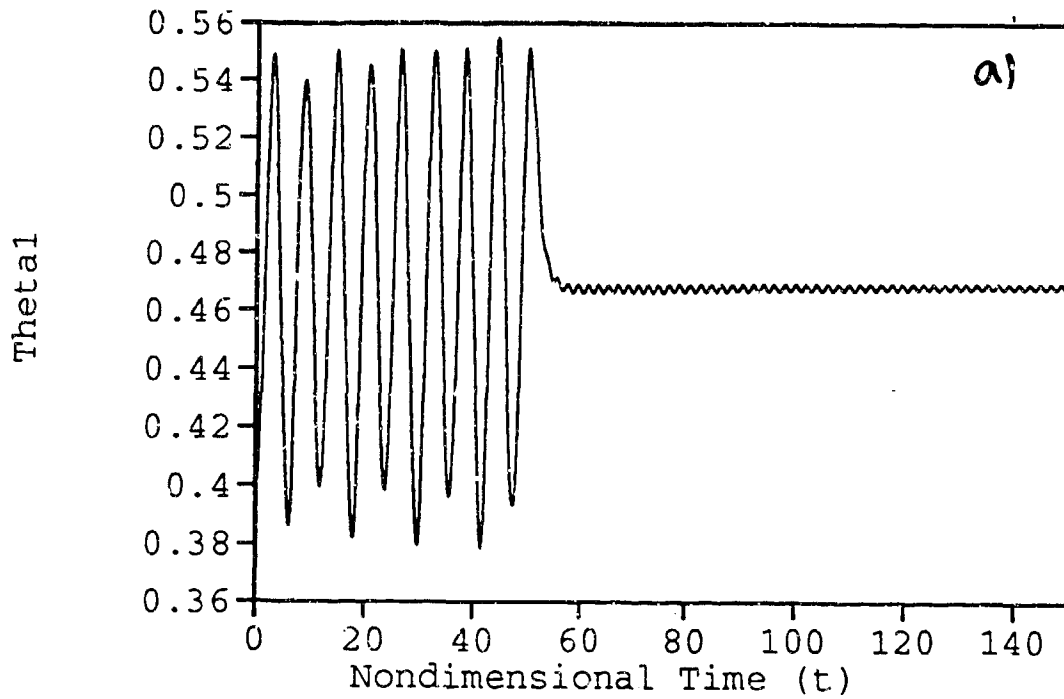
Figure 8. Time response of the system for $\Omega^{*}=1$, $M^{*}=0.1$, $K^{*}=1.5$ and $K_{v}=2.5$, when the velocity feedback is activated at $\tau=50$.
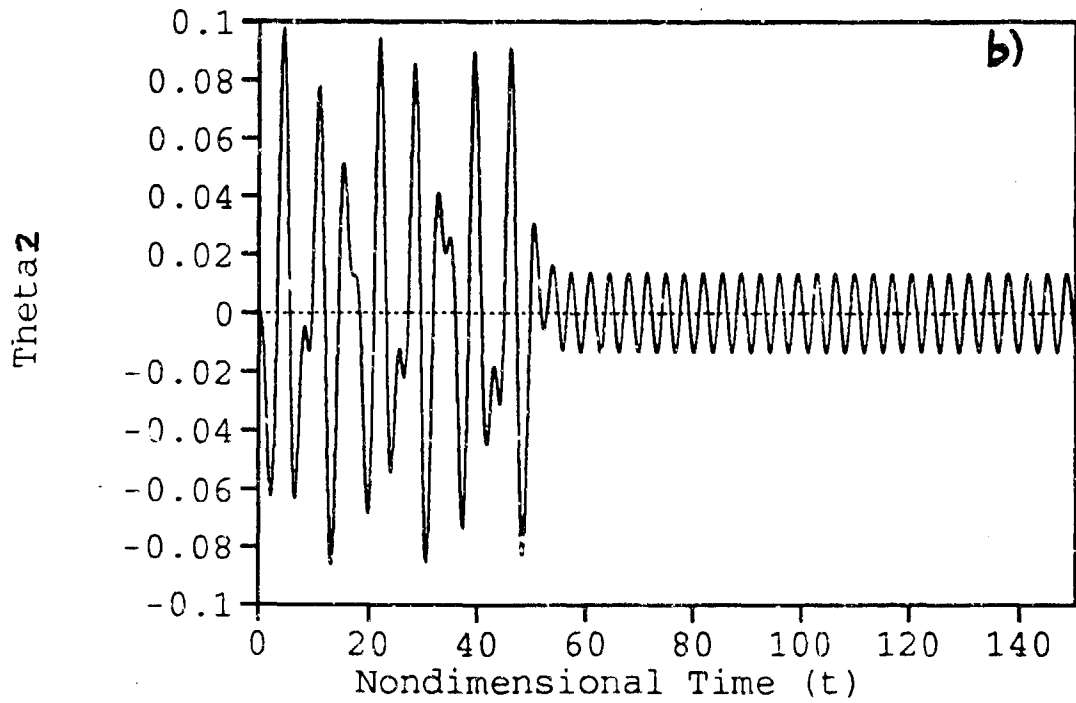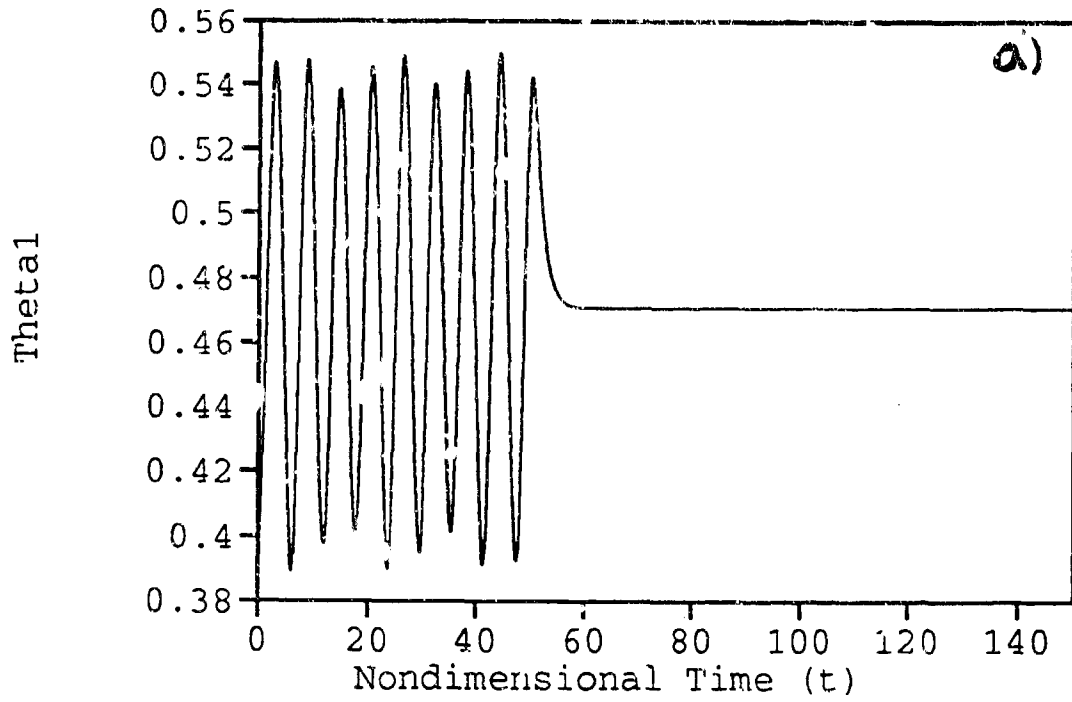
Figure 9. Time response of the system for $\Omega^*=1$, $M^*=0.1$, $K^*=20$ and $K_v=2.5$, when the velocity feedback is activated at $\tau=50$.
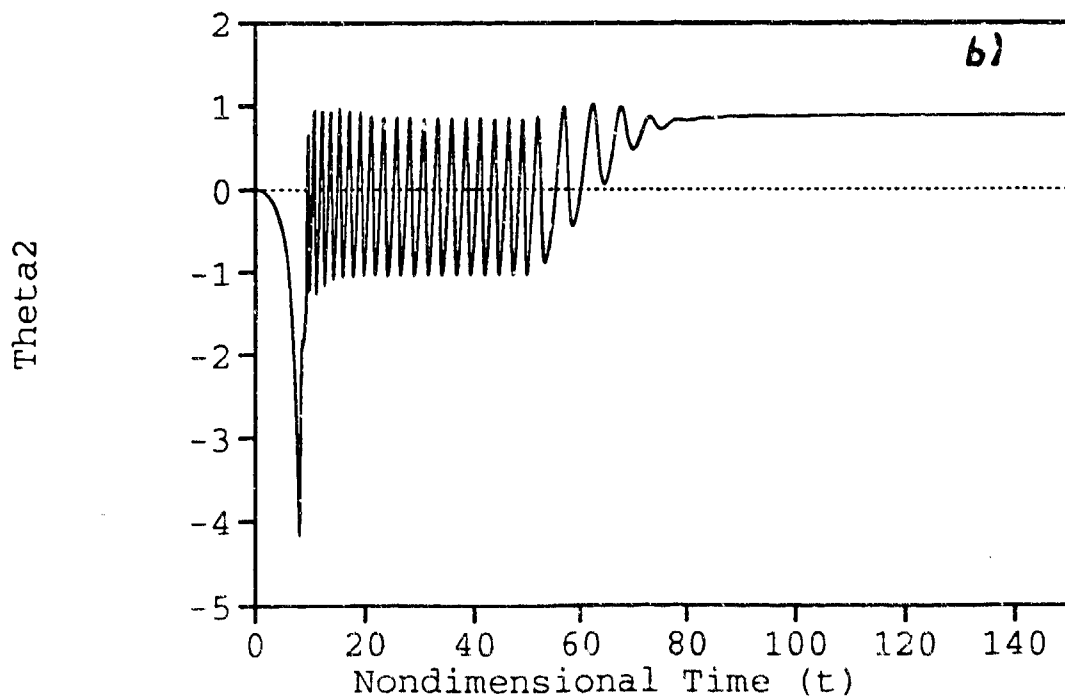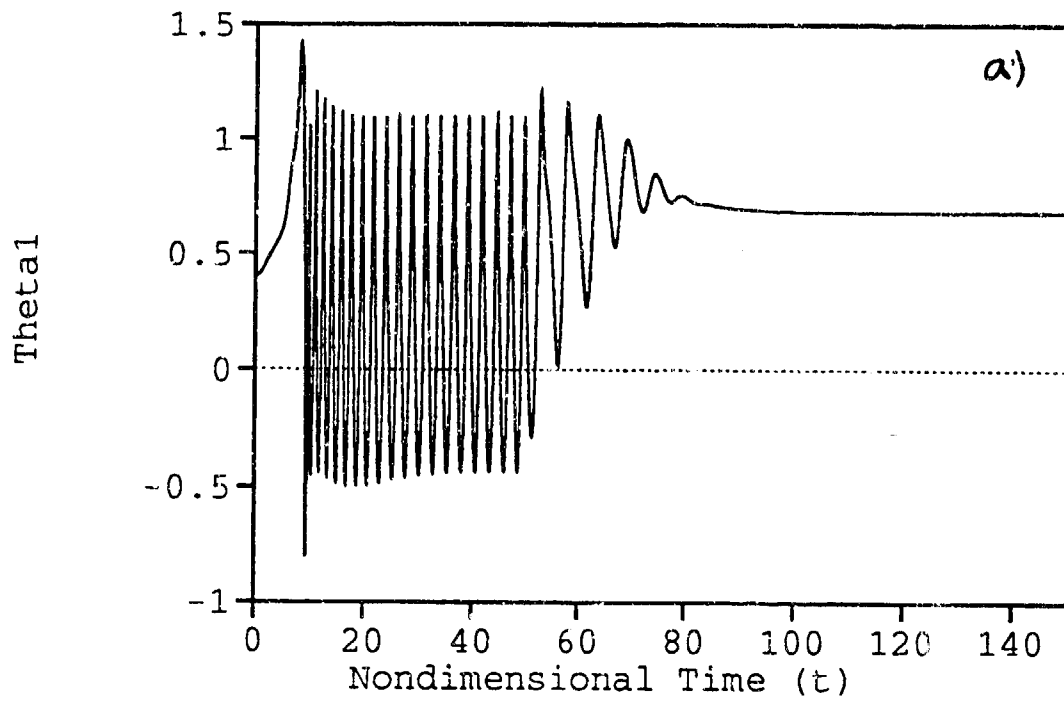
Figure 10. Time response of the system from $\Omega^*=0.7$, $M^*=4.0$, $K^*=1.0$ and $K_v=2.5$, when the velocity feedback is activated at $\tau=50$.

Nonlinear Robust Control: Theory, Examples, and Applications

Zhihua Qu
Assistant Professor
Department of Electrical and Computer Engineering
University of Central Florida
Orlando, FL 32626, U.S.A.
Phone: (407) 823-5976
Fax: (407) 823-5835
E-mail: quz@engr.ucf.edu

Abstract

Robust control design for stabilizing nonlinear uncertain systems is investigated. Four issues are covered in the paper. First, existing and most recent research results in the area of nonlinear robust control design are summarized. Second, properties and features of nonlinear robust control are exposed through simple examples. To show the potential that robust control theory can be applied to weapons systems, a electrical-mechanical system, flexible-joint robot, is used as a prototype to proceed the design. Finally, the current research topics in theory and applications of nonlinear robust control are outlined.

1 Introduction

Robust control theory addresses the problem of designing an implementable control to stabilize a dynamical system in which uncertainties are nonlinear and large but bounded, while meeting the design requirements. A system under study is described either by state space model

$$\dot{x} = f(x,t) + \Delta f(x,t) + g(x,u,t), \tag{1}$$

or by input-output model

$$A_p(s,t)[1 + \Delta A_p(s,t)][y(t)] = k_p(t)B_p(s,t)[1 + \Delta B_p(s,t)][u(t) + d(y,t)]. \tag{2}$$

In equation (1), $x \in \Re^n$, $u \in \Re^m$, $f(x,t)$ is known, $\Delta f(\cdot)$ contains large unknown dynamics but bounded by known function, and $g(\cdot)$ is known or partially known. In equation (2), $A_p(\cdot,\cdot)$, $B_p(\cdot,\cdot)$ are unknown, monic time-varying differential operators, $d(y,t)$ is the lumped nonlinear uncertainty, $\Delta A_p(\cdot,\cdot)$ and $\Delta B_p(\cdot,\cdot)$ represent additive and multiplicative unmodelled dynamics, respectively. The analytical method used in nonlinear robust control is the direct method of Lyapunov.

A nonlinear uncertain system is a system which is both nonlinear and uncertain. The importance of controlling a nonlinear uncertain system rests on the fact that an uncertain model reflects the imperfect knowledge of most physical systems of any consequence. The uncertainties in the system model can be variations of system parameters, modelling or model reduction errors, unknown dynamics, disturbances, etc. Based on minimum aprior information on the uncertainties, one can bound the uncertainties in magnitude by a *known* function of system states and time. A successful robust control should be designed such that it requires at most the bounding function of the uncertainties. Incorporating uncertainty into control design is in most cases the only way to improve stability and performance. It is the purpose of this paper to present the main results and features of nonlinear robust control.

The paper is organized as follows. In section two, design steps of robust control using Lyapunov approach are explained using an intuitive argument. Counterexample is given to show that not all uncertain systems are stabilizable. Features and shortcomings of existing results on stabilizable uncertain systems are reviewed. In second three, several examples will be used to show that nonlinear robust control is superior to other existing control techniques. This is because nonlinear robust control can deal with nonlinear and fast varying uncertainties. In section four, two class of systems will be used to illustrate applicability of nonlinear robust control to weapon systems. The first class

Qu

is represented by general second-order vector nonlinear differential equation which subsumes most rigid mechanical systems. As the second class, control of flexible systems is briefly discussed. To overcome the shortcomings of existing results, several new research directions are proposed in section five with summary of approaches and preliminary results.

2 Overview of Nonlinear Robust Control

The robust control problem is the problem of designing an implementable control to stabilize a dynamical system and to meet the design requirements while the dynamics system has large but bounded uncertainties.

Of the different analysis and design approaches, direct method of Lyapunov is of central importance, first because time varying or nonlinear uncertainties can be easily bounded in the time domain, and second because time-varying and nonlinear systems can also be treated by this method. This paper focuses on the problem of robust control design of nonlinear uncertain systems by the direct method of Lyapunov.

The robust control problem has been widely studied over the last fifteen years, and many important robust control schemes have been proposed. There are mainly three classes of robust controllers: linear high-gain control, variable structure control [61], and min-max controller [19] and its derivatives [9, 4, 1]. The high-gain approach guarantees in many cases only local stability and usually cause actuator saturation, and can be viewed as special cases of general nonlinear robust controls. A variable structure control is inherently discontinuous and chattering. Along the line of min-max controller, robust control and stability analysis are done using Lyapunov functions, an early review can be found in [10]. Robust control we design here is based on Lyapunov technique and, although the resulting controllers are continuous, they will be categorically of min-max controllers. This choice is made to generate smooth robust controls guaranteeing global stability.

The design of a robust control typically involves three steps. First, the nominal system, that is, the system without uncertainties, is stabilized or is assumed to be stable. Moreover, a Lyapunov function for the nominal system can either be found or is assumed to be known. Second, the uncertainties are bounded by a known function. Third, a control is then designed based on the Lyapunov function of the nominal system and the bounding function of the uncertainties. The ideal result would be that the control can stabilize the uncertain system as a whole as long as the bounding function of the uncertainties is available, and that the stability result satisfies the design requirements.

The main results in stabilization of nonlinear uncertain systems will be reviewed in this section. The review will be proceeded in two parts: state space method and input-output method.

2.1 State Space Approach

Most existing results on controlling nonlinear uncertain systems are in terms of state space model. The uncertain system is usually assumed to be described by

$$\dot{x} = f(x,t) + \xi'(x,t) + B(x,t)[\xi(x,t) + u] \qquad x(t_0) = x_0, \tag{3}$$

where $t \in \Re$ is time, $x(t) \in \Re^n$ is the state, $u(t) \in \Re^m$ is the control, $\xi(x,t)$ is the "matched" uncertainties [9], and $\xi'(x,t)$ is the "unmatched" uncertainties. For simplicity, uncertainties that are a function of the control are not included in the following discussion. Both $\xi'(x,t)$ and $\xi(x,t)$ are assumed to be bounded in magnitude, usually in their Euclidean norm denoted by $\|\cdot\|$. The corresponding system without uncertainty, called the nominal system, is described by

$$\dot{x} = f(x,t) + B(x,t)u \qquad x(t_0) = x_0, \tag{4}$$

where $f(\cdot) : \Re^n \times \Re \to \Re^n$ and $B(\cdot) : \Re^n \times \Re \to \Re^{n \times m}$ are known. Moreover the so called uncontrolled, nominal system of system (3) is defined by

$$\dot{x} = f(x,t) \qquad x(t_0) = x_0, \tag{5}$$

An uncertain system does not have to be affine in control. That is, an uncertain system can be in the form (1), which is more general than (3), or element by element,

$$\dot{x}_i = f_i(x,t) + \Delta f_i(x,t) + g_i(x,u,t),$$

where $x \in \Re^n$, $u \in \Re^m$, $f(x,t)$ is known, $\Delta f(\cdot)$ contains large unknown dynamics but bounded by known function, and $g(\cdot)$ is known or partially known. For system (3), we have $\Delta f(x,t) = \xi'(x,t) + B(x,t)\xi(x,t)$ and $g(x,u,t) = B(x,t)u$. For simplicity, we shall use the model (3) unless mentioned otherwise.

System (3) is assumed to satisfy the following assumptions.

Assumption 1: The *uncertain* function $\xi(\cdot)$ is bounded in Euclidean norm by a *known* function; namely, there is a *known* non-negative function $\rho(\cdot)$ such that

$$\|\xi(x,t)\| \leq \rho(x,t) \qquad \|\xi'(x,t)\| \leq \rho'(x,t) \qquad \forall (x,t) \in \Re^n \times \Re.$$

Assumption 2: The known functions $f(\cdot)$, $B(\cdot)$, and $\rho(\cdot)$ as well as the *unknown* function $\xi(\cdot)$ are Caratheodory, and $f(0,t) = 0$ for all $t \in \Re$. Moreover, given a compact set $E \subset \Re^n$ and a compact interval $[a, b] \subset \Re$, there exist non-negative Lebesgue integrable functions $m_i(\cdot)$, $i = 1, 2$, such that for all $(x,t) \in \Re^n \times [a, b]$

$$\|f(x,t)\| \leq m_1(t), \qquad \|B(x,t)\|\rho(x,t) \leq m_2(t).$$

Assumption 3: The uncontrolled, nominal system $\dot{x} = f(x,t)$ is uniformly asymptotically stable in the large. More specifically, there is a Lyapunov function $V(x,t)$ for system (5), specified as follows. There is a C^1 function $V(\cdot) : \Re^n \times \Re \rightarrow \Re^+$, continuous, strictly increasing, scalar functions $\gamma_i(\cdot) : \Re^+ \rightarrow \Re^+$, $i = 1, 2$, and a continuous, positive definite, scalar functions $\gamma_3(\cdot) : \Re^+ \rightarrow \Re^+$, which satisfy

$$\gamma_i(0) = 0, \quad i = 1, 2, 3 \qquad\qquad \lim_{s \to \infty} \gamma_j(s) = \infty, \quad j = 1, 2$$

such that for all $(x,t) \in \Re^n \times \Re$

$$\gamma_1(\|x\|) \leq V(x,t) \leq \gamma_2(\|x\|),$$

$$\frac{\partial V(x,t)}{\partial t} + \nabla_x^T V(x,t) f(x,t) \leq -\gamma_3(\|x\|).$$

This Lyapunov function will be used to develop state feedback controls.

It is worth noting that Assumption 2 is made to guarantee the existence of a classical solution for system (3) under any control that is nonsingular and bounded by $\rho(\cdot)$. It is also worth noting that Assumption 3 is equivalent to the assumption that the nominal system (4) is uniformly asymptotically stabilizable.

It would be ideal if one would find a robustly stabilizing control under the above general assumptions. Unfortunately, not all uncertain systems in the form of (3) are stabilizable. For example, consider the system

$$\dot{x}_1 = x_2 + \Delta_1(x_1, x_2), \qquad \dot{x}_2 = u,$$

in which the uncertainty is bounded as $|\Delta_1(x_1, x_2)| \leq |x_1| + |x_2|$. One can easily see that the system is not stabilizable since the additive uncertainty $\Delta_1(x_1, x_2)$ could be $-x_2 + x_1$. Similarly, an uncertain system may not be stabilizable either if there is a large multiplicative uncertainty, which can be seen from the system

$$\dot{x} = x + [1 + \Delta_2(x)]u,$$

where $|\Delta_2(x)| \leq 1$. Robust control theory is to identify the class of all stabilizable uncertain systems and to provide stabilizing control guaranteeing desired performance. Therefore, the main issue is what is the minimum structural requirement on the system or uncertainties under which a stabilizing control can be found. The other important issues are the search of Lyapunov function for nonlinear system and the performance. The following synopsis is proceeded around the issues.

2.1.1 Structural Requirements on Uncertainties

Most robust control schemes are concerned with systems for which the uncertainties are "matched", that is, the uncertainties satisfy *the matching conditions* (MCs), or equivalently, $\xi'(x,t) = 0$ in (3). The MCs were originally introduced in [19, 9] based on the following intuitive observation: Taking derivative of $V(x,t)$ along the trajectory of system (3) yields

$$
\begin{aligned}
V(x,t) &= \frac{\partial V(x,t)}{\partial t} + \nabla_x^T V(x,t) f(x,t) + \nabla_x^T V(x,t) \xi'(x,t) \\
&\quad + \nabla_x^T V(x,t) B(x,t)[\xi(x,t) + u] \\
&\leq -\gamma_3(\|x\|) + \nabla_x^T V(x,t) \xi'(x,t) + \nabla_x^T V(x,t) B(x,t)[\xi(x,t) + u],
\end{aligned}
\tag{6}
$$

315

Qu

where the last step follows from Assumption 3. If the MCs are satisfied, we have

$$\dot{V}(x,t) - \gamma_3(\|x\|) + \nabla_x^T V(x,t) B(x,t)[\xi(x,t) + u] \tag{7}$$

in which all uncertainties can be reached directly by the control input, and robust controllers can be found in [19, 9]. Without the MCs, since the number of inputs is usually less than the number of state variables, the so-called null set $\nabla_x^T V(x,t) B(x,t) = 0$ is nontrivial, and, on the null set, the derivative of Lyapunov function is

$$\dot{V}(x,t) \leq -\gamma_3(\|x\|) + \nabla_x^T V(x,t) \xi'(x,t). \tag{8}$$

It is obvious that no stability can be concluded if the bounding function of the un-matched uncertainty $\xi'(x,t)$ is larger than $\gamma_3(\cdot)$.

The concept of matching conditions is introduced basically for mathematical convenience and therefore not necessary. In fact, most physical systems do not satisfy the restriction. Therefore, conditions much less restrictive than the matching conditions must be developed for both mathematical and practical considerations. This relaxation is the crucial step in order to make nonlinear robust control a viable mean.

There has been some work to loosen this restriction for *linear, uncertain systems,* that is, uncertainties are the entries in the matrices of linear state space model and are bounded by constant. For example, stability margin against unmatched uncertainties was studied in [28, 29]. Later, the Riccati approach [33, 53] was introduced. The uncertain system under consideration is linear and the control is of linear form. In the control synthesis, the bound of the uncertainties does not enter explicitly into the control scheme but instead appears implicitly in an associated Riccati equation for solution of the feedback control gain. Also available are structural conditions on uncertainties that are less restrictive than the matching conditions, such as '$l - th$ step matching conditions [21]' and 'generalized matching conditions [59]' and 'quadratic stabilizability [62].' These results are however *inherently limited to linear uncertain systems.*

In much of the literature on *nonlinear, uncertain systems,* for instance [8, 6, 5, 2], the problem of uncertainties not satisfying the matching conditions is treated by dividing the uncertainties into two parts, the matched uncertainties and unmatched, or mismatched, uncertainties, as shown in (3). The control applied is the same one that would be applied if there were no unmatched uncertainties. Consequently the norm of the unmatched portion of the uncertain term is required to be smaller than a threshold value determined by the control law, namely, by (8)

$$\| \nabla_x V(x,t) \xi'(x,t) \| \leq \gamma_3(\|x\|) \quad \forall (x,t) \in \mathbf{N} \tag{9}$$

This merely says that as long as the unmatched uncertainties are reasonably small the system will remain stable under the proposed control law. The case where the norm of the unmatched uncertainties exceeds the threshold is common in engineering applications but has not been addressed.

The problem of loosening the matching conditions or the size restriction (9) is the major topic in the research of the author. The approach taken is to investigate whether there exists a class of uncertain systems whose nominal system possess certain properties which allow the class of uncertain systems to be stabilized for all possible bounded uncertainties. This idea is different from that in the existing literature. That is, the properties of the nominal system are exploited in order to remove unnecessary assumptions about the uncertainties. The followings are primary results on loosening the matching conditions achieved recently by the author.

Composition of Lyapunov Functions: A new approach of designing robust control is proposed [44]. The method uses the property that the Lyapunov function is not unique for a stable or stabilizable system and reveals that there is a class of uncertain dynamic systems which can be asymptotically stabilized under the proposed control law. The class of systems can be defined as follows. First, the nominal system must have two Lyapunov functions such that the intersection of the null sets of the two Lyapunov functions contains at most the equilibrium point. A composite Lyapunov function can then be defined, consisting of these two Lyapunov functions, defined on disjoint subsets whose union is the whole space. Second, there are no possible trajectories that exhibit aberrant intensive chattering, where the meaning of intensive chattering is quantified.

Convergence Rate: A general control law and a set of conditions on the uncertainties in a uncertain dynamic system are proposed in [45] to guarantee the stability of the uncertain system. The development is carried out without the matching conditions. It is also shown that an uncertain system can always be stabilized under the proposed control law if its nominal system can be stabilized with an arbitrarily large convergence rate. The conditions for a linear nominal system to be stabilizable with arbitrarily large convergence rate are discussed. In addition, previous results based on the matching conditions are shown to be special cases of the new results.

316

Systems with Cascaded Structure: Many engineering systems consist of subsystems that are serially connected. For these systems, high-gain controller [34] and nonlinear robust controller [42] are available provided that the matching conditions are satisfied not at the system level but at the level of subsystems.

Feedback Linearization Method: Feedback linearization technique has been integrated in [43] into robust control theory in order to design robust control for uncertain nonlinear systems. The overall system do not have to be feedback linearizable or to satisfy the matching conditions.

Equivalently Matched Uncertainties: It is shown in [37] that uncertainties not satisfying MCs can always be stabilized as long as they are equivalently matched. Or loosely speaking, the unmatched uncertainty $\nabla_x^T V(x,t)\xi'(x,t)$ in (6) is in the range of the input space $\nabla_x^T V(x,t)B(x,t)u$ so that the derivative of Lyapunov function can be written in the same form as (7). This approach requires judicious choice of Lyapunov functions.

Generalized Matching Conditions: The generalized matching conditions (GMCs) was recently introduced [35] under which nonlinear uncertain systems are stabilizable. The GMCs are defined based on (1) as $\Delta f_i(x,t) = \Delta f_i(x_1, \cdots, x_i, t)$ and $g_i(x,u,t) = g_i(x, x_{n+1}, t)$, with $x_{n+1} = u$, satisfying without loss of any generality the relation: there exist known continuous, positive definite functions α_i and non-negative functions φ_i such that

$$x_{i+1}g_i(x, x_{i+1}, t) \geq \alpha_i(\|x_{i+1}\|)(1 + \varphi_i(x,u,t)) \quad \forall(i,x,u,t).$$

Globally stabilizing robust controller can be designed under GMCs using the recursive procedure in [35]. The procedure is conceptually the same as but mathematically more complicated than the back-stepping procedure [23].

The above results represent significant progress in loosening size or structural restrictions on the uncertainties. Especially, the three approaches, GMCs, equivalently matched uncertainties, and feedback linearization, form a powerful set of tools to solve many control problems in engineering such as large-scale power systems, rigid-body robots, and other rigid electrical-mechanical systems. A new idea beyond GMC on further relaxation of the matching conditions in the state space will be discussed in section five. Another powerful method that does not require the matching conditions is robust control design using input-output model, which is the subject of section 2.2.

2.1.2 Search of Lyapunov Functions

As made by Assumption 3, Lyapunov function for designing robust control must be assumed to be known. However, for nonlinear systems, finding a Lyapunov function is itself a challenging problem. Several approaches recently proposed by the author provide answers to the problem, which includes GMCs [35], feedback linearization method [43], and systems with cascaded structure [42]. For example, under GMCs, the structure of nominal systems is almost known and Lyapunov function can always be chosen as quadratic functions. If feedback linearization method is applicable, the nominal systems after nonlinear transformation is in Brunowsky canonical form, and the search for Lyapunov function becomes trivial.

2.1.3 Stability Results

It is well known that, if the bounding functions on the uncertainties are known and if system (5) is asymptotically stable in the large, there are a variety of feedback control laws, yielding various types of stability for system (3).

Among existing feedback control laws, the two primary ones are the minmax control [19, 20] and the saturation-type control [9]. If $\xi'(x,t) = 0$ in (3), the minmax control, that makes system (3) asymptotically stable in the large, is given by

$$u(x,t) = \begin{cases} -\rho(x,t)\frac{\alpha(x,t)}{\|\alpha(x,t)\|} & \forall(x_t,t) \notin \mathbf{N} \\ \{u(x,t) \in \Re^m\} & \forall(x,t) \in \mathbf{N} \end{cases}, \tag{10}$$

where $\alpha(x,t) \triangleq B^T(x,t)\nabla_x V(x,t)\rho(x,t)$ and $\mathbf{N} \triangleq \{(x_t,t) : \alpha(x,t) = 0\}$.

Although the above min-max control achieves asymptotic stability for system (3), the control is computationally poorly behaved when $\|\alpha\|$ is very small. Moreover, the minmax control is discontinuous and consequently does not satisfy the usual concept of a solution.

It was subsequently noted that the choice of control law on the set **N**, where $\alpha(x,t) = 0$, is essentially arbitrary, and that a proper choice could make the control continuous [9]. Corless and Leitmann [9] proposed the following continuous state feedback control law, which is a modification of the Lyapunov min-max control law.

$$u(x,t) = \begin{cases} -\rho(x,t)\frac{\alpha(x,t)}{\|\alpha(x,t)\|} & \text{if } \|\alpha(x,t)\| > \epsilon \\ -\rho(x,t)\frac{\alpha(x,t)}{\epsilon} & \text{if } \|\alpha(x,t)\| \leq \epsilon \end{cases} \quad (11)$$

where $\epsilon > 0$ is given. It is easy to show that, if $\xi'(x,t) = 0$, under the control (11),

$$\dot{V}(x,t) \leq -\gamma_3(\|x\|) + 2\epsilon \qquad \forall (x,t) \in \Re^n \times \Re, \quad (12)$$

where ϵ is chosen small enough to make $\dot{V}(x,t)$ negative definite outside a sufficient small neighborhood around the origin.

Since $\gamma_3(0) = 0$, this Lyapunov function does not give global asymptotic stability but rather stability of UUB. Several other control laws, equivalent to the min-max control and the saturation-type control have subsequently been proposed [4, 1]. These saturation-type controls are continuous and therefore guarantee the existence of a classical solution. Instead of asymptotic stability, saturation-type controls render system (3) UUB. Recently, modified design procedures are proposed by the author to generate uniformly continuous robust controllers [39, 41, 38]. These continuous controls guarantee exponential or asymptotic stability as long as the nominal system has the corresponding property.

2.2 Input-Output Approach

Input-output control is desired in many applications since it requires far less information than state-feedback control. For *known* linear time invariant (LTI) systems, there are several input-output design approaches: classical design based on transfer functions; state observation together with numerous state-feedback control methods [32]. For *unknown* LTI systems, there are mainly two methods: adaptive control [30] and *linear* robust control such as H^∞ and H^2 [16, 15], which design methodologies have been studied extensively in the past two decades. Although they are popular, widely used, and have many outstanding features, both methods are limited for systems that are slow time-varying and contain only soft nonlinearities (that is, nonlinearities satisfying global Lipchitzian condition). That is, these approaches are not applicable to systems with nonlinear uncertainties, fast time-varying parameters, significant unmodelled dynamics, large and varying time delays, etc. New control design methodology has to be developed for the listed problems.

Recently, a pioneer work on nonlinear robust control design based on I/O model was proposed by the author, in which the design technique is somewhat analogous to but much more powerful than adaptive control. A system under consideration is represented by (2), in which only the following information are assumed to be known: bounds on time-varying parameters, upper bound on system order and relative degree, and bounding functions on the uncertainties and unmodelled dynamics. Robust input-output control (Model Reference Robust Control, or MRRC) is designed by a four-step systematic procedure using a straightforward Lyapunov argument for stability analysis. More specifically, a nominal control is first designed under the assumed perfect knowledge of the system; a nonlinear robust control problem is then formulated with aid of the unknown, nominal control; state space model is built using filtered version of input and output signals; and finally nonlinear robust control guaranteeing global stability is generated using a systematic design procedure. As shown in [47], a basic setup of the new control scheme is proposed to solve tracking problem for any unknown minimum-phase, linear SISO systems. In [46], synthesis procedure is provided for unknown systems with arbitrarily fast-varying parameters. In [36], nonlinear robust control is designed for time-invariant systems with nonlinear uncertainties and unmodelled dynamics that are arbitrarily large, unstable, and of infinite dimension.

Due to space limitation, it is impossible to discuss here the details of the I/O robust control design procedure for different classes of systems. Instead, the main ideas will be exposed through the examples and applications in the next two sections. Complete analysis can be found in the references cited for interested readers

3 Characteristics of Nonlinear Robust Control

In the previous sections, extensive discussions are made on design methodologies, applicability, stability and performance results of existing and most recent nonlinear robust controls. In this subsection we choose to expose the basic

feature of nonlinear robust controls through simple examples. The examples not only show theoretical approach to be used but also provide intuitive explanation of how and how well robust control works.

Example 1: First-order SISO system:

$$\dot{e} = ae + u + d(e, t), \tag{13}$$

where we assume without loss of generality that $a = -0.1$, since any unstable part of the nominal system can be included in $d(e, t)$. The function d is a continuous uncertainty satisfying $|d(e, t)| \leq 1 + e^2 \triangleq \rho(e)$. There are two important points about uncertain systems that need to be emphasized before we proceed. First, the uncertain system may not have any equilibrium point, or if an equilibrium point exists it may not be known. Thus, stability must be discussed with respect to the equilibrium point of the uncontrolled nominal system, that is, the system with the disturbance set to zero. Second, the uncertainty is bounded pointwise by a bounding function, and hence there is no limitation on how, or how fast, the uncertainty varies within the bound. The fact that the rate of variation of the disturbance can be arbitrarily large makes it clear any *explicit* adaptation or learning law will be inadequate.

We will use Lyapunov's direct method to determine the stability of the system. We note that the proof of stability will yield a robust control design. Letting $V(e) = 0.5e^2$, we have

$$
\begin{aligned}
\dot{V} &= e\dot{e} \\
&= ae^2 + e(u + d) \\
&\leq ae^2 + eu + |e| \cdot |d| \\
&\leq 2aV + eu + |e| \cdot \rho(e).
\end{aligned}
$$

By introducing the *known* function ρ in the last step, we obtain a known form from which an *explicit* robust control can be designed. It is also clear that we should choose u so that, in the limit, the term ue exactly cancels the term $|e| \cdot \rho(e)$.

Because we want a *continuous* robust control, we choose

$$u = -\frac{e\rho(e)}{|e|\rho(e) + \epsilon\exp(-\beta t)}\rho(e),$$

where $\epsilon, \beta > 0$ are design parameters. Substituting the control into $\dot{V}$ yields

$$\dot{V} \leq 2aV + \epsilon\exp(-\beta t).$$

The details of how this inequality is obtained and the property of V are given explicitly in the proof of robustness for the general case which follows this example.

Solving the above differential inequality shows that V or equivalently $|e|$ converges to zero exponentially. The convergence rate can be adjusted by changing $|a|$ and ϵ. Note that u is continuous at any finite instant of time and is uniformly bounded since e is uniformly bounded and since $|u| \leq \rho(e)$. Therefore, there is a classical solution for e. Since e is continuous and uniformly bounded, e is uniformly continuous. It follows from the system dynamics (13) that, for any $\delta > 0$,

$$\lim_{t \to \infty} \int_t^{t+\delta} (u + d)d\tau = 0,$$

which implies that u tends to $-d(e, t)$ almost everywhere in the limit. To gain some intuition as to why the proposed robust control guarantees exponentially asymptotic stability, first note that the ratio

$$\frac{e\rho(e)}{|e|\rho(e) + \epsilon\exp(-\beta t)}$$

is always in the interval $[-1, 1]$. It is also important to note that the state e and the exponential term tend to zero simultaneously. Thus the ratio can in general stay well inside $[-1, 1]$ as time goes to infinity. The control u is then simply this ratio times ρ. This ratio has the potential of converging in the limit to the time-varying ratio $d(e, t)/\rho(e)$. That is, over time, the control can actually correlate ρ and an *arbitrary* but continuous time varying uncertainty, so that as time goes to infinity the ratio identifies a scaled version of the uncertainty. In other words the control will, as time evolves, implicitly learn *any* smooth, time-varying function.
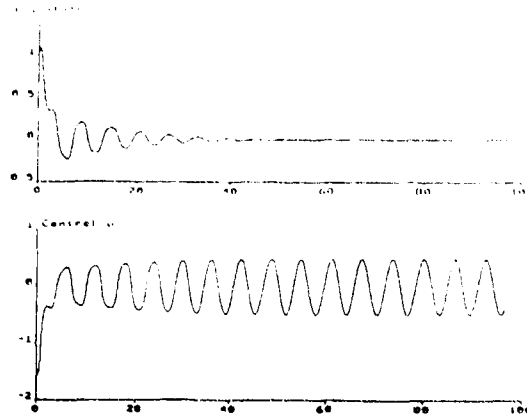
Figure 1: Simulation results of Example 1

Figure 1 shows the simulation using SIMNON© in which the control parameters are $\epsilon = 1$, $\beta = 0.1$, and the "uncertainty" is chosen to be

$$d = 0.5 \sin t + \epsilon \cos 2t + 0.5e^2 \cos t.$$

The horizontal time axis is marked in terms of seconds.　　　　　　　　　　　　　　　　　　□

Example 2: A second-order LTV system:

$$\ddot{y} + a_1(t)\dot{y} + a_2(t)y = \dot{u} + b_1(t)u,$$

where $a_1(t)$, $a_2(t)$, $b_1(t) > 0$ are time-varying parameters. The plant output y is required to tracking the output of the reference model

$$\dot{y}_m + 2y_m = r,$$

where r is any given bounded and continuous reference input. Note that the reference model is strictly proper.

As will be shown later, $\alpha(s) = 1$ should be chosen for this system. It follows from the discussion in [46] that the following control is a perfect nominal tracking control (i.e., $\lim_{t \to \infty}(y_m - y) = 0$)

$$
\begin{aligned}
\dot{w}_1 &= -w_1 + \theta_1^* u \\
\dot{w}_2 &= -w_2 + \theta_2^* y \\
u^*(t) &= r(t) + \theta_0^* y + w_1 + w_2,
\end{aligned}
$$

where θ_i^* are given by

$$\theta_1^*(t) = 1 - b_1(t), \quad \theta_0^*(t) = a_1(t) - 3 \quad \theta_2^*(t) = a_2(t) - 2 - \theta_0^*(t) - \dot{\theta}_0^*(t).$$

Since perfect knowlege of system parameters is not available, we can not let $u = u^*(t)$. However, since $u^*(t)$ is the perfect control, we can rewrite

$$u = (u - \theta_0^* y - w_1 - w_2) + \theta_0^* y + w_1 + w_2,$$

which implies that

$$\dot{y} + 2y = u + r(t) - u^*(t).$$

Define the error signal $e(t) = y_m(t) - y(t)$ yields

$$\dot{e} + 2e = -u + u^*(t).$$

It is noted that $u^*(t)$ can be viewed as a bounded uncertainty since θ_i^* can be easily bounded using the bounds on the system parameters. The uncertainty $u^*(t)$ satisfies the matching conditions [19]. So, robust control can be designed to compensator for $u^*(t)$, as shown in Example 1.　　　　　　　　　　　　□

Example 3: Second order LTV system with relative degree two:

$$\ddot{y} + a_1(t)\dot{y} + a_2(t)y = u,$$

where $a_1(t)$ and $a_2(t)$ are time-varying parameters. The plant output y is required to tracking the output of the reference model

$$\ddot{y}_m + 3\dot{y}_m + 2y_m = r.$$

As shown in [46], the following control ensures perfect nominal tracking control under perfect knowledge, i.e., $\lim_{t \to \infty}(y_m - y) = 0$.

$$\dot{w}_1 = -w_1 + \theta_1^* u$$
$$\dot{w}_2 = -w_2 + \theta_2^* u$$
$$u^*(t) = r(t) + \theta_0^* y + w_1 + w_2,$$

where θ_i^* are given by

$$\theta_1^*(t) = a_1(t) - 3, \quad \theta_0^*(t) = -5 + a_1(t) + \dot{a}_1(t) + a_2(t) - \theta_1^*(t)a_1(t),$$

$$\theta_2^*(t) = a_2(t) + \dot{a}_2(t) - \theta_1^*(t)a_2(t) - \theta_0^*(t) - \dot{\theta}_0^*(t) - 2.$$

Due to the lack of perfect knowlege, we can not let $u = u^*(t)$. However, since $u^*(t)$ is the perfect control, the system can be rewritten as

$$\ddot{y} + 3\dot{y} + 2y = u + r(t) - u^*(t),$$

or

$$\ddot{e} + 3\dot{e} + 2e = -u + u^*(t). \tag{14}$$

It is noted that $u^*(t)$ can again be viewed as a bounded uncertainty.

Unlike Example 1, robust control can not be designed directly unless state feedback is available. This is because, although the uncertainty is matched [19], the reference model as well as (14) is not strictly proper. That is, a robust control designed using standard robust control theory will require measurement not only y but also $\dot{y}$, which violates the objective of I/O robust control. To get around this problem, let

$$\overline{u} = \frac{1}{s + 1.5} u$$

which yields

$$\ddot{e} + 3\dot{e} + 2e = -\dot{\overline{u}} - 1.5\overline{u} + u^*(t)$$
$$\dot{\overline{u}} = -1.5\overline{u} + u.$$

The above system can be viewed as two cascaded, strictly proper subsystems. Since the subsystems are strictly proper, output robust control can be designed for each one of them, and cascaded connection can be used to generate the overall control $u(t)$ in a similar fashion as those in [42, 43, 35]. The treat-off is that the uncertainty $u^*(t)$ is now not matched but satisfies the generalized matching conditions [35].

As shown in [42, 43, 35], the loss of matching conditions for uncertainty implies that asymptotic stability or expoenential stability can not be achieved in general. An intuitive explanaton is the following. The intermediate control variable $\overline{u}$ could be designed in a similar form as explained in Example 1 to compensate any continuous $u^*(t)$. There is no limitation on the uncertainty $u^*(t)$ except its size bounding function $\|\|u^*(t)\|\|$. However, inside the given size bounding function, the uncertainty may vary continuous but arbitrarily fast, this implies that robust control $\overline{u}$ has the capability to change arbitrarily fast as well in order to match up with the change in the uncertainty Therefore, the time derivative of $\overline{u}$ can not be bounded apriori. Thus, to achieve exponential stability for plant of high relative degree, the control u may be excessively large since $u = \dot{\overline{u}} + 1.5\overline{u}$. Because of this reason, exponential stability for plant of relative degree greater than one will not pursued in this paper. The control objective for these systems is to make the tracking error arbitrarily small to achieve any given accuracy requirement. $\square$

Example 4: Minimum phase system with unmodelled dynamics: $G_p(s)[1 + \Delta G(s)]$ where $\lim_{s \to \infty} \Delta G(s) \neq -1$,

$$G_p(s) = k_p \frac{B_p(s)}{A_p(s)} = b_{p0} \frac{1}{s + a_{p1}},$$

and a_{p1} and b_{p0} are unknown parameters with $b_{p0} > 0$.

321
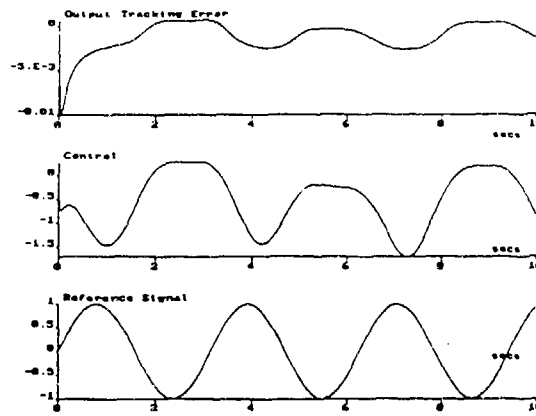
Figure 2: Simulation results of Example 4

For this system, there are only two known information. First,

$$\left| \mathcal{L}^{-1} \left\{ \frac{\Delta G(s)}{1 + \Delta G(s)} \right\} \right| \leq C_{\Delta G} e^{-0.1t}$$

for some unknown constant $C_{\Delta G}$. Second, the lumped uncertainty $\xi(y, t)$ is bounded by

$$|\xi(y, t)| \leq 1 + y^2 + e^{-t} * y^2 \triangleq \rho(y, t).$$

Choose the desired reference model to be

$$G_m(s) = \frac{1}{s + 1}.$$

It is easy to check that $\overline{G}_m(s) = G_m(s)$ is SPR.

A stabilizing control can be designed using the MRRC approach. A specific choice in [36] is

$$u = \nu_1 = \frac{\mu_1(e, y, u, t)}{|\mu_1(e, y, u, t)| + \epsilon_1} g_1(y, u, t) = \frac{e g_1^2}{|e| g_1 + \epsilon_1},$$

where

$$g_1(y, r, u, t) = k_g \left\{ r^2(t) + y^2(t) + \rho^2(y, t) + e^{-0.1t} * y^2(t) \right\},$$

$\epsilon_1 > 0$ is a constant, $\mu_1(e, y, u, t) = e(t) g_1(y, u, t)$, and $k_g > 0$ is a scalar gain.

The simulation was done using SIMNON$^{©}$ with the following choices:

Plant: $G_p(s) = \frac{1}{s-1}$, $\Delta G(s) = \frac{5}{s-2}$. Reference signal: $r(t) = \sin 2t$.

Lumped uncertainty: $\xi(y, t) = 0.25 \cos t + 0.5 \cos y + y \sin 2t + e^{-t} * [y^2 \sin(y \cdot t)]$.

Initial conditions: zero. Parameters in the controller: $k_g = 5.0$, $\epsilon_1 = 0.3$.

Simulation results are shown in Figure 2. We note that the tracking error can be made smaller by choosing a smaller value for the design parameter ϵ_1. □

Example 5: Consider the plant described by $G_p(s)[1 + \Delta G(s)]$ where

$$G_p(s) = k_p \frac{B_p(s)}{A_p(s)} = b_{p0} \frac{1}{s + a_{p1}},$$

a_{p1} and b_{p0} are unknown parameters with $b_{p0} > 0$, and the uncertainty $\Delta G(s)$ has relative degree no less than -1.

Two known information are assumed for this system. It is assumed that the lumped uncertainty $\xi(y, t)$ be bounded by

$$|\xi(y, t)| \leq 1 + y^2 + e^{-t} * y^2 \triangleq \rho(y, t).$$

About unmodelled dynamics, it is assumed that $p_0' \geq 0.1$.

The same reference model and MRRC as those in Example 4 are used. The simulations were done using SIMNON$^{©}$ with the following choices:

322
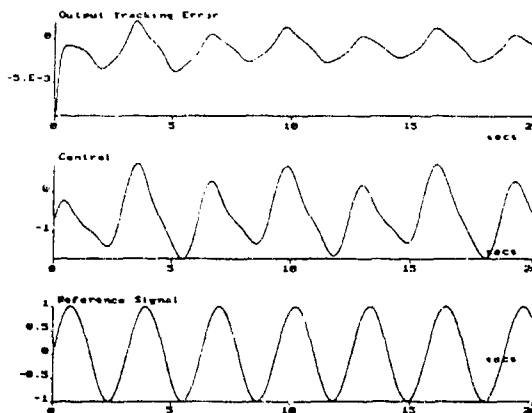
Figure 3: Simulation of Example 5: Plant (1)
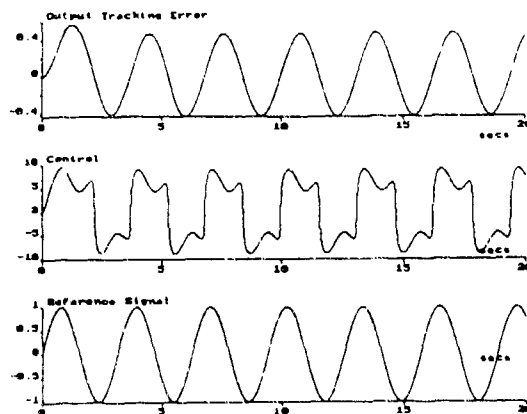
Figure 4: Simulation of Example 5: Plant (2)

Plant: (1) $G_p(s) = \frac{1}{s-1}$, $\Delta G(s) = \frac{-1.2}{s+1}$; (2) $G_p(s) = \frac{1}{s-1}$, $\Delta G(s) = \frac{-1.001s}{s+1}$. Reference signal: $r(t) = \sin 2t$.

Lumped uncertainty: $\xi(y,t) = 0.25 \cos t + 0.5 \cos y + y \sin 2t + e^{-t} * [y^2 \sin(y \cdot t)]$.

Initial conditions: zero. Parameters in the controller: $k_g = 5.0$, $\epsilon_1 = 0.3$.

The same MRRC applies to two different nonminimum phase plants. Simulation results of two plants are shown in Figures 3 and 4, respectively. We note that, if the high-frequency gain of the overall system is different from that of the nominal system, the output tracking error is not very small and in fact can not be made smaller by choosing a smaller value for the design parameter ϵ_1. *Box*

For general systems, control design steps and theoretical analysis are, although much more complicated, conceptually the same as those in the above examples.

4 Applications

This section is organized into two subsections. In the first subsection, general discussions are made on applicability of nonlinear robust control for both rigid and flexible systems. In the second subsection we use flexible-joint robot as a prototype to show how to design robust control for systems that are high-dimensional, uncertain, highly nonlinear.

4.1 General Discussions

The need of the proposed research in robust control come naturally from many applications including control of weapon systems. For example, any mechanical, rigid motion in weapon systems can be described by

$$\tau = M(q)\ddot{q} + N(q,\dot{q})$$

$$N(q, \dot{q}) \quad = \quad V_m(q, \dot{q})\dot{q} + G(q) + F_d(t)\dot{q} + F_s(\dot{q}) + T_d.$$

where q represents $n \times 1$ vector of generalized coordinates, u is $n \times 1$ vector of generalized force inputs, $M(q)$ is an $n \times n$ inertia matrix, $V_m(q, \dot{q})$ is an $n \times n$ matrix of centripetal and Coriolis terms, $G(q)$ is an $n \times 1$ vector of gravity terms, $F_d(t)$ and $F_s(\dot{q})$ are diagonal matrices of dynamic and static friction terms, and T_d is an $n \times 1$ vector of any unknown but bounded disturbances. $N(q, \dot{q})$ provides a consolidated notation for the nonlinear effects and disturbances. If necessary, dynamics of electrical subsystems can be included as well. It is apparent that system (15) fits naturally into the setup of nonlinear robust control, especially the generalized matching conditions.

In many cases, a weapon system contains not only rigid mechanical parts but also flexible parts, for example, helicopter blades made of composite materials. This class of systems is usually referred as flexible systems. From Hamilton's principle, dynamics of a flexible system are governed by partial differential equation (PDE). For instance, the motion of a planar and homogeneous flexible beam is described by a forth-order linear PDE with four boundary conditions [3]. For complicated systems, PDE is in general nonlinear and difficult to derive. The main differences between control of rigid systems and control of flexible systems are: (1) control objective can not be achieved directly but rather through oscillatory propagation, which is reflected mathematically by the fact that control inputs do not appear the PDE but rather enter through its boundary conditions; (2) any model of a flexible system is of infinite dimension, contains significant nonlinearity, and is only known approximately. These characteristics makes flexible system a robust control problem.

Since control problem of PDE is not solvable in general and since almost all control results are based on ordinary differential equations (ODEs), one has to approximate the dynamics of flexible systems by ODEs. The popular approach for modelling flexible systems using ODEs is to use finitely truncated modal expansions. That is, first define the assumed modes and then use Lagrange formulation to yield a high-order complicated nonlinear ODEs. Another approach is to model a flexible system as an infinite dimensional systems subject to significant nonlinearities. The ODE models from both techniques will obviously contain large uncertainties, which makes nonlinear robust control be the natural candidate for this control problem.

To apply robust control, both methods of approximation need to be studied. The first approximation approach yields a nonlinear state space model in which uncertainties may not satisfy the generalized matching conditions, which requires new research as proposed in section five. The second method provides a linear input-output model which is time-varying (and implicitly state-dependent), contains nonlinear uncertainties and unmodelled dynamics of infinite order, and is also non-minimum phase. The non-minimum phase feature of flexible systems has been shown in [26] for an Euler-Bernoulli beam. This represents the class of systems tackled by the newly proposed MRRC method.

In a word, the nonlinear robust control schemes are very much applicable to weapon systems that contain both flexible subsystems and rigid subsystems

4.2   Robust Control Design for Flexible-Joint Robots

Control design for robot manipulators with joint flexibility has attracted much attention from control researchers in recent years. The main reason is that, as shown by experimental study in [58], joint flexibility must be taken into account in both modelling and control design in order to achieve high tracking performance. Common sources of joint flexibility are gear elasticity (for example, harmonic drives), shaft windup, etc. Most researchers have adopted the model of flexible joint robots presented in [54].

Several methods, such as feedback linearization, observer design, adaptive control, singular perturbation, and robust control, have been investigated to design effective control for flexible joint robots. A list of references on these results can be found in the survey paper [56], we shall only brief synopsis of the most recent developments and provide comparison of different approaches. In feedback linearization method [54, 25], control is designed based on feedback linearization transformation which requires the knowledge of the dynamics and acceleration and jerk measurements. Under the assumption that joint flexibility is "small", there are two time scales in system dynamics, and a control can be designed using singular perturbation technique. Adaptive version of this slow/fast control was studied in [17, 18]. The resulting control is intuitively simple since it usually contains two parts: a control for rigid body and a corrective control, however, the control does not guarantee global stability. The most recent adaptive control scheme proposed in [27] guarantees global stability under the standard assumption that dynamics can be fully parameterized. On the front of robust control design, local stability was shown [34] which can be viewed as extension of robust control results for rigid robots [48, 50]. Later, a robust control guaranteeing global stability was presented in [13], this full state feedback robust control design is an application of the result in [42] and an extension of the robust control law [12] for

rigid robots. Hybrid control, or combined robust and adaptive control, of flexible joint robots has also been studied [49, 14].

So far all existing control laws for elastic robots require full state feedback. There are some results [31, 60] on designing state observer for flexible joint robots, but no result has been reported on the subject of how to close the control loop, that is, how to design a control based on the estimates of the states. Since the separation principle does not hold in general for nonlinear systems, it appears unlikely that full state feedback control can be changed to an estimate-based control to guarantee global stability.

In this section we use flexible joint manipulators as eample to design input-output robust control. The control objective is to design a robust control which guarantees global stability and good tracking performance but requires only feedback of link position and velocity. The proposed control design is not only more attractive in practice since it requires less feedback information, but also allows the presence of significant but bounded nonlinear uncertainties including fast time varying parameters, modelling errors, load change, and unknown flexibility.

Dynamics of a robot with flexible joints are described by the following nonlinear differential equations:

$$0 = M(q_1)\ddot{q}_1 + N(q_1, \dot{q}_1) + K(q_1 - q_2) \tag{15}$$

$$J\ddot{q}_2 = K(q_1 - q_2) - D\dot{q}_2 + \tau + P(q_1, \dot{q}_1) \tag{16}$$

$$N(q_1, \dot{q}_1) = V_m(q_1, \dot{q}_1)\dot{q}_1 + G(q_1) + F_d\dot{q}_1 + H(q_1, \dot{q}_1)$$

$$H(q_1, \dot{q}_1) = F_s(\dot{q}_1) + T_d,$$

where q_1 and q_2 represent $n \times 1$ vectors of joint angles and motor angles, respectively, τ is $n \times 1$ the control vector of motor output torques, $M(q_1)$ is an $n \times n$ inertia matrix(symmetric and positive definite) for the rigid links, K is a diagonal matrix representing the joint stiffness. $V_m(q_1, \dot{q}_1)$ is an $n \times n$ matrix of centripetal and Coriolis terms, $G(q_1)$ is an $n \times 1$ vector of gravity terms, F_d is an $n \times n$ diagonal matrix of dynamic friction coefficients, $H(q_1, \dot{q}_1)$ includes static friction $F_s(\dot{q}_1)$ and any unknown but bounded disturbances. It is worth noting that T_d is in general a *unknown* nonlinear functional of $q_1, \dot{q}_1$. In equation (16), J is a diagonal matrix of actuator inertias reflected to the link side of the gears, D is also a diagonal matrix of torsional damping coefficients, $P(q_1, \dot{q}_1)$ denotes any possible nonlinearity whose bounding function depends only on q_1, and $\dot{q}_1$.

Let q_1^d characterize the desired, smooth trajectory that the robot should track. The assumption of q_1^d being smooth implies that q_1^d and its derivatives up to the forth order are continuous and bounded functions of time.

The followings are the important properties of robot dynamics.

P.1 It has been shown in [11] that the inertia matrix satisfies

$$\underline{m}I \leq M(q_1) \leq \overline{m}(q_1)I, \qquad \forall q_1 \in \Re^{n \times 1}$$

where it is assumed that $\underline{m}$ and $\overline{m}(q_1)$ be known. Note that $\overline{m}(q_1)$ is a non-negative function and reduces to a constant for robots with only revolute joints.

P.2 It has been shown in [11] that $V_m(q_1, \dot{q}_1)$ is a function at most of first order in q_1 and $\dot{q}_1$. Therefore,

$$\|V_m(q_1, \dot{q}_1)\| \leq \beta_1 + \beta_2\|x_1\| = \rho_1(x_1),$$

where $\| \cdot \|$ denotes Euclidean norm, x_1 is the *output vector* defined by $x_1 = \begin{bmatrix} e_1^T & \dot{e}_1^T \end{bmatrix}^T$, and e_1 is an $n \times 1$ vector representing the trajectory error, i.e. $e_1 = q_1^d - q_1$.

The robust control design proposed requires only the following assumptions:

A.1 *Unknown* functionals in dynamics equations (15) and (16) include dynamic and static friction, bounded disturbances, etc. It is assumed that they be bounded by known functions as

$$\|G(q_1) + F_d\dot{q}_1 + F_s(\dot{q})\| \leq \beta_3 + \beta_4\|x_1\| = \rho_2(x_1).$$

$$\|T_d\| \leq \rho_3(x_1, t), \quad \|P(q_1, \dot{q}_1)\| \leq \rho_4(x_1), \quad \|M(q_1)\| \leq \rho_5(x_1).$$

A.2 The feedback information for control design are only the measurements of joint position and velocity, i.e., q_1 and $\dot{q}_1$. The position and velocity deformations $q_2 - q_1$ and $\dot{q}_2 - \dot{q}_1$ are unknown, but initial deformations are bounded, that is,

$$\|x_2(t_0) - x_1(t_0)\| \leq \rho_6 \quad \text{or} \quad \|x_2(t_0)\| \leq \rho_7$$

for some constant ρ_6 or ρ_7, where x_2 is the internal state defined by $x_2 = \begin{bmatrix} q_2^T & \dot{q}_2^T \end{bmatrix}^T$.

A.3 If the parameters K, J, and D are unknown, it is assumed that their value are limited within compact sets as

$$0 < \underline{K} \le K \le \overline{K}, \quad 0 < \underline{J} \le J \le \overline{J}, \quad 0 < \underline{D} \le D \le \overline{D}, \quad .$$

In addition, if they are time-varying, their derivatives up to third order are bounded.

We can rewrite system dynamics (16) into the following state space representation:

$$\dot{x}_2 = A_2 x_2 + B_2[\tau + K q_1 + P(q_1, \dot{q}_1)], \quad q_2 = C_2 x_2 \tag{17}$$

where

$$A_2 = \begin{bmatrix} 0 & I \\ -J^{-1}K & -J^{-1}D \end{bmatrix}, \quad B_2 = \begin{bmatrix} 0 \\ J^{-1} \end{bmatrix}, \quad C_2 = \begin{bmatrix} I & 0 \end{bmatrix}, \quad x_2 = \begin{bmatrix} q_2^T & \dot{q}_2^T \end{bmatrix}^T.$$

Note that the matrix A_2 is stable, which is always physically guaranteed. It follows from (17) that

$$q_2(t) = C_2 e^{A_2 t} x_2(0) + \tau' + C_2 e^{A_2 t} * B_2 K q_1 + C_2 e^{A_2 t} * B_2 P(q_1, \dot{q}_1), \tag{18}$$

where $*$ denotes the convolution operation and

$$\tau' = C_2 e^{A_2 t} * B_2 \tau.$$

To make the analysis easier to understand, let us proceed the I/O robust control design for two different cases. In the next subsection, we shall first study the simple case that the parameters K, J, and D are known. The general case that the parameters K, J, and D are unknown will be investigated in the subsequent subsection.

4.2.1 Simplified I/O Control

In this section, I/O robust control design is studied for the case that $J = J_o$, $K = K_o$, and $D = D_o$ for some nominal value matrices J_o, K_o, and D_o. With the knowledge of A_{2o} and B_{2o} where

$$A_{2o} = \begin{bmatrix} 0 & I \\ -J_o^{-1}K_o & -J_o^{-1}D_o \end{bmatrix}, \quad B_{2o} = \begin{bmatrix} 0 \\ J_o^{-1} \end{bmatrix}.$$

the transition matrix $e^{A_{2o}t}$ can be calculated. Consequently, the intermediate variable

$$\tau'_o = \tau' |_{J=J_o, D=D_o, K=K_o} = C_2 e^{A_{2o}t} * B_{2o}\tau$$

is available in control design. In stead of calculating directly $e^{A_{2o}t}$ off-line, one can use the following augmented system to generate τ'_o:

$$\dot{z} = A_{2o}z + B_{2o}\tau, \quad \tau'_o = C_2 z, \tag{19}$$

where z is the augmented state of appropriate order. More specifically, letting

$$z = \begin{bmatrix} z_1^T & z_2^T \end{bmatrix}^T$$

yields

$$\begin{aligned} \tau'_o &= z_1 \\ \dot{z}_1 &= z_2 \\ \dot{z}_2 &= -J_o^{-1}K_o z_1 - J_o^{-1}D_o z_2 + J_o^{-1}\tau. \end{aligned} \tag{20}$$

It is worth noting here that, although matrices in (17) are known, q_2 or x_2 can not be calculated due to the uncertainty $P(q_1, \dot{q}_1)$.

Substituting solution (18) and (21) into (15) yields the error system:

$$\begin{aligned} \dot{x}_1 &= A_1 x_1 + B_1(\Delta A - \tau'_o + q_1) \\ &= \overline{A}x_1 + B_1(\Delta A' - \tau'_o + q_1), \end{aligned} \tag{22}$$

326

where $K_p > 0$ is gain matrices chosen by the designer,

$$A_1 = \begin{bmatrix} 0 & I \\ 0 & 0 \end{bmatrix}, \quad \overline{A} = \begin{bmatrix} 0 & I \\ -M^{-1}(q_1)K_p & 0 \end{bmatrix}, \quad B_1 = \begin{bmatrix} 0 \\ M^{-1}K_o \end{bmatrix},$$

$$\Delta A = K_o^{-1} M(q_1) \ddot{q}_1^d + K_o^{-1} N(q_1, \dot{q}_1) - C_2 e^{A_{2o} t} x_2(0) - C_2 e^{A_{2o} t} * B_{2o} P(q_1, \dot{q}_1),$$

and

$$\Delta A' = \Delta A + K_o^{-1} K_p e_1 - C_2 e^{A_{2o} t} * B_{2o} K_c q_1.$$

Input-output robust control design as well as corresponding stability and tracking performance will be investigated in terms of error system (22) and augmented system (19) The analysis is done using Lyapunov's direct method. To apply the Lyapunov technique, let us choose Lyapunov function candidate to be

$$V = V_1 + V_2, \quad V_1 = x_1^T P x_1, \quad V_2 = \frac{1}{2}(z - u)^T(z - u), \tag{23}$$

where u is the vector to be chosen later, $\alpha > 0$ is a constant scalar, and

$$P = \frac{1}{2} \begin{bmatrix} K_p + \alpha^2 M(q_1) & \alpha M(q_1) \\ \alpha M(q_1) & M(q_1) \end{bmatrix}.$$

It follows from the definition

$$V = \frac{1}{2} e_1^T K_p e_1 + \frac{1}{2}(\alpha e_1 + \dot{e}_1)^T M(q_1)(\alpha e_1 + \dot{e}_1) + \frac{1}{2}\|z - u\|^2$$

that V is a positive definite function with respect to x_1 and $z - u$.

The following lemma illustrates the property of the derivative of sub-Lyapunov function $V_1(x_1)$ along every trajectory of system (22).

Lemma: [51] *Consider system (15) and (16) under Properties P.1 and P.2 and Assumptions A.1 and A.2. Assume in addition that the matrices K, D, and J be constant and known. Then, the sub-Lyapunov function $V_1(x_1)$ satisfies the following inequality:*

$$\dot{V}_1(x_1) \leq -\lambda_1 \|e_1\|^2 + \|w(x_1)\| \varrho_1(x_1) - w^T(x_1) K_o(\tau_o' - q_1 - K_c^{-1} K_p e_1 + C_2 e^{A_{2o} t} * B_{2o} K_o q_1), \tag{24}$$

where $\lambda_{min}(\cdot)$ and $\lambda_{max}(\cdot)$ represent the operation of taking the minimum and maximum eigenvalues, respectively,

$$\lambda_1 = \alpha \lambda_{min}(K_p), \quad w(x_1) \triangleq \begin{bmatrix} \alpha I & I \end{bmatrix} x_1,$$

$$\varrho_1(x_1) = \overline{m}(q_1)\|\ddot{q}_1^d\| + \rho_1(x_1)\|\dot{q}_1\| + \rho_2(x_1) + \rho_3(x_1) + \|w(x_1)\|\rho_5(x_1) + \alpha \overline{m}(q_1)\|\dot{e}_1\|$$
$$+ \|K_c C_2 e^{A_{2o} t}\| \cdot \rho_7 + \int_{t_0}^{t} \|K_o C_2 e^{A_{2o}(t-s)} B_{2o}\| \rho_4(x_1(s)) ds.$$

Remark: The bounding function $\varrho_1(x_1)$ does not depend on internal state x_2 and only requires an estimate (or bound) on the initial condition of x_2.

Upon having Lemma, we can proceed input-output robust control design The proposed I/O controller is generated by the following recursive mapping:

$$u = \begin{bmatrix} u_1^T & u_2^T \end{bmatrix}^T$$

$$u_1 = u_{11} + u_{12}$$

$$u_{11} = q_1 + K_o^{-1} K_p e_1 + K_o^{-1} \overline{m}(q_1) w(x_1) - C_2 e^{A_{2o} t} * B_{2o} K_o q_1$$

$$u_{12} = K_c^{-1} \frac{\mu_1(x_1, t)|\mu_1(x_1, t)|^{\nu_1}}{(|\mu_1(x_1, t)|^{\nu_1 + 1} + \epsilon_1^{1+\nu_1})} \varrho_1(x_1),$$

$$u_2 = u_1 - z_1 + K_o^T w(x_1) + \frac{\mu_2(x_1, t)|\mu_2(x_1, t)|^{\nu_2}}{(|\mu_2(x_1, t)|^{\nu_2 + 1} + \epsilon_2^{1+\nu_2})} g_2(x_1, t),$$

$$\tau = J_o u_2 + J_o u_1 + (K_o - J_o)z_1 + (D_o - J_o)z_2$$
$$+ J_o \frac{\mu_3(x_1, t)|\mu_3(x_1, t)|^{\nu_3}}{(|\mu_3(x_1, t)|^{\nu_3 + 1} + \epsilon_3^{1+\nu_3})} g_3(x_1, t), \tag{25}$$

327

where $\epsilon_j > 0$ and $\nu_j \geq 0$, $j = 1, 2, 3$, are constants, the constants ν_j are chosen such that the first order partial derivatives of u_j with respect to their variables are well-defined, $||| \cdot |||$ denotes a known bounding function on the magnitude of the argument, and

$$\mu_1(x_1, t) = w(x_1)\varrho_1(x_1),$$

$$g_2(x_1, t) = |||\dot{u}_1|||, \quad \mu_2(x_1, t) = (u_1 - z_1)g_2(y, u, t),$$

$$g_3(x_1, t) = |||\dot{u}_2|||, \quad \mu_3(x_1, t) = (u_2 - z_2)g_3(x_1, t).$$

The recursive mapping basically involves finding bounding functions of $|\dot{u}_1|$ and $|\dot{u}_2|$ for obtaining u_2 and τ, respectively. The terms $|\dot{u}_1|$ and $|\dot{u}_2|$ can be bounded by first developing bounds for the first-order partial derivatives of u_i with respect to its variables, and then by determining the bounds for the first-order time derivatives of its variables using dynamic equations (19) and (22). The bounding functions are usually obtained by taking Euclidean norm. There are several ways to guarantee differentiability of u_1 and u_2. The easiest way is to use some user-defined norm such as $||y||_\epsilon \triangleq \sqrt{||y||^2 + \epsilon}$ for some $\epsilon > 0$. It is worth mentioning here that $\dot{u}_1$ will contain $\dot{x}_1$ which in turn depends on x_2. However, the bounding function on $|\dot{u}_1|$ will only depend on x_1 and τ'_o since x_2 can be bounded using (18) with $\tau' = \tau'_o$.

We are now in a position to state the following theorem on control (25) which requires only input-output measurements and is for now robust with respect to any bounded uncertainties except the parameter variation of J, D, and K.

Theorem: [51] *Consider system (15) and (16) under Properties P.1 and P.2 and Assumptions A.1 and A.2. Assume in addition that the matrices K, D, and J be constant and known. If I/O robust controller τ is chosen to be the outcome of the mapping procedure (25), then the trajectory tracking error x_1 (both e and $\dot{e}$) is globally and uniformly ultimately bounded. That is, as time approaches infinity, the magnitude of the tracking error characterized by $V_1(e, \dot{e})$ becomes no larger than the design parameter ϵ^* where*

$$-\frac{1}{\min\{\frac{2\alpha\lambda_{min}(K_p)}{\lambda_{max}(K_p)}, 2\}} \sum_{i=1}^{3} \epsilon_i.$$

Furthermore, the robust control τ is continuous and globally, uniformly bounded.

4.2.2   General I/O Control

In this section, input-output control design is proceeded without knowledge of matrices J, D, and K. When these matrices are not known, the intermediate variable τ' defined in (18) can not be calculated. However, it is noted that, if a nominal augmented system similar to (19) can be obtained by defining τ'_o properly, most of the analysis in the previous section follows. Therefore, we shall focus on how to generate from (17) an equation similar to (19) which depends only on nominal values.

Consider the following linear time-varying system:

$$F(s, t)y = v + d, \tag{26}$$

where y, v and d are column vectors of n dimension, y is the output, v is the corresponding input, d is disturbance. $F(s, t)$ is the so-called time-varying differential operator defined by

$$F(s, t) = Js^2 + Ds + K.$$

That is, system (26) can be rewritten in terms of differential equation as

$$J\ddot{y} + D\dot{y} + Ky = v + d.$$

More details on time-varying differential operator can be found in [57, 22].

The problem to be studied is under what input v the closed-loop system becomes

$$F_o(s)J_o^{-1}Jy = r + d', \tag{27}$$

328

where J_o, D_o, and K_o are constant matrices represents any choice of nominal values of J, D, K respectively, r is any reference input, d' is the equivalent disturbance, and differential operator $F_o(s)$ is given by

$$F_o(s) = J_o s^2 + D_o s + K_o.$$

Let us introduce the following auxiliary signals:

$$\dot{\eta}_1 = -\eta_1 + G_1 v, \tag{28}$$

$$\dot{\eta}_2 = -\eta_2 + G_2 y, \tag{29}$$

where η_1 and η_2 are n-th order column vectors, initial conditions of η_1 and η_2 are assumed without loss of any generality to be zero and G_1 and G_2 are n-th order diagonal matrices.

The input v is selected as

$$v = G_3 y + r + \eta_1 + \eta_2, \tag{30}$$

where G_3 is also an n-th order diagonal matrix. Utilizing differential operator, we can rewrite the input v as

$$v = G_3 y + r + (s + 1)^{-1}[G_1 v + G_2 y],$$

or

$$v = (sI + I - G_1)^{-1}\{[(s + 1)G_3 + G_2]y + (s + 1)r\}.$$

Substituting the above equation into (26) yields

$$[(sI + I - G_1)(Js^2 + Ds + K) - (s + 1)G_3 - G_2]y = (s + 1)r + (sI + I - G_1)d.$$

It then follows that the closed loop system is given by (27) with

$$d' = (s + 1)^{-1}(sI + I - G_1)d$$

iff the following identity holds:

$$[(sI + I - G_1)(Js^2 + Ds + K) - (s + 1)G_3 - G_2] = (s + 1)(J_o s^2 + D_o s + K_o)J_o^{-1} J. \tag{31}$$

Since all matrices are diagonal, the above equality can be rewritten as

$$[(s + 1 - G_{1i})(J_i s^2 + D_i s + K_i) - (s + 1)G_{3i} - G_{2i}] = (s + 1)(J_{oi} s^2 + D_{oi} s + K_{oi})\frac{J_i}{J_{oi}},$$

where subscript i denotes the i-th element on the diagonal. It is easy to verify that the above equality holds if G_1, G_2, and G_3 are chosen such that

$$G_{1i} = \frac{D_i}{J_i} - 2\frac{\dot{J}_i}{J_i} - \frac{D_{oi}}{J_{oi}},$$

$$G_{3i} = \dot{D}_i + K_i + (1 - G_{1i})D_i - 3\ddot{J}_i - 2\dot{J}_i - 2\frac{D_{oi}}{J_{oi}}\dot{J}_i - \frac{K_{oi}}{J_{oi}}J_i - \frac{D_{oi}}{J_{oi}}\dot{J}_i,$$

$$G_{2i} = \dot{K}_i + (1 - G_{1i})K_i - \dot{G}_{3i} - \frac{d^3 J_i}{dt^3} - (1 + \frac{D_{oi}}{J_{oi}})\ddot{J}_i - \frac{K_{oi} + D_{oi}}{J_{oi}}\dot{J}_i - \frac{K_{oi}}{J_{oi}}J_i. \tag{32}$$

Solution (32) guarantees identity (31) which in turn guarantees that the closed-loop system is internally stable. The above relations will be used to determine known bounds on G_1, G_2, and G_3. These bounds are required in designing robust control.

It should be emphasized here that the introduction of differential operators implies zero initial conditions. It is noted that systems given by (17) and (26) are both uniformly asymptotically stable. Consequently, non-zero initial conditions contribute only exponentially decaying terms with which a similar Lyapunov stability proof can be proceeded to yield the same stability results.

Now, reconsider dynamic equation (16) by rewriting as

$$
\begin{aligned}
J\ddot{q}_2 + D\dot{q}_2 + Kq_2 &= \tau + Kq_1 + P(q_1, \dot{q}_1) \\
&= [G_3 q_2 + \tau + \eta_1 + \eta_2] + [Kq_1 + P(q_1, \dot{q}_1) - G_3 q_2 - \eta_1 - \eta_2] \\
&\triangleq v + d,
\end{aligned}
$$

where η_1 and η_2 are given by (28) and (29) with $r = \tau$ and $y = q_2$, and G_i are given by the solution (32). It follows from the discussion from (26) to (32) that dynamics (16) becomes

$$
\ddot{q}_2' + J_o^{-1} D_o \dot{q}_2' + J_o^{-1} K_o q_2' = \tau + P'(q_1, \dot{q}_1, \zeta) \tag{33}
$$

where

$$
q_2' = Jq_2, \quad \zeta_1 = e^{-t} * \tau, \quad \zeta_2 = e^{-t} * \zeta_2, \quad \zeta_3 = e^{-t} * \zeta_3, \quad \zeta = \begin{bmatrix} \zeta_1^T & \zeta_2^T & \zeta_3^T \end{bmatrix}^T,
$$

$$
P'(q_1, \dot{q}_1, \zeta) = (s+1)^{-1}(sI + I - G_1)[Kq_1 + P(q_1, \dot{q}_1) - G_3 q_2 - \eta_1 - \eta_2].
$$

Hence, the solution for q_2 is given by

$$
q_2(t) = J^{-1} C_2 e^{A_{2o}t} x_2'(0) + J^{-1}\tau_o'' + J^{-1} C_2 e^{A_{2o}t} * B_{2o} J_o P'(q_1, \dot{q}_1, \zeta), \tag{34}
$$

where

$$
x_2'(0) = \begin{bmatrix} q_2^T(t_0)J(t_0) & \dot{q}_2^T J(t_0) + q_2^T(t_0)\dot{J}(t_0) \end{bmatrix}^T
$$

and τ_o'' is defined by

$$
\begin{aligned}
z' &= \begin{bmatrix} z_1' \\ z_2' \end{bmatrix} \\
\tau_o'' &= C_2 z' \\
\dot{z}' &= A_{2o} z' + B_{2o} J_o \tau, \tag{35}
\end{aligned}
$$

which is similar to (19). Thus, the results obtained in the previous subsection can be duplicated here and therefore omitted.

5   Current and Future Research

The current and future research is divided into three parts: loosening the existing restrictions on uncertainties (mainly the GMCs), strengthening existing stability results by studying performance indices under robust control, and improving the nonlinear I/O control method so that it becomes applicable to more classes systems, especially general non-minimum phase systems.

There have been several preliminary results along these directions. First, for systems without GMCs, we propose a new design procedure in which several interlacings are performed in each recursion. The intuition is that interlacing allows one to deal with the uncertainties not satisfying GMCs. The procedure has been proven to work for systems such as those with $\Delta f_i(x, t) = \Delta f_i(x_{i+2}, \cdots, x_n, t)$. It became apparent in the preliminary study that the procedure can be used not only for control design but also for identifying the class of stabilizable systems. Second, using performance index to quantify the transient performance of nonlinear robust control has been studied in [40]. Third, it has been shown in [52] that MRRC is applicable to nonminimum phase systems provided that nonminimum phase zeros are due to sufficiently small unmodelled dynamics.

References

[1] B.R.Barmish, M.J.Corless and G.Leitmann "A new class of stabilizing controllers for uncertain dynamical systems," *SIAM J. Contr. Optimiz.*, Vol.21, No.2, pp.246-255, 1983.

[2] B.R.Barmish and G.Leitmann "On ultimate boundedness control of uncertain systems in the absence of matching assumptions," *IEEE Transaction on Automat. Contr.*, Vol.27, No 1, pp.153-158, 1982.

[3] G.Chen, "Control and stabilization for the wave equation in a bounded domain," *SIAM J. Contr. & Opti.*, Vol.17, 66-81, 1979.

[4] Y.H.Chen, "Design of robust controllers for uncertain dynamical systems," *IEEE Trans. Automat. Contr.*, Vol.33, No.5, pp.487-491, 1988.

[5] Y.H.Chen, "Reducing the measure of mismatch for uncertain dynamical systems," *Proceeding ACC*, 229-236, 1986

[6] Y.H.Chen, "On the robustness of mismatched uncertain dynamical systems," *J. of Dynamic Systems, Measurement, and Control*, Vol. 109, 29-35, 1987

[7] Y.H.Chen, "Deterministic control for a new class uncertain dynamical systems," *IEEE Trans. Automat. Contr.*, Vol.32, No.1, pp.73-74, 1987.

[8] Y. H. Chen and G.Leitmann "Robustness of uncertain systems in the absence of matching assumptions," *Int. J. Control*, Vol.45, No.5, pp.1527-1542, 1987.

[9] M.J.Corless and G.Leitmann "Continuous state feedback guaranteeing uniform ultimate boundedness for uncertain dynamic systems," *IEEE Trans. Automat. Contr.*, Vol.26, No.5, pp.1139-1144, May, 1981.

[10] M.J.Corless and G.Leitmann "Controller design for uncertain systems via Lyapunov functions," *Proceeding of ACC*, pp.2019-2025, 1988

[11] J.J.Craig, *Adaptive Control of Mechanical Manipulators*, Reading, MA., Addison-Wesley, 1988.

[12] D.M.Dawson, Z.Qu, F.L.Lewis, and J.F.Dorsey, "Robust control for the tracking of robot motion," *International Journal of Control*, Vol.52, No.3, pp. 581-595, September, 1990.

[13] D.M.Dawson, Z.Qu, M.Bridges, and J.C.Carroll, "Robust tracking of rigid-link flexible-joint electrically-driven robot," *The 30th IEEE Conference on Decision and Control*, pp.1409-1412, Brighton, U.K. December 1991.

[14] D.Dawson, Z.Qu, and M.Bridge, "Hybrid adaptive control for the tracking of rigid-link flexible-joint robots," *Modelling and Control of Compliant and Rigid Motion Systems, 1991 ASME Winter Annual Meeting*, pp.95-98, Atlanta GA. December 1991.

[15] J.C.Doyle, K.Glover, P.P.Kharogonekar, and B.A.Francis, "State space solutions to standard H^2 and H^∞ control problems," *IEEE Trans. Automat. Contr.*, Vol.34, No.8, pp.831-847, 1989.

[16] B.A.Francis, *A Course in H^∞ Control Theory*, Springer-Verlag, New York, 1987.

[17] F.Ghorbel, J.Y.Hung, and M.W.Spong, "Adaptive control of flexible-joint manipulators," *the 1989 IEEE International Conference on Robotics and Automation*, Scottsdale, Arizona, pp.15-19, 1989.

[18] F.Ghorbel and M.W.Spong, "Stability analysis of adaptively controlled flexible joint manipulators," *Proc. of the 29th IEEE Conference on Decision and Control*, Honolulu, HI., pp.2538-2544, 1990.

[19] S.Gutman, "Uncertain Dynamical Systems — A Lyapunov Min-Max Approach," *IEEE Trans. Automat. Contr.*, Vol.24, No.3, pp.437-443, June, 1979.

[20] S.Gutman and Z.Palmor, "Properties of min-max controllers in uncertain dynamic systems," *SIAM J. Contr. & Optimiz.*, Vol.20, No.6, pp.850-861, 1982.

[21] C.V.Hollot and M.Arabacioglu, "$l-th$ step Lyapunov min-max controllers: Stabilizing discrete-time systems under real parameter variations," *Proceeding ACC*, 496-501, 1987.

[22] A.Ilchmann, I.Nurnberger, and W.Schmale, "Time-varying polynomial matrix systems," *Int. J. Control*, Vol.40, No.2, pp.329-362, 1984.

[23] I.Kanellakppoulos, P.V.Kokotovic, and A.S.Morse, "Systematic design of adaptive controllers for feedback linearizable systems," *IEEE Trans. Automat. Contr.*, Vol.36, 1241-1253, 1991.

[24] V.L.Kharitonov, "Asymptotic stability of an equilibrium position of a family of systems of differential equations," *Differentsial'nye Uravneniya*, Vol.14, pp.2086-2088, 1978.

[25] K.Khorasani, "Nonlinear feedback control of flexible joint manipulators: A single link case study," *IEEE Transactions on Automatic Control*, Vol.35, No.10, pp.1145-1149, 1990.

[26] D.S.Kwon and W.J.Book, "Tracking control of a nonminimum phase flexible manipulator," in *Modelling and Control of Compliant and Rigid Motion Systems, 1991 ASME Winter Annual Meeting*, pp.27-37, Atlanta GA. December 1991.

[27] R.Lozano and B.Brogliato, "Adaptive control of robot manipulators with flexible joints," *IEEE Transactions on Automatic Control*, Vol.37, No.2, pp.174-181, 1992.

[28] G.Leitmann, "Guaranteed asymptotic stability for some linear systems with bounded uncertainties," *J. Dynamic Systems, Measurement and Control*, Vol.101, pp.212-216, 1979.

[29] G.Leitmann, "On the efficacy of nonlinear control in uncertain linear systems," *J. Dynamic Systems, Measurement and Control*, Vol.102, 95-102, 1981

[30] K.S.Narendra and A.M.Annaswamy, *Stable Adaptive Systems*, Prentice-Hall, Englewood Cliffs, 1989.

[31] S.Nicosia, P.Tomei, and A.Tornambe, "A nonlinear observor for elastic robots," *IEEE Transactions on Robotics and Automation*, Vol.4, No.1, pp.45-52, 1988.

[32] K.Ogata, *Modern Control Engineering*, Prentice-Hall, Englewood Cliffs, 2nd edition, 1990.

[33] I.R.Petersen and C.V.Hollot, "A Riccati equation approach to the stabilization of uncertain linear systems," *Automatica*, Vol.22, No.4, pp.397-411, 1986.

[34] Z.Qu, "Robust control of a class of nonlinear uncertain systems," *IEEE Transactions on Automatic Control*, Vol.37, No.9, pp.1437-1442, September, 1992.

[35] Z.Qu, "Robust control of nonlinear uncertain systems under generalized matching conditions," *Automatica, The Journal of IFAC*, Vol.29, No.4, July, 1993. (Full paper)

[36] Z.Qu, "Model reference robust control of SISO systems with significant unmodelled dynamics," *American Control Conference*, to appear June 1993. Also submitted to *SIAM Journal of Control and Optimization*, 10/14/92.

[37] Z.Qu, "Global stabilization of nonlinear systems with a class of unmatched uncertainties," *Systems & Control Letter*, Vol.18, No.3, pp.301-307, May, 1992.

[38] Z.Qu, "A new class of robust controllers for nonlinear uncertain systems," *The 31st IEEE Conference on Decision and Control*, pp.743-744, Tucson, Arizona, December, 1992.

[39] Z.Qu, "Asymptotic stability of controlling uncertain dynamical systems," *1992 American Control Conference*, Chicago, IL., pp.592-593, June, 1992. Also in *International Journal of Control*, to appear.

[40] Z.Qu, "Continuous robust control guaranteeing functional performance index for nonlinear uncertain systems," *1993 American Control Conference*, San Francisco, June 1993.

[41] Z.Qu and D.M.Dawson, "Continuous feedback control guaranteeing exponential stability for uncertain dynamical systems," *The 30th IEEE Conference on Decision and Control*, pp. 2036-2638, Brighton, U.K. December 1991.

[42] Z.Qu and D.M.Dawson, "Lyapunov direct design of robust tracking control for classes of cascaded nonlinear uncertain systems without matching conditions," *The 30th IEEE Conference on Decision and Control*, pp. 2521-2526, Brighton, U.K. December 1991.

[43] Z.Qu and D.M.Dawson, "Constructive robust control design for cascaded and individually feedback linearizable nonlinear uncertain systems," in *Control of Systems with Inexact Dynamic Models, 1991 ASME Winter Annual Meeting*, pp.63-71, Atlanta GA. December 1991. Also submitted to *Automatica*, 2/12/92, revised 10/26/92 and 3/17/93.

[44] Z.Qu and J.F.Dorsey, "Robust control by two Lyapunov functions," *International Journal of Control*, Vol.55, No.6, pp.1335-1350, June, 1992.

[45] Z.Qu and J.F.Dorsey, "Robust control of generalized dynamic systems without matching conditions," *Transactions of the ASME, Journal of Dynamic Systems, Measurement, And Control*, Vol.113, No.4, pp.582-589, December, 1991.

[46] Z.Qu, J.F.Dorsey, and D.M.Dawson, "Continuous input-output robust tracking control of SISO continuous time systems with fast time-varying parameters: A model reference approach," *The 31st IEEE Conference on Decision and Control*, pp.2767-2772, Tucson, Arizona, December, 1992.

[47] Z.Qu, J.F.Dorsey, and D.M.Dawson, "Model reference robust control of a class of SISO systems," submitted to *IEEE Trans. Automat. Contr.*, 2/5/92, revised 10/6/92 and 3/29/93. (Regular paper.) Preliminary version in *1992 American Control Conference*, 1182-1186, 1992.

[48] Z.Qu, J.F.Dorsey, X.Zhang, and D.M.Dawson, "Robust control of robots by computed torque law," *Systems & Control Letters*, Vol. 16, No. 1, pp.25-32, 1991.

[49] Z.Qu, D.M.Dawson, and J.F.Dorsey, "Exponentially stable trajectory following of robotic manipulators under a class of adaptive controls," *Automatica, The Journal of IFAC*, Vol.28, No.3, pp.579-586, May 1992.

[50] Z.Qu and J.F.Dorsey, "Robust tracking control of robots by a linear feedback law," *IEEE Transactions on Automatic Control*, Vol. 36, No. 9, pp.1081-1084, September, 1991.

[51] Zhihua Qu, "Globally stable I/O robust control of flexible joint robots," *IEEE International Conference on Robotics and Automation*, Altlanta, GA., May, 1993.

[52] Zhihua Qu, "Model reference robust control of weakly non-minimum phase systems," submitted to *The 32nd IEEE Conference on Decision and Control*, 2/26/93.

[53] W.E.Schmitendorf, "Designing stabilizing controllers for uncertain systems using the Riccati equation methods," *Proceeding ACC*, 502-505, 1987; also in *IEEE Transaction on Automat. Contr.*, Vol. 33, No.4, pp.376-379, 1988

[54] M.W.Spong, "Modelling and control of elastic joint robots," *Journal of Dynamic Systems, Measurement, and Control*, Vol.109, pp.310-319, 1987.

[55] M.W.Spong, "Adaptive control of flexible-joint manipulators," *Systems & Control Letters*, Vol.13, pp.15-21, 1989.

[56] M.W.Spong, "The control of flexible joint robots: A survey," in *New Trends and Applications of Distributed Parameter Control Systems*, Lecture Notes in Pure and Applied Mathematics, G.Chen, E.B.Lee, W.Littman, and L.Markus, Eds., Marcel Dekker Publisher, New York, 1990.

[57] A.V.Solodov, *Linear Automatic Control Systems with Varying Parameters*, New York, NY., American Elsevier, 1966.

[58] L.M.Sweet and M.C.Good, "Redefinition of the robot motion control problem: effects of plant dynamics, drive system constraints, and user requirement," *The 23rd IEEE Conference on Decision and Control*, Las Vegas, NV, 1984.

[59] J.S.Thorp and B.R.Barmish, "On guaranteed stability of uncertain linear systems via linear control," *J. of Optimiz. Theory and Applic.*, Vol.35, 559-579, 1981

[60] P.Tomei, "An observer for flexible joint robots," *IEEE Transactions on Automatic Control*, Vol.35, No.6, pp.739-743, 1990.

[61] V.I.Utkin, *Sliding Modes in Control and Optimization*, Springer-Verlag:Berlin, 1992.

[62] K.Wei, "Quadratic stabilizability of linear systems with structural independent time-varying uncertainties," *IEEE Trans. Automat. Contr.*, Vol.35, pp.268-277, 1990.

Biography

Zhihua QU was born in Shanghai, China in 1963. He received the B.Sc. and M.Sc. degrees in electrical engineering from the Changsha Railway Institute, P.R.China, in 1983 and 1986, respectively. From June 1986 to March 1988, he was an instructor at Changsha Railway Institute. He received the Ph D degree in electrical engineering from the Georgia Institute of Technology in June 1990. Since then, he has been an Assistant Professor of Electrical Engineering at the University of Central Florida. His research interests are in robust control, robotics, adaptive control, power system, and nonlinear system theory.

Design of Robust Structural Controllers for Gun-Turret Systems

VITTAL S. RAO*
DEPARTMENT OF ELECTRICAL ENGINEERING
AND INTELLIGENT SYSTEMS CENTER,
UNIVERSITY OF MISSOURI-ROLLA
ROLLA, MO 65401

MICHAEL S. MATTICE AND
NORMAN P. COLEMAN, JR.
US ARMY ARDEC
SMCAR-FSF-RC, B95N
PICATINNY ARSENAL, NJ 07806

Abstract:

Improvements in robust performance of gun-turret system mounted on helicopters, can significantly enhance the mission capabilities of light attack helicopters. A significant research effort has been directed toward the design and implementation of controllers which can guarantee the stability and performance. Some of the specific gun-turret problems are impulse loads near the first flexible mode of the system, time-varying friction in the recoil slider, lack of barrel tip position sensors, presence of non-linear elements, and lack of proper mathematical models of the gun-turret systems. One of the major sources of fire control error is due to the excitation of several structural modes by gun firing. Designing controllers for such system whose mathematical model is subject to uncertainties is an interesting and challenging problem.

To design active controllers for flexible gun systems, a mathematical representation of the system is needed. We have derived mathematical models of gun-turret systems by analytical methods and model validation is accomplished by using structural identification methods. In order to accomplish simplicity in the controller implementation, we have derived reduced order models by using optimal projection methods.

To account for uncertainties in the structural models and to accomplish good closed loop system performance and sensor noise suppression properties, we have developed robust control design methodologies for gun-turret systems. The reduced order models are utilized in the design of robust controllers. We have utilized a modified linear quadratic Gaussian with loop transfer recovery (LQG/LTR) robust control design methodology for accommodating the limited control force provided by the actuators.

Design of Robust Structural Controllers for Gun-Turret Systems

Vittal S. Rao*
Professor and Director
Department of Electrical Engineering
and Intelligent Systems Center
University of Missouri - Rolla
Rolla, MO 65401

Michael S. Mattice and
Norman P. Coleman, Jr.
US Army ARDEC
SMCAR-FSF-RC, B95N
Picatinny Arsenal, NJ 07806

I. INTRODUCTION

Improvements in robust performance of Gun-Turret System mounted on helicopters, can significantly enhance the mission capabilities of light attack helicopters. Designing a controller for such a system whose mathematical model is subject to uncertainties is an interesting and challenging problem. The uncertainties in the model may arise due to unmodeled dynamics, firing disturbances, helicopter motion, linearization of nonlinear elements, train rate sensor noise etc. A control strategy which can guarantee stability and provide satisfactory performance in the presence of model uncertainties is called a robust controller. Among the various design methods for robust controllers, the linear quadratic Gaussian with loop transfer recovery (LQG/LTR) design procedure [1], has many advantages. This methodology will result in control systems with excellent stability robustness, command following, disturbance rejection and sensor noise suppression properties. A significant research effort has been directed toward the design and implementation of robust controllers for turret-gun system.

One of the important problems in the control of a Gun-Turret system is to approximate a high-order, complex mathematical model of the system with a low-order, simpler model. The resulting reduced order models are useful for designing and implementing robust controllers for a Gun-Turret System. This methodology will provide simplicity of implementation and reduction in hardware requirements.

The Gun-Turret System contains nonlinear elements, such as gear trains, servo valves, hydraulic motors etc. In this system, the firing disturbances excite the structural modes. Integrated Systems Inc. (ISI) has developed a detailed nonlinear model and identified various parameters of the model [2]. A linear quadratic Gaussian with loop transfer recovery (LQG/LTR) controller is designed for the gun system using linearized models. We encountered the convergence/numerical integration problems in the simulation of this controller along with the non-linear plant. It is also noticed that there is a large spread of eigenvalues of the linear model [3]. For the convergence of the control algorithms and their easy implementation, controllers are designed using reduced order models.

Optimal projection theory was developed by Bernstein and Hyland [4] to design low-order fixed compensators for multivariable systems. The optimal projection method was later extended to model reduction [5], parameter robust control [6,7], H_2/H_∞ method for model reduction [8] and various other control problems. The salient feature of the optimal projection theory is that it will provide a common mathematical framework for designing low order controllers with multiple performance criterion.

The optimal projection method methodology has been employed to derive a reduced order model and a lower order controller for the Gun-Turret System. The results are compared with balance-truncation [9], modal method [10] and Routh Approximation methods [11].

Hyland an Bernstein [4] have presented a technique for model reduction by minimizing the steady state error between the outputs of the original system and reduced order mode. A detailed description of this procedure along with a proposed numerical solution algorithm is presented in this report.

In order to accommodate the limited control force of the actuators, we have modified the robust contorl design methodology.

II. BRIEF DESCRIPTION OF THE GUN-TURRET SYSTEM

The gun-turret system (Fig.1) under investigation consists of a medium caliber chain gun mounted to a turret capable of slewing ± 120 degrees in azimuth and +15 to -60 degrees in elevation. The impulse-like disturbance due to firing is sinusoidal in nature and near the natural frequency of the system. In addition, the firing disturbances produce structural deformations which are unobservable at the sensors.

The current gun-turret system is controlled by an analog controller which resides in the turret control box (TCB). The TCB receives the gun reference commands from the fire control computer (FCC). The FCC is responsible for compensating for the helicopters rigid body motion and the addition of the lead angle prediction.

The gun is mounted within a cradle using a brass slide mechanism that allows for recoil movement. Recoil adapters are mounted between the recoiling mass of the gun and the cradle to dampen the recoil force. The cradle and gun assemblies are attached to a fork using two trunnion pins. One trunnion pin has a resolver built into it. this resolver provides the elevation pointing error to the TCB. The elevation axis positioning is accomplished through the use of a servo-valve controlled, double-acting hydraulic cylinder. A pressure transducer measures the pressure differential across the cylinder and provides this to the TCB.

The fork is held in place by the azimuth housing. The azimuth axis positioning is accomplished through the use of a rotary hydraulic motor and a gearbox. A train rate sensor measures the azimuth angular velocity and a resolver provides the pointing error. The azimuth housing is mounted to the helicopter hull.

A detailed model of the turret-gun system was developed by Shah and Kosut [3]. The nonlinear simulation model includes the effects of hydraulic servo-valve nonlinearities, backlash in the drive train and freeplay in the fork, cradle and barrel attachment points [2]. Preliminary testing has shown that besides geometry dependent inertial variations, very little coupling exists between the axes. Hence, independent models were developed for the elevation and azimuth axes. The rest of this report will deal with only the azimuth axis, however, the results can easily be applied to elevation.

III. MODEL REDUCTION TECHNIQUE USING OPTIMAL PROJECTION

A Method

Hyland and Bernstein [5] have presented a technique for model reduction by minimizing the steady state error between the outputs of the original system and reduced order model. The necessary conditions for optimality will result in two modified Lyapunov equations which determine the structure of the reduced order model. These Lyapunov equations are coupled by a projection parameter whose rank is equal to the order of the reduced model. A detailed description of the procedure is presented in this section. The principal references for this section are Hyland and Bernstein [5] and Ngo[12]. A reduced order model for gun-turret system is derived by using optimal projection equations and a critical comparison is made between other reduced order models.
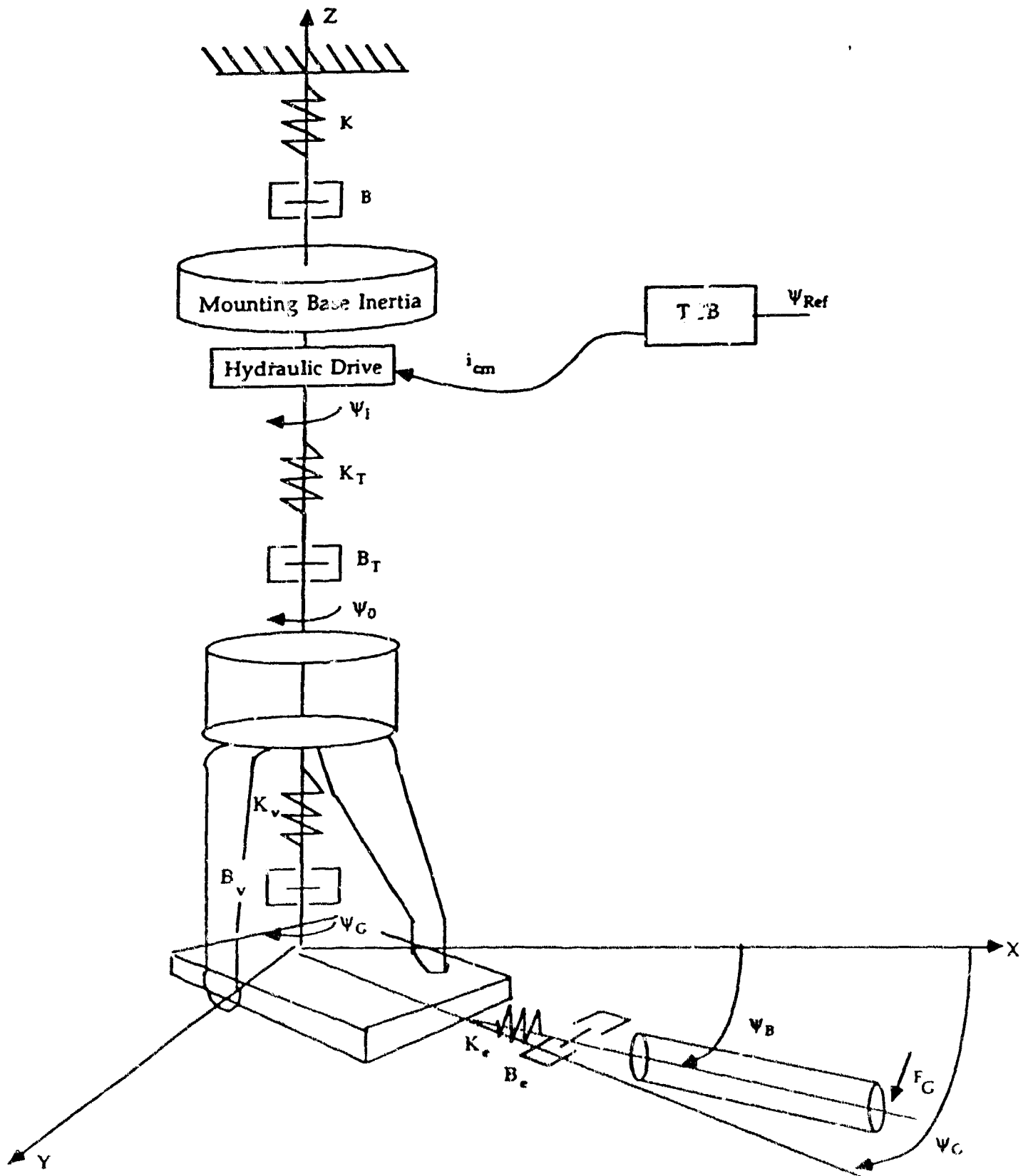
Fig 1. Schematic Diagram of Azimuth Axis System.

Statement of Problem:

For an nth order stable, controllable and observable system

$$\dot{x} = Ax + Bu \tag{1}$$

$$y = Cx \tag{2}$$

where u is white noise with spectral density V>0, find a n_mth order reduced model

$$\dot{x}_m = A_m x_m + B_m u \tag{3}$$

$$y = C_m x_m \tag{4}$$

by minimizing the model reduction error criterion

$$J(A_m, B_m, C_m) \underline{\Delta} \lim_{t \to \infty} E\left[(y - y_m)^T R(y - y_m)\right] \tag{5}$$

where R is symmetric, positive definite matrix.
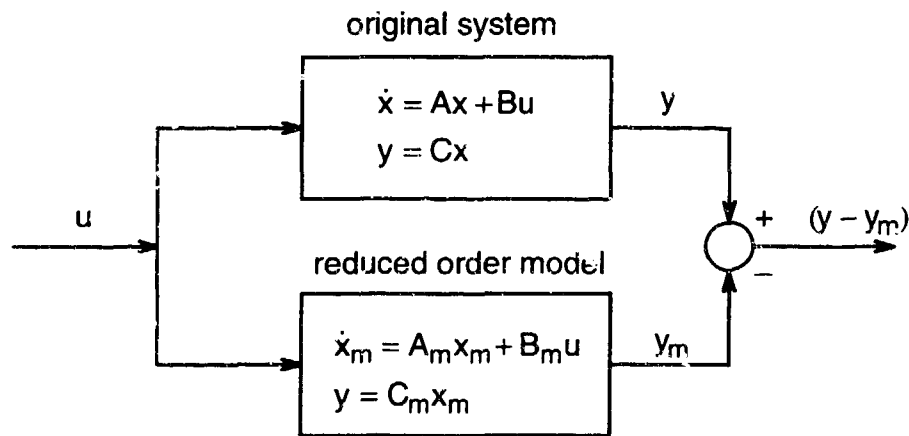
original system

Fig. 2. Representation of Original and Reduced Order Models.

Consider the augmented system

$$\begin{bmatrix} \dot{x} \\ \dot{x}_m \end{bmatrix} = \begin{bmatrix} A & O \\ O & A_m \end{bmatrix} \begin{bmatrix} X \\ X_m \end{bmatrix} + \begin{bmatrix} B \\ B_m \end{bmatrix} u \tag{6}$$

$$\dot{\tilde{x}} = \tilde{A} \quad \tilde{x} + \tilde{B}u$$

The model reduction criterion J can be written as

$$J = \lim_{t \to \infty} tr\left[\bar{Q}(t)\tilde{R}\right] \tag{7}$$

where
$$R = \begin{bmatrix} C^T Rc & -C^T Rc_m \\ -C_m^T RC & C_m^T RC_m \end{bmatrix} \tag{8}$$

and $\qquad \left[\tilde{Q}(t) \right] = E \left[\tilde{x}\,\tilde{x}^T \right]$. $\qquad\qquad$ (9)

If $\tilde{A}$ is stable, then $\tilde{Q}(t)$ has limiting solution, $\lim_{t \to \infty} \hat{Q}(t) = \hat{Q}$ satisfying equation

$$\tilde{A}\tilde{Q} + \tilde{Q}\tilde{A}^T + \tilde{V} = 0 \qquad\qquad (10)$$

where $\qquad \tilde{V} = \tilde{B}\tilde{B}^T = \begin{bmatrix} BVB^T & BVB_m^T \\ B_m VB^T & B_m VB_m^T \end{bmatrix}$ $\qquad\qquad$ (11)

Now the problem is transformed into minimizing

$$J\left(A_m, B_m, C_m\right) = tr\ \tilde{Q}\tilde{R} \qquad\qquad (12)$$

subject to a constraint

$$\tilde{A}\tilde{Q} + \tilde{Q}\tilde{A}^T + \tilde{V} = 0 \qquad\qquad (13)$$

The constrained minimization problem can be solved by introducing the Lagrange multiplier $\left(\tilde{P}\right)$ and modifying the performance index as

$$L = tr\left[\tilde{Q}\tilde{R} + \left(\tilde{A}\tilde{Q} + \tilde{Q}\tilde{A}^T + \tilde{V}\right)\tilde{P}\right] \qquad\qquad (14)$$

The necessary conditions for optimality are:

(i) $\qquad \dfrac{\partial L}{\partial \tilde{Q}} = \tilde{R}^T + \tilde{A}^T \tilde{P} + \tilde{P}\tilde{A} = 0 = \tilde{A}^T \tilde{P} = \tilde{P}\tilde{A} + \tilde{R} = 0$ $\qquad\qquad$ (15)

(ii) $\qquad \dfrac{\partial L}{\partial \tilde{P}} = \tilde{A}\tilde{Q} + \tilde{Q}\tilde{A}^T + \tilde{V} = 0$ $\qquad\qquad$ (16)

(iii) $\qquad \dfrac{\partial L}{\partial A_m} = 2\dfrac{\partial}{\partial A_m}\left(\tilde{A}\tilde{Q}\tilde{P}\right) = 0$ $\qquad\qquad$ (17)

The results of model reduction technique based on optimal projection method are summarized in the following theorem [5]:

Theorem

Suppose (A_m, B_m, C_m) solves the optimal model-reduction problem. Then there exist nonnegative definite matrices $\hat{P}$, $\hat{Q}$ such that, for some factorization of $\hat{Q}\hat{P} = G^T M\Gamma$, the matrices A_m, B_m and C_m are given by

$$A_m = \Gamma A G^T \qquad (18)$$

$$B_m = \Gamma B \qquad (19)$$

$$C_m = C G^T \qquad (20)$$

and such that with $\tau = G^T \Gamma$, the following conditions are satisfied:

$$A\hat{Q} + \hat{Q}A^T + BVB^T - \tau_\perp BVB^T \tau_\perp^T = 0 \qquad (21)$$

$$A^T \hat{P} + \hat{P}A + C^T RC - \tau_\perp^T C^T RC \tau_\perp = 0 \qquad (22)$$

$$rank(\hat{Q}) = rank(\hat{P}) = rank(\hat{Q}\hat{P}) = n_m \qquad (23)$$

where $\qquad \tau_\perp = I_n - \tau$

The minimum model reduction cost is given by

$$J_{min} = tr\left[(Q_1 - \hat{Q})C^T RC\right] \qquad or \qquad (24)$$

$$J_{min} = tr\left[BVB^T(P_1 - \hat{P})\right] \qquad (25)$$

B The Properties of Projection Parameter τ

The projection parameter, τ plays an important role in the model reduction procedure. The properties of projection parameter are discussed below:

(i) In general, τ is an oblique projection and not necessarily an orthogonal projection since it may not be symmetric.

(ii) Projection parameter, τ is an idempotent matrix, since

$$\tau^2 = \tau \qquad (26)$$

(iii) The matrix τ satisfies the following identities:

$$\tau\hat{Q} = \hat{Q} = \hat{Q}\tau^T \qquad (27)$$

$$\hat{P}\tau = \hat{P} = \tau^T\hat{P} \qquad (28)$$

(iv) Eigenvalues and eigenvectors of τ.

The eigenvalues of τ are either 1 or 0.

(v) There exists an invertible matrix $\Phi \in R^{n \times n}$ such that

$$\hat{Q}\hat{P} = \Phi^{-1}\begin{bmatrix} \Lambda & 0 \\ 0 & 0 \end{bmatrix}\Phi \quad , \quad \Lambda \in R^{n_m \times n_m} \quad \text{is a diagonal matrix.} \tag{29}$$

$$\tau = \Phi^{-1}\begin{bmatrix} I_{n_m} & 0 \\ 0 & 0 \end{bmatrix}\Phi \tag{30}$$

C Numerical Solution of Optimal Projection Equations for Model Reduction

In order to find reduced order models, we need to solve a coupled Liapunov type equations. Essentially, two distinct approaches have been developed for solving the optimal projection equations: (1) iterative procedure balancing [9] using or component cost analysis [13] and (2) homotopic continuation method [14]. In this paper iterative procedure is described.

Recall that the objective is to determine $\hat{Q}$, $\hat{P}$ and $\tau_\perp$ such that the following conditions are satisfied:

$$A\hat{Q} + \hat{Q}A^T + BVB^T - \tau_\perp BVB^T \tau_\perp^T = 0 \tag{31}$$

$$A^T\hat{P} + \hat{P}A + C^T RC - \tau_\perp^T C^T RC\tau_\perp = 0 \tag{32}$$

$$rank(\hat{Q}) = rank(\hat{P}) = rank(\hat{Q}\hat{P}) = n_m \tag{33}$$

For the sake of simplicity, it is assumed that $V = R = I_n$.

Ngo [12] has developed a numerical procedure for solving Equations (31) and (32) by utilizing balanced realization of the original system. He has also shown the similarities between optimal projection equations and controllability observability Grammians of balanced realizations. Let the original system be represented by

$$\dot{x} = Ax + Bu \tag{34}$$

$$y = Cx \tag{35}$$

This representation will be transformed into an internally balanced representation with

$$x_b = Tx \tag{36}$$

A procedure for determining similarity transformation, T, is given in the reference [15].
Then internally balanced realization is given by

$$\dot{x}_b = A_b x_b + B_b u \tag{37}$$

$$y = C_b x_b \tag{38}$$

where $\qquad A_b = TAT^{-1}, \quad B_b = TB, \quad C_b = CT^{-1}$ \hfill (39)

The controllability and observability Grammians of internally balanced realization $(\Sigma_c = \Sigma_0 = \Sigma)$ satisfy the following equations:

$$A_b\Sigma + \Sigma A_b^T + B_b B_b^T = 0 \tag{40}$$

$$A_b^T\Sigma + \Sigma A_b + C_b^T C_b = 0 \tag{41}$$

341

Now the optimal projection equations for model reduction can be written as

$$A_b\hat{Q} + \hat{Q}A_b^T + B_bB_b^T - \tau_\perp B_b B_b^T \tau_\perp^T = 0 \tag{42}$$

$$A_b^T\hat{P} + \hat{P}A_b + C_b^T C - \tau_\perp C_b^T C_b \tau_\perp = 0 \tag{43}$$

Equations (40) and (41) can be written as

$$A_b\hat{Q}_0 + \hat{Q}_0 A_b^T + B_b B_b^T - \tau_{\perp 0} B_b B_b^T \tau_{\perp 0}^T + \begin{bmatrix} 0 & A_{12}\Sigma_2 \\ \Sigma_2 A_{12}^T & 0 \end{bmatrix} = 0 \tag{44}$$

$$A_b\hat{P}_0 + \hat{P}_0 A_b + C_b C_b^T - \tau_{\perp 0}^T C_b^T C_b \tau_{\perp 0} + \begin{bmatrix} 0 & A_{21}^T\Sigma_2 \\ \Sigma_2 A_{21} & 0 \end{bmatrix} = 0 \tag{45}$$

The similarity between Equations (44), (45) and (42), (43) gives a procedure for the selection of initial guess for $\hat{Q}$, $\hat{P}$ and $\tau_\perp$ in the numerical solution of optimal projection equations.

Numerical Algorithm

Step 1: Determine the balanced realization (A_b, B_b, C_b) and Σ from the general state variable representation (A, B, C) of the original system.

$$Let \qquad \Sigma = diag\left(\sigma_1, \sigma_2, \ldots \sigma_{n_n}\right) \tag{46}$$

$$with \qquad \sigma_1 \geq \sigma_2 \geq \ldots \geq \sigma_n \tag{47}$$

where σ_i's are Hankel Singular values

Select the order of the reduced model, n_m such that

$$\sigma_{n_m} \gg \sigma_{n_m+1} \tag{48}$$

$$then \qquad \Sigma_1 = diag\left(\sigma_1, \ldots \sigma_{n_m}\right) \tag{49}$$

$$\Sigma_2 = diag\left(\sigma_{n_m+1}, \ldots \sigma_n\right) \tag{50}$$

Step 2: Choose the initial values of $\tau_\perp$ and $\tau_\perp$ as

$$\hat{Q}_0 = \hat{P}_0 = \begin{bmatrix} \Sigma_1 & 0 \\ 0 & 0 \end{bmatrix} \tag{51}$$

then

$$\tau_0 = \left(\hat{Q}_0\hat{P}_0\right)\left(\hat{Q}_0\hat{P}_0\right)^\# = \begin{bmatrix} I_{n_m} & 0 \\ 0 & 0 \end{bmatrix} \tag{52}$$

Step 3:

$$Let \qquad \tau_{\perp i} = I_n - \tau_i \qquad for \ i = 0, 1, \ldots \tag{53}$$

Solve the following equations for $\hat{Q}_{i+1}$ and $\hat{P}_{i+1}$

$$A_b\hat{Q}_{i+1} + \hat{Q}_{i+1}A_b^T + B_bB_b^T - \tau_{\perp i}B_bB_b^T\tau_{\perp i} = 0 \tag{54}$$

$$A_B^T\hat{P}_{i+1} + \hat{P}_{i+1}A_b + C_b^TC_b - \tau_{\perp i}C_b^TC_b\tau_{\perp i} = 0 \tag{55}$$

$$for \quad i = 0,1,2,\ldots$$

Step 4:   For a given value of i, the solutions of (126) and (127), $\hat{Q}_{i+1}$ and $\hat{P}_{i+1}$ may have the rank greater than n_m. One of the requirements of optimal projection is that

$$rank \; \hat{Q} = rank \; \hat{P} = n_m \tag{56}$$

To reduce the rank of $\hat{Q}_{i+1}$ and $\hat{P}_{i+1}$, find the singular value decomposition, such that

$$\hat{Q}_{i+1} = U_{i+1}^q\overline{Q}_{i+1}V_{i+1}^{q^T} \tag{57}$$

$$\hat{P}_{i+1} = U_{i+1}^p\overline{P}_{i+1}V_{i+1}^{p^T} \tag{58}$$

Partition $\hat{Q}_{i+1}$ and $\hat{P}_{i+1}$ as

$$\hat{Q}_{i+1} = \begin{bmatrix} \overline{Q}_{11} & 0 \\ 0 & \overline{Q}_{22} \end{bmatrix} \quad ; \quad \hat{P}_{i+1} = \begin{bmatrix} \overline{P}_{11} & 0 \\ 0 & \overline{P}_{22} \end{bmatrix} \tag{59}$$

The rank of $\hat{Q}_{i+1}$ and $\hat{P}_{i+1}$ is reduced by defining

$$\overline{\overline{Q}}_{i+1} = U_{i+1}^q\overline{\overline{Q}}_{i+1}V_{i+1}^{q^T} \tag{60}$$

$$\overline{\overline{P}}_{i+1} = U_{i+1}^p\overline{\overline{P}}_{i+1}V_{i+1}^{p^T} \tag{61}$$

$$where \quad \overline{\overline{Q}}_{i+1} \underset{\Delta}{=} \begin{bmatrix} \overline{Q}_{11} & 0 \\ 0 & 0 \end{bmatrix} \quad ; \quad \overline{\overline{P}}_{i+1} = \begin{bmatrix} \overline{P}_{11} & 0 \\ 0 & 0 \end{bmatrix} \tag{62}$$

Step 5:   Update the value of the projection parameter

$$\tau_{i+1} = \left(\overline{\overline{Q}}_{i+1}\overline{\overline{P}}_{i+1}\right)\left(\overline{\overline{Q}}_{i+1}\overline{\overline{P}}_{i+1}\right)^{\#} \tag{63}$$

Step 6:   Define the error

$$e_1 = \frac{\left\|\overline{\overline{Q}}_{i+1} - \overline{\hat{Q}}_i\right\|}{\|\Sigma\|} \quad and \quad e_2 = \frac{\left\|\overline{\overline{P}}_{i+1} - \overline{\hat{P}}_i\right\|}{\|\Sigma\|} \tag{64}$$

and e = max (e₁, e₂)
If e is less than a prespecified value go to Step 7, otherwise go to Step 3

Step 7: Decompose $\left(\overline{\widehat{Q}}\,\overline{\widehat{P}}\right)$ as

$$\left(\overline{\widehat{Q}}\,\overline{\widehat{P}}\right) = \Phi^{-1}\begin{bmatrix} \Lambda & 0 \\ 0 & 0 \end{bmatrix}\Phi \qquad (65)$$

Then $\qquad \tau = \Phi^{-1}\begin{bmatrix} I_{n_m} & 0 \\ 0 & 0 \end{bmatrix}\Phi \qquad (66)$

$$\Gamma = \begin{bmatrix} I_{n_m} & 0 \end{bmatrix}\Phi \quad and \quad G = \begin{bmatrix} I_{n_m} & 0 \end{bmatrix}\Phi^{-T} \qquad (67)$$

The reduced order model matrices are given by

$$A_m = \Gamma A_b G^T \qquad (68)$$

$$B_m = \Gamma B_b \quad ...(69)$$

$$C_m = C_b G^T \qquad (70)$$

Ngo[12] has developed a program code in Matrixx to solve the optimal projection equations.

IV. DERIVATION OF REDUCED ORDER MODELS FOR GUN TERRET SYSTEM

A 12th order linear state variable model of the Gun-Turret system is derived from a nonlinear representation by using analyzing system features of Matrixx Software. The input and output variables are azimuth current and train rate respectively. The reduced order models are derived by using balance-truncation, optimal projection methods. For the sake of comparison purposes the eigenvalues and zeros of original system and reduced order models are given in Table 1 and Table 2 respectively. From Table 2 it can be noticed that the non-minimum phase zeros are introduced in the reduced order models.

Table 1. Comparison of EigenvalueTs

Original System		Balance-Truncation		Optimal Projection	
-1.7134D-03	+0.0000D+00j	-1.7134D-02	+.0000D+00j	-1.7134D-02	+0.0000D+00j
-5.3756D+00	+5.2045D+01j	-5.3828D+00	+5.2046D+01j	-5.3828D+00	+5.2046D+01j
-5.3756D+00	-5.2045D+01j	-5.3828D+00	-5.2046D+01j	-5.3828D+00	-5.2046D+01j
-2.0265D+01	+1.3794D+02j	-2.0733D+01	+1.3771D+02j	-2.0737D+01	+1.3770D+02j
-2.0265D+01	-1.3794D+02j	-2.0733D+01	+1.3771D+02j	-2.0737D+01	-1.3770D+02j
-1.9819D+01	+2.9484D+02j	-1.9985D+01	+2.9457D+02j	-1.9986D+01	+2.9456D+02j
-1.9819D+01	-2.9484D+02j	-1.9985D+01	-2.9457D+02j	-1.9986D+01	-2.9456D+02j
-9.4526D+02	+0.0000D+00j				
-1.5732D+03	+4.5507D+03j				
-1.5732D+03	-4.5507D+03j				
-1.2223D+02	+6.3979D+03j				
-1.2223D+02	-6.3979D+03j				

Table 2. Comparison of Transmission Zeros

Original System		Balance-Truncation		Optimal Projection	
-1.6245D+01	+1.7280D+02j	-6.5481D+02	+8.7498D+02j	-6.5544D+02	+8.7524D+02j
-1.6245D+01	-1.7280D+02j	-6.5481D+02	-8.7498D+02j	-6.5544D+02	-8.7524D+02j
-3.3961D+00	+8.2848D+01j	-1.6459D+01	+1.7352D+02j	-1.6464D+01	+1.7352D+02j
-3.3961D+00	-8.2848D+01j	-1.6459D+01	-1.7352D+02j	-1.6464D+01	-1.7352D+02j
		-3.3051D+01	+8.2825D+01j	-3.3052D+01	+8.2825D+01j
		-3.3051D+01	-8.2825D+01j	-3.3052D+01	-8.2825D+01j

V.   DESIGN OF ROBUST CONTROLLERS

Among the various mehtods available for design of robust controllers, the linear quadratic Gaussian with loop transfer recover (LQG/LTR) design procedure has many advantages. This methodology seeks to define a compensator so that the stability robustness and performance specifications are met to the extent possible. Initially we have designed a robust controller without restricting the control effort of the actuators. Since the control effort produced by the actuators do not meet the LQG/LTR controller needs, we have designed a modified LQG/LTR controller, which speeds up the loop transfer recover process. The quickening of the loop transfer recovery process can be shown using an expression, $E_0(s)$, defined as the error between the desired loop shape and the actual loop shape at the output of the plant.

$E_0(s)$ for nominal LQG/LTR structure is given by

$$E_o(s) = \left[I + C\Phi K_f\right]\left[I + N(s)\right]^{-1} N(s) \tag{71}$$

where $\qquad N(s) = C(sI - A + BK_c)^{-1} K_f$ $\tag{72}$

The error expression $E_0(s)$ for modified structure is

$$E_o(s) = N(s) = C\left(sI - A + BK_c\right)^{-1} K_f \tag{73}$$

Note that perfect recover is obtained when $E_0(s)=0$. Using this modified structure, we have designed robust controllers for full and reduced order systems. The plant output controller effort needed in each case is shown in figures (3 and 4).

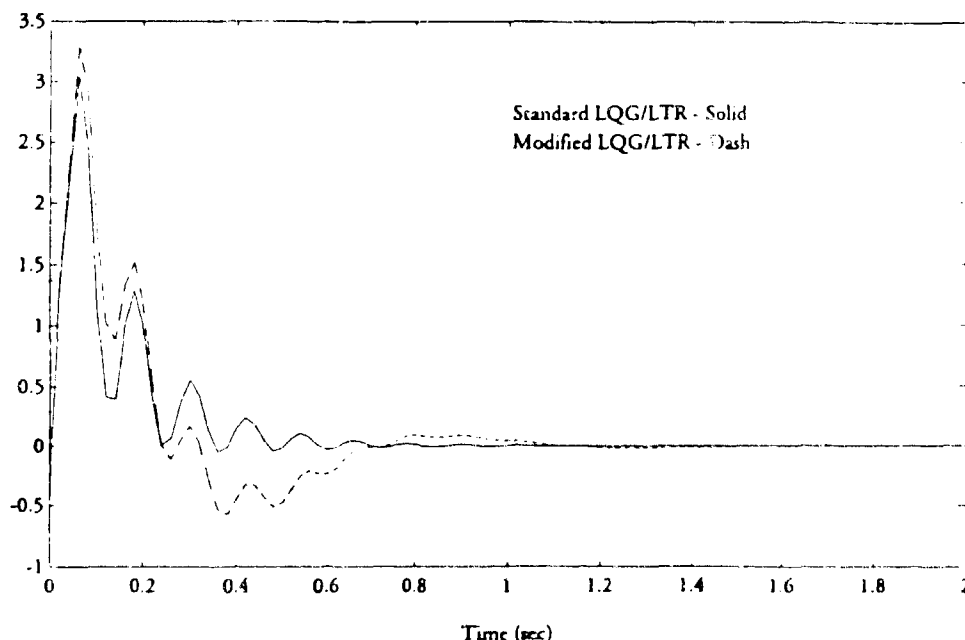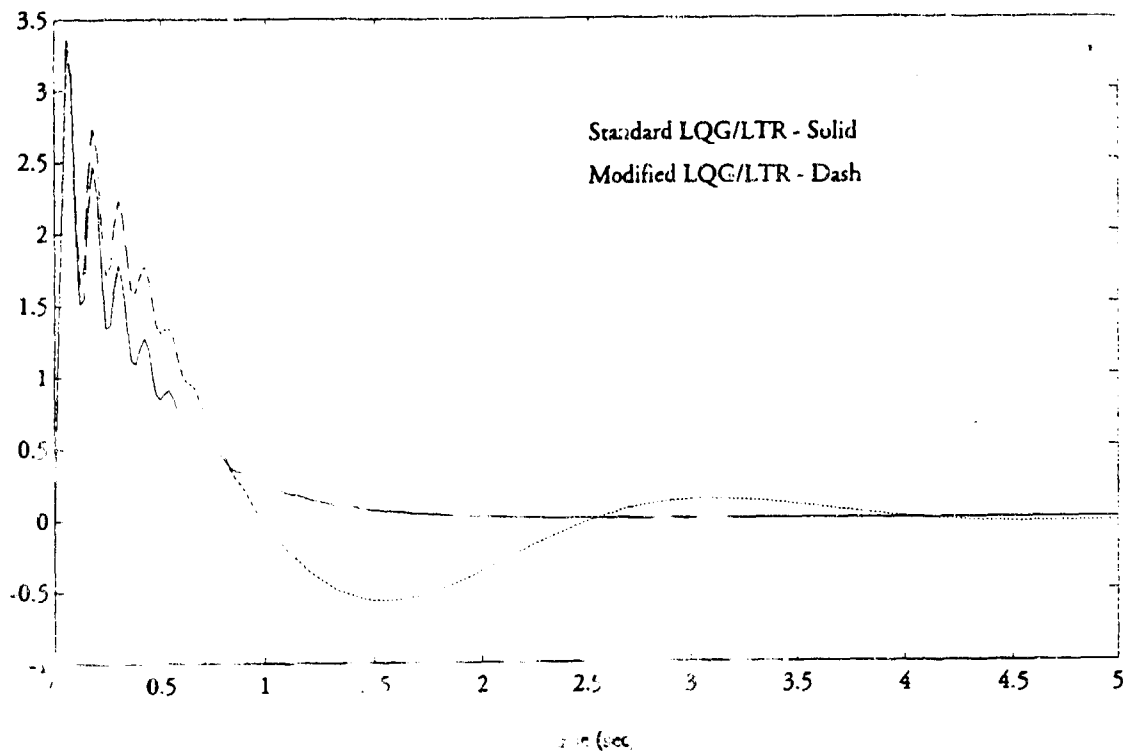Figure 3a.   Plant Output of Original System

Standard LQG/LTR - Solid
Modified LQG/LTR - Dash

Figure 3b.   Plant Output of Reduced Order Models

Standard LQG/LTR - Solid
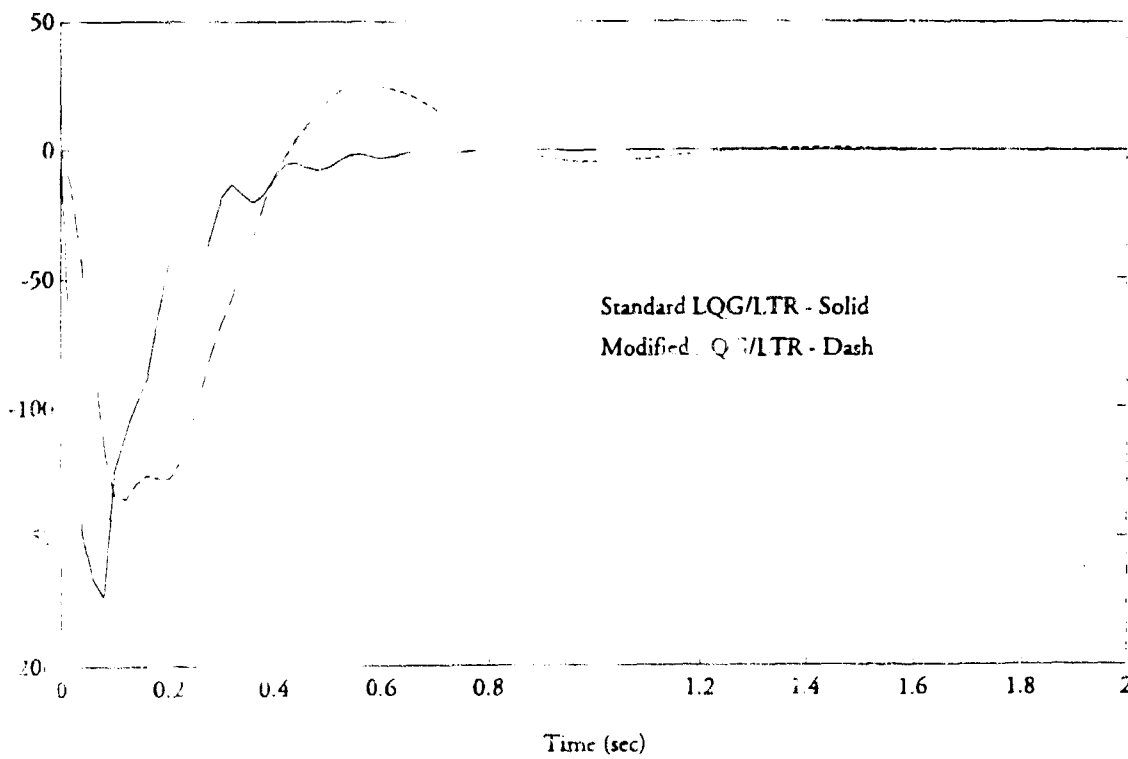Modified LQG/LTR - Dash

Time (sec)

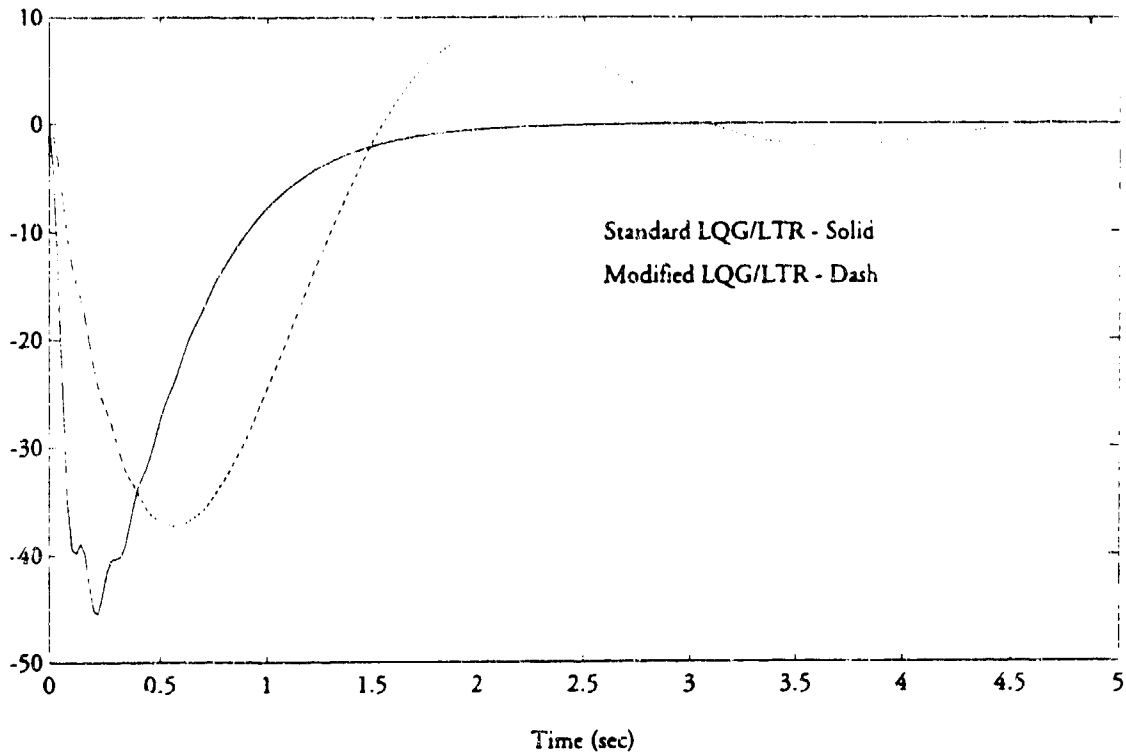Figure 4a.   Controller Effort of Original System

346

Figure 4b. Controller Effort of Reduced Order Model

VI. CONCLUSIONS

The optimal projection and balance-truncate methodologies have been employed in the derivation of reduced order models for the gun-turret system. In general, the optimal projection theory provides a common mathematical framework for designing low order controllers with multiple performance criterion. A critical comparison of the reduced order models reveal that the results of optimal projection reduced order models are similar to balance-truncate models. We have developed a numerical algorithm for solving the optimal projection equations.

The robust controllers were designed for the gun-turret system by using both original and reduced order models. The reduced order models have introduced nonminimal phase zeros in the models. The presence of nonminimal phase zeros introduced complexities in the design of controllers. In order to minimize the control effort needed, we have developed a modified LQG/LTR algorithm for designing robust controllers. A comparison of controller effort has been indicated for full order and reduced order controllers. We intend to implement these controllers on test beds at ARDEC.

VII. REFERENCES

[1]   S. Vittal Rao. M.S. Mattice and N.P. Coleman Jr., "Design of Reduced Order LQG/LTR Controllers for Turret-Gun System," Proceedings of American Control Conference, Pittsburgh, pp 312-315, June 1989.

[2]   S. Shah, "Gun/Turret Adaptive Controller for Integrated Air-to-Air Weapon Systems," Report No. 127, Integrated Systems Inc., July 1988.

[3] S. Shah and R.L. Kosut, "Control of Articulated Structures on Maneuvering Platforms" Proceedings of American Control Conference, pp 33-36, May 1990.

[4] D. S. Bernstein and D.C. Hyland, "Optimal Projection Approach to Robust Fixed-Structure Control Design," AIAA Progress in Astronautics and Aeronautics 'Mechanics and Control of Large Flexible Structures' Edited by J.L. Junkins, Vol. 129 pp 237-293, 1990.

[5] D.C. Hyland and D.S. Bernstein, "The Optimal Projection Equations for Model Reduction and the Relationships Among the Methods of Wilson, Skelton and Moore," IEEE Trans. on Automatic Control, Vol. AC-30, No. 12, Dec. 1985, pp 1201-1211.

[6] D.S. Bernstein and D.C. Hyland, "The Optimal Projection/Maximum Entropy Approach to Designing Low-Order, Robust Controllers for Flexible Structures," Proceedings of the IEEE Conference on Decision and Control, pp. 745-752, 1985.

[7] N. Madiwale, W.M. Haddad and D.S. Bernstein, "Robust H_∞ Control Design for Systems with Structured Parameter Uncertainty," Proceedings of the IEEE Conference on Decision and Control Austin, Texas, pp. 965-972, 1988.

[8] W.M. Haddad and D.S. Bernstein, "Combined L_2/H_∞ Model Reduction," Int. J. of Control, Vol. 49, No. 5, pp 1523-1435, 1989.

[9] B.C. Moore, "Principal Component Analysis in Linear Systems: Controllability, Observability and Model Reduction," IEEE Trans. on Automatic Control, Vol, AC-26, 1981, pp 17.32.

[10] D. Bonvin and D.A. Mellichamp, "A Unified Derivation and Critical Review of Modal Approaches to Model Reduction," Int. J. Control, Vol. 35, No. 5, pp 829-848, 1982.

[11] J.V. Ramarkrishan, S. Vittal Rao and L.R. Koval, "Multivariable Routh-Approximant Model Reduction Method in the Time Domain," Optimal Control Applications & Methods, Vol. 11, pp 233-247, Sept 1990.

[12] K.T. Ngo, "Design of Reduced Order Robust Controller Using Optimal Projects on Method," M.S. Thesis, University of Missouri-Rolla.

[13] R.E. Skelton, "Cost Decomposition of Linear Systems with Application to Model Reduction," Int. J. of Control, Vol. 32, No. 6, pp 1031-1055, 1980.

[14] S. Richter and E.G. Collins, Jr., "A Homotopy Algorithm for Reduced Order Controller Design Using the Optimal Projection Equations," Proceedings of the IEEE Conference on Decision and Control, Tampa, pp 506-511, Dec. 1989.

[15] L. Pernebo and L.M. Silverman, "Model Reduction via Balanced State Space Representations," IEEE Transactions on Automatic Control, Vol. AC-27, pp. 382-387, 1982.

SENSING AND ACTUATION ARRAYS FOR STRUCTURAL CONTROL

PROF. DOUGLAS K. LINDNER
BRADLEY DEPARTMENT OF ELECTRICAL ENGINEERING
VIRGINIA TECH
BLACKSBURG, VA 24061
(703) 231-4580
FAX: (703) 231-3362
EMAIL: LINDNER@VTVM1.CC.VT.EDU

Abstract

In this paper we consider vibration suppression in flexible structures using active control. The design of active control systems for structures has been a topic of investigation for more than a decade. One of the common threads linking previous research in this area is the assumption that the control system will have relatively few sensors and actuators. This assumption was necessary, considering the actuation and sensing technology available in the past. The last decade, however, has seen the development of the next generation of actuators and sensors. This instrumentation consists of low power, miniaturized devices that can be incorporated directly into the material of the structure. Coupled with advancements in digital electronics, we can imagine dense arrays of sensors and actuators for structural control. In this paper we investigate the possible impact these arrays would have on control system design. In particular we note that these arrays provide a direct spatial measurement of the structure. We present a framework that takes into account this novel capability of the actuator/sensor arrays. Application to the active suppression of acoustic radiation is discussed.

Biography:

Douglas K. Lindner is presently an Associate Professor in the Bradley Department of Electrical Engineering at Virginia Tech.

From June to December 1992 we was on sabbatical leave as a Navy/ASEE Faculty Fellow with the Mechanics of Material Branch at the Naval Research Laboratory in Washington, DC. He has also spent the summers of 1985 and 1986 with the Spacecraft control branch at NASA Langley as a NASA/ASEE Faculty Fellow. His current research interests are in structural control using embedded sensors and actuators.

Douglas K. Lindner received his Ph.D from the University of Illinois at Urbana-Champaign, specializing in control theory.

SENSING AND ACTUATION ARRAYS FOR STRUCTURAL CONTROL

PROF. DOUGLAS K. LINDNER
BRADLEY DEPARTMENT OF ELECTRICAL ENGINEERING
VIRGINIA TECH
BLACKSBURG, VA 24061

1. INTRODUCTION

The suppression of vibration in flexible structures using active feedback control has received a great deal of attention in the last decade. Current research has focused on the instrumentation required to implement these control laws, particularly, through the use of embedded sensors and/or actuators - so-called Smart Structures. In this paper we discuss the impact this new generation of actuators and sensors will have on the design and implementation of control algorithms for the suppression of acoustic radiation from flexible structures.

Recently there has emerged a new class of sensors for structures which respond over a significant gauge length; we call these sensors distributed-effect sensors. The most well known sensor of this type is piezoelectric laminate PVDF film. Another sensors in this class are modal domain optical fiber sensors [1]. In their simplest configuration, the use of modal domain optical fiber sensors in a control loop for vibration suppression of a cantilevered beam has recently been demonstrated [2].

In some cases, distributed-effect sensors have a unique capability in that they can be fabricated to locally alter their sensitivity to the measurand. Because these sensors have a scalar output, we see that a multidimensional signal in space and time has been reduced to a scalar function of time. Thus, these sensors act as a spatial filter. This spatial filter is defined by the spatial variation of the sensitivity of the sensor; this function of space is called the weighting function. By various choices of the weighting function, these sensors can be configured to measure a wide variety of structural parameters which can not be measured directly with point sensors.

Spatial filtering has been demonstrated using PVDF film. The distributed actuation can be described in terms of boundary forces and moments [3], in terms of modes [4] or wave number filters [5]. To achieve this weighting function, PVDF film is cut into the required shape. Several ways in which modal domain optical fiber sensors may be configured as spatial filters have been suggested [6,7].

In this paper we investigate the use of spatial sensors and actuators for control of flexible structures. These actuators and sensors inherently include spatial information about the structure. Therefore, it is convenient to place this discussion within the framework of structural acoustics. When a vibrating structure immersed in a fluid the structure will radiate acoustic power. Only part of the vibrations contribute to the far field acoustic power. Therefore, the control system should sense the shape that is radiating acoustic power and suppress this shape while leaving the rest of the vibrations alone. Spatial filters are ideally suited for this application [8-10]. In this

paper we use this application as a motivation for the investigation into spatial sensing and actuation.

In addition to the development of distributed-effect sensors. the last decade has seen the development of miniaturized actuators and sensors. Combined with recent advances in electronics including miniaturized power converters [11], we can suppose that these small sensors and actuators could be configured as actuator or sensor array. When these arrays become dense (as measured with respect to the structural dynamics), these arrays are an approximation to a distributed actuator or sensor. If these arrays are linked using a digital communication network, then output of the sensors, say, can be combined into weighted sum. These weightings on the sensor outputs form the weighting function for a spatial filter. We assume a similar configuration for the actuator array. In this paper we assume that these actuator and sensor arrays can be approximated by distributed actuators and spatial filters for sensors.

The focus of this paper is the selection of the actuator and sensors for improvement of the control system performance. For simplicity, we assume that the controller is a LMS algorithm. This type of controller is widely used for the suppression of acoustic radiation.

In Section 2 we discuss the models of the structure and instrumentation. Section 3 we briefly review the framework for determining the structural shape that radiate. Section 4 describes the model of the control system; the LMS controller. Section 5 explains the relationship between the actuator and sensor weighting functions and the performance of the control system. Section 6 has the conclusions.

2. STRUCTURAL MODEL AND INSTRUMENTATION

Here we consider a lightly fluid loaded, baffled, uniform clamped-clamped beam acted on by a point force disturbance as shown in Figure 2.1.
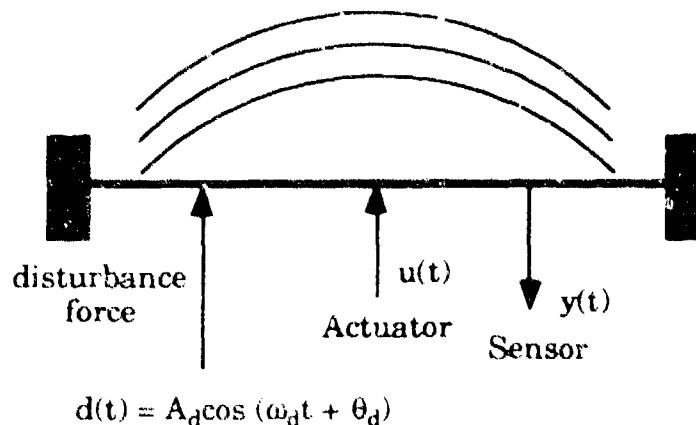

$$d(t) = A_d \cos (\omega_d t + \theta_d)$$

Figure 2.1. Instrumented Clamped-Clamped Beam.

This beam is modeled with an Euler-Bernoulli model

$$EI\frac{\partial^4 w(z,t)}{\partial z^4} + \rho_A \frac{\partial^2 w(z,t)}{\partial z^2} = \delta(z-z_u)u(t) + \delta(z-z_d)d(t),$$

$$w(0,t) = w(L,t) = 0, \frac{\partial w(0,t)}{\partial z} = \frac{\partial w(L,t)}{\partial z} = 0,$$ (2.1)

where $t \geq 0$ is the time variable, z, $0 \leq z \leq L$ is the space variable, and $w(z,t)$ is the displacement of the beam. We assume that a disturbance force enters into the structure as a point force at z_d. The beam is also instrumented with a point force actuator, $u(t)$, located at z_u. The coordinate system is shown in Figure 2.2.
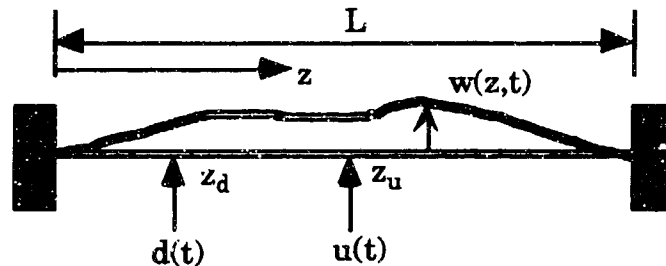

Figure 2.2. Coordinate system of the Instrumented
Clamped-Clamped Beam.

The parameters for this beam are given in Table 2.1.

TABLE 2.1. BEAM PARAMETERS

Young's Modulus	E	2.04×10^{11} Pa
Mass Density	ρ_A	0.491 kg/m
Length	L_b	1.0 m
Width	h_b	0.125 m
Thickness	t_b	0.5 mm

The displacement of the beam can be approximated by a finite number (n_r) of the modes, $\psi_k(z)$, and the modal amplitudes, $\eta_k(t)$, as

$$w(z,t) = \sum_{k=1}^{n_r} \psi_k(z)\eta_k(t)$$ (2.2)

where $w(z,t)$ is the displacement, $\psi_k(z)$ is the kth mode shape and $\eta_k(t)$ is the kth modal amplitude. This approximation leads to a reduced order model

$$\ddot{\eta}(t) + D\dot{\eta}(t) + \Omega^2\eta(t) = H_c u(t) + H_d d(t),$$

$$y(t) = C\eta(t)$$ (2.3)

where

$$\eta(t) = \left[\eta_1(t), \quad \eta_2(t), \quad \cdots, \quad \eta_{n_r}(t) \right]^T. \tag{2.4}$$

In (2.3)

$$H_d = \left[h_{d1}, \quad \cdots, \quad h_{dn_r} \right]^T \tag{2.5}$$

is the vector of modal influence coefficients for the disturbance force . The vector of modal influences for the control input, H_c, is determined similarly. The natural frequencies are contained in

$$\Omega^2 = \text{diag}\left\{ \omega_k^2 \right\}, \quad D = \text{diag}\left\{ 2\xi_k \omega_k \right\}, \quad i = 1, \cdots, n_r, \tag{2.6}$$

and 1% proportional damping was added to the model (2.3) via the damping matrix D in (2.3). The second equation in (2.3) models the sensors on the beam.

In this paper we consider sinusoidal disturbance forces of the form

$$d(t) = A_d \cos(\omega_d t + \theta_d) \tag{2.7}$$

where θ_d is a random variable uniformly distributed between $-\pi$ and π. The signal $d(t)$ is then a wide sense stationary harmonic process. To remove an arbitrary scale constant from the problem, we set $A_d = 0$. After the system has reached steady state, all of the modal amplitudes will be harmonic. These modal amplitudes can be computed from the transfer function

$$\eta(s) = \left[s^2 I + Ds + \Omega^2 \right]^{-1} H_d d(s) = Q(s) H_d d(s) \tag{2.8}$$

where

$$Q(s) = \text{diag}(Q_i(s)) = \text{diag}\left((s^2 + 2\xi_i \omega_i s + \omega_i^2)^{-1} \right). \tag{2.9}$$

The modal amplitude of the kth mode as computed from (2.8) is

$$\eta_k(t) = \eta_{dk} \cos(\omega_d t + \theta_{dk} + \theta_d) \tag{2.10}$$

where

$$\eta_{dk} = |Q_k(j\omega_d)||h_{dk}| = q_k |h_{dk}|, \quad \text{and,}$$

$$\theta_{dk} = \begin{cases} \angle Q_k(j\omega_d) & \text{if } h_{dk} > 0 \\ \angle Q_k(j\omega_d) + \pi & \text{if } h_{dk} < 0 \end{cases} \tag{2.11}$$

LINDNER

Here h_{dk} is the kth element of the vector of modal influence coefficients H_d and

$$Q_k(s)\Big|_{s=j\omega_d} = \left[\frac{1}{s^2 + 2\xi_k\omega_k s + \omega_k^2}\right]_{s=j\omega_d} = |Q_k(j\omega_d)|\exp(\angle Q_k(j\omega_d)). \qquad (2.12)$$

When the beam has reached steady state, the displacements of the beam are given by

$$w_d(z,t) = \sum_{k=1}^{n_r} \psi_k(z)\eta_{dk}\cos(\omega_d t + \theta_d + \theta_{dk}). \qquad (2.13)$$

In this paper we are concerned with sensors that respond over a significant gauge length. Let the spatial variable, z, belong to the domain Γ_b. Let $\Gamma_s \subseteq \Gamma_b$ such that Γ_s is an open set that contains more than one element of Γ_b.

Definition: A signal, m(z,t), is called a <u>distributed signal</u> if it depends on time, t, and the spatial variable, z, which belongs to Γ_s, $z \in \Gamma_s$.

Here we are concerned with sensors that can be modeled as

$$y(t) = \int_{\Gamma_s} g(z)m(z,t)dz. \qquad (2.14)$$

Definition: If the function g(z) is given by $g(z) = \delta(z - z_0)$, we say that the sensor is a <u>point</u> sensor. If g(z) is not an impulse function, then we say the sensor is a <u>distributed-effect</u> sensor.

In some cases a distributed-effect sensor can be physically altered in a controlled way such that the function g(z) can be selected independently of the sensor. In that case, (2.14) can be interpreted as filtering the distributed signal m(z,t) according to g(z) to produce the scalar signal y(t).

Definition: If the function g(z) in (2.14) can be chosen independently of the sensor, then g(z) is called a <u>weighting function</u>.

Definition: Any device with an input of the distributed signal m(z,t) and an output of the scalar signal y(t) which can be modeled as in (2.14) where g(z) is a weighting function is called a <u>spatial filter</u>.

For simplicity, let the domain of the distributed-effect sensor, Γ_s, be defined on the entire spatial domain of the structure, $\Gamma_b = \{z \mid 0 \le z \le L\}$. We assume that the distributed signal to be measured is the strain at the surface of the beam. This strain can be expressed as

$$\varepsilon(z,t) = h_b \sum_{j=1}^{\infty} \psi_{sj}''(z)\eta_j(t) \tag{2.15}$$

where h_b is the distance from the neutral axis. Let the weighting function of the distributed-effect sensor be

$$g(z) = \sum_{k=1}^{n_r} g_k \psi_k''(z). \tag{2.16}$$

Then the sensor output is given by

$$y(t) = \int_0^L g(z)\varepsilon(z,t)dz = h_b \int_0^L \left[\sum_{k=1}^{n_r} g_k \psi_k''(z) \right]\left[\sum_{k=1}^{n_r} \psi_k''(z)\eta_k(t) \right] dz$$

$$= \sum_{k=1}^{n_r} c_k \eta_k(t) = C\eta(t). \tag{2.17}$$

So we see that choosing the weights of the weighting function is the same as specifying the output matrix for the beam model.

3. ACOUSTIC RADIATED POWER

In this section we review the framework for relating the vibrations in the beam to the far field radiated acoustic power [12-13]. When a structure is excited by the disturbance signal, $d(t)$, in (2.7) the velocity of each point on the structure is given by

$$v_d(z,t) = \sum_{k=1}^{n_r} \psi_k(z)v_{dk} \cos(\omega_d t + \theta_d + \theta_{dk}). \tag{3.1}$$

Certain combinations of these vibrational modes in (3.1) generate far field pressure waves in the surrounding fluid medium. The total radiated power from the beam can be determined as follows. Define the vector

$$V_d = \begin{bmatrix} v_1 \cos\theta_{d1} \\ \vdots \\ v_{n_r} \cos\theta_{dn_r} \end{bmatrix} \tag{3.2}$$

where the components of V_d are defined in (3.2). Then the expected value of the total far field radiated power is

$$\Pi = V_d^T M(\omega_d) V_d. \tag{3.3}$$

Remark: From this analysis we see that for sinusoidal disturbances the far field radiated acoustic power is determined by the vector V_d in (3.2). The vector V_d contains information about the relative phase relationship between the modes in the numbers $\cos(\theta_{dk})$.

Next we examine the structure of the quadratic form (3.3). The matrix $M(\omega_d)$ is symmetric and positive definite so that its singular value decomposition is given by

$$M(\omega_d) = S \Sigma S^T \tag{3.4}$$

where

$$S = \begin{bmatrix} s_1 & s_2 & \cdots & s_N \end{bmatrix}, \quad \text{and} \quad \Sigma = \begin{bmatrix} \sigma_1 & & \\ & \ddots & \\ & & \sigma_n \end{bmatrix}, \quad \sigma_1 \geq \sigma_2 \geq \cdots \geq \sigma_n > 0. \tag{3.5}$$

In (3.5) all of the vectors, s_i, are orthonormal.

The decomposition of the matrix $M(\omega_d)$ in (3.4) lends insight into which structural modes contribute to the far field acoustic power. For a given vector of modal velocity amplitudes, V_{d0}, the total radiated power is given by

$$\Pi = V_{d0}^T M(\omega_d) V_{d0} = V_{d0}^T S \Sigma S^T V_{d0} = \sum_{i=1}^N \left(V_{d0}^T s_i \right)^2 \sigma_i. \tag{3.6}$$

From (3.6) we see that the contributions of the various velocity vectors to the far field acoustic power can be decomposed into principle directions, s_i. These directions are rank ordered according to the attached singular value, σ_i. The maximum power that can be radiated per unit excitation is given by $V_{d0} = s_1$, (because of the orthonormality of the vectors, s_i) and the minimum is given by $V_{d0} = s_N$.

Example. Suppose that the beam described in Section 2.1 is excited by a sinusoidal disturbance with frequency $\omega_d = 95.4$ rad/sec. For this excitation, the matrix $M(\omega_d)$ in (3.4) is

$$M(95.4) = \begin{bmatrix} 5.49 & 0 & 2.4 \\ 0 & 0.007 & 0 \\ 2.4 & 0 & 1.05 \end{bmatrix} \times 10^{-2}. \tag{3.7}$$

This matrix has singular values

$$\Sigma = \text{diag}\begin{bmatrix} 0.0654 & 7.4 \times 10^{-5} & 2.7 \times 10^{-8} \end{bmatrix} \tag{3.8}$$

with corresponding singular vectors

$$\begin{bmatrix} 0.916 \\ 0 \\ 0.401 \end{bmatrix}, \begin{bmatrix} 0 \\ 1 \\ 0 \end{bmatrix}, \begin{bmatrix} 0.401 \\ 0 \\ -0.916 \end{bmatrix}. \tag{3.9}$$

Suppose that the beam is driven with a sinusoidal source such that

$$v_{d\,max}(z, t) = \psi_1(z)(0.916)\cos(95.4t) + \psi_3(z)(0.401)\cos(95.4t). \tag{3.10}$$

For this excitation frequency, the acoustic power radiated by the structure is

$$\Pi = \sigma_1 = 0.0654. \tag{3.11}$$

The spatial distribution of the peak amplitude of the signal in (3.10) is shown in Figure 3.1.
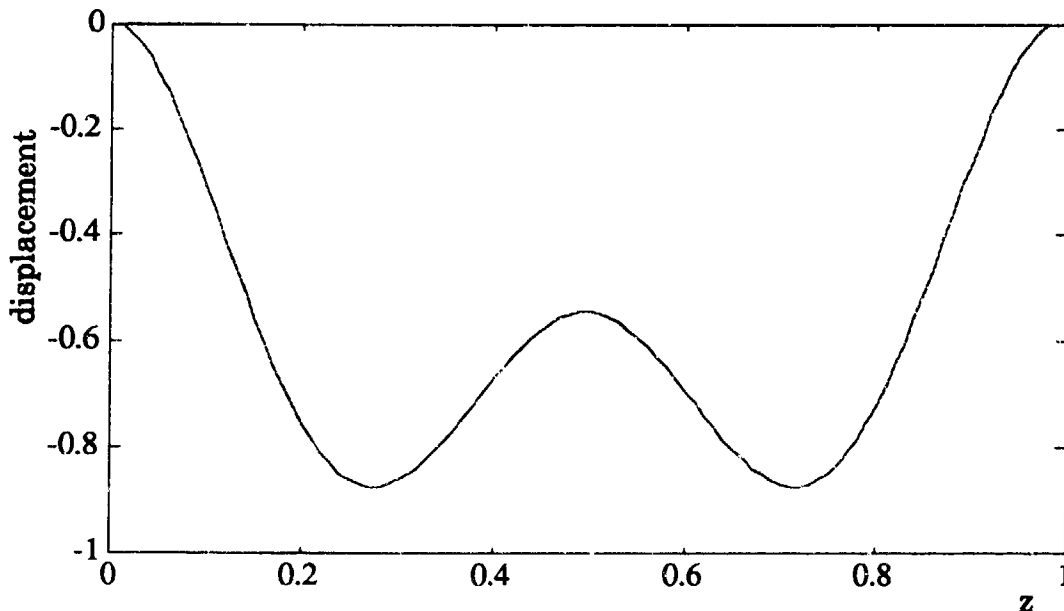

Figure 3.1. Maximun Radiator.

To compute the total radiated acoustic power, the velocity profile is required. This velocity profile can be calculated from the vector of modal displacements by scaling η_d by ω_d. The expression for the total radiated power becomes

$$\Pi = (\omega_d^2)\eta_d^T M(\omega_d)\eta_d. \tag{3.12}$$

4. THE LMS CONTROL ALGORITHM

For a beam driven by a sinusoidal disturbance at a known frequency, the LMS algorithm has been proposed as a controller for the suppression of acoustic radiation [14]. The LMS controller is shown schematically in Figure 4.1 for the beam.
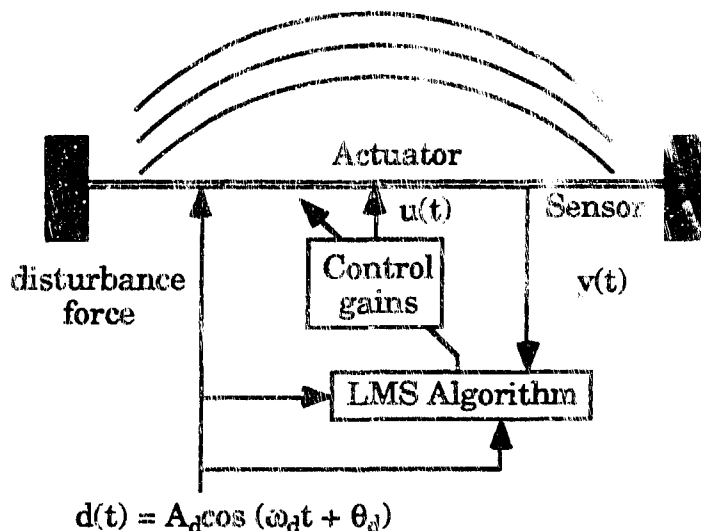

$$d(t) = A_d \cos(\omega_d t + \theta_d)$$

Figure 4.1. The LMS Controller.

The LMS algorithm can be thought of as containing a transient response and a steady state sinusoidal response. During the transient the controller locks on to the phase of the disturbance signal. Then in steady state operation the controller works to zero the sensor output. It is with the steady state operation that we are concerned.

Given the steady state disturbance

$$d(t) = \cos(\omega_d t + \theta_d) \tag{4.1}$$

the output signal at the sensor is

$$y_{ds}(t) = A_{ds} \cos(\omega_d t + \theta_{ds}). \tag{4.2}$$

The LMS controller assumes that the control force is of the form

$$u(t) = A_c \cos(\omega_d t + \theta_c). \tag{4.3}$$

We call A_c the control gain and θ_c the control phase. The controller selects the parameters A_c and θ_c based on the sensor output. If the disturbance force is not present, the response of the beam to the control force (4.3) at the output of the sensor is

$$y_{cs}(t) = A_{cs} \cos(\omega_d t + \theta_{cs}). \tag{4.4}$$

When both input forces are present, the sensor output is

$$y(t) = A_{ds} \cos(\omega_d t + \theta_{ds}) + A_{cs} \cos(\omega_d t + \theta_{cs}). \tag{4.5}$$

The controller chooses the amplitude, A_c, and phase, θ_c, of the control input signal such that the sensor output signal (4.5) is driven to zero;[1] i.e. $y(t) \to 0$. When the LMS controller is operational the sensor output signal is driven to zero. If the sensor is a displacement point sensor, then that point of the beam is pinned to zero displacement. The change in total radiated acoustic power is then computed from the beam velocity distributions for the controlled and uncontrolled system.

With this controller there is no freedom to choose the control gains (for steady state operation). All of the "control design" is in the selection of the sensor and actuator locations. To describe the relationship of the sensor and actuator to the total radiated acoustic power we develop an internal description of the LMS controller.

The state equations of the controlled system are

$$\ddot{\eta}(t) + D\dot{\eta}(t) + \Omega^2 \eta(t) = H_d A_d \cos(\omega_d t + \theta_d) + H_c A_c \cos(\omega_d t + \theta_c). \tag{4.6}$$

The vector of modal displacement amplitudes due to the disturbance force is

$$\eta_d(t) = \begin{bmatrix} \eta_{d1} \cos\theta_{d1} \\ \vdots \\ \eta_{dn_r} \cos\theta_{dr_r} \end{bmatrix} \cos(\omega_d t + \theta_{ds}) = \eta_d \cos(\omega_d t + \theta_{ds}). \tag{4.7}$$

The vector of modal amplitudes associated with the control force has a similar form. The corresponding sensor output signal is

$$\begin{aligned} y(t) &= C(\eta_d(t) + A_c \eta_c(t)) \\ &= C\eta_d \cos(\omega_d t + \theta_{ds}) + CA_c \eta_c \cos(\omega_d t + \theta_{cs}). \end{aligned} \tag{4.8}$$

It follows that

$$C\eta_d - A_c C\eta_c = C[\eta_d - A_c \eta_c] = 0 \tag{4.9}$$

which essentially nulls the output of the sensor. From (4.9) the control gain is

$$A_c = \frac{C\eta_d}{C\eta_c}. \tag{4.10}$$

---

[1] Technically, a small residual vibration remains due to steady state operating conditions. For our purposes here, we set this amplitude to zero.

After the controlled system has reached steady state, the residual vibration left in the beam is given by

$$\eta_r(t) = (\eta_d - A_c\eta_c)\cos(\omega_d t + \theta_{dc})$$
$$= A_r\eta_r\cos(\omega_d t + \theta_{dc})$$

(4.11)

We call the vector in (4.11) the residual vector of modal displacement amplitudes. The radiated acoustic power from the controlled system is the residual radiated acoustic power.

Now the total radiated acoustic power of the uncontrolled beam is

$$\Pi_u = (\omega_d)^2 \eta_d^T M(\omega_d)\eta_d,$$

(4.12)

and the total radiated acoustic power of the controlled beam is

$$\Pi_c = (\omega_d)^2 \eta_r^T M(\omega_d)\eta_r.$$

(4.13)

Example: Consider the beam in Section 2. Suppose that a disturbance force with a frequency $\omega = 95.4$ rad/s is located at $z_d = 0.36$. If the actuator is located at $z_c = 0.45$ and a strain gage is located at $z_s = 0.75$ m. The vector of amplitude displacements for the control gain is

$$\eta_c = \begin{bmatrix} -11.46 \\ -1.344 \\ -0.88 \end{bmatrix} \times 10^{-5}.$$

(4.14)

From (4.10) the control gain is $A_c = 0.5272$. The residual vector of modal displacements is

$$\eta_c = \begin{bmatrix} -3.80 \\ -2.40 \\ -0.45 \end{bmatrix} \times 10^{-5}.$$

(4.15)

The uncontrolled total radiated acoustic power is 4.83×10^{-6} W, while the total acoustic power for the controlled system is 7.96×10^{-7} W. The displacement amplitudes for the controlled and uncontrolled system are shown in Figure 4.2.
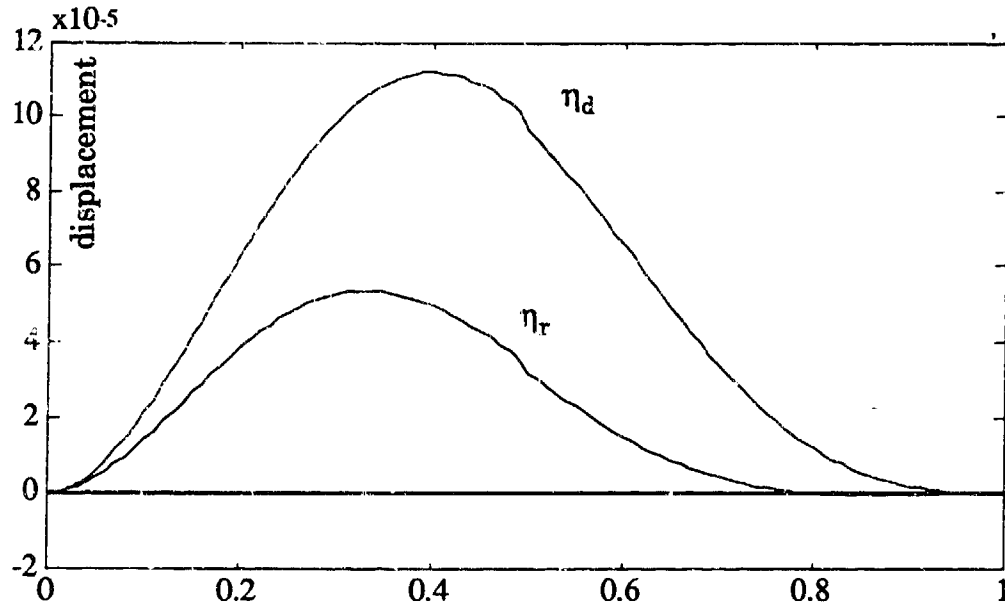
Figure 4.2. Controlled and Uncontrolled Radiating Shapes. z

5. GEOMETRIC INTERPRETATION OF RADIATED ACOUSTIC POWER

Let R^{n_r} be the vector space with a basis determined by the modal displacements η_i. This vector space is shown in Figure 5.1 for R^2.
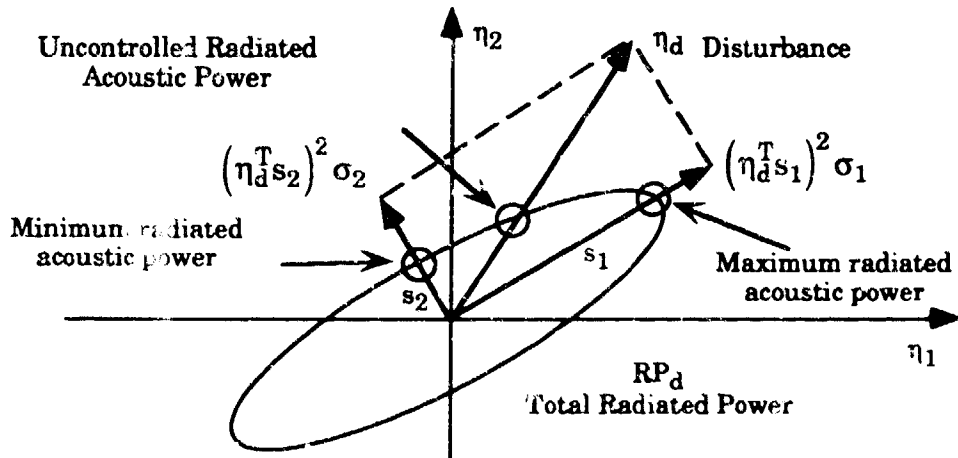

Figure 5.1. Geometric Representation of the LMS Controller.

In the vector space R^{n_r} we identify the set, RP_d,

$$RP_d = \left\{ \eta \in R^{n_r} \mid \eta = \alpha \eta_{d0}, \alpha = \left(\omega_d\right)^2 \eta_{d0}^T M(\omega_d)\eta_{d0}, \|\eta_{d0}\| = 1 \right\}. \qquad (5.1)$$

called the set of normalized total radiated power. Each element of this set is the total radiated power for the corresponding modal displacement amplitudes for $\|\eta_{do}\| = 1$. This set is an ellipse whose principle axes are the principle directions, s_i, of the matrix $M(\omega_d)$ in (5.1) scaled by the eigenvalue σ_i^2. The set RP_d is identified in Figure 5.1.

For a given disturbance, $d(t)$, the vector of modal displacement amplitudes is given by η_d, and the corresponding vector of modal velocities is $\omega_d\eta_d$. The total radiated power for this excitation is

$$\Pi = (\omega_d^2)\eta_d^T M(\omega_d)\eta_d = (\omega_d^2)\eta_d^T S\Sigma S^T\eta_d = (\omega_d^2)\sum_{i=1}^{N}\left(\eta_d^T s_i\right)^2 \sigma_i. \qquad (5.2)$$

From (5.2) we see that the contributions of the various velocity vectors to the far field acoustic power can be decomposed into principle directions, s_i. So we see that the quadratic expression for the total radiated power is as the intersection of the set RP_d and the vector η_d.

Similarly, the actuator and disturbance location can be described geometrically. If the disturbance, say, is located at $z = z_d$ then from (2.5) the vector of modal influence coefficients is

$$H_d = \begin{bmatrix} h_{d1} & \cdots & h_{dn_r} \end{bmatrix}^T. \qquad (5.3)$$

This vector is shown in Figure 5.2 where we have assumed that the components of the vector are positive.
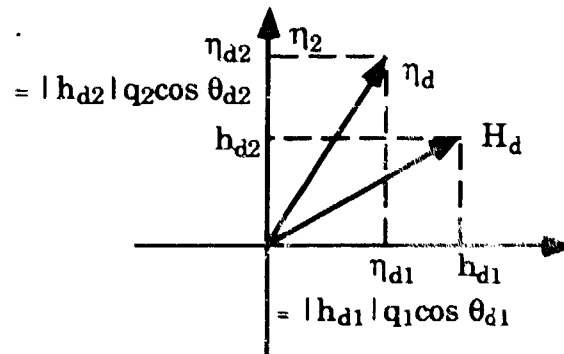

Figure 5.2. Geometric Description of the Vector of Modal Amplitudes for the Sinusoidal Disturbance.

When computing the total far field radiated acoustic power, we are interested in the vector of modal displacements corresponding to the disturbance $d(t)$. This vector is related to the vector of modal influence coefficients through the beam dynamics. From (2.11) the vector of modal displacements is

$$\eta_d = \begin{bmatrix} |h_{d1}|q_1 \cos\theta_{d1} \\ \vdots \\ |h_{dn_r}|q_{n_r} \cos\theta_{dn_r} \end{bmatrix}. \tag{5.4}$$

This vector, (5.4) is shown in Figure 5.2.

Geometrically, the radiated acoustic power can be determined by intersecting the vector of displacement amplitudes, η_d, with the set of total radiated power, RP_d. This intersection is shown in Figure 5.1. Note that this vector is fixed once the structure and the frequency of the disturbance have been specified. Also note that not all vectors in R^2 stand in a one-to-one relationship with possible vectors of modal displacement amplitudes.

As with the disturbance force, the object of interest is the vector of modal displacements, η_c, due to the action of the control force. The steady state vibrations due to the control force are described by the location of the actuator and the (disturbance) frequency of the control force. The construction of this vector is exactly the same as the construction of disturbance vector of modal displacements. The vector η_c is shown in Figure 5.3.
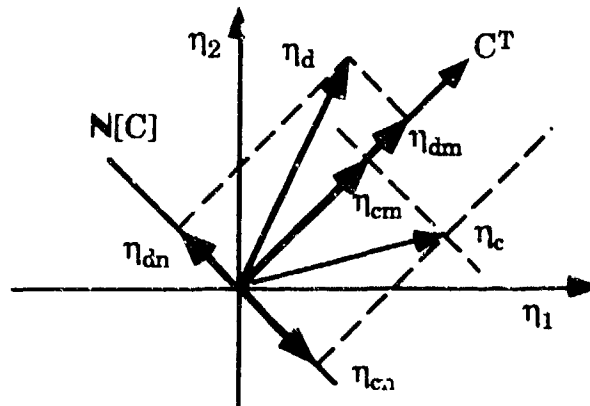

Figure 5.3. Decomposition of the Vectors of Modal Displacements
Along the Range Space of C^T.

The sensor on the beam is modeled as the output matrix C in the model of the system in (2.3). In the space R^{n_r} the output matrix, C, is a map $C: R^{n_r} \to R$. This map is characterized by the nullspace of C, $N[C]$. Since $N[C]^\perp = R[C^T]$, the range space of C^T, $N[C]$ is orthogonal to the vector C^T. These two spaces are shown in Figure 5.3. Since the output matrix C is determined by the type and location of the sensor, geometrically the sensor is represented by the vector C^T.

The controlled beams vectors of displacement amplitudes satisfy

$$0 = C\eta_d - A_c C\eta_c = C[\eta_d - A_c\eta_c]. \tag{5.5}$$

Geometrically, the calculation of the control gain can be broken into two steps. First, the vector of modal displacements for the disturbance, η_d, is decomposed in terms of the two subspaces

$$\eta_d = \eta_{dm} + \eta_{dn}, \quad \eta_{dm} \in \mathbf{R}\left[C^T\right], \quad \eta_{dn} \in \mathbf{N}[C],$$

$$\eta_c = \eta_{cm} + \eta_{cn}, \quad \eta_{cm} \in \mathbf{R}\left[C^T\right], \quad \eta_{cn} \in \mathbf{N}[C] \tag{5.6}$$

shown in Figure 5.3. The same projection is applied to the control vector of modal displacement amplitudes, η_c. Second, the same vector multiplied by the control gain, $A_c\eta_c$, as shown in Figure 5.3. Then the two vectors η_d and $A_c\eta_c$, $\eta_r = A_d\eta_d - A_c\eta_c$, are added component-wise. We have

$$0 = C\eta_d - A_cC\eta_c = C\left[\eta_{dm} + \eta_{dn}\right] - A_cC\left[\eta_{cm} + \eta_{cn}\right]$$

$$= C\eta_{dm} - A_cC\eta_{cm} = C\left[\eta_{dm} - A_c\eta_{cm}\right]. \tag{5.7}$$

Their sum, the residual vector of modal amplitudes, is shown in Figure 5.4.
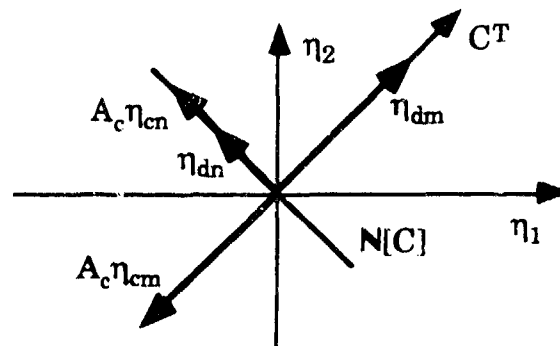

Figure 5.4. Decomposition of the Disturbance and Control
Vectors of Modal Displacements.

The total radiated power of the uncontrolled system is determined from the intersection of the vector of modal displacements corresponding the disturbance with the set of total radiated power as shown in Figure 5.5.
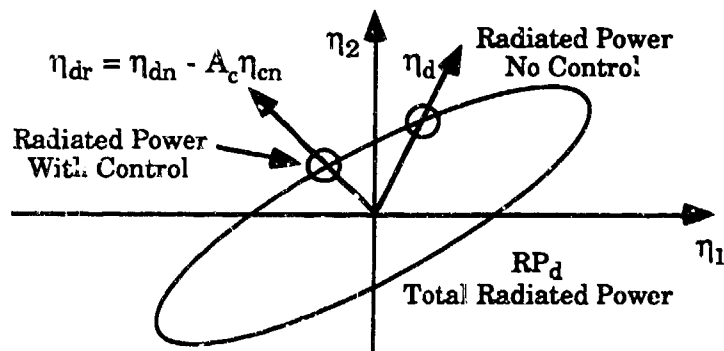
Figure 5.5. Radiated Acoustic Power for the Uncontrolled
and Controlled Beam.

The total radiated power for the controlled system is found from the intersection of the residual vector of modal displacements with the set of total radiated power.

From the discussion above, it is clear that the LMS controller doesn't directly incorporate any measure of the radiated acoustic power. A reduction of power is realized if the total acoustic power corresponding to the residual power is less than the acoustic power that is radiated by the uncontrolled beam. The LMS controller drives to zero the linear combination of modeshapes $C[\eta_d(t) - A_c \eta_c(t)]$. As a result of this action the sum of modes corresponding to the residual vector of displacement amplitudes may increase or decrease. Hence, the total radiated power of the controlled system must be evaluated on a case by case basis.

Remarks. In this discussion about we assumed perfect knowledge of the structure and truly distributed actuators and sensors. In practice errors will be present. These errors can be modeled as a perturbation to the desired shape of the sensor. Then the effects of these errors on the control system performance can be determined using the results in [6,15].

The problem formulation discussed in this paper is based on a modal model of the structure. These results, however, can be extended to finite element models with only minor modifications.

6. CONCLUSIONS

In this paper we have considered the use of distributed-effect actuator and sensor arrays for the vibration suppression in flexible structures. We have formulated the control problem in such a way that spatial information can be incorporated directly into the control system design. Using this formulation we have shown how to place the actuator and sensors for optimum control system performance. This theory was applied to the suppression of acoustic radiation from a vibrating structure.

Acknowledgement

7. REFERENCES

1. Murphy, K. A., M. S. Miller, A. M. Vengasarkar, and R. O. Claus, 1990. "Elliptical-Core Two Mode, Optical Fiber Sensor Implementation Methods," *Journal of Lightwave Technology*, Vol. 8, pp. 1688-1696.

2. Cox, D. E. and D. K. Lindner, "Active Control for Vibration Suppression in a Flexible Beam Using a Modal Domain Optical Fiber Sensor," *ASME Journal of Vibration and Acoustics*, Vol 113, 1991, pp. 369-382.

3. Burke, S. E. and J. E. Hubbard, 1988. "Distributed Actuator Control Design for Flexible Beams," *Automatica*, Vol. 24, No. 5, pp 619-627.

4. Lee, C.-K. and F. C. Moon, "Modal Sensors/Actuators, *"Journal of Applied Mechanics*, Vol. 57, 1990., pp. 434-441.

5. Collins, S.A., D. W. Miller, and A. H. von Flotow, 1991. "Piezopolymer Spatial Filters for Active Structural Control," *Proceedings of the Workshop on Recent Advances in Active Control of sound and Vibration*, Blacksburg, VA, pp. 219-236.

6. Reichard, K. M., 1991. "Distributed-Effect Modal Domain Optical Fiber Sensors for Flexible Structure Control," Ph.D. Thesis, Bradley Department of Electrical Engineering, Virginia Tech, Blacksburg, VA.

7. Reichard, K. M. and Lindner, D. K., 1991. "Modeling the Effects of Arbitrary Stress on the Response of Modal Domain Optical Fiber Sensors," Internal Report, Bradley Department of Electrical Engineering, Virginia Tech, Blacksburg, VA.

8. Clark, R. L. and Fuller, C. R., 1991. "Active Structural Acoustic Control With Adaptive Structures Including Wave Number Considerations," *Proceedings of the Workshop on Recent Advances in Active Control of Sound and Vibration*, Blacksburg, VA, April, pp. 507-524.

9. Lindner, D. K., W. T. Baumann, F. Ho, and E. Bielecki, 1991. "Modal Domain Optical Fiber Sensors for Control of Acoustic Radiation," *Proceedings of the Workshop on Recent Advances in Active Control of Sound and Vibration*, Blacksburg, VA, April, pp. 839-850.

10. *Procedings for the second conference on Recent Advances in Active Control of Sound and Vibration*, R. A. Burdisso, editor, Technomics Lancaster, PA, 1993.

11.   Lindner, Douglas K. and Wojciech Tabisz, "Miniaturized Power Converters for Smart Structure Actuators," accepted for SPIE's 1993 North American Conference on Smart Structures and Materials, Albuquerque, NM, February 1-4, 1993.

12.   Baumann, W.T., W. R. Saunders, and Harry H. Robertshaw, 1990a "Active Suppression of Acoustic Radiation from Impulsively Excited Structures." 119th Meeting of the Acoustical Society of America.

13.   Baumann, W. T., F. Ho, and H. H. Robertshaw, 1990b "Active Acoustic Control of Broadband Structural Disturbances." 120th Meeting of the Acoustical Society of America.

14.   Elliott, S. J., I. M. Stothers, and P. A. Nelson, 1987."A Multiple Error LMS Algorithm and Its Application to the Active Control of Sound and Vibration." *IEEE Trans. on Acoustics, Speech, and Signal Processing*, ASSP-35:1423-1434.

15.   Lindner, D. K. and Reichard, K. M., "Weighted Distributed-Effect Sensors for Smart Structure Applications," *Proceedings of the ADPA/AIAA/ASME/SPIE Conference on Active Materials and Adaptive Structures*, Washington, D.C., Nov., 1991, pp. 53 - 58.

TITLE: Development of a Hybrid Distributed-Lumped Parameter
Openloop Model of Elevation Axis for a Gun System.

D. K. Dholiwar.
DRA, Fighting Vehicles & Systems Sector
Chobham Lane, Chertsey
Surrey. KT16 OEE. UK

ABSTRACT:

A hybrid distributed-lumped parameter model of the elevation
axis of a gun system has been developed which links together the
dynamics of the flexible barrel, modelled using finite element
technique with the electro-mechanical servo system modelled in the
lumped parameter method.   The barrel is modelled by specifying the
dimensions of the elements, thus eliminating the need for gross
approximations.

A generic gun system is modelled and the effects of changing
system parameters such as barrel stiffness, breech mass, gearbox
stiffness and structural damping are investigated in the frequency
domain using Bode diagrams.

The simulation also provides the response of the barrel at a
number of locations, the muzzle motion being of particular interest for
future work on muzzle reference systems, active muzzle control, and for
predicting accuracy when firing on the move.

BIOGRAPHY:
PRESENT ASSIGNMENT: DRA, Chertsey, Surrey. UK.
Head of Dynamics and Control Section.

PAST EXPERIENCE: G E C Engineering Research Centre, Whetstone,
Leicester, UK. Research Engineer Control Group.

DEGREES HELD: Bsc. Mechanical Engineering(1977).
University of Bath, Claverton Down, Bath. UK.
Msc. Fluid Power and Control Systems.(1980).
University of Bath.

Development of a Hybrid Distributed-Lumped Parameter Openloop Model of Elevation Axis for a Gun System.

D. K. Dholiwar.
DRA, Fighting Vehicles & Systems Sector
Chobham Lane, Chertsey
Surrey KT16 OEE. UK

INTRODUCTION

To satisfy the demands of speed and precision modern control systems have to influence or compensate for the dynamics of flexible structures.

The development of effective control systems for flexible structures are attracting considerable attention as these systems are now prevalent in a wide variety of products and industrial applications. Typical examples are disk drives in consumer electronics, satellite structures in the aerospace industry, robot arms in manufacturing applications, and gun systems in ground based weapons such as Main Battle Tanks.

In Main Battle Tank gun systems the flexing and the movement of the barrel in its mounting, under the influence of the gunners demand and due to terrain-induced disturbances, causes significant loss of gun accuracy and a low hit probability when firing on the move or tracking moving targets.

It has been suggested that by directly measuring the muzzle motion and incorporating it in Fire Control Systems significant improvements in accuracy can be achieved. Firstly, by correcting for errors due to droop, barrel bend and misalignments and secondly, by controlling or compensating for structural deformations using predictive control methods[1].

To enable engineers to develop effective control systems, improved computer simulations of the weapon system are required which incorporate the effects of structural flexibility more accurately. Distributed parameter modelling, using the Finite Element Modelling (FEM) technique is primarily used for analyzing mode shapes, natural frequencies and stress-strain relationships in structural and mechanical components. In lumped parameter models the effects of structural dynamics are either ignored or approximated using several mass-spring elements. The models are then tuned by matching with measured results in the frequency domain. This leads to arbitrary selection of lumped parameters and the models are only valid at the measured locations. These models can not be used , with confidence, to predict the motion at points remote from the measured locations.

The work described in this paper is a study into the development of hybrid distributed-lumped parameter model. This approach links together the dynamics of the structure, modelled using FEM techniques,

with lumped parameter models of the actuator and other servo components. The simulation thus incorporates the effects of flexibility while still retaining the simplicity of the lumped parameter approach. For this initial study the openloop linear model of the elevation axis of a gun system is considered.

The simulation is developed using modules which represent system components such as amplifier, motor and gearbox. These modules are then linked together using measurable quantities such as volts, amps, torques, displacement etc. The modules themselves are constructed using primitive blocks which are assembled using hierarchical facilities provided in the MATRIX$_x$ simulation package. The simulation can be easily modified to include improved component models and permits structural models with varying number of elements to be incorporated.

THEORY

The elevation axis illustrated in Figure 1, consists of several electro-mechanical components - motor, gearbox and gun. These components, together with the servo amplifier and the primary feedback transducer (rate gyro) constitute the openloop elevation model. The equations in the subsequent subsections describe the behaviour of each component and collectively they form the hybrid model.
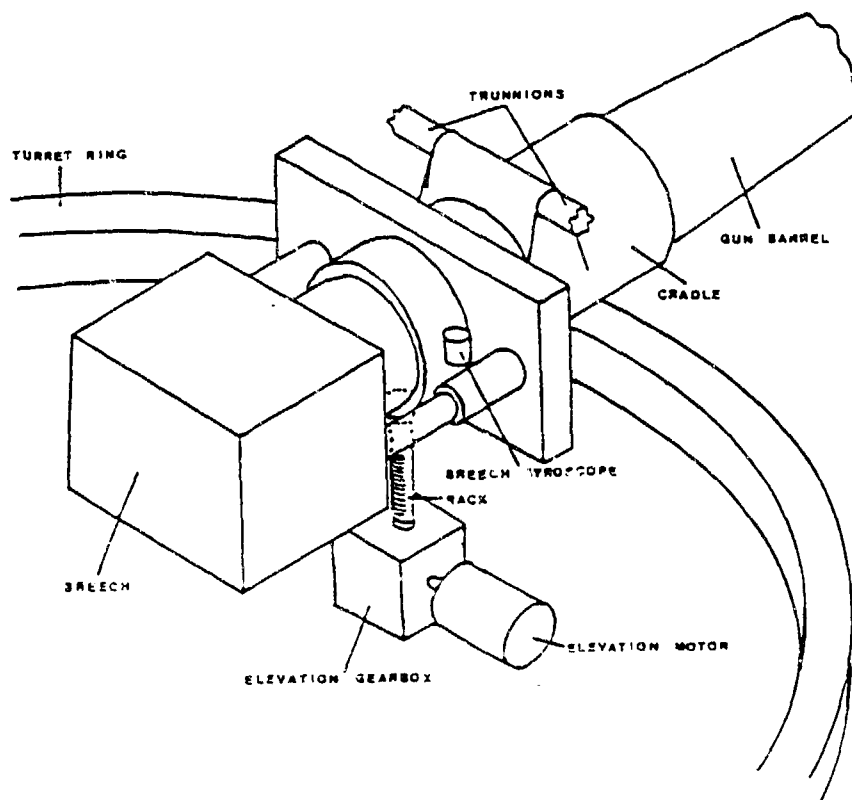

Figure 1 Main components of elevation axis servo system

Distributed Parameter Model

The gun, which is shown in Figure 2, consists of 3 main components. These are the breech, cradle and barrel.

In the FEM technique the structure is divided into discrete elements which are then assembled together at the node points to represent the system. The following assumptions are used in modelling the gun :-

a) The breech is modelled as a single element which has a rectangular cross section.

b) The bearing clearances in the cradle which support the barrel are small and neglected.

c) The cradle and the barrel within it are modelled as a single compound element which is cylindrical.

d) The cradle and breech are held together in close contact by the recoil mechanism until firing takes place.

e) The barrel is divided into several cylindrical sections which have constant cross-sectional area. Average values are used for tapered sections.
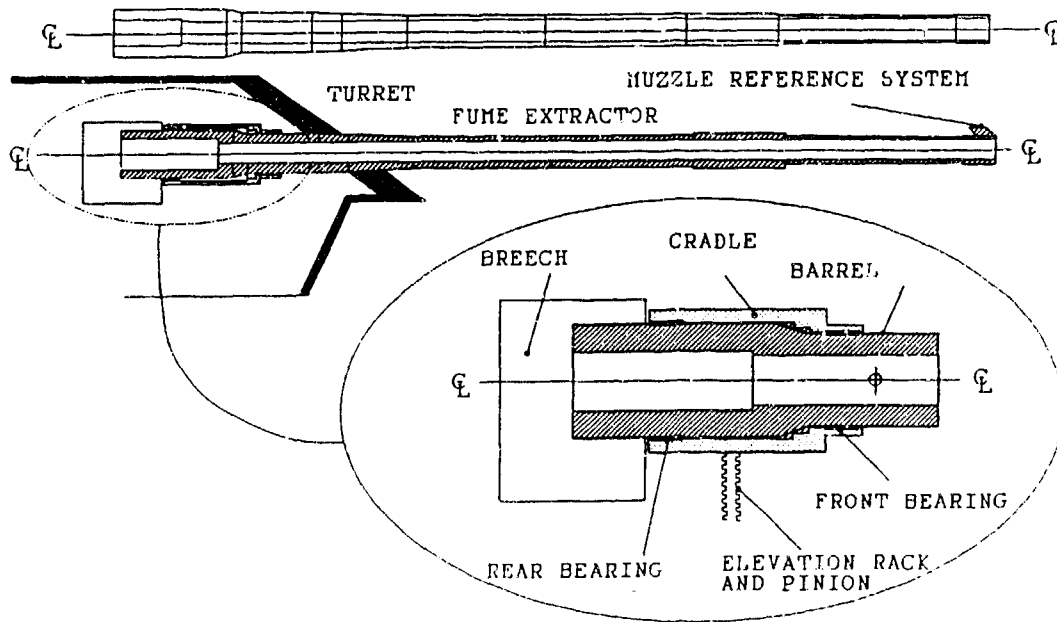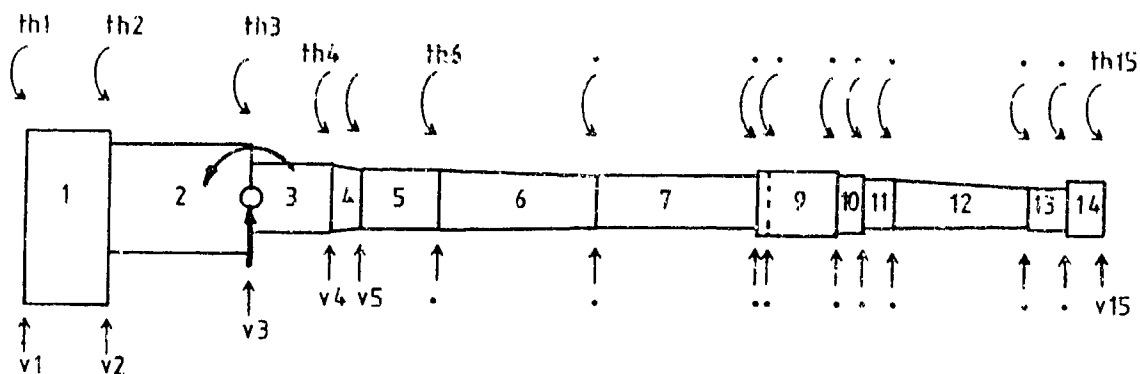
Figure 2 Details of gun system

vldot, thldot, etc. are the rates

Figure 3 Finite element representation of the gun system

The representation in Figure 3 is used to model the system as with this arrangement it is easier to decouple the pitch and heave motions of the hull. The pitch and heave motions and the torque from the elevation servo system act through the pivot located at the front end of the cradle.

The mass and stiffness properties for the Bernoulli-Euler element are derived by considering mode shapes [2].

$$[m] = \frac{\rho A L_e}{420} \begin{pmatrix} 156 & 22L_e & 54 & -13L_e \\ 22L_e & 4L_e^2 & 13L_e & -3L_e^2 \\ 54 & 13L_e & 156 & -22L_e \\ -13L_e & -3L_e^2 & -22L_e & 4L_e^2 \end{pmatrix} \quad (1)$$

$$[k] = \frac{EI}{L_e^3} \begin{pmatrix} 12 & 6L_e & -12 & 6L_e \\ 6L_e & 4L_e^2 & -6L_e & 2L_e^2 \\ -12 & -6L_e & 12 & -6L_e \\ 6L_e & 2L_e^2 & -6L_e & 4L_e^2 \end{pmatrix} \quad (2)$$

A = Area
E = Young's modulus
I = Moment of Inertia (cross-sectional area)
L_e = element length
ρ = density

When these elements have been assembled the following equation of
motion results.

$$[M]\{\ddot{x}\}+[F]\{\dot{x}\}+[k]\{x\}=\{Fo\} \tag{3}$$

F = Damping matrix
Fo= Forcing function
K = Stiffness matrix
M = Mass matrix
x = displacement

The damping matrix F can be obtained using similar techniques as those
used to derive the stiffness and mass matrices, however as damping in
structures is primarily determined by friction in joints, bearings,
surface covering etc. it is advantageous to define damping for the
structure as a whole. A commonly used procedure for deriving damping
is called Rayleigh damping [2].

$$[F] = a_o[M] + a_1[K] \tag{4}$$

The variables a_0 and a_1 can be selected by choosing ζ for two modes.

$$\zeta_r = \frac{1}{2}\left(\frac{a_o}{\omega_r} + a_1\omega_r\right) \tag{5}$$

The main disadvantage with procedure is that damping can not be
selected for each mode individually. By transforming equation 3 into
a set of uncoupled equations damping can be selected for each mode[3].

$$x = \Phi q, \quad M = \Phi^T M \Phi, \quad K = \Phi^T K \Phi \tag{6}$$

$$[M]\{\ddot{q}\} + [F]\{\dot{q}\} + [K]\{q\} = \Phi^T\{Fo\}, \quad F = diag\{2\,\zeta_r\,\omega_r\,M_r\} \tag{7}$$

Φ = modal matrix
q = Principle coordinates

The value of ζ is selected for each mode and the resulting damping
matrix transformed back to physical coordinates using the transpose and
inverse of modal matrix.

The equations of motion are represented in state space form and linked
with models of the servo system.

$$\dot{x}(t) = Ax(t) + Bu(t) \tag{8}$$

$$y = Cx(t) + Du(t) \tag{9}$$

A = Coefficient matrix
B = Driving matrix
C = Output matrix
D = Transmission matrix
u = input vector
x = state vector
y = output vector

The MATRIX$_x$ window with the state space model is shown in Figure 4. The co-ordinates v1dot, th1dot, etc, describe the rates at element boundaries and v1, th1, etc the displacements.

Lumped Parameter Models

The electro-mechanical servo components considered in this section are modelled using the lumped parameter technique.

Gyro

The gyro, which is located on the cradle, measures the absolute angular rate of the gun and the pitch motion of the hull. The gyro is modelled as a damped second order system which has the following transfer function

$$\frac{\omega_n^2 * K_{gy}}{s^2 + 2\zeta\omega_n s + \omega_n^2} \tag{10}$$

K_{gy} = Gyro gain
S = Laplace transform
ζ = Damping ratio
ω = Natural frequency

Servomotor

The servomotors used in control systems are usually DC machines which may have separately excited field or permanent magnet stators. A schematic diagram of the motor [5], with the associated variables, is shown in Figure 5

The voltage equation for the armature is given by

$$V_i = R_a i_a + L_a \frac{di_a}{dt} + V_b \tag{11}$$

where V_b is the voltage generated when a conductor moves through a field. According to Faraday's Law, the voltage induced in a conducting loop rotating in a magnetic flux is given by equation 12.

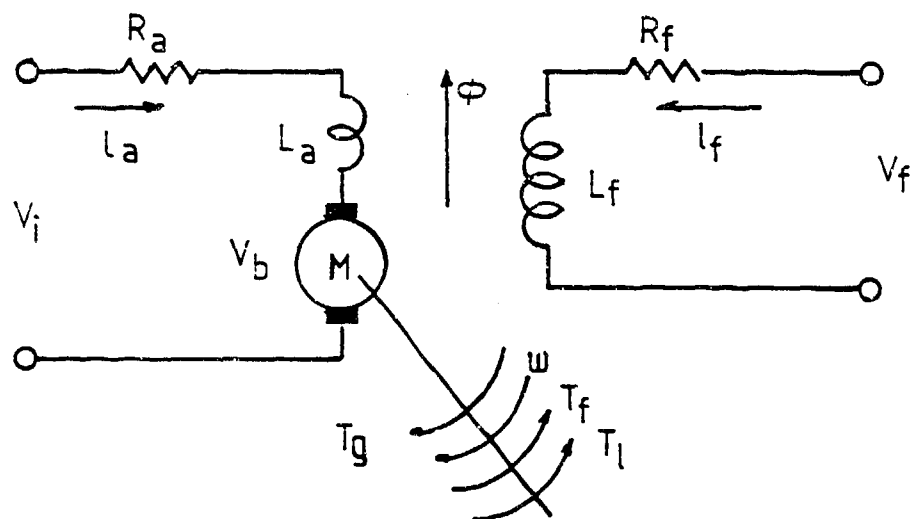Where λ represents the flux linkage in the coil. The rate of

DHOLIWAR

Figure 4 State Space model of the gun

Figure 5 Schematic of DC Motor

$$V = \frac{d\lambda}{dt} \tag{12}$$

change of λ is proportional to the magnetic flux in the air gap and the angular velocity $\omega(t)$

$$V_b = K \phi \, \omega(t) \tag{13}$$

Now, if we assume constant field voltage or current and ignoring second order effects, the above equation simplifies to

$$V_b(t) = K_e \, \omega(t) \tag{14}$$

where K_e is the motor voltage constant. The torque generated in the armature with field flux which remains constant is given by

$$T_g = K_t \, i_a \tag{15}$$

K_t is called the torque constant of the motor.

The torque generated by the motor is equal to the torque required to overcome the motor inertia, the frictional and external load torques.

$$T_{\varsigma} = T_f + T_L + J_m \frac{d\theta^2_m}{dt} + F_m \frac{d\theta_m}{dt} \tag{16}$$

T_f consists of all other losses.

Servo amplifier

Servo amplifiers used in gun control systems are usually switching amplifiers whose output power is controlled by varying the on-off time ratio, pulse-width, of the output. The switching frequency of these amplifiers can be as high as 100 kHz[6]. Because of the high switching rates accurate models of the amplifiers require very small integration step lengths, which results in long simulation run times. To overcome this difficulty switching amplifiers in control simulations are often modelled as equivalent linear amplifiers.

Servo amplifiers use a combination of current and voltage feedback for stable operation. In many applications the current feedback is dominant and the amplifier is modelled as a gain which converts a low input voltage to a current output. When this representation of the amplifier is used, the motor model simplifies to a constant term which produces motor torque. After accounting for torques due to friction, external loading and acceleration, the output can be integrated to give a transfer function between input voltage and speed. The block diagram in figure 6 shows the simplified amplifier and motor model.

Gearbox

The gearbox model used in this simulation consists of two gears. The total gearbox stiffness is lumped at the output shaft and in the nonlinear model the backlash in the gearbox is lumped between the two gears. Figure 7 shows the block diagram of the complete system.

DISCUSSION OF RESULTS

The results from the simulation, which does not represent any specific gun system, are presented in the frequency domain. The Bode diagrams, with normalised frequency, show the openloop response of the system with voltage input at the amplifier and the output at the gyro.

The effects of varying the system parameters such as barrel stiffness, breech mass, gearbox stiffness and system damping are investigated.

Figure 8 shows the effects on the response when the stiffness of the gun is changed. The stiffness may change due to length, moment of inertia, or because of changes in the Young's modulus; which may occur in barrels made from composite materials. As the stiffness is increased the resonant frequencies associated with the gun also increase. The resonance at normalised frequency of 0.2 which is associated with the gearbox and motor inertia remains unchanged. In figure 9 the effects changing gearbox stiffness are shown.

The breech and muzzle masses may change to account for improvements in design or to accommodate sensor systems, such muzzle mirrors. Figure 10 shows the variations in the system response when the breech mass is changed. Breech mass mainly effects the frequencies beyond the gearbox

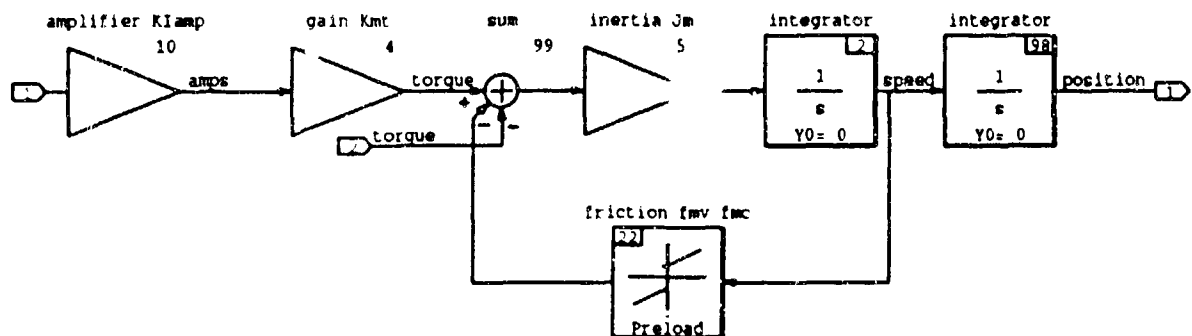| Continuous SuperBlock | Ext.Inputs | Ext.Outputs |
| Amp_motor_simple | 2 | 1 |

Figure 6 Block diagram of a simplified DC motor and amplifier

resonance although some modification is noted at frequency of 0.04.

Figure 11 shows the response of the system along the barrel. Figure 11a,b,c show the response at the breech, fume extractor and muzzle respectively. For ease of comparison the rate at each location is measured using the same gyro model.

The effects of changing the damping in the gun structure are presented in figure 12. Figure 12a shows the undamped system while 12b and c show the effects of increasing the damping. Again the resonance associated with the gearbox and motor remains unaffected.

CONCLUSIONS

The results of this study indicate that:

a) The hybrid technique used to simulate the elevation axis of a gun system is a valid technique which links together Finite Element Model of the gun with lumped parameter models of the servo components.

b) Using the hybrid technique flexible components which have changing cross-sections, such as the barrel, can be modelled by specifying the dimensions of each element. This eliminates the need for guesswork and gross assumptions. Some tuning is required to allow for irregular mass distribution at the cradle. The
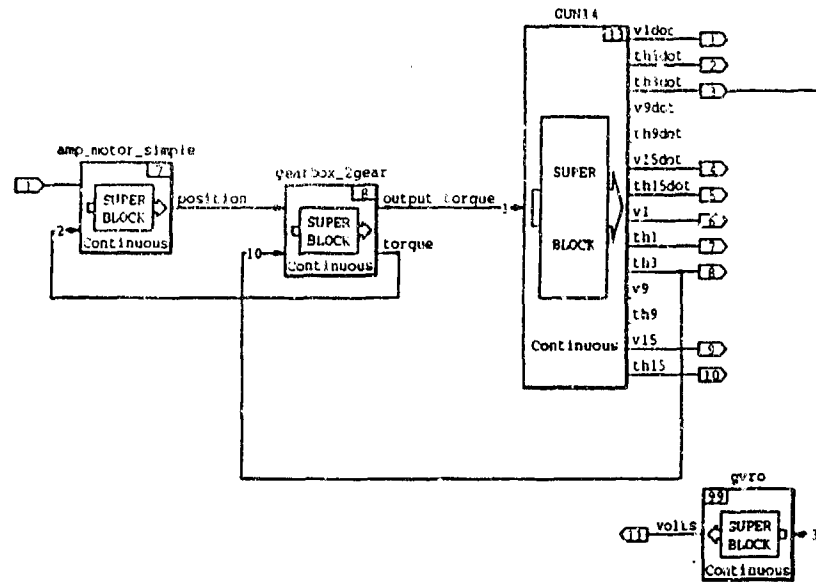
DHOLIWAR

Figure 7 Block diagram of the system

accuracy of the model can be improved by using several elements to model the cradle but this would further increase the complexity of the model.

c) The simulation also provides the response of the gun at a number of locations. The motion of muzzle is of particular interest for future work on muzzle reference systems and for predicting accuracy when firing on the move.

d) The modular nature of the simulation allows easy modification of the simulation so that different or improved component models can be readily incorporated. The validation of the component models is also simplified as the input and outputs are measurable quantities such as speed and voltages.

e) The greater accelerations at higher frequencies may excite nonlinearities which will cause discrepancies between the measured and the predicted results. At these frequencies the simplifications regarding the bearing clearances and the recuperator may be incorrect. Transient responses from the vehicle and nonlinear models are required to confirm this conclusion.

DHOLIWAR

REFERENCES

1   Bird J. S., Measurement of tank gun dynamics in support of a
     Dynamic Muzzle Referencing system. Defence Research
     Establishment, Ottawa, Canada. December 1990 Report No 1053.

2   Mierovitch L., Elements of vibrational analysis, 1st edition
     1975, Published McGraw-Hill.

3   Tung F. C., Application of system identification technique to the
     modelling of large space structures. American Institute of
     Aeronautics and Astronautics. 1981 pp 333-340

4   Shinners S. M., Modern control systems theory and applications
     2nd edition 1979, Addison Wesley.

5   Kuo B., Tal J., Incremental motion control, 1978, SRL Publishing.

6   Tako S. L, Understanding DC servo amplifiers. Machine design May
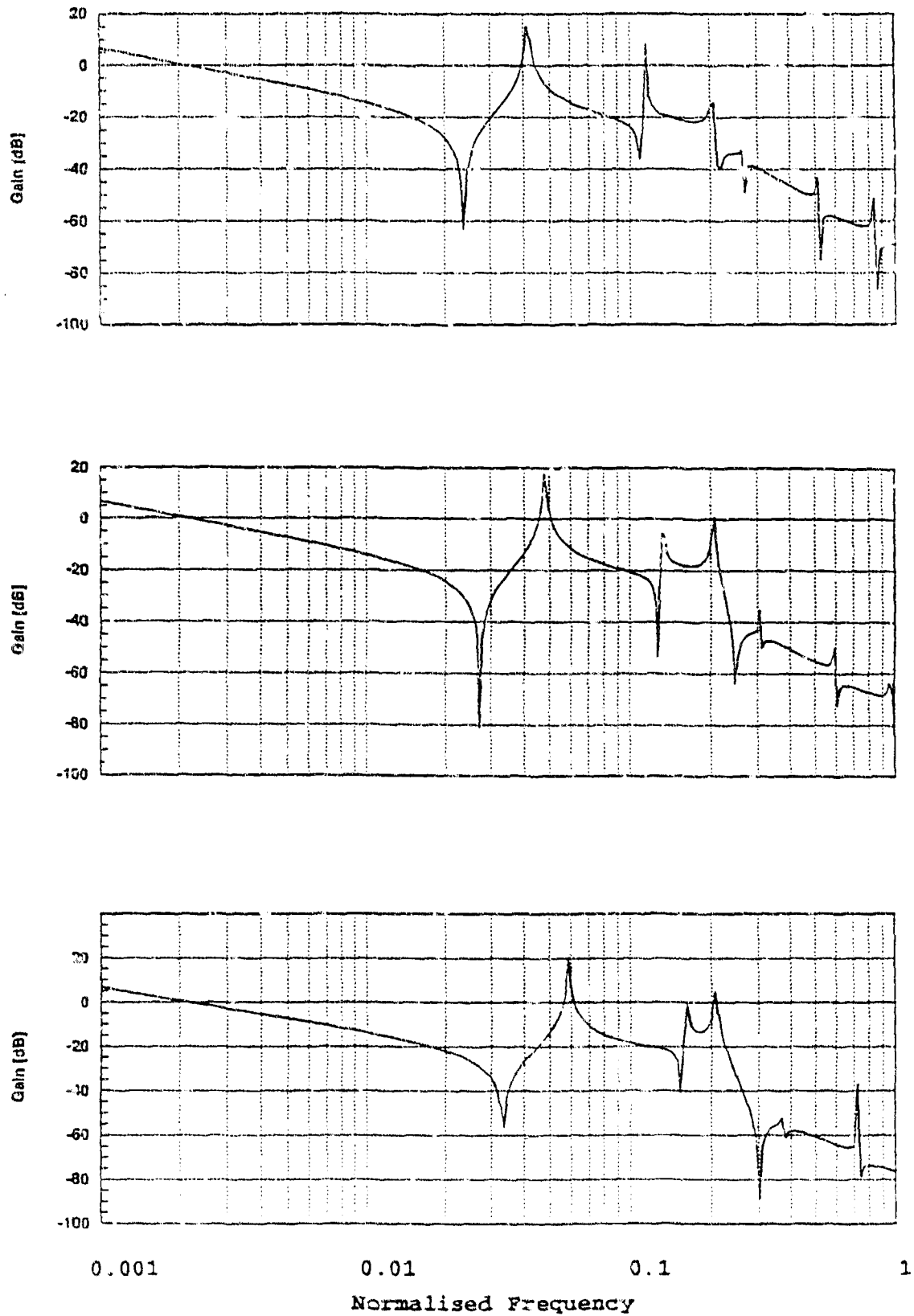   10, May 24, June 7 1979. Penton Publishing Inc.
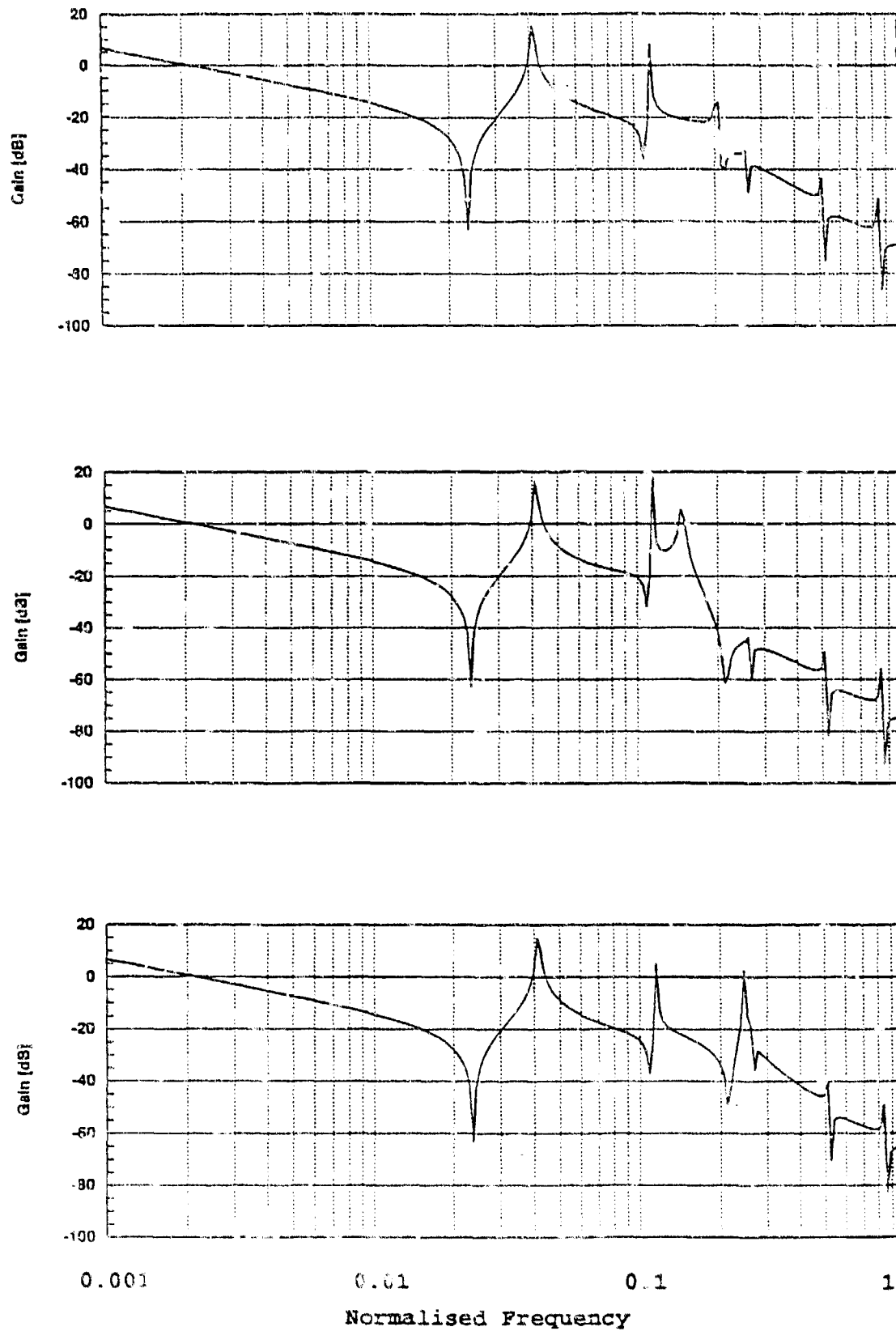
Figure 8 Effects of increasing barrel stiffness

Figure 9 Effects of changing gearbox stiffness
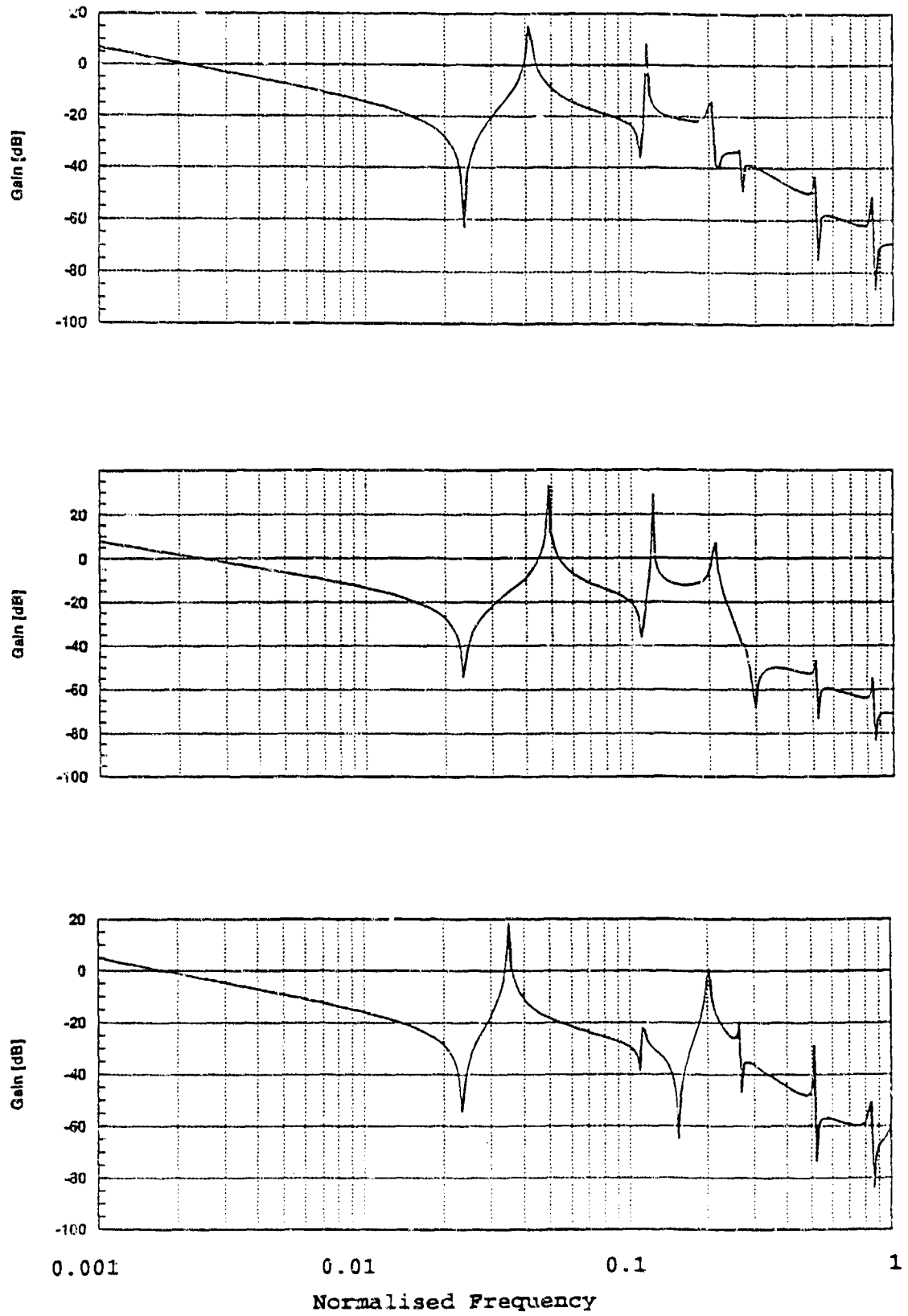(a) standard (b) reducing (c) increasing

Figure 10 Effects of changing breech mass
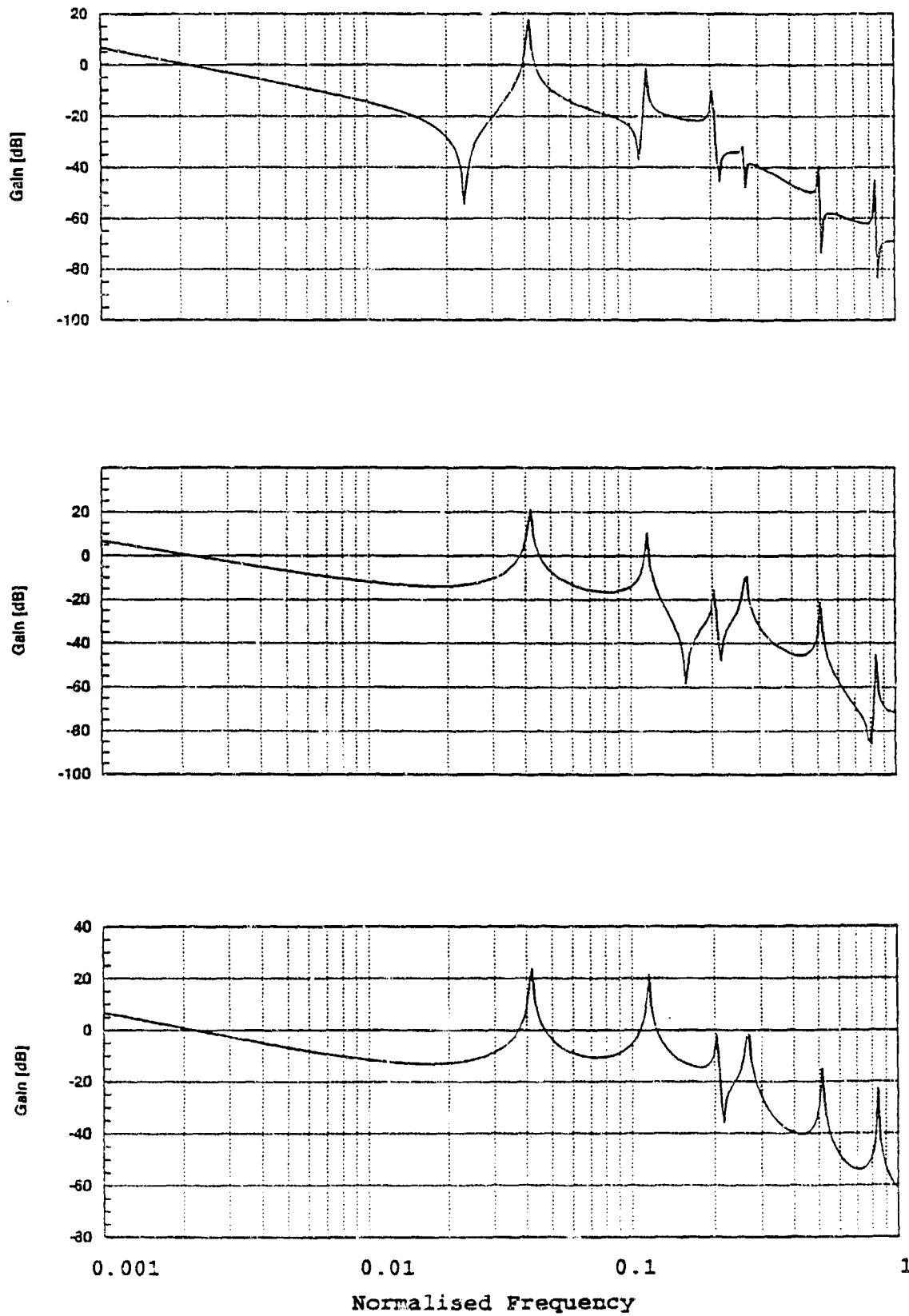(a) standard (b) reducing (c) increasing

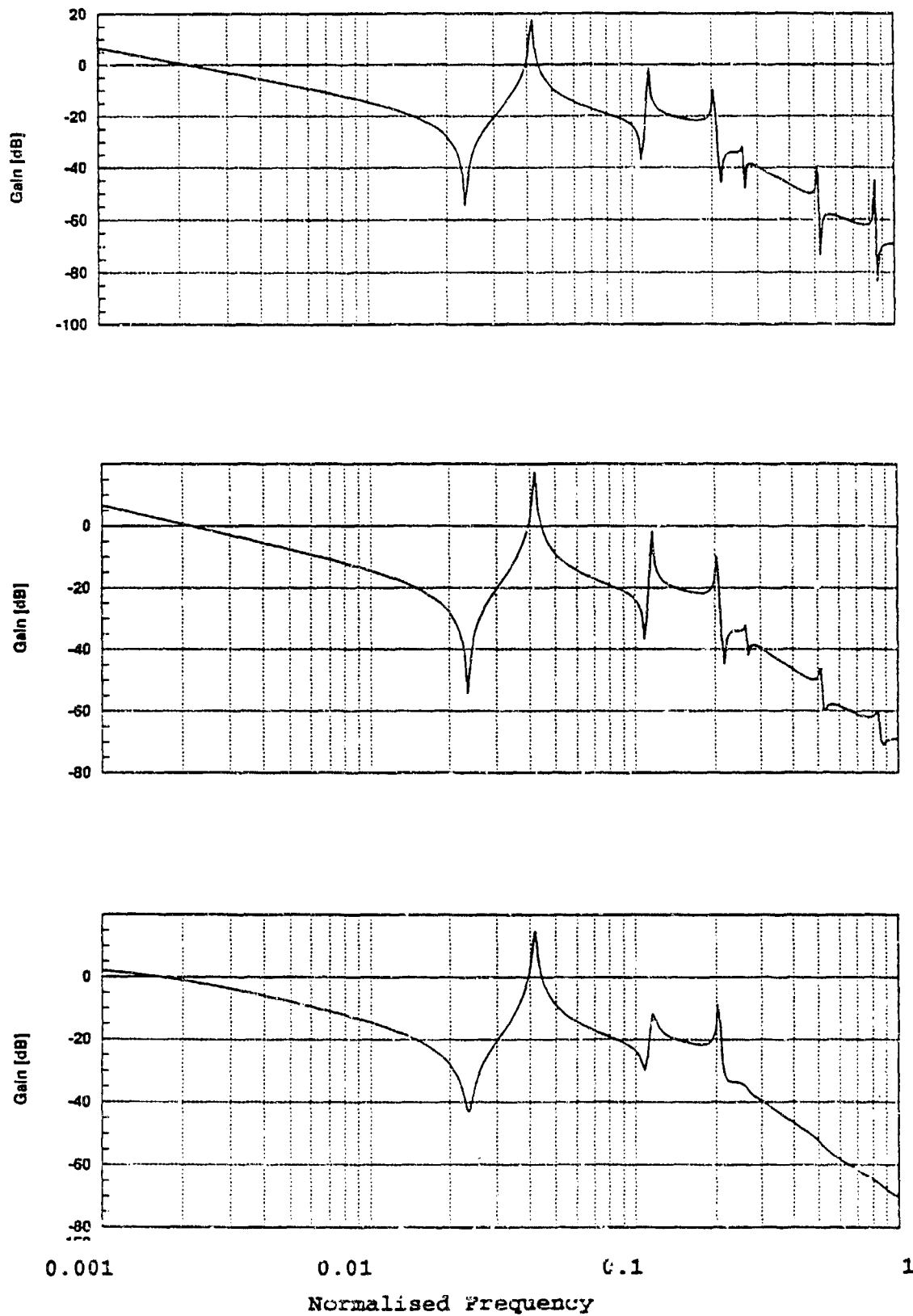Figure 11 Response at (a) breech (b) fume extractor (c) muzzle

Figure 12 Effects of increasing structural damping

Adaptive Feedforward and Feedback Compensation
For Flexible Weapon Pointing Systems

Farshad Khorrami   Sandeep Jain

Control/Robotics Research Laboratory
School of Electrical Engineering & Computer Science
Polytechnic University, Six Metrotech Center
Brooklyn, NY 11201

M. Mattice   N. Coleman, Jr.

U.S. Army, Armament Research
Development and Engineering Center
Automation and Robotics Team
Picatinny Arsenal, NJ 07806

J. Rastegar

Department of Mechanical Engineering
State University of New York at Stony Brook
Stony Brook, NY 11794

Abstract

In this paper, active control of flexible structures, e.g., weapon systems, using feedback and feedforward compensation is considered. Specifically, dynamic feedback design utilizing signals from the accelerometer mounted on the structure is discussed. Furthermore, utilization of adaptive input precompensators in conjunction with nonlinear controllers for flexible structures is proposed. The flexible pointing system considered here is the test-bed at the Army Research Development Engineering Center (ARDEC) at Picatinny Arsenal, which is a scaled-down representation of real-life targetting systems. The approaches advocated here are based on Youla's parametrization of stabilizing controllers, Wiener-Hopf design, feedback linearization and input preshaping. The results on the ARDEC setup indicate a significant improvement in performance with the Weiner-Hopf design. Results on the adaptive feedback and feedforward scheme are presented for the flexible arm at CRRL.

Biography

Farshad khorrami recieved his Bachelor's degrees in mathematics and electrical enigneering at The Ohio State University in 1982 and 1984 respectively. He received the master's degree in mathematics in 1984 and the Ph.D. in electrical engineering in 1988 both from The Ohio State University. He is currently an assistant professor of electrical engineering at Polytechnic University in Brooklyn, NY. His research interests include robotics and high speed positioning applications, large scale systems and decentralized control, adaptive and nonlinear systems, flexible structures, and microprocessor based control and instrumentation. He has developed the Control/Robotics Research Laboratory (CRRL) at Polytechnic University. He was the General Chairman of the IEEE Regional Control Conference held at Polytechnic on July 1992.

Adaptive Feedforward and Feedback Compensation
For Flexible Weapon Pointing Systems

Farshad Khorrami   Sandeep Jain

Control/Robotics Research Laboratory
School of Electrical Engineering & Computer Science
Polytechnic University, Six Metrotech Center
Brooklyn, NY 11201

M. Mattice   N. Coleman, Jr.

U.S. Army, Armament Research
Development and Engineering Center
Automation and Robotics Team
Picatinny Arsenal, NJ 07806

J. Rastegar

Department of Mechanical Engineering
State University of New York at Stony Brook
Stony Brook, NY 11794

1 Introduction

Rapid retargetting of pointing systems in the face of external disturbances poses generic control problems [1–7]. The problems arise mainly due to the flexible nature of the pointing system. Excitation of the structural modes grossly affects the pointing accuracy of these systems. The structural frequencies of these setups are clustered in the low frequency range and are well within the control bandwidth. Thus, it becomes imperative to consider control designs based on models which take these flexural effects into account.

An advanced weapon tracking testbed (AWTB) has been developed at the Army Research Development Engineering Center (ARDEC) at Picatinny Arsenal. This setup will be described in more detail later in this paper. The AWTB mimics the behavior of real-life targetting systems, e.g., helicopter and gun-turret systems, etc. In this paper, our efforts and results on control design for AWTB at ARDEC are presented. We have also developed several experimental setups on flexible structures at the Control/Robotics Research Laboratory (CRRL) which exhibit similar dynamics and control issues. Several control schemes for flexible pointing systems are being tried at CRRL. These include the trajectory synthesis approach [7] and utilization of piezoceramics for vibration damping [8], to name a few. Other ongoing approaches for flexible targetting systems will be discussed in this paper.

The noncollocated nature of the sensors and actuators complicates the problem of controller synthesis for these structures as the input/state map is not externally feedback linearizable. Furthermore, the distributed parameter nature of the dynamics is an additional complication as it results in an infinite dimensional system. A finite dimensional model which ignores the high frequency modes is reasonable to consider due to the actuator/sensor bandwidth limits. However, control and observation spillover need to be considered.

An important consideration in gun-pointing applications is that significant parameter variations may exist, for example, varying environmental conditions or different barrel configurations. Such variations may be modeled as a disturbance; however, considerable performance degradation may result for unmodeled parameter variations. Most approaches for disturbance reduction result in a high-gain feedback. For flexible gun-pointing systems, due to the non-minimum phase nature of the system, high-gain feedback is not possible and/or desirable. A better approach to handling such plant uncertainties is using adaptive (self-tuning) control schemes. These involve on-line system identification and control, yielding a closed-loop system with reduced sensitivity and improved performance over non-adaptive algorithms.

In this paper, two different control designs incorporating feedforward and feedback compensation for vibration suppression and pointing purposes are proposed. The first scheme is based on a two-stage control design. The inner-loop control performs the base slew, whereas the outer-loop is designed to maintain a good pointing accuracy at the tip. The feedback for the tip pointing accuracy is obtained from the accelerometer mounted at the tip. The outer-loop control is a dynamic compensation derived from Youla's parameterization of stabilizing controllers [9] and frequency shaping techniques [10]. Control designs are based on two and three-mode models of the AWTB.

The second approach utilizes a nonlinear control scheme with an adaptive feedforward compensation. The feedforward controller basically preshapes the reference trajectory for the inner-loop nonlinear control which is based on feedback linearization of the rigid-body motion of the system. It has been shown in [11] that the feedback linearizing control reduces the effect of geometric configuration on the frequencies. Thus, the preshaping scheme applied in conjunction with this inner-loop nonlinear control is more effective for different slew configurations as compared to a linear, independent joint inner-loop PD control. However, in case of *significant* parameter variations, for instance, for different barrel configurations, an adaptive scheme needs to be implemented. A self-tuning frequency domain adaptation mechanism is invoked to adjust the nonlinear controller and the input preshaper to parameter changes. Here, the estimation and control can be carried out simultaneously without the need for any test-slews to generate estimates unlike most adaptive control schemes. Results are presented for the advocated control design implemented on the experimental setup at the Control/Robotics Research Laboratory (CRRL).

2   Description and Modelling of the Flexible Pointing Test-bed at ARDEC

The testbed at ARDEC is designed to simulate real-life targetting systems viz., helicopter and gun-turret systems. The main body of the setup consists of an aluminum disk, appended to which is a replaceable plate which simulates a barrel. The system is actuated by a direct drive brushless DC motor with a variable compliance torque transmission. Figure 1 shows a picture of the setup.
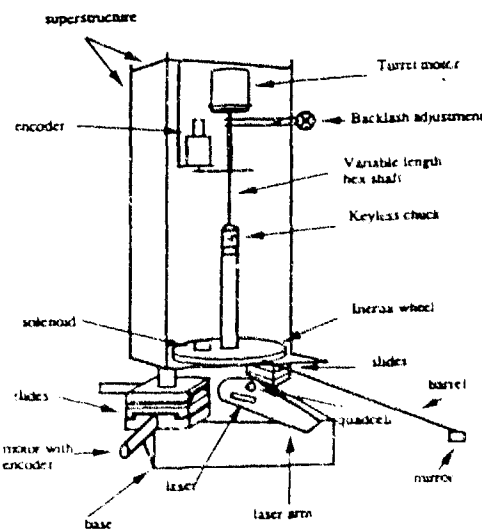

Figure 1: Experimental test-bed at ARDEC.

A piezoelectric accelerometer is mounted at the tip of the barrel. The angular position of the turret motor is measured using an optical encoder with 10.986 millidegree resolution. The angular velocity information

is obtained by differentiating the encoder output. Other accessories are mounted on the setup to emulate practical conditions (e.g., disturbances, variable compliance, backlash, etc.) as closely as possible. These include a variable backlash mechanism, four slide motors for base-motion disturbances, a variable friction mechanism, and a solenoid firing equipment to generate periodic and impulsive type disturbances due to firing. The compliance of the torque transmission unit is $34.0\frac{N-m}{rad}$. Tracking and pointing performance of the barrel can be obtained using a laser-based system mounted on the setup.

Modelling

The modelling of the test bed has been done on similar lines to modelling procedures for flexible multi-body systems. A lumped model for the turret actuator has been obtained taking into account all the associated inertias, viz. inertias of the disk and the coupling assembly, and friction effects. The parameters for different components on the set-up were obtained in technical reports [12,13]. A careful modelling of the turret actuator was done through frequency response analysis. The following table lists the turret actuator parameters obtained from our experiments on the motor.

Parameters of Turret Actuator	
$J_{motor+tach.+enc.}$	$0.0023\ Kg-m^2$
$J_{disk+solenoid}$	$0.08556\ Kg-m^2$
B_{eff}	$0.125\ \frac{N-m}{rad/sec}$
K_{eff}	$0.98\ \frac{N-m}{Volt}$

The barrel is modelled as a flexible beam with the following parameters.

Barrel Parameters	
Length	$0.83\ m$
Thickness	$\frac{1}{16}\ inch$
Mass/Length	$0.177368\ \frac{Kg}{m}$
EI	$2.21857\ N-m^2$

The dynamics of the system are obtained using the extended Hamilton principle. In general, for a weapon pointing system, the barrel exhibits flexibility along both the azimuth and elevation motions. However, for the setup considered here, the barrel flexibility is only in one direction and can be represented by the flexure variable α. Another flexible pointing test-bed with flexure along both azimuth and elevation motions is currently being built. The flexure variable α can be approximated by a finite-dimensional representation ignoring the high frequency modes as follows:

$$\alpha(l,t) = \sum_{j=1}^{p} \eta_j(t)\Phi_j(l). \tag{1}$$

Choosing the first p eigenfunctions (mode-shapes), ϕ_j, as the complete set of functions, the kinetic and potential energy terms are discretized in terms of the generalized coordinate vector $X = [\theta^T | \eta^T]^T$ as follows:

$$T = \frac{1}{2}X^T M(X)X$$

and

$$W_r = \frac{1}{2}X^T K X.$$

Here $\underline{\theta}$ and $\underline{\eta}$ are the rigid body and flexure variables respectively. Using these expressions for kinetic and potential energies and following the Euler-Lagrangian formulation, we obtain the lumped representation of the system including the actuator dynamics

$$\mathcal{M}\ddot{X} + \mathcal{D}\dot{X} + KX = F(X, \dot{X}) + BV_{in} \tag{2}$$

where $\mathcal{M}, K, \mathcal{D}, F$, and B are the inertia, stiffness, damping, vector of non-linearities due to Coriolis and centripetal forces, and input matrix respectively.

Model Validation

A precise validation of the model is done by comparing the frequency response obtained from the simulation model of the set-up with the experimental frequency response shown in Figure 2. A two-mode model of the system is considered here. FFT analysis of the accelerometer data of the open-loop system shows the first two vibrational modes at 4.18 and 22.6 Hz. respectively and the mode due to joint flexibility at 9.17 Hz. The frequency response of the simulated model is given in Figure 3. From the figures, we see that the experimental and analytical frequency responses match quite closely thus validating the accuracy of the model.
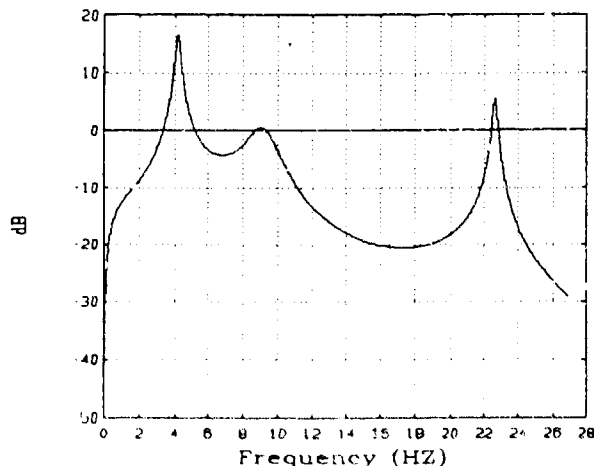

Figure 2: Frequency response of the experimental set-up.

3   Controller Designs and Experimental Results

Rapid retargetting and external disturbances result in the excitation of the vibrational modes of the structure which affects the pointing of the barrel tip. A controller design which maintains a good pointing accuracy during rapid slewing and in face of external disturbances is hence quite essential. Different control designs using structure mounted sensors and actuators are being considered for the experimental testbed at ARDEC.

3.1   Friction Compensation

It was observed that stiction played an important role in the performance of the turret motor. It is thus important to identify and compensate for this nonlinearity. Different techniques for friction compensation can be utilized. One possible approach is to feed narrow pulse signals to the motor at zero speed instants. The sign and magnitude of the pulse corresponds to the minimum voltage required to turn the motor in
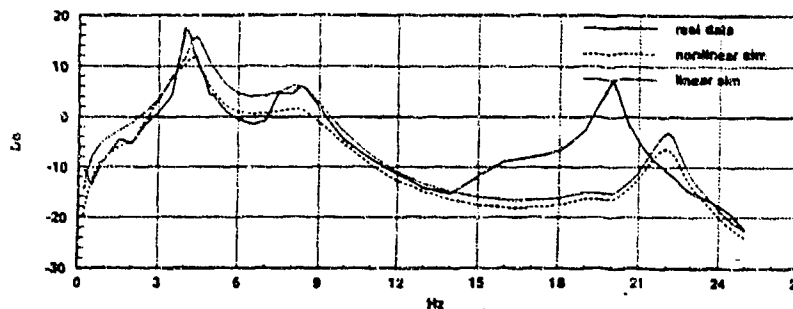
Figure 3: Frequency response of the simulated model.

that direction. Another approach which has proven quite effective is to incorporate a velocity feedback loop around the motor. This has the effect of stiffening up the motor and hence help in overcoming friction.

3.2   Dynamic Compensation Based on Youla's Parameterization

A two-stage control design is considered in this paper. The inner-loop controller is a joint based controller for tracking a desired slew trajectory. The PD gains for the inner loop were chosen to be -4.0 and -0.5 respectively. With this choice of the PD gains, a reasonably good performance at the joint is achieved. A step slew maneuver of 0.5 radians is completed in 0.6 seconds with a critically damped joint response. However, significant vibrations are noticed at the barrel tip resulting in poor pointing accuracy. To damp out the barrel vibrations, an outer-loop controller is designed. The controller designed here is a dynamic compensator based on the linear system model with the PD control in the inner-loop. The feedback utilized here is from the accelerometer mounted at the tip of the barrel. The design is based on Youla's parameterization of stabilizing controllers [9]. To increase the bandwidth for tracking, a prefilter C_r was placed on the command signal. The two degree of freedom linear controller is depicted in Figure 4. C_w is designed for stabilization and could also be used for decoupling [14].
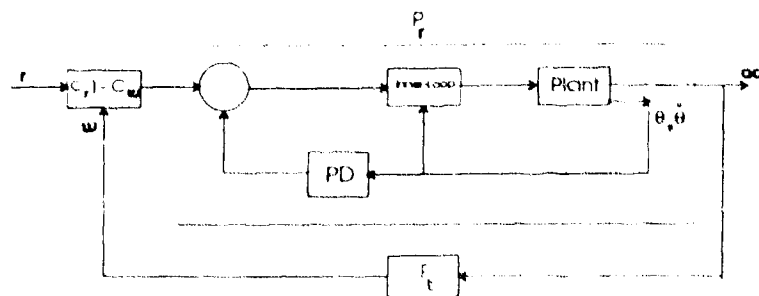

Figure 4: Two-degree-of-freedom control structure.

The generic transfer function of the test-bed retaining n_m vibrational modes of the barrel, from input

actuator voltage to the end-point acceleration under the PD control is given by:

$$\frac{acc(s)}{V_{in}(s)} = \frac{s^2 \Pi_{i=1}^{n-m}(s^2 - \alpha_i^2)}{(s^2 + 2\zeta_a \omega_a s + \omega_a^2)(s^2 + 2\zeta_c \omega_c s + \omega_c^2)\Pi_{i=1}^{n-m}(s^2 + 2\zeta_i \omega_i s + \omega_i^2)} \tag{3}$$

where subscripts a and c correspond to the modes corresponding to the actuator and the compliance respectively. Note that the plant is nonminimum phase. Hence, high gain feedback schemes cannot be utilized for vibration compensation and disturbance rejection. A two mode model of the flexible barrel is considered for the dynamic compensator design.

The parameters of the transfer function under the PD control corresponding to 3 are given by: $\alpha_1 = 58.48$, $\alpha_2 = 192.35$, $\zeta_a = 1.2$, $\omega_a = 75.67$, $\zeta_c = 0.73$, $\omega_c = 4.16$, $\zeta_1 = 0.037$, $\omega_1 = 26.68$, $\zeta_2 = 0.0054$, $\omega_1 = 142.02$. The vibrational modes are lightly damped (with damping ratios below 10%). A dynamic compensator is now designed to increase the damping of the first mode to 40% as well as maintaining the stability of the second mode. For this purpose, the controller must roll-off sufficiently fast so that the second mode is not excited. The following controller transfer function was obtained:

$$G_c(s) = \frac{17.1233(s^2 + 22s + 146)}{s^2 + 80s + 2500} \tag{4}$$

The effect of the above compensator on the system modes is shown by the root-locus plot of Figure 5.
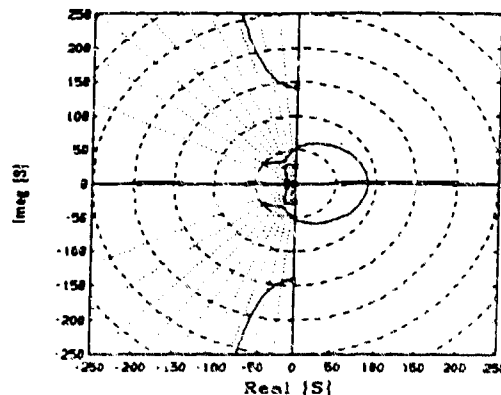

Figure 5: Root-locus plot using the dynamic compensator.

Experiments were conducted to study the barrel tip performance using the above controller. The solid plot in Figure 6 shows end-point response of the compensated system for a 0.5 radian slew maneuver. The response is compared with the case where only a PD control is utilized (refer to dotted plot in Figure 6). The plots show an improvement in tip-performance for the case where the dynamic compensator is utilized as compared with the PD control only. Utilizing the dynamic compensator, the end-point vibrations using the dynamic compensator are damped out in 1.3 seconds for a 0.6 second, 0.5 radian slew maneuver, whereas the vibrations are sustained for about 8 seconds for the same slew under the PD control. The joint behaviour using dynamic compensation is shown in Figure 7. The slight oscillations at the joint compensate for vibrations at the tip.
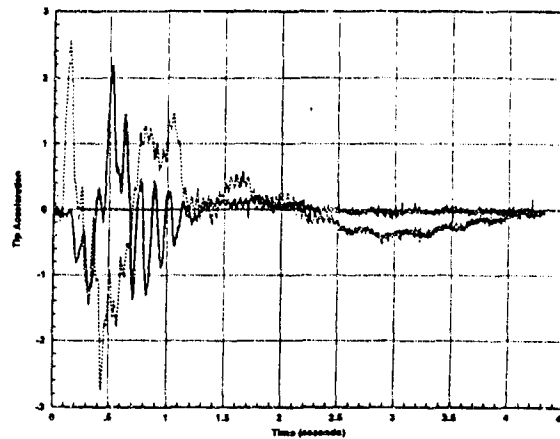
Figure 6: Tip performance with and without dynamic compensation for a 0.5 radian slew.
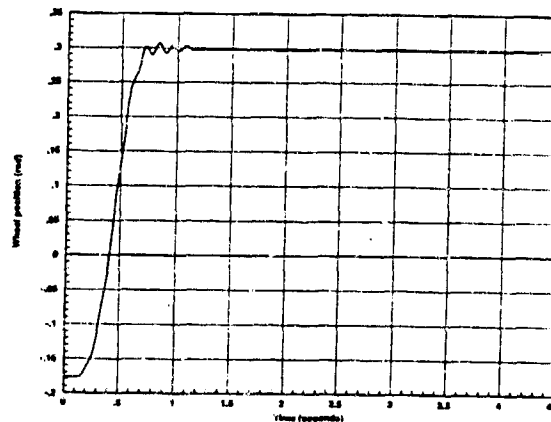

Figure 7: Joint trajectory under dynamic compensation.

3.3 Adaptive Nonlinear Feedback and Feedforward Compensation

As was mentioned before, an important consideration in gun-pointing applications is that significant parameter variations may exist, for example, varying environmental conditions or different barrel configurations. For robustness to such variations, an adaptive scheme utilizing a nonlinear feedback and feedforward control is proposed next. The dynamics of a flexible gun-pointing system with azimuth and elevation motions is similar to that of a flexible two-link arm. The experimental results presented here are for the adaptive scheme implemented on the two-link flexible arm at CRRL.

3.3.1 Nonlinear Control with PD Inner-Loop

The nonlinear control design is derived from the asymptotic expansion analysis for flexible structures derived in [15]. The expansion was performed by embedding a small purturbation parameter in the distributed

parameter model and performing an asymptotic expansion. The small parameters are $\epsilon_i = \frac{m_i L_i^3}{E_i I_i}$. The choice of these parameters signifies that as the barrel becomes shorter or as the bending stiffness becomes larger, the perturbation parameter becomes smaller. In turn, this corresponds to the fact that as this parameter vanishes the barrel behaves as if it were rigid. It was shown [15] that the flexure variable was of order ϵ. Furthermore, analytical representation of flexural variables can be obtained through the asymptotic expansion approach. The $\mathcal{O}(1)$ linearizing control turns out to be identical to the computed-torque controller for a rigid gun-pointing system, since as $\epsilon \to 0$, the barrel behaves as if it were rigid. The rigid-body dynamics

$$\mathcal{M}_r \underline{\ddot{\theta}} + \mathcal{D}_r \underline{\dot{\theta}} = F_r(\theta, \dot{\theta}) + B_r V_{in}$$

can be linearized using the following control law

$$B_r V_{in} = \mathcal{M}_r \underline{v} + \mathcal{D}_r \underline{\dot{\theta}} - F_r(\theta, \dot{\theta})$$

where the entries v_i of v are given by

$$v_i = -K_{p_i}(\theta_i - \theta_{iref}) - K_{d_i}(\dot{\theta}_i - \dot{\theta}_{iref}) + \ddot{\theta}_{iref}.$$

Since this control eliminates the nonlinearities in the $\mathcal{O}(1)$ dynamics, the performance is expected to be better as compared to the case of a linear rigid body controller. Furthermore, cancellation of some of the nonlinearities would reduce the configuration dependence of the barrel frequencies. Also, the nonlinear control results in smaller and smoother actuator torques. These facts have been discussed in detail in [11] for multi-link flexible arms, and are extended in the sequel for application of the adaptive input preshaping scheme. However, application of the non-linear control would still result in significant vibrations induced at the end-point of the barrel. For further suppression of tip-vibrations, the input preshaping technique is employed. Implementation of the input preshaping scheme, requires an estimate of the vibrational frequencies. To this effect, the tip acceleration signal is utilized. This measurement can be easily obtained by mounting an accelerometer at the tip of the barrel or considering the frequency content of the turret position or velocity signals.

3.3.2 Input Preshaping

The input preshaping scheme adjusts the input command to the manipulator so that vibrations are eliminated. This is achieved by convolving impulses with the reference signal [16]. Implementation of the input preshaping scheme, requires an estimate of the vibrational frequencies of the system for which the tip acceleration signal is utilized. The details on the input preshaping scheme are given in [16,17,11].

The important assumptions upon which the input preshaping scheme is based on are that the system be linear and time-invariant. These assumptions do not hold for a multi-axis flexible pointing system as a result of which the input-preshaping scheme would not be as effective in vibration suppression for such systems. However, since the aforementioned nonlinear control alleviates the effects of some of the nonlinearities resulting in a *close to* linear system, the input preshaping scheme has been shown to be effective. The results for flexible-link manipulators are presented in [11].

3.3.3 Adaptive Control for Parameter Variations

To increase robustness of the input preshaping and nonlinear control to parameter and frequency variations, a self-tuning regulator is utilized to identify the modal frequencies and the variable parameters on-line to adjust both the inner-loop nonlinear control and the timing of impulses for input preshaping (Figure 8).
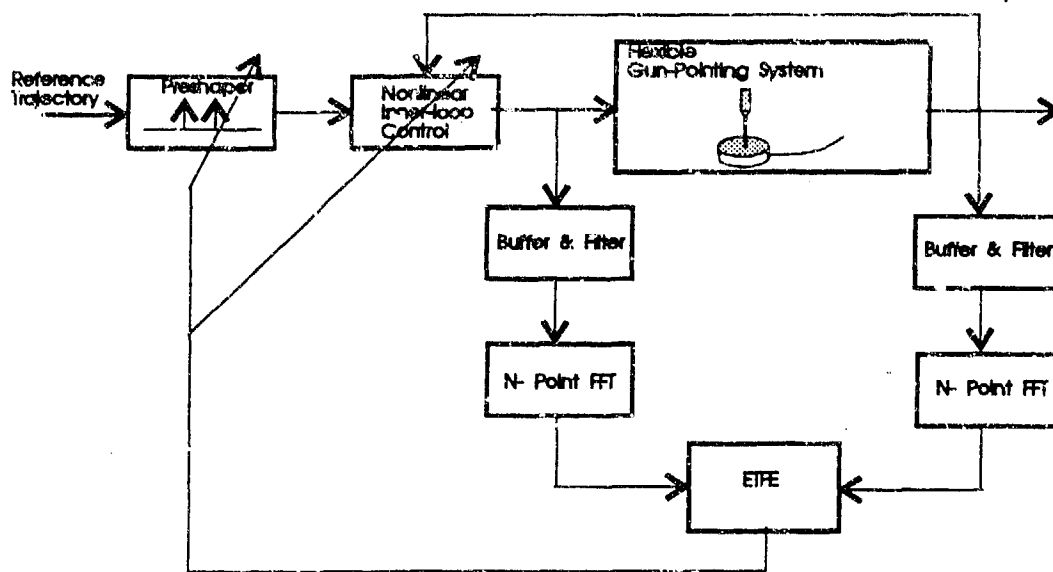
Figure 8: Block diagram for implementation of the adaptive nonlinear control and preshaping.

The input signal $u(n)$ and output $y(n)$ are accumulated into buffer memories to form N-point data blocks. These blocks are then transformed by N-point Fast Fourier Transforms (FFTs) to their equivalent frequency transformed blocks U, Y at the kth time instant. A simple yet effective representation for transfer function identification is the so called- Empirical Transfer Function Estimate (ETFE) [18]. A non-recursive updating scheme for the transfer function in the frequency domain, at a given time k, is utilized in the manner $H_i(k) = Y_i(k)/U_i(k)$, $H_{N-i}(k) = H_i^*(k)$, for $i \in \{0 \leq i \leq \frac{N}{2}, U_i(k) \neq 0\}$, where i corresponds to i^{th} bin in the frequency domain, and $H_i^*(k)$ is the complex conjugate of $H_i(k)$.

A recursive implementation of this idea is possible via the Time-varying Transfer Function Estimation (TTFE) method [1?]. This is basically an extension of the ETFE by performing a Recursive Least Squares on the frequency bins. The TTFE technique can be used to reduce the variance of the estimated frequency response. The adjacent frequency bins $H_i(k), H_j(k)$ are correlated through the relation

$$H_i(k) = \frac{\sum_{j=(i-\Delta_i)\bmod N}^{(i+\Delta_i)\bmod N} \varepsilon_j^i H_j(k)}{\sum_{j=(i-\Delta_i)\bmod N}^{(i+\Delta_i)\bmod N} \varepsilon_j^i} \tag{5}$$

which indicates that the estimate $H_i(k)$ is related to all the adjacent frequencies within a modulus Δ_i with a corresponding weight ε_j^i for the frequency point ω_j.

The critical information for control purposes sought by frequency domain methods is the location of poles and zeroes of the assumed *linear slowly time-varying* transfer function. These locations correspond to the peaks and the valleys of the estimated magnitude response. Due to the lightly damped nature of the flexible-structures, these locations are easily recognizable with the TTFE technique, even with low signal-to-noise ratios. For the case of large signal-to-noise ratios, however, the simpler non-recursive ETFE technique is quite effective, as has been shown in the ensuing experimental results.

3.3.4 Experimental Results

As was stated before, a flexible gun-pointing system with azimuth and elevation motions exhibits similar dynamics to a two-link flexible arm. The experimental results presented here are for the flexible two-link arm at CRRL. The variable parameter in this case is the payload at the tip

The advantages of the $\mathcal{O}(1)$ feedback linearizing control over the linear PD control were discussed in detail in [11]. It was shown that the end-point performance under the $\mathcal{O}(1)$ feedback linearizing control is significantly better than that using an independent joint PD control, since the nonlinearities in the $\mathcal{O}(1)$ dynamics are eliminated in the case of the nonlinear control. The nonlinear control also offers other advantages over the linear, independent joint PD Control in terms of smaller and smoother actuator torques and reduced configuration dependence of modal frequencies. The following tables list the modal vibration frequencies for different configurations of the arm locked under these controls, thus validating the reduced configuration dependence of vibrational frequencies under the nonlinear control as compared to the linear, independent joint PD Control. Due to these advantages of the nonlinear control, the ensuing adaptive preshaping technique is applied with the $\mathcal{O}(1)$ linearizing control in the inner-loop.

Table II

Independent Joint PD Control		
Configuration (degrees)	Mode I (Hz.)	Mode II (Hz.)
(0,0)	0.852	8.731
(0,30)	0.826	8.549
(0,45)	0.792	8.265
(0,60)	0.762	8.080
(0,90)	0.731	7.896

Table III

$\mathcal{O}(1)$ Linearizing Control		
Configuration (degrees)	Mode I (Hz.)	Mode II (Hz.)
(0,0)	0.788	8.404
(0,30)	0.786	8.388
(0,45)	0.783	8.362
(0,60)	0.780	8.320
(0,90)	0.776	8.284

The modal frequencies of vibration under the $\mathcal{O}(1)$ feedback linearizing control were estimated for different payloads. The estimates of vibrational modes were obtained using the ETFE algorithm since the signal to noise ratio of the data was quite high and distinct peaks were obtained corresponding to the lightly damped vibrational modes. The data for system identification was sampled at 250 Hz, while the control loop was executed at 1KHz. Radix-2 decimation in frequency (DIF) 2048 point FFT algorithms were implemented for estimation. The FFT routines were written in assembler for faster execution. The TMS320C30 DSP board was utilized for FFT computations, with a '486 based PC as the host for control loop computations. The architecture and special instruction set of the DSP provide efficient and optimized implementation of the FFT routines. The table of twiddle-factors (sines/cosines) for FFT computations was prepared and stored separately in DRAM and linked with the FFT routines to provide faster execution speed. The execution time for each set of 2048 point FFT computations was 1.2 msec. Since the FFT computations were done in parallel with the execution of the control-loop on the host '486, the time for FFT computations was not a critical factor governing the sampling time. The crucial factors governing the

accuracy of the frequency estimates are the sampling time of data and the number 'N' of points of FFT. For small frequency quantization error, the sampling frequency must be smaller and 'N' must be as large as possible. It was found that a sampling rate of 250Hz and 2048 points of FFT gave reasonably precise estimates so as to delineate the variation of vibrational frequency with payload. Figure 9 shows typical plots for the FFTs computed on the accelerometer data for the no payload and 100 gm. payload case. Similar plots were obtained for other sets of payloads.
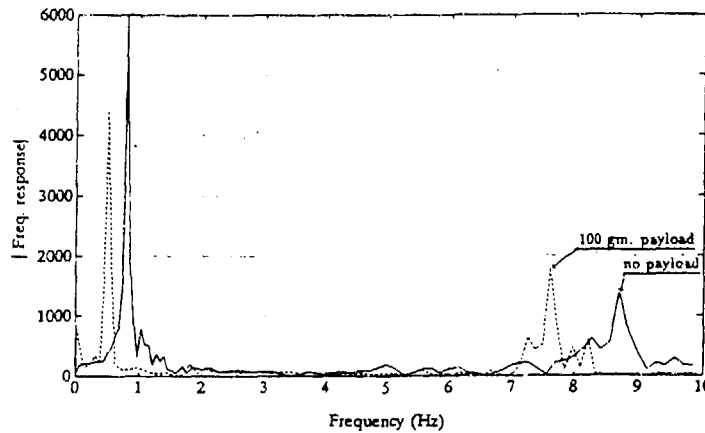

Figure 9: FFT plots obtained from the accelerometer data for the arm locked in (60,60) degree configuration under the $O(1)$ linearizing control for $m_p=0$ (solid plot); 100 gm. (dashed plot).

The frequencies of the vibrational modes are next correlated with the variable parameters; in this case the variable payload. A fourth order polynomial relation between the payload and vibrational modes was obtained. The details on correlation of the first and second vibrational modes with payload are given in [20]. Figures 10 and 11 show the variation of the second and first modes with payload.
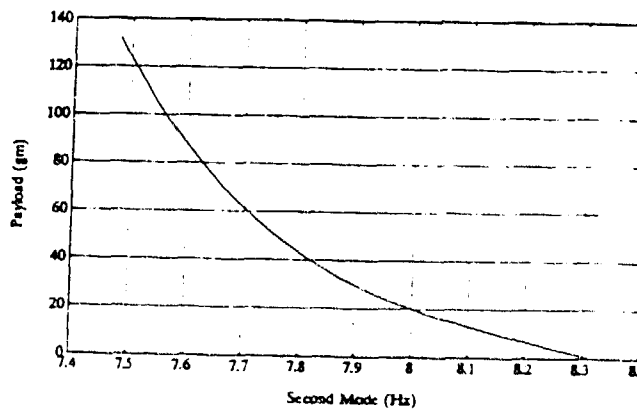

Figure 10: Payload estimation based on the second vibrational mode.

An accurate estimation of payload plays a significant role in the performance of the $O(1)$ feedback linearing control scheme. The performance of the feedback linearizing control can deteriorate if it is designed based on incorrect payload estimates. Experiments were conducted to study the performance of the nonlinear
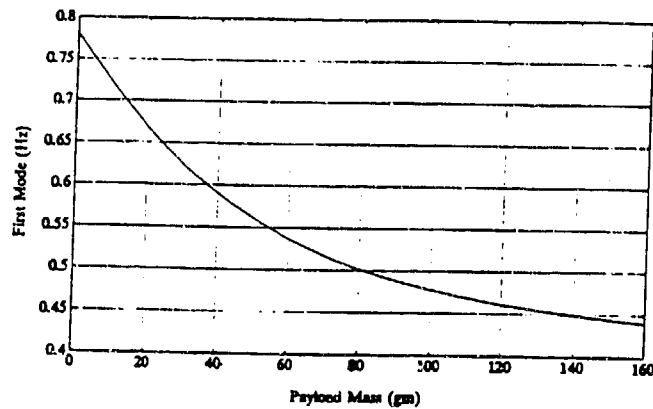
Figure 11: Variation of first vibrational mode with payload.

control for different payload estimates. The plots in Figure 12 indicate an improvement in the end-effector performance when the controller was obtained using the correct payload estimate generated online. The solid plot in the figure shows the end-point response under the $\mathcal{O}(1)$ linearizing control for a (0-60,0-60) degree[1] slew with a 100 gm. payload attached, whereas the control is generated using an estimate of 0 gm. An adaptive estimation of this payload results in an improved end-point response as shown by the dashed plot in Figure 12.
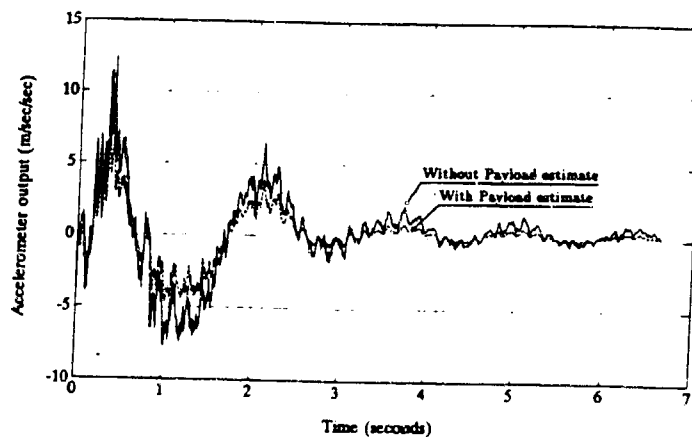

Figure 12: Tip vibrations under $\mathcal{O}(1)$ linearizing control with and without payload estimate (m_p =100gm).

Next, a two pulse preshaping controller obtained from the adaptive estimation of the first mode and payload, was applied to the two-link arm for the (0-60,0-60) degree slew under the $\mathcal{O}(1)$ linearizing control. Although the experimental plots show two vibrational modes, only the dominant first mode is targeted using the preshaper. A 30 gm. payload was applied in this case. The plots in Figure 13 show the results in sequence with and without preshaping. Next, a 100 gm. payload was attached to the tip. The result of applying the adaptive preshaper for this case is shown by the last plot in Figure 13. The plots validate the fact that an adaptive preshaper can effectively improve the end-point performance for varying payloads.

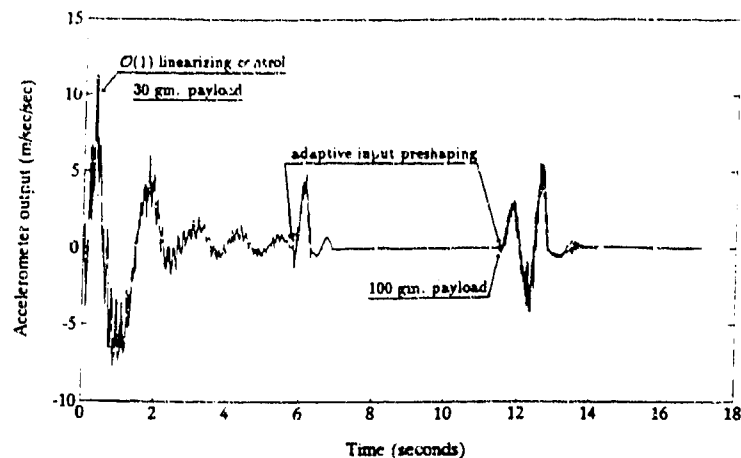[1]The notation ($-,-$) implies (θ_1^{ini}-θ_1^{ref},θ_2^{ini}-θ_2^{ref}).

Figure 13: Adaptive preshaping for different payloads.

4   Conclusion

In this paper, control of flexible weapon pointing systems using feedback and feedforward schemes is considered. Experimental results using dynamic feedback from the accelerometer mounted at the tip indicate that superior performance and robustness properties can be attained using such a compensation. Adaptive input precompensation and nonlinear feedback for robustness enhancement is discussed. The initial experimental effort at CRRL using this scheme shows that significant improvement on tip pointing performance alongwith robustness to parameter variation can be achieved. This effort is on going at ARDEC.

References

[1] J. N. Juang, L. G. Horta, and H. H. Robertshaw, "A slewing control expe·· ment for flexible structures," in *Proceedings of the 5th VPI& SU/AIAA Symposium on Dynamics and Control of Large Structures*, (Blacksburg, Virginia), June 1985.

[2] F. Khorrami and I. Zeinoun, "Rapid slewing and pointing of a flexible structure with embedded piezoceramics," in *Proceedings of the Conference on Smart Structures and Materials*, (Albuquerque, New Mexico), Feb. 1993.

[3] Ü. Özgüner, F. Khorrami, and A. İftar, "Two controller design approaches for decentralized systems," in *Proceedings of the AIAA Conference*, (Minneapolis, Minnesota), pp. 237–244, Aug. 1988.

[4] R. C. Montgomery and N. Sundararajan, "Identification of the dynamics of a two-dimensional grid structure using least squares lattice filters," *Journal of the Astronautical Sciences*, vol. 33, no. 1, pp. 35–47, 1985.

[5] M. J. Balas, "Feedback control of flexible structure," *IEEE Trans. on Automatic Control*, vol. AC–23, pp. 673–679, 1978.

[6] F. Khorrami and S. Jain, "Nonlinear control with end-point acceleration feedback for a two-link flexible manipulator: Experimental results," *Journal of Robotic Systems*, vol. 10, pp. 505–530, June 1993. (To appear).

[7] J. Rastegar, Q. Tu, and F. Tangerman, "Trajectory synthesis and inverse dynamics formulation for minimal vibrational excitation for flexible structures based on trajectory patterns," in *Proceedings of the 1993 American Control Conference,* (San Francisco, CA), June 1993. (To appear).

[8] F. Khorrami, I. Zeinoun, and E. Tome, "Experimental results on active control of flexible-link manipulators with embedded piezoceramics," in *Proceedings of the 1992 IEEE International Conference on Robotics & Automation,* (Atlanta, GA), 1993. (To appear).

[9] D. C. Youla, H. A. Jabr, and J. J. Bongiorno, "Modern wiener-hopf design of optimal controllers part II: The multivariable case," *IEEE Transactions on Automatic Control,* vol. AC-21, June 1976.

[10] F. Khorrami and Ü. Özgüner, "Frequency-shaped cost functional for decentralized systems," in *Proceedings of the 27th Conference on Decision and Control,* (Austin, Texas), pp. 417–422, Dec. 1988.

[11] F. Khorrami, S. Jain, and A. Tzes, "Experiments on rigid-body based controllers with input preshaping for a two-link flexible manipulator," in *Proceedings of the 1992 American Control Conference,* (Chicago, Illinois), pp. 2957–2961, June 1992.

[12] S. P. Bhat, "ATB-1000 user guide," tech. rep., Integrated Systems Inc., Santa Clara, California, June 1991.

[13] M. Mattice, N. Coleman, and S. Banks, "Summary of the ARO workshop on the design of real-time controllers," tech. rep., Army Research Laboratory, Picatinny Arsenal, NJ, Aug. 1991.

[14] H. Lee and J. Bongiorno, "Weiner-Hopf Design of Optimal Decoupling Multivariable Feedback Control Systems," *IEEE Transactions on Automatic Control,* 1993. to appear.

[15] F. Khorrami, "Analysis of multi-link flexible manipulators via asymptotic expansions," in *Proceedings of the 28th Conference on Decision and Control,* (Tampa, FL), pp. 2089–2094, Dec. 1989

[16] G. H. Tallman and G. H. Smith, "Analog study of dead-beat posicast control," *IRE Transactions on Automatic Control,* vol. AC-3, pp. 14–21, 1958.

[17] N. C. Singer and W. P. Seering, "Preshaping command inputs to reduce system vibration," *Trans. ASME: J. Dyn., Meas., and Control,* vol. 112, pp. 76–82, Mar. 1990.

[18] L. Ljung, *System Identification Theory For The User.* Englewood Cliffs, NJ: Prentice–Hall, 1987.

[19] A. Tzes and S. Yurkovich, "A Frequency Domain Identification Scheme for Flexible Structure Control," *Trans. ASME, J. Dyn., Meas., and Control,* vol. 112, pp. 427–434, Sept. 1990.

[20] F. Khorrami, S. Jain, and A. Tzes, "Adaptive nonlinear control and input preshaping for flexible-link manipulators," in *Proceedings of the 1993 American Control Conference,* (San Francisco, CA), June 1993. (To appear).

SESSION V

VIBRATIONS AND MATHEMATICAL METHODS

*TITLE: A MODAL SURVEY OF THE M1A1 MAIN WEAPON SYSTEM

Dr. Stephen Wilkerson, Mr. Morris Berman, and Mr. Ting Li
U.S. Army Research Laboratory
ATTN: AMSRL-WT-PD
Aberdeen Proving Ground, MD 21005-5066
(410) 278-6131

*ABSTRACT:

When a tank fires its main weapon system, a complex chain of dynamic events begins. The projectile is accelerated down an imperfect gun tube (gun tubes are never perfectly straight) being forced by the burning propellant gases. During this time, considerable forces and interactions between the projectile and gun tube are possible. In some cases, the response of the two systems (i.e., the projectile and gun tube) are not fully understood. One method of examining the dynamics of these complicated chain of events is to develop straightforward numerical models. As a first step in assuring the accuracy of these models, verification of the assumptions, such as geometry and boundary conditions, must be examined.

This paper discusses an experimental modal survey of the M1A1 main weapon system. Both horizontal and vertical components are examined to find the actual frequencies and mode shapes of the system. A simple numerical model is developed using the finite element method and subsequently compared to the experimental results of the modal survey. A discussion of the system's attributes, as well as the techniques and assumptions used to develop the finite element model are discussed at length. Possible shortcomings in the numerical approximation are outlined as well.

*BIOGRAPHY:
*PRESENT ASSIGNMENT: October 1989 to Present: Research Engineer, The U.S. Army Research Laboratory, Aberdeen Proving Ground, MD 21005-5066.

*PAST EXPERIENCE:

July 1983 to October 1989: Mechanical Engineer, The Naval Surface Weapons Center, 10901 New Hampshire Ave., Silver Spring, MD 20903-5000

1982 to 1983: Aerospace Engineer, Naval Air Systems Command, Washington, DC.

*DEGREES HELD:

The Johns Hopkins University, Baltimore, MD. Ph.D., Department of Mechanics, April 6, 1990. Dissertation title: "A Boundary Integral Approach to Three-Dimensional Underwater Explosion Bubble Dynamics."

George Washington University, Washington, DC. Masters of Science, Structural Engineering, May 1985. Thesis title: "Ship and Submarine Response to an Underwater Explosion." GPA - 3.50.

The Johns Hopkins University, Baltimore, MD. Bachelor of Science, Mechanical Engineering, May 1982, GPA - 3.00.

A MODAL SURVEY OF THE M1A1 MAIN WEAPON SYSTEM

Dr. Stephen Wilkerson, Mr. Morris Berman, and Mr. Ting Li
U.S. Army Research Laboratory
ATTN: AMSRL-WT-PD
Aberdeen Proving Ground, MD 21005-5066
(410) 278-6131

OBJECTIVE

The primary purpose of this modal test was to provide experimental verification for a finite element (FE) model of the M1A1 tank M256 main gun. The FE model is being developed for the gun accuracy improvement program. Major vertical and horizontal rigid body and bending modes of the main gun will be obtained from experimental modal analysis (EMA). The realism of the FE boundary conditions (between the main gun and its supporting structures) may be enhanced by comparison to the EMA model. The secondary objectives of this experiment included measuring the nonlinearity of the gun modal responses and determining, if any, the effects of the hydraulic gun elevation mechanism on the gun dynamics.

TEST SETUP

All of the heat shields on the gun were removed and the accelerometers were attached directly to the gun tube. The accelerometer locations were situated in two lines, 90° apart. This positioning permits one set of vertical data and one set of horizontal measurements to be obtained. In order to resolve the fifth bending mode, 15 locations, 10 inches apart, were chosen from the muzzle to the king nut. Only four locations, due to inaccessibility, were measured within the turret. Table 1 and Figure 1 detail the placement of the measurement locations. The chosen excitation locations were at the muzzle (location 200) and in the king-nut area (location 100). Both vertical and horizontal excitation was utilized. The excitation source was a 50-lb electrodynamic shaker. To ensure uniform energy distribution over the frequency range of interest, a controlled true random signal was utilized as the excitation signal.

SIGNAL PROCESSING

A 16-channel Genrad 2515 spectrum analyzer was utilized to acquire the measurements. Since more than 16 measurement channels were utilized, 2 runs were required for each configuration. Frequency response functions (FRFs) and coherence functions were retained in the final data set. In addition, several auto spectra were also retained to evaluate the excitation signal. The FRFs were collected with the following parameters:

Maximum Frequency	640 Hz
Frame Size	2560 Frequency
Frequency	0.25 Hz
Number of	50
Window Type	Hanning

FRFs collected to assess nonlinearity of the structure utilized a higher frequency resolution in order to detect small frequency shifts.

FINITE ELEMENT MODEL DESCRIPTION

The M256 120-mm gun system consists of a number of important parts which contribute to the system's dynamic characteristics. Figure 2 is a cut-a-way, three-dimensional view showing some of the parts in the cradle assembly area. This figure, as well as the model, do not consider the mantelet or trunnion mounts. This is discussed in the conclusion section of this paper. The objective of this first FE model, namely, a beam element representation of the system, was to make a simple, easily modified, numerical model of the M256 gun-recoil system. Then this simple model will be used as a learning tool for more sophisticated FE models in the future. The complicated set of boundary conditions in the system is first examined with the simplistic model. That model is then compared with experiments and improved based on observed discrepancies. Model attributes are incrementally changed until a satisfactory numerical representation of the M256's dynamic characteristics is made. The characteristics (realistic geometric and boundary conditions) of the simple model are then incorporated into more sophisticated and robust three-dimensional FE models which are not so quickly modified or analyzed.
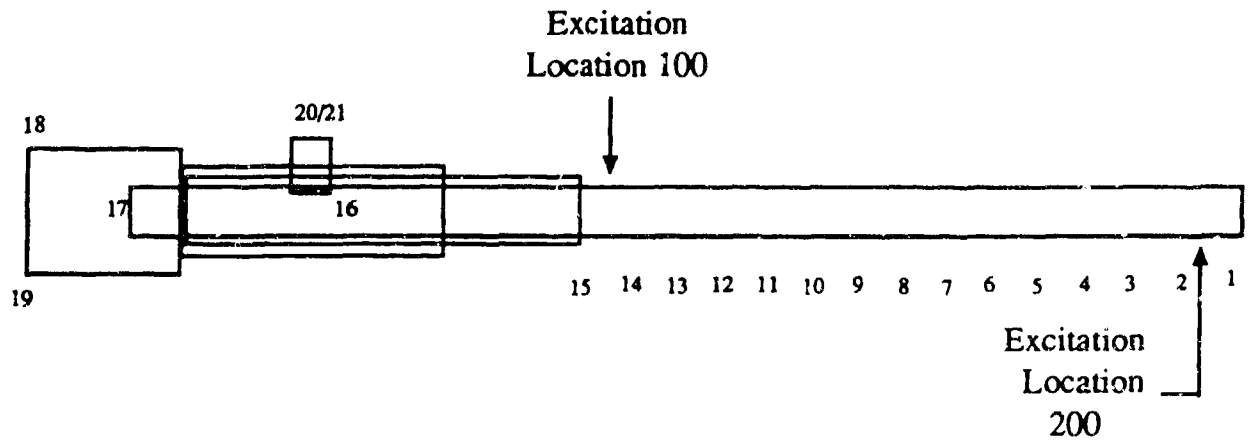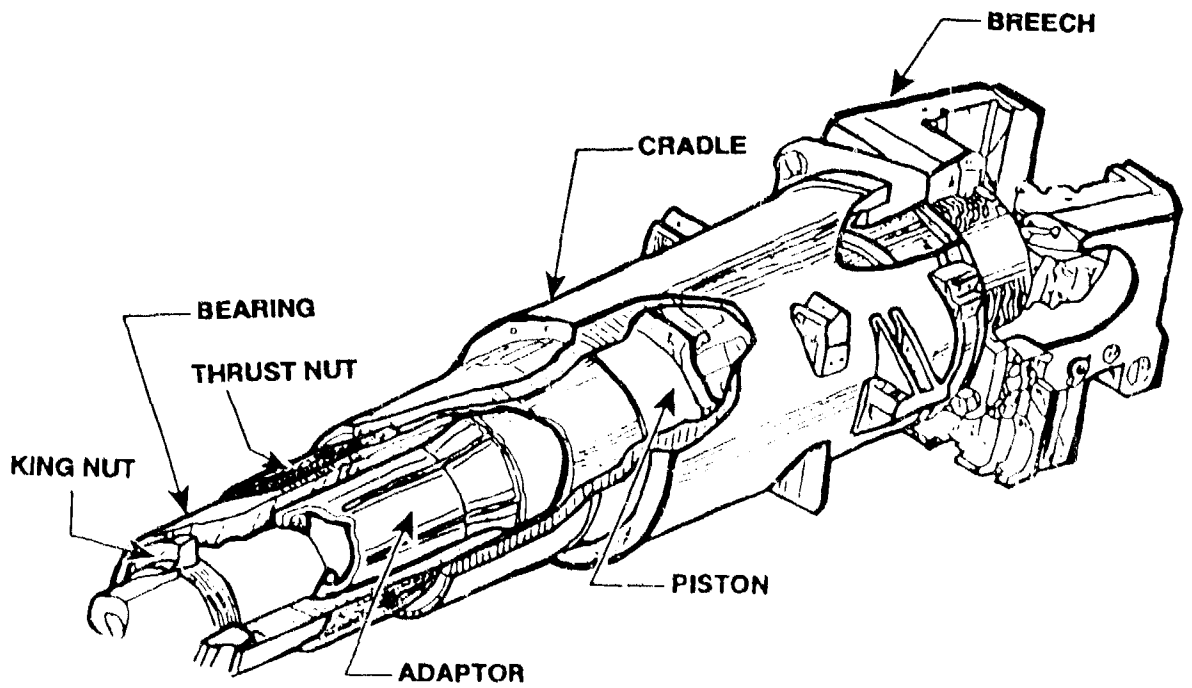
Figure 1. Measurement Location Diagram.

Figure 2. Cut-a-Way View of the M256 Assembly.

Table 1. Measurement Location Dimension

Location No.	Distance From Muzzle	Description of Gauge Location
1	.05	@ Muzzle
2	10.	On Gun Tube
3	20.	On Gun Tube
4	30.	On Gun Tube
5	40.	On Gun Tube
6	50.	On Gun Tube
7	60.	On Gun Tube
8	70.	On Gun Tube
9	80.	On Gun Tube
10	90.	On Gun Tube
11	100.	On Gun Tube
12	110.	On Gun Tube
13	120.	On Gun Tube
14	130.	On Gun Tube
15	135.	On Gun Tube
16	180.	On Cradle
17	208.7	On RF of Gun Tube
18	218.	On Breech
19	218.	On Breech
20	~191.	On Elev. Mechanism
21	~191.	On Elev. Mechanism

After examining the mechanical drawings of the system and then examining its associated parts, as well as its assembly and disassembly, a simplified model of the M256 consisting of what is believed to be critical components was developed. The critical components were combined into nine individual parts. These nine essential parts are highlighted in Figure 2. Additionally, Figure 3 shows a computer aided design/computer aided manufacture (CAD/CAM) drawing of the simplified parts which are going to be included in the FE model. For the beam element model, each of the parts is represented using concentric cylindrical beam elements with associated properties to the pieces shown in Figure 3. However, the adapted bearing, king-nut, and thrust nut were included in the beam element model of the piston. The piston was assumed to be rigidly attached, as was the breech, to the gun tube at the contact points. Similarly, the cradle, which supports the structure, was modeled, at first, with rigid contact points where the piston rested on the cradle's surfaces (Wilkerson et al. 1993). Initially, it was understood that this would be insufficient for modeling the recoil system's motion. Nonetheless, it was assumed that this would be sufficient for finding the first five vertical flexural frequencies and associated mode shapes correctly. Due to clearances between the piston and cradle in the real system, that was not the case. In particular, the contact
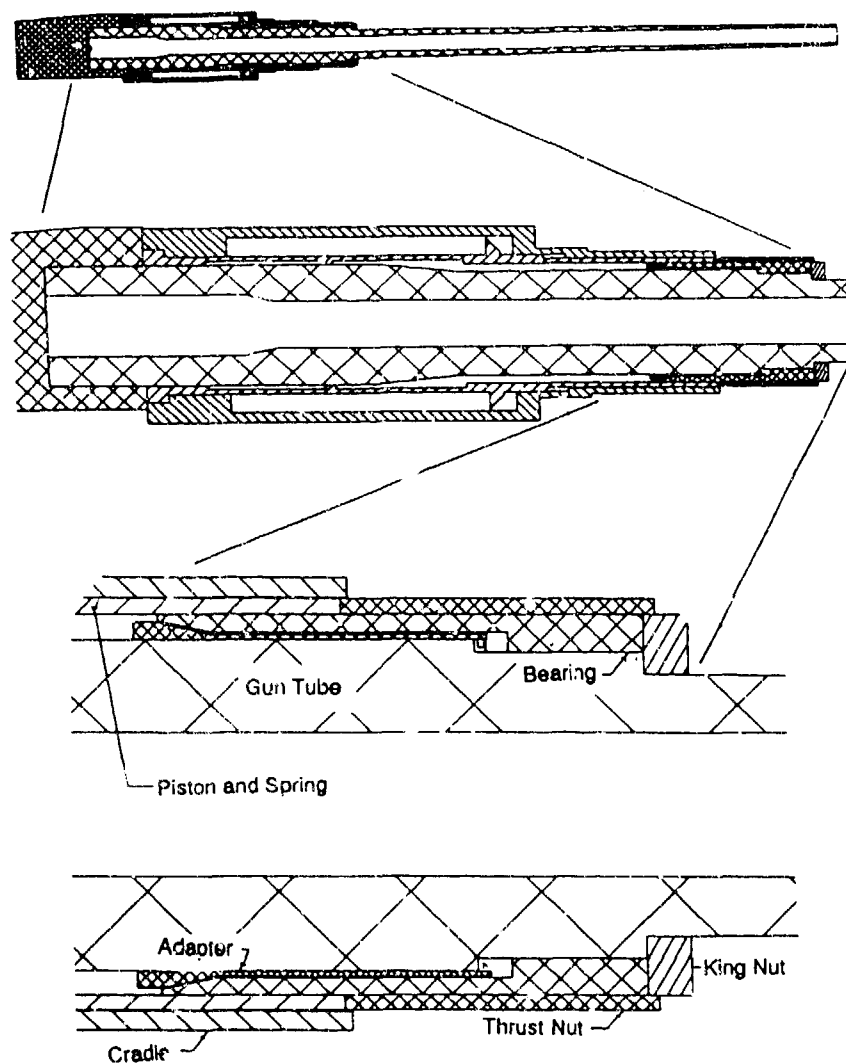
Figure 3. CAD/CAM Simplification of M256 Critical Components.

points, where the piston slides inside the cradle, required more flexibility than the rigid connections allowed. Subsequently, the rigid connections were replaced by gap elements. These gap elements gave the system more flexibility and better approximated the actual systems dynamic characteristics. (Note: gap elements are simulated with regard to the vertical modal analysis as spring-dashpots, but act as gap elements allowing the system to recoil.) The final model consisted of the gun tube, breech, piston, and cradle assembly. The cradle was simply supported at the same location as the trunnions. The elevating mechanism was approximated in the model as a spring-dashpot which attached between the cradle assembly and a rigid mount.

In order to check the FE model's geometric properties, it was assembled incrementally. First, the model of just the gun tube was compared with some experimental results of the free-free vibrational frequencies of that part (Rowekamp 1987). This was a good initial check of the model's most important part, namely, the gun tube. Afterwards, the breech, piston, and cradle assembles were included in the model. Results comparing experimental frequencies to the numerical model's predictions are given in Table 2 and Figure 4 for the gun tube alone. A comparison of the experimental and numerical model for the assembled M256's frequencies and mode shapes are given in the results section of this paper.

Table 2. Gun Tube ..ly - Free-Free

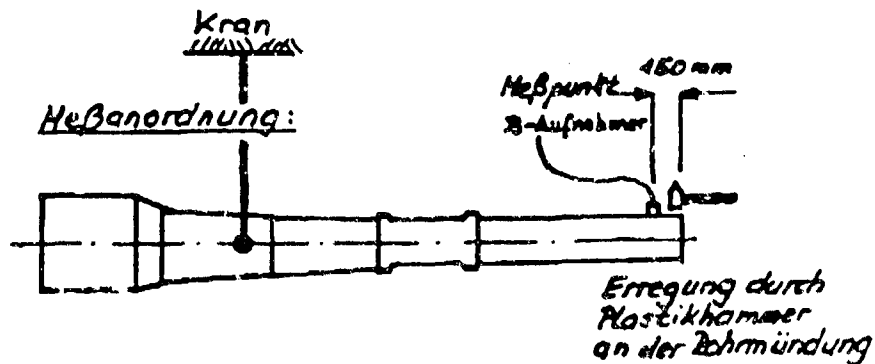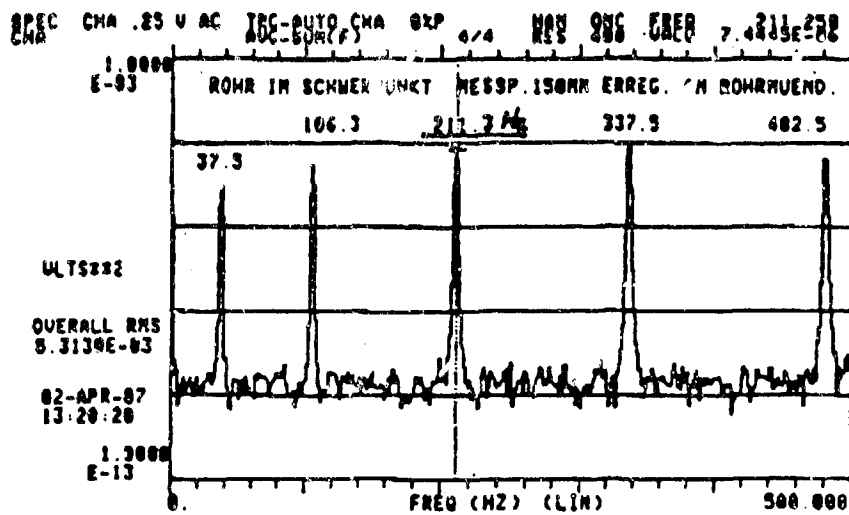| Mode Shape	Experimental Results	Beam Model		3-D Model	
		Freq.	Error	Freq.	Error
1	37.5	36.4	3.0	35.6	5.3
2	106.3	106 1	0.2	104.5	1.75
3	211.3	214.4	1.5	210.6	0.34
4	337.0	394.3	3.6	336.5	0.15
5	482.5	510.3	5.8	488.6	1 3

Figure 4. Frequency Response Function for Gun-Tube in Free-Free Mode.

RESULTS

The natural frequencies found in the experimental analysis for vertical and horizontal flexural components are summarized in Tables 3 and 4. Table 3 also summarizes the numerical predictions from the model in the vertical direction. No numerical predictions have been made for the horizontal flexural components. The mode indicator functions for frequency ranges 0-200 Hz and 200-640 Hz are given in Figures 5 and 6 for the vertical and Figures 7 and 8 for the horizontal, respectively.

Table 3. Vertical Modal Parameters

Mode Label	Flexural Mode	Damping % of Critical	Magnitude in Driving Point, FRF	Frequency		Error (%)
				Exp.	Calc.	
1	—	2.724	11.24	11.6	10.5	11
2	1	1.096	20.02	30.27	31.4	3.8
3	2	4.074	4.78	79.5	85.7	7.8
4	3	1.127	4.37	182.	178.9	1.7
5	4	1.143	4.66	276.	287.9	4.0
6	4	2.355	11.9	376.	366.	2.8
7	5	2.392	1 37	495.	455.	8.8

Table 4. Horizontal Modal Parameters

Mode Label	Damping % of Critical	Magnitude in Driving Point FRF	Frequency (Hz)
1	1.33	25.65	16.57
2	2.17	2.36	40.85
3	4.74	4.96	73.8
4	2.33	1.88	134.6
5	2.49	2.56	170.5
6	4.69	1.70	240.0
7	3.91	.925	332.4
8	.512	1.24	342.0
9	2.53	3.24	479.4

A small nonlinearity study was performed on the M256 cannon. This study was performed in only the vertical configuration with the excitation force at the king nut. Data was collected at six excitation levels (1 lb, 4 lb, 6.2 lb, 8 lb, 10 lb, 12.5 lb) from 0 Hz to 320 Hz at seven locations. The first two modes were quite linear. Modes 3 (80 Hz) and 4 (182 Hz) manifested some interesting effects (Figure 9). Both of these modes showed two lower amplitude peaks preceding the frequency from which the modal parameters were extracted. In the nonlinearity study, these initial peaks showed a large variation in amplitude and frequency compared to the third (primary) peak. This observation is a good indicator that the system can exhibit nonlinear behavior, particularly in certain frequency ranges. No attempt was made to simulate this behavior with the numerical model. Further, it is very likely that the two peaks observed are primarily the result of boundary conditions (interfaces between tube and piston, or piston and cradle) and not the dynamic properties of the M256 tube itself.
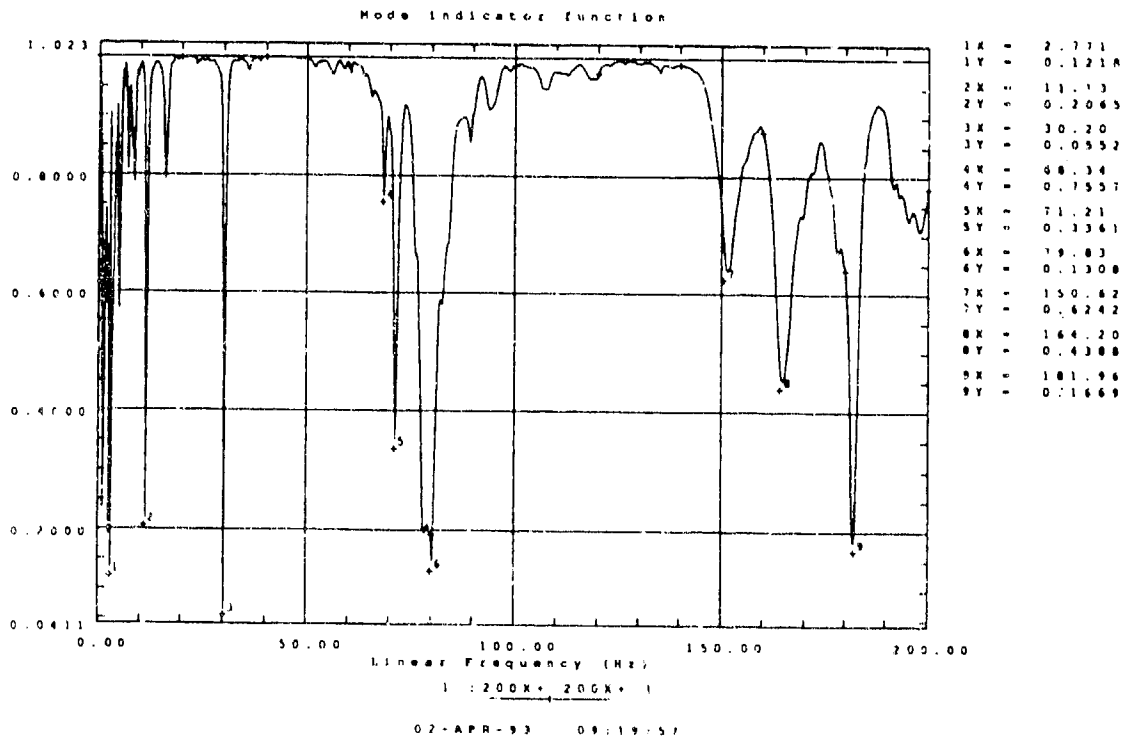
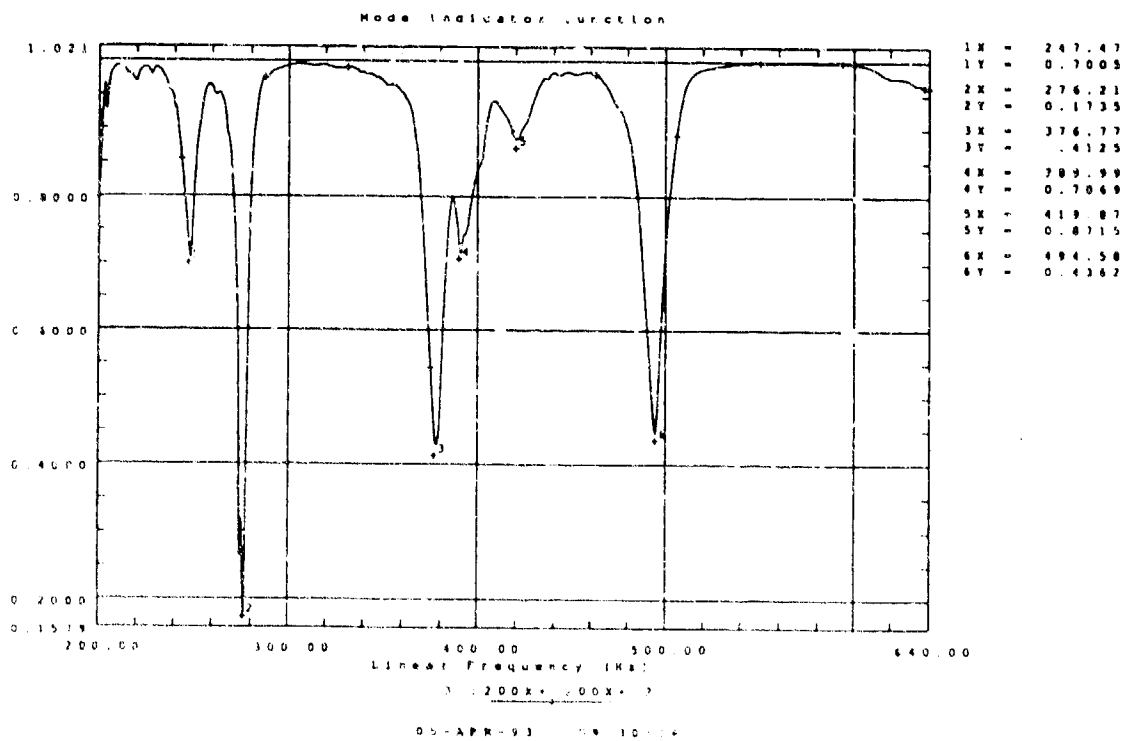Figure 5. Mode indicator function for vertical frequencies out to 200 Hz.

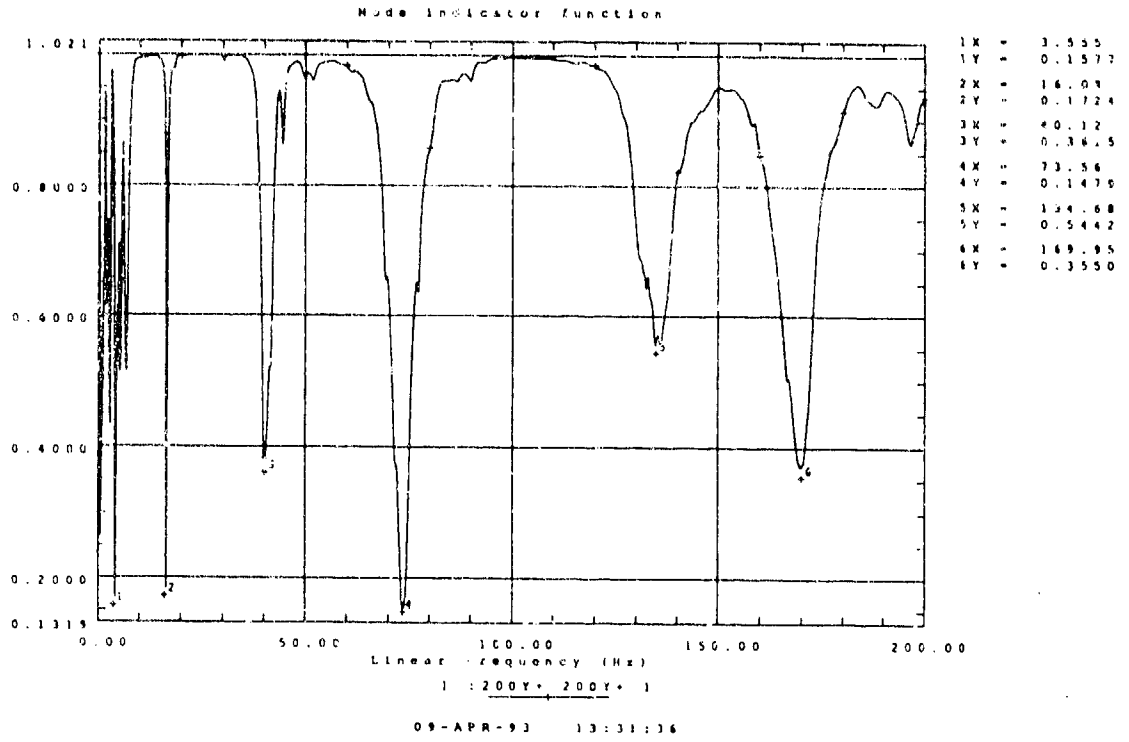Figure 6. Mode indicator function for vertical frequencies from 200 to 640 Hz.

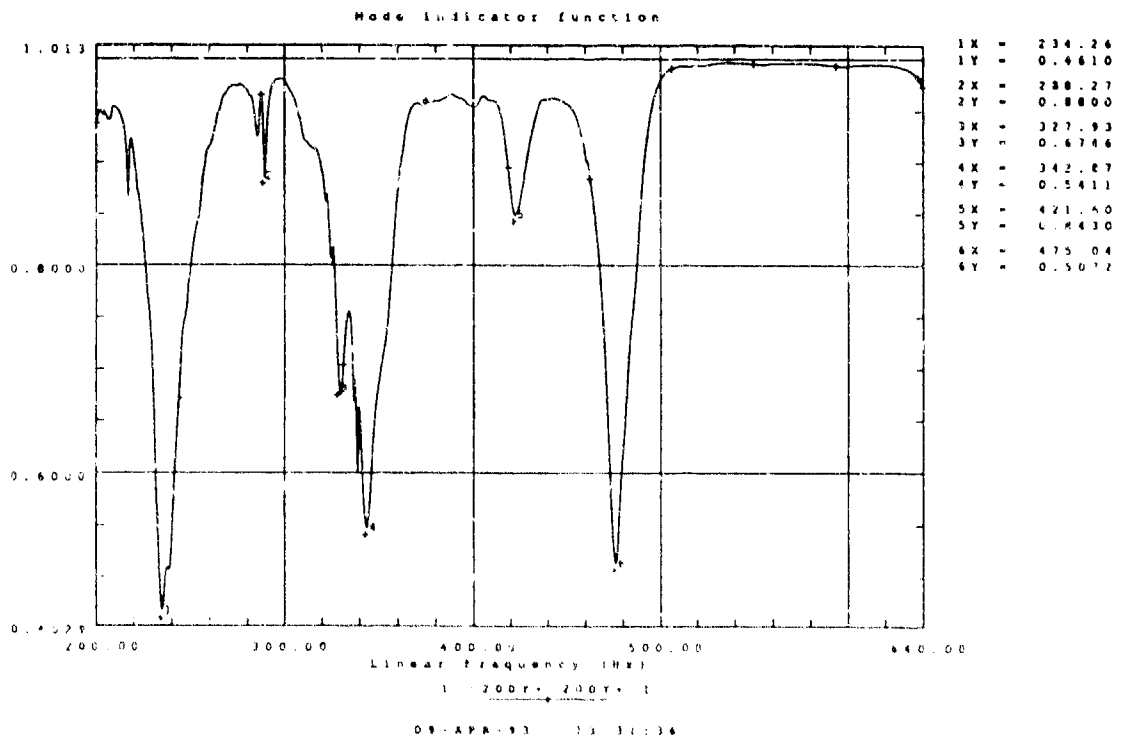Figure 7. Mode indicator function for horizontal frequencies out to 200 Hz.

Figure 8. Mode indicator function for horizontal frequencies from 200 to 540 Hz.
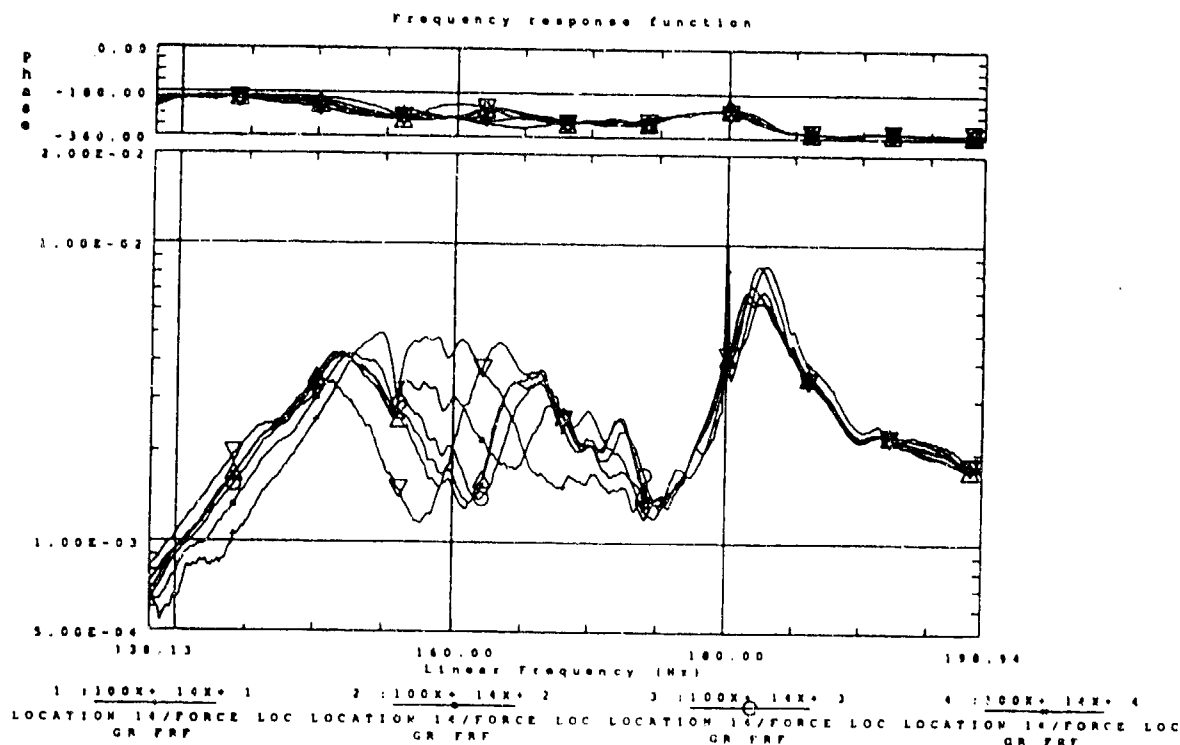
Figure 9. Nonlinear study, mode indicator function for 0 to 320 Hz.

Figures 10–16 show the numerical and experimental mode shapes for each of the first seven major frequencies obtained. As can be seen in the figures, the early mode shapes (i.e., rigid body mode and the first two flexural frequencies) compare with the numerical predictions quite well. However, due to insufficient accessibility in the cradle region of the M256, the shapes of flexural modes 3–5 are not completely resolved in the experiment. Consequently, the actual assumed shape is penciled into the experimental figures based on the estimations made by the numerical model.

CONCLUSIONS

The confidence in the accuracy of the modal parameters for the first five modes of the vertical configuration and the first four modes of the horizontal configuration is high. There is significantly less confidence in the accuracy of the damping and frequency values for the higher order modes. In the vertical configuration, several modes appear in the mode indicator function and frequency response functions which were not extracted in the modal analysis. These modes have mode shapes which are extremely similar to mode shapes which were extracted. It is believed that these extraneous modes result from complex boundary conditions and are not present in the dynamics of the tube itself, but only the system as a whole (tube, plus its supporting structure).

The current FE model shows reasonable agreement with the experimental results. However, the experimental mode shapes for flexural modes 4 and 5 must be resolved to determine if the numerical predictions are correct and to verify that there are multiple flexural mode 4 shapes. This can only be done by increasing the number of sensors on the gun tube inside of the cradle. This could have been accomplished by attaching the sensors to the inside of the gun tube; however, it was not thought of at the time of the test.

There was also a fair amount of difficulty in numerically predicting both the first rigid body mode and the first flexural mode. Both modes are dependent on the spring constant used to simulate the elevating mechanism. A stiffer spring constant makes it easier to duplicate the rigid body frequency while making the first flexural mode too stiff. Therefore, it was
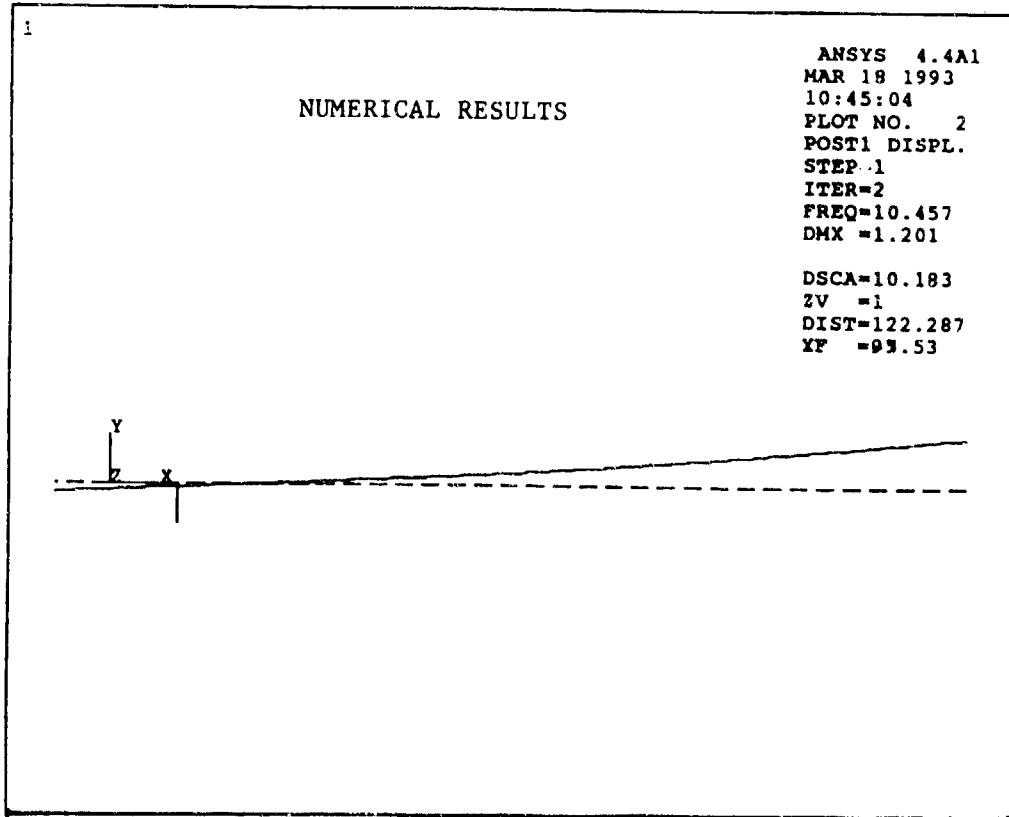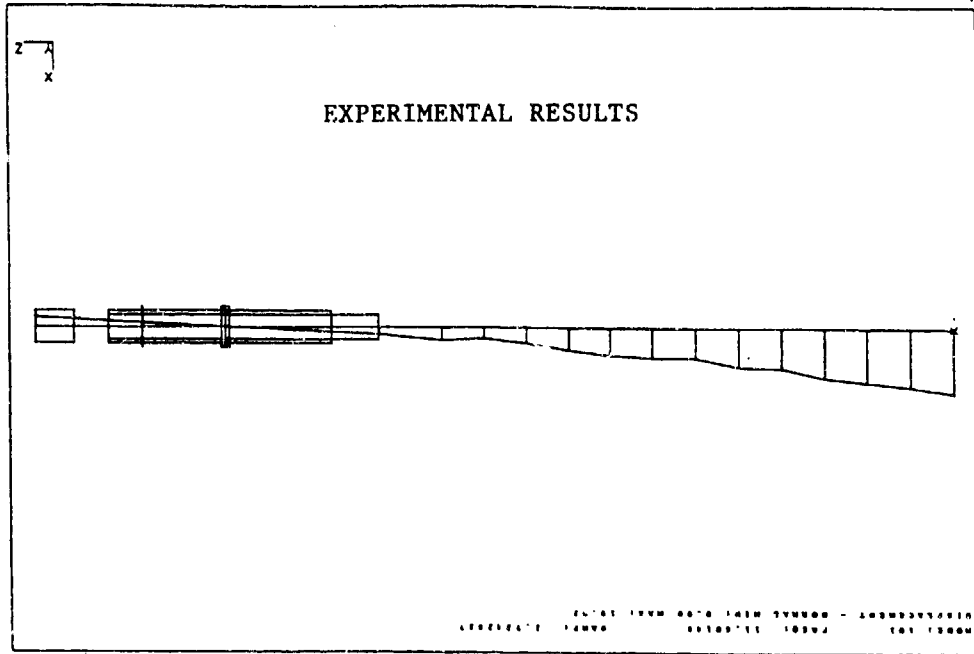
410

Figure 10. Comparison of numerical and experimental vertical mode shapes (rigid body mode)
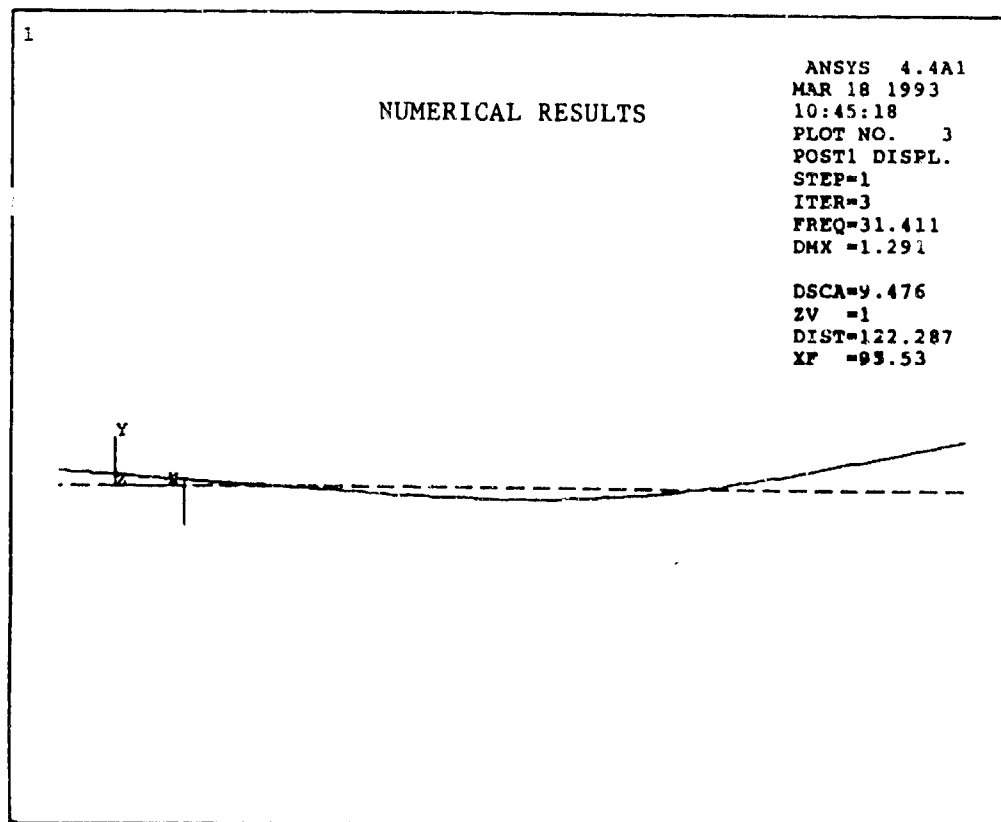
411

Figure 11. Comparison of numerical and experimental vertical mode shapes (first flexural mode).

EXPERIMENTAL RESULTS

NUMERICAL RESULTS

```
                                              ANSYS  4.4A1
                                              MAR 18 1993
                                              10:45:26
                                              PLOT NO.    4
                                              POST1 DISPL.
                                              STEP=1
                                              ITER=4
                                              FREQ=85.74
                                              DMX =1.472

                                              DSCA=8.365
                                              ZV  =1
                                              DIST=122.287
                                              XF  =95.53
```

Figure 12. Comparison of numerical and experimental vertical mode shapes (second flexural mode).
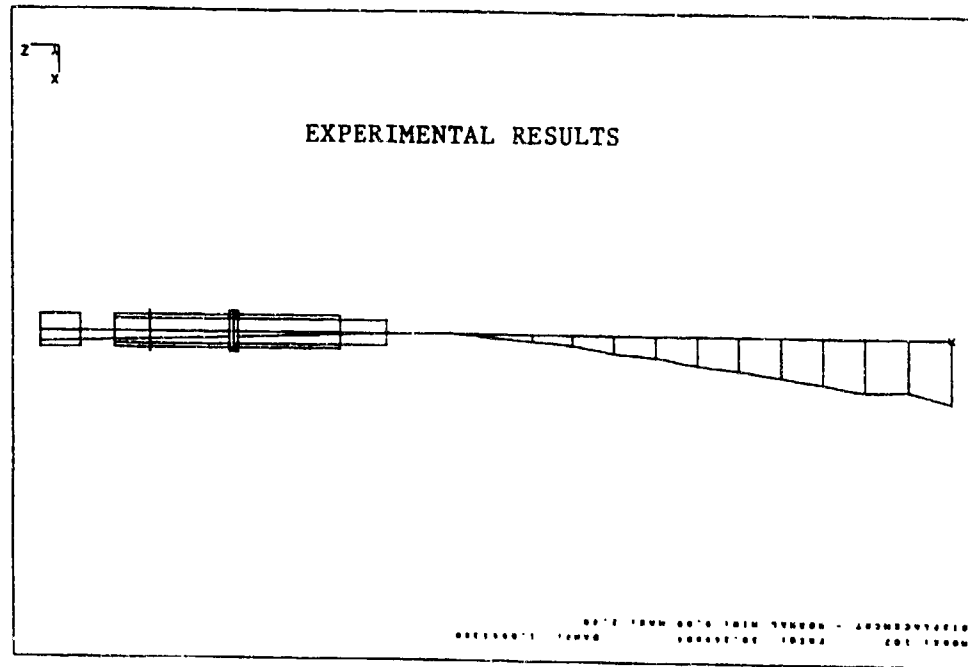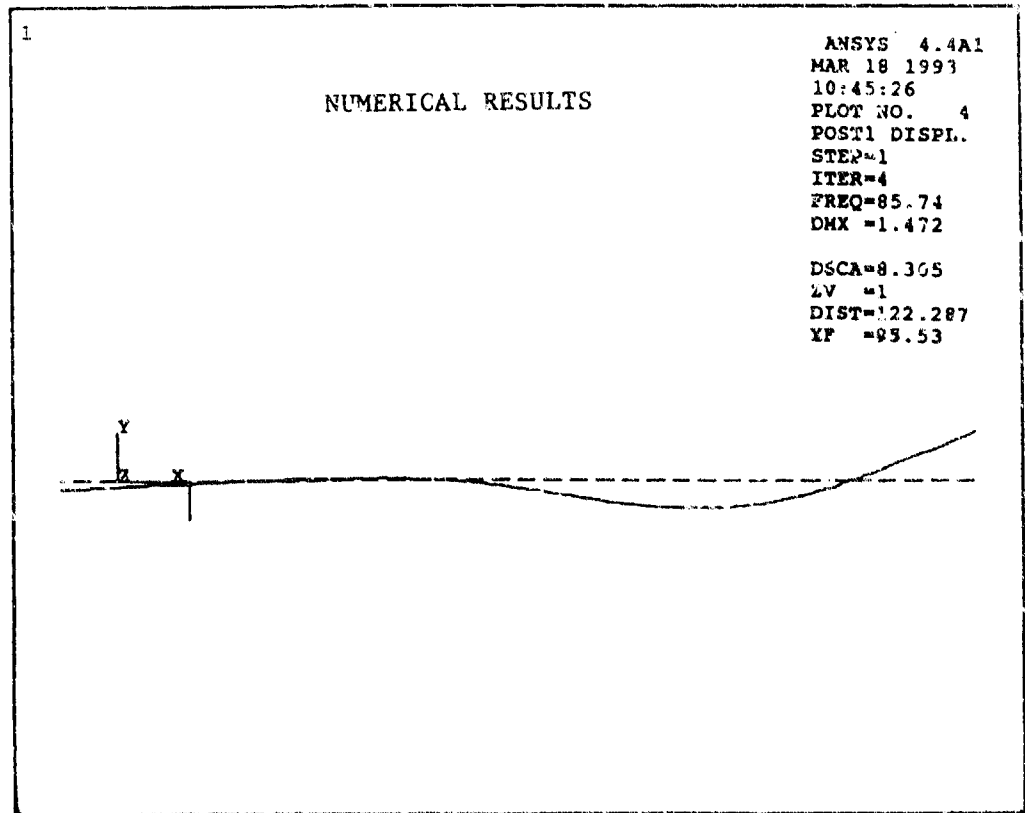
413

Figure 13. Comparison of numerical and experimental vertical mode shapes (third flexural mode).
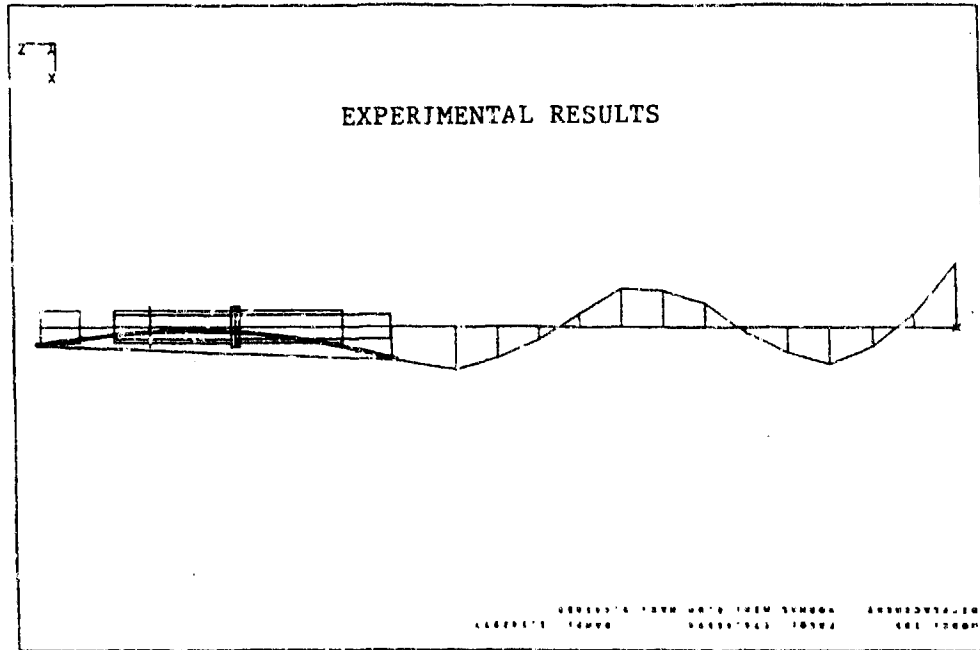
Figure 14. Comparison of numerical and experimental vertical mode shapes (fourth flexural mode).

EXPERIMENTAL RESULTS

NUMERICAL RESULTS

```
ANSYS   1.4A1
MAR 18 1993
10:53:07
PLOT NO.    3
POST1 DISPL.
STEP=1
ITER=7
FREQ=365.945
DHX =0.551369

DSCA=22.179
ZV  =1
DIST=122.287
XF  =95.53
```
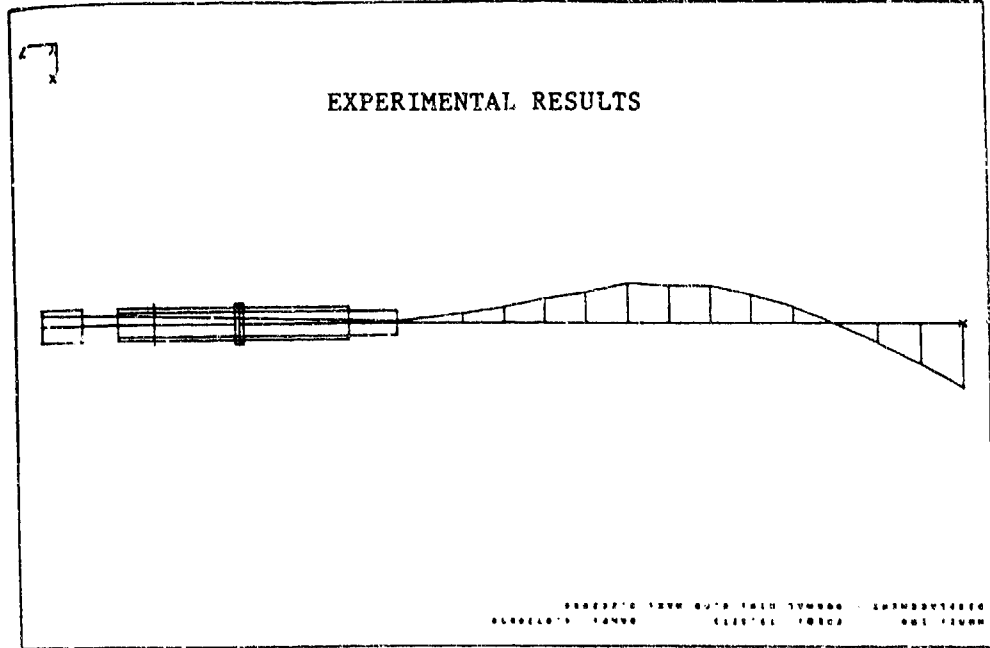
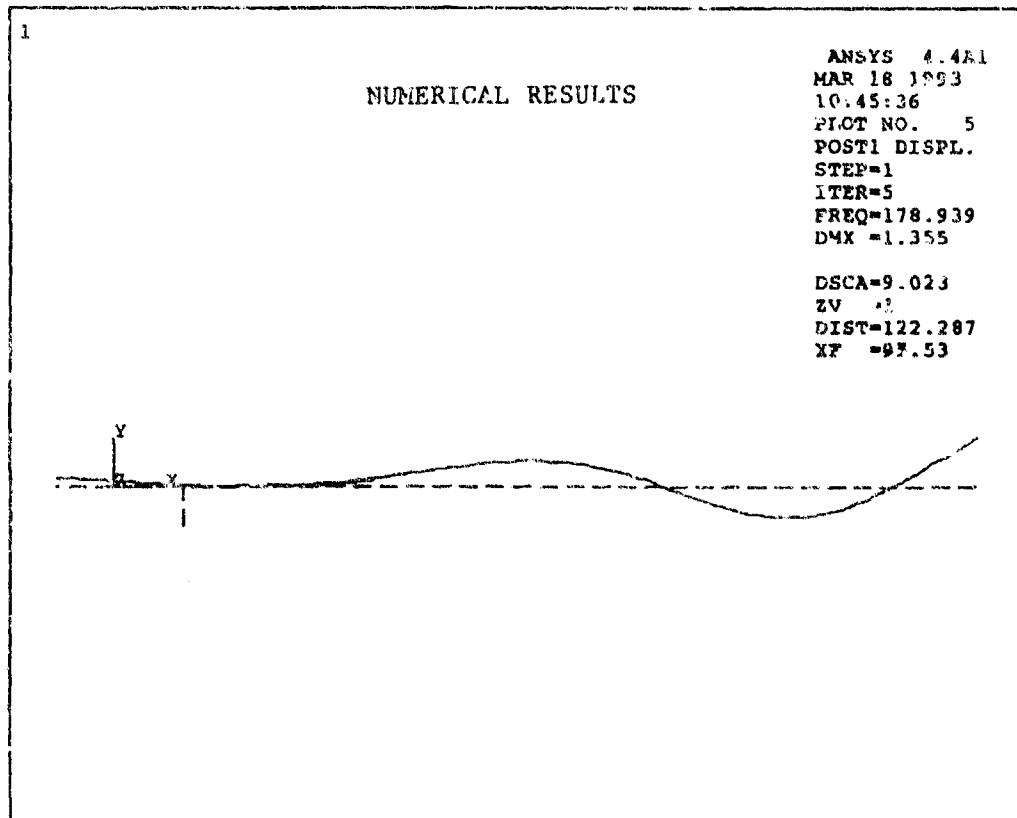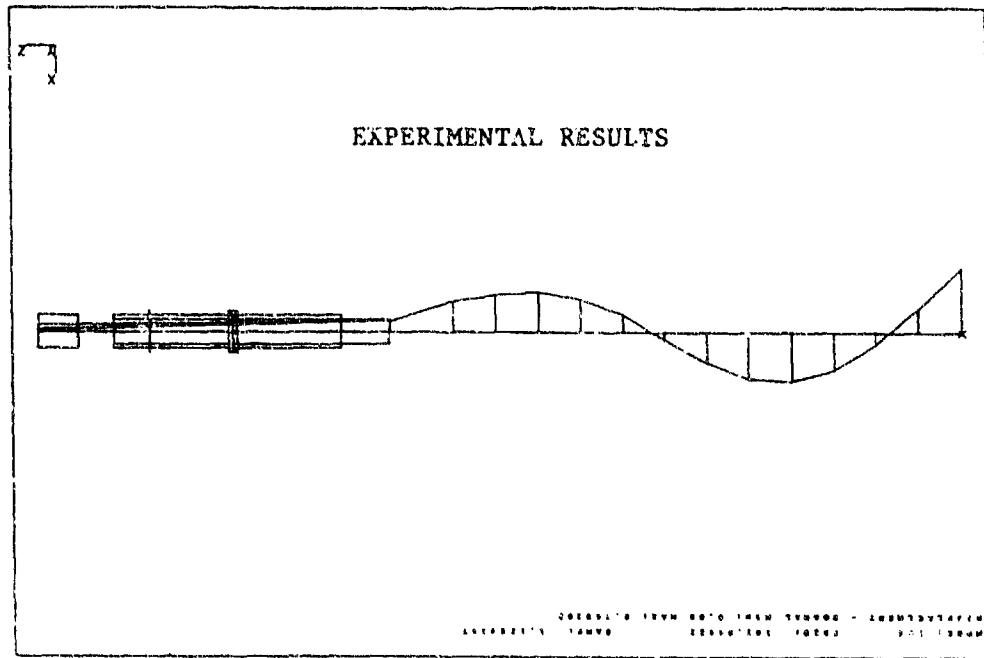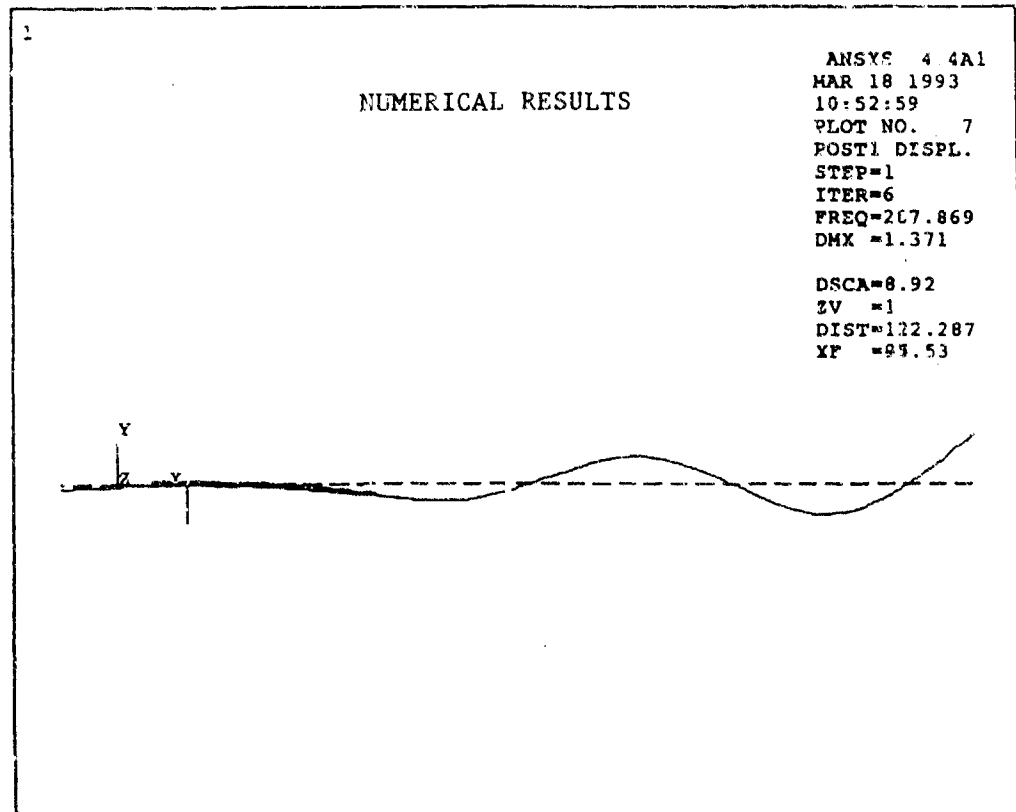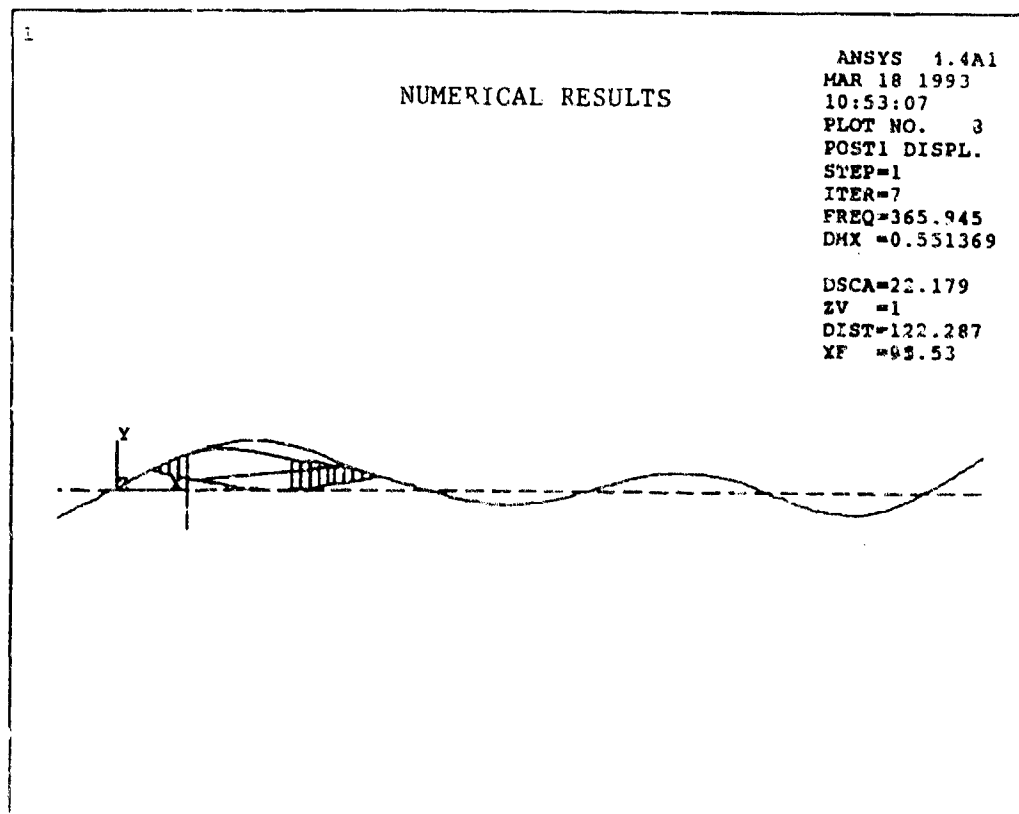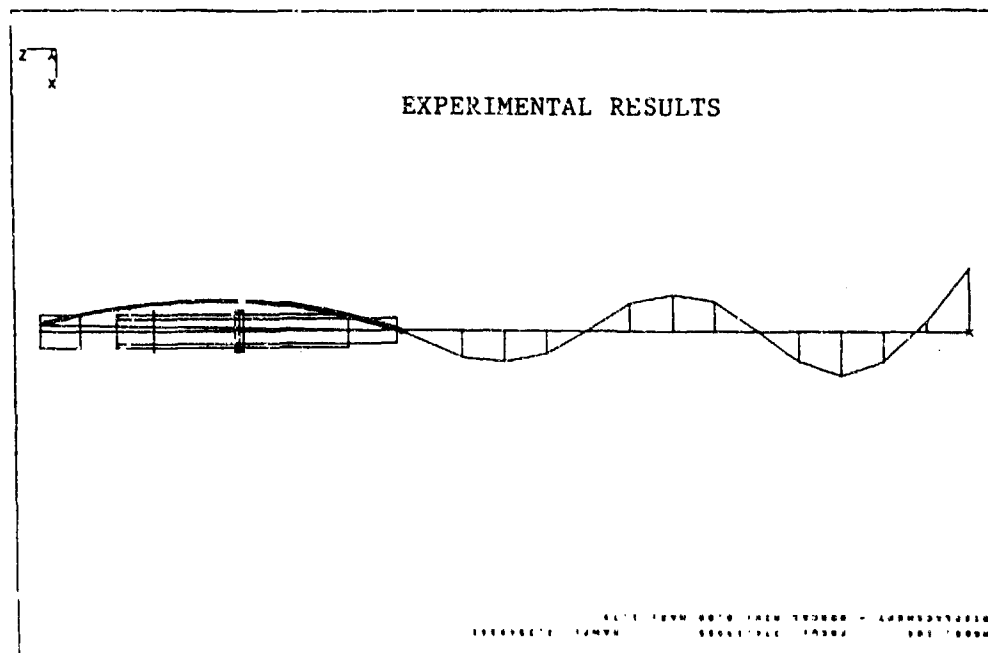Figure 15. Comparison of numerical and experimental vertical mode shapes (fourth flexural mode ?).
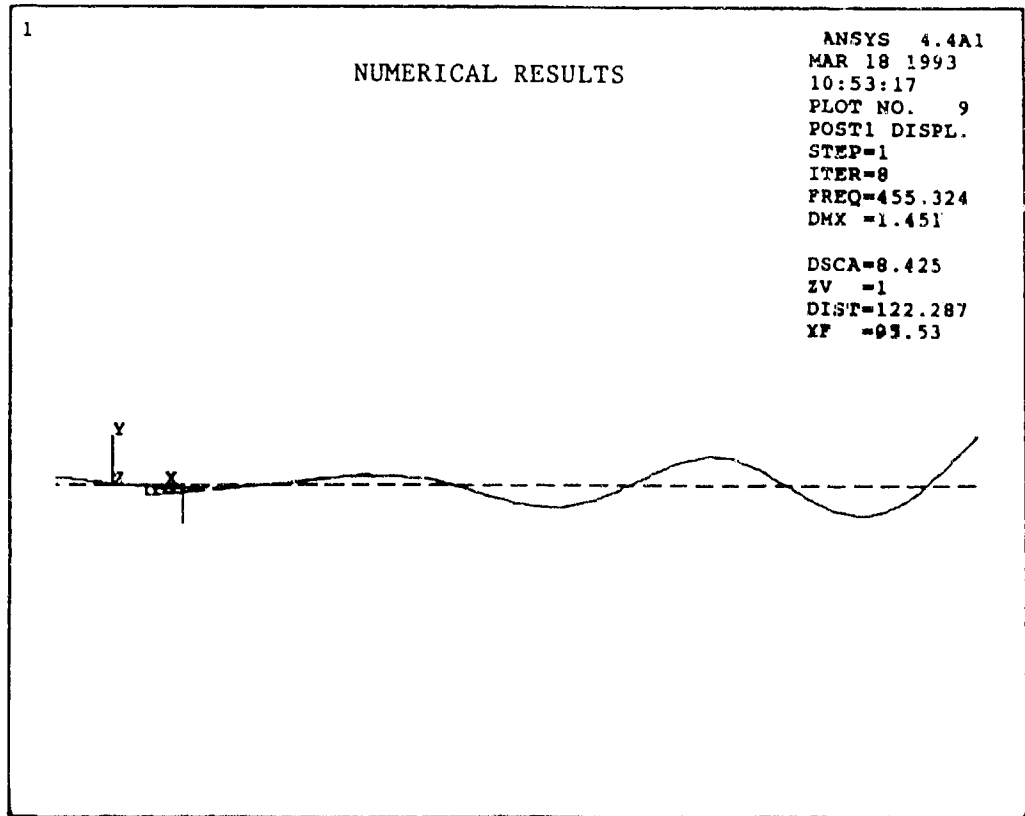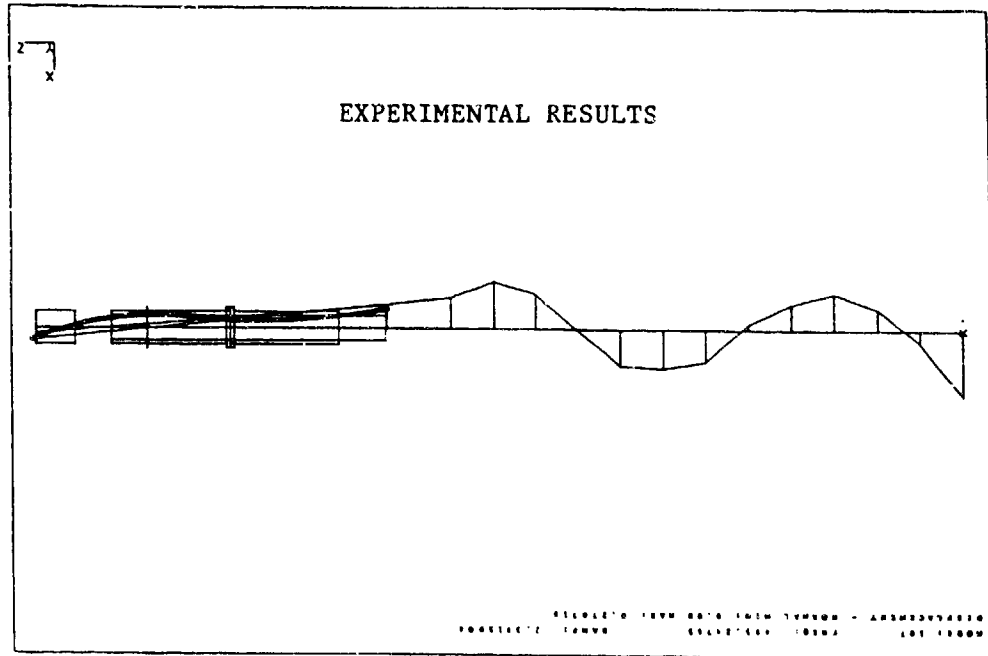
Figure 16. Comparison of numerical and experimental vertical mode shapes (fifth flexural mode ?).

speculated that the trunnions were exhibiting some resistance to rotation and a rotational spring was added at that location, which improved both predictions.

Finally, some of the parts that were not originally represented in the model need to be included. These parts include the thermal shrouds, bore sight, mantelet, and trunnion mounts. Future models will incorporate these parts and hopefully better represent the whole system.

REFERENCES

1. Wilkerson, S. A., et al. "Static Load Test on the M256 System." In print March 1993.

2. Rowekamp, B. J. "120-mm Tank Main Armament System Test Acord; Breech Mechanism Interchangeability Documentation for Hybrid Cannon." Benet Laboratories, Watervliet, NY, August 1987.

Hierarchical Solution of PDEs Using Wavelets

John R. Williams[†]   and   Kevin Amaratunga[‡]

†Associate Professor ‡Graduate Student

Intelligent Engineering Systems Laboratory,

Massachusetts Institute of Technology, Cambridge, MA 02139

Abstract

In engineering problems, we often require a quick rough estimate of the solution at the preliminary stage, which may later be refined as the design or investigation progresses. The multiresolution properties of wavelets suggest that is possible to obtain an initial coarse description of the solution with little computational effort and then successively refine the solution in regions of interest with a minimum of extra effort. The problem of successive refinement is one of the main drawbacks of the finite element method.

This paper demonstrates how a hierarchy of solutions to a PDE can be obtained by using Mallat's multiresolution transform [1] in conjunction with the wavelet-Galerkin method. This approach provides a rational means to trade off accuracy for solution speed. In contrast to the example of Beylkin et. al. [2, 3], where the discrete wavelet transform is applied to the matrix differential operator $\frac{d}{dx}$, we decompose the inverse of the differential operator matrix. We note that the structure of the inverse matrix is particularly suitable for developing hierarchical solutions.

Hierarchical Solution of PDEs Using Wavelets

John R. Williams† and Kevin Amaratunga‡

†Associate Professor ‡Graduate Student

Intelligent Engineering Systems Laboratory,

Massachusetts Institute of Technology, Cambridge, MA 02139

1 Introduction

Wavelets are a family of orthonormal functions which are characterized by the translation and dilation of a single function $\psi(x)$. This family of functions, denoted by $\psi_{m,k}(x)$ and given by

$$\psi_{m,k}(x) = 2^{\frac{m}{2}} \psi(2^m x - k); \qquad m, k \in Z$$

is a basis for the space of square integrable functions $L^2(R)$ i.e.

$$f(x) = \sum_m \sum_k d_{m,k} \, \psi_{m,k}(x) \qquad \in L^2(R)$$

Wavelets are derived from scaling functions i.e. functions which satisfy the recursion

$$\phi(x) = \sum_k a_k \, \phi(2x - k) \tag{1}$$

in which a finite number of the filter coefficients a_k are nonzero. Any $L^2(R)$ function $f(x)$ may be approximated at resolution m by

$$P_m(f)(x) = \sum_k c_{m,k} \, \phi_{m,k}(x) \qquad k \in Z$$

where, using Daubechies notation [4], $P_m f$ represents the projection of the function f onto the space of scaling functions at resolution m.

$$\phi_{m,k}(x) = 2^{\frac{m}{2}} \phi(2^m x - k); \qquad k \in Z$$

is a scaling function basis for the scale m approximation of $L^2(R)$. The set of approximations $P_n(f)(x)$ constitutes a multiresolution representation of the function $f(x)$ [1].

In two dimensions, the space of square integrable functions is $L^2(R^2)$ and any function $f(x, y)$ which lies in this space may be expressed in terms of the orthonormal basis

$$\psi_{i,k}(x)\psi_{j,l}(y); \qquad i, k, j, l \in Z$$

This is simply the tensor product of the one dimensional bases in the two coordinate directions, x and y. $f(x, y)$ may be represented at resolution m by

$$P_m(f)(x, y) = \sum_k \sum_l c_{m,k,l} \, \phi_{m,k}(x)\phi_{m,l}(y) \qquad k, l \in Z$$
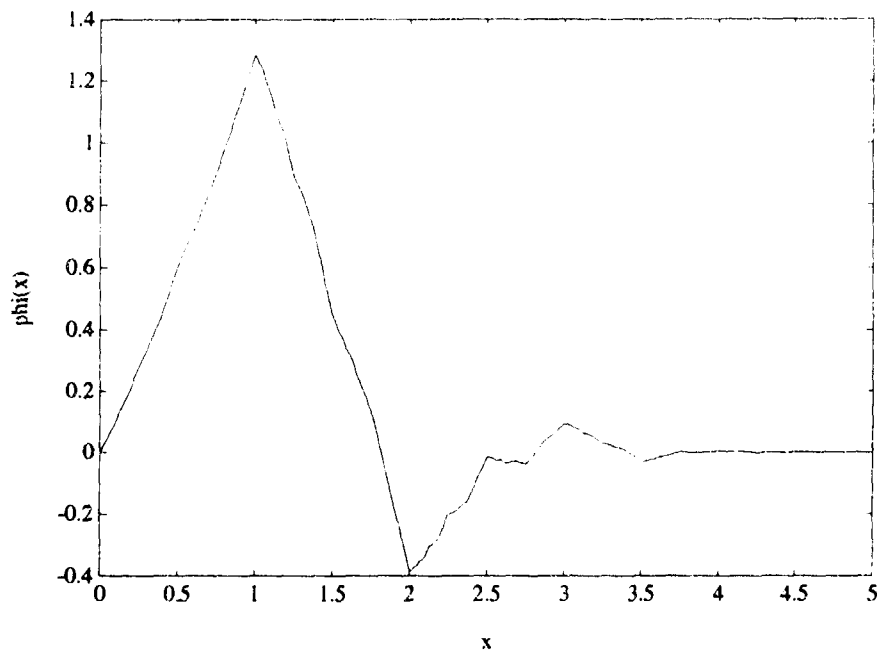
Figure 1: Daubechies D6 scaling function

This work details how a hierarchy of wavelet solutions to partial differential equations may be developed using wavelet bases. In order to demonstrate the wavelet-Galerkin technique, we consider Poisson's equation in two dimensions i.e.

$$u_{,xx} + u_{,yy} = f$$

where $u = u(x, y)$. $f = f(x, y)$. We limit ourselves to the solution of the problem on a periodic domain (the enforcement of boundary conditions on the periodic solution is discussed in [5].) We then consider how Mallat's multiresolution transform [1] may be used in conjunction with the wavelet-Galerkin technique to trade off accuracy for solution speed in a rational manner.

2 Wavelet-Galerkin Solution of Poisson's Equation

The wavelet-Galerkin method [6, 7, 8, 9, 10] entails representing the solution u and the right hand side f as expansions of scaling functions at a particular scale m. The values of the scaling function, ϕ, may be calculated using the recursion in equation (1) (see e.g. [11]). Orthogonal compactly supported scaling functions, such as those belonging to the Daubechies family of wavelets [4], are found to be particularly suitable for the solution of partial differential equations. Figure 1 depicts the Daubechies 6 coefficient scaling function.

The wavelet-Galerkin solution of the Poisson equation is slightly more complicated than a conventional finite difference solution, since the solution procedure involves transformations to and from wavelet space. Consider the Poisson equation

$$u_{,xx} + u_{,yy} = f \qquad (2)$$

The wavelet-Galerkin approximation to the solution $u(x,y)$ at scale m is

$$u(x,y) = \sum_k \sum_l \check{c}_{k,l}\, 2^{\frac{m}{2}}\phi(2^m x - k) 2^{\frac{m}{2}}\phi(2^m y - l) \qquad k, l \in Z \tag{3}$$

where $\check{c}_{k,l}$ are the wavelet coefficients of u. The transformation from wavelet space to physical space (or vice versa) can be easily accomplished using the FFT if the wavelet expansion is expressed as a discrete convolution. To do this make the substitutions

$$X = 2^m x$$
$$Y = 2^m y$$

to create a function of X and Y:

$$U(X,Y) = u(x,y) = \sum_k \sum_l c_{k,l}\,\phi(X - k)\phi(Y - l) \qquad c_{k,l} = 2^m \check{c}_{k,l} \tag{4}$$

Discretizing $U(X,Y)$ at integer values of X and Y leads to a discrete periodic convolution

$$U_{i,j} = \sum_k \sum_l c_{k,l}\,\phi_{i-k}\phi_{j-l} = \sum_k \sum_l c_{i-k,j-l}\,\phi_k \phi_l$$

where $\phi_k = \phi(\kappa)$. This may be written in matrix form as

$$U = \Phi_{n_x}\, c\, \Phi_{n_y}{}^T \tag{5}$$

where Φ_n is a size n circulant matrix of scaling function values. Equation (5) may be rewritten as

$$U = \left(\Phi_{n_y}\left(\Phi_{n_x}\, c\right)^T\right)^T.$$

It is easy to see that this is a one-dimensional convolution of the first column of Φ_{n_x} with each column of c, followed by a transposition of the rows and columns of the result, followed by a one-dimensional convolution of the first column of Φ_{n_y} with each column of this result, followed by another transposition of the rows and columns of the result. The one-dimensional convolutions are efficiently and exactly computed using the FFT.

Similar relationships to equations (4) and (5) exist for the right hand side function, f i.e

$$F(X,Y) = f(x,y) = \sum_k \sum_l g_{k,l}\,\phi(X - k)\phi(Y - l) \tag{6}$$

and

$$F = \Phi_{n_x}\, g\, \Phi_{n_y}{}^T \tag{7}$$

where g is the matrix of wavelet coefficients of $F(X,Y)$.

The differential equation in wavelet space may now be formulated by substituting equations (4) and (6) into equation (2). This leads to a system of equations of the form

$$\sum_k c_{k,q}\,\Omega_{p-k} + \sum_l c_{p,l}\,\Omega_{q-l} = \frac{1}{2^{2m}}\,g_{p,q}$$

where

$$\Omega_{j-k} = \int \phi''(y-k)\phi(y-j)dy$$

are the connection coefficients described by Latto et al [7]. In matrix form. this becomes

$$R_{n_x} c + c R_{n_y}{}^T = \frac{1}{2^{2m}} g \tag{8}$$

where R_n is a size n circulant matrix of connection coefficients. The system of equations (8) may be decoupled by taking the two-dimensional FFT:

$$\Lambda_{n_x} \hat{c} + \hat{c} \Lambda_{n_y} = \frac{1}{2^{2m}} \hat{g} \tag{9}$$

where Λ_n are diagonal and $\hat{(\cdot)}$ denotes the two-dimensional FFT. It then follows that

$$\hat{K}_\Omega \cdot \hat{c} = \frac{1}{2^{2m}} \hat{g} \tag{10}$$

where

$$K_\Omega = \begin{bmatrix} 2\Omega_0 & \Omega_1 & \ldots & \Omega_{N-2} & \ldots & \Omega_{2-N} & \ldots & \Omega_{-1} \\ \Omega_1 & 0 & \ldots & 0 & \ldots & 0 & \ldots & 0 \\ \ldots & \ldots & \ldots & \ldots & \ldots & \ldots & \ldots & \ldots \\ \Omega_{N-2} & 0 & \ldots & 0 & \ldots & \ldots & \ldots & 0 \\ 0 & 0 & \ldots & 0 & \ldots & \ldots & \ldots & 0 \\ \ldots & \ldots & \ldots & \ldots & \ldots & \ldots & \ldots & \ldots \\ 0 & 0 & \ldots & \ldots & \ldots & 0 & \ldots & 0 \\ \Omega_{2-N} & 0 & \ldots & \ldots & \ldots & 0 & \ldots & 0 \\ \ldots & \ldots & \ldots & \ldots & \ldots & \ldots & \ldots & \ldots \\ \Omega_{-1} & 0 & \ldots & 0 & \ldots & 0 & \ldots & 0 \end{bmatrix}_{(n_x, n_y)}$$

Combining equation (10) with the two-dimensional FFTs of equations (5) and (7) gives

$$\hat{U} = \frac{1}{2^{2m}} \hat{F} / \hat{K}_\Omega$$

Taking the inverse two dimensional Fourier transform yields the solution U.

3 Convergence of the Wavelet-Galerkin Method

The wavelet-Galerkin method as described above compares extremely favourably with a five point finite difference solution. The following are some results for a test problem.

Figure 2 shows the decay of the maximum residual error with increasing sample size n. The figure clearly indicates the high rate of convergence that is obtained with the wavelet method.

Figure 3 indicates the variation of computation time, in seconds, with increasing sample size. The wavelet solution takes slightly longer than the finite difference solution owing to the need to transform the sample from physical space into wavelet space and back again. This overhead becomes less significant as the sample size increases.
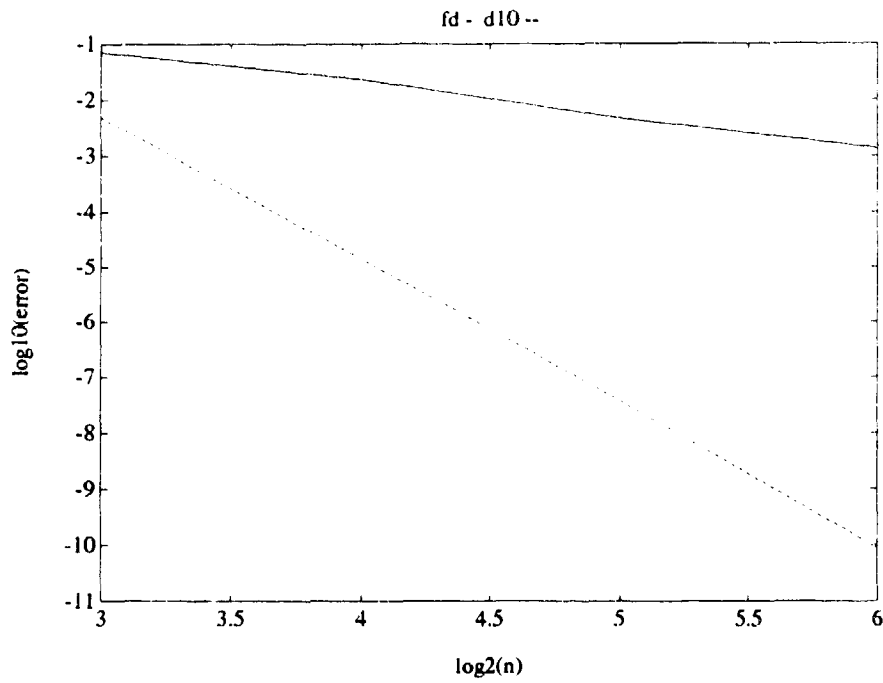
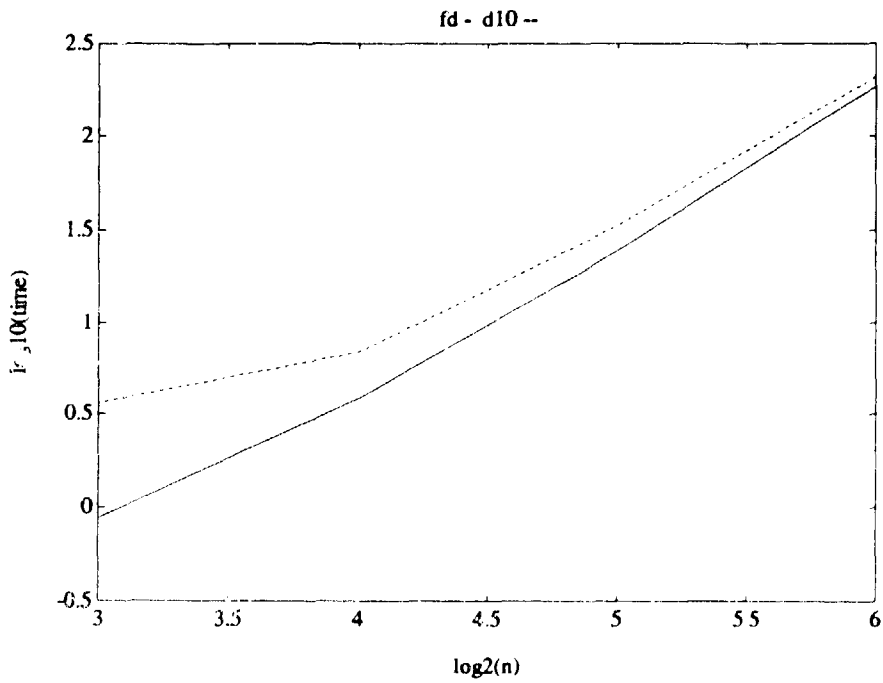Figure 2: Decay in error of d10 wavelet and finite difference solutions with increasing sample size

Figure 3: Variation of computation times with increasing sample size

Figure 4: A 256 × 256 greyscale image

4 The Fast Wavelet Transform and PDEs

One of the attractive features of wavelets is their multiresolution property, which is their ability to represent a function at different levels of resolution. The wavelet-Galerkin approach, while being a competitive solution procedure for PDEs, does not exploit the multiresolution properties of wavelets.

The multiresolution decomposition of a vector of data may be accomplished in $O(N)$ operations using the fast wavelet transform or FWT [12]. Figures 4 and 5 illustrate how the two-dimensional FWT may be applied to an image to produce an "averaged" low resolution picture and several detail components. A similar operation may be carried out on matrix operators. Beylkin, Coifman and Rokhlin [2, 3] have described in detail how matrix differential operators may be transformed into sparse matrices using the FWT. This sparsification facilitates the rapid evaluation of derivatives numerically. Among the examples given in their work are the construction of the non-standard form of the operators $D \equiv \frac{d}{dx}$ and $D^n \equiv \frac{d^n}{dx^n}$. The elements of these wavelet transformed matrix differential operators are self-similar at all scales.

In our experiments we have futher noticed that it may be advantageous to apply the FWT to the *inverse* of a matrix differential operator. The application of the FWT to an inverse matrix differential operator also gives rise to self-similar behaviour at different scales. As an example we consider the standard form of the inverse matrix differential operator, $(D^2 + 1)^{-1}$. Figure 6(a) shows the 64 × 64 inverse matrix differential operator, $(D^2 + 1)^{-1}$, for the Daubechies D6 wavelet system [4] at scale $m = 6$. Figure 6(b) shows a single stage wavelet decomposition of the inverse operator into components at scale $m = 5$, giving a low

Figure 5: A single stage decomposition of the image in the previous figure

frequency block in the upper left hand corner and three high frequency blocks. Figures 6(c) and (d) show further stages of decomposition of the low frequency block.

It is apparent from these results that the sparsification of the inverse matrix differential operator by the FWT occurs in a much more orderly way than if the matrix differential operator itself were decomposed. The low frequency block of the wavelet transformed inverse matrix differential operator contributes most significantly to the solution and from Figure 6 it is easy to see that the operator may be compressed without performing any thresholding operations. Furthermore, the high frequency blocks (which, although small, are non-zero) provide us with the information necessary to get to a finer level of resolution.

An important observation is that the discrete wavelet transform preserves the circulant structure of the original inverse matrix differential operator i.e. both the low frequency block and the high frequency blocks are circulant in nature. This means that the FFT can still be used to evaluate the solution in $O(NlogN)$ operations, where N is now the size of the reduced problem.

5 Conclusions

The wavelet-Galerkin approach is an efficient technique for the numerical solution of PDEs which has a very high rate of convergence, especially for high order Daubechies wavelets. The attractiveness of the wavelet-Galerkin approach is further enhanced by the fact that the multiresolution properties of wavelets provide a rational way to trade off accuracy for solution speed.
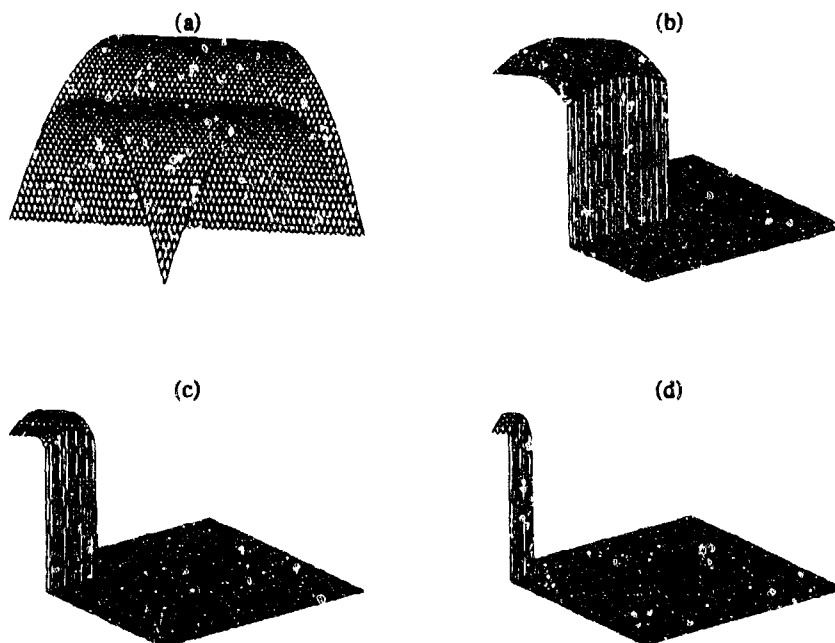
Figure 6: (a) The inverse differential operator $(D^2 + 1)^{-1}$ (b) First level of decomposition (c) Second level of decomposition (d) Third level of decomposition

6 Acknowledgements

References

[1] S. G. Mallat, 'A theory for multiresolution signal decomposition: the wavelet representation', *Comm. Pure and Appl. Math.*, **41**, 7, 674-693 (1988).

[2] G. Beylkin, R. Coifman and V. Rokhlin, 'Fast wavelet transforms and numerical algorithms I', *Comm. Pure Appl. Math.*, **44**, 141-183 (1991).

[3] G. Beylkin, R. Coifman and V. Rokhlin, 'Wavelets in numerical analysis', in Wavelets and their applications, M. B. Ruskai ed., Jones and Bartlett, Boston, 1992.

[4] I. Daubechies, 'Orthonormal bases of compactly supported wavelets', *Comm. Pure and Appl. Math.*, **41**, 909-996 (1988).

[5] K. Amaratunga and J. R. Williams, 'Wavelet based Green's function approach to 2D PDEs', IESL Technical Report No. 92-06, Intelligent Engineering Systems Laboratory, M.I.T., September 1992.

[6] R. Glowinski, W. Lawton, M. Ravachol and E. Tenenbaum, 'Wavelet solution of linear and nonlinear elliptic, parabolic and hyperpolic problems in one space dimension', *proc. 9th International Conference on Numerical Methods in Applied Sciences and Engineering*, SIAM, Philadelphia (1990).

[7] A. Latto, H. Resnikoff and E. Tenenbaum, 'The evaluation of connection coefficients of compactly supported wavelets', to appear in *proc. French - USA workshop on Wavelets and Turbulence*, Princeton Univ., June 1991, Springer-Verlag, 1992.

[8] A. Latto and E. Tenenbaum, 'Les ondelettes a support compact et la solution numerique de l'equation de Burgers', *C. R. Acad. Sci. Paris*, **311**, 903-909 (1990).

[9] J. Weiss, 'Wavelets and the study of two dimensional turbulence', *proc. French - USA workshop on Wavelets and Turbulence*, Princeton Univ., June 1991, Y. Maday, Ed. Springer-Verlag, NY.

[10] S. Qian and J. Weiss, 'Wavelets and the numerical solution of partial differential equations', Aware Technical Report AD920318 and submitted for publication to *J. Comp. Phys.*, March 1992.

[11] J. R. Williams and K. Amaratunga, 'Introduction to wavelets in engineering', IESL Technical Report No. 92-07, Intelligent Engineering Systems Laboratory, M.I.T., October 1992.

[12] G. Strang, 'Wavelet transforms versus Fourier transforms', Department of Mathematics, Massachusetts Institute of Technology (1992).

TITLE: TRANSFER OF ENERGY FROM HIGH-FREQUENCY TO
LOW-FREQUENCY MODES
A. H. NAYFEH*, S. A. NAYFEH, T. A. ANDERSON, and
B. BALACHANDRAN
DEPARTMENT OF ENGINEERING SCIENCE AND MECHANICS
VIRGINIA POLYTECHNIC INSTITUTE AND STATE UNIVERSITY
BLACKSBURG, VA 24061

ABSTRACT:

In some recent experimental studies, we observed that energy can be transferred from high-frequency to low-frequency modes in structures with weak nonlinearities. In these experiments, a structure was subjected to a simple-harmonic, low-amplitude excitation. The frequency of the excitation was near one of the high natural frequencies; yet after a very long time the contribution of the first mode to the multi-frequency response was larger than the contribution of the high-frequency mode that was directly excited. Subsequently, we developed analytical models to explain the interactions between widely spaced modes of structures and used them to determine conditions under which energy can be transferred from high-frequency to low-frequency modes, as observed in the experiments.

BIOGRAPHY:

NAME: Ali Hasan Nayfeh

CITIZENSHIP: USA

CURRENT FIELDS OF INTEREST:

Perturbation methods, nonlinear oscillations, structural dynamics, ship motion, acoustics, hydrodynamic stability, aerodynamic, nonlinear waves, flight mechanics, optical resonance

EDUCATION:

1962, B.S., Stanford University, Engineering Science, Great Distinction 1963, M.S., Stanford University, Aeronautics and Astronautics 1964, Ph.D., Stanford University, Aeronautics and Astronautics

PUBLICATIONS - BOOKS:

1. PERTURBATION METHODS, Wiley-Interscience, New York, 1973; Russian Translation, Mir Publishers of Moscow, USSR, 1976.

2. NONLINEAR OSCILLATIONS, with D. T Mook, Wiley-Interscience, New York, 1979.

3. INTRODUCTION TO PERTURBATION TECHNIQUES, Wiley-Interscience, New York, 1981; Russian Translation, Mir Publishers of Moscow, USSR, 1984.

4. PROBLEMS IN PERTURBATION, Wiley-Interscience, New York, 1985.

5. METHOD OF NORMAL FORMS, Wiley-Interscience, New York, 1993.

6. NONLINEAR DYNAMICS-CONCEPTS AND APPLICATIONS, with B. Balachandran, Wiley-Interscience, New York, 1993, in press.

PUBLICATIONS - PAPERS IN REFEREED JOURNALS: 267

CHAPTERS OF BOOKS 18

NAYFEH, NAYFEH, ANDERSON, BALACHANDRAN

CONFERENCE PAPERS: 96

TALKS AT NATIONAL AND INTERNATIONAL MEETINGS AND SEMINARS Over 350

PH.D DISSERTATIONS SUPERVISED: 41

M.S. THESES SUPERVISED: 27

PRESENT ASSIGNMENT:	University Distinguished Professor of Engineering
	Virginia Polytechnic Institute and State University
PAST EXPERIENCE:	Heliodyne Corporation
	Aerotherm Corporation
DEGREES HELD:	Ph.D.

1. Introduction

Nonlinear modal interactions have been the subject of a great deal of recent research. It has been found that, in weakly-nonlinear systems where there exists a special relationship between two or more natural frequencies of the linear modes and an excitation frequency, the long-time responses can contain significant contributions in many modes of vibration [1-5]. The presence of significant responses in more than one mode increases the number of modal equations that must be treated and this generally serves to complicate the dynamics the system. More importantly, modal interactions can lead to dangerously large responses in modes that are predicted by linear analysis to have insignificant response amplitudes.

Most of the research on modal interactions focuses on autoparametric resonances in systems where the linear natural frequencies ω_i are commensurate or nearly commensurate. The types of possible internal resonances depend on the degree of the nonlinearity. When the nonlinearity is cubic, to the first approximation, internal resonances may occur if $\omega_n \approx \omega_m$, $\omega_n \approx 3\omega_m$, $\omega_n \approx |\pm 2\omega_m \pm \omega_k|$, or $\omega_n \approx |\pm \omega_m \pm \omega_k \pm \omega_l|$. If quadratic nonlinearities are added, additional resonances may occur if $\omega_n \approx 2\omega_m$ or $\omega_n \approx \omega_m + \omega_k$. These autoparametric resonances have been successfully treated with perturbation methods [1-27]. There also exists a large body of experimental results which are in good general agreement with the perturbation results [1,2,5,11,12,19,22,28-37]. Autoparametric resonances may provide a coupling or an energy exchange between a system's modes. Consequently, excitation of a high-frequency mode may produce a large-amplitude response in a low-frequency mode involved with it in an autoparametric resonance.

In externally excited multi-degree-of-freedom systems, combination resonances may occur in response to a single-harmonic external excitation of frequency Ω. The type of combination resonance that can be excited depends on the degree of the nonlinearity, the number of modes involved, and Ω. For a cubic nonlinearity, to the first approximation, combination resonances may occur if $\Omega = |\pm \omega_m \pm \omega_k|/2$, $\Omega \approx |\pm 2\omega_m \pm \omega_k|$, or $\Omega \approx |\pm \omega_m \pm \omega_k \pm \omega_l|$. If quadratic nonlinearities are added, additional combination resonances may occur if $\Omega \approx |\pm \omega_m \pm \omega_k|$. Thus, a high-frequency excitation may produce large-amplitude responses in low-frequency modes that are involved in the combination resonance. Dugundji and Mukhopadhyay [38] conducted experiments on a cantilever beam subjected to external base excitation at a frequency close to the sum of the natural frequencies of the first torsional and first bending modes, which are approximately in the ratio of 18 to one. They found that the high-frequency excitation can produce a large-amplitude response in the low-frequency (first bending) mode.

In parametrically excited systems, modal interactions can occur when the excitation frequency is near the sum or difference of two or more linear natural frequencies. These so-called combination resonances have been studied extensively in the literature [1,2,5,39]. Again, these combination resonances can lead to interactions between high- and low-frequency modes.

Often, when the response of a system becomes chaotic, low-frequency modes can be excited. Haddow and Hasan [40] conducted an experiment by parametrically exciting a cantilever beam near twice the natural frequency of its fourth mode. They found that, as the excitation frequency was decreased, a planar periodic response consisting essentially of the fourth mode lost stability, giving way to a nonplanar chaotic motion. They observed that as a result the energy seemed to cascade down through the modes, resulting eventually in a low-frequency steady-state response. Burton and Kolowith [41] conducted an experiment similar to that of Haddow and Hasan. In certain regions of the parameter space, they observed chaotic motions where the first seven in-plane bending modes as well as the first torsional mode were present in the response. Cusumano and Moon [42] conducted an experiment with an externally excited cantilever beam. They observed a cascading of energy to low-frequency components in the response associated with chaotic non-planar motions.

Two recent studies suggest that another type of interaction may occur between high-frequency and low-frequency modes. In the first study, we [43] conducted experiments on a parametrically excited cantilever. We found that interactions occur between two high-frequency modes and the first mode. The presence of the first mode is accompanied by slow modulation of the amplitudes and

phases of the higher-frequency modes with the frequency of the modulation being equal to that of the first mode. Our results indicate that the mechanism for the excitation of the first mode is neither a classical internal resonance nor an external or parametric combination resonance involving the first mode. Rather, it seems that slow modulation of the high-frequency modes allows for the energy to be transferred to the first mode.

In the second study, we [44] conducted experiments on an externally excited, circular cross-section, cantilever rod. Because of the axial symmetry, one-to-one autoparametric resonances occur at each natural frequency of the rod and the mode in the plane of the excitation interacts with the out-of-plane mode at the same natural frequency, resulting in non-planar whirling motions. In addition, it is found that when the rod is excited near the natural frequency of its third or any higher mode, a large first-mode response occurs. Moreover, the degree of the coupling between the first mode and the higher modes is qualitatively observed to increase as we drive progressively higher modes. As in the first experiment, the appearance of the first mode is accompanied by modulation of the amplitudes and phases of the high-frequency modes.

The interaction between high- and low-frequency modes observed experimentally is of great practical importance. In many engineering systems, high-frequency excitations can be caused by rotating machinery. Through this mechanism, energy from high-frequency sources can be transferred to low-frequency modes of supporting structures or foundations, resulting in harmful large oscillations. Moreover, some preliminary results indicate that the use of conventional methods for decreasing modal interactions, such as increasing the dissipation or decreasing the forcing amplitude, may have undesirable effects. In the next section, we present a summary of our experiments.

2. Experiments on a Parametrically Excited Cantilever Beam

A schematic of the experimental setup for a base excitation along the axis of the beam is shown in Figure 1. The test specimen is a vertically mounted carbon steel cantilever beam of dimensions 33.56″ x 0.75″ x 0.032″. The beam was clamped to a 250 lb modal shaker with a custom table and suspension to allow base excitation of the beam. We note that the beam is slightly bent in the static configuration. The first four natural frequencies of the beam are 0.65 Hz, 5.65 Hz, 16.19 Hz, and 31.91 Hz, respectively.

The base motion was monitored with an accelerometer. A digital voltmeter was used to measure the root-mean-square (rms) value of the acceleration. A measure of the response was obtained from two strain gages: one located at $x/L = 0.06$ and the other located at $x/L = 0.25$, where x is the distance along the undeformed beam measured from the base and L is the length of the beam.

The accelerometer and strain-gage spectra were monitored as the excitation frequency was varied. Also, the autocorrelation function R_{xx} and the pointwise dimension were examined for selected motions. For the spectral analyses, we used 1280 lines of resolution in a 40 Hz baseband. A flat top window was used during periodic excitations, and a Hanning window with thirty overlap averages was used during random excitations. The two strain-gage signals were plotted against each other on the digital oscilloscope, thereby producing a pseudo-phase plane. To obtain a Poincaré section [45] we used the excitation frequency as the clock frequency for the oscilloscope. Due to the manner in which the points are stored in the digital scope, the final Poincaré section effectively corresponds to one obtained at one-half of the clock frequency. We used Fourier spectra, pseudo-phase planes, autocorrelation functions, and dimension calculations to analyze the different motions.

The excitation frequency was chosen to be the control parameter, and the base acceleration was held constant at 0.85 g rms, where the symbol g stands for the acceleration due to gravity. Initially when the excitation frequency f_e was at 33.5 Hz, there was a peak in the response spectrum at the excitation frequency. This peak is due to a primary resonance of the fourth mode. As the excitation frequency was gradually decreased to 32.31 Hz, the third mode appeared in the response. It was

excited by a principal parametric resonance. The response spectrum, shown in Figure 2a, has peaks at f_e and $f_e/2$. The Poincaré section, shown in Figure 2b, is characteristic of a periodic motion. The scatter in the points is due to noise. When the excitation frequency was decreased to 32.298 Hz, the periodic response consisting of the third and fourth modes lost stability, resulting in a modulated motion. During this modulated motion, the amplitudes and phases associated with the third and fourth modes varied with time. The spectrum of this response is shown in Figure 3a, with the sidebands around the carrier frequency at $f_e/2$ indicating a modulated motion. The sideband spacing f_m is 0.58 Hz, which is close to the first natural frequency of the beam.

Once the modulated motions set in, the contribution of the first mode to the response became large. The modulated response is indicative of an energy transfer from the third and fourth modes to the first mode. During the experiments, the presence of the first mode was very apparent visually. The presence of the first mode in the response leads to a scattering of points along a curve in the corresponding Poincaré section, as shown in Figure 3b. This observation indicates that the response is not periodic. When the excitation frequency was further reduced to 32.289 Hz, the motion appeared to become chaotic with a large out-of-plane component. The associated spectrum, shown in Figure 4a, has a continuous character in many frequency bandwidths. This characteristic is a signature of chaotic motion [45]. The Poincaré section, displayed in Figure 4b, is typical of nonperiodic motions; it does not have any obviously discernible structure.

In Figure 5, we show a time record obtained during the transient phase of the motion after f_e was changed form 32.298 H to 32.289 Hz. During the initial phase, the third and fourth modes are dominant in the response. Subsequently, there is a transition from the response composed mainly of modulated high-frequency (fast-time scale) motion to one dominated by the low-frequency (slow-time scale) first mode. In Figure 5, the strain is plotted versus time. The displacements observed during the low-frequency dominated phase of the motion are much larger than those observed during the high-frequency dominated phase. The change in the time history is striking.

3. Experiments on an Externally Excited Rod

In the second study, we conducted experiments on a slender, circular cross-section, steel, cantilever rod. The length of the cantilever is 34.5" and the diameter of its cross-section is 0.0625". The first five linear natural frequencies of the rod, as determined by examination of the frequency spectra of decaying free oscillations, are shown in Table 1.

Figure 6 is a schematic diagram of the experimental setup. A vertical beam is clamped to a 100-lb shaker that supplies a simple-harmonic motion at the base so that an external (i.e., transverse to the axis of the beam) excitation is applied. The excitation is monitored by means of an accelerometer mounted to the shaker head. The motion of the tip of the beam is measured by two linear-array cameras, one oriented to measure the motion in the plane of the excitation (camera 0) and the other oriented to measure the motion out of the plane of the excitation (camera 1).

The linear-array camera system employs a hardware-implemented peak detector to determine the location of the target in real-time. At a specified sampling frequency, it returns two eleven-bit numbers representing the displacement of the tip of the beam in the in-plane and out-of-plane directions. This data is acquired in real-time by a personal computer where it is displayed, processed, and stored.

We present frequency-response curves for the fifth in-plane and out-of-plane modes of the cantilever beam. The excitation level was held constant at 2.00 g rms and the excitation frequency was varied in the neighborhood of the fifth natural frequency. Changes in the excitation frequency were made very gradually and transients were allowed to die out before the amplitude of the response was recorded The data in the plots is a composite of the responses obtained by performing both forward and backward frequency sweeps. In addition, to ensure that even isolated branches of the frequency-response curves were located, we performed a third sweep where at increments in the

excitation frequency, we applied several disturbances to the beam in an effort to find all possible long-time responses.

The results of this procedure are shown in Figure 7. Well away from the fifth natural frequency of 83.105 Hz, the only possible response is planar and periodic. The response of the beam is strictly in the plane of the excitation and a visual inspection of the motion indicates that the response is composed almost entirely of the fifth mode. This is confirmed by examination of the response spectrum which shows only a single peak at the excitation frequency.

As the frequency of excitation is swept upward from well below the fifth natural frequency, a jump occurs from a planar-periodic to a non-planar strongly-modulated motion. Here, visual inspection of the response clearly detects the modulation of the response of the fifth mode as well as the presence of a low-frequency component in the response.

Increasing the excitation frequency further, we observe a jump to a non-planar weakly-modulated whirling motion. Again, visual inspection of the motion clearly reveals a large low-frequency component in the response. In this case, however, visual inspection does not detect any modulation of the fifth mode. A more detailed discussion of both the weakly- and strongly-modulated motions follows.

The observed weakly-modulated responses contain a large low-frequency component superimposed on a nearly constant amplitude fifth-mode whirling motion. Typical time traces of in-plane and out-of-plane responses of this type are shown in Figure 8a. Visual inspection of these plots does not readily reveal any modulation of either the high- or low-frequency components of the response.

A typical FFT of this type of response is shown in Figure 9. The FFT shows two main peaks, one at the frequency of the excitation (near the fifth natural frequency) and the other at the natural frequency of the first mode. Sidebands around the peak corresponding to the fifth mode indicate that the response of the fifth mode is modulated. Moreover, the frequency spacing between the fifth-mode peak and its sidebands is equal to the first natural frequency, confirming that the frequency of modulation of the fifth-mode response is equal to the natural frequency of the first mode.

As indicated by the dense set of sidebands clustered around the peak at the first natural frequency, the response of the first mode is also modulated. Examination of the time-domain data from which this FFT was computed, shown in Figure 8b, confirms that the amplitude of the first-mode response is not constant. The time traces in Figure 8b contain 170 seconds of data, illustrating the extremely slow variation of the amplitude of the first mode.

The most obvious feature of the strongly-modulated motions is the modulation of the fifth mode. A typical time trace of this type of motion is shown in Figure 10a. In contrast to the case of the weakly-modulated motions of Figure 8, the modulation of the fifth mode is clearly distinguishable without the aid of FFT's. It is also apparent from the asymmetry in the envelope of the traces shown in Figure 10a that there is a significant low-frequency component present in the response.

In Figure 10b a longer time trace of this motion is presented. Here, the scaling of the time axis is such that both the low-frequency component present in the response and the envelope of the fifth-mode response are clearly discernible. The erratic character of the evolution of the fifth-mode response suggests that the fifth mode is chaotically modulated. This assertion can be further sustained by examination of the FFT of this signal shown in Figure 11 where the narrow-band of response present in the neighborhood of the fifth natural frequency is characteristic of chaotically-modulated motions.

Turning our attention to the low-frequency component present in the response, we find that there is a peak at the first natural frequency of the system and conclude that the low-frequency component in the response is due to the first mode. As in the case of the weakly-modulated motions, there appears a dense set of sidebands clustered about the first-natural frequency peak, indicating that the first-mode response is also modulated.

4. A Paradigm for the Transfer of Energy from High-Frequency to Low-Frequency Modes

The results presented in Sections 2 and 3 show modal interactions occurring between high- and low-frequency modes in a flexible structure. The mechanism for the interaction appears to be neither a classical internal resonance nor an external or parametric resonance involving the low-frequency modes. Rather, it seems that these interactions can occur whenever there exist modes whose natural frequencies are much lower than the natural frequencies of the modes being directly driven.

To investigate possible mechanisms for the transfer of energy from high- to low-frequency modes, we [46] studied a representative system made up of two coupled oscillators. These equations are in a form that may be obtained by a two-mode discretization of a continuous system with cubic nonlinearities or, alternatively, they could model a discrete two-degree-of-freedom system. The equations are given by

$$\ddot{u}_1 + 2\varepsilon\mu_1\dot{u}_1 + \varepsilon^2 u_1 = -\varepsilon^2(4\alpha_1 u_1^3 + \alpha_2 u_1 u_2^2) \tag{1}$$

$$\ddot{u}_2 + 2\varepsilon\mu_2\dot{u}_2 + u_2 = \varepsilon(\alpha_3 u_2^3 + \alpha_4 u_1^2 u_2 + f\cos\Omega t) \tag{2}$$

where ε, the ratio of the linear natural frequencies of the system, is positive and small. The high-frequency mode, whose undamped linear natural frequency is nondimensionalized to unity, has coordinate u_2, and the low-frequency mode, whose normalized undamped linear natural frequency is ε, has coordinate u_1. The system has linear viscous damping given by the coefficients μ_1 and μ_2, cubic nonlinearities with the coefficients α_i, and an external forcing function $f\cos\Omega t$ which is applied only to the high-frequency mode of the system. Of principal interest is whether an excitation applied to the high-frequency mode near its linear natural frequency can, as observed in the experiments, generate a large response in the low-frequency mode. To answer this question, we used the method of averaging to construct an approximation of the solutions of Eqs. (1) and (2).

The method of averaging is based on the assumption that small perturbations, such as weak nonlinearities or light damping, cause slow (low-frequency) variations in the response of a system [47]. The fast (high-frequency) variations due to the perturbations are assumed to be insignificant. Essentially, the averaging approximation yields a simplified mathematical representation of the dynamics of the system by smoothing away these fast variations. Thus, it is of basic importance that the components which make up the response be correctly classified as either fast or slow.

Neglecting the damping and nonlinearities, one can write the solution to Eq. (1) as $u_1 = A_0 \cos(\varepsilon t + \phi_0)$. In this solution, it is apparent that whereas u_1 is an $O(1)$ quantity, $\dot{u}_1$ is $O(\varepsilon)$ and $\ddot{u}_1$ is order $O(\varepsilon^2)$. This leads us to assume that u_1 itself is slowly varying. Because the natural frequency of u_2 is not small, its motion can be treated in the usual way by assuming that its amplitude and phase are slowly varying as described below.

To explicitly show that u_2 is driven near its linear natural frequency, we set $\Omega^2 = 1 + \varepsilon\sigma$, where σ is a measure of the closeness of the excitation frequency to the unperturbed natural frequency of u_2. Next, we apply the variation of parameters transformation

$$u_2 = a(t)\cos(\Omega t + \beta(t)) \tag{3}$$

$$\dot{u}_2 = -a(t)\Omega\sin(\Omega t + \beta(t)) \tag{4}$$

to Eqs. (1) and (2) and obtain

$$\ddot{u}_1 + 2\varepsilon\mu_1\dot{u}_1 + \varepsilon^2 u_1 = -\varepsilon^2(4\alpha_1 u_1^3 + \alpha_2 u_1 a^2 \cos^2(\Omega t + \beta)) \tag{5}$$

$$\dot{a}\Omega = -\varepsilon g \sin(\Omega t + \beta) \tag{6}$$

$$a\dot{\beta}\Omega = -\varepsilon g \cos(\Omega t + \beta)$$ (7)

where

$$g = \sigma a \cos(\Omega t + \beta) + \alpha_3 a^3 \cos^3(\Omega t + \beta) + \alpha_4 u_1^2 a \cos(\Omega t + \beta)$$
$$+ 2\mu_2 a\Omega \sin(\Omega t + \beta) + f \cos \Omega t$$ (8)

Keeping only the slowly-varying terms on the right-hand sides of Eqs. (5)-(7), we obtain the averaged or modulation equations

$$\ddot{u}_1 + 2\varepsilon\mu_1\dot{u}_1 + \varepsilon^2 u_1 = -\varepsilon^2(4\alpha_1 u_1^3 + \frac{1}{2}\alpha_2 u_1 a^2)$$ (9)

and

$$\dot{a} = -\varepsilon(\mu_2 a + \frac{1}{2} f \sin \beta)$$ (10)

$$\dot{\beta} = -\varepsilon\left(\frac{1}{2}\sigma + \frac{1}{2}\alpha_4 u_1^2 + \frac{3}{6}\alpha_3 a^2 + \frac{f}{2a}\cos \beta\right)$$ (11)

where we have set $\Omega \approx 1$. Equation (9) can be rewritten as a pair of first-order equations as

$$\dot{u}_1 = \varepsilon v_1$$ (12)

$$\dot{v}_1 = -\varepsilon(u_1 + 2\mu_1 v_1 + 4\alpha_1 u_1^3 + \frac{1}{2}\alpha_2 u_1 a^2)$$ (13)

The fixed-point solutions of the averaged equations represent constant amplitude and phase motions of the high-frequency mode accompanied by static (DC) responses of the low-frequency mode. Setting the time derivatives in Eqs. (10)-(13) equal to zero and solving for σ and u_1 in terms of a, we obtain

$$u_1 = 0$$ (14)

or

$$u_1 = \pm \sqrt{-\frac{1 + \frac{1}{2}\alpha_2 a^2}{4\alpha_1}}$$ (15)

and

$$\sigma = -\frac{3}{4}\alpha_3 a^2 - \alpha_4 u_1^2 \pm \sqrt{\frac{f^2}{a^2} - 4\mu_2^2}$$ (16)

The stability of a fixed-point solution is studied by examination of the eigenvalues of the Jacobian matrix of Eqs. (10)-(13) evaluated at the fixed point of interest. If all of the eigenvalues have negative real parts, the fixed point is asymptotically stable and any motion in the neighborhood of this fixed point is expected to be attracted to it. These solutions are called stable nodes and are denoted by solid lines in the frequency-response curves of Figure 12. If a real eigenvalue becomes positive, the fixed point loses stability and the motion is expected to diverge from it. These unstable solutions are called saddles and are denoted by dotted lines in Figure 12.

If instead a Hopf bifurcation occurs (a complex conjugate pair of eigenvalues crosses transversely from the left-half of the complex plane into the right-half of the complex plane), the fixed point loses stability, but in this case the motion is expected to oscillate about the fixed point. These unstable fixed points (called unstable foci and denoted by dashed lines in Figure 12) are of great interest because, in their neighborhood, we expect to find motions where u_1 oscillates and u_2 is modulated at the frequency of oscillation of u_1 as observed in the experiments.

437

In Figure 12, we present frequency-response curves for a case in which nontrivial solutions for u_1 occur. It should be noted that, although we show only the fixed-point solutions corresponding to positive values of u_1 in Figure 12, there exists a second set of solutions corresponding to negative values of u_1. The trivial solutions are unstable with a positive real eigenvalue in the central region of the plot. In this region, a nontrivial solution for u_1 exists. The upper branch of this solution consists of two regions of stable nodes joined by a region of unstable foci. Where the stable nodes exist, the motion will consist of periodic oscillations in u_2 and either a positive or negative nonzero static deflection in u_1. Where the unstable foci exist, oscillatory u_1 motions accompanied by modulated u_2 responses will occur.

In Figure 13, we present Hopf bifurcation sets for the values of the α_i used in Figure 12 and various values of the damping coefficients. Below these curves, oscillations in u_1 decay to a constant value and above them oscillations in u_1 are sustained. From the curves in Figure 13a, it is apparent that at any particular excitation frequency, increasing the damping coefficient μ_2 of the high-frequency mode increases the critical forcing amplitude required to generate oscillations in u_1. From Figure 13b however, we see that increasing the damping coefficient μ_1 of the low-frequency mode does not always increase the value of the critical forcing amplitude. At some excitation amplitudes and frequencies, increasing μ_1 actually destabilizes the system.

To study the dynamics of the system in the neighborhood of unstable foci, we employed a fourth-order Runge-Kutta-Fehlberg algorithm and integrated the averaged equations using the same parameter values as used in Figure 12. As predicted by the stability analysis, oscillatory responses of u_1 are found to occur here. The dynamics of the system are very complicated in these regimes and various nonlinear phenomena, such as period-doubling bifurcations culminating in chaos, symmetry-breaking bifurcations, the existence of multiple attractors, and the merging of attractors are found.

In Figure 14, we present a sequence of responses obtained for the parameter values used in Figure 12, $f = 2.5$, and various values of σ. As shown in Figure 12, as σ is decreased through $\sigma = 0.349$, a Hopf bifurcation occurs. In Figure 14a, we plot the motion in the $a - u_1$ plane just before the supercritical Hopf bifurcation occurs. As expected, the long-time response consists of only the stable fixed point. It should be noted that there exists a second fixed-point solution corresponding to negative values of u_1 which is not plotted here.

In Figure 14b, we show the motion just after the bifurcation. As predicted, the response changes from the point in the plane shown in Figure 14a to the limit cycle shown in Figure 14b. As σ is further decreased, the size of the limit cycle increases as shown in Figures 14b-e. Decreasing σ further, we obtain the period-doubling bifurcation sequence of Figures 14f-g which culminates in the creation of the chaotic attractor shown in Figure 14h. It should be noted that only a short sample of the chaotic attractor is shown. As the motion continues, the trajectory would fill the area outlined roughly by the portion of the trajectory shown.

For all of the responses shown in Figure 14, there exists a mirror image with opposite signs of u_1 and v_1 in the left half of the plane. Decreasing σ further, the chaotic attractors in the left and right halves of the $a - u_1$ plane merge into a single attractor. That is, the motion does not remain in either the left or right half of the plane but rather jumps erratically from one to the other. This response is shown in Figure 15a. As σ is further decreased through roughly -0.41, this attractor loses stability. The motion is no longer attracted to it but rather diverges from it after some time and jumps to another attractor (depicted in Figure 16a) which, for values of σ less than roughly -0.2, coexists with the attractors discussed thus far.

As shown in Figure 16a this attractor is periodic and symmetric at $\sigma = -0.41$. As σ is decreased, a symmetry-breaking bifurcation occurs; one of the two resulting nonsymmetric attractors is shown in Figure 16b. As σ is further decreased, these attractors undergo a period-doubling bifurcation sequence leading to chaos as shown in Figure 16c-e. The chaotic attractor in Figure 16e is nonsymmetric and an attractor with its mirror image also exists. Another decrease in σ causes these attractors to merge, resulting in the symmetric attractor shown in Figure 16f. As σ is further

decreased, a great variety of nonlinear dynamical phenomena are observed until a reverse Hopf bifurcation occurs at the end of the unstable branch leading to stable fixed-point solutions.

The analysis of this two-degree-of-freedom system shows interactions between high- and low-frequency modes through which an excitation applied to the high-frequency mode results in large-amplitude responses in the low-frequency mode. The response of the system is similar to that reported in the two experiments.

5. Concluding Remarks

The interaction between high- and low-frequency modes observed experimentally and demonstrated theoretically is of great practical importance. In many engineering systems, high-frequency excitations can be caused by rotating machinery. Through the mechanism discovered at VPI&SU, energy from high-frequency sources can be transferred to low-frequency modes of supporting structures or foundations, resulting in harmful large oscillations. Moreover, the results obtained in this research indicate that the use of conventional methods for decreasing modal interactions, such as increasing the dissipation or decreasing the forcing amplitude, may have undesirable effects.

6. References

1. Evan-Iwanowski, R. M., **Resonance Oscillations in Mechanical Systems,** Elsevier, 1976.

2. Nayfeh, A. H. and D. T. Mook, **Nonlinear Oscillations,** Wiley-Interscience, 1979.

3. Ibrahim, R. A., **Parametric Random Vibration,** Wiley-Interscience, 1985.

4. Schmidt, G. and A. Tondl, **Non-Linear Vibrations,** Akademie-Verlag, Berlin, 1986.

5. Nayfeh, A. H. and Balachandran, B., "Modal interactions in dynamical and structural systems," ASME Applied Mechanics Reviews 42, 1989, 175-202.

6. Pai, P. F. and Nayfeh, A. H., "Nonlinear nonplanar oscillations of a cantilever beam under lateral base excitations," International Journal of Non-Linear Mechanics 25, 1990, 454-474.

7. Feng, Z. C. and Sethna, P. R., "Symmetry-breaking bifurcations in resonant surface waves," Journal of Fluid Mechanics 199, 1989, 495-518.

8. Bajaj, A. K. and Johnson, J. M., "On the amplitude dynamics and crisis in resonant motions of stretched strings," Philosophical Transactions of the Royal Society of London 338, 1992, 1-41.

9. Miles, J. W., "Resonant motion of a spherical pendulum," Physica 11D, 1984, 309-323.

10. Crespo da Silva, M. R. M., "On the whirling of a base-excited cantilever beam," Journal of Acoustical Society of America 67, 1980, 704-707.

11. Haddow, A. G., Barr, A. D. S., and Mook, D. T., "Theoretical and experimental study of modal interaction in a two-degree-of-freedom structure," Journal of Sound and Vibration 97, 1984, 451-473.

12. Hatwal, H., Mallik, A. K., and Ghosh, A., "Forced nonlinear oscillations of an autoparametric system - Part 2: Chaotic responses," Journal of Applied Mechanics 50, 1983, 663-668.

13. Yasuda, K. and Kushida, G., "Nonlinear forced oscillations of a shallow spherical shell," Bulletin of the Japanese Society of Mechanical Engineering 27, 1984, 2233-2240.

14. Streit, D. A., Bajaj, A. K., and Krousgrill, C. M., "Combination parametric resonance leading to periodic and chaotic response in two-degree-of-freedom systems with quadratic nonlinearities," Journal of Sound and Vibration 124, 1988, 297-314.

15. Mook, D. T., HaQuang, N., and Plaut, R. H., "The influence of an internal resonance on non-linear structural vibrations under combination resonance conditions," Journal of Sound and Vibration 104, 1985, 229-241.

16. Maewal, A. "Miles' evolution equations for axisymmetric shells: simple strange attractors in structural dynamics," International Journal of Non-Linear Mechanics 21, 1986, 433-438.

17. O'Reilly, O. and Holmes, P. J., "Nonlinear, non-planar, and non-periodic vibrations of a string," Journal of Sound and Vibration 153, 1992, 413-435.

18. Lee, C. L. and Perkins, N. C., "Nonlinear oscillations of suspended cables containing a two-to-one internal resonance," Nonlinear Dynamics 3, 1992, 465-490.

19. Afaneh, A. A. and Ibrahim, R. A., "Nonlinear response of an initially buckled beam with 1:1 internal resonance to sinusoidal excitation," ASME DE-Vol. 50/AMD-Vol. 144, Nonlinear Vibrations, 1992, pp. 69-81.

20. Raouf, R. A. and Nayfeh, A. H., "One-to-one autoparametric resonance in infinitely long cylindrical shells," Computers & Structures 35, 1990, 163-173.

21. Restuccio, J. M., Krousgrill, C. M., and Bajaj, A. K., "Nonlinear nonplanar dynamics of a parametrically excited inextensional elastic beam," Nonlinear Dynamics 2, 1991, 263-289.

22. Samaranayake, S., Bajaj, A. K., and Nwokah, O. D. I., "Amplitude modulated dynamics and bifurcations in the resonant response of a structure with cyclic symmetry," ASME DE-Vol. 50/AMD-Vol. 144, Nonlinear Vibrations, 1992, pp. 139-150.

23. Vakakis, A. F., "Study of the resonances of a nonlinear, periodic, cyclic structure," ASME DE-Vol. 50/AMD-Vol. 144, Nonlinear Vibrations, 1992, pp. 151-158.

24. Crespo da Silva, M. R. M. and Zaretzky, C. L., "Nonlinear flexural-flexural-torsional interactions in beams including the effect of torsional dynamics. I: primary resonance," Nonlinear Dynamics, in press, 1993.

25. Natsiavas, S., "Free vibration of two coupled nonlinear oscillators," Nonlinear Dynamics, in press, 1993.

26. Tousi, S. and Bajaj, A. K., "Period-doubling bifurcations and modulated motions in forced mechanical systems," Journal of Applied Mechanics 52, 1985, 446-452.

27. Tadibakhsh, I. G. and Wang Y., "Wind-driven nonlinear oscillations of cables," Nonlinear Dynamics 1, 1990, 265-291.

28. Nayfeh, A. H. and Zavodney, L. D., "Experimental observation of amplitude- and phase-modulated responses of two internally coupled oscillators to a harmonic excitation," Journal of Applied Mechanics 55, 1988, 706-710.

29. Nayfeh, A. H., Balachandran, B., Colbert, M. A., and Nayfeh, M. A., "An experimental investigation of complicated responses of a two-degree-of-freedom structure," Journal of Applied Mechanics 56, 1989, 960-967.

30. Ibrahim, P. A. and Barr, A. D. S., "Autoparametric resonance in a structure containing a liquid, Part II: Three mode interaction," Journal of Sound and Vibration 42, 1975, 181-200.

31. Ibrahim, R. A., Woodall, T. D., and Heo, H., "Modal analysis of structural systems involving nonlinear coupling," The Shock and Vibration Bulletin 54, 1984, 19-27.

32 Bux, S. L. and Roberts, J. W., "Non-linear vibratory interactions in systems of coupled beams," Journal of Sound and Vibration 104, 1986, 497-520.

33. Ashworth, R. P. and Barr, A. D. S., "The resonances of structures with quadratic inertial non-linearity under direct and parametric harmonic excitation," Journal of Sound and Vibration 118, 1987, 47-68.

34. Ibrahim, R. A., "Multiple internal resonance in a structure-liquid system," Journal of Engineering for Industry 98, 1976, 1092-1098.

35. Cartmell, M. P. and Roberts, J. W., "Simultaneous combination resonances in an autoparametrically resonant system," Journal of Sound and Vibration 123, 1988, 81-101.

36. Balachandran, B. and Nayfeh, A. H., "Nonlinear motions of a beam-mass structure," Nonlinear Dynamics 1, 1990, 39-61.

37. Fujino, Y., Pacheco, B. M., and Warnitchai, P., "An experimental and analytical study of autoparametric resonance in a 3DOF model of cable-stayed-beam," Nonlinear Dynamics 4, 1993, 111-138.

38. Dugundji, J. and Mukhopadhyay, V., "Lateral bending-torsion vibrations of a thin beam under parametric excitation," Journal of Applied Mechanics 40, 1973, 693-698.

39. Nayfeh, A. and Jebril, A. E. S., "The response of two-degree-of-freedom systems with quadratic and cubic nonlinearities to multifrequency excitation," Journal of Sound and Vibration 115, 1987, 83-101.

40. Haddow, A. G. and Hasan, S. M., "Nonlinear oscillations of a flexible cantilever: experimental results," Proceedings of the Second Conference on Non-linear Vibrations, Stability, and Dynamics of Structures and Mechanics, Blacksburg, VA, June 1-3, 1988.

41. Burton T. D. and Kolowith, M., "Nonlinear resonance and chaotic motion in a flexible parametrically excited beam," Proceedings of the Second Conference on Non-Linear Vibrations, Stability, and Dynamics of Structures and Mechanics, Blacksburg, VA, June 1-3, 1988.

42. Cusumano, J. P., and Moon, F. C., "Low dimensional behavior in chaotic nonplanar motions of a forced elastic rod: experiment and theory," Nonlinear Dynamics in Engineering Systems, IUTAM Symposium, Germany, 1989

43. Anderson, T. J., Balachandran, B., and Nayfeh, A. H., "Observations of modal interactions among modes with widely spaced frequencies," ASME Winter Annual Meeting, Nonlinear Vibration Symposium, November 8-13 1992 b.

44. Nayfeh, S. A. and Nayfeh, A. H., "Energy transfer from high to low-frequency modes in flexible structures," ASME Annual Winter Meeting, Nonlinear Vibration Symposium, November 8-13, 1992.

45 Moon, F., Chaotic Vibrations, Wiley interscience, New York, 1987.

46. Nayfeh, S. A. and Nayfeh, A. H., "Nonlinear interactions between widely spaced modes," International Journal of Bifurcation and Chaos 3, 1993, in press.

47. Nayfeh, A. H., Perturbation methods, Wiley, 1973.

Table 1. The first five natural frequencies of the test specimen.

Mode	Natural Frequency (Hz)
1	1.303 ± 0.005
2	9.049 ± 0.005
3	25.564 ± 0.005
4	50.213 ± 0.007
5	83.105 ± 0.011

Table 2. Experimentally and theoretically determined natural frequencies of the aluminum cantilever plate.

Mode No.	Experiment (Hz)	Finite element (Hz)
1	9.67	9.23
2	32.34	30.62
3	58.93	57.22
4	108.1	103.61
5	147.9	142.25
6	166.1	164.94
7	221.1	212.15
8	237.4	225.76
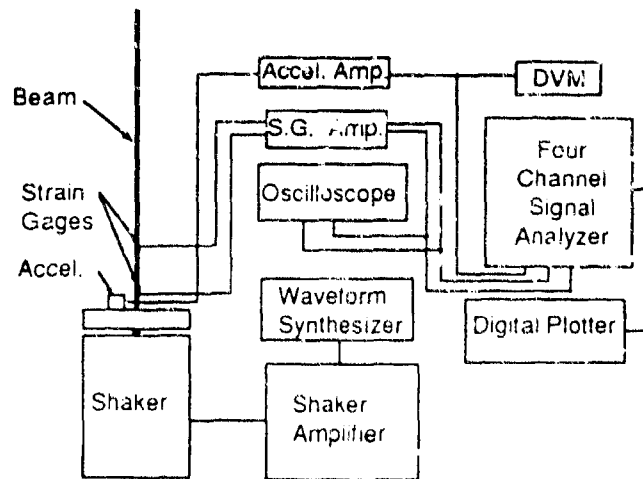
Figure 1. Experimental setup for the parametrically excited cantilever beam.
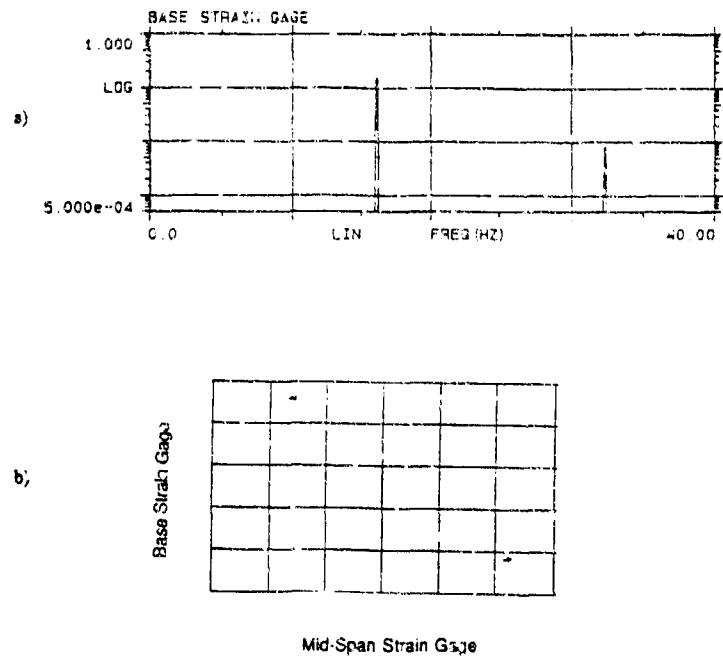
Figure 2. Response at $f_o = 32.31$ Hz: a) Fourier spectrum and b) Poincaré section.
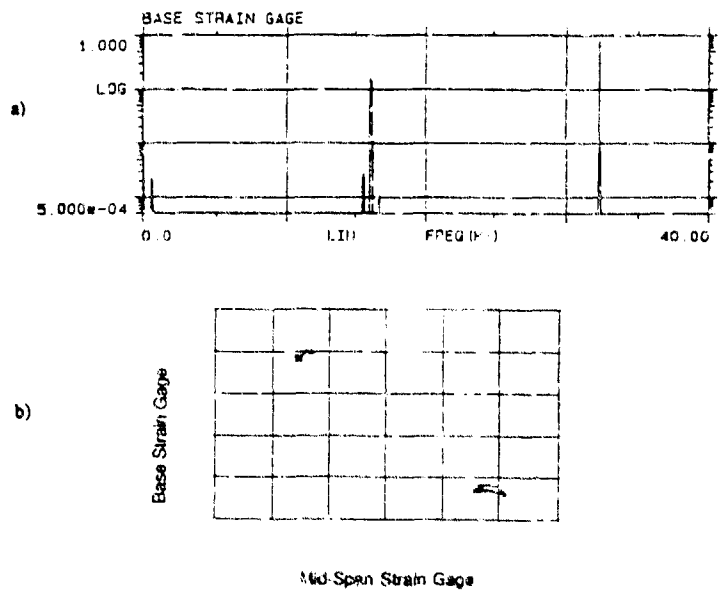
Figure 3. Response at $f_o = 32.298$ Hz: a) Fourier spectrum and b) Poincare section.
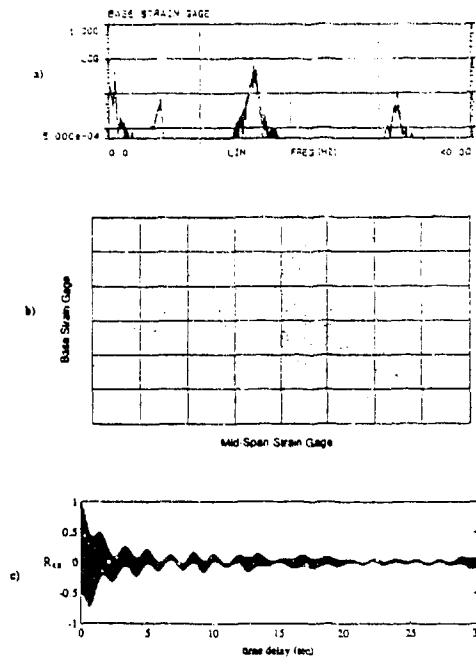
Figure 4. Response at f_o = 32.289 Hz: a) Fourier spectrum, b) Poincaré section, and c) autocorrelation function.
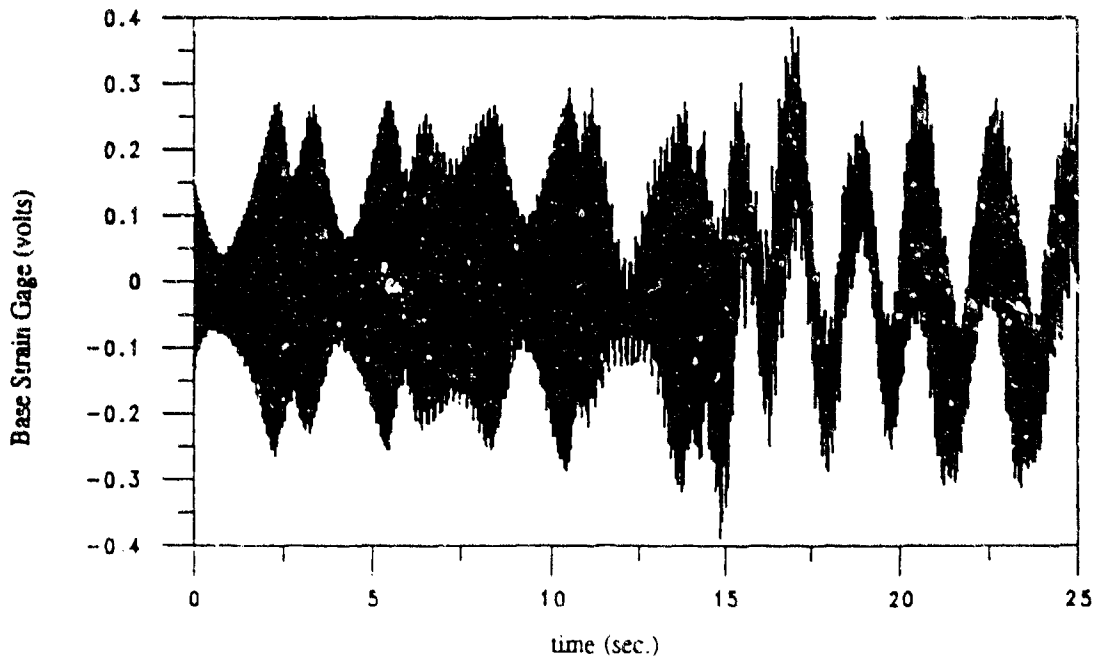

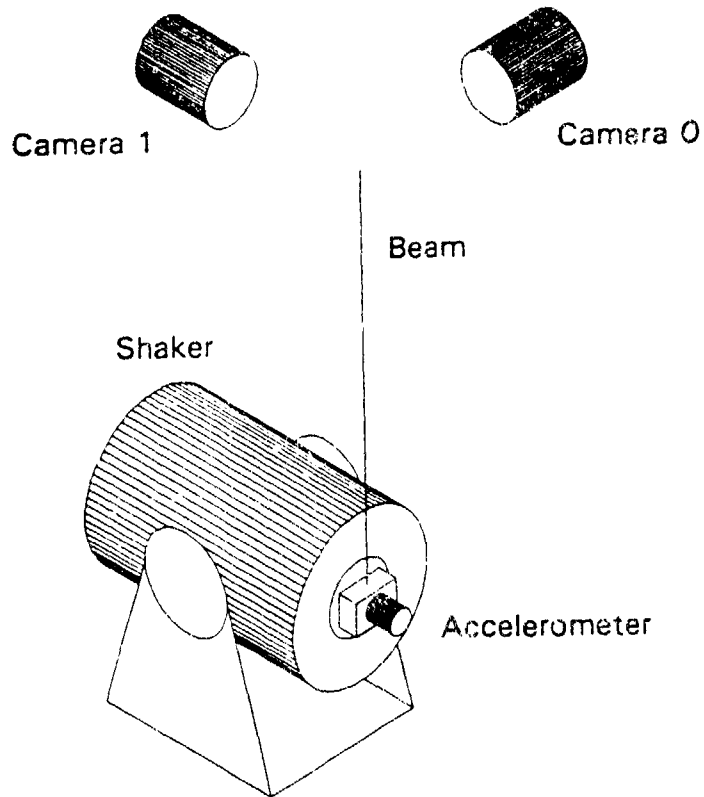**Figure 5.** A time trace of a transient motion.

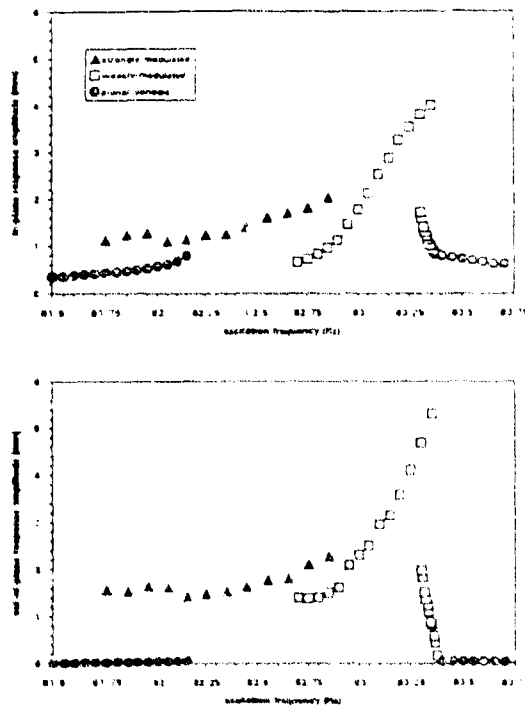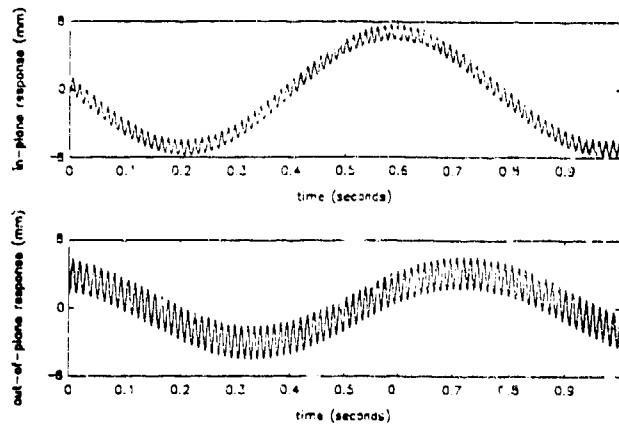**Figure 6.** Experimental setup for the externally excited cantilever rod.
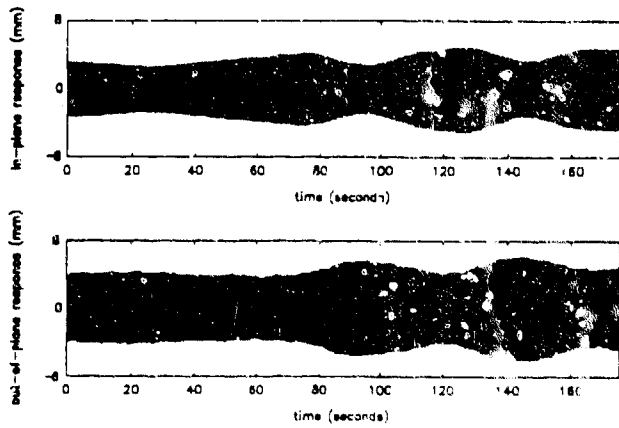

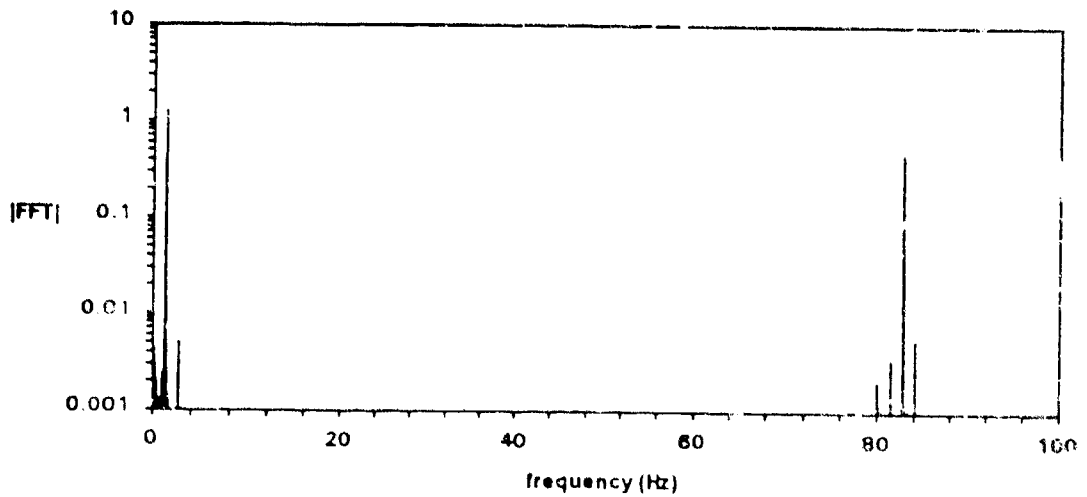**Figure 7.** Frequency-response curves of the fifth mode for an excitation amplitude of 2.00 gs rms.
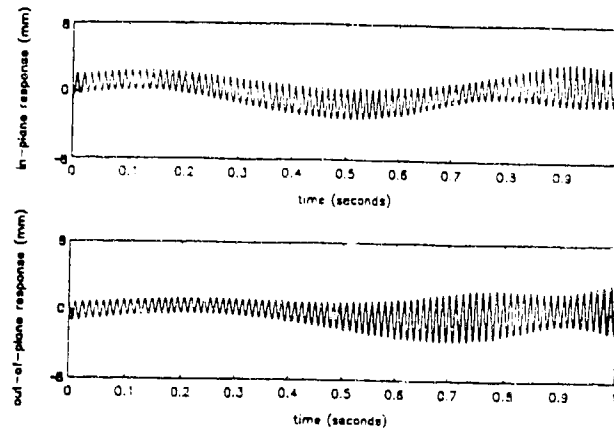
(a) Trace showing one second of the response
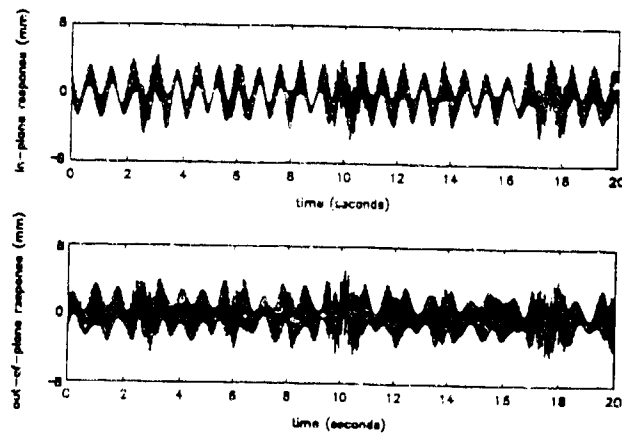

(b) Trace showing 170 seconds of the response

Figure 8. Time traces of a typical weakly modulated motion.

Figure 9. Magnitude of the FFT of a typical weakly modulation motion.

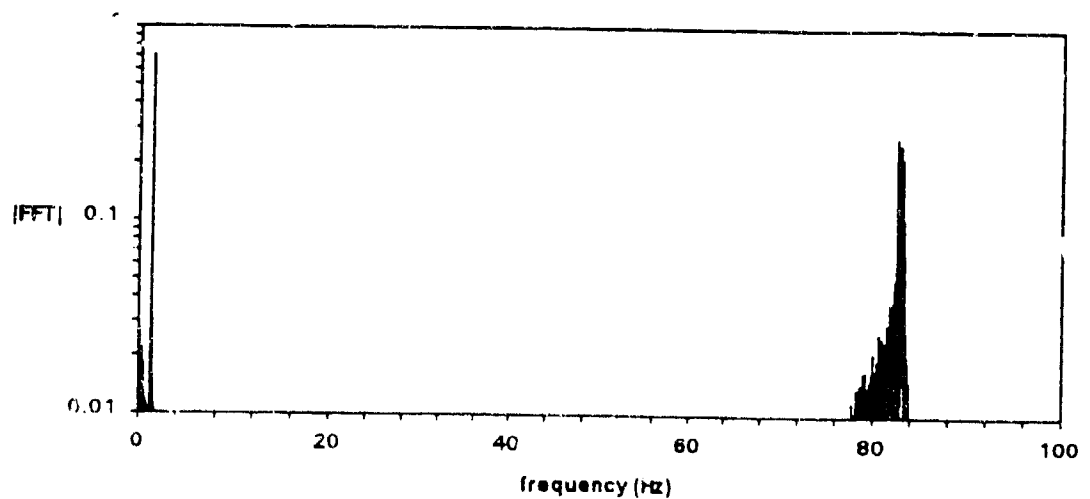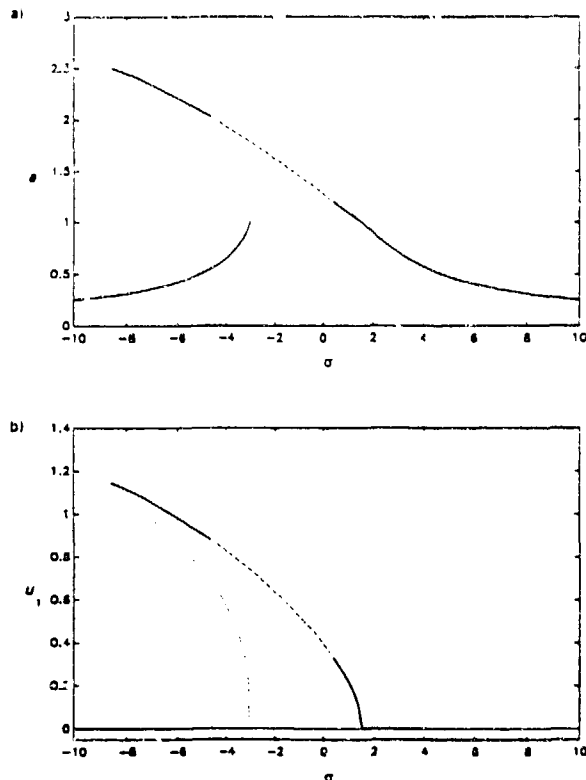Figure 10. Time traces of a typical strongly modulated motion.

Figure 11. Magnitude of the FFT of a typical strongly modulated motion.

Figure 12. Frequency-response curves for $\alpha_1 = \alpha_3 = 1$, $\alpha_2 = -2$, $\alpha_4 = 3$, $\mu_1 = 0.25$, $\mu_2 = 0.5$, and $f = 2.5$. Solid lines denote stable solutions, dotted lines denote unstable solutions with a positive real eigenvalue, and dashed lines denote unstable solutions with a complex-conjugate pair of eigenvalues in the right half-plane.
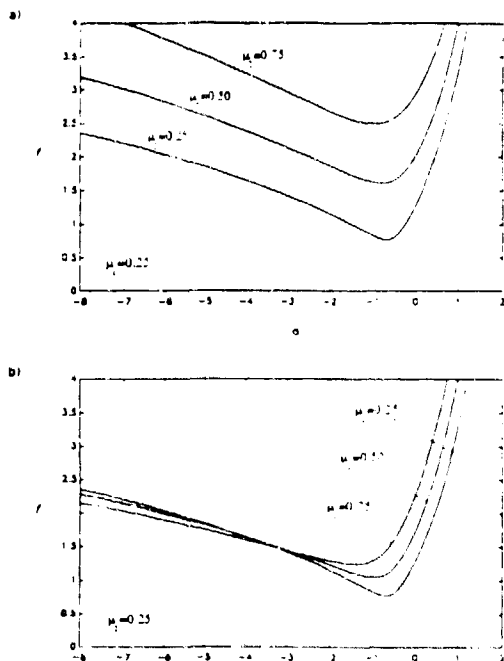
Figure 13. Boundaries between constant and oscillatory motions of u_1 for $\alpha_1 = \alpha_3 = 1$, $\alpha_2 = -2$, $\alpha_4 = 3$, and various damping values.

Figure 14. Numerical simulation of the averaged equations for $\alpha_1 = \alpha_3 = 1, \alpha_2 = -2, \alpha_4 = 3$, $\mu_1 = 0.25, \mu_r = 0.5, f = 2.5$, and $\sigma =$ (a) 0.350, (b) 0.348, (c) 0.300, (d) 0.200, (e) 0.000, (f) -0.170, (g) -0.243, and (h) -0.260.
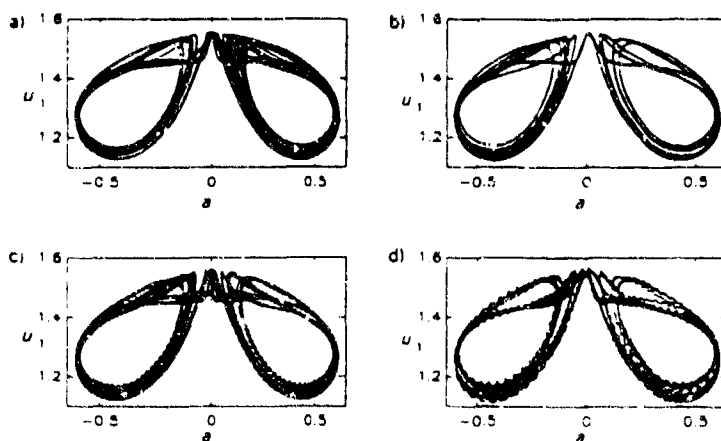
Figure 15. Numerical simulation of (a) the averaged equations and (b)-(d) the exact equations for $\alpha_1 = \alpha_3 = 1, \alpha_2 = -2, \alpha_4 = 3, \mu_1 = 0.25, \mu_2 = 0.5, f = 2.5$, and $\sigma = -0.27$, and $\varepsilon =$ (b) 0.01, (c) 0.03, and (d) 0.05.
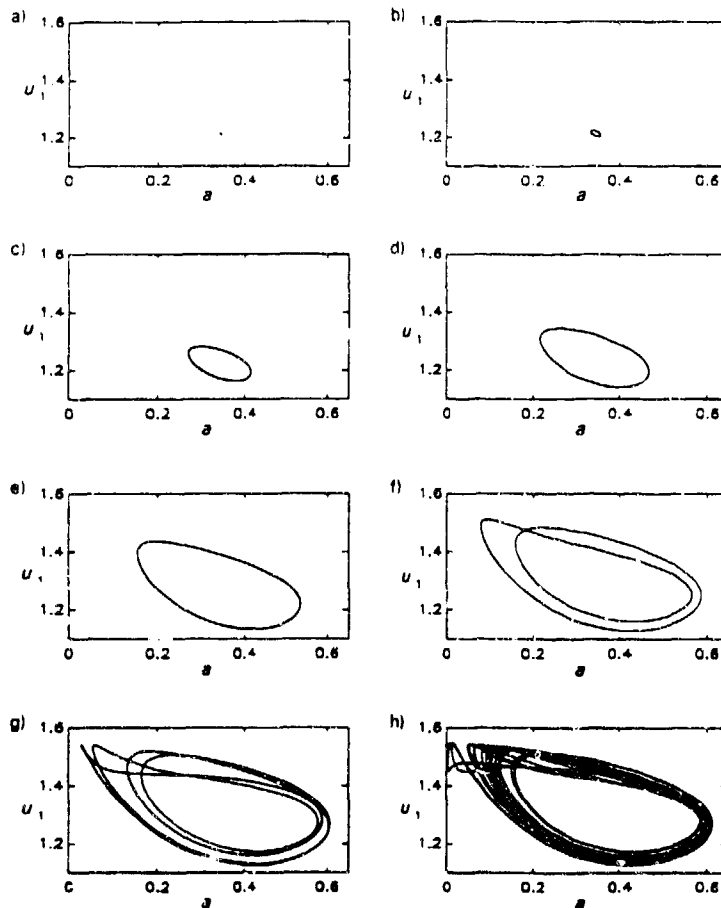
449
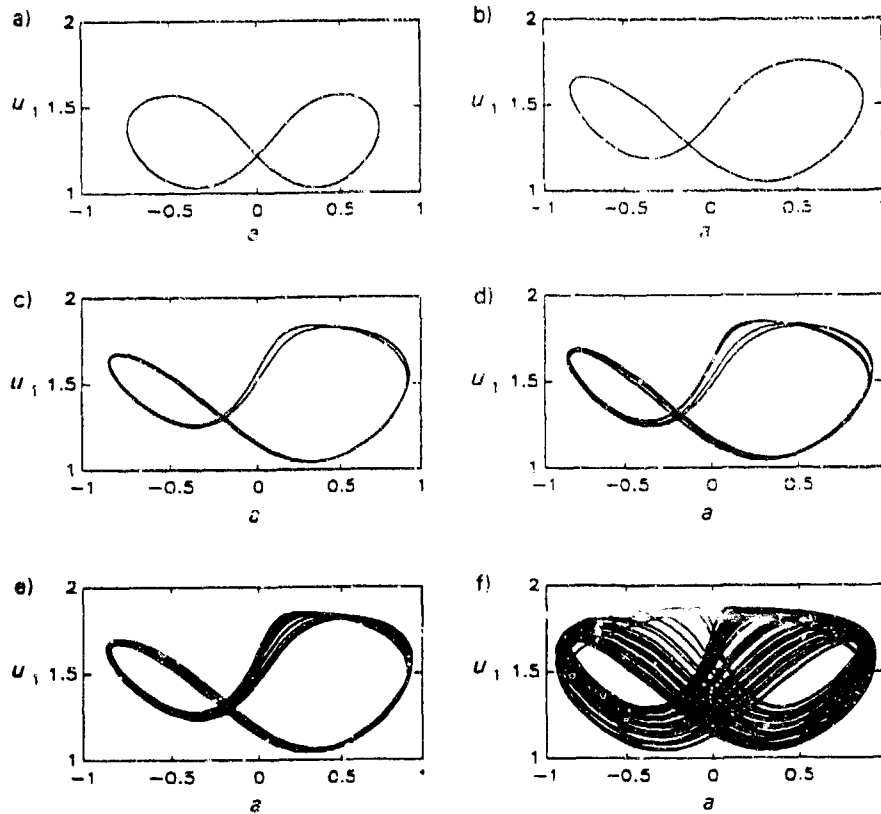
Figure 16. Numerical simulation of the averaged equations for $\alpha_1 = \alpha_3 = 1$, $\alpha_2 = -2$, $\alpha_4 = 3$, $\mu_1 = 0.25$, $\mu_2 = 0.5$, $f = 2.5$, and $\sigma =$ (a) -0.41, (b) -1.10, (c) -1.28, (d) -1.31, (e) -1.32, and (f) -1.36.

VAKAKIS, BENTSMAN

TITLE: PASSIVE MOTION CONFINEMENT OF IMPULSES IN A
         SYSTEM OF COUPLED NONLINEAR BEAMS

ALEXANDER F. VAKAKIS AND JOSEPH BENTSMAN
DEPT OF MECHANICAL AND INDUSTRIAL ENGINEERING
UNIVERSITY OF ILLINOIS
1206 W. GREEN STREET, URBANA, IL 61801

ABSTRACT:

A system of weakly coupled, geometrically nonlinear beams is examined. A Galerkin procedure is used to express the motions of the two beams in terms of their linearized flexural modes. Transient, impulsive excitations are considered, and the response of the system is analytically and numerically computed. For small values of a coupling nonlinear parameter, the vibrational energy injected into the system is proved to mainly localize at the directly forced beam, and only a small portion of this energy "leaks" to the unforced one. This passive, transient motion confinement is solely due to nonlinear localized modes of the unforced system, and it becomes more profound as the nonlinearity increases and/or the coupling stiffness connecting the two beams decreases. In the absence of nonlinearity, the injected vibrational energy is continuously transferred between the two beams, and thus, no passive motion confinement is possible.

BIOGRAPHY: Alexander F. Vakakis

PRESENT ASSIGNMENT: Assistant Professor
                        Department of Mechanical & Industrial Engineering
                        University of Illinois at Urbana - Champaign

PAST EXPERIENCE: Research and Teaching Assistant
                     California Institute of Technology

DEGREES HELD: PhD, California Institute of Technology
                  MSc, Imperial College, University of London (United Kingdom)
                  BSc, University of Patras (Greece)

Passive Motion Confinement of Impulses in a System of Coupled Nonlinear Beams

Alexander F. Vakakis (*), and Joseph Bentsman
University of Illinois at Urbana - Champaign
Urbana, Illinois

1. INTRODUCTION

Repetitive structures are common in engineering practise. They consist of a number of identical substructures coupled by means of resilient elements. Such systems are commonly used in aerospace and turbomachinery applications: an assembly of helicopter blades can be regarded as a cyclic system of highly flexible (and hence geometrically nonlinear) coupled beams; periodically stiffened plates and shells are used for a long time as parts of aeroplane fuselages; and continuously shrouded bladed disc assemblies are essential parts of all turbomachines. In this work, a system consisting of two linearly coupled isotropic beams will be considered to model a two-helicopter blade assembly. Due to the flexibility of the beams, geometric and inertial nonlinearities occur, giving rise to a variety of nonlinear phenomena, having no counterpart in existing linear or linearized theories. In particular, for weak interblade coupling and/or strong blade nonlinearities, the assembly will be shown to possess nonlinear localized modes of vibration. *The implementation of the mode localization properties of this system in the design for passive motion confinement of external disturbances, is the main objective of this work.*

In a number of recent works, the phenomenon of mode localization in "perturbed" linear periodic systems was investigated [1-5]. In these references it was shown that the (extended) normal modes of weakly coupled, symmetric linear systems become localized when weak perturbations of the periodicity are introduced. Linear mode localization was detected when the coupling between subsystems was of the order or smaller than the spread in natural frequencies of the component systems. The phenomenon of mode localization in discrete periodic oscillators with nonlinear stiffnesses was analytically and numerically studied in [6-8]. This was accomplished using the notion of "nonlinear normal mode," [9], i.e., of a free motion during which all coordinates of the system oscillate equiperiodically, reaching their extremum values at the same instant of time. As pointed out in other works [10-12], although superposition of modal responses is not valid in nonlinear systems, forced nonlinear steady state motions occur in the neighborhoods of the nonlinear normal modes (as in linear systems); thus, the examination of nonlinear normal modes provides valuable insight into the dynamic response of discrete nonlinear oscillators. Recently, the notion of "nonlinear normal mode" was extended to one-dimensional nonlinear continuous systems [13,14].

In [8], a discrete cyclic system composed of n identical substructures possessing grounding nonlinearities of the third degree, and linear coupling stiffnesses was studied. In all numerical examples, it was found that, for sufficiently weak coupling between substructures (of $O(\varepsilon)$, $|\varepsilon| << 1$), the periodic system contained a "strongly" localized mode during only one coordinate vibrated with $O(1)$ amplitude, the remaining coordinates oscillating with amplitudes of at least $O(\varepsilon)$. Moreover, this "strongly localized" mode was found to be orbitally stable and thus, physically realizable. Some additional results on nonlinear normal modes were recently reported in [15], were a new methodology for

detecting nonlinear normal modes was described; this method is based on the computation of invariant manifolds for the motion, and is valid even for systems with damping.

Localized modes in *linear* cyclic assemblies of beams modeling large space reflectors were investigated in [4,5,16]. Linear mode localization in such flexible structures occurred only in the presence of structural disorders, and the localized linear modes were investigated both analytically and numerically. It was shown that higher flexible modes were more susceptible to localization than lower ones. Moreover, the strength of the localization phenomenon was found to depend on the position of the coupling stiffness. A recent experiment [17] proved the existence of certain linear localized modes in a circular antenna with twelve flexible ribs and a gimballed central-hub. In accordance to existing theories, the "second bending group" of the antenna (ribs oscillating in the second flexible mode) was more effectively localized than the first group. Moreover, stronger localization was observed with increasing modal band. Mode localization in systems of flexible nonlinear beams was first examined in [18]. In that work, a configuration of two coupled, geometrically nonlinear beams was investigated. A variety of localized modes was determined. The topology of the localized branches of modes was found to be greatly influenced by an "internal resonance" existing between the second and third linearized cantilever modes, and by the position of the coupling stiffness.

A number of existing works investigates the spatial confinement of propagating disturbances in structures with localized modes. In [19], localization of propagating disturbances in one-dimensional disordered coupled oscillators and in beams with irregularly spaced constraints is studied using ensemble averaging procedures. Analytic and numerical logarithmic averages for the transmission of disturbances along such systems were given. In [20], a wave propagation formulation for studying transmission in disordered periodic systems is adopted. Multiplication of random transmission matrices is carried out in order to compute the "localization factors" inside the passbands of the unperturbed system. An extension of these statistical analyzes was given in [21], were theoretical results on the localization factors were confirmed by Monte Carlo simulations. Localization of flexural propagating waves along a fluid-loaded plate with an irregular array of line attachments is presented in [22]. A structural acoustics formulation is adopted in that work, and localization is studied by means of numerical simulations. Additional numerical computations of motion confinement of external disturbances due to mode localization were carried out for models of linear [4,5,23] and nonlinear [8] structures. These works demonstrated the beneficial effects of the mode localization phenomenon on the passive and/or active vibration isolation of periodic systems. This is because *in a structure with localized modes the energy induced from an impulse in any of its substructures remains confined to that substructure and does not "spread" throughout the remaining system.* Motion confinement due to nonlinear mode localization in impulsively loaded cyclic systems was demonstrated in [8], where the impulsive response of a nonlinear cyclic system with 50 DOF was numerically computed using a finite-element technique. For sufficiently weak coupling and *no disorder*, the energy of the impulse was confined to the point of its application, in contrast to the corresponding linear system where the energy "leaked" to the other components of the system. This motion confinement in the nonlinear system was attributed to the nonlinear localized modes, which did not exist in the corresponding linear structure.

The present work investigates the passive motion confinement properties of a system of two coupled, geometrically nonlinear beams. In section 2, the mathematical model is described and the nonlinear localized modes of the system are discussed. In section 3, both beams are forced to vibrate in their first cantilever mode, and motion

confinement of a general class of induced impulses is proved analytically and numerically. A discussion of the implications of the main findings of this work is given in section 4.

2. NONLINEAR LOCALIZED MODES OF THE UNFORCED SYSTEM

The flexible system under consideration is shown in figure 1. The structure consists of two isotropic, linearly elastic beams of identical material properties and dimensions, which are coupled by means of a linear stiffness. Assuming no out-of-plane components of motion, and increased beam flexibility, the nonlinear relation between curvature and transverse displacement and the longitudinal inertia of the beams give rise to geometric nonlinearities which can greatly influence the dynamic response [24-27]. Assuming that the

beams are rigidly fixed to a non-moving rigid base, and that weak coupling stiffness $K = \epsilon k$ exists, where $|\epsilon| \ll 1$, a rescaling of the transverse displacements, , $v_p \to \epsilon^{1/2} v_p$, leads to the following governing equations of motion:

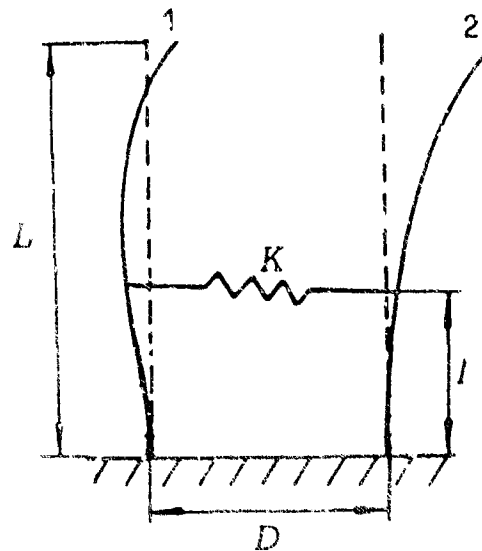Figure 1. The flexible nonlinear assembly under consideration.

$$ v_{ptt} + v_{pxxxx} = -\epsilon \left\{ v_{px} [v_{px} v_{pxx}]_x + (1/2) v_{px} \int_1^X [\int_0^s v_{px}^2 \, du]_{tt} \, ds \right\}_x - $$

$$ - \epsilon (kL^4/EI) \left\{ v_p(l/L,t) - v_m(l/L,t) \right\} \delta(x-l/L) + F_p(x,t) $$

$$ u_p(x,t) = O(\epsilon) \, , \, p, \, m = 1,2 \, , \, p \neq m \tag{1} $$

where v_p and u_p denote the transverse and longitudinal displacements of beam p, and x the arclength per unit length of the two beams. In (1), t is the scaled time, defined by $t = \tau \{ EI/\rho L^4 \}^{1/2}$, where τ represents physical time, E the modulus of elasticity of the material of the beams, I the moment of inertia of the cross section of the beams about axes

orthogonal to the plane of their motion, and ρ the material density per unit length. In (1), no shear deformations of the cross-section, nor any rotary inertia effects are taken into account. The first nonlinear term in the right-hand-side of (1) is due to the nonlinear relation between the curvature and the transverse displacement, and the second nonlinear term represents the nonlinear coupling effects due to the nonlinear longitudinal inertia of the beam. Note that, *expressions (1) indicate that the longitudinal displacement u(x,t) is of higher order than the transverse displacement v(x,t), and therefore of much smaller magnitude and importance.* In the following analysis, longitudinal motions are neglected.

For small values of ε, equations (1) form a set of weakly nonlinear, and weakly coupled partial differential equations. This set can be discretized by expressing the transverse displacements $v_p(x,t)$ in the following series form:

$$v_p(x,t) = \sum_{m=1}^{n} \phi_m(x) \, q_{pm}(t) \, , \, p=1,2 \tag{2}$$

where the functions $\phi_m(x)$ are the normalized cantilever eigenfunctions of the linear parts of (1, corresponding to $\varepsilon=0$), and $q_{pm}(t)$ new generalized coordinates. Substituting (2) into (1), then multiplying by the i-th normalized eigenfunction $\phi_i(x)$, integrating from $x = 0$ to $x = 1$ with respect to the spatial variable, and using the orthogonality properties of the linearized eigenfunctions, the following set of ordinary differential equations for $q_{pi}(t)$ is obtained:

$$\ddot{q}_{pi} = \varepsilon \left\{ \sum_{b=1}^{n} \sum_{k=1}^{n} \sum_{l=1}^{n} \left[a_{iblk} \, q_{pb} \, q_{pk} \, q_{pl} + \frac{b_{iblk}}{2} q_{pb} \, [q_{pk} \, q_{pl}]_{tt} \right] + \right.$$

$$\left. + \sum_{k=1}^{n} \gamma_{ki} \, (q_{pk} - q_{(p+1)k})) \right\} + F_{pi}(t) \tag{3}$$

where the first subscript of q_{pi} represents the beam number, $p = 1, 2$ $p = 3 \equiv 1$, and the second subscript denotes the order of the linearized mode-shape. $i = 1,2...n$. The various terms in (3) are defined as follows:

$$a_{iblk} = \int_0^1 \phi_i \, [\phi_b'(\phi_k'\phi_l'')']' \, dx, \quad b_{iblk} = \int_0^1 \phi_i \, [\phi_b' \int_1^x \int_0^\zeta \phi_k'\phi_l' \, d\lambda d\zeta]' \, dx,$$

$$\gamma_{ki} = \frac{k \, L^4}{E \, I} \, \phi_k(^a/L) \, \phi_i(^a/L) \quad F_{pi}(t) = \int_0^1 F_p(x,t) \, \phi_i \, dx \tag{4}$$

where prime denotes differentiation with respect to the argument. The numerical values for some of coefficients (4) are provided in [18]

The objective of the present work is to study the response of systems (1) and (3) due to general impulsive excitations $F_{pi}(t)$. Before analyzing the forced responses, it is of interest to review the nonlinear mode localization properties of the unforced system, corresponding to $F_{pi}(t)=0$ in (3). A detailed dynamic analysis of the unforced system was carried out in [18] by employing the method of multiple scales. To this end, the responses q_{pi} in (3) are expressed in the form:

$$q_{pi} (t) = q_{pi} (T_0,T_1) = A_{pi}(T_1) \, e^{j\omega_i T_0} + \bar{A}_{pi}(T_1) \, e^{-j\omega_i T_0} + O(\varepsilon) \tag{5}$$

where $T_0 = t$ and $T_1 = \varepsilon t$ are "fast" and "slow" time-scales [24], $A_{ip}(T_1)$ are complex amplitudes, $(\cdot)$ denotes the complex conjugate, and ω_i is the natural frequency of the i-th linearized cantilever mode. The complex amplitudes in (5) are computed by substituting (5) into (4) and eliminating "secular terms" of the $O(\varepsilon)$ equations, i.e., terms which lead to unbounded and, thus, non-uniformly valid solutions in time [18]. At this point, it is noted that a low-order "internal resonance" exists between the second and third flexural cantilever modes $\phi_2(x)$ and $\phi_3(x)$, since their corresponding linearized natural frequencies are nearly integrably related: $\omega_3 \sim 3\omega_2$. *Such a low-order "internal resonance" is well known [24-27] to lead to nonlinear transfer of energy between the associated linearized modes and hence, is expected to influence the nonlinear mode localization in the flexible system under consideration.* To study the effects of this low-order "internal resonance" one introduces a "detuning" parameter, σ, defined as:

$$\omega_3 = 3\omega_2 + \varepsilon\sigma. \tag{6}$$

Parameter σ quantifies the closeness of the multiples of the natural frequencies of the modes participating in the "internal resonance." Truncating expression (2) to three modes per blade (n=3), expressing the complex amplitudes as, $A_{pi}(T_1) = (1/2) a_{pi}(T_1) e^{j\theta_{pi}(T_1)}$, where a_{pi} and θ_{pi} are real amplitudes and phases, substituting (5) into (3), and eliminating "secular terms," the following set of differential equations governing the amplitude- and phase-modulations is derived:

(Mode 1)
$$\omega_1 a_{11}' = (1/2) \gamma_{11} a_{21} \sin(\theta_{21}-\theta_{11})$$

$$\omega_1 a_{21}' = - (1/2) \gamma_{11} a_{11} \sin(\theta_{21}-\theta_{11})$$

$$\omega_1 a_{11} \theta_{11}' = (1/2) \gamma_{11} \left(a_{11} - a_{21} \cos(\theta_{21}-\theta_{11})\right) - (a_{11}/8) \sum_{k=1}^{3} \eta_{1k} a_{1k}^2$$

$$\omega_1 a_{21} \theta_{21}' = (1/2) \gamma_{11} \left(a_{21} - a_{11} \cos(\theta_{11}-\theta_{21})\right) - (a_{21}/8) \sum_{k=1}^{3} \eta_{1k} a_{2k}^2 \tag{7i}$$

(Mode 2) $\omega_2 a_{12}' = (1/2) \gamma_{22} a_{22} \sin(\theta_{22}-\theta_{12}) + (\xi/8) a_{13} a_{12}^2 \sin(\theta_{13}-3\theta_{12}+\sigma_1 T_1)$

$$\omega_2 a_{22}' = (1/2) \gamma_{22} a_{12} \sin(\theta_{12}-\theta_{22}) + (\xi/8) a_{23} a_{22}^2 \sin(\theta_{23}-3\theta_{22}+\sigma_1 T_1)$$

$$\omega_2 a_{12} \theta_{12}' = (1/2) \gamma_{22} \left(a_{12} - a_{22} \cos(\theta_{22}-\theta_{12})\right) - (a_{12}/8) \sum_{k=1}^{3} \eta_{2k} a_{1k}^2 -$$

$$-(\xi/8) a_{13} a_{12}^2 \cos(\theta_{13}-3\theta_{12}+\sigma_1 T_1)$$

$$\omega_2 a_{22} \theta_{22}' = (1/2) \gamma_{22} \left(a_{22} - a_{12} \cos(\theta_{12}-\theta_{22})\right) - (a_{22}/8) \sum_{k=1}^{3} \eta_{2k} a_{2k}^2 -$$

$$- (\xi/8) a_{23} a_{22}^2 \cos(\theta_{23}-3\theta_{22}+\sigma_1 T_1) \tag{7ii}$$

(Mode 3) $\omega_3 \, a_{12}' = (1/2) \, \gamma_{33} \, a_{23} \sin(\theta_{23}-\theta_{13}) - (\delta/8) \, a_{12}^3 \sin(\theta_{13}-3\theta_{12}+\sigma_1 T_1)$

$\omega_3 \, a_{23}' = (1/2) \, \gamma_{33} \, a_{13} \sin(\theta_{13}-\theta_{23}) - (\delta/8) \, a_{22}^3 \sin(\theta_{23}-3\theta_{22}+\sigma_1 T_1)$

$\omega_3 \, a_{13} \, \theta_{13}' = (1/2) \, \gamma_{33} \left(a_{13} - a_{23} \cos(\theta_{23}-\theta_{13})\right) - (a_{13}/8) \sum_{k=1}^{3} \eta_{3k} \, a_{1k}^2 \; -$

$- (\delta/8) \, a_{12}^3 \cos(\theta_{13}-3\theta_{12}+\sigma_1 T_1)$

$\omega_3 \, a_{23} \, \theta_{23}' = (1/2) \, \gamma_{33} \left(a_{23} - a_{13} \cos(\theta_{13}-\theta_{23})\right) - (a_{23}/8) \sum_{k=1}^{3} \eta_{3k} \, a_{2k}^2 \; -$

$- (\delta/8) \, a_{22}^3 \cos(\theta_{23}-3\theta_{22}+\sigma_1 T_1)$ (7iii)

In (7), primes denote differentiation with respect to the "slow time" T_1. The various parameters appearing in (7) are defined as:

$$\eta_{ii} \equiv 2\omega_i^2 \, b_{iiii} - 3a_{iiii}, \quad \eta_{pi} \equiv 2b_{pipi} \, (\omega_p^2 + \omega_i^2) - 2(a_{ppii} + a_{piip} + a_{pipi})$$

$$\zeta \equiv b_{2232} \, (\omega_3 - \omega_2)^2 + 2\omega_2^2 \, b_{2322} - a_{2223} - a_{2232} - a_{2322}. \quad \delta \equiv 2\omega_2^2 \, b_{3222} - a_{3222} \quad (8)$$

The free nonlinear *periodic* solutions of the system are investigated by replacing the angle-variables θ_{pi} with the new phase-variables $\Phi_1 = \theta_{21} - \theta_{11}$, $\Phi_2 = \theta_{22} - \theta_{12}$, $\Phi_3 = \theta_{23} - \theta_{13}$, and $\Psi_1 = \theta_{13} - 3\theta_{12} + \sigma T_1$, and reducing equations (7) to a set of ten *autonomous* ordinary differential equations of first order [18]. The periodic solutions of the system are then obtained by imposing stationarity conditions on the amplitude- and phase-variables, i.e., by setting $a_{pi}' = 0$, $\Phi_i' = 0$, and $\Psi_1' = 0$ in the reduced set of equations, and solving the resulting set of stationary algebraic equations. This calculation was performed in [18], where it was found that, *certain of the periodic solutions of the system are localized.* During such motions (localized normal oscillations), the modal amplitudes of one beam are much larger in magnitude than the corresponding amplitudes of the other beam, and thus, the vibrational energy is spatially confined and nearly restricted to only one of the two subsystems. In a localized normal oscillation, the motions of the two beams are approximately given by:

$$v_p(x,t) \approx \sum_{i=1}^{3} [\, a_{pi}^* \cos(\omega_i t + \theta_{pi}^*(\varepsilon t)) + O(\varepsilon) \,] \, \phi_i(x), \qquad p = 1, 2 \quad (9)$$

where a_{pi}^* and $\theta_{pi}^*(\varepsilon t)$ denote the localized modal amplitudes and angles, obtained by solving the stationary equations. The stability of the periodic solutions (9) can be studied by Floquet analysis, i.e., by forming the appropriate system of linear variational equations in terms of the amplitude and phase modulations and computing the eigenvalues of the associated Floquet matrix [24].

It turns out that there exist two basic classes of localized nonlinear modes in the system. The first category involves participation of only the first cantilever mode of the two blades, i.e., $a_{11}^* \neq 0$, $a_{21}^* \neq 0$, $a_{pi}^* = 0$, $p=1,2$, $i=2,3$, and the localized modes are depicted in figure 2a. Note that nonlinear localization depends on the ratio $r=\gamma_{11}/\eta_{111}$. From definitions (4) and (8) it can be seen that γ_{11} is a parameter related to the strength and

position of the coupling stiffness, whereas η_{11} relates to the geometric nonlinearities of the beam. As $r \to 0$, the bifurcating modes become localized, $\lim_{r \to 0} \{ a_{11}{}^*/a_{21}{}^* \} = 0$ or ∞, and the energy of the corresponding free motion is mainly confined to only one of the two beams (figure 2a). When r increases, the localized branches become non-localized and eventually coalesce with the antisymmetric mode in a hamiltonian pitchfork bifurcation. *This bifurcation point can be regarded as the point of generation of the nonlinear mode localization phenomenon.* In physical terms, parameter r represents the ratio of coupling over nonlinear forces, and thus, figure 2a shows that *when both beams oscillate in their first bending mode, nonlinear mode localization occurs only when the coupling forces are weak, and/or the beam nonlinearities are strong.*
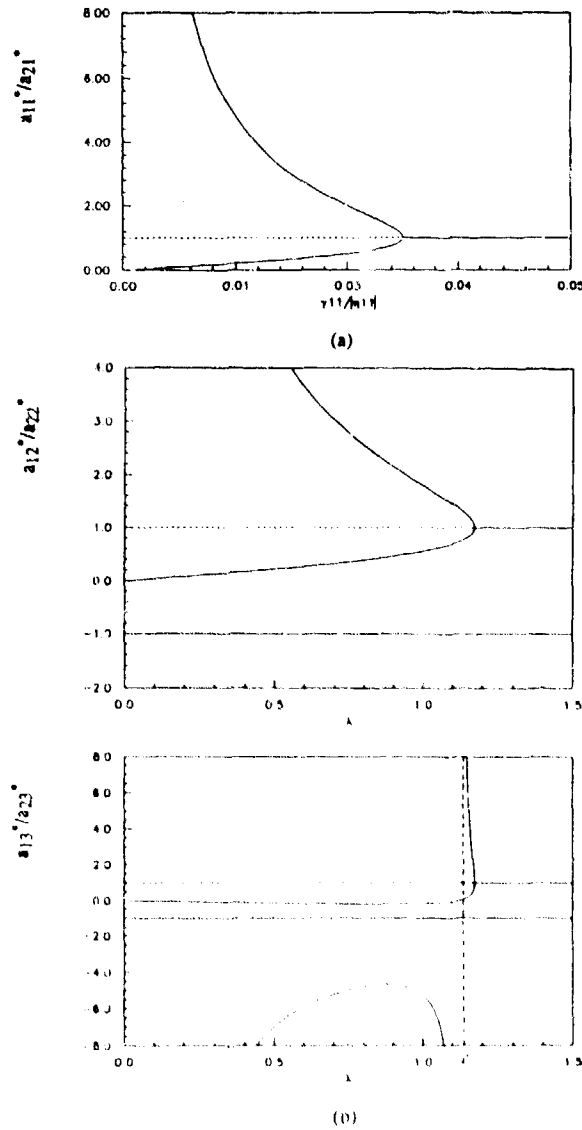

Figure 2. Nonlinear mode localization for beams oscillating in (a) their first cantilever mode, and (b) in their second and third cantilever modes.
————————— Stable modes, ------------------ Unstable modes.

VAKAKIS, BENTSMAN

The second class of nonlinear localized modes involves participation of only the second and third cantilever modes, i.e., $a_{11}^* = a_{21}^* = 0$, $a_{pi}^* \neq 0$, p=1,2, i=2,3. In this case, the "internal resonance" between modes 2 and 3 greatly affects the topology of the localized branches. For c = 1 / L = 0.7650 (where 1 is the coupling position), the branches of localized modes are depicted in figure 2b. In each of the two diagrams the ratio of the modal amplitudes (a_{1i}^*/a_{2i}^*), i=2,3 is plotted versus the parameter $\lambda = (kL^4/EI)/a_{3223}$. Again, it is observed that $\lim_{\lambda \to 0} \{a_{1i}^*/a_{2i}^*\} = 0$ or ∞, i=2,3, i.e., that as the coupling decreases and/or the nonlinearity increases nonlinear mode localization occurs. As λ increases, the localized modes become non-localized, until they coalesce with the symmetric mode in a pitchfork bifurcation. An interesting feature of mode localization in the presence of internal resonance is its essential dependence on the position of the coupling stiffness. Indeed, when c=l/L is close to 0.783, the value corresponding to the node of the second (lower) cantilever mode, a complicated sequence of bifurcations of certain solution branches takes place [18]. Additionally, it can be shown that *high modes are more susceptible to nonlinear mode localization than lower ones*. In figure 3, the values of the coupling stiffness at the points of generation of the localized mode branches are plotted as functions of the position of the coupling stiffness. Both categories of localized solutions are depicted, and it can be seen that localization for modes 2 and 3 is generated at much higher values of the coupling stiffness than for mode 1. Similar results hold for higher modes. It is concluded that, *if the coupling stiffness is low enough to localize the first cantilever mode, then it is sufficient to localize all higher modes;* this result is in full agreement with existing theories on mode localization of disordered, linear beam assemblies [4,5,16,17,23].
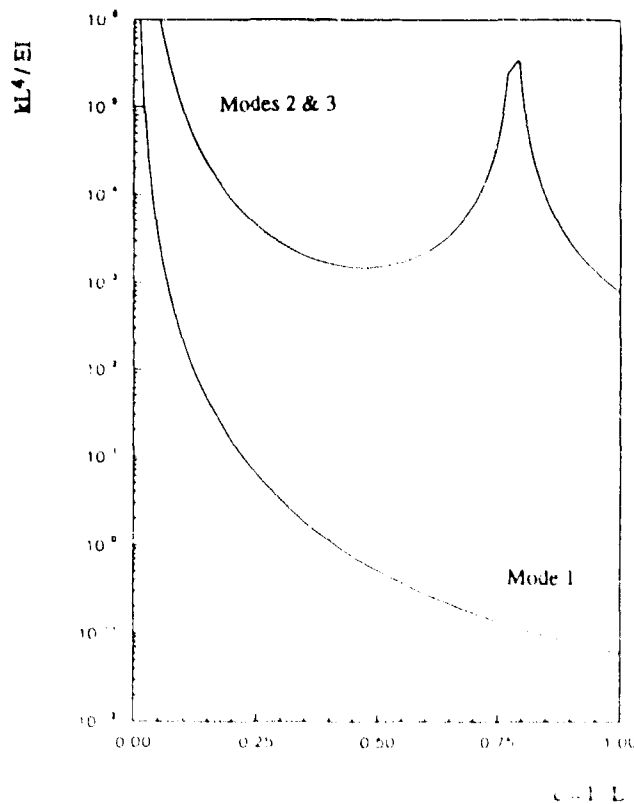

Figure 3. Coupling strength at the point of generation of nonlinear mode localization, versus coupling position.

VAKAKIS, BENTSMAN

The results presented in this section establish the existence of stable nonlinear localized modes in the unforced flexible assembly of figure 1. These modes were found to exist only for sufficiently small coupling stiffnesses and/or large nonlinear forces. Moreover, the nonlinear localization phenomenon becomes much more profound for high-mode vibrations. In the next sections it will be shown that, due to nonlinear mode localization, a spatial confinement of a general class of externally induced transient impulses results. Thus, it will be proven that the symmetric two-beam nonlinear system possesses passive motion confinement characteristics, a result with no counterpart in existing linear theories.

3. IMPULSIVE MOTION CONFINEMENT

Passive confinement of externally induced impulses in a *discrete* nonlinear cyclic system was studied in [8], by employing purely numerical techniques. To initiate the study of the motion confinement properties of the nonlinear flexible system of figure 1, excitations of the following form are assumed to be applied to the two beams:

$$F_1(x,t) = (1/\varepsilon) f_1(t) \phi_1(x) \text{ for } 0 \leq t < \varepsilon D, \text{ and } F_1(x,t) = 0 \text{ for } t \geq \varepsilon D$$
$$F_2(x,t) = 0, \ 0 \leq t < \infty \tag{10}$$

Thus, a general impulsive excitation of duration εD is assumed to act on beam 1, with a spatial distribution identical to that of the first linearized cantilever mode. Beam 2 is not directly excited at this stage. Forcing functions with more general spatial distributions will be considered in the next session. Expressing the displacements $v_p(x,t)$, $p=1,2$, in terms of the linearized cantilever modes, the discretized set of forced ordinary differential equations (3) is obtained. Taking into account definitions (4) and (10), the forcing terms in equations (3) assume the form,

$$(1/\varepsilon) F_{pi}(t) = (1/\varepsilon) \int_0^1 f_1(t) \phi_i^2(x) \, dx \, \delta_{p1} \, \delta_{i1} \text{ for } 0 \leq t < \varepsilon D, \ F_{pi}(t) = 0 \text{ for } t \geq \varepsilon D \tag{11}$$

where δ_{ij} is Kroenecker's symbol. It is therefore concluded that by using the impulse distributions (10), it is ensured that only the first cantilever mode of beam 1 is *directly* excited by the forcing distributions (10). *It is of interest to study the transfer of the energy of the impulse from the directly excited mode to the other modes of the system; clearly, spatial motion confinement of the external impulse is achieved if and only if minimal amounts of vibrational energy eventually "leak" to the modes of the unforced beam 2.*

In the previous section, it was found that a low order "internal resonance" exists between the second and third cantilever modes; moreover, the first cantilever mode was found not to possess any nonlinear coupling with any higher modes. Hence, no energy transfer is expected to occur from the directly excited first mode of beam 1, to any other higher modes of the two beams, and thus, the only possible energy exchange is anticipated to take place only between the first cantilever modes of the two beams. This theoretical prediction will be verified in the following analysis. The dynamics of the forced system (3) will now be analyzed, by examining the modal responses in two distinct phases. For the sake of simplicity, the analysis is limited to n=3 cantilever modes per beam.

Phase 1. $0 \leq t < \varepsilon D$. During this phase, the applied force is non-zero, and the response is asymptotically approximated by introducing the new time T, defined by $t=\varepsilon T$. The range of values of the new time variable during this phase of the motion is, $0 \leq T < D$.

VAKAKIS, BENTSMAN

Expressing the time derivatives in (3) in terms of the new variable T, the governing equations for the modal amplitudes are written as:

(Mode 1)

$$d^2(q_{p1}) / dT^2 = \varepsilon \left\{ -\sum_{b=1}^{3} \sum_{k=1}^{3} \sum_{l=1}^{3} \frac{b_{1bkl}}{2} q_{pb} [q_{pk} q_{p1}]_{TT} + \hat{p}_1(T)\delta_{p1} \right\} -$$

$$- \varepsilon^2\omega_1^2 q_{p1} - \varepsilon^3 \left\{ \sum_{b=1}^{3} \sum_{k=1}^{3} \sum_{l=1}^{3} a_{1bkl} q_{pb} q_{pk} q_{p1} + \sum_{k=1}^{3} \gamma_{ik}(q_{pk} - q_{(p+1)k})) \right\}, \ p=1,2 \quad (12)$$

with similar expressions holding for the modal displacements q_{p2}, and q_{p3}, p=1,2, of the higher modes. Complementing (12), is the set of initial conditions $q_{pi}(0)=0$, $d(q_{pi}(0))/dT=0$, p=1,2, i=1,2,3, since at t=T=0 the system is assumed to be at rest. In equations (12), all depended variables are functions of T, and the new forcing function is defined as,

$$\hat{p}_1(T) = F_{11}(\varepsilon T) \quad (13)$$

The response of system (12) is approximated using regular perturbation expansions, i.e.,

by expressing the responses in the form, $q_{pi}(T) = \sum_{m=1}^{\infty} \varepsilon^m q_{pi}^{(m)}(T)$, and substituting in

(12). By matching the coefficients of respective powers of ε, one determines the various orders of approximation. Omitting the calculations, and transforming in terms of the original time variable, the response of the system during this phase is computed as:

$$q_{11}(t) = \varepsilon \int_0^{(t/\varepsilon)} \int_0^\eta \hat{p}_1(s) \, ds \, d\eta + O(\varepsilon^3), \quad \dot{q}_{11}(t) = \int_0^{(t/\varepsilon)} \hat{p}_1(s) \, ds + O(\varepsilon^2)$$

$$q_{ij}(t) = O(\varepsilon^4), \quad \dot{q}_{ij}(t) = O(\varepsilon^3), \quad \text{otherwise} \quad (14)$$

Hence, the analysis predicts that for $0 \leq t < \varepsilon D$ (the duration of the impulse), the response of the system is mainly determined by the impulse itself and not by any structural parameters (the system "does not have time to oscillate"). Note that, the velocity of the directly excited mode is of O(1), whereas the response of all unforced modes are orders of magnitudes smaller than that of the directly forced mode. The resulting physical motions of the two beams are given by:

$$v_1(x,t) \approx \phi_1(x) \, q_{11}(t) + O(\varepsilon^3), \quad v_2(x,t) \approx O(\varepsilon^4), \quad \text{for} \ 0 \leq t < \varepsilon D \quad (15)$$

Phase 2, $t \geq \varepsilon D$. During this phase of the motion, the impulse ceases to apply, and, thus, *the system performs free oscillations*, with initial conditions determined from (14). Introducing the time translation $\hat{t}=t-\varepsilon D$, the governing equations (3) are expressed as:

$$\ddot{q}_{pi} + \omega_i^2 q_{pi} = -\varepsilon \left\{ \sum_{b=1}^{3} \sum_{k=1}^{3} \sum_{l=1}^{3} \left[a_{ibkl} q_{pb} q_{pk} q_{p1} + \frac{b_{ibkl}}{2} q_{pb} d^2(q_{pk} q_{p1})/d\hat{t}^2 \right] + \right.$$

$$\left. + \sum_{k=1}^{3} \gamma_{ik} (q_{pk} - q_{(p+1)k})) \right\} \quad , \ p=1,2, \ i=1,2,3 \quad (16)$$

461

where differentiation is carried out with respect to $\hat{t}$, and $q_{pi} = q_{pi}(\hat{t})$. From (14), the set of initial conditions complementing (16) is, $q_{11}(0)=\varepsilon\int_C^D \int_0^\eta \hat{p}_1(s) \, ds \, d\eta +O(\varepsilon^3)$, $\dot{q}_{11}(0)=\int_0^D \hat{p}_1(s) \, ds +O(\varepsilon^2)$, $q_{pi}(0) = O(\varepsilon^4)$, and $\dot{q}_{pi}(0) = O(\varepsilon^3)$, otherwise. Since equations (16) represent *free* oscillations of the system, their solutions can be analytically approximated by the multiple-scales singular perturbation analysis outlined in section 2. To this end, the modal responses are expressed according to (5), with time scales $T_0 = \hat{t}$ and $T_1 = \varepsilon\hat{t}$. Introducing the transformations $A_{pi}(T_1) = (1/2) \, a_{pi}(T_1) \, e^{j\theta_{pi}(T_1)}$, p=1,2, i=1,2,3, the modulation equations (7) governing the real amplitudes $a_{pi}(T_1)$ and angles $\theta_{pi}(T_1)$ are obtained. In order to compute the amplitude and phase modulations of the response, one should solve equations (7), with initial conditions, $a_{11}(0)=-(1/\omega_1)\int_0^D \hat{p}_1(s) \, ds$, $a_{21}(0)=0$, $\theta_{11}(0)=\pm\pi/2$, $\theta_{21}(0)=0$, $a_{pi}(0)=0$, otherwise. The resulting physical motions of the beams are then approximated by:

$$v_p(x,t) \approx \sum_{i=1}^{3} \left[a_{pi}(\varepsilon(t-\varepsilon D)) \cos\left(\omega_i(t-\varepsilon D) + \theta_{pi}(\varepsilon(t-\varepsilon D))\right)+O(\varepsilon) \right] \phi_i(x), \quad t \geq \varepsilon D. \quad p = 1, 2 \quad (17)$$

Considering the structure of equations (7ii) and (7iii), it can be mathematically proven that, if $a_{12}(0) = a_{13}(0) = a_{22}(0) = a_{23}(0) = 0$, then $a_{12}(T_1) = a_{13}(T_1) = a_{22}(T_1) = a_{23}(T_1) = 0$, $\forall$ T_1. Therefore, in this case, the modulation equations (7), can be reduced into the set:

$$a_{11}' = (\gamma/2\omega) \, a_{21} \sin(\theta_{21}-\theta_{11})$$

$$a_{21}' = -(\gamma/2\omega) \, a_{11} \sin(\theta_{21}-\theta_{11})$$

$$a_{11}\theta_{11}' = \left[(3\alpha/8\omega_1) - (\beta\omega_1/4)\right] a_{11}^3 + (\gamma/2\omega) \, a_{11} - (\gamma/2\omega) \, a_{21} \cos(\theta_{21}-\theta_{11})$$

$$a_{21}\theta_{21}' = \left[(3\alpha/8\omega_1) - (\beta\omega_1/4)\right] a_{21}^3 + (\gamma/2\omega) \, a_{21} - (\gamma/2\omega) \, a_{11} \cos(\theta_{21}-\theta_{11}) \quad (18a)$$

where primes denote differentiation with respect to the "slow time" T_1, and the simplified notation, $\alpha \equiv a_{1111}$, $\beta \equiv b_{1111}$, and $\gamma \equiv \gamma_{11}$, is adopted from now on. *Hence, it is proven that the only possible energy transfer is between the first modes of the two beams, and that no other energy exchange involving higher modes occurs.* In order to investigate the energy transfer between the modes of beams 1 and 2, one needs to integrate equations (18a). Define at this point the quantity $J=\gamma/\left(\left[(3\alpha/2)-(\beta\omega_1^2)\right]\rho\right)$, where $\rho=(2\omega_1)^{-1}\int_0^D \hat{p}_1(s) \, ds$;

Parameter J is recognized as the ratio of the coupling over the nonlinear forces. It will be now shown that, for $J<<1$, the response of the system can be analytically approximated. This is achieved by expressing the amplitudes and angles as, $a_{p1}(T_1)= \sum_{m=0}^{\infty} J^m a_{p1}^{(m)}(T_1)$,

$\theta_{p1}(T_1) = \sum_{m=0}^{\infty} J^m \, \theta_{p1}^{(m)}(T_1)$ p=1, 2, and substituting into (18a). Matching terms proportional to the same power of J, leads to the following analytical expressions for the amplitude modulations:

$$a_{11}(T_1)=\pm\left\{2\rho-(J^2/\rho)\sin^2\left(\left[(3\alpha/4\omega_1)-(\beta\omega_1/2)\right]\rho^2 T_1\right)+O(J^3)\right\}$$

$$a_{21}(T_1)=\pm\left\{-2J\sin\left(\left[(3\alpha/4\omega_1)-(\beta\omega_1/2)\right]\rho^2 T_1\right)+O(J^2)\right\}\quad (J<<1)\quad(18b)$$

Similar analytical expressions hold for the angles $\theta_{p1}(T_1)$. Solutions (18b) predict that, *when* $J<<1$, *the transient impulsive response of the system is mainly confined to the directly excited blade, since* $a_{11}(T_1) >> a_{21}(T_1)$. Now, based on the results of section 2, the condition $J<<1$ (weak coupling and/or strong nonlinearities) is also recognized as the condition for the existence of localized nonlinear modes in the system. It is therefore concluded that, *when the system possesses nonlinear localized modes, it also possesses passive motion confinement properties: when an external impulse acts at one beam of the system, the disturbance remains spatially confined to its point of application, and only a small portion of the injected energy "leaks" to the unforced beam.* Moreover, from (18b), it is predicted that the responses of the forced and unforced beams contain $O(J^2)$ and $O(J)$-amplitude modulations respectively. This is consistent with energy conservation considerations. Indeed, from (18b), a direct computation gives, $a_{11}^2(T_1) + a_{21}^2(T_1) = 4\rho^2$ + $O(J^3)$. Correct to $O(\epsilon)$, this relation can be shown to represent conservation of energy of the free, undamped system under consideration [28]. It must be stated that the analytic approximations (18b) hold only for small values of the quantity J.
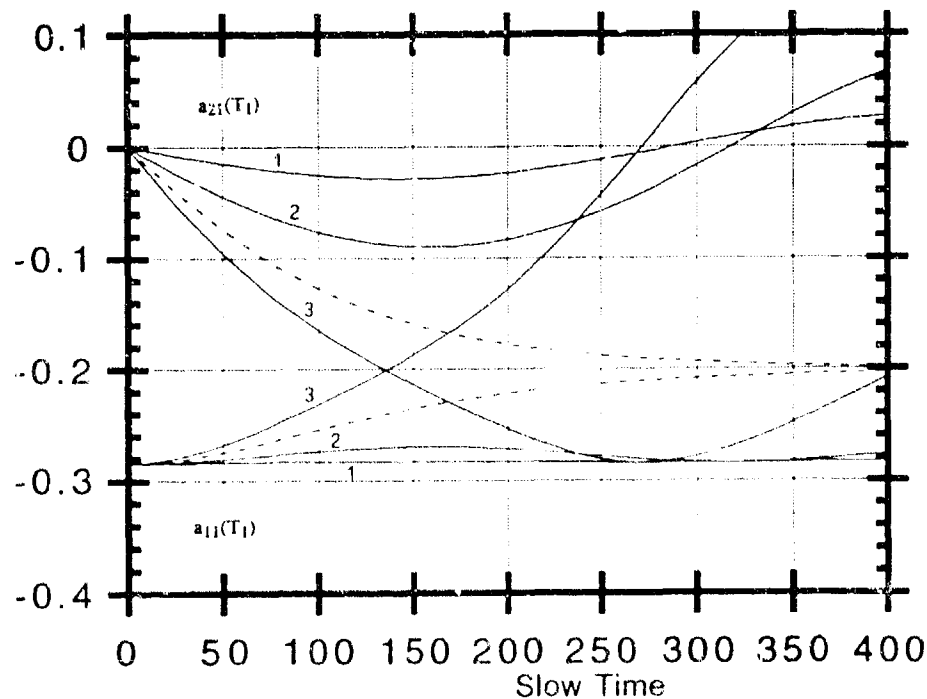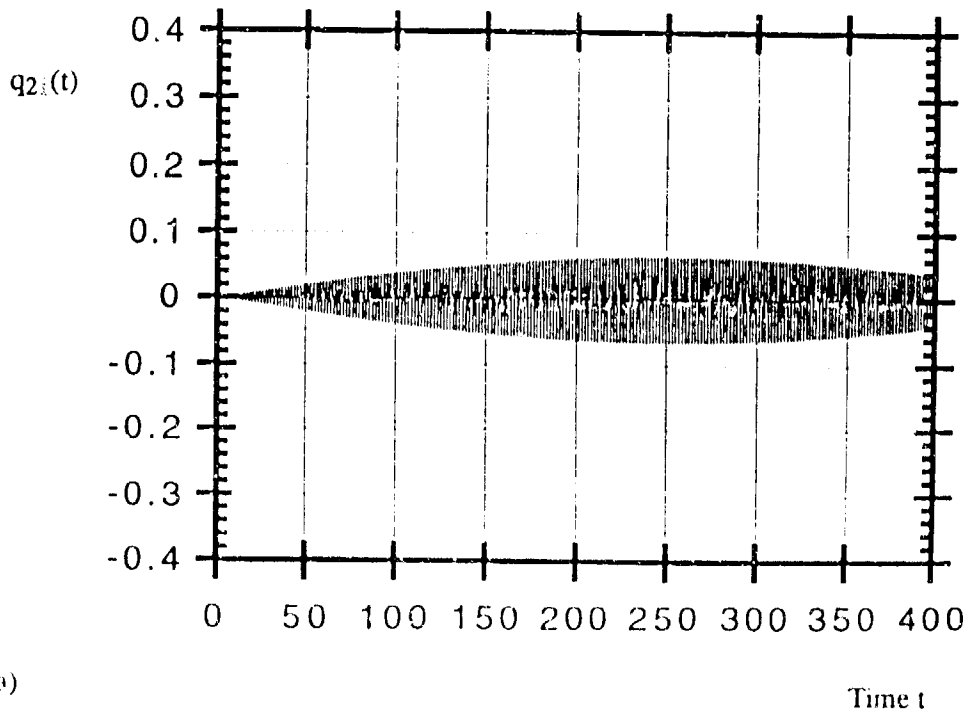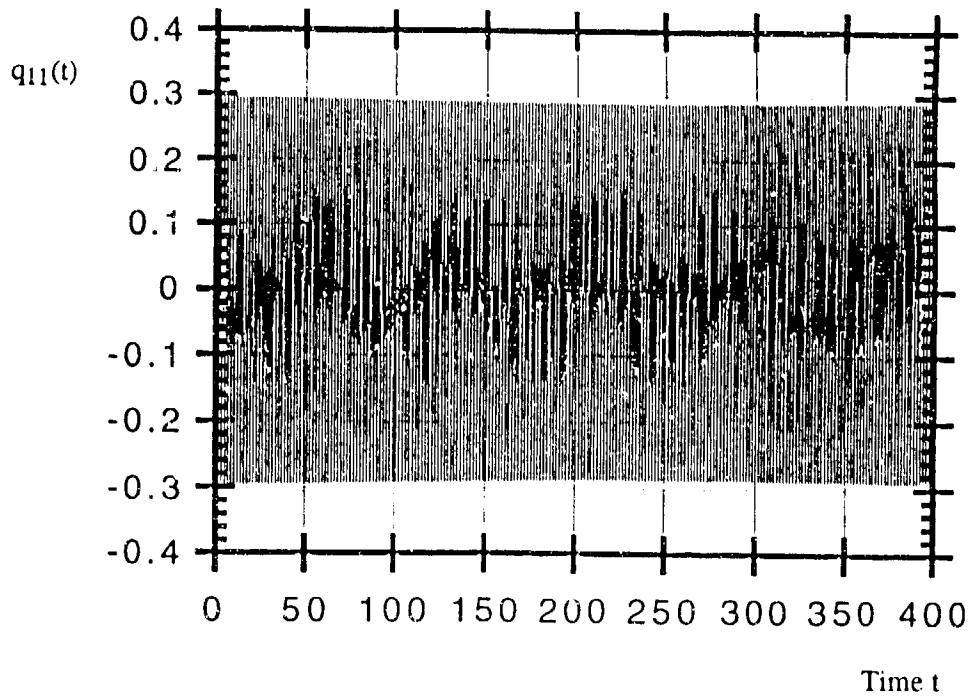

Figure 4. Single-mode oscillations, amplitude modulations computed by numerically integrating the reduced set of modulation equations (18a): (1) J=0.0142, (2) J=0.0426, (3) J=0.0924, ------------------ J=J$_{cr}$=0.0711.

As J increases to finite values, i.e., when the coupling increases and/or the nonlinear forces decrease, one needs to resort to numerical integrations in order to compute the solutions of system (18a). The numerical integrations verify the theoretical predictions. The numerically computed amplitude modulations for $\alpha=40.44$, $\beta=4.59$, $\varepsilon=0.5$, $\omega_1^2=12.38$ (rad/sec)^2, and $\rho=0.1421$ are depicted in figure 4. For the sake of clarity, only the "lower" pair of modulations is shown. The parameter J was varied by changing the coupling variable γ. For $J\ll1$, the modal amplitude of the unforced beam 2 is small, whereas the directly excited beam undergoes a modulated oscillation close to its initial amplitude value, $a_{11}(0) = -(1/\omega_1)\int_0^D \hat{p}_1(s)\, ds = -2\rho$. *Hence, for $J\ll1$, passive motion confinement of the impulse to the directly excited beam is observed.* As J increases, the amplitude a_{21} of the unforced beam grows, indicating an increased transfer of energy out of the directly excited beam, or equivalently, a diminishing of the motion confinement capacity of the system. At a critical value, $J=J_{cr}=\rho/2$, *all* vibrational energy of the directly excited beam is eventually transferred to the unforced one. For values of J above the critical value, energy is continuously transferred between the two beams, and the system does not possess passive motion confinement properties anymore. To verify the results of the multiple-scales analysis, an impulsive distributed excitation of magnitude $F_1(x,t) = 5\,\phi_1(x)$ $\Rightarrow (1/\varepsilon)\,F_{11}(t) = \int_0^1 10\,\phi_i\, dx$, and duration $\varepsilon D=0.1\text{sec}$ was applied to beam 1, and the structural parameters were assigned the values, $\varepsilon=0.5$, $a_{1111}=40.44$, $b_{1111}=4.59$, $\gamma_{1i}=0.02$, $\omega_1=3.51$ (rad/sec), $J=0.0367\ll1$; the response was numerically computed by directly integrating the differential equations of motion (12) with $q_{12}=q_{13}=q_{22}=q_{23}=0$, and assuming zero initial conditions at $t=0$. In figure 5a the responses of the two beams are shown as functions of time, and in figure 5b, a projection of the phase space of the motion is depicted. Note that the energy of the injected impulse is mainly confined to the directly forced beam, according to theoretical predictions. *The amplitude of the unforced beam can be further diminished by decreasing the coupling stiffness and/or increasing the nonlinear coefficients.* For comparison purposes, the theoretically predicted amplitude modulations (18b) are also presented in figure 5c. Clearly, the asymptotic theory agrees well with the numerical computations for this low value of J. Note, that in the absence of nonlinearities, all injected energy is continuously transferred between the forced and unforced beams, in the well-known "beat phenomenon." *Hence, the detected passive motion confinement phenomenon is solely attributed to the geometric nonlinearities of the system.*

Summarizing, the results of this section prove that, for small values of the parameter J (i.e., for small coupling stiffness and/or large nonlinear forces), impulsive forces with spatial distributions identical to the first cantilever mode become spatially confined to the directly excited beam. The only possible energy exchange in this case is between the first modes of the two beams, and no higher modes are indirectly excited. As J increases, the amount of energy "leaking" to the unforced beam also increases, and the passive motion confinement of the induced disturbance becomes less profound. For J greater than a critical value no motion confinement becomes possible anymore.
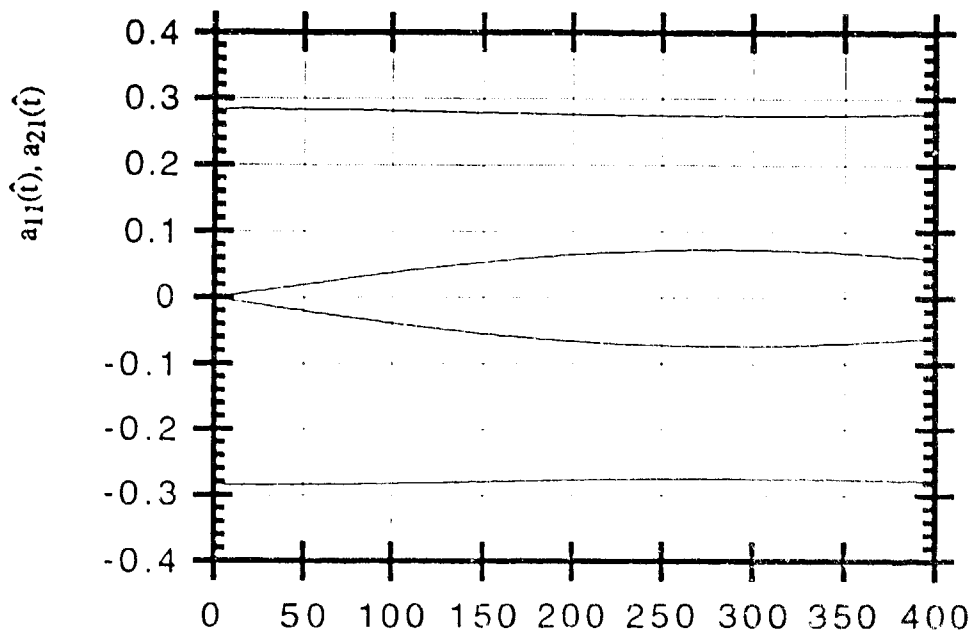
Figure 5. Single-mode oscillations, amplitude modulations computed by, (a) direct integrations of the equations of motion, time responses, (b) direct integrations of the equations of motion, responses in a projection of the phase space, (c) theoretical results, eq.(18b).

465

(b)

$q_{11}(t)$, $q_{21}(t)$

(c)

Time $\hat{t}$

VAKAKIS, BENTSMAN
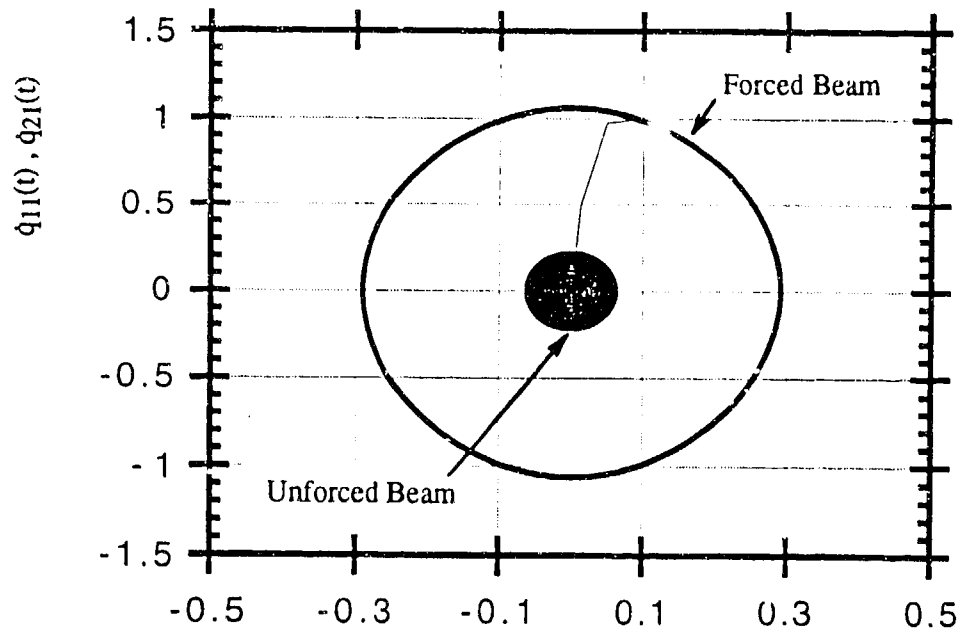
4. DISCUSSION

In this work it was proved that a geometrically nonlinear and weakly coupled system of beams can possess passive spatial motion confinement properties. The presented analysis employed regular and singular perturbation techniques, combined with numerical integrations of the corresponding modulation equations. For motions of the beams in their first cantilever mode, it was found that spatial motion confinement of the induced disturbance occurs only when the coupling is sufficiently small and/or the nonlinear effects large.

Although the analysis presented herein dealt with a configuration of only two beams, the obtained results can be extended to a more general class of multiple connected flexible systems with or without symmetry. By designing such systems so that their coupling stiffnesses are small or/and their geometric nonlinearities large, applied impulses are ensured not to "spread" through the entire structure, but to remain confined to the subsystem where they are originally applied. *Note that this confinement of vibrational energy is purely passive*, and is solely due to orbitally stable localized nonlinear modes of the system. The implications of such a dynamical feature are profound. Indeed, a system whose inherent dynamics lead to motion confinement of external disturbances is much more amenable to active or passive isolation than a structure possessing "extended" dynamic modal responses (i.e., motions during which all of its substructures vibrate with finite amplitudes). Therefore, the class of nonlinear systems under consideration in this work are expected to possess enhanced controllability features, since in the planning of passive or active control algorithms one needs only consider the dynamic response of only a limited number of substructures instead of the whole system; however, issues of performance, "spill-over" and robustness must be addressed in such active designs.

ACKNOWLEDGEMENTS

REFERENCES

1. Hodges, C.H., "Confinement of Vibration by Structural Irregularity," *Journal of Sound and Vibration*, Vol. 82, No 3, 1982, pp. 411-424.
2. Pierre, C., Dowell, E.H., "Localization of Vibrations by Structural Irregularity," *Journal of Sound and Vibration*, Vol. 114, No. 3, 1987, pp. 549-564.
3. Wei, S.-T., and Pierre, C., "Localization Phenomena in Mistuned Assemblies with Cyclic Symmetry Part I: Free Vibrations & II: Forced Vibrations" *ASME Journal of Vibration, Acoustics and Reliability in Design*, Vol. 110, 1988, pp. 429-448.
4. Bendiksen, O.O., "Mode Localization Phenomena in Large Space Structures," *AIAA Journal*, Vol. 25, No 9, 1987, pp. 1241-1248.
5. Cornwell, P.J., and Bendiksen, O.O., "Localization of Vibrations in Large Space Reflectors," *AIAA Journal*, Vol. 27, No 2, 1989, pp. 219-226.
6. Vakakis, A.F., "Nonsimilar Normal Oscillations in a Strongly Nonlinear Discrete System," *Journal of Sound and Vibration*, Vol. 158, No 2, 1992, pp. 341-361.
7. Vakakis, A.F., and Cetinkaya, C., "Mode Localization in a Class of Multi-Degree-of-Freedom Nonlinear Systems With Cyclic Symmetry," *SIAM Journal on Applied Mathematics*, Vol. 53, 1993, pp. 265-282.

8. Vakakis, A.F., Nayfeh, T., and King, M.E., "A Multiple-Scales Analysis of Nonlinear, Localized Modes in a Cyclic Periodic System," *ASME Journal of Applied Mechanics,* 1993, (in press).

9. Rosenberg, R.M., "On Nonlinear Vibrations of Systems with Many Degrees of Freedom," *Advances in Applied Mechanics,* Vol. 9, 1966, pp. 155-242.

10. Caughey, T.K., and Vakakis, A.F., "A Method for Examining Steady State Solutions of Forced Discrete Systems with Strong Non-linearities," *International Journal of Non-Linear Mechanics,* Vol. 26, 1991, pp. 89-103.

11. Vakakis, A.F., and Caughey, T.K., "A Theorem on the Exact Nonsimilar Steady-States of a Nonsimilar Oscillator," *ASME Journal of Applied Mechanics,* Vol. 59, 1992, pp. 418-424.

12. Vakakis, A.F., "Fundamental and Subharmonic Resonances in a System with a '1-1' Internal Resonance," *Nonlinear Dynamics,* Vol. 3, 1992, pp. 123-143.

13. Shaw, S.W. and Pierre, C., "Normal modes of vibration for nonlinear continuous systems," *Journal of Sound and Vibration,* 1993, (in press).

14. King, M.E. and Vakakis, A.F., "An Energy-Based Formulation for Computing Nonlinear Normal Modes in Undamped Continuous Systems," *ASME Journal of Vibration and Acoustics,* 1993 (submitted).

15. Pierre, C., and Shaw, S., "Mode Localization due to Symmetry-Breaking Nonlinearities," *International Journal of Bifurcation and Chaos,* Vol.1, No 2, 1991, pp. 471-475.

16. Pierre, C. and Cha, P., "Strong Mode Localization in Nearly Periodic Disordered Structures," *AIAA Journal,* Vol. 27, No. 2, 1989, pp. 227-241.

17. Levine, M.B. and Salama, M.A., "Mode Localization Experiments on a Ribbed Antenna," *Proceedings of the 33rd AIAA / ASME / ASCE / AHS / ASC Structures, Structural Dynamics, and Materials Conference,* 1992, pp. 2038-2047.

18. King, M.E. and Vakakis A.F., "Mode Localization in a System of Coupled Flexible Beams with Geometric Nonlinearities." *Zeitschrift fur Angewandte Mathematik und Mechanik (ZAMM),* 1993, (in press).

19. Hodges, C.H., Woodhouse, J., "Confinement of Vibration by One-Dimensional Disorder, I: Theory of Ensemble Averaging & II: A Numerical Experiment on Different Ensemble Averages," *Journal of Sound and Vibration,* Vol. 130, No. 2, 1989, pp. 237-268.

20. Kissel, G.J., "Localization in Disordered Periodic Structures," Ph.D. Thesis, Massachusetts Institute of Technology, Boston, Massachusetts, 1988.

21. Pierre, C., "Weak and Strong Localization in Disordered Structures: A Statistical Investigation," *Journal of Sound and Vibration,* 1993 (in press).

22. Photiadis, D.M., "Anderson Localization of One-Dimensional Wave Propagation on a Fluid-Loaded Plate," *Journal of the Acoustical Society of America,* Vol. 91, No. 2, 1992, pp. 771-780.

23. Lust, S.D., Friedmann, P.P. and Bendiksen, O.O., "Free and Forced Response of Nearly Periodic Multi-Span Beams and Multi-Bay Trusses," *Proceedings of the 32nd AIAA / ASME / ASCE / AHS / ASC Structures, Structural Dynamics, and Materials Conference,* 1991, pp. 2831-2842.

24. Nayfeh, A. and Mook, D., "Nonlinear Oscillations," Wiley & Sons, New York, 1984.

25. Crespo Da Silva, M.R.M. and Zaretzky, C.L., "Non-Linear Modal Coupling in Planar and Non-Planar Responses of Inextensional Beams," *International Journal of Nonlinear Mechanics,* Vol. 25, No.2, 1990, pp. 227-239.

26. Crespo Da Silva, M.R.M. and Glynn, C.C., 1978, "Nonlinear Flexural-Torsional Dynamics of Inextensional Beams I: Equations of Motion II: Forced Motions," *Journal of Structural Mechanics,* Vol. 6, No.4, 1978, pp. 437-461.

VAKAKIS, BENTSMAN

27. Pai, Perng-Jin F., "Nonlinear Flexural - Flexural - Torsional Dynamics of Metallic and Composite Beams," Ph.D. Thesis, Virginia Polytechnic Institute and State University, Blacksburg, Virginia, 1992.
28. Vakakis, A.F. and Rand, R.H., "Normal Modes and Global Dynamics of a Two Degree-of-Freedom Nonlinear System 1: Low Energies," *International Journal of Nonlinear Mechanics*, Vol. 27, No. 5, 1991, pp. 861-874.

APPENDIX: Numerical values of the coefficients of equations (7).

Using the definitions (8) and (4), and taking into account that the linearized cantilever eigenfunctions are given by:

$$\phi_i(x) = \cosh\psi_i x - \cos\psi_i x + N(\psi_i) [\sinh\psi_i x - \sin\psi_i x] \qquad (A\text{-}1)$$

where $N(\psi_i) = (\sin\psi_i - \sinh\psi_i) / (\cos\psi_i + \cosh\psi_i)$, and $\cos\psi_i \cosh\psi_i = -1$, the various coefficients in equations (7) assume the following numerical values:

$$\eta_{11}=-7.69, \ \eta_{12}=\eta_{21}=1114.79, \ \eta_{13}=\eta_{31}=15916.42, \ \eta_{22}=100271.71,$$

$$\eta_{23}=\eta_{32}=75688.97, \ \eta_{33}=6816895.85, \ \xi=-13715.76, \ \delta=-7566.34 \qquad (A\text{-}2)$$

LOCAL AND GLOBAL NONLINEAR DYNAMICS
OF HARMONICALLY EXCITED RECTANGULAR PLATES

S. I. CHANG, A. K. BAJAJ[*], P. DAVIES
SCHOOL OF MECHANICAL ENGINEERING, PURDUE UNIVERSITY,
WEST LAFAYETTE, INDIANA 47907.

ABSTRACT:

Nonlinear flexural vibrations of rectangular plates with uniform stretching and transverse harmonic excitations are studied. The analysis results for the case when two distinct plate modes have nearly coincident natural frequencies, are based on the multi-mode approximation of von Karman plate equations. Local bifurcation analysis of the averaged equations, governing the time evolution of the response amplitudes of modes in internal resonance, shows that the plate motion can be either in the directly excited mode, or in a mixed-mode where both the interacting modes participate. The presence of Hopf bifurcation in the coupled-mode responses leads to amplitude modulated traveling waves as well as period doubling bifurcations to chaos. A global bifurcation analysis is also initiated which shows the existence of heteroclinic loops for an integrable limit of transformed and properly scaled averaged equations. Perturbation of these heteroclinic loops can lead to Smale horseshoes and chaotic behavior for the plates.

BIOGRAPHY:
Seo Il Chang is currently working on his doctoral research in the School of Mechanical Engineering at Purdue University and will graduate in 1993. His research is in the area of nonlinear vibrations focusing on the complex behavior of weakly nonlinear multi-modal systems. He is a graduate of Seoul National University, and he was awarded his Master's degree from Syracuse University in 1988.

Local and Global Dynamics
of Harmonically Excited Rectangular Plates

Seo Il Chang, Anil K. Bajaj and Patricia Davies
School of Mechanical Engineering, Purdue University,
West Lafayette, Indiana 47907-1288.

INTRODUCTION AND MODELING THE PLATE DYNAMICS

The nonlinear response of thin, as well as thick, plates has been the subject of extensive studies and many recent reviews exist on the subject [1]. Sridhar, Mook and Nayfeh [2,3] used the dynamic analogue of von Karman equations to study the forced response of thin plates. They analyzed symmetric as well as asymmetric vibrations, and traveling waves in a clamped circular plate subjected to harmonic excitations, when the frequency of excitation is near one of the natural frequencies. Their analysis showed that for the symmetric responses in the presence of an internal resonance among the first three modes, when more than one mode is directly excited, the lower modes can dominate the response even when the frequency of the excitation is near that of the highest mode. When the response is asymmetric, they found that in the absence of internal resonance, or when the frequency of excitation is near one of the lower frequencies involved in internal resonance, the steady-state response can only have the form of a standing wave. However, when the frequency of excitation is near the highest frequency involved in the internal resonance it is possible for a traveling wave component of the highest mode to appear in the steady-state response. In a more recent study Hadian and Nayfeh [4] showed that in the case of a symmetric response, a multi-mode motion loses its stability through a Hopf bifurcation, resulting in periodically- or chaotically-modulated motions of the plate.

Yang and Sethna [5] studied nonlinear flexural vibrations of nearly square plates subjected to parametric in-plane excitations. The spatial symmetry of the plate resulted in 1:1 resonance in the various m:n and n:m plate modes. For dynamically unstable motions in the region of principal parametric instability, the asymptotic method of averaging was used to obtain a set of four amplitude equations governing the evolution of interacting modes. Local bifurcation analysis of the amplitude equations showed that the system is capable of extremely complex standing as well as traveling wave motions including periodic, almost-periodic and chaotic oscillations. These motions were physically interpreted in terms of rotations of the nodal patterns. A global bifurcation analysis, based on a Melnikov type theory for two degree-of-freedom Hamiltonian systems [6], was also undertaken. It showed the existence of heteroclinic loops which, when they break, lead to Smale horseshoes and chaotic behavior on an extremely long time scale. Yang and Sethna [7] did a similar analysis of plate motions subjected to antisymmetric harmonic excitations normal to the midplane of the plates.

Earlier, Yasuda and Torii [8] had also studied the response of square membranes to transverse harmonic excitations which can lead to a coupled-mode response arising from 1:1 internal resonance. Following the analytical and experimental work of Yasuda and Asano [9], in which they analytically predicted, as well as experimentally observed amplitude-modulated motions, Chang et al. [10]

investigated nonlinear flexural vibrations of rectangular plates with uniform stretching subject to excitations normal to the midplane. They showed that, when two plate modes are in 1:1 internal resonance, depending on the spatial distribution of the external forces, the plate can undergo harmonic motions either in one of the two individual modes or in a combination of the two modes. For low damping levels, the presence of a Hopf bifurcation in the multi-mode response leads to complicated amplitude-modulated dynamics including period-doubling bifurcations, chaos, coexistence of multiple chaotic motions, and crisis, whereby the chaotic attractor suddenly disappears and the plate resumes small amplitude harmonic motions in a single-mode.

The work presented here is part of an ongoing research project undertaken by the authors on the nonlinear dynamical behavior of thin elastic plates. In [10], the authors studied the case of primary external resonance with 1:1 internal resonance, by using a two-mode approximation to the response of a rectangular plate. The von Karman plate equations for a pinned-pinned rectangular plate that also account for membrane forces, were reduced via the Galerkin procedure, to two coupled second-order nonlinear modal equations. The method of averaging [11,12] was then utilized to obtain amplitude equations, and these amplitude equations were studied both analytically and numerically to determine steady-state harmonic, almost-periodic and amplitude-modulated chaotic responses.

In the present study, the plate deflection is assumed to be a superposition of MxN distinct linear modes of the thin plate as follows:

$$w(x,y,t) = \sum_{m}^{M} \sum_{n}^{N} W_{mn}(t)\,\phi_m(x)\psi_n(y) = \sum_{m}^{M} \sum_{n}^{N} W_{mn}(t) \sin m\pi x \sin n\pi y , \qquad (1)$$

where $W_{mn}(t)$ is the time dependent modal amplitude of the (m,n) spatial mode of oscillation of the plate. Employing the Galerkin method with equation (1) as the solution, the von Karman equations are transformed into a set of MxN nonlinear ordinary differential equations governing the modal amplitudes of response as follows:

$$\ddot{W}_{mn} + \omega_{mn}^2 W_{mn} + c\dot{W}_{mn} + \sum_{r,i,k}^{M} \sum_{s,j,l}^{N} L_{mnrsijkl} W_{rs} W_{ij} W_{kl} = F_{mn}(t) , \qquad (2)$$

where $\omega_{mn}^2 = (m^2 + \kappa^2 n^2) + D\pi^4(m^2 + \kappa^2 n^2)^2$ is the nondimensional natural frequency for the (m,n) plate mode, $L_{mnrsijkl}$'s are the coefficients for nonlinear terms, and $F_{mn}(t) = F_{mn} \cos \omega t$ is the contribution of the transverse excitation, F, to the (m,n) mode.

The physical phenomena of interest arise when two or more spatial modes participate in various kinds of internal and combination resonances, and it can be shown [13] that the response, at the lowest order, is a combination of only the modes in resonance. The particular modes in internal or combination resonance are determined by the appropriate frequency conditions, the mode numbers (m,n), and the aspect ratio κ. As an example we choose to investigate 1:1 internal resonance of two modes specified by mode numbers (m,n) and (r,s).

We now wish to study these equations to find out parameter regions where interesting types of behavior are possible. The approach in the local and global bifurcation analysis is to derive a set of, so called, averaged equations [11,12] and examine the slowly varying amplitude and phase characteristics

of the response. In the local bifurcation analysis the conditions for steady state (constant amplitude) solutions are examined and parameter region boundaries are defined when the nature of the steady state solutions change. In the global bifurcation analysis the characteristics of the averaged equations are examined directly to determine nature and interaction of possible solutions. The critical elements to be identified are the parameter values for which trajectories joining different saddle points exist. These parameter regions are the regions for which chaotic solutions are certainly possible.

In order to analyze the averaged equations analytically and to perform global analysis [6], several transformations must be performed. The aim of these transformations is to produce a set of equations that are solvable. To this end the approach in the global bifurcation is slightly different to that adopted in the local bifurcation analysis, where equations in the slowly varying amplitude and phase [11,12] are derived. In the global analysis the final averaged equations are equations in variables that are related to the system energy, and hence while the transformati   may seem a little obscure they do result in a direct examination of the behavior of quantities that are physically meaningful.

LOCAL BIFURCATION ANALYSIS

Let $W_{mn} = R_1 \cos(\omega t - \gamma_1)$, $W_{rs} = R_2 \cos(\omega t - \gamma_2)$. Then, by using a variation of constants procedure and the method of averaging [11,12], and noting that the excitation frequency ω is near the two close natural frequencies ω_{mn} and ω_{rs}, equations (2) result in the following averaged equations for the amplitudes R_i and the phases γ_i [13]:

$$\dot{R}_1 = -\frac{c}{2}R_1 + \frac{F_{mn}}{2\omega}\sin\gamma_1 + \frac{\varepsilon A_2}{8\omega}R_2^2 R_1 \sin 2(\gamma_1 - \gamma_2),$$ (3)

$$\dot{\gamma}_1 = \frac{\omega^2 - \omega_{mn}^2}{2\omega} + \frac{F_{mn}}{2\omega R_1}\cos\gamma_1 + \frac{3\varepsilon A_1}{8\omega}R_1^2 + \frac{\varepsilon A_2}{8\omega}R_2^2\left[2 + \cos 2(\gamma_1 - \gamma_2)\right],$$

$$\dot{R}_2 = -\frac{c}{2}R_2 + \frac{F_{rs}}{2\omega}\sin\gamma_2 + \frac{\varepsilon A_2}{8\omega}R_1^2 R_2 \sin 2(\gamma_2 - \gamma_1),$$

$$\dot{\gamma}_2 = \frac{\omega^2 - \omega_{rs}^2}{2\omega} + \frac{F_{rs}}{2\omega R_2}\cos\gamma_2 + \frac{3\varepsilon A_3}{8\omega}R_2^2 + \frac{\varepsilon A_2}{8\omega}R_1^2\left[2 + \cos 2(\gamma_2 - \gamma_1)\right].$$

These equations were studied in [10] for the case when only one mode (the (1,2) mode) is directly excited, that is, $F_{12} \neq 0$ and $F_{31} = 0$. It was shown that the plate can undergo harmonic motions either in the directly excited individual mode or in a coupled-mode, and that stable single-mode and coupled-mode solutions can coexist over a wide range in parameters (the amplitudes and frequency of excitation). It was further shown that for low damping levels, the presence of Hopf bifurcations in the coupled-mode response leads to complicated amplitude-modulated dynamics including period-doubling bifurcations, chaos, coexistence of multiple chaotic motions, and crisis. These equations were also derived and studied by Yasuda and Asano in [9] for the case of a rectangular membrane.

Given a specific value of the aspect ratio κ, and the degeneracy of two specific modes, the plate and the membrane have the same averaged or amplitude equations. The nonlinear coefficients A_1, A_2 and A_3 depend only on the mode combinations, the Poisson's ratio, and the form of the nonlinearity assumed (von Karman-type nonlinearities). The values of the natural frequencies ω_{mn} and ω_{rs} for the degeneracy of two specific plate modes, are, however, different from those for the membrane.

We should note that the procedure used here in deriving the averaged equations is the method of harmonic balance along the lines of [9], although it can be easily formalized by introducing a small parameter and by appropriately scaling the modal amplitudes W_{mn} and W_{rs}, the damping c, and the external force amplitudes F_{mn} and F_{rs}. The resulting amplitude equations will be identical to equations (3), except for the small parameter multiplying the right hand side. Thus, the amplitude equations should be treated in the sense of a slow time scale. We will use the formal scaling approach in the second part of this study dealing with global bifurcation analysis.

In a general external loading case, the force amplitudes F_{mn} and F_{rs} are not zero. We are here interested in the situation when only one mode is externally excited and the second mode is driven due to its nonlinear coupling to the excited mode. Two such specific cases arise, that is, $F_{mn} \neq 0$ and $F_{rs} = 0$, or $F_{mn} = 0$ and $F_{rs} \neq 0$. For these cases, due to the similar nature of the equations for (R_1, γ_1) and for (R_2, γ_2), the analytical expressions for various steady-state constant solutions of equations (3) turn out to be identical except for the role of the nonlinear coefficients A_1 and A_3. In view of the possible bifurcations and stability considerations, however, considerable qualitative as well as quantitative differences in the overall response can arise in the two cases. We describe these below, where a local bifurcation analysis of equations (3) is carried out. In fact, it is shown in [10] that the qualitative behavior is strongly dependent on the nonlinear coefficients, and hence on the mode combinations (m,n) and (r,s), and rectangular plates with two interacting modes in 1:1 resonance can be classified based on the nonlinear coefficients.

Steady-State Constant Solutions

As already discussed, we emphasize the cases when only one of the two modes is externally excited. First, consider the case when $F_{rs} = 0$ and $F_{mn} \neq 0$. Thus, the (m,n) mode is directly excited by an external harmonic force. There are two types of steady-state constant solutions. One set of solutions is characterized by the fact that $R_2 = 0$, that is, the indirectly excited mode is absent. Then the only response is in the (m,n) mode with $R_1 \neq 0$ and this is called the single-mode solution. The other class of solutions corresponds to both R_1 and R_2 being nonzero and such motions are called the coupled-mode response. A similar situation exists when the (r,s) mode is directly excited and $F_{mn} = 0$.

From equations (3), the steady-state constant solutions for single-mode motions ($\bar{R}_2 = 0$) are determined by

$$\frac{c}{2}\bar{R}_1 - \frac{F_{mn}}{2\omega}\sin\bar{\gamma}_1 = 0, \qquad \frac{\omega^2 - \omega_{mn}^2}{2\omega}\bar{R}_1 + \frac{3\varepsilon A_1}{8\omega}\bar{R}_1^3 + \frac{F_{mn}}{2\omega}\cos\bar{\gamma}_1 = 0, \qquad (4)$$

where an overbar indicates the single-mode steady-state solutions. Combining the equations for $\bar{R}_1$ and $\bar{\gamma}_1$ results in the following polynomial in $\bar{R}_1$:

$$\bar{R}_1^6 + \frac{8(\omega^2 - \omega_{mn}^2)}{3\varepsilon A_1}\bar{R}_1^4 + \frac{16[\omega^2 c^2 + (\omega^2 - \omega_{mn}^2)^2]}{9\varepsilon^2 A_1^2}\bar{R}_1^2 - \frac{16F_{mn}^2}{9\varepsilon^2 A_1^2} = 0. \qquad (5)$$

Real roots of equation (5), which is identical to those arising in the primary resonant response of the harmonically excited Duffing equation [11], determine the single-mode steady-state constant solutions.

Differentiating equation (5) with respect to $\bar{R}_1$ and setting $\partial\omega/\partial\bar{R}_1 = 0$ gives, the saddle-node bifurcation points [14] or, the points of vertical tangency for single-mode steady-state solutions:

$$\left[\bar{R}_1^2\right]_{SNS} = \frac{4}{9\varepsilon A_1}\left[-2(\omega^2 - \omega_{mn}^2) \pm \sqrt{(\omega^2 - \omega_{mn}^2)^2 - 3c^2\omega^2}\right].\qquad(6)$$

Here the subscript SNS implies the saddle-node bifurcation for single-mode solutions.

The problem of finding steady-state constant solutions for the coupled-mode response $(R_1 \neq 0, R_2 \neq 0)$ can also be formulated as that of finding the real roots of a polynomial of the 8th order in $\hat{R}_2^2$, where a hat indicates the coupled-mode steady-state solution. Due to its complexity, the polynomial expression in $\hat{R}_2$ has been determined by using symbolic algebra programs (e.g. SMP, MACSYMA), and is not presented here. The corresponding expression for the coupled-mode steady-state solution $\hat{R}_1$ is given in terms of $\hat{R}_2$ by

$$\hat{R}_1^2 = -2\left[\frac{A_3}{A_2}\hat{R}_2^2 + \frac{4}{3}\frac{(\omega^2 - \omega_{rs}^2)}{\varepsilon A_2}\right] \pm \sqrt{\left[\frac{A_3}{A_2}\hat{R}_2^2 + \frac{4}{3}\frac{(\omega^2 - \omega_{rs}^2)}{\varepsilon A_2}\right]^2 - \frac{16}{3}\frac{\omega^2 c^2}{\varepsilon^2 A_2^2}}.\qquad(7)$$

When damping is absent, the equation governing the amplitude $\hat{R}_2$ is of the form

$$C_1\hat{R}_2^8 + C_2\hat{R}_2^6 + C_3\hat{R}_2^4 + C_4\hat{R}_2^2 + C_5 = 0,\qquad(8)$$

where the coefficients of the polynomial are functions of the parameters $A_1, A_2, A_3, \omega, \omega_{mn}, \omega_{rs}, \varepsilon$ and F_{mn}. These expressions for coefficients C_i, i=1,2,3,4,5, are given in the work of Chang et al. [10].

Setting $\hat{R}_2 = 0$ in equation (7), we can obtain the critical points for the onset of coupled-mode steady-state harmonic response. The condition for the occurrence of pitchfork bifurcation from the single-mode response is

$$\left[\hat{R}_1^2\right]_{PF} = \frac{4}{3\varepsilon A_2}\left[-2(\omega^2 - \omega_{rs}^2) \pm \sqrt{(\omega^2 - \omega_{rs}^2)^2 - 3c^2\omega^2}\right],\qquad(9)$$

where PF refers to a pitchfork bifurcation [14].

It is clear from the polynomials (5) and (8) that, given the mode numbers (m,n) and (r,s), and the aspect ratio κ, the number of real solutions of the single-mode and the coupled-mode type depends on the physical parameters $\omega_{mn}, \omega_{rs}, c, \omega,$ and F_{mn}. While the condition of $\kappa = 1.633$ fixes the two natural frequencies $\omega_{mn} = \omega_{rs}$, any small deviations from the precise value of the aspect ratio lead to small mistuning in the internally resonant modes and thus $(\omega_{mn}^2 - \omega_{rs}^2)$ is an important "internal" mistuning parameter. The other frequency parameter is $(\omega^2 - \omega_{mn}^2)$ or $(\omega^2 - \omega_{rs}^2)$ which represents the "external" mistuning. Numerical values of the natural frequencies ω_{mn} and ω_{rs}, as indicated earlier, depend also on the bending stiffness D and the Poisson's ratio ν. The nonlinear coefficients $A_1, A_2,$ and A_3, however, depend only on the Poisson's ratio.

In Figures 1(a) and 1(b) are shown the various single-mode and coupled-mode steady-state constant solutions R_1 and R_2 as a function of the excitation frequency ω. These response curves are for (1,2) and (3,1) interacting modes with the damping c=0.0, and force amplitudes $F_{12} = 10.0$ and $F_{31} = 0.0$. This situation arises when the loading is symmetric about $x = 0.5$ and is antisymmetric about $y = 0.5$.
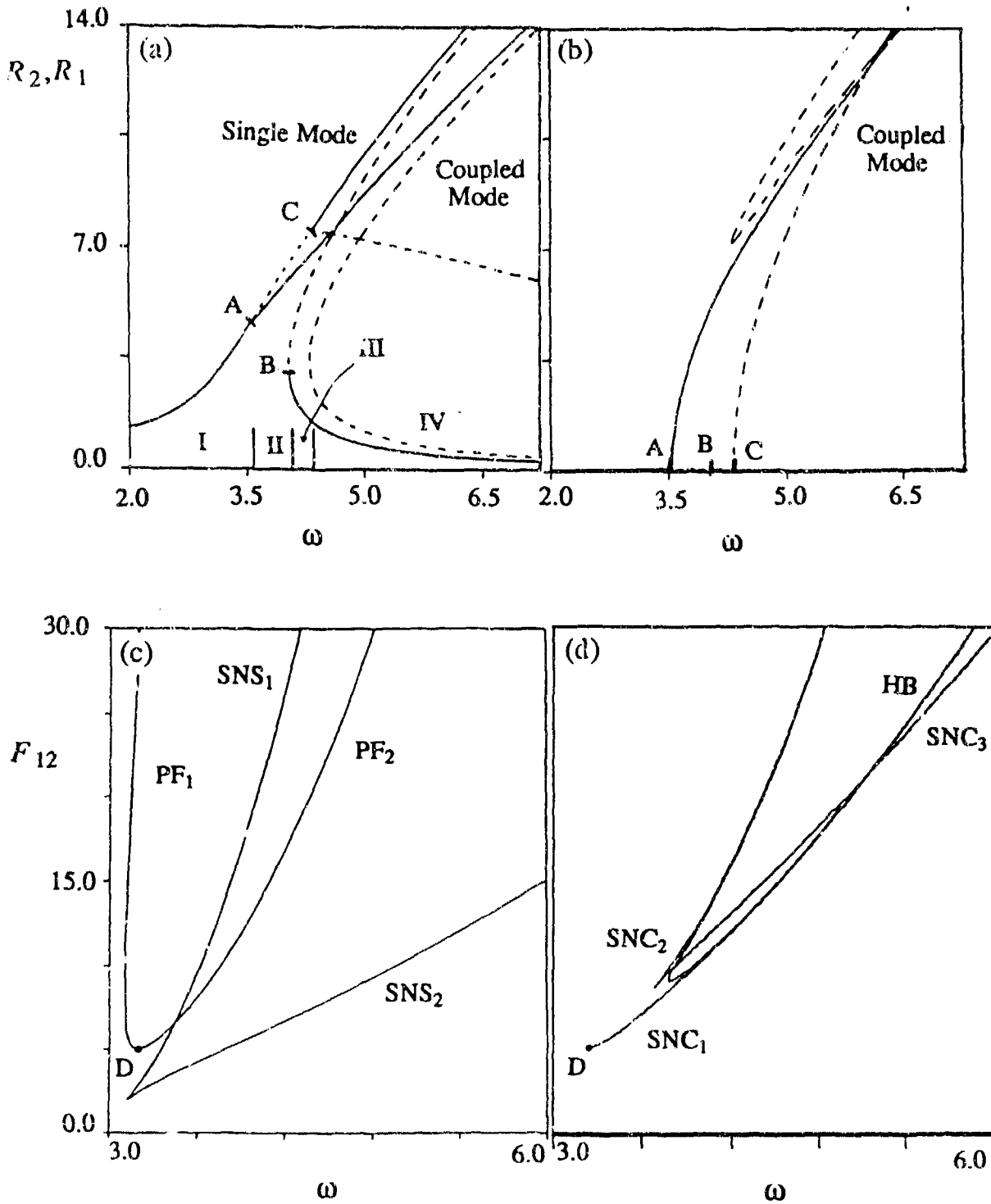
Figure 1: (a) Constant-amplitude response R_1, for the (1,2) plate mode, and (b) constant-amplitude response R_2, for the (3,1) plate mode $F_{21} = 10.0$, $F_{31} = 0.0$, $c = 0.0$. (c) Saddle-node and pitchfork bifurcation sets for single-mode solutions; $F_{31} = 0.0$, $c = 0.195$. (d) Saddle-node and Hopf bifurcation sets for coupled-mode solutions; $F_{31} = 0.0$, $c = 0.195$.
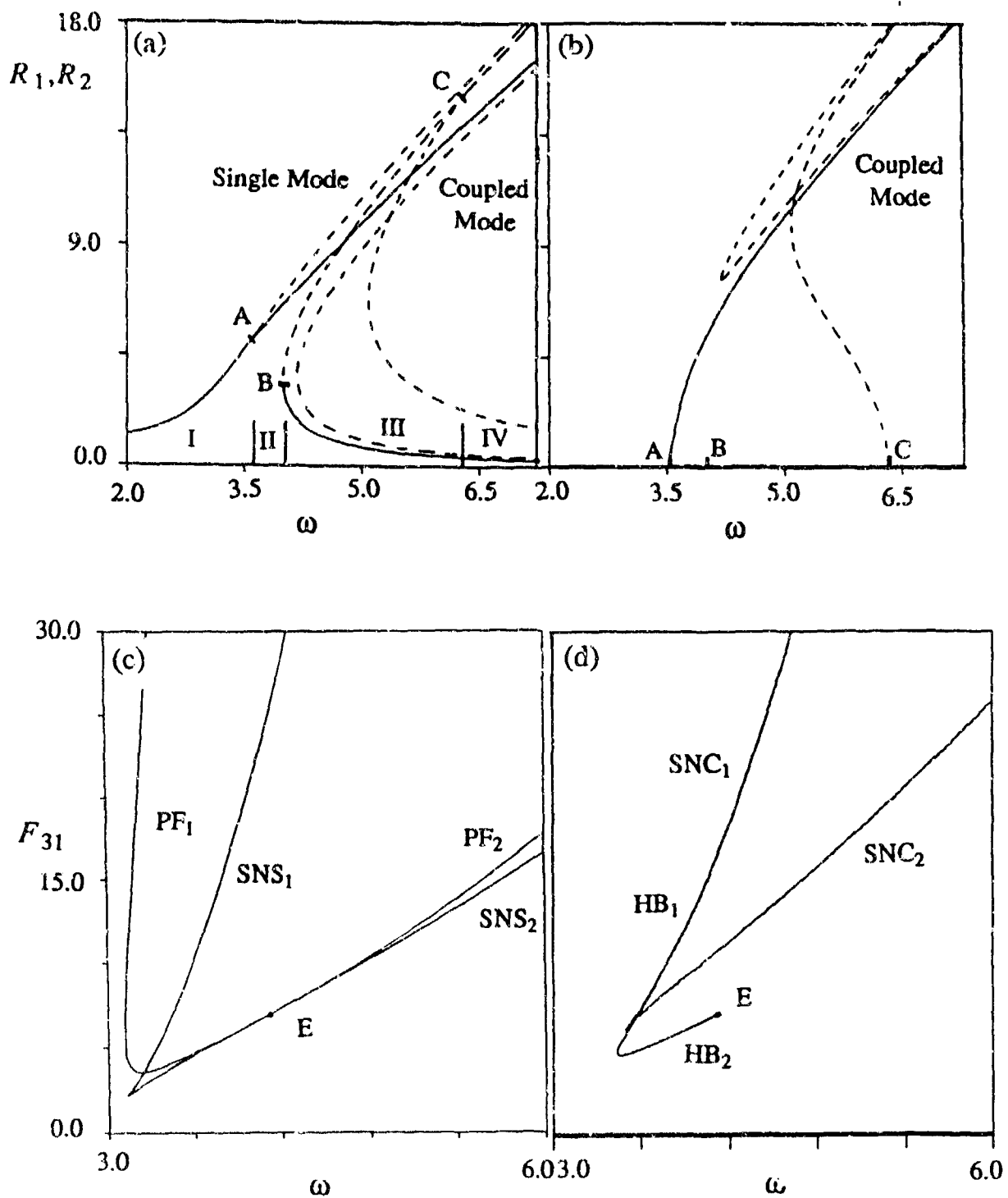
Figure 2: (a) Constant amplitude response R_1, for the (1,2) plate mode, and (b)constant amplitude response R_2, for the (3,1) plate mode $F_{12} = 0.0$, $F_{31} = 10.0$, c = 0.0. (c) Saddle-node and pitchfork bifurcation sets for single-mode solutions; $F_{12} = 0.0$, c = 0.195. (d) Saddle-node and Hopf bifurcation sets for coupled-mode solutions; $F_{12} = 0.0$, c = 0.195.

For all the numerical results presented in this work $\varepsilon = 6 \times 10^{-4}$, $v = 0.3$, $\omega_{12}^2 = \omega_{31}^2 = 35/3$, and $D = 0.0$. The nonlinear coefficients for the (1,2) and (3,1) modes are $A_1 = -326.27$, $A_2 = -274.79$ and $A_3 = -268.32$. The frequency axis is divided into 4 intervals, I, II, III, and IV, according to the nature of solutions. Over the interval I, there exists only one single-mode solution. Over the interval II, we have a stable coupled-mode solution and an unstable single-mode solution. Therefore, in the intervals I and II, the initial conditions are not critical to determining the final steady-state response. In frequency intervals III and IV, there exists a stable single-mode and a stable coupled-mode solution. In frequency interval IV, two stable single-mode solutions and a stable coupled-mode solution exist. Thus, in intervals III and IV, the initial conditions are very important in determining the final steady-state response reached in any experiment or numerical simulation. Note also, that for every mixed-mode solution with some γ_2, there is another solution with phase angle $\gamma_2 + \pi$ for the same amplitude R_2. Thus, the response curves really represent two coupled-mode solutions which are phase shifted by π radians. The points A and C in Figure 1 are associated with equation (9), that is, the pitchfork bifurcation points, and the point B is associated with equation (6), that is, a saddle-node bifurcation point for single-mode solution. The corresponding frequencies at the points A, B, and C coincide with the boundaries of the intervals.

The single-mode and the coupled-mode harmonic motions of the plate can also be interpreted in terms of standing and rotating nodal patterns. Clearly, for the single-mode response, the nodal lines are stationary and the plate vibrates harmonically in the (1,2) mode. When both (1,2) and (3,1) modes are present in the response, the nodal pattern depends on the phases γ_1 and γ_2. Only in the case of $\gamma_1 = \gamma_2$ or $\gamma_1 = \gamma_2 \pm \pi$ are the nodal patterns stationary. Otherwise, the nodal pattern changes continuously in a periodic manner, resulting in a traveling wave motion of the plate.

A similar analysis can be performed for the case when $F_{mn} = 0$ and $F_{rs} \neq 0$. This situation arises when the transverse forcing is symmetric about both $x = 0.5$ and $y = 0.5$. In Figures 2(a) and (b) are shown the response curves for this case with $F_{12} = 0$ and $F_{31} = 10.0$. From the figure, it is seen that over the intervals I, II, and III, we have qualitatively the same results. Over the interval IV, however, there exist two solutions: one stable single-mode and one stable coupled-mode, whereas, there are two stable single-mode solutions and one stable coupled-mode solution for the case with $F_{12} = 10.0$ and $F_{31} = 0$. This qualitative difference arises because here one of the pitchfork bifurcations from the single-mode solutions occurs in the lower branch (point C), while in the earlier case both the pitchfork bifurcations occur only in the upper branch of the single-mode solutions. This is a consequence of the relative magnitude of the nonlinear coefficients A_i, i=1,2,3, and can be used to classify the various nonlinear responses of rectangular plates [10]. Further discussion about other qualitative differences between the responses in the two cases are given below.

Periodic and Chaotic Solutions of Averaged Equations

A numerical study of periodic solutions of the averaged equations has been performed by using direct time integration as well as using AUTO [15]. We present the results for two cases of (i) $F_{mn} \neq 0$, $F_{rs} = 0$, and (ii) $F_{mn} = 0$, $F_{rs} \neq 0$. Both cases exhibit qualitatively different behavior as described below. For ease of computation of some of the results, a different set of averaged equations, called the Cartesian form, are used. These are derived from equations (3) by using: $u_i = R_i \cos \gamma_i$ and $v_i = R_i \sin \gamma_i$. This results in the following set of equations,

$$\dot{u}_1 = -\frac{c}{2}u_1 - \frac{\omega^2-\omega_{mn}^2}{2\omega}v_1 - \frac{3\varepsilon A_1}{8\omega}v_1(u_1^2 + v_1^2) + \frac{\varepsilon A_2}{8\omega}(-v_1u_2^2 - 3v_1v_2^2 - 2u_1u_2v_2),\qquad(10)$$

$$\dot{v}_1 = -\frac{c}{2}v_1 + \frac{F_{mn}}{2\omega} + \frac{\omega^2-\omega_{rs}^2}{2\omega}u_1 + \frac{3\varepsilon A_1}{8\omega}u_1(u_1^2 + v_1^2) + \frac{\varepsilon A_2}{8\omega}(3u_1u_2^2 + u_1v_2^2 + 2v_1u_2v_2),$$

$$\dot{u}_2 = -\frac{c}{2}u_2 - \frac{\omega^2-\omega_{rs}^2}{2\omega}v_2 - \frac{3\varepsilon A_3}{8\omega}v_2(u_2^2 + v_2^2) + \frac{\varepsilon A_2}{8\omega}(-v_2u_1^2 - 3v_2v_1^2 - 2u_2u_1v_1),$$

$$\dot{v}_2 = -\frac{c}{2}v_2 + \frac{F_{rs}}{2\omega} + \frac{\omega^2-\omega_{rs}^2}{2\omega}u_2 + \frac{3\varepsilon A_3}{8\omega}u_2(u_2^2 + v_2^2) + \frac{\varepsilon A_2}{8\omega}(3u_2u_1^2 + u_2v_1^2 + 2v_2u_1v_1).$$

(i) $F_{mn} \neq 0$, $F_{rs} = 0$, mn$\equiv$12, rs$\equiv$31:

The bifurcations sets for the single-mode and coupled-mode solutions are, for this case, shown in Figures 1(c) and (d). These are values of the parameters where a steady-state constant solution loses its stability or undergoes a change in it. Here SNS and PF refer to saddle-node and pitchfork bifurcation sets (zero eigenvalue) for the single-mode solutions. The notation SNC and HB is used to signify saddle-node and Hopf sets for the coupled-mode solutions.
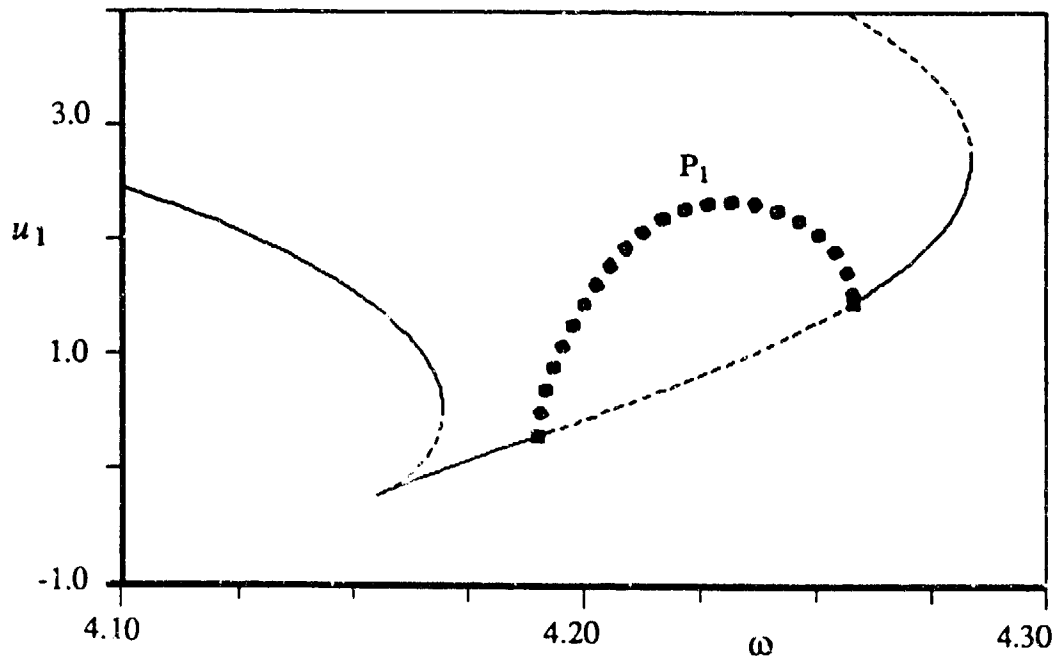
Figure 3: Response amplitude for the limit cycle solution for u_1 as a function of the excitation frequency; $F_{12} = 10.0$, $F_{31} = 0.0$, c = 0.20.

For sufficiently low F_{12}, the response of the averaged equations is limited to equilibrium points in the directly excited (1,2) mode. For higher level of F_{12}, however, the (3,1) mode also contributes to the response. As the excitation F_{mn} increases further, some of the coupled-mode steady-state constant solutions lose stability due to a Hopf bifurcation [14] and the averaged system develops periodic

solutions from the Hopf bifurcation points. These periodic solutions, denoted as P_1 solutions, correspond to amplitude- and phase-modulated motions of the rectangular plate and result in a slow oscillation of the nodal pattern. In Figure 3, the solutions of the averaged equations (10) for c = 0.20 are shown. The P_1 solutions are stable (denoted by solid circles) over the whole frequency interval connecting the two Hopf points. With a further increase in F_{12}, these P_1 solutions become unstable via period-doubling bifurcations and develop P_2 solutions. At some value of F_{12}, there arises a cascade of period-doublings leading to chaotic solutions.
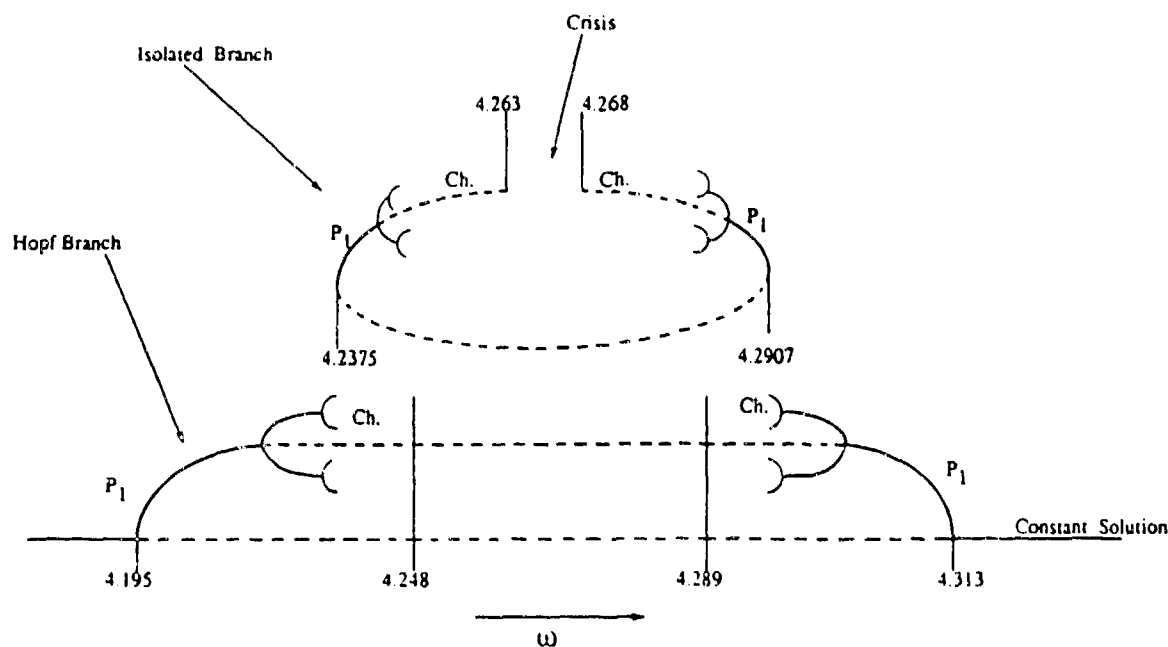
Figure 4: Qualitative relationship between the Hopf and the isolated solution branches; $F_{12} = 10.0$, $F_{31} = 0.0$, c = 0.19.

While numerically investigating the Hopf solution branch, a new periodic solution branch was discovered. This branch of periodic solutions arises due to a saddle-node bifurcation with periodic solutions as the primary solution. That is, a stable and an unstable limit cycle arise due to a saddle-node bifurcation [14] at some low enough damping and the branch exists over a small frequency interval. As the damping c is reduced, the stable periodic solution branch undergoes a sequence of period-doubling bifurcations which ultimately lead to chaotic attractors. For c = 0.19, $F_{12} = 10.0$, the isolated branch arises at $\omega \simeq 4.238$, goes through bifurcations and ultimately terminates at $\omega \simeq 4.291$. In Figure 4 is presented the qualitative relationship between the isolated branch and the branch originating at Hopf points, $\omega \simeq 4.195$ and $\omega \simeq 4.313$. Over the frequency intervals (4.2375, 4.248) and (4.289, 4.2907), stable steady-state solutions are found to exist in both the branches. The chaotic solutions in the isolated branch are found to undergo 'boundary crisis' [16,17], at $\omega \simeq 4.263$ and 4.268. Phase plane plots of this behavior are shown in Figure 5. 'Boundary crisis' occurs when the chaotic attractor touches the stable manifold of the saddle-type coupled-mode equilibrium point (denoted by CM) and ceases to exist. Near the above listed frequencies, the averaged equations exhibit transient chaos where the solution, when initiated in the neighborhood of the chaotic solution, traces the ghost of the previous attractor for some

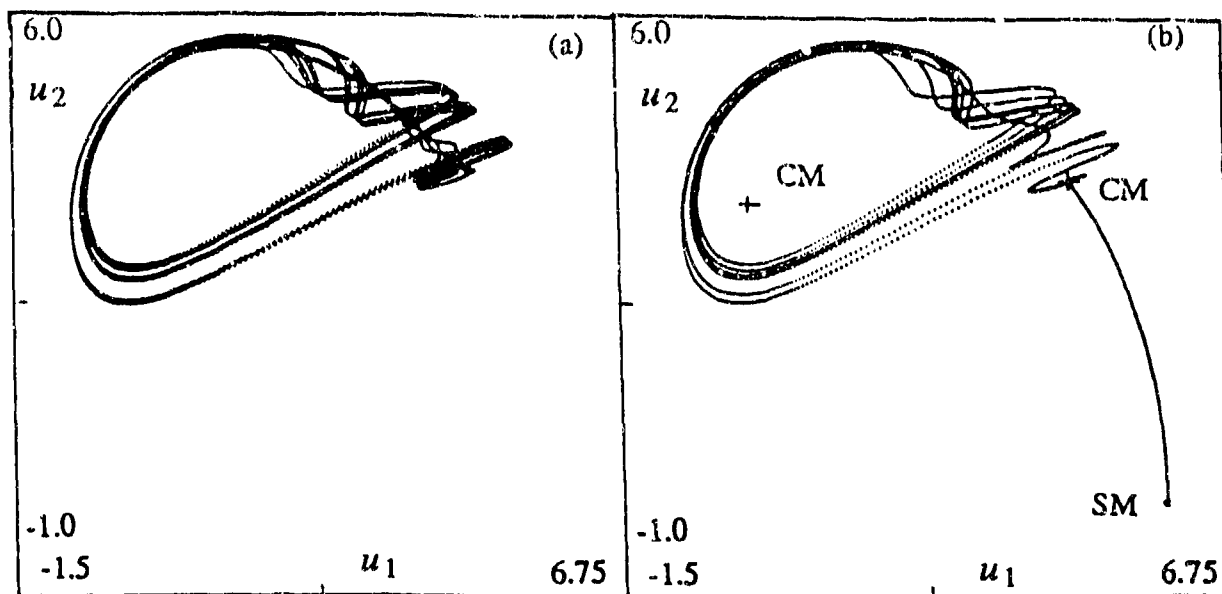time and is then quickly attracted by the single-mode constant solution (SM).

Figure 5: 'Crisis' in the averaged equations; $F_{12} = 10.0$, $F_{31} = 0.0$, $c = 0.19$. (a) chaotic attractor, $\omega = 4.262$, (b) transient chaos, $\omega = 4.264$.

The fact that an isolated solutions branch exists can also be verified using tools of numerical bifurcation analysis. AUTO [15] is one of the powerful packages available for bifurcation analysis and continuation of solutions for ordinary differential equations. It can also compute periodic solution branches, given approximate starting points, and can help construct 'saddle-node' bifurcation sets in two parameter space. Numerical results for the continuation of periodic solutions starting at the two Hopf points are shown, for $c = 0.18755$, in Figure 6. Four turning points are found in each of the curves started from the left and the right Hopf points. These points are identified by numbers 1-4 and 5-8, respectively. As the frequency ω is varied the turning points 2,4,6 and 8 correspond to locations where the isolated branches are created, whereas, the points 1,3,5 and 7 correspond to frequencies where they merge with other periodic solution branches. Thus, as damping is increased the turning points 1 and 5, and 3 and 7 collide to form isolated branches. This bubble structure is typical of the transition to chaotic behavior observed in various dynamical systems [16].

In Figure 7 are shown the saddle-node bifurcation sets for the isolated periodic solution branches corresponding to the points 1-8 in Figure 6. For damping $c > 0.193$, no isolated branch exists and numerical simulations show that there are chaotic solutions in the Hopf branch. The set now confirms that at $c = 0.19$ (corresponding to the qualitative diagram shown in Figure 4), the isolated branch has not yet merged with the Hopf branch. In fact, the bifurcation sets indicate that on lowering the damping further, another isolated branch is created which merges with the first isolated branch before the merging with the Hopf branch takes place. Thus, the cascade of isolated branch creations and mergers is quite complex.
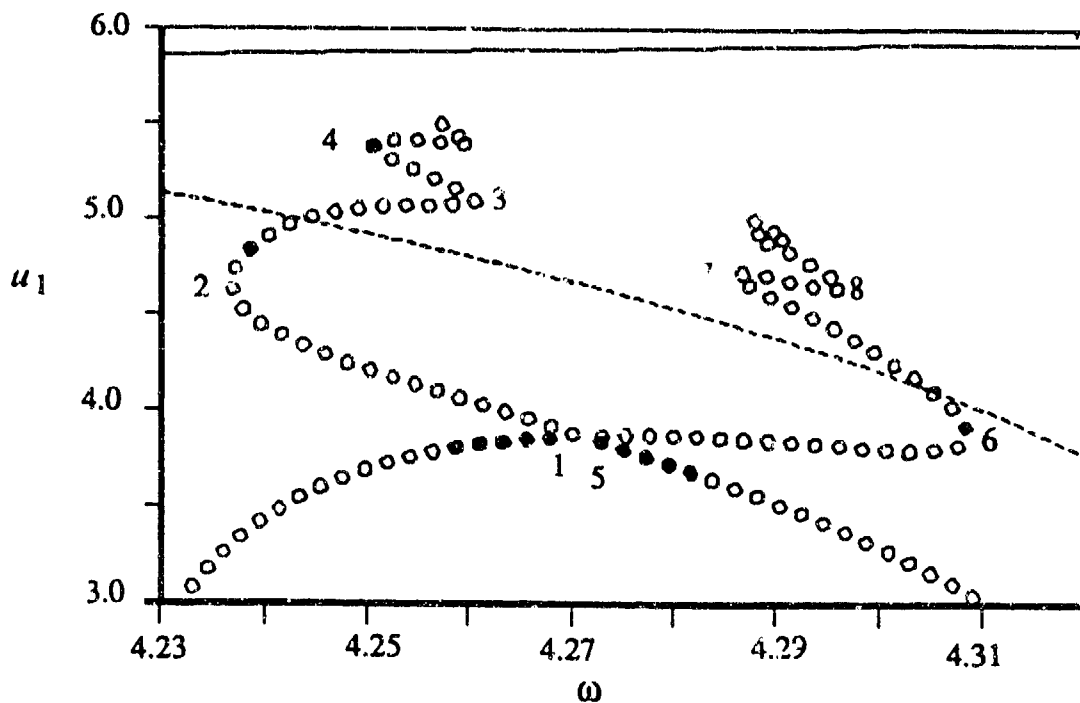
Figure 6: Periodic solution branches continued from the two Hopf points on the coupled-mode branch; $F_{12} = 10.0$, $F_{31} = 0.0$, $c = 0.18755$.
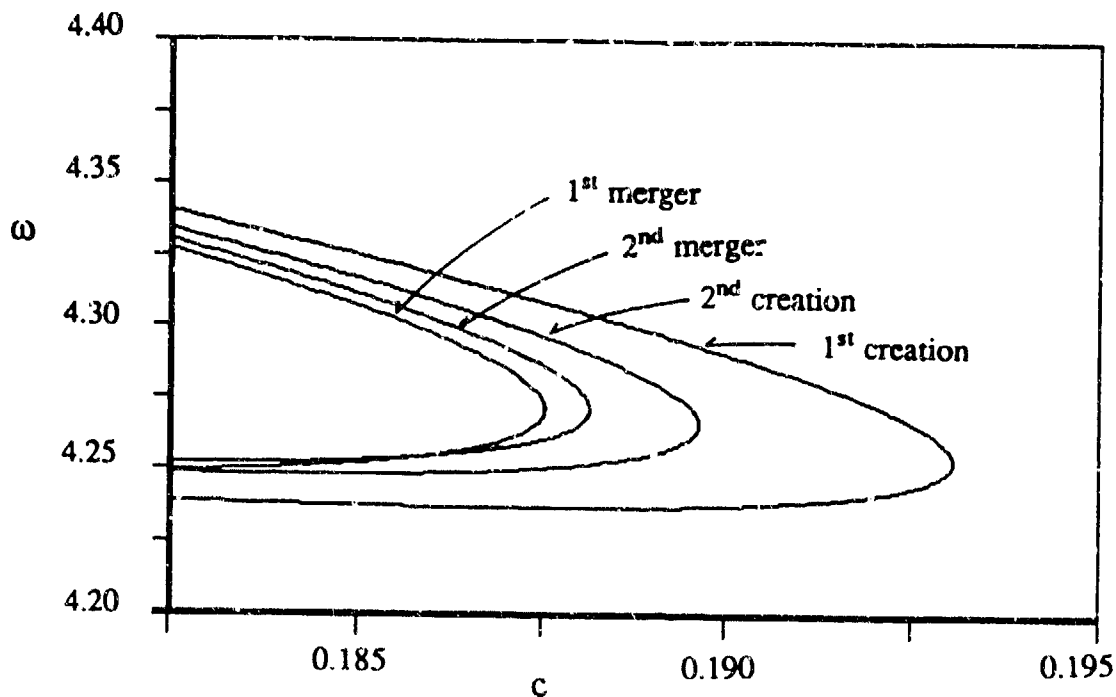

Figure 7: Saddle-node bifurcation sets for the first and second isolated periodic solution branches in (c-ω) plane; $F_{12} = 10.0$, $F_{31} = -0.0$.

Before closing this discussion let us point out that, because of the symmetry inherent in the system when $F_{rs} = 0$, there is another image branch of coupled-mode solutions in which the solutions undergo an identical evolution as the system parameters are varied. As is shown in the next section, the response exhibited by the averaged equation in the case of $F_{mn} = 0$ is quite different from the one presented here, and these differences are intimately associated with the existence of this twin.

ii) $F_{mn} = 0$, $F_{rs} \neq 0$, mn≡12, rs≡31:
The bifurcation sets for the single-mode and coupled-mode solutions are, for this case, shown in Figures 2(c) and (d). For a fixed damping (c = 0.195), the Hopf unstable region in the coupled-mode branch arises only when $F_{31} \geq 4.5$. For values of F_{31} slightly above $F_{31} = 4.5$, there are two Hopf points in the solution branch, the bifurcating limit cycles (P_1 solutions) are found to be supercritical and the P_1 solutions join the two Hopf points. This behavior is very similar to the one observed in case (i) above. Note now that the averaged equations (10) with $F_{mn} = 0$ enjoy symmetry under the transformation (u_1, v_1, u_2, v_2) → ($-u_1$, $-v_1$, u_2, v_2) and thus the coupled-mode solutions exist in pairs or are themselves symmetric about the invariant (u_2, v_2) plane. There are two identical Hopf branches.
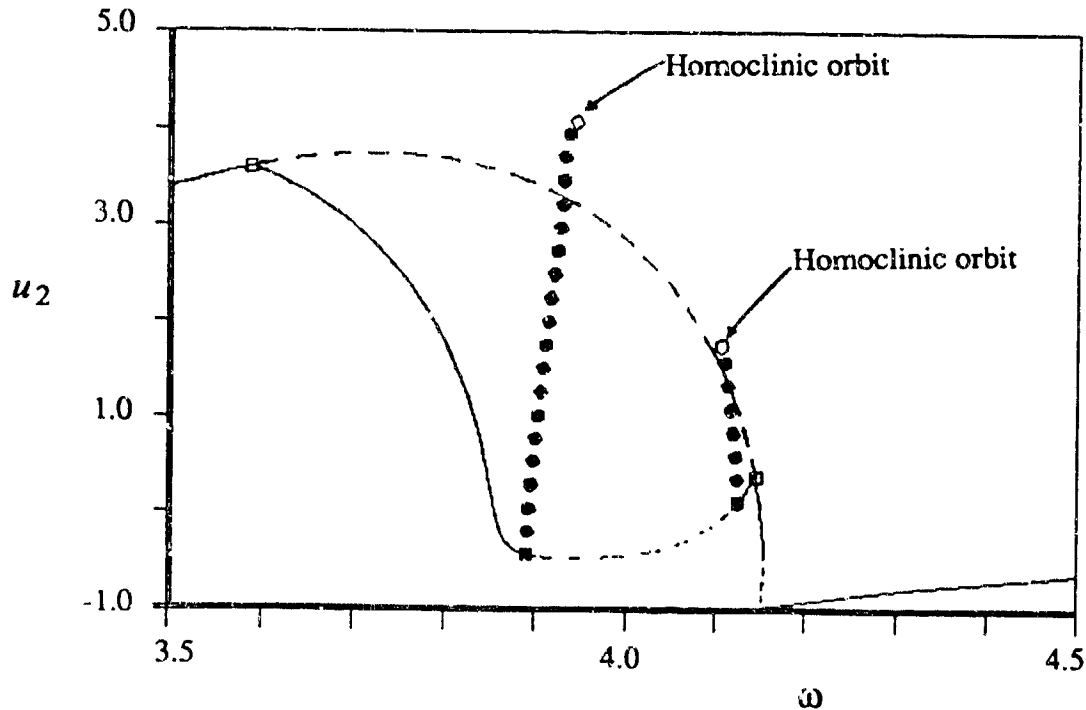
Figure 8: Response amplitude u_2 as a function of the excitation frequency; $F_{12} = 0.0$, $F_{31} = 5.5$, c = 0.195.

For higher force (F_{31}), the P_1 solution branch, instead of undergoing a period-doubling bifurcation, as is the behavior in case (i), develops homoclinic orbits and AUTO is unable to continue periodic solutions beyond those points. In Figure 8 are shown the response curves for $F_{31} = 5.5$. In the frequency interval (3.946 - 4.106), no results for periodic solutions are found. A careful direct time integration study in this region shows very interesting behavior, as exemplified by the sequence of phase
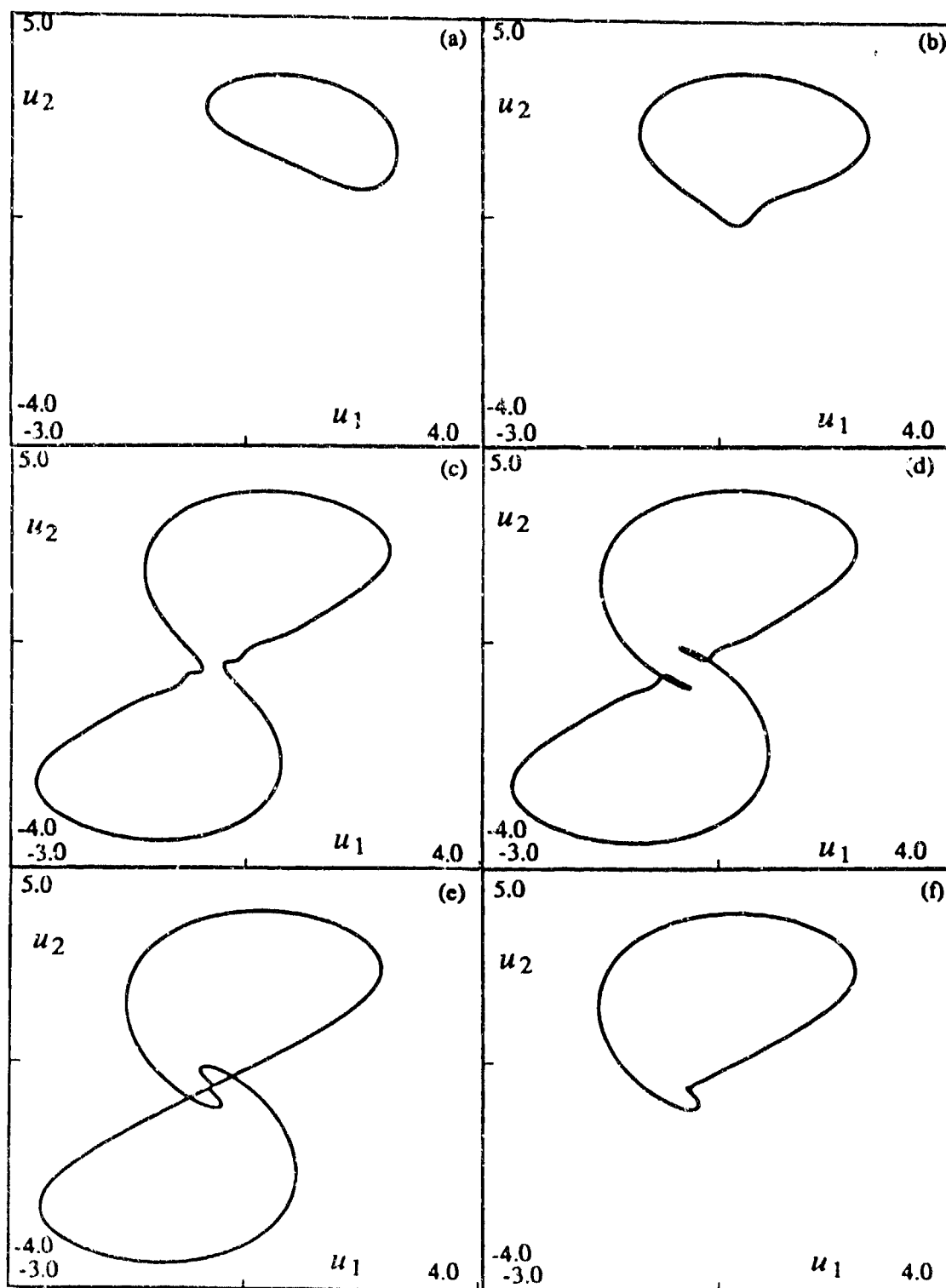
Figure 9: Phase plots (u_1 vs. u_2) for the steady-state solutions; $F_{12} = 0.0$, $F_{31} = 5.5$, c = 0.195. (a) $\omega = 3.93$, (b) $\omega = 3.94$, (c) $\omega = 3.95$, (d) $\omega = 3.96$, (e) $\omega = 3.9615$, (f) $\omega = 3.962$.

plots shown in Figure 9. The Hopf bifurcating periodic solution at $\omega = 3.93$ (Figure 9(a)) deforms ($\omega = 3.94$, Figure 9(b)) and then merges with its symmetric twin to give the periodic solution shown in Figure 9(c) ($\omega = 3.95$). In between the frequencies with phase plots shown in Figure 9(b) and 9(c), there is a frequency for which the upper and the lower limit cycles just touch each other at the origin in (u_1, v_1) plane. This is the homoclinic orbit, which is bi-asymptotic to the saddle-type single-mode solution. This phenomenon of merging of the two limit cycles via a homoclinic orbit is called a glueing bifurcation [18]. Further increases in ω result in the phase plots of Figures 9(d) - 9(f), where the single limit cycle again undergoes a glueing bifurcation and this time unglues (detaches) back to the pair of limit cycles (Figure 9(f), only one shown).

At much higher excitation amplitudes, each of the two Hopf branches terminating in a homoclinic orbit, already shown in Figure 8, deform to develop turning points and period-doubling instabilities. A representative periodic solution response curve is shown in Figure 10 for $F_{31} = 10.0$. In the frequency intervals over which the P_1 solutions are unstable, period-doubling cascades arise leading to chaotic solutions. The accompanying graph shows the variation of the period of the limit cycle solution, and it is clear that the period approaches that of a homoclinic orbit about some excitation frequency.
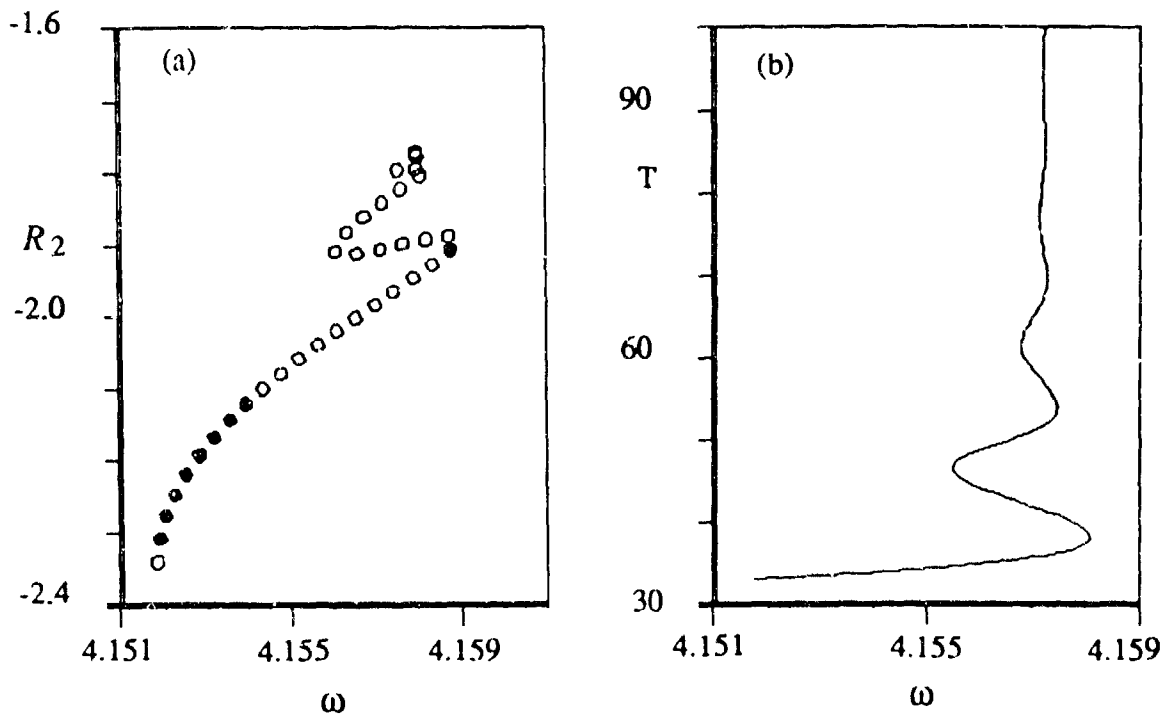

Figure 10: The periodic solution branch continued from the left Hopf point; $F_{12} = 0.0$, $F_{31} = 10.0$, $c = 0.19$. (a) amplitude of response, (b) the variation of the period.

GLOBAL BIFURCATION ANALYSIS

Most results for equations (3), as reported above, are based on local analysis of them near equilibria and on their direct numerical integration. A completely general nonlinear analysis is at present not possible and therefore we investigate the possibility of identifying conditions on the system parameters under which chaotic dynamics can occur. This analysis is based on the identification of homoclinic and/or heteroclinic orbits in some limiting, as well as intergrable, Hamiltonian case of equations (3), and then using a generalized Melnikov method on equations (3) treated as a perturbation of the integrable Hamiltonian system. Through this global analysis [6], the existence of Smale horseshoes, and hence chaotic motions, can be shown for the plate system. The following development closely follows the work of Feng and Sethna [19].

Consider first a two-mode approximation to the plate equations [13] where the modal amplitudes are governed by:

$$\ddot{W}_{mn} + \omega_{mn}^2 W_{mn} = \epsilon \left[A_1 W_{mn}^2 + A_2 W_2^2 \right] W_{mn} - c\dot{W}_{mn} + F_{mn}\cos \nu t \tag{11}$$

$$\ddot{W}_{rs} + \omega_{rs}^2 W_{rs} = \epsilon \left[A_2 W_{mn}^2 + A_3 W_{rs}^2 \right] W_{rs} - c\dot{W}_{rs} + F_{rs}\cos \nu t$$

These can be rewritten in state space form as:

$$\dot{q}_1 = \dot{W}_{mn} = + \frac{\partial H}{\partial p_1} = p_1 \tag{12}$$

$$\dot{p}_1 = \ddot{W}_{mn} = - \frac{\partial H}{\partial q_1} - cp_1 = - \omega_{mn}^2 q_1 + \epsilon \left[A_1 q_1^2 + A_2 q_2^2 \right] q_1 - cp_1 + F_{mn}\cos \nu t$$

$$\dot{q}_2 = \dot{W}_{rs} = + \frac{\partial H}{\partial p_2} = p_2$$

$$\dot{p}_2 = \ddot{W}_{rs} = - \frac{\partial H}{\partial q_2} - cp_2 = - \omega_{rs}^2 q_2 + \epsilon \left[A_2 q_1^2 + A_3 q_2^2 \right] q_2 - cp_2 + F_{rs}\cos \nu t,$$

where, $$H = \frac{1}{2}(p_1^2 + p_2^2) + \frac{1}{2}(\omega_{mn}^2 q_1^2 + \omega_{rs}^2 q_2^2) \tag{13}$$

$$- \frac{1}{4}\epsilon(A_1 q_1^4 + 2A_2 q_1^2 q_2^2 + A_3 q_2^4) - (F_{mn}q_1 + F_{rs}q_2)\cos \nu t .$$

We will now introduce some scalings that are consistent with the assumption of small motions: $p_i = \delta^{1/2}\hat{p}_i$, $q_i = \delta^{1/2}\hat{q}_i$, $i=1,2$, and $c = \delta\hat{c}$, $F_{mn} = \delta^{3/2}\hat{F}_{mn}$, and $F_{rs} = \delta^{3/2}\hat{F}_{rs}$, $0 < \delta << 1$. The natural frequencies are written in a form that suggests a detuning around the excitation frequency ν, $\omega_{mn}^2 = \nu^2 - \delta\sigma_1$, $\omega_{rs}^2 = \nu^2 - \delta\sigma_2$. This yields the following set of equations,

$$\dot{\hat{q}}_1 = \frac{\partial H}{\partial \hat{p}_1} = \hat{p}_1 \tag{14}$$

$$\dot{\hat{p}}_1 = -\frac{\partial H}{\partial \hat{q}_1} - \delta\hat{c}\hat{p}_1 = -v^2\hat{q}_1 + \delta\left[\epsilon\left[A_1\hat{q}_1^2 + A_2\hat{q}_2^2\right]\hat{q}_1 + \sigma_1\hat{q}_1 - \hat{c}\hat{p}_1 + \hat{F}_{mn}\cos vt\right]$$

$$\dot{\hat{q}}_2 = +\frac{\partial H}{\partial \hat{p}_2} = \hat{p}_2$$

$$\dot{\hat{p}}_2 = -\frac{\partial H}{\partial \hat{q}_2} - \delta\hat{c}\hat{p}_2 = -v^2\hat{q}_2 + \delta\left[\epsilon\left[A_2\hat{q}_1^2 + A_3\hat{q}_2^2\right]\hat{q}_2 + \sigma_2\hat{q}_2 - \hat{c}\hat{p}_2 + \hat{F}_{rs}\cos vt\right]$$

where $H = H_o + \delta H_1$, $H_o(\hat{p},\hat{q}) = \frac{1}{2}\left[\hat{p}_1^2 + \hat{p}_2^2\right] + \frac{1}{2}v^2\left[\hat{q}_1^2 + \hat{q}_2^2\right]$ (15)

and $H_1(\hat{q},t) = -\left[\frac{1}{4}\epsilon\left[A_1\hat{q}_1^4 + 2A_2\hat{q}_1^2\hat{q}_2^2 + A_3\hat{q}_2^4\right]\right.$

$$\left. + \frac{1}{2}\left[\sigma_1\hat{q}_1^2 + \sigma_2\hat{q}_2^2\right] + \left[\hat{F}_{mn}\hat{q}_1 + \hat{F}_{rs}\hat{q}_2\right]\cos vt\right].$$

Transforming the equations (14) by using the canonical transformation:

$$\hat{q}_i = v^{-\frac{1}{2}}\left[2I_i\right]^{\frac{1}{2}}\sin\left[\theta_i + vt\right], \quad \hat{p}_i = v^{\frac{1}{2}}\left[2I_i\right]^{\frac{1}{2}}\cos\left[\theta_i + vt\right], \tag{16a}$$

introducing the scalings: $\tau = \delta t$, $\bar{A}_i = \epsilon A_i$, $F_{mn} = \mu f_1$, and $F_{rs} = \mu f_2$, time averaging the resulting equations [11,12] and finally transforming from (I_i, θ_i) to new variables (P_i, Q_i) by using,

$$\theta_2 = Q_2, \ I_1 = P_1, \ \theta_1 = Q_1 - Q_2, \text{ and } I_2 = P_2 - P_1. \tag{16b}$$

yields, for the case of no damping ($\hat{c}=0$),

$$P'_1 = \frac{1}{2v^2}\bar{A}_2 P_1(P_1 - P_2)\sin 2Q_1 + \mu\frac{f_1}{\sqrt{2v}}\sqrt{P_1}\cos(Q_1 + Q_2) \tag{17}$$

$$Q'_1 = \frac{1}{4v^2}\left[\bar{A}_2(2P_1 - P_2)(2 + \cos 2Q_1) + 3\bar{A}_3(P_2 - P_1) - 3\bar{A}_1 P_1 + 2v(\sigma_2 - \sigma_1)\right]$$

$$+ \mu\frac{\sqrt{2}}{4\sqrt{v}}\left[-f_1\frac{\sin(Q_1 + Q_2)}{\sqrt{P_1}} + f_2\frac{\sin Q_2}{\sqrt{P_2 - P_1}}\right]$$

$$P'_2 = \mu \frac{1}{\sqrt{2v}} \left[f_1 \sqrt{P_1} \cos(Q_1 + Q_2) + f_2 \sqrt{P_2 - P_1} \cos Q_2 \right]$$

$$Q'_2 = \frac{1}{4v^2} \left[-\bar{A}_2 P_1(2 + \cos 2Q_1) + 3\bar{A}_3(F_1 - P_2) - 2v\sigma_2 \right].$$

Note that the ′ notation stands for a derivative with respect to τ, whereas the ˙ indicates a derivative with respect to t.

Consider now the special case of no forcing, $\mu = 0$. This results in $P'_2 = 0$, that is P_2 is a constant, and the removal of Q_2 from the equations for P'_1 and Q'_1. Setting P_2 equal to a constant P_{20} gives the following reduced set of equations in P_1 and Q_1.

$$P'_1 = - \frac{\partial H_2^{\circ\circ}}{\partial Q_1} = \frac{1}{2v^2} \bar{A}_2 P_1(P_1 - P_{20}) \sin 2Q_1 \tag{18}$$

$$Q'_1 = \frac{\partial H_2^{\circ\circ}}{\partial P_1} = \frac{1}{4v^2} \left[\bar{A}_2(2P_1 - P_{20})(2 + \cos 2Q_1) + 3\bar{A}_3(P_{20} - P_1) - 3\bar{A}_1 P_1 + 2v(\sigma_2 - \sigma_1) \right]$$

where $H_2^{\circ\circ} = \frac{1}{8v^2} \left[(-3\bar{A}_1 + 4\bar{A}_2 - 3\bar{A}_3)P_1^2 + (-4\bar{A}_2 + 6\bar{A}_3)P_1 P_{20} - 3\bar{A}_3 P_{20}^2 \right.$ $\tag{19}$

$$\left. + 4v(\sigma_2 - \sigma_1)P_1 - 4v\sigma_2 P_{20} + 2\bar{A}_2 P_1^2 \cos 2Q_1 - 2\bar{A}_2 P_1 P_{20} \cos 2Q_1 \right].$$

It can also be shown, by reversing the transformations, that:

$$P_2 = \frac{v^{-1}}{2} \left[v^2 \left(\hat{q}_1^2 + \hat{q}_2^2 \right) + \left(\hat{p}_1^2 + \hat{p}_2^2 \right) \right] = v^{-1} H_o(\hat{p}, \hat{q})$$

where $H_o(\hat{p}, \hat{q})$, first defined in equation (15), is the total energy for a linear conservative system.

Consider now the equilbrium points of equations (18), that are defined by the solutions of $P'_1 = 0$ and $Q'_1 = 0$. To also examine the nature of these equilibrium points, the determinant of the Jacobian of equations (18) was evaluated at the equilibrium points (note that tr $J = 0$ as equations (18) define a conservative system).

$$\det J = -\frac{1}{4v^4} \bar{A}_2^2 \left[2P_1 - P_{20} \right]^2 \sin^2 2Q_1 \tag{20}$$

$$-\frac{1}{2v^4} \bar{A}_2 P_1 \left[P_1 - P_{20} \right] \cos 2Q_1 \left[2\bar{A}_2(2 + \cos 2Q_1) - 3\bar{A}_3 - 3\bar{A}_1 \right].$$

The four equilibrium points of equations (18) are:

$$(i) \quad P_1 = 0; \quad \cos 2Q_1 = -2 + 3\frac{\bar{A}_3}{\bar{A}_2} + \frac{2v}{\bar{A}_2 P_{20}}\left[\sigma_2 - \sigma_1\right], \tag{21a}$$

$$(ii) \quad P_1 = P_{20}; \quad \cos 2Q_1 = -2 + 3\frac{\bar{A}_1}{\bar{A}_2} - \frac{2v}{\bar{A}_2 P_{20}}\left[\sigma_2 - \sigma_1\right], \tag{21b}$$

$$(iii) \quad Q_1 = 0,\pi; \quad P_1 = \frac{3(\bar{A}_3 - \bar{A}_2)}{-6\bar{A}_2 + 3\bar{A}_3 + 3\bar{A}_1}P_{20} + \frac{2v}{-6\bar{A}_2 + 3\bar{A}_3 + 3\bar{A}_1}\left[\sigma_2 - \sigma_1\right], \tag{21c}$$

$$(iv) \quad Q_1 = \frac{\pi}{2}; \quad P_1 = \frac{(3\bar{A}_3 - \bar{A}_2)}{-2\bar{A}_2 + 3\bar{A}_3 + 3\bar{A}_1}P_{20} + \frac{2v}{-2\bar{A}_2 + 3\bar{A}_3 + 3\bar{A}_1}\left[\sigma_2 - \sigma_1\right]. \tag{21d}$$

From these equations we can see that in (i) and (ii) the equilibrium points only exist if $\cos 2Q_1$ has values between ± 1. The determinant is always negative in these cases and so if there are equilibrium points they will be saddle points. Note that since P_1, and $P_2 - P_1$ are positive by definition, then $P_2 > P_1$. In cases (iii) and (iv) both saddle points and centers are possible, which is determined by the sign of the determinant. Using these results it is possible to define regions for $(\sigma_2 - \sigma_1)/P_{20}$ where only certain types of equilibrium points are possible. These regions are shown graphically in Figure 11.
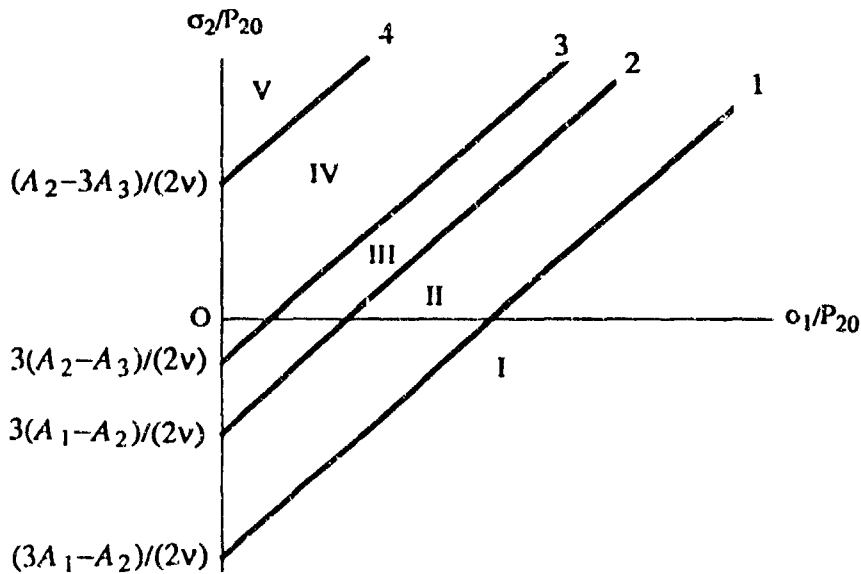
Figure 11: Regions of $(\sigma_2 - \sigma_1)/P_{20}$ that contain the same equilibrium point characteristics, see table 1 for the types of equilibrium points present in each region.

For the first equilbrium point (i), we have saddle points if:

$$\frac{\bar{A}_2 - 3\bar{A}_3}{2v} \geq \frac{\sigma_2 - \sigma_1}{P_{20}} \geq \frac{3(\bar{A}_2 - \bar{A}_3)}{2v}.$$

This defines, respectively, the lines labelled 4 and 3 in Figure 11. For the second equilibrium points (ii), we have saddle points if:

$$-\frac{\bar{A}_2 - 3\bar{A}_1}{2v} \leq \frac{\sigma_2 - \sigma_1}{P_{20}} \leq -\frac{3(\bar{A}_2 - \bar{A}_1)}{2v}.$$

This defines, respectively, lines 1 and 3 in Figure 11. From (iii), we have saddle points if:

$$\frac{3(\bar{A}_2 - \bar{A}_3)}{2v} > \frac{\sigma_2 - \sigma_1}{P_{20}} > \frac{3(\bar{A}_1 - \bar{A}_2)}{2v},$$

and centers if this inequality is not satisfied. This also defines, respectively, lines 3 and 2 in Figure 11. Finally from (iv), we have saddle points if:

$$\frac{\sigma_2 - \sigma_1}{P_{20}} > \frac{\bar{A}_2 - 3\bar{A}_3}{2v}, \quad \text{or} \quad \frac{\sigma_2 - \sigma_1}{P_{20}} < \frac{-\bar{A}_2 + 3\bar{A}_1}{2v}.$$

Otherwise the equilibrium points will be centers. These inequalities also define lines 4 and 1, respectively, in Figure 11. From Figure 11 we can see five clear regions. Within these regions the number and type of equilibrium points are constant. In table 1 are summarized the results.

	(i)	(ii)	(iii)	(iv)
I	×	×	center	saddle
II	×	saddle	center	center
III	×	×	saddle	center
IV	saddle	×	center	center
V	×	×	center	saddle

Table 1: Types of equilibrium points possible in regions defined in Figure 11.

Using the same values for A_1, A_2 and A_3 that were used in the local bifurcation analysis examples, and recalling that $\bar{A}_i = \epsilon A_i$, the solution orbits for $\sigma_1/P_{20} = .006$, and $\sigma_2/P_{20} = -.072$ (region I), $= -.03$ (region II), $= -.0012$ (region III), $= .03$ (region IV), $= .072$ (region V), were calculated. These are shown in Figure 12. Note that chaotic behavior is not possible in parameter regions I and V since the heteroclinic cycles or trajectories joining saddle points occur in regions of the phase plane that are not physically meaningful (recall that $0 \leq P_1 < P_{20}$).

The next step in the analysis is to use the Melnikov technique for two-degree-of-freedom autonomous systems [6,19] and to study the way in which the heteroclinic connections, in cases II, III and IV above, are destroyed by the introduction of perturbations to the system, that is, when $\mu \neq 0$. For the case in [19], it was shown that in each of the cases II, III, and IV, chaotic behavior results when $\mu = 0$. We are pursuing this analysis approach and results will be reported shortly.
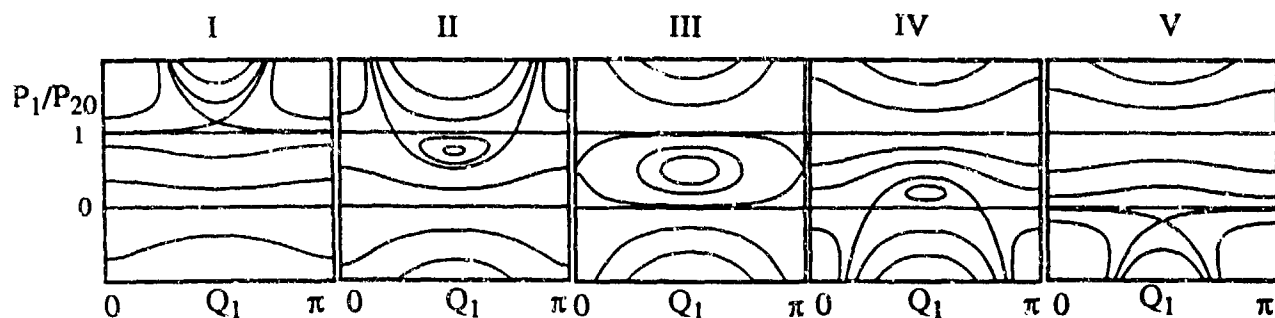
Figure 12: Solution orbits in P_1 and Q_1 phase space for $\sigma_1/P_{20} = .006$, and $\sigma_2/P_{20} = -.072$ (I), $= -.03$ (II), $-.0012$ (III), $= .03$ (IV), $= .072$ (V).

SUMMARY

This work considered the nonlinear vibratory response of a uniformly stretched rectangular plate pinned to immovable supports at its edges. The plate is harmonically excited near primary resonance when two distinct spatial modes are in 1:1 internal resonance. The method of averaging is used to investigate the response representing the dynamics of the two modes in resonance.

Steady-state solutions of the averaged equations are studied in considerable detail. Emphasis is on determining the conditions which lead to a coupled-mode response when only one of the modes in resonance is externally excited. It is shown that, depending on the mode combinations in resonance, as well as the mode that is excited, qualitatively distinct response diagrams can be obtained. Stable single-mode and coupled-mode responses are found to coexist over a wide frequency interval. At low damping levels, the mixed-mode periodic response undergoes Hopf bifurcation to amplitude- and phase-modulated motions. In one case, these limit cycles in the averaged equations are found to lead to period-doubling bifurcations which in turn lead to chaotic motions which represent a chaotic amplitude and phase modulated response of the plate. At lower levels of damping, a "crisis" can interrupt the chaotic behavior and the plate can unexpectedly jump to small amplitude single-mode harmonic motions as the frequency of excitation is varied. In the second case, the phenomenon of glueing bifurcation is found to occur.

The averaged equations are then formulated in a way that facilitates their global analysis. In the limit of zero forcing these new equations are shown to be integrable and heteroclinic loops are found for different combinations of system parameters. These loops can be destroyed by the presence of external excitation leading to chaotic behavior.

CHANG, BAJAJ & DAVIES

REFERENCES

1. Sathyamoorthy, M., "Nonlinear Vibration Analysis of Plates: A Review and Survey of Current Developments", Appl. Mech. Rev., 40, 1553-1561 (1987).
2. Sridhar, S., Mook, D.T. and Nayfeh, A.H., "Nonlinear Resonances in the Forced Responses of Plates, Part I: Symmetric Responses of Circular Plates", J. Sound and Vib., 41, 359-373 (1975).
3. Sridhar, S., Mook, D.T. and Nayfeh, A.H., "Nonlinear Resonances in the Forced Responses of Plates, Part II: Asymmetric Responses of Circular Plates", J. Sound and Vib., 59, 159-170 (1978).
4. Hadian, J. and Nayfeh, A.H., "Modal Interaction in Circular Plates", J. Sound and Vib., 142, 279-292 (1990).
5. Yang, X.L. and Sethna, P.R., "Local and Global Bifurcations in Parametrically Excited Vibrations of Nearly Square Plates", Int. J. Non-Lin. Mech., 26, 199-220 (1991).
6. Wiggins, S., Global Bifurcations and Chaos, Springer-Verlag, New York, 1988.
7. Yang, X.L. and Sethna, P.R., 'Nonlinear Phenomena in Forced Vibrations of a Nearly Square Plate-antisymmetric Case', Journal of Sound and Vibration 155, 413-441, (1992).
8. Yasuda, K. and Torii, T., "Multi-Mode Response of a Square Membrane", JSME Inter. J., 30, 963-969 (1987).
9. Yasuda, K. and Asano, T., "Nonlinear Forced Oscillations of a Rectangular Membrane with Degenerate Modes", Bull. JSME, 29, 3090-3095 (1986).
10. Chang, S.I., Bajaj, A.K. and Krousgrill, C.M., "Non-Linear Vibrations and Chaos in Harmonically Excited Rectangular Plates with One-to-One Internal Resonance", Nonlinear Dynamics (to appear).
11. Nayfeh, A.H. and Mook. D.T., Nonlinear Oscillations, Wiley Interscience, New York, 1979.
12. Hale, J.K., Ordinary Differential Equations, Wiley-Interscience, New York, 1969.
13. Chang, S.I., 'Nonlinear Vibrations in Rectangular Plates', Doctoral Dissertation, Purdue University, West Lafayette, IN., 1993.
14. Guckenheimer, J. and Holmes, P.J., "Nonlinear Oscillations, Dynamical Systems, and Bifurcations of Vector Fields", Springer-Verlag, New York (1983).
15. Doedel, E., "AUTO: Software for Continuation and Bifurcation Problems in Ordinary Differential Equations", Report, Dept. of Appl. Math., Cal Tech., Pasadena (1986).
16. Bajaj, A.K. and Johnson, J.M., "On the Amplitude Dynamics and 'Crisis' in Resonant Motion of Stretched Strings", Phil. Trans. Soc. Lond., A338, 1-41 (1992).
17. Grebogi, C., Ott, E. and Yorke, J.E., "Crisis, Sudden Changes in Chaotic Attractors, and Transient Chaos", Physica D, 7, 181-200 (1983).
18. Glendinning, P., "Global Bifurcations in Flows, "In New Directions in Dynamical Systems, edited by T. Bedford and J. Swift, Cambridge University Press, Cambridge, 120-149 (1988).
19. Feng, Z.C. and Sethna, P.R., "Global Bifurcation and Chaos in Parametrically Forced systems with One-One Resonance", Dyn. and Stab. of Syst., 5, 201-225, 1990.

TITLE: An Analysis of the 120mm M829 Screening in Operation Desert Storm

Robert E. Dillon, Jr., Lieutenant Colonel, USA
Dept. of Civil and Mechanical Engineering
US Military Academy, West Point, New York

ABSTRACT:

The screening results for the 120mm M829 APFSDS round fired from one tank battalion deployed to Southwest Asia from Germany are presented and analyzed in an effort to explain the deviation from expected accuracy. A background history of the ammunition prior to the screening is presented as well as a detailed description of the screening process, measurements of hits on the screening panels, a statistical analysis of the target impacts, and an exterior ballistic analysis to determine the loss of muzzle velocity needed to account for the low hits observed. It was found that a loss of about 170m/s muzzle velocity was necessary to cause the low hits. A mean point of impact was computed for the battalion and compared to the Computer Correction Factor for the M829.

BIOGRAPHY: Robert E. Dillon, Jr.
PRESENT ASSIGNMENT: Associate Professor and Director of Mechanical Engineering Design
PAST EXPERIENCE: Armor officer in company, battalion, and brigade level positions; R&D Coordinator, Benet Weapons Lab, 1981-1984; Associate Professor, Dept. of Mechanics, US Military Academy, 1984-1987.
DEGREES HELD: BS., US Military Academy, West Point, NY, 1974; M. Eng. (Aero), Rensselaer Polytechnic Institute, Troy, NY, 1981; Ph.D., (Aero) Rensselaer Polytechnic Institute, Troy, NY, 1983.

AN ANALYSIS OF THE 120mm M829 SCREENING IN OPERATION DESERT STORM

Robert E. Dillon, Jr., LTC, USA
Dept. of Civil and Mechanical Engineering
US Military Academy
West Point, New York 10996-1792

INTRODUCTION

During Operation Desert Storm it became necessary to Screen the M1A1 tanks prior to entering combat. This paper describes the screening process followed by one battalion and the efforts taken to correct for the unacceptable accuracy obtained from the fleet Computer Correction Factor (CCF) for the M829 round for this occasion.

During the screening in Saudi Arabia about 20 tanks in the battalion failed to hit the screening panel. There were 10 other tanks who hit the screening panel but failed to satisfy the screening criterion [1:A-20]. This was a drastic change from past gunnery experiences where this battalion had to proof fire four out of 58 tanks at worst. Now there were 30 out of 58 tanks that failed to screen. The screening failures were analyzed by the battalion master gunner, the brigade master gunner, the company commander, the brigade operations officer, and the battalion commander. Most of the shots were observed to be low. The mean point of impact of the battalion across the board was likewise observed to be low.

BACKGROUND

Wet Ammunition

There is some history of poor performance of 120mm training ammunition used in Germany. This same battalion, while at annual tank gunnery qualification in Grafenwöhr in March 1988 was issued training ammunition that had been exposed to the weather for a prolonged period. The soldiers in the battalion had to chip ice off the casing of their M831 and M865 training rounds with screwdrivers in order to get them to fit inside the ammunition ready racks. This all occurred despite published guidance on how to store the 120mm ammunition. During this gunnery rotation the battalion consistently fired low on targets beyond 1700 meters range. At the time it was theorized by the battalion master gunner the water content of the ammunition was to blame for

the low shots at long range. The battalion also drew water damaged ammunition in 1989 and some rounds could not be chambered due to excessive swelling of the cartridge case. The rotation in March 1990 saw mostly new ammunition issued and no problems were encountered with water soaked ammunition.

The battalion had finished off cycle gunnery two months prior to notification of deployment to SWA and had not encountered any mechanical difficulties with the their fire control systems nor were any problems reported with the M865 and M831 ammunition. The battalion had just received its M1A1 (Heavy) tanks in July 1990 and all were in excellent mechanical condition. The battalion had been uploaded since February of 1987 until the fall of 1988 when the ammunition was placed in subterranean bunkers. During the time the battalion was up-loaded, the ammunition was subjected to the constant rain and high humidity of the north German weather. To exacerbate this problem, the environmental cover at the rear of the turret bustle allowed water to leak into the ammunition compartment. This, along with any scratches or gouges on the cartridge case, created a condition allowing the ammunition to absorb water. This was known by PM, TMAS and the ammunition units in Germany[7,8]. In November 1989, one ammunition surveillance team from PM, TMAS found ammunition that had been submerged in water, had soft casings, rusty primers and rusty stub cases. Some turret bustle ammunition compartments had standing water along with condensation droplets forming on the inside walls [7]. One quality control inspection by an ammunition unit to the battalion studied in this report showed such findings as: soft cartridge cases, 63% of the ammunition inspected had corrosion on the base and primer, and 100% with scrapes and scratches on the combustible cartridge case [8].

Screening Doctrine

The current doctrine, as put forth by the Armor School, states that tanks will not be zeroed but rather calibrated by boresight, then screened using a fleet CCF for each type of main gun ammunition [1:A-17]. There has been debate in the armor community for several years on the necessity of zeroing. The Armor School maintains that zeroing is good for only a specific occasion and despite the increase in accuracy for this occasion, the costs [of the ammunition] for zeroing make this practice "irresponsible" [6]. This argument unfortunately does not quantify the costs of destroyed tanks and incinerated solders as a result of not zeroing. The tank manufacturer, however, states that to get the maximum accuracy from the tank it must be zeroed [2:2-276]. The manufacturer also states that zeroing will only need to be done once and unless the gun tube, mount, or recoil spring are removed there is no need to re-zero the tank [2:2-76]. To further complicate the issue, FM 17-12-1 does not give any instructions for screening prior to combat. The only references to screening are made when referring to a training situation and not combat.

As the last of the old M60 tankers leave the army so does the institutional memory on zeroing. Since the M1 and M1A1 tankers have only screened during gunnery and few have proof fired their tanks, there is little experience save for the master gunner in zeroing. When a tank does not pass screen and has to be proofed, the master gunner usually supervises the crew.

GENERAL APPROACH

Research

A literature search of the Defense Technical Information Center discovered some problems with accuracy during tests of early production M1A1 tanks [3:1]. However, there was no consistent pattern of low hits mentioned in the literature.

Reduction of Raw Firing Data

All the tanks in the battalion fired M829 at screening panels placed at 1500 meters. Figure 1 shows the 1500 meter screening panel. Initially, each tank was boresighted and applied the fleet CCF for the M829 round and attempted to fire for confirmation. Each hit was measured and the distance from the center of the panel to the hit was recorded. Figure 2 shows the mean point of impact (MPI) of the shots fired from the fleet CCF. Not shown on the figure are the locations of all the hits nor the 17 shots that missed the target short, one that missed to the right and three that flew over the target.

At this point we decided to correct for the poor hit distribution observed in the M829 rounds brought from Germany. We computed a modified CCF for those tanks missing the panel or hitting low. Based on the distribution of hits the modified CCF was L0.13, U0.30. This is in comparison to the published CCF for the M829 of L0.13, U0.65. Figure 2 shows the MPI of those shots fired from tanks using the modified CCF. As a result of this correction, the MPI was brought closer to the aim point.

After a closer look at the strike of all the rounds a more precise computation of the MPI was computed. From these data a corrected CCF was found to be L0.01, U0.34. This would be the CCF for these rounds fired for this screening occasion. Compared to our field estimate CCF of L0.13, U0.30 we came close to the true mean point of impact for the vertical jump be since we ignored horizontal jump we were off roughly one tenth of a mil. Table 1 compares the fleet CCF with the modified CCF computed at the range and the corrected CCF computed in this report. The MPI based on the corrected CCF is also shown on figure two and the proximity of the MPI with the aim point is

evident. As an added comment, the crews whose shot hit close to the center were very comfortable with the screening process. However, those crews whose shot hit 80 cm from their aim point had considerably less confidence in their ability to hit a hostile target even though reference 1 said they were "properly screened".

Table 1 Comparison of Fleet with Modified CCFs

CCF	Horizontal (mils)	Vertical (mils)
Fleet	Left 0.13	Up 0.65
Modified at Range (Dillon)	Left 0.13	Up 0.30
Modified in Report (Dillon)	Left 0.01	Up 0.34

Discussion

At the firing range, figure 3, our immediate concern was to find the cause of the poor accuracy of some of the M829 rounds. One source of error we considered was optical path bending The high temperatures in the desert and the convex curvature of the range from the firing line to the target area caused considerable heat striations distorting the image of the targets. If the gunners were aiming at the apparent center of the target, this could explain the poor accuracy. We tested this hypothesis by firing some available M865 rounds from tanks that failed the M829 screening. All these tanks hit very close to the aim point with M865. This narrowed our alternatives to two possible causes: 1) the M829 CCF was not correct, 2) the M829 ammunition was faulty. To narrow our alternatives down we reasoned that the CCF was for the M829 was correct and our history of wet rounds gave us some insight into the cause of the low hits. Based on this experience and after some lengthy discussion at the range we assumed one or two things were happening. One was some of the M829 ammunition had absorbed enough water to slow the round down to the point that the lost muzzle velocity would cause the round to hit low. The other was the lower muzzle velocity would cause the slower round to arrive at the muzzle late which would cause the projectile to exit the tube with different horizontal and vertical velocities and displacements due to gun dynamics. We thought this could have a very large and random effect on dispersion. We were not in a position to do anything about narrowing down the source of error(s) but we did have to come up with a solution and fast. The time and ammunition constraints we faced prohibited us from zeroing 30 tanks. Our modified CCF was our interim solution. Our modified CCF allowed all tanks in the battalion to pass screen except two which had to be zeroed.

In order to present a possible cause of the low hits by some of the M829 rounds an exterior ballistic analysis was conducted to determine how much muzzle velocity would have to be lost to cause an M829 round fired from the fleet CCF to miss a screening panel 1500 meters away. Following the exterior ballistic analysis an initial interior ballistic analysis was conducted to attempt to quantify how much muzzle velocity could be lost from a wet casing.

Exterior Ballistic Analysis

An exterior ballistic analysis was conducted on the M829 ammunition in an effort to determine how much muzzle velocity would have to be lost to miss a screening panel 1500 meters away. From the size of our panel, the round would have to pass 0.67 mils below the aim point to miss the panel.

A solution to this can be calculated by modeling the trajectory of the M829 round in two dimensions. The differential equations of motion in the x and y directions are:

$$x'' = -(1/m)K_d d^2 x' \tag{1}$$

$$y'' = -(1/m)K_d d^2 y' - g \tag{2}$$

where m is the projectile mass, K_d is the ballistic drag coefficient, d is the projectile body diameter, and g is the acceleration due to gravity. The values for the drag coefficient were obtained from reference 9 and are a function of the flight Mach number.

These equations were integrated for several initial conditions of muzzle velocity to determine how much loss would cause the round to fall 0.67 mils at 1500 meters. Table 2 shows the results of this. In order for a round to miss the panel the muzzle velocity would have to be below about 1500 m/s which is a loss of about 170 m/s at the muzzle. A cursory interior ballistic analysis was done to explore the feasibility of the wet ammo theory.

Table 2 Projectile Strike vs Muzzle Velocity

Muzzle Velocity (m/s)	Strike at 1500 m (cm below baseline)	Change in Vmuz (m/s)
1670	0.0	0.0
1570	-40.5	-100
1500	-100.5	-170

This analysis was done assuming the low hits were a result of low muzzle velocity only. In actuality, it is presumed the gun dynamics would be different with a loss of 170 m/s of muzzle velocity. With this lower velocity and time of arrival at the muzzle, we theorize the projectile would experience a different jump due to the lateral and vertical displacement and velocity of the muzzle at the time of shot ejection. So, in addition to the greater fall from low muzzle velocity, the projectile would have a different jump due to different gun dynamics during launch.

Interior Ballistic Analysis

In order to study the possibility of wet ammo causing a loss of muzzle velocity sufficient to cause a round to miss the panel, a simple interior ballistic parametric study was done using IBCODE [4:--]. To establish a baseline from which to compare, the interior ballistic solution for the M829 was calculated.

Since there was no way of determining how much water permeation existed in the rounds already fired we decided to remove the combustible cartridge case from the initial conditions of the calculation. Although very crude this allowed us to see how much the cartridge case contributed to the interior ballistic solution [5:--]. By removing the cartridge case from the input deck an 8.3% loss of muzzle velocity resulted. This corresponds to 137 m/s in the M829. If the cartridge case was water soaked, the water would act as an energy sink and presumably reduce the muzzle velocity even further. As a result of the interior ballistic analysis, wet ammo theory could cause the low shots seen in the screening.

DILLON

CONCLUSIONS

The M829 fleet CCF was not acceptable for all tanks during Operation Desert Storm.

The field modified CCF provided an interim solution for the M829 rounds during the ground campaign in Operation Desert Storm.

Wet ammunition is suspected as the major cause of poor accuracy with the fleet CCF.

RECOMMENDATIONS

A more precise analysis of the interior ballistics of the M829 ammunition be conducted to determine the effect of moisture in the propellant on the performance of this ammunition.

A full scale firing test be conducted using water soaked ammunition to provide an insight on the applicability of the fleet CCF for water soaked ammunition.

A study is recommended to investigate the effect of gun dynamics on the accuracy of the M829 round with lower than nominal muzzle velocities.

ACKNOWLEDGMENTS

DILLON

REFERENCES

1. US., Department of the Army, Field Manual 17-12-1, "Tank Combat Tables," w/c3, Government Printing Office, Washington, DC: 1989.

2. US., Department of the Army, Technical Manual 9-2350-264-10-2, "Tank Combat, Full Tracked, 120mm Gun, M1A1," w/c10, Government Printing Office, Washington, DC: 1990.

3. Compton, Louis D., "Final Report Follow-On Production Test of the M1A1 Abrahms Tank, sn L10193U," Combat Vehicle Division, Automotive and Support Equipment Directorate, US. Army Combat Systems Test Activity, Aberdeen Proving Ground, MD: 1990.

4. O'Hara, Peter, G., Benet Weapons Laboratory, Private Communication on IBCODE, an MS-DOS interior ballistic code developed by Mr. Fred Robin of Army Research Laboratory, Aberdeen MD, 1991.

5. Vottis, P., Benet Weapons Laboratory, Private Communication, 1991.

6. Letter, Weapons Department, US Army Armor Center, Subject: Zero vs Boresight, 12 Sep 90.

7. Katz, Walter, et al, "Surveillance of 120mm Tank Ammunition, Preliminary Report, Visits to Vilseck/Grafenwoehr, Wildflecken & Schweinfurt, 15-21 October 1989," PM-TMAS Report No. TMAS-SUR-2P, 1 November 1989, Picatinny Arsenal, NJ.

8. Memorandum, AEROD-N-QAB, Subject: Inspection of downloaded 120mm Sabot rounds, M829 (APFSDS-T), 8 Nov 89.

9. Leiske, R., Army Research Laboratory, Aberdeen, MD.

FIGURES

1500 Meter Screening Panel
120mm M1A1
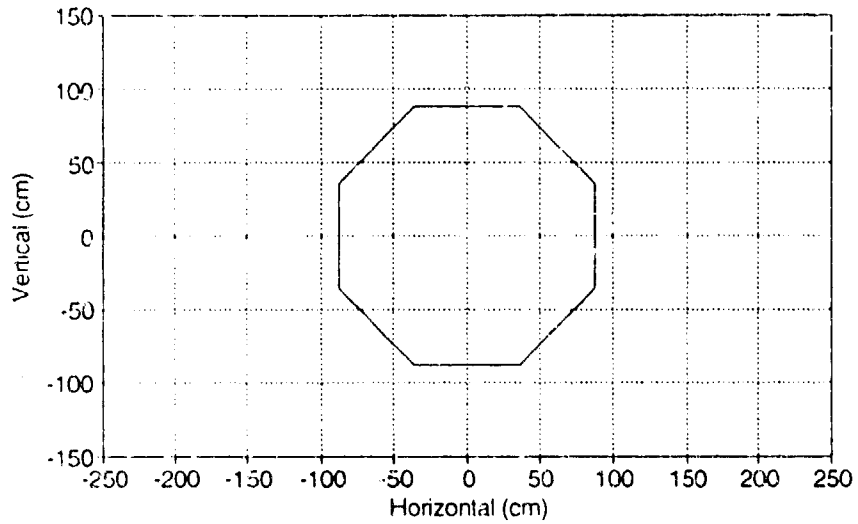
Figure 1. 120mm 1500 meter screening panel.

M829 1500 Meter Screening
Mean Points of Impact
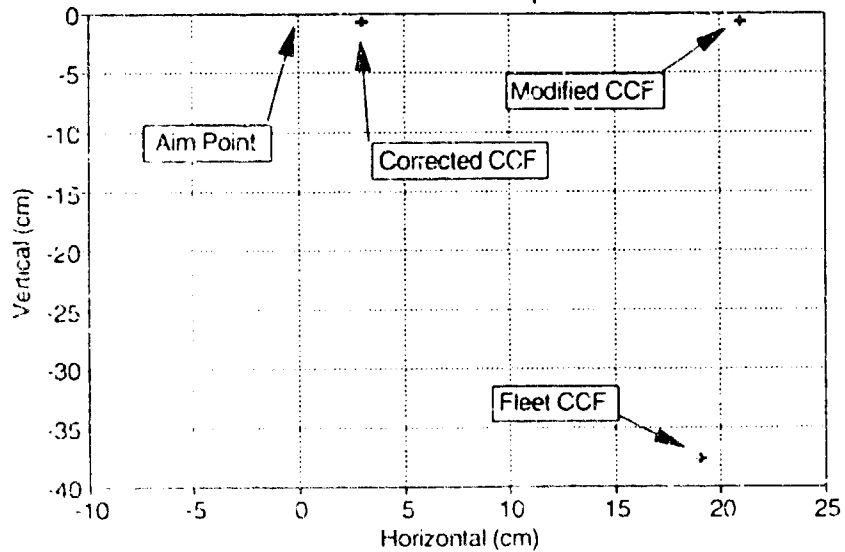
Figure 2. Mean Points of Impact.
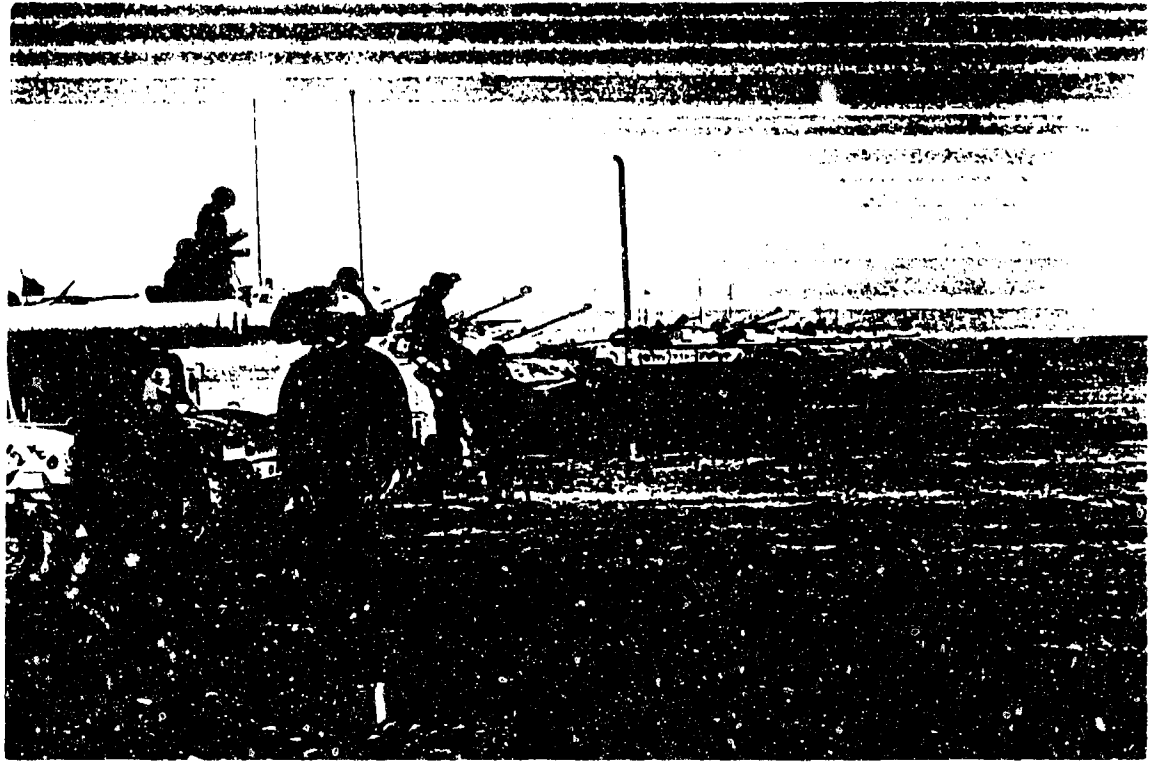
Figure 3. Tanks at the Screening Range

TITLE: DYNAMIC STRAIN WAVES AND PERMANENT BORE ENLARGEMENT

R. HASENBEIN AND E. HYLAND
U.S. ARMY ARMAMENT RESEARCH, DEVELOPMENT & ENGINEERING CENTER
BENET LABORATORIES
WATERVLIET, NY 12189-4050

ABSTRACT:

The purpose of this study was to explore the effect of dynamic strain waves on tube strength, specifically to determine whether they are capable of causing permanent radial expansion of the bore. To accomplish this, previous test firings of three tubes were studied. The first two (the 120-mm TT2 and the 105-mm CT2) were experimental tubes fired in the mid-1980s, and the third (the 120-mm M256) is the standard main gun for the M1A1 Abrams Tank. Inspection reports after test firings indicated that the first two tubes had undergone permanent radial expansion, despite having static factors of safety of 2.5 and 2.0 respectively. There are no known reports that the third tube experiences permanent bore deformations due to firing ammunition in current production.

A non-linear, elastic-plastic, dynamic finite element analysis was performed that emulates firing tests of each of the above tubes. The analysis successfully reproduced the permanent bore dilations actually experienced by the first two tubes, and it also correctly predicted that the third tube would not fail in this manner.

Based on this study, the following conclusions are reached:

• Dynamic strain waves can cause permanent radial expansion of a tube's bore if the combined von Mises' (dynamic) stress exceeds the static yield strength of the tube material.

• This permanent bore deformation can be predicted using the above analytical techniques.

• Static elastic strength pressure curves alone are not a sufficient indicator of a tube's ability to withstand the effects of firing a given projectile. An analysis such as that described above must also be performed to confirm that stresses are not dynamically amplified beyond the yield strength of the material, thereby causing permanent bore enlargement.

BIOGRAPHY: R. Hasenbein
PRESENT ASSIGNMENT: Mechanical Engineer, Systems Engineering Branch, Development Engineering Division, Benet Laboratories, ARDEC.

DEGREES HELD: M.S. - Union College, Schenectady, NY;
                  B.S. - University of Rochester, Rochester, NY

DYNAMIC STRAIN WAVES AND PERMANENT BORE ENLARGEMENT

R. Hasenbein and E. Hyland
U.S. Army Armament Research, Development, and Engineering Center
Benet Laboratories
Watervliet, NY 12189-4050

INTRODUCTION

A discussion of dynamic strain waves in large caliber cannon tubes, an extensive analytical treatment of this phenomenon, and experimental results using a sub-scale firing fixture have previously been presented by Simkins at the Fifth and Sixth U.S. Army Symposia on Gun Dynamics [1,2]. At the latter symposium, a paper by the author [3] documented the work of several cannon designers, analysts, and experimentalists, exploring the implications of dynamic strains from the development point of view. This paper speculated that dynamic strain waves may have the following implications for cannon tubes:

● effect on tube strength (permanent bore deformation);

● effect on tube fatigue life (high strain rate loading, multiple cycles per round fired);

● effect on projectile behavior due to local clearances or constrictions at tube-projectile interfaces;

● effect on adhesion/cohesion of bore coatings such as chromium plating,

● creation of local accelerations in the tube walls.

As of that date, none of these possible implications had been studied in any detail except for the last one (i.e., the effect of dynamic strain waves on muzzle reference system collimators).

The purpose of this paper is to further explore the first item on the above list: the effect of dynamic strain waves on tube strength. The specific question to be answered is this. "Is it possible for dynamic strain waves to cause permanent radial expansion of a tube's bore?"

BACKGROUND: DYNAMIC STRAINS

Beginning in the mid-1980s, the presence of dynamic strain waves in cannon tubes firing high velocity projectiles was first observed and documented. A short background is provided here in order to review the terminology that accompanies this phenomenon.

Figure 1 is an artist's sketch showing a projectile moving at low velocity down the bore of a cannon tube. Well ahead of the projectile where there is no significant pressure, the bore has hardly

dilated at all. Behind the projectile, the bore is pressurized by the propelling charge gases, and the resulting bore dilation is easily calculated by classical static equations [4]. Note that slightly ahead of the projectile obturator there is a small contraction of the bore, and slightly behind it there is a minor over-expansion beyond the calculated dilation; both are due to local wall flexures.

Figure 2 shows a second artist's sketch depicting a projectile moving at a much higher velocity. In the region well behind the projectile, classical equations can again be used to calculate the static component of the bore dilation, and of course there is still no significant dilation in the unpressurized zone well ahead of the projectile. The major difference between Figure 2 and Figure 1 is what happens in the areas just behind and just ahead of the projectile obturator. The moving pressure front significantly amplifies the slight bore contraction (fore) and over-expansion (aft) that were present at low projectile velocities. Note that in this area the strain response has taken on a wavelike nature that (in this case) builds up as the projectile approaches, then decays after it passes by. This dynamic strain wave travels down the tube along with the projectile. The frequency and amplitude achieved by this wave at a given axial location on the tube are the subject of the following paragraph.

Figure 3 shows a representative tangential strain gage trace a specific downbore location on a tank cannon tube. In this figure, the "static strain" has been calculated and labeled; its value at a given axial position depends primarily on the following factors:

● material properties of the cannon tube (Young's modulus and Poisson's ratio);

● inside diameter (I.D.) of the cannon tube (i.e., its caliber);

● wall thickness (or, alternatively, the wall ratio) of the cannon tube;

● pressure applied at the I.D. (bore) of the cannon tube at the base of the projectile by the propelling charge gases.

Also labeled in this figure is the "peak dynamic strain"; its value at a given axial position depends on all of the above factors and, in addition, the velocity of the projectile (which is also, of course, the velocity of the suddenly applied pressure front located at the projectile obturator) and tube material density. The term "strain amplification" is defined simply as the "peak dynamic strain" divided by the "static strain" at any given distance from the rear face of the tube (RFT). The frequency of these dynamic strain waves has previously been observed to be on the order of 15,000 Hertz for large caliber tank guns.

Note that the "projectile passage" label in Figure 3 indicates the approximate time at which the projectile passes under the strain gage, and "projectile exit" shows when it has left the muzzle.

Dynamic strain amplifications are potentially greatest at any given axial location when the projectile velocity approaches the so-called "critical velocity" of the cannon tube. For given tube material properties (usually those of A723 gun steel) and caliber, the "critical velocity" at any axial position is primarily a function of wall thickness (ref 1).

● If the projectile velocity and tube "critical velocity" are about equal, a resonant condition is established; therefore, the projectile velocity in this case is also termed "critical." For an undamped system, amplifications can theoretically become infinite; however, in actual firing tests in which projectile velocities have been at or near "critical," dynamic strain amplifications on the order of 4 to 6 have been measured.

● If the projectile velocity is less than "critical," amplifications decrease. If it remains significantly below "critical" (as it usually does for a slower HEAT-T round), amplifications may be on the order of 1.1 or lower. In these cases, the projectile velocities are termed "subcritical."

● If the projectile velocity increases above "critical," amplifications also begin to decrease, asymptoting down to a value of 2.0 for very high velocities. These projectile velocities are termed "supercritical."

Dynamic strain firing tests at Aberdeen Proving Ground have indicated that local longitudinal dynamic strains in the tube walls are also very high. In fact, it is not uncommon for these to equal or exceed the tangential dynamic strains in amplitude.

BACKGROUND: DYNAMIC FINITE ELEMENT ANALYSIS

Reference 3 describes the techniques that have evolved for performing dynamic finite element analyses (FEA) to predict the dynamic strain response of cannon tubes when fired. These are summarized below:

● Performance of a ballistic analysis that emulates the ammunition being fired. Outputs of interest include:

• projectile in-bore position as a function of time, and

• in-bore pressure at the base of the projectile as a function of time (and, therefore, projectile location).

● Preparation of an axisymmetric gridwork for FEA that emulates the cannon tube in reasonable detail. Early models included only the last 2000 mm of the muzzle end of the tube in order to reduce computational time (which was still considerable); however, the current technique models the entire tube in order to minimize artificial "start-up" oscillations.

● Execution of an FEA using the ABAQUS non-linear finite element code running in dynamic mode. Input files include:

• results of the above ballistic analysis,

• the tube gridwork, and

• elastic properties of the tube material.

Outputs of the analysis may include stresses, strains, and displacements. These are typically presented as a function of time (at a given axial location on the tube) or as a function of distance from RFT (peak values only). Stress and strain can be shown either in their orthogonal components (radial, tangential, longitudinal), or they can be tensorially combined (for instance, into a von Mises stress).

As an example, to demonstrate the accuracy of this analytical technique, a previous FEA was performed that modelled the 120-mm XM25 tube firing the M865 TPCSDS-T cartridge conditioned to 21°C. The upper curve of Figure 4 shows the tangential strains that the FEA predicts will be experienced by the tube on its outside diameter (O.D.) as a function of distance from RFT. The lower curve represents strains that would have resulted if the pressure from the propelling charge gases had been

applied statically. In Figure 5, the peak dynamic strain was divided by the static strain at each axial location, resulting in an amplification curve. Since the FEA of this particular tube/ammunition combination emulated the conditions of a dynamic strain firing test conducted at Aberdeen Proving Ground, experimental data are available as a comparison. The asterisks (*) shown in Figure 5 represent the amplifications actually observed in that test, and it can be seen that these compare very favorably with the results of the FEA.

BACKGROUND: TUBE STRENGTH

Prior to the mid-1980s, the single-shot strength of a cannon tube was predicated solely on its static characteristics. For example, ballistic drawings were generated showing the tube's "Elastic Strength Pressure" (ESP) as a function of distance from RFT. These drawings stated that the ESP "is that pressure which must not be exceeded at the indicated section without risk of tube failure" by permanent bore deformation. ESP curves were calculated based on:

- the minimum yield strength allowable for the tube's material;

- its "least material condition" geometry (minimum allowable O.D., maximum allowable I.D.); and

- the smallest elastic-plastic radius due to autofrettage (if applicable).

The drawing advised that the factor of safety for the tube firing a specific type of ammunition could be calculated by dividing the ESP by the internal pressure applied by the propelling charge gases at any given axial location. If the result was greater than 1.0, the implication was that no permanent bore deformation should be expected.

As previously stated, in the mid-1980s the dynamic strain phenomenon was first observed and documented. The presence of high strain amplifications created an intuitive suspicion that static factors of safety may be inadequate in cases when a projectile is fired at high velocity (more specifically, when it approaches tube critical velocities). As a result, ESP curves were still generated for developmental cannons, but only for reference and not as part of a ballistic drawing to be included in a formal Technical Data Package. Moreover, great care was exercised when distributing any ESP curve to be sure that the recipient understood its limitations. The following caveat was included on most ESP curves prepared by Benet:

"Pressure and dynamic strains influence stresses at the muzzle end of the tube. Each ballistic solution will have to be reviewed by Benet Labs to determine muzzle end stress implications."

The above conservativism, which dynamic strains have imposed on developers when considering the strength of cannon tubes, seemed to be qualitatively logical and appropriate; to date, however, a quantitative analysis has not been performed linking dynamic strains to tube strength (specifically, permanent bore deformation). The intent of this study and report is to formally make that link.

BACKGROUND: FIRING TESTS OF TWO EXPERIMENTAL TUBES

In 1984 and 1985, two different experimental tubes (described in more detail below) were fired at Aberdeen Proving Ground, both of which had wall thicknesses near the muzzle that were somewhat thinner than conventional tubes. At that time, the dynamic strain phenomenon had not yet been

discovered, so the designers were comforted that the static factor of safety (ESP divided by expected pressure) was 2.0 or greater. After firings were completed, the tubes were inspected, and it was discovered that the bores of both had undergone a permanent radial expansion in the region near the muzzle. The origin of these failures was not understood at the time the tests were performed; however, during the following years as Simkins identified and explained the nature of the dynamic strain phenomenon being observed during test firings of the 120-mm XM25 tube (ref 1), a suspicion arose that the two failures previously encountered were in some way related. The data were therefore stored safely for a later time when more advanced analytical techniques might become available, and the era of conservativism with regard to ESP curves began.

Since that time, several new capabilities have evolved:

● The ABAQUS non-linear finite element computer code came into widespread use within Benet and became recognized as an important design tool.

● Analytical FEA techniques (described above) were developed that utilized the attributes of ABAQUS. These successfully emulated the dynamic strain waves, both qualitatively and quantitatively, and it was found that they could be applied to a variety of specific tube/ammunition combinations.

● Computational speed dramatically increased with the acquisition of the Convex C220 mini-supercomputer at Benet.

All of the above have combined to make it possible to perform "large-scale, non-linear, dynamic" FEA of an entire cannon tube, emulating firing of ammunition. In this study, these capabilities have been extended to also include the term "elastic-plastic" in the above descriptor list, thus allowing the prediction of possible plastic deformations and residual stresses. With this, the proper tools are now in place to re-study the two tubes mentioned in the first paragraph above. The results are described in the following three case studies.

CASE STUDY: 120-mm TT2 TUBE

The first tube to be studied was designated "120-mm TT2," and it was a pre-prototype for the 120-mm XM25 tube. In many ways, it was similar to the 120-mm M256 tube, having the same overall length, same smooth bore, and same chamber; it was therefore capable of firing the same ammunition. Moreover, it had the same O.D. details from RFT to roughly 2000 mm from RFT (see comparison in Figure 6). From that point forward, the wall thickness for TT2 was significantly thinner than for the M256, decreasing to a minimum of about 12.7 mm (0.5 inch). The ESP in this thinnest section was approximately 175 MPa (25 kpsi); since the expected pressure during firing at that axial location was about 70 MPa (10 kpsi), the static factor of safety was judged to be about 2.5.

Figure 7 is a graph showing wall thickness of TT2 as a function of distance from RFT. The tube's critical velocity is directly related to this parameter, and it too has been estimated and plotted in Figure 8. It can be seen that the lowest critical velocity is in the region of minimum wall thickness. Superimposed on the critical velocity curve is a second curve that shows the in-bore velocity of a projectile fired from this tube. The latter was estimated using a ballistic computer code calibrated to the average muzzle velocity observed during several test rounds. Qualitatively, it can be observed that the projectile velocity and tube critical velocity come into close proximity in the region of thinnest wall, and a near-resonant condition would be expected.

As described above, the ballistics and tube geometry were modeled and used as inputs to the ABAQUS non-linear, elastic-plastic, dynamic FEA. In an elastic-plastic analysis, material yield strength is a required input, and this was estimated to be 1117 MPa (162 kpsi) based on forging inspection data. The most important results of this FEA are summarized in the following two figures:

- Figure 9 is a curve showing the analytical predictions of permanent bore enlargement as a function of distance from RFT. For reference, the actual post-firing bore inspection data are also superposed as shaded circles. It can be observed that the predicted and actual results compare very favorably, both qualitatively and quantitatively.

- Figure 10 is an interesting curve showing the plastic strains (i.e., the elastic strain component has been subtracted from the total dynamic strain) experienced by the bore at an axial location 4850 mm from RFT as a function of time. It can be seen for the tangential strain (solid line) that, as the projectile approaches, the bore first deforms plastically in compression, then reverses itself to deform permanently in tension. The strain curve for the longitudinal direction (dashed line) does just the opposite. This creates an overall strain environment at the bore that is extremely severe.

- Figure 11 shows a plot of tangential strains at the I.D. as a function of distance from RFT. The lower curve shows the strains that would result if the pressure created by the combustion gases were applied statically, and the upper curve indicates the peak dynamic strain response predicted by the FEA.

- Figure 12 is a graph of dynamic strain amplifications as a function of distance from RFT. This is essentially obtained by dividing the upper curve of Figure 11 by the lower curve.

- Figure 13 depicts the von Mises combined stresses in the tube wall as a function of distance from RFT. The three curves portray inside, outside, and midwall stresses, respectively. Note that the I.D. stress achieves its theoretical limit (the tube material's yield strength) at about 4600 nm from RFT, the location beyond which permanent bore enlargements were observed. The combined stresses at midwall and the O.D. lie well below this limit except near 4900 mm from RFT (the initial axial location of high permanent bore deformation) and at the extreme muzzle (the second zone of high deformation).

CASE STUDY: 105-mm CT2 TUBE

The second tube to be studied was designated "105-mm CT2." Actually, it was the steel liner for an experimental organic composite tube; during this particular firing test, however, the composite jacket had been removed. This tube was similar to the 105-mm M68E1, having the same overall length, same rifled bore, and same chamber; it was therefore capable of firing the same ammunition. Moreover, it had the same O.D. details from RFT to about 3250 mm from RFT (see comparison in Figure 14). From that point forward, the wall thickness for CT2 was significantly thinner than for the M68E1, decreasing to a minimum of about 7.6 mm (0.3 inch) as measured from the O.D. to the rifling grooves. The ESP in the thinnest section was roughly 140 MPa (20 kpsi); since the expected pressure during firing in that axial location was about 70 MPa (10 kpsi), the static factor of safety was judged to be about 2.0.

Figure 15 is a graph showing wall thickness of CT2 as a function of distance from RFT. Since this is a rifled tube, wall thickness could have been calculated using either the land-to-land or the groove-to-groove I.D.; in this case, however, an effective "smoothbore" I.D. was used that produced the same sectional mass as the rifled tube. Based on this, critical velocities have been estimated and plotted as a function of distance from RFT in Figure 16. It can be seen that the lowest critical velocity is in the region of minimum wall thickness. Superimposed on the critical velocity curve is the projectile's in-bore velocity; the latter was estimated using a ballistic computer code calibrated to the average of muzzle velocities

observed during testing. Qualitatively, it can be observed that the projectile velocity and tube critical velocity come into close proximity in the region of thinnest wall, and a near-resonant condition would be expected.

Again, the ballistics and tube geometry were modelled and used as inputs to the ABAQUS non-linear, elastic-plastic, dynamic FEA. Tube yield strength based on forging data was estimated to be 1138 MPa (165 kpsi). The results of this FEA for CT2 are qualitatively the same as for TT2 and will therefore not be repeated here, with the exception of the one most crucial to this study:

⊙ Figure 17 is a curve that shows the analytical predictions of permanent bore deformation as a function of distance from RFT. For reference, the actual post-firing bore inspection data are also superposed as shaded circles. It can be observed that the predicted and actual results compare very favorably, both qualitatively and quantitatively.

CASE STUDY: 120-mm M256 TUBE

Test firings have indicated that this tube does not undergo permanent bore deformations when firing standard ammunition. Therefore, for completeness, the analytical techniques described above were applied to this tube, emulating the firing of the same ammunition as in the TT2 case study. As hoped, the FEA also predicted that no permanent bore deformation should be expected.

OBSERVATIONS AND CONCLUSIONS

The most important results of the above study can be seen in Figures 9 and 17. The FEA computer predictions agree, both qualitatively and quantitatively, with the results of post-firing inspection reports for two experimental tubes test-fired in the mid-1980s. In both cases, permanent bore deformations were observed, and current analytical methods (if they had been available at that time) would have predicted these events. Equally important are the results of a third case study for the 120-mm M256 tube in which permanent bore deformation is neither observed in the field nor predicted by these analytical techniques.

It is therefore concluded that the non-linear, elastic-plastic, dynamic FEA techniques that have been developed can be used to predict not only the dynamic strain response of a cannon tube to firing, but also whether or not it should be expected to undergo permanent bore deformation as a result of it.

It is also concluded that the answer to the question posed near the beginning of this report (i.e., "Is it possible for dynamic strain waves to cause permanent radial expansion of a tube's bore?") can clearly be answered, "Yes." This study quantitatively affirms the previous suspicion that static ESP curves must never be used as a final predictor of tube strength. An analysis such as that described above must also be performed to confirm that stresses are not dynamically amplified beyond the yield strength of the material, thereby causing permanent bore enlargement. As in static stress analyses of a pressurized cylinder,

- it appears that when the von Mises' combined (dynamic) stresses exceed the static yield strength, permanent radial expansion of the bore may occur, and

- the degree of permanent bore deformation depends on how much of the tube wall is in the plastic regime.

HASENBEIN, HYLAND

ESP curves still have some intrinsic value, particularly in assessing the strength of a gun tube towards its breech end. However, in the downbore regions, the curve may give false comfort in this regard since it does not take into account dynamic amplifications.

Finally, the results shown in Figure 10 must also be carefully studied. It appears that if ammunition is fired near the critical velocity of a cannon tube, causing its combined stresses to exceed the static yield strength of the material, the local bore deformations can become quite severe, alternately undergoing plastic tensile and compressive deformations in two orthogonal directions. The intuitive implication is that this may have a significant effect on:

- the formation and propagation of fatigue cracks, and

- the adhesion and cohesion of chromium near the bore surface.

These possibilities are offered here as topics for further studies.

REFERENCES

1. T.E. Simkins, "Resonance of Flexural Waves in Gun Tubes," in: *Proceedings of the Fifth U.S. Army Symposium on Gun Dynamics*, ARCCB-SP-87023, Benet Laboratories, Watervliet, NY, 23-27 September 1987, pp. 65-78.

2. T.E. Simkins, "Dynamic Strains in a 60-mm Gun Tube--An Experimental Study," in: *Proceedings of the Sixth U.S. Army Symposium on Gun Dynamics*, ARCCB-SP-90015, Benet Laboratories, Watervliet, NY, 15-17 May 1990, Vol. II, pp. 253-271.

3. R.G. Hasenbein, A. Gabriele, D. Finlayson, B. Artus, G. Cunningham, and R. Gast, "Dynamic Strain Waves--A Development Perspective," in: *Proceedings of the Sixth U.S. Army Symposium on Gun Dynamics*, ARCCB-SP-90015, Benet Laboratories, Watervliet, NY, 15-17 May 1990, Vol. II, pp. 286-297.

4. R.C. Juvinall, *Stress, Strain, and Strength*, McGraw-Hill Book Co., New York, NY, 1967.

Figure 1. Near-static tube wall dilation (low velocity firing).

DYNAMIC TUBE WALL DILATION
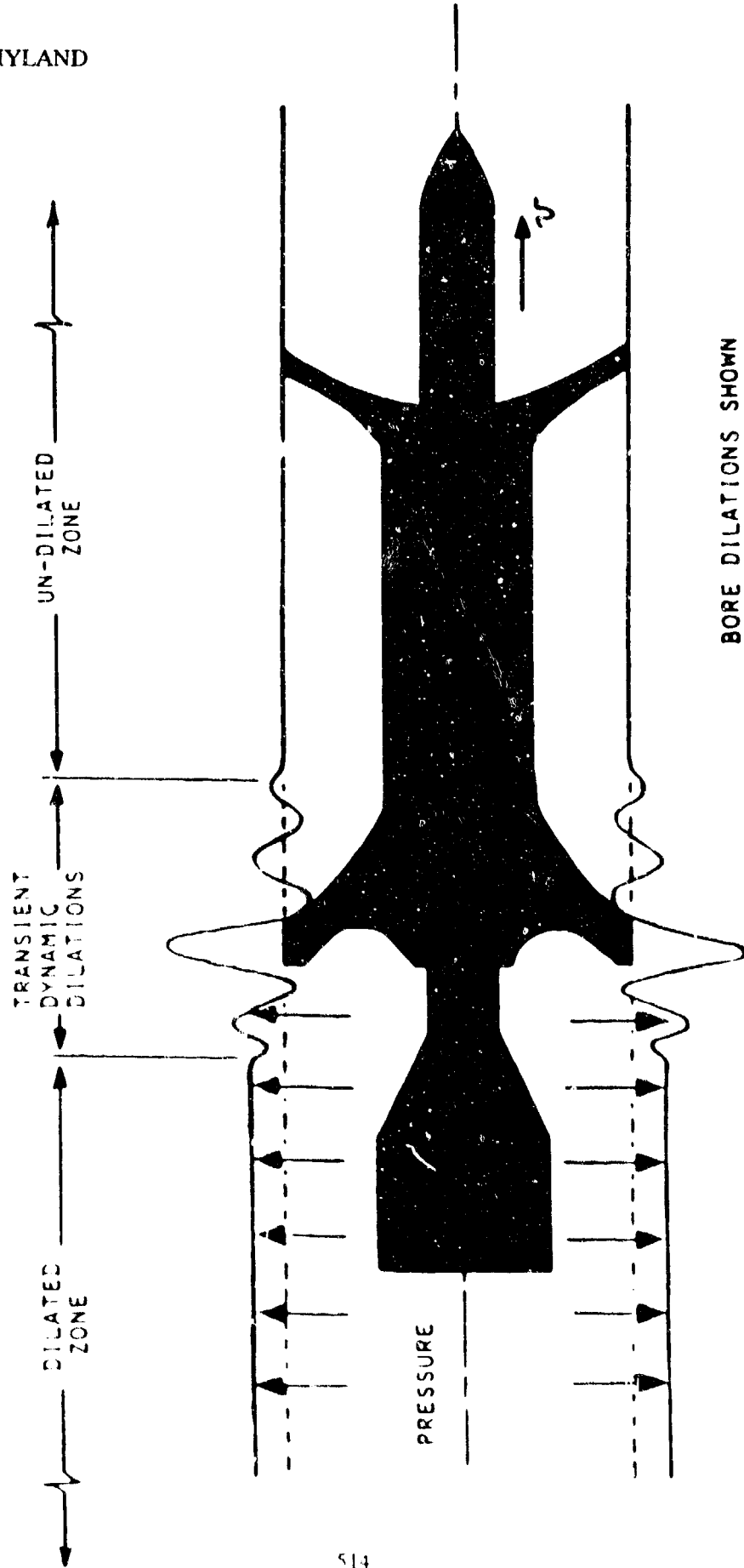
BORE DILATIONS SHOWN
EXAGGERATED FOR CLARITY

Figure 2. Dynamic tube wall dilation (high velocity firing).

REPRESENTATIVE STRAIN TRACE
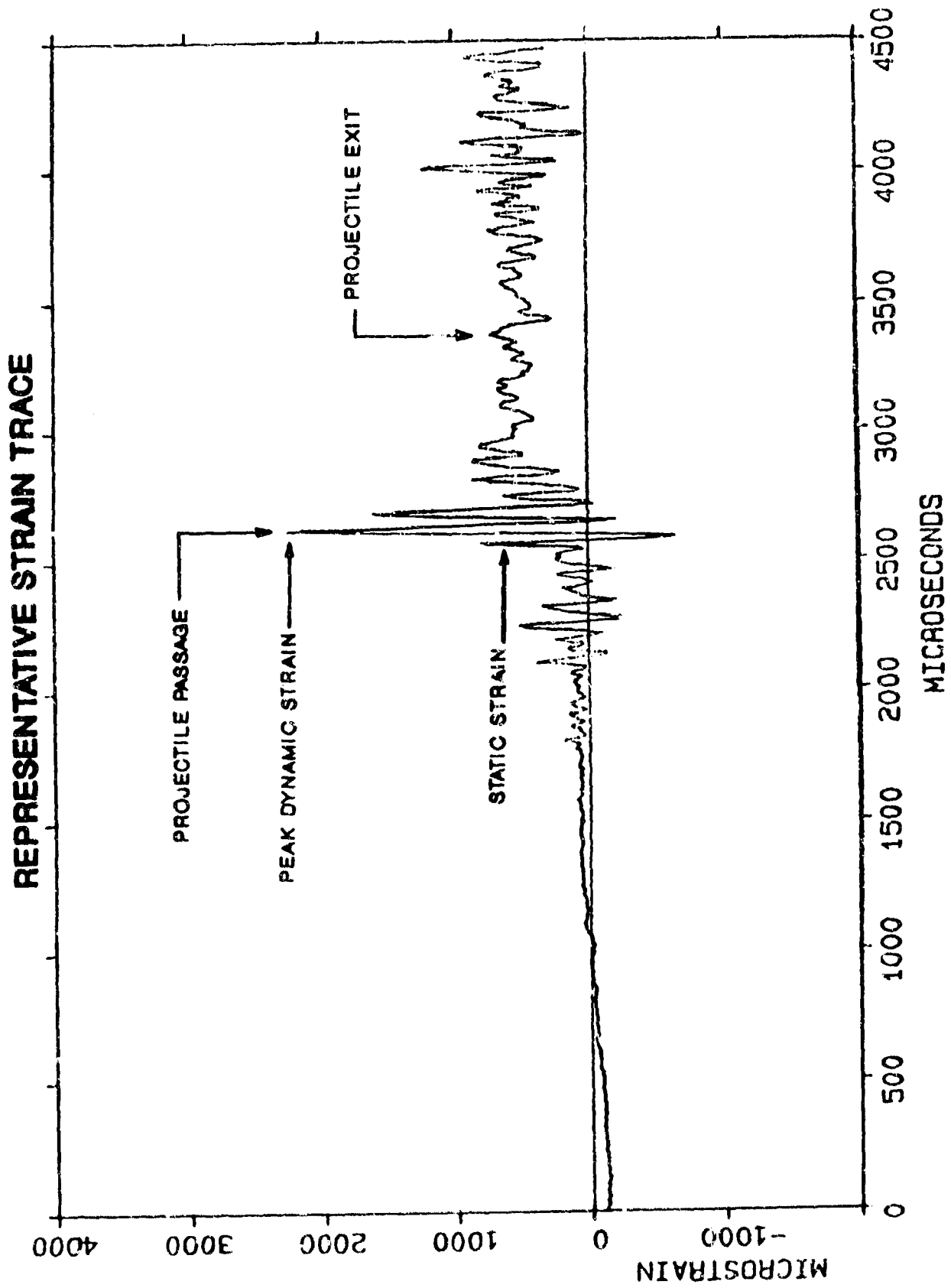
Figure 3. Representative dynamic strain trace (strain gage).

Figure 4. 120-mm XM25 tube tangential strains when firing the M865 TPCSDS-T cartridge conditioned to 21°C (static and dynamic) versus distance from RFT.

ALL-STEEL TUBE
@ OUTSIDE DIAMETER
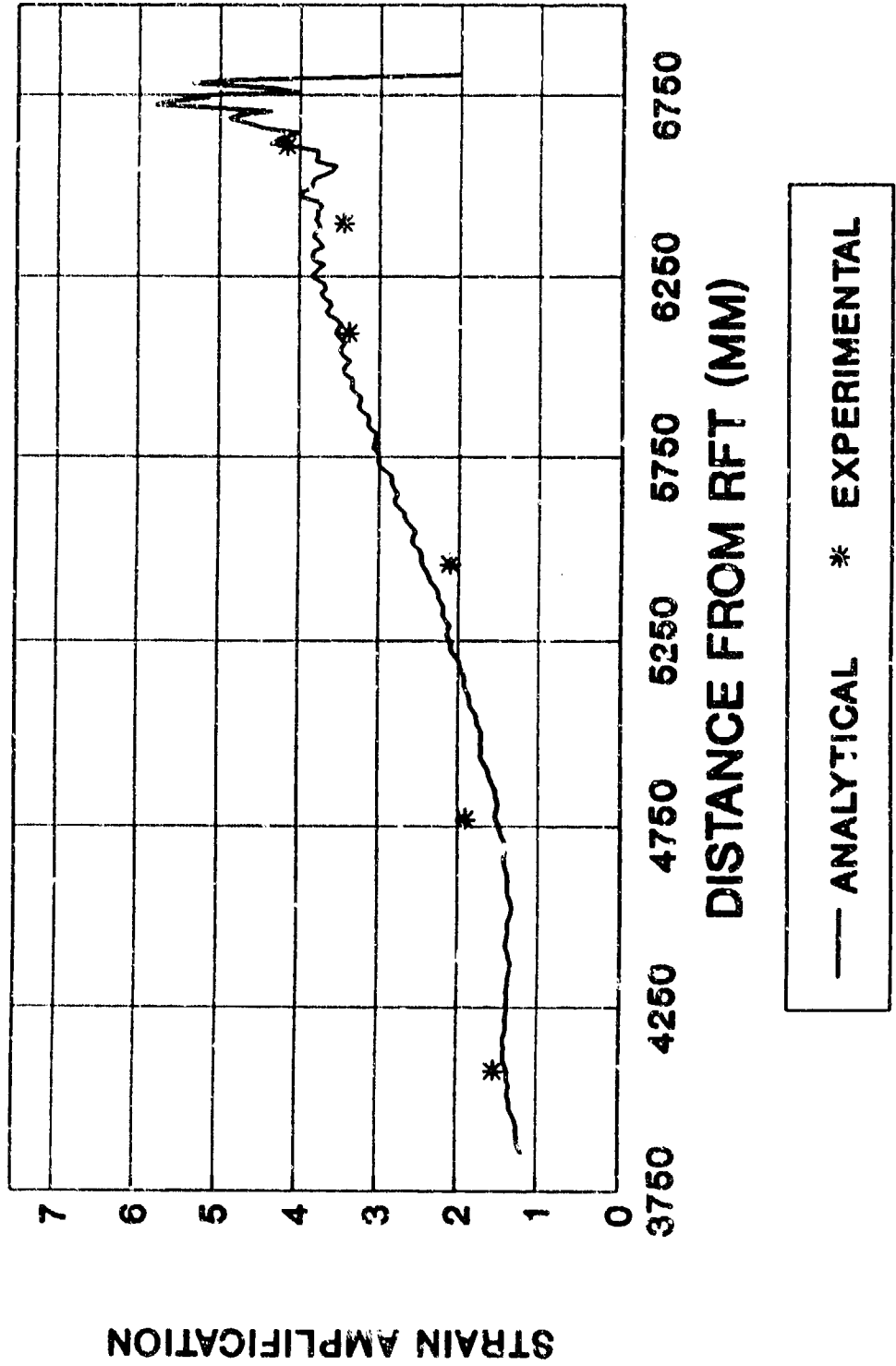
Figure 5. 120-mm XM25 tube strain amplifications when firing the M865 TPCSDS-T cartridge conditioned to 21°C (analytical and experimental) versus distance from RFT.

Figure 6. Comparison of diametral profiles of the 120-mm TT2 and M256 tubes.
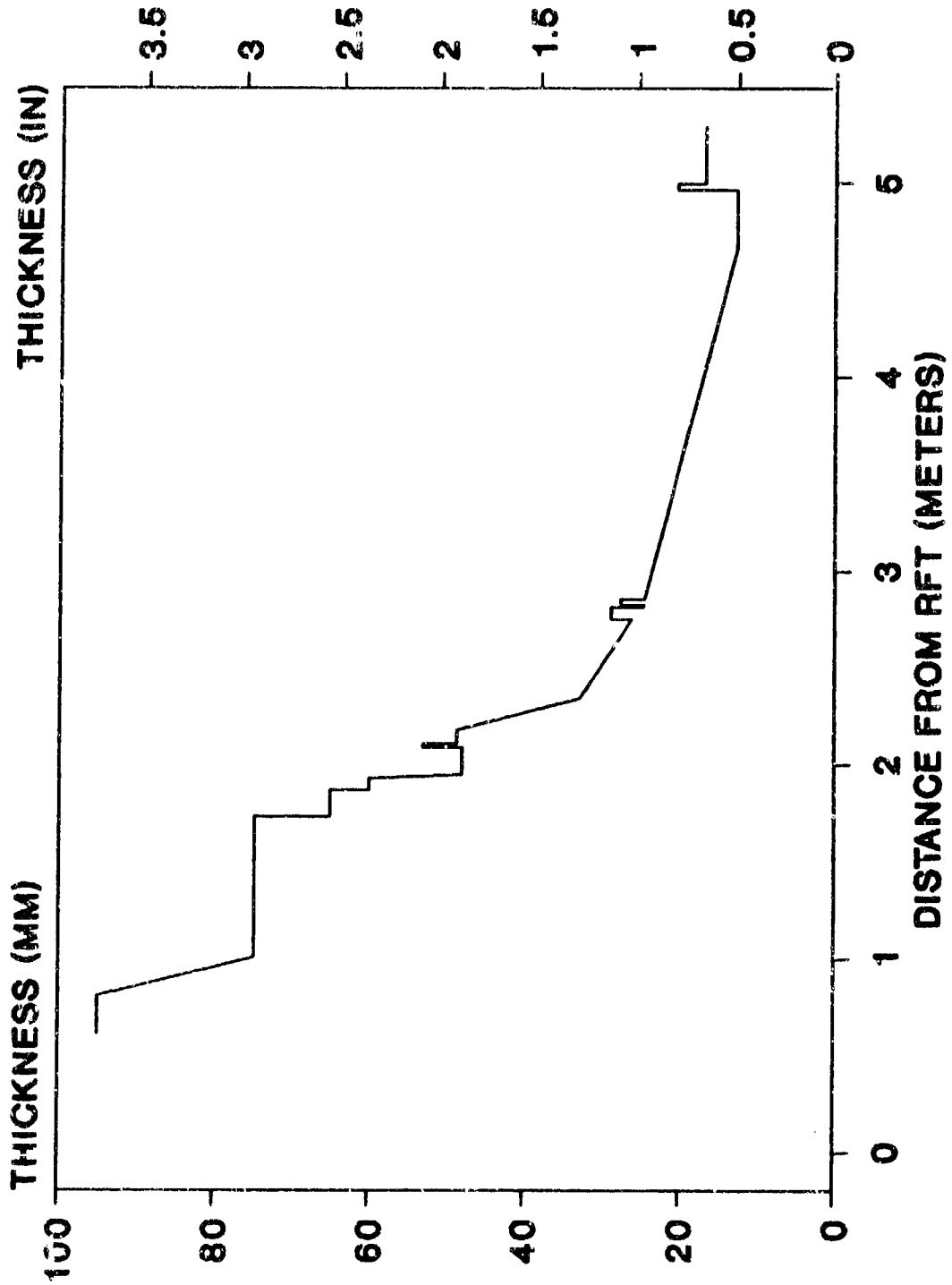
Figure 7. Wall thicknesses of 120-mm TT2 tube.
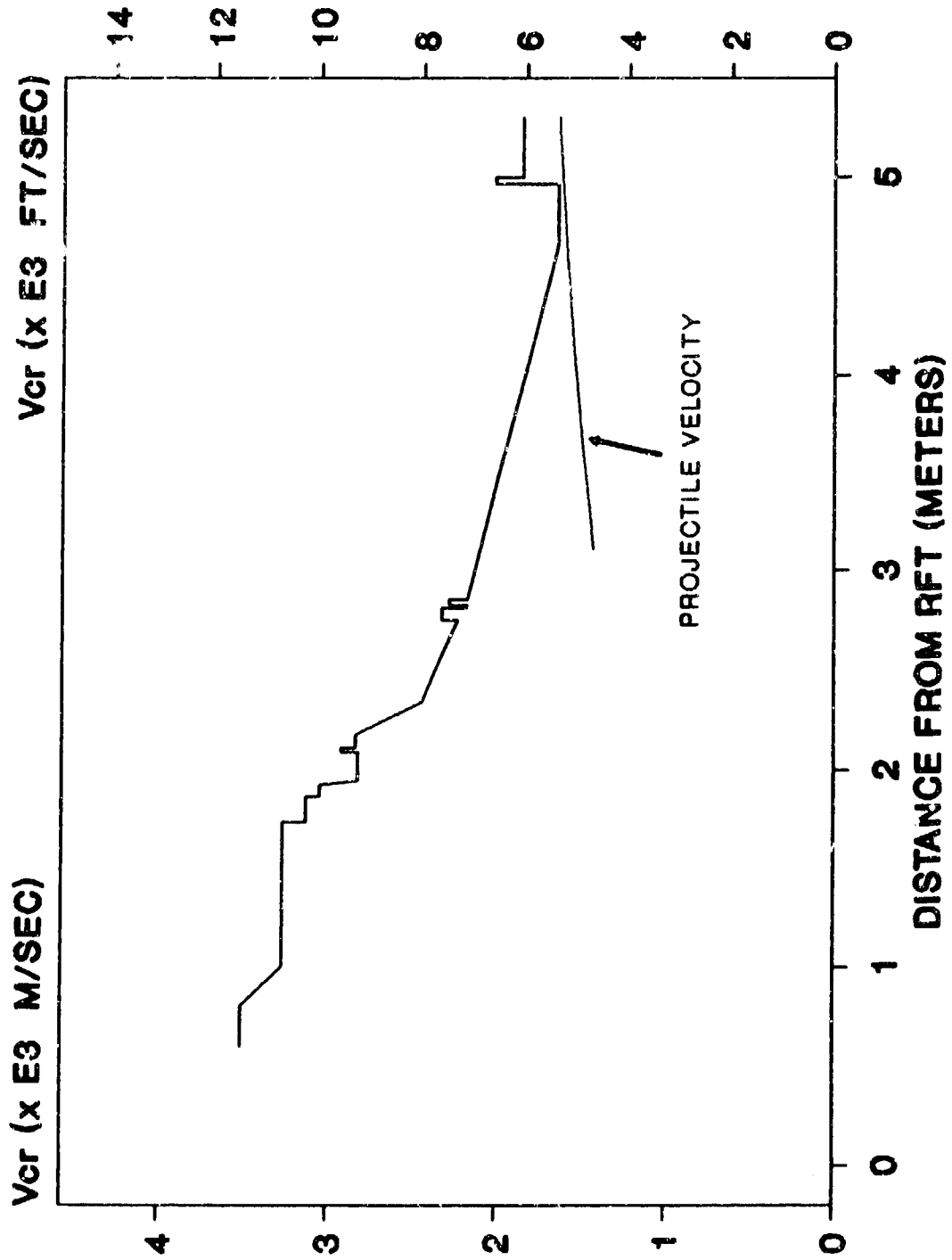
Figure 8. Estimated critical velocities of 120-mm TT2 tube and reference projectile velocity during test.
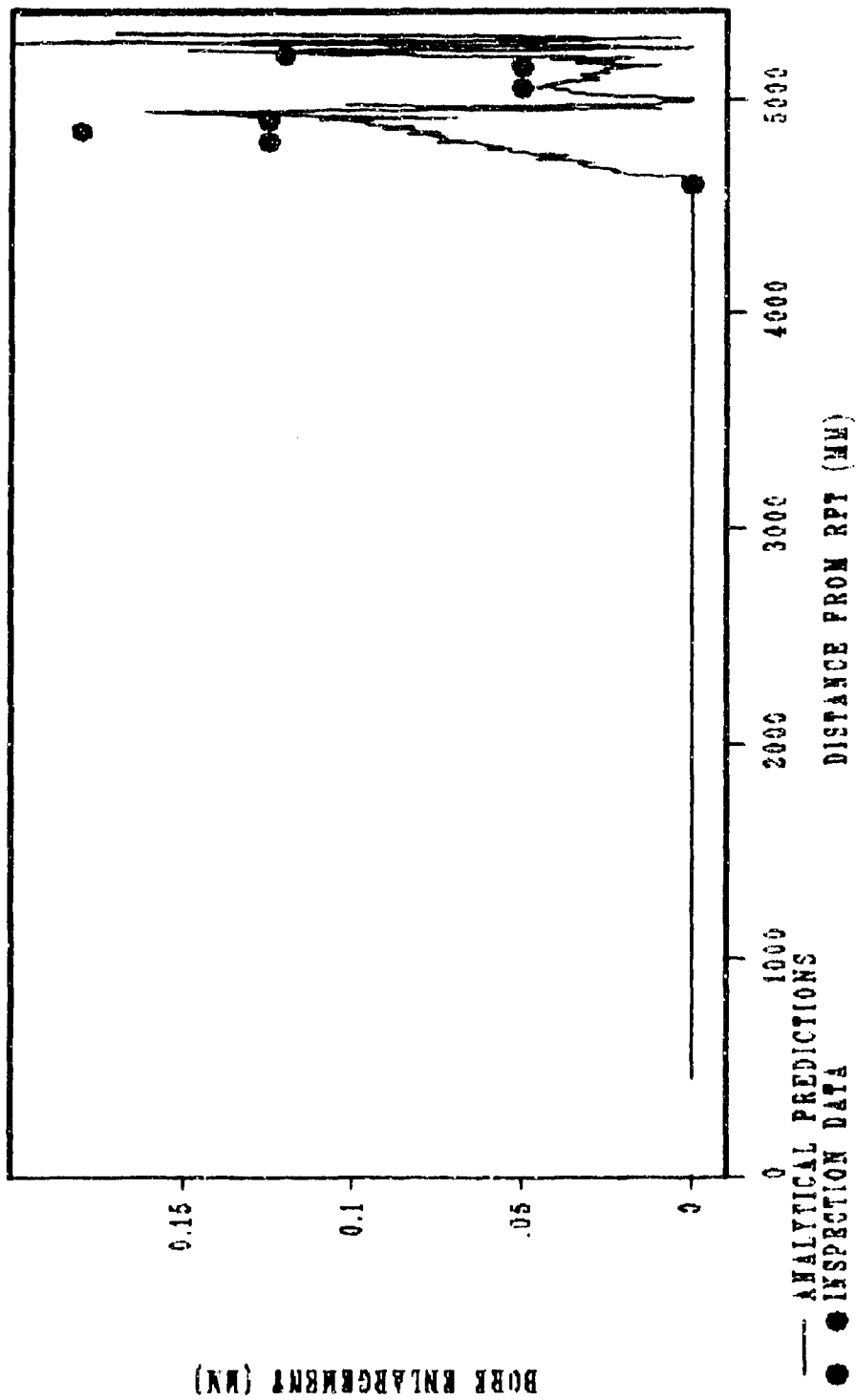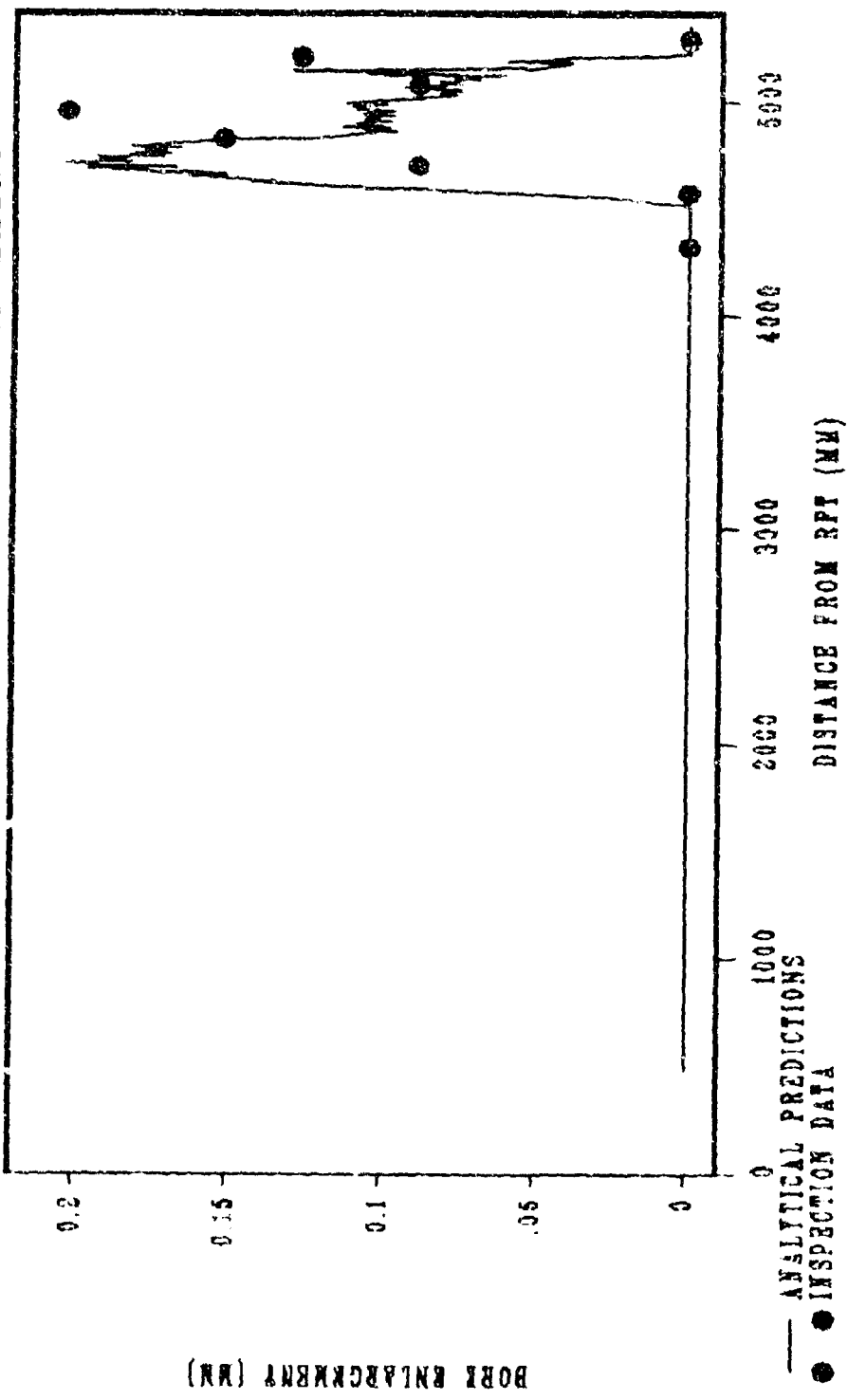
Figure 9. Permanent bore deformation due to firing 120-mm TT2 tube (analytical and experimental) versus distance from RFT.
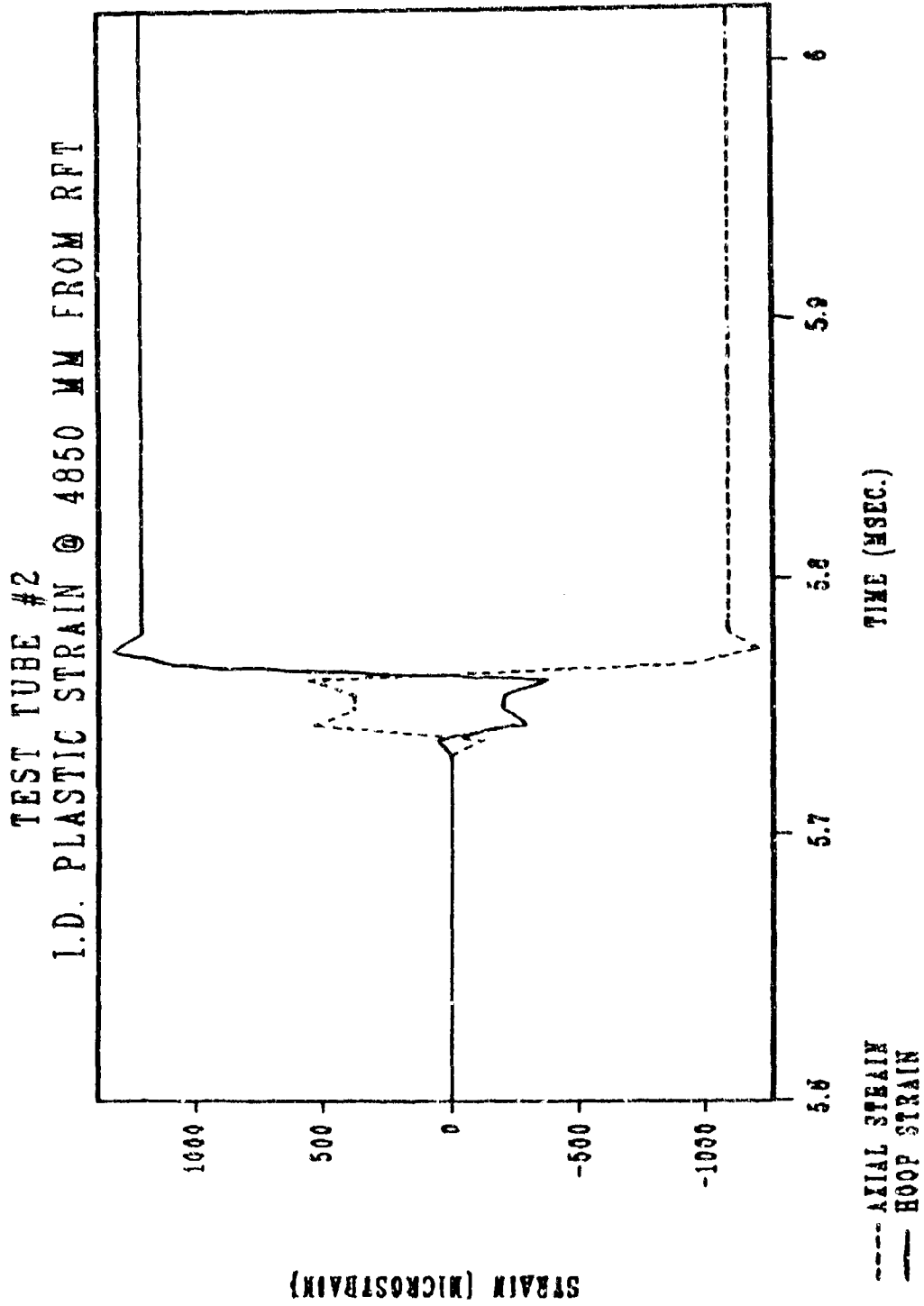
Figure 10. Plastic strains at the bore due to firing 120-mm TT2 tube (tangential and longitudinal) versus time.
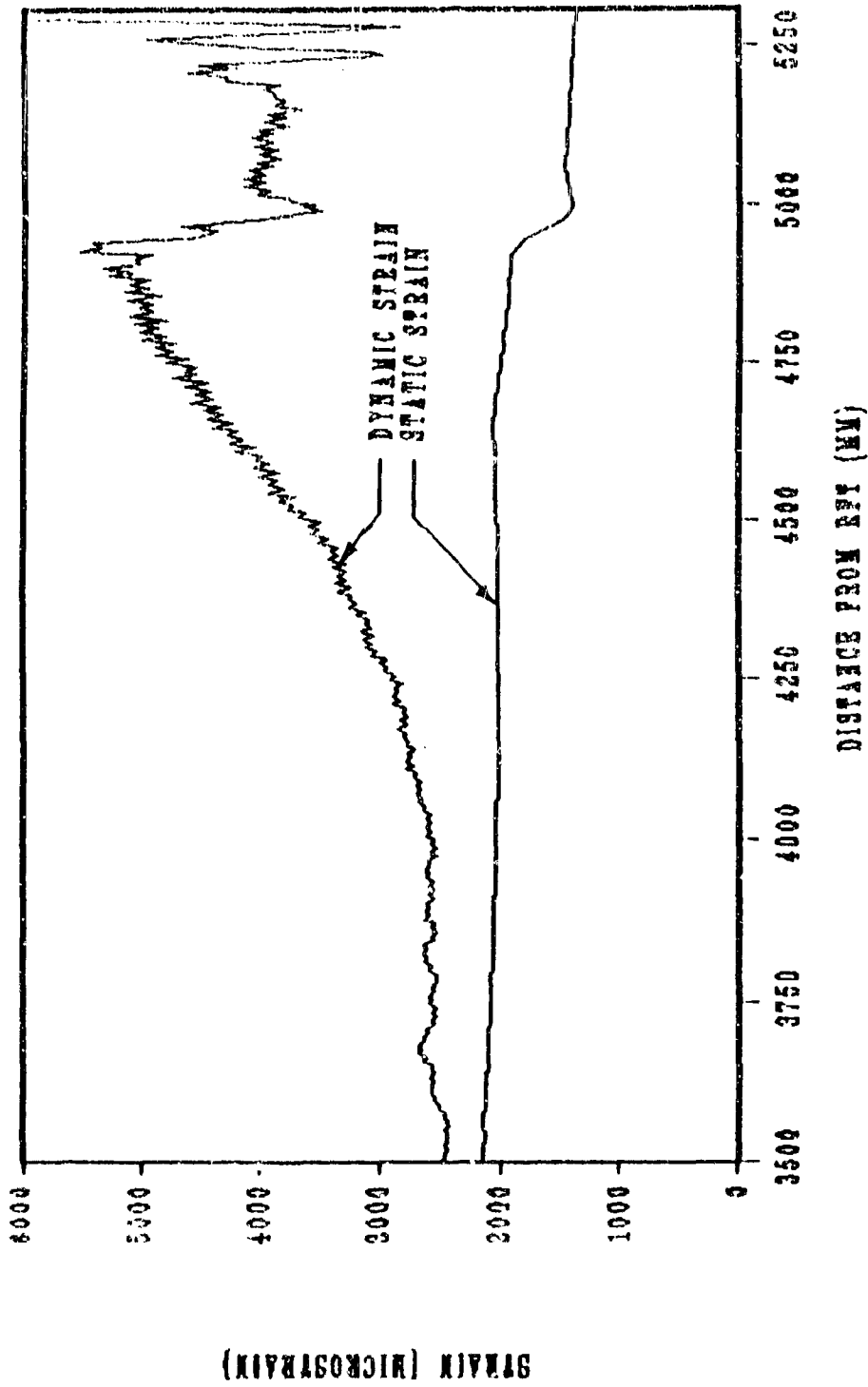
Figure 11. Tangential strain due to firing 120-mm TT2 tube at inside diameter (static and peak dynamic) versus distance from RFT
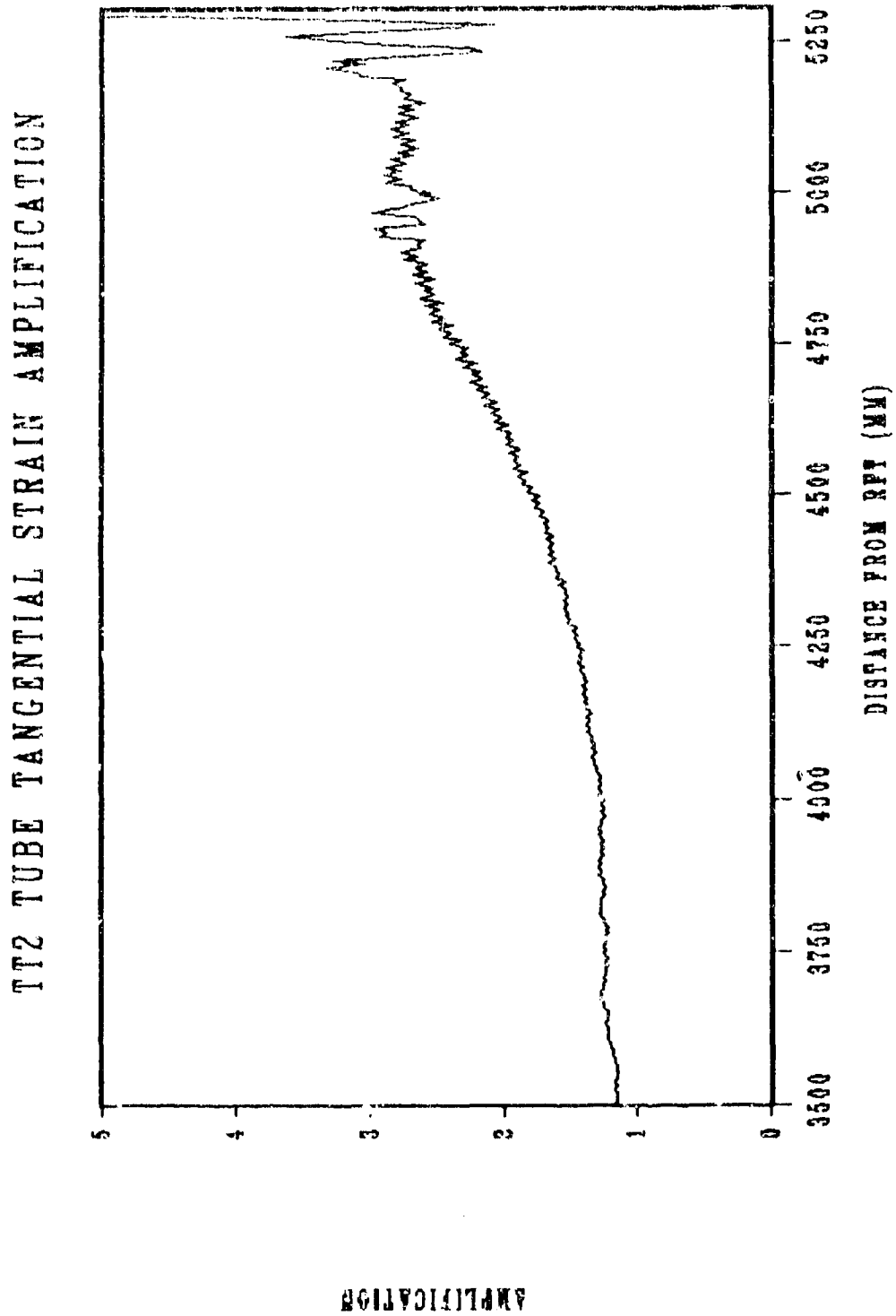
Figure 12. Tangential dynamic strain amplifications due to firing 120-mm TT2 tube versus distance from RFT.
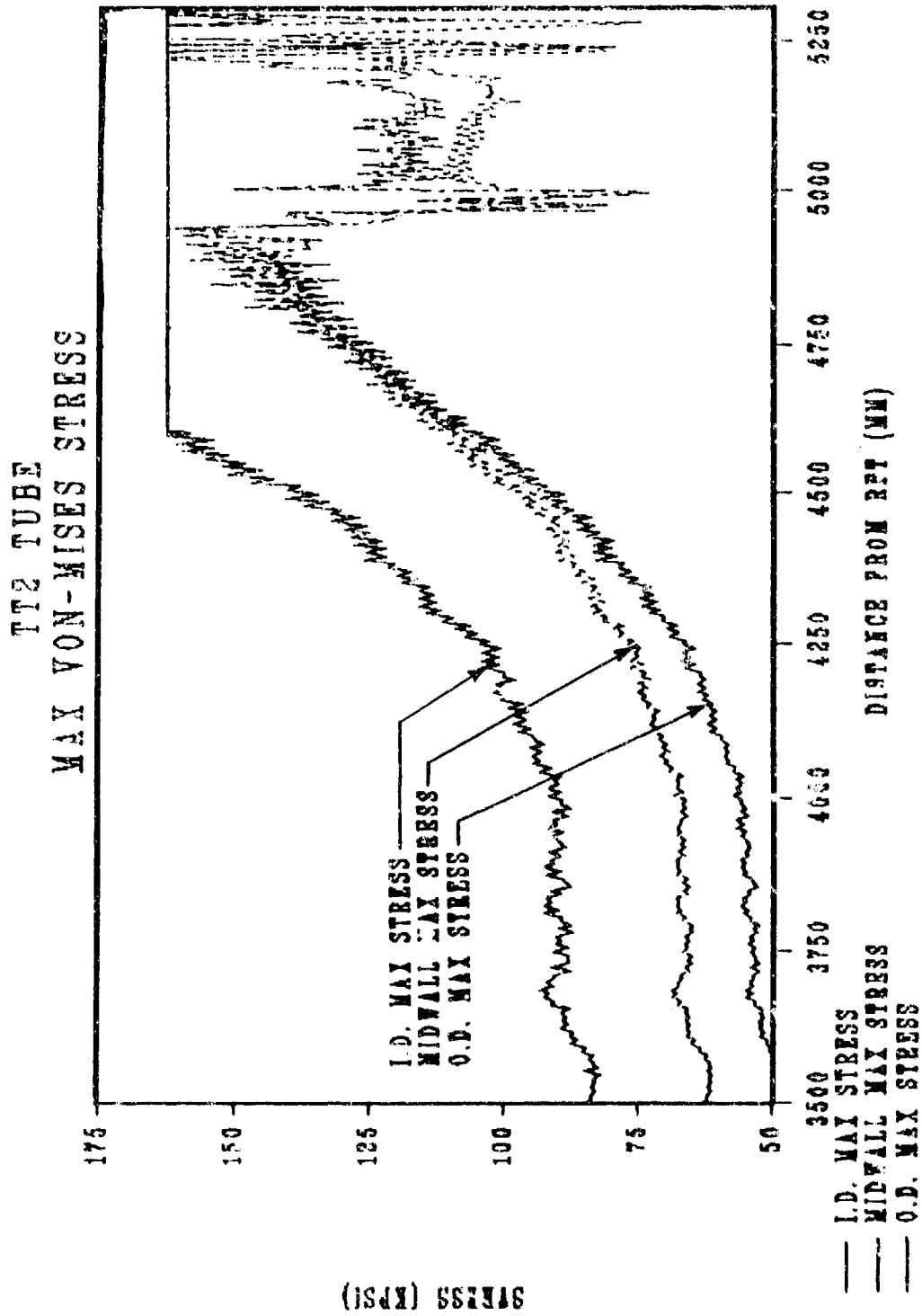
Figure 13. Peak von Mises' combined stresses due to firing 120-mm TT2 tube (inside, outside, and midwall) versus distance from RFT.

TUBE PROFILE COMPARISON
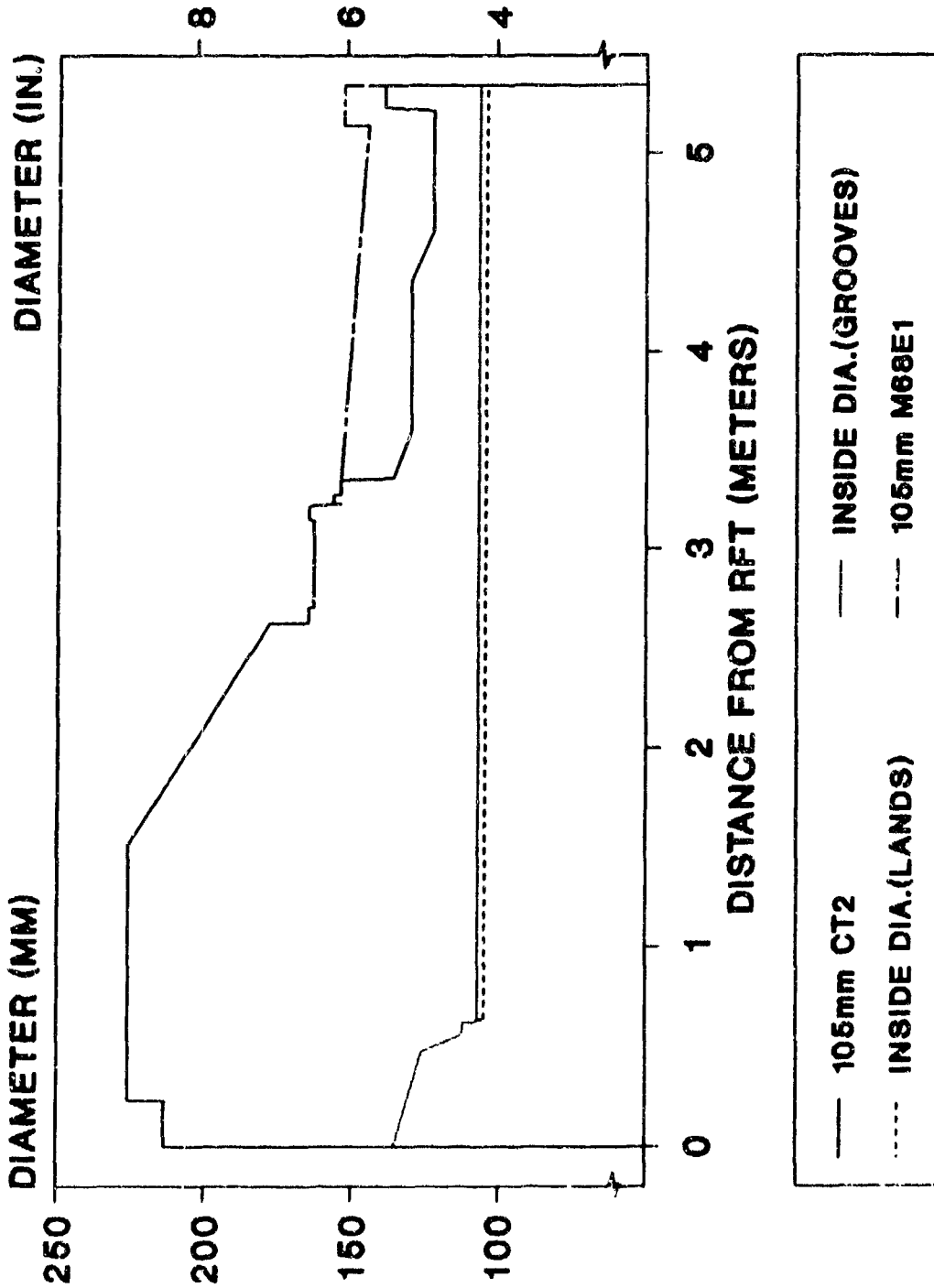
Figure 14. Comparison of diametral profiles of the 105-mm CT2 and M68E1 tubes.

CT2 WALL THICKNESS
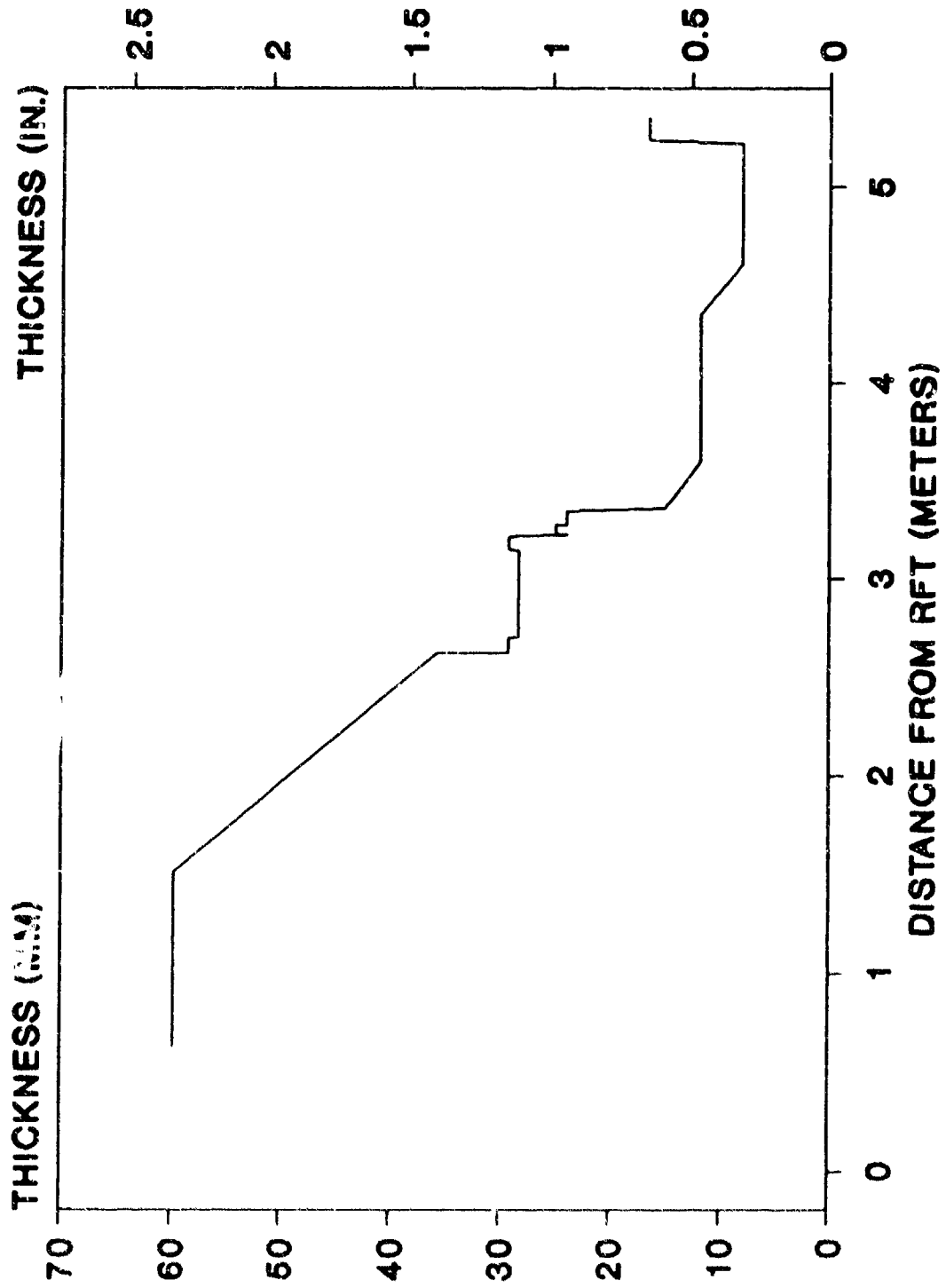
Figure 15. Wall thicknesses of 105-mm CT2 tube.
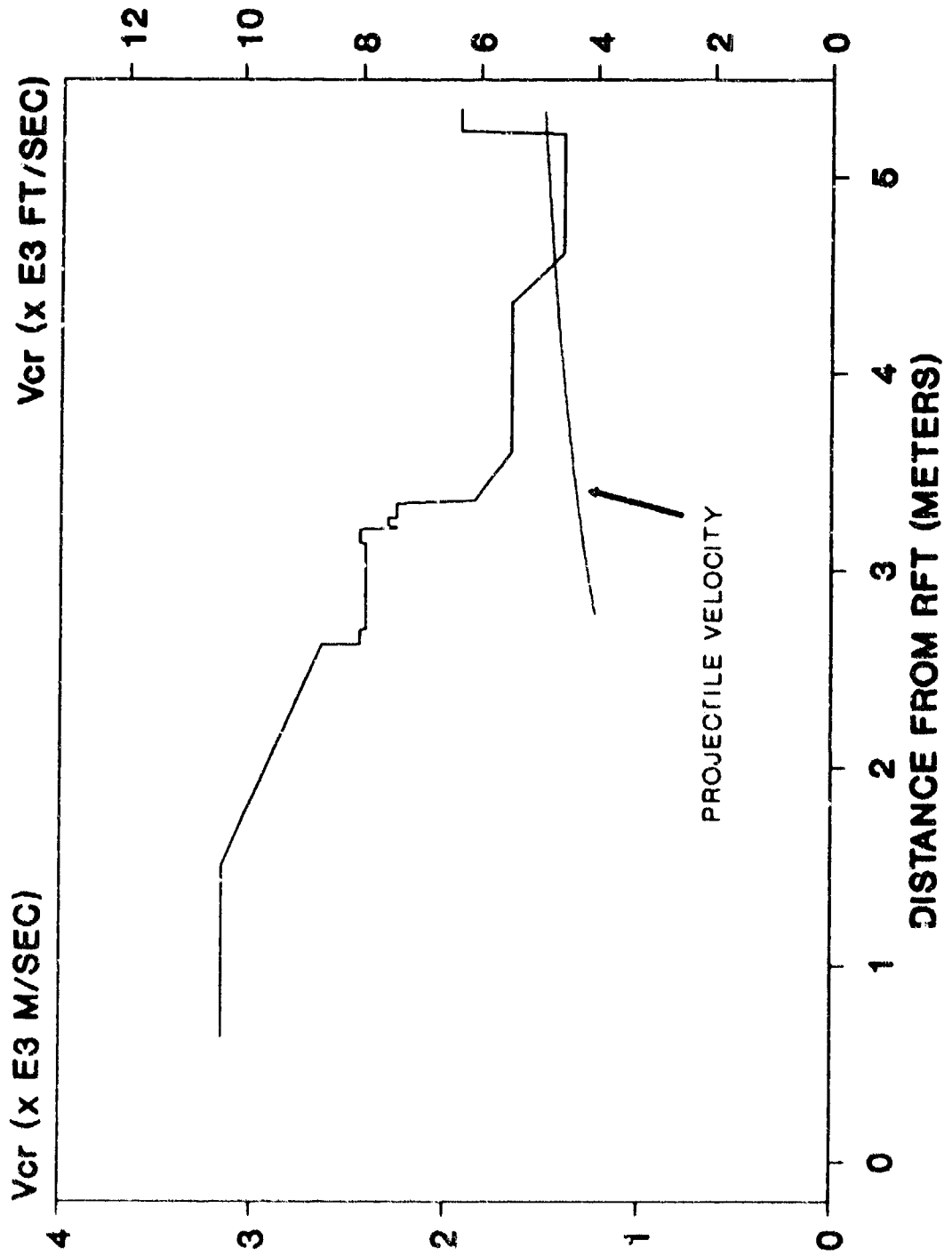
Figure 16. Estimated critical velocities of 105-mm CT2 tube and reference projectile velocity during test.

Figure 17. Permanent bore deformation due to firing 105-mm CT2 tube (analytical and experimental) versus distance from RFT.

TITLE: Beat Phenomena in Travelling Waves in Cylinders

Thomas E. Simkins
US Army Armament Research and Development Center
Close Combat Armaments Center
Benet Laboratories
Watervliet Arsenal
Watervliet, NY 12189

ABSTRACT:

The displacement response of a semi-infinite, thin-walled cylinder to a pressure moving at a constant velocity has been solved by Sing-chih Tang in closed form except for an integral term which Tang was forced to evaluate numerically. In this paper, an asymptotic evaluation of this integral is given which adds considerably to the physical interpretation of the solution. In brief, the asymptotic evaluation represents the long term propagation of transients in the cylinder and their interaction with the steady-state solution.

BIOGRAPHY: Thomas E. Simkins

PRESENT ASSIGNMENT: Research Mechanical Engineer, Benet Laboratories, Watervliet Arsenal, NY.

PAST EXPERIENCE: Began career with Benet Laboratories in 1963. General Chairman of six US Army Gun Dynamics Symposiums.

DEGREES HELD: B.S., Mechanical Engineering, Northeastern University (1961); M.Sc. (1963) and Ph.D. (1968), Department of Mechanics, Rensselaer Polytechnic Institute.

Nomenclature

$X = \sqrt{12}x/h$

$v_d^2 = E/(1 - \nu^2)\rho$

$V_p = v_p/v_d$

$W = w/h$

$q^2 = \frac{E}{12\kappa G}\left(\frac{h}{R}\right)^2$

$\Omega^2 = K^4 + \delta^2 q^2$

$T = \sqrt{12}v_d t/h$

$\delta^2 = (1 - \nu^2)\kappa G/E$

$\lambda_1^2 = \delta q/2$

$P = p/12\kappa G$

$G = \frac{E}{2(1+\nu)}$

$K = kh/\sqrt{12}$

E=Young's modulus

x=distance from tube entrance

h=tube wall thickness

w= midwall radial displacement

t=time

p=pressure

κ=shear correction factor

ν=Poisson's ratio

ρ=density

R=tube radius at midwall

v_p=pressure velocity

k= wave number

V_c=critical value of $V_p = \sqrt{2\delta q}$

$K_c = \sqrt{\delta q}$

Beat Phenomena in Travelling Waves in Cylinders

Thomas E. Simkins
Research Mechanical Engineer
Benet Laboratories
Watervliet Arsenal
Watervliet, NY 12189

1. Introduction and Background

The problem of a cylinder of infinite length subjected to a uniform pressure load moving at constant velocity has been studied by Jones and Bhuta (1964), Reismann (1965), and Tang (1965). These studies have resulted in steady-state solutions to the problem, employing somewhat different paradigms. In his publication, Tang also gave the solution to the initial value problem of a uniform pressure entering and travelling along a semi-infinite cylinder at a constant velocity. Dörr (1943) also studied this problem. Of the two, Tang's work will be referred to in the sequel. Tang's solution to this problem, however, includes an integral that he was only able to evaluate numerically making a qualitative interpretation of the result incomplete. The work herein makes use of the method of stationary phase to obtain an asymptotic evaluation of this integral from which significant additional information is obtained.

A synopsis of progress to date requires a brief review of the steady state solution and its physical interpretation. The physics involved can be represented by the simplest possible model of the problem. To this end, a thin-walled cylinder, extending to infinity in both directions, is first assumed. The cylinder is subjected to a uniform and axisymmetric steplike pressure moving at a constant velocity, V_p, in the axial direction as shown in figure 1.
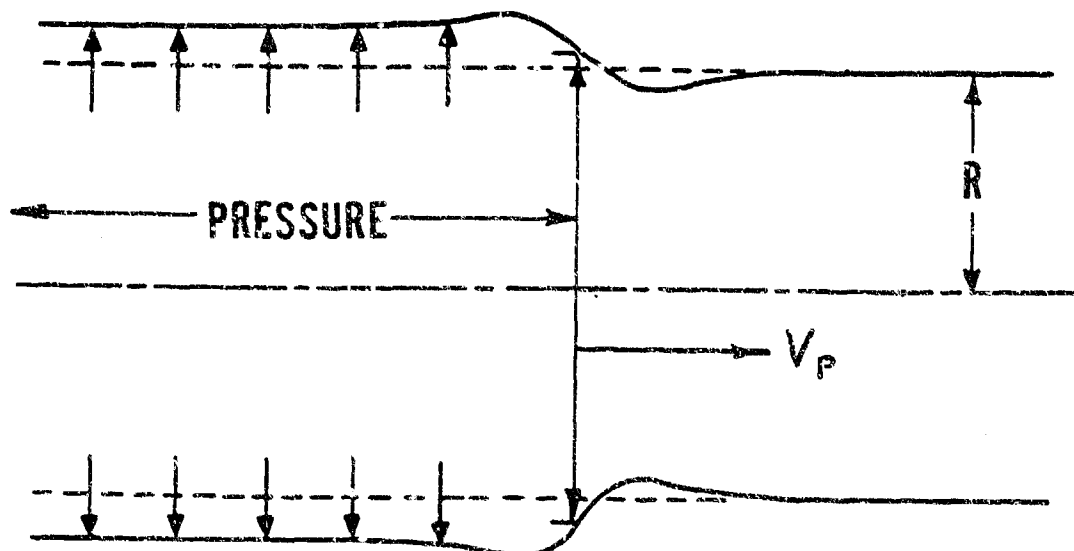

Figure 1 - Infinite Cylinder with Moving Pressure

SIMKINS

Using Tang's notation, the equation of motion under these conditions is:

$$\frac{\partial^4 W}{\partial X^4} + \delta^2 q^2 W + \frac{\partial^2 W}{\partial T^2} = \delta^2 P \left(1 - H(X - V_p T)\right) \tag{1}$$

$$-\infty < X < \infty \text{ and } T \geq 0$$

P is constant and represents the magnitude of the moving pressure. H is the Heaviside step function:

$$H(X - V_f T) = 0 \quad X \leq V_p T$$

$$= 1 \quad X > V_p T$$

The steady-state solution to this system has been given in the previously cited references. Letting V_c denote the lowest *critical velocity* of the moving pressure, Tang's results for this problem appear as follows:
For $V_p < V_c$:

$$W(X, T) = W_1(X - V_p T) \tag{2}$$

where

$$W_1(\eta) = \frac{P}{2q^2} \{2 - e^{m\eta}[\cos n\eta + \frac{n^2 - m^2}{2mn} \sin n\eta]\}; \quad \eta \leq 0$$

$$W_1(\eta) = \frac{P}{2q^2} \{e^{-m\eta}[\cos n\eta - \frac{n^2 - m^2}{2mn} \sin n\eta]\}; \quad \eta \geq 0$$

where $K = \pm n \pm im$ is a (complex) root of the equation:

$$K^4 - V_p^2 K^2 + \delta^2 q^2 = 0 \tag{3}$$

For $V_p > V_c$:

$$W(X, T) = W_0(X - V_p T) \tag{4}$$

where

$$W_0(\eta) = \frac{P}{q^2} - \frac{P\delta^2}{n_2^2(n_1^2 - n_2^2)} \cos n_2\eta; \quad \eta \leq 0$$

$$W_0(\eta) = -\frac{P\delta^2}{n_1^2(n_1^2 - n_2^2)} \cos n_1\eta; \quad \eta \geq 0$$

and where $K = \pm n_1, \pm n_2$ is a real root of Equation (3).

Eq. (3) is identical to the dispersion equation for freely propagating flexural waves if $V_{ph}(K)$ is substituted for V_p, where V_{ph} represents the *phase velocity* of a flexural wave having real wave number K. The *group velocity* of such a wave is then simply:

$$V_g(K) = K V_{ph}'(K) + V_{ph}(K); \quad Im(K) = 0 \tag{5}$$

As pointed out by Reismann (1965), a condition for resonance is established when $V_g(K) = V_{ph}(K) = V_p$. From Equation (5) this condition amounts to the vanishing of $V_{ph}'(K)$.

Setting V'_{ph} equal to zero gives a value $K_c = \sqrt{bq}$ such that $V_{ph}(K_c) = V_c = \sqrt{2bq}$, a critical velocity of the pressure load which will cause W_1 to become unbounded. While there are other critical pressure velocities, only the lowest, V_c, is available from this elementary model. The curves representing $V_g(K)$ and $V_{ph}(K)$ are shown in Figure 2.
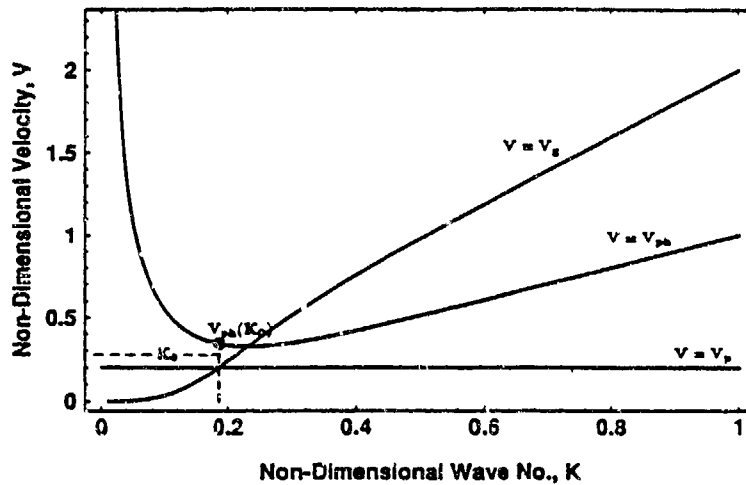

Figure 2 - Dispersion Characteristics of the Infinite Tube

Figures 3a and 3b show the radial displacement, W_1, in the neighborhood of the moving pressure front when $V_p = .85V_c$ and $V_p = .985V_c$ respectively. The plots have been normalized with respect to P/q^2, the deformation caused by a static application of P throughout the entire cylinder. The abcissa represents the non-dimensional distance measured from the pressure front. The figures exemplify the displacement amplification which occurs as V_p approaches V_c. Figure 4 summarizes this amplification as a function of the pressure velocity, V_p, and somewhat resembles that derived from the harmonic excitation of a single degree of freedom system in which the abcissa is the forcing frequency. Thus one is tempted to draw at least a loose analogy between the two problems.
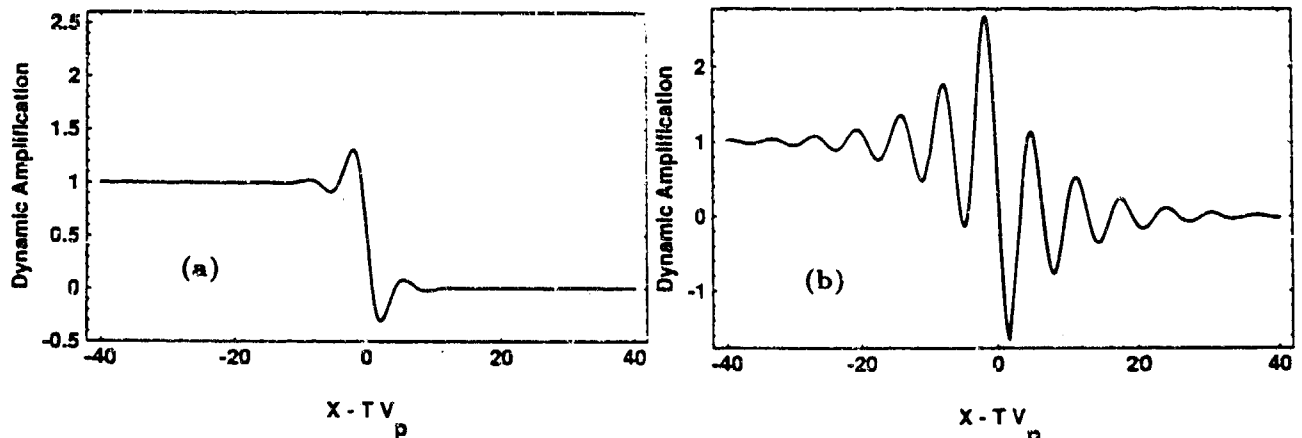
Figure 3 - Radial Displacement at Pressure Front
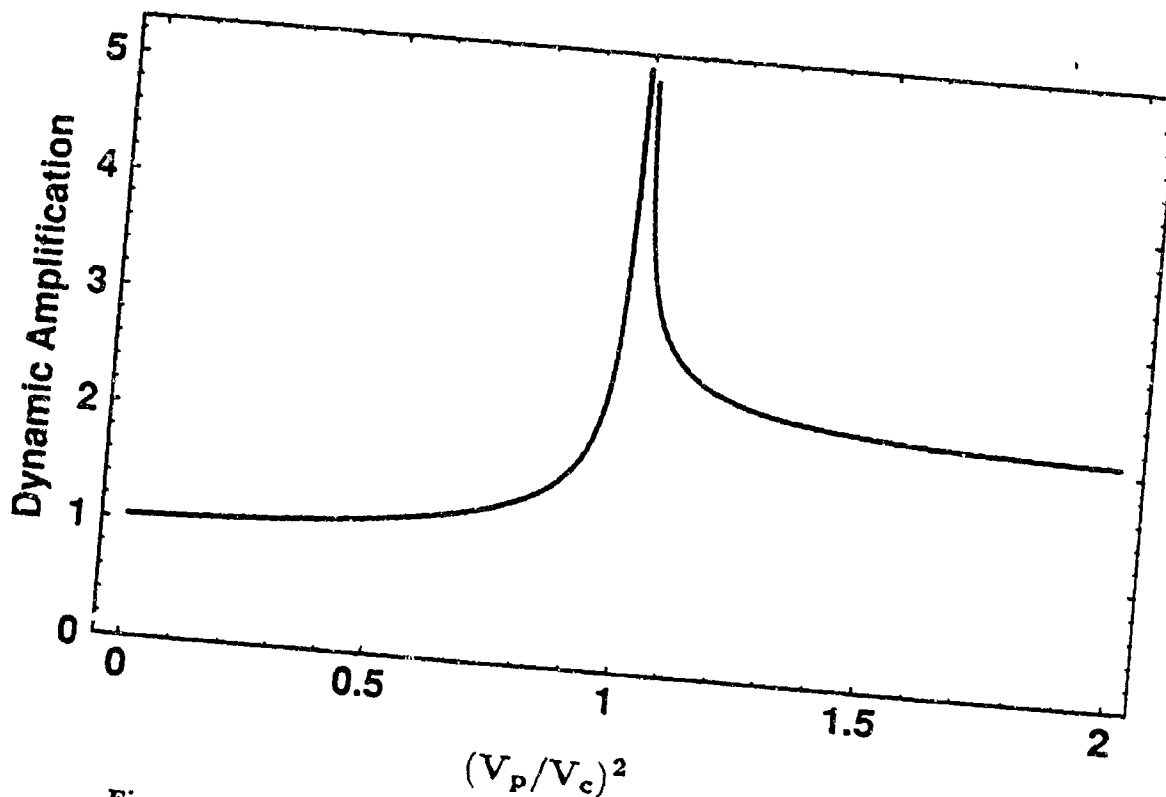**(a) $V_p = .85V_c$, (b) $V_p = .985V_c$**

Figure 4 - Effect of Pressure Velocity on Maximum Radial Displacement

2. Semi-infinite Cylinder - the Initial Value Problem

Once again the governing differential equation is taken to be (1). In treating this problem, Tang chose zero values for the initial velocity and displacement. Diaphragm end conditions were chosen at $X = 0$ and the displacement was required to be bounded as $X \to \infty$. Tang found that when $V_p < V_c$, the radial displacement of the tube wall in response to a moving pressure entering the tube at $X = 0$ at constant velocity, V_p, to be:

$$W(X,T) = W_1(X - V_p T) + W_2(X + V_p T) + W_3(\lambda_1 X) + I(X,T)$$

where $W_1(\eta)$ is as defined in the previous section and

$$(6)$$

$$W_2(\eta) = \frac{P}{2q^2} e^{-m\eta}(\cos n\eta - \frac{n^2 - m^2}{2mn} \sin n\eta)$$

$$W_3(\eta) = -\frac{P}{q^2} e^{-\eta} \cos \eta$$

and

$$I(X,T) = \frac{-2\delta^2 P}{\pi} \int_0^\infty (\frac{i}{\Omega^2} - \frac{1}{\Omega^2 - V^2 K^2}) \frac{\cos \Omega T \sin KX}{K} dK$$

$$\Omega^2 = K^4 + \delta^2 q^2$$

535

Physically it can be expected that the pressure, which enters the tube at velocity V_p, will excite a strong transient as it suddenly expands the tube at the entrance, $X = 0$. However, even without damping, dispersion can be expected to attenuate the effect of this transient deformation as it travels sufficiently far into the tube at which time the deformation near the pressure front should appear very much like the steady state solution $W_1(X - V_pT)$, given in the previous section. This expectation is supported by the explicit appearance of W_1 in the displacement expression (6). Except for $W_1(X - V_pT)$ and $I(X,T)$, the remaining terms in Eq.(6) are needed to satisfy the diaphragm boundary condition and have negligible effects at sufficiently large X. This restriction on X depends on the difference between V_p and V_c. i.e., X must increase as $V_p \rightarrow V_c$ if the same level of approximation is to be maintained. The deformation near the pressure front, $X = V_pT$, is of particular interest.

As noted by Tang, all of the terms in Equation (6) except $I(X,T)$ can be interpreted as steady-state solutions to particular loadings of the infinite cylinder. It follows that any transient effects are contained in $I(X,T)$. This term is analogous to that which appears in the solution to the harmonically forced oscillator and, in keeping with this analogy, can be thought of as a *transition* or *start-up* transient . Thus (at sufficiently large X) the two main terms in the solution in regions of the tube not too close to the entrance, especially in the neighborhood of the pressure front, are the steady-state solution corresponding to a moving pressure in an infinite tube and the transition term, $I(X,T)$.

Pursuing the analogy of the harmonically forced oscillator, where the 'start-up' transient results in the formation of *beats* (a harmonic modulation of the steady-state response) which become more and more apparent as the natural and forcing frequencies approach each other, it might be expected that a similar effect occurs for the case at hand.

3. Asymptotic Expansion of $I(X,T)$

Substituting

$$\cos \Omega T \sin KX = \frac{1}{2} Im\{ e^{i(KX+\Omega T)} + e^{i(KX-\Omega T)} \}$$

gives:

$$I(X,T) = \frac{-2\delta^2 P}{\pi} \int_0^\infty F(K) \cos \Omega T \sin KX \, dK$$

$$= -\frac{\delta^2 P}{\pi} Im\{ \int_0^\infty F(K) e^{ih_1(K)T} \, dK + \int_0^\infty F(K) e^{ih_2(K)T} \, dK \} \tag{7}$$

where

$$F(K) = \frac{1}{K} \{ \frac{1}{\Omega^2} - \frac{1}{\Omega^2 - V^2 K^2} \}$$

and

$$h_1(K) = \frac{KX}{T} + \Omega(K); \quad h_2(K) = \frac{KX}{T} - \Omega(K)$$

Using the method of stationary phase as described by Whittam (1974), the first term of an asymptotic expansion of (7) can be obtained. The contribution from the first integral of (7) is negligible since $h_1(K)$ has no stationary point in the region $K > 0$. The major contribution from the second integral is from the neighborhood of $K = K_0$ where K_0 is the value of K such that $h_2(K)$ is stationary, i.e.:

$$h_2'(K_0) = \frac{X}{T} - \Omega'(K_0) = 0$$

or

$$\Omega'(K_0) = \frac{X}{T} \tag{8}$$

It is noted that $\Omega'(K_0)$ is simply the group velocity associated with the wave number K_0.

The stationary phase result for the second integral of (7) can then be written:

$$-\frac{\delta^2 P}{\pi} Im \int_0^\infty F(K) e^{i(\frac{K_0}{?}X - \Omega(K))T} dK$$

$$= -\frac{\delta^2 P}{?} Im\left\{ F(K_0)\sqrt{\frac{2\pi}{T|\Omega'(K_0)|}} e^{-i\Omega(K_0)T + iK_0 X - \frac{i\pi}{4}sgn\ \Omega''(K_0)} \right\}$$

$$= F(K_0)\delta^2 P \sqrt{\frac{2}{\pi T|\Omega'(K_0)|}} \sin[\Omega(K_0)T - K_0 X + \frac{\pi}{4}sgn\ \Omega''(K_0)]$$

From the expression for Ω^2:

$$\Omega''(K_0) = \frac{2K_0^2}{\Omega(\ )}[\Omega^2(K_0)\ 2q^2\delta^2] > 0$$

Thus the asymptotic evaluation for (X, T)

$$F(K_0)\delta^2 \sqrt{\frac{2}{\pi T(K_0)}} \sin[\Omega(\ )T - K_0 X + \frac{\pi}{4}] \tag{9}$$

4. Interpretation of Results

The stationary phase result states that the dominant part of the transient disturbance initiated at $(X = T = 0)$ that arrives at a particular location X at time will have travelled with a group velocity X/T and will consist of the dominant wave number K_0 determined from Equation (7). If the motion at a fixed value of X is observed, where X is large enough for Eq. (9) to be satisfied and $W_2 + W_3$ to be ignored, the displacement will consist of the steady-state terms, $(X - V_p T)$ having frequency nV_p and $I(X, T)$ oscillating with frequency $\Omega(K_0)$. Referring again to Figure K_0 is the wave number of a freely propagating wave (excited at $= 0$ by the sudden entrance of the pressure front) having Vp as its group velocity. The figure also shows that the phase velocity of this free wave, $V(K_0)$ is greater than V_p. The beat frequency observed at fixed X is u $(n)_p$ $\Omega(K_0))$.

Moving along with the moving pressure front, $X = V_p t$ Eq. (9) can be written:

$$I(X, T) = F(K_0)\delta^2 P \sqrt{\frac{1}{\pi T \Omega'}}\ \overline{K_0}\ \{\cos \beta T + \sin \beta T\} \tag{10}$$

where

$$\beta = \Omega(K_0) - K_0 V_p$$

Thus, for large T such that (9) is valid and $W_2 + W_3$ can be ignored, the radial displacement response (6) at the pressure wave essentially consist of a harmonic modulation of the steady-state response function $(X - V_p T)$ decreasing amplitude as $\sqrt{T}$. It is noted that β vanishes as $V_p \to V_c$.

Figure 5 shows this displacement at several closely spaced stations along the tube at successive times the case $V_p/V = .018$.
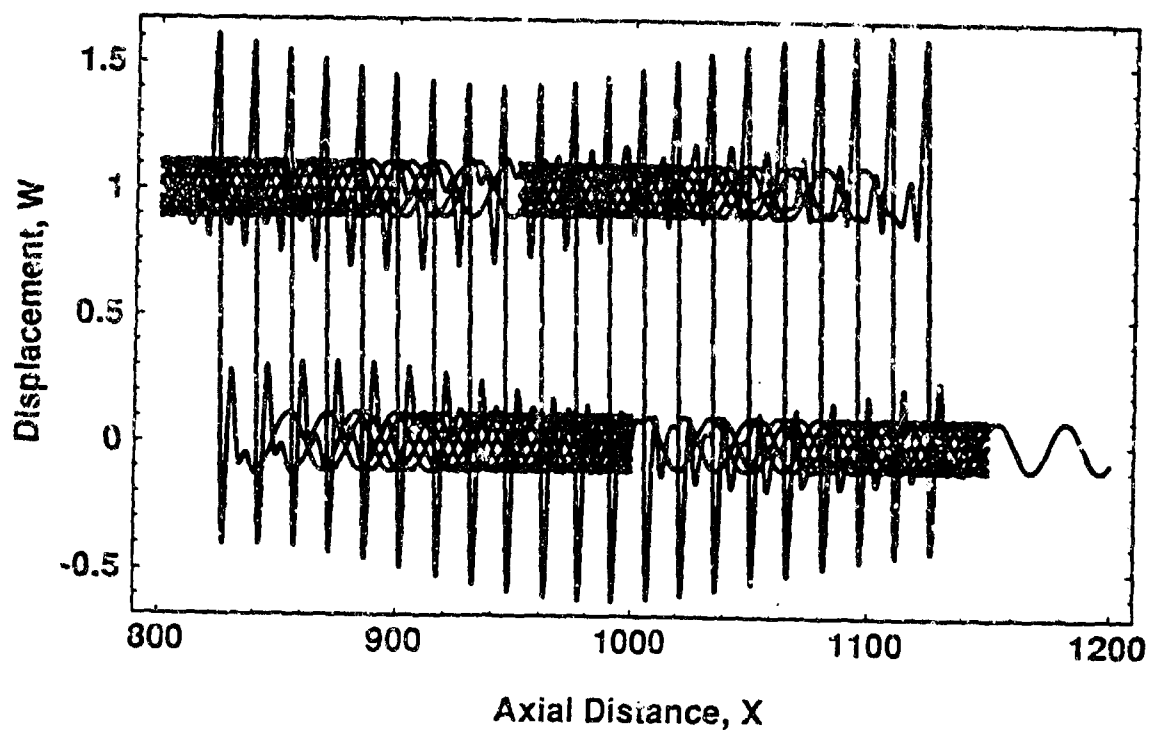
Figure 5 - Successive Radial Displacements Along Tube

From figure 5 a *beat wavelength* can be observed - the distance, λ, along the cylinder corresponding to one period of the modulation. Substituting $T = X/V_p$ in Eq. (10):

$$\lambda = \frac{2\pi}{\left[\frac{\Omega(K_0)}{V_p} - K_0\right]} \tag{11}$$

λ h. engineering significance in that it represents the distance between strain maxima along the tube. The net effect of the transient is thus to periodically raise the strain levels in the tube to values greater than those predicted by the steady-state theory alone.

References

Dörr, J. 1943 *Injenieur-Archiv*, volume 14, 1943, 167-192. Der unenlichen federnd gebetteten Balken unter dem Einfluss einer gleichförmig bewegten Last.

Jones, J.P., and Bhuta, P.G., 1964 *Journal of Applied Mechanics* 86, Trans. ASME, 31, 105 - 111. Response of Cylindrical Shells to Moving Load.

Reismann, H., 1965 *Solid Mechanics* volume 2, part 2, S. Ostrach and R. H. Scanlon, Oxford, Pergamon Press, 349-363. Response of a Pre-stressed Cylindrical Shell to Moving Pressure Load.

Tang, S., 1965 *Journal of the Engineering Mechanics Division*, Proceedings of the ASME, Vol 91, No. EM 5, October, 1965, 97 - 121. Dynamic Response of a Tube Under Moving Pressure.

Whittam, G. B., 1974 *Linear and Nonlinear Waves*, Wiley & Sons, 371 - 374.

ALPHABETICAL INDEX OF AUTHORS

TECHNICAL REPORT INTERNAL DISTRIBUTION LIST

NOTE: PLEASE NOTIFY DIRECTOR, BENET LABORATORIES, ATTN: SMCAR-CCB-TL, OF ANY ADDRESS CHANGES.

TECHNICAL REPORT EXTERNAL DISTRIBUTION LIST

	NO. OF COPIES		NO. OF COPIES
ASST SEC OF THE ARMY RESEARCH AND DEVELOPMENT ATTN: DEPT FOR SCI AND TECH THE PENTAGON WASHINGTON, D.C. 20310-0103	1	COMMANDER ROCK ISLAND ARSENAL ATTN: SMCRI-ENM ROCK ISLAND, IL 61299-5000	1
ADMINISTRATOR DEFENSE TECHNICAL INFO CENTER ATTN: DTIC-FDAC CAMERON STATION ALEXANDRIA, VA 22304-6145	12	MIAC/CINDAS PURDUE UNIVERSITY P.O. BOX 2634 WEST LAFAYETTE, IN 47906	1

COMMANDER
US ARMY ARDEC

ATTN: SMCAR-AEE	1
SMCAR-AES, BLDG. 321	1
SMCAR-AET-O, BLDG. 351N	1
SMCAR-CC	1
SMCAR-CCP-A	1
SMCAR-FSA	1
SMCAR-FSM-E	1
SMCAR-FSS-D, BLDG. 94	1
SMCAR-IMI-I (STINFO) BLDG. 59	2

PICATINNY ARSENAL, NJ 07806-5000

COMMANDER
US ARMY TANK-AUTMV R&D COMMAND
ATTN: AMSTA-DDL (TECH LIB)   1
WARREN, MI 48397-5000

COMMANDER
US MILITARY ACADEMY   1
ATTN: DEPARTMENT OF MECHANICS
WEST POINT, NY 10996-1792

US ARMY MISSILE COMMAND
REDSTONE SCIENTIFIC INFO CTR   2
ATTN: DOCUMENTS SECT, BLDG. 4484
REDSTONE ARSENAL, AL 35898-5241

DIRECTOR
US ARMY BALLISTIC RESEARCH LABORATORY
ATTN: SLCBR-DD-T, BLDG. 305   1
ABERDEEN PROVING GROUND, MD 21005-5066

COMMANDER
US ARMY FGN SCIENCE AND TECH CTR
ATTN: DRXST-SD   1
220 7TH STREET, N.E.
CHARLOTTESVILLE, VA 22901

DIRECTOR
US ARMY MATERIEL SYSTEMS ANALYSIS ACTV
ATTN: AMXSY-MP   1
ABERDEEN PROVING GROUND, MD 21005-5071

COMMANDER
US ARMY LABCOM
MATERIALS TECHNOLOGY LAB
ATTN: SLCMT-IML (TECH LIB)   2
WATERTOWN, MA 02172-0001

DIRECTOR
US ARMY RESEARCH LABORATORY
ATTN: AMSRL-WT-PD (DR. B. BURNS)   1
ABERDEEN PROVING GROUND, MD 21005-5066

NOTE: PLEASE NOTIFY COMMANDER, ARMAMENT RESEARCH, DEVELOPMENT, AND ENGINEERING
         CENTER, US ARMY AMCCOM, ATTN: BENET LABORATORIES, SMCAR-CCB-TL,
         WATERVLIET, NY 12189-4050, OF ANY ADDRESS CHANGES.

	NO. OF COPIES		NO. OF COPIES
COMMANDER US ARMY LABCOM, ISA ATTN: SLCIS-IM-TL 2800 POWDER MILL ROAD ADELPHI, MD 20783-1145	1	COMMANDER AIR FORCE ARMAMENT LABORATORY ATTN: AFATL/MN EGLIN AFB, FL 32542-5434	1
COMMANDER US ARMY RESEARCH OFFICE ATTN: CHIEF, IPO P.O. BOX 12211 RESEARCH TRIANGLE PARK, NC 27709-2211	1	COMMANDER AIR FORCE ARMAMENT LABORATORY ATTN: AFATL/MNF EGLIN AFB, FL 32542-5434	1
DIRECTOR US NAVAL RESEARCH LAB ATTN: MATERIALS SCI & TECH DIVISION CODE 26-27 (DOC LIB) WASHINGTON, D.C. 20375	1 1		